Geochemical aspects of early diagenesis, submarine volcanism and hydrothermalism in an intraplate tectonic setting

A Thesis submitted to the Goa University for the Award of the Degree of Doctor of Philosophy
in
Marine Sciences
by

Maria Brenda Luzia Mascarenhas

Research Supervisor: **Dr. B. Nagender Nath**
(CSIR) National Institute of Oceanography
Dona Paula, Goa-403004.

Goa University,
Taleigao, Goa
July 2014

Dedicated to

My beloved Husband, Edwin

&

loving children, Simone & Eduardo

CONTENTS

Statement

As required under the University ordinance 0.91.8 (vi), I state that the present thesis entitled "Geochemical aspects of early diagenesis, submarine volcanism and hydrothermalism in an intraplate tectonic setting", is my original contribution and the same has not been submitted on any previous occasion. To the best of my knowledge, the present study is the first comprehensive work of its kind from the area mentioned.

The literature related to the problem investigated has been cited. Due acknowledgements have been made wherever facilities and suggestions have been availed of

Maria Brenda Luzia Mascarenhas
National Institute of Oceanography
Council of Scientific and Industrial Research,
Dona Paula, Goa-403004
September 2013

Certificate

This is to certify that the thesis entitled "Geochemical aspects of early diagenesis, submarine volcanism and hydrothermalism in an intraplate tectonic setting", submitted by Ms Maria Brenda Luzia Mascarenhas for the award of the degree of Doctor of Philosophy in Marine Science is based on her original studies carried out by her under my supervision. The thesis or any part thereof has not been previously submitted for any other degree or diploma in any universities or institutions.

Place: Dona Paula
Date:

Dr. B. Nagender Nath
Research Guide,
CSIR- National Institute of Oceanography,
Dona Paula- 403 004.

ACKNOWLEDGEMENTS

This dissertation would not have been possible without the guidance and the help of several individuals who in one way or another contributed and extended their valuable assistance in the preparation and completion of this study.

Of all the people who inspired, influenced, supported or assisted with this work, I would like to particularly thank Dr. B. Nagender Nath, Chief Scientist, Geological Oceanography Division, National Institute of Oceanography, Goa, my research guide, who acted in all four of these capacities. Together we participated on two oceanographic cruises in the Central Indian Basin, during which he kindled and nurtured my interest in geochemistry through his tremendous enthusiasm for science. His constant availability for discussion, both scientific and personal, could always be counted on and was invaluable. He has also been a constant source of novel interpretive ideas through this research and his guidance and encouragement, both as a friend and teacher, have evolved a truly meaningful learning experience for which I shall always be grateful. His patience and support helped me overcome many crisis situations and finish this thesis. I hope that one day I would become as good an advisor to my students as Dr. Nath has been to me.

I wish to thank Dr. S. W. A. Naqvi, Director, National Institute of Oceanography, Goa, Dr. S. R. Shetye and Dr E Desa former Directors, National Institute of Oceanography, Goa for their support and permission to carry out my Ph. D work. I am very much indebted to my co-guide Dr. G. N. Nayak, Faculty of Life Sciences and Environment, Goa University for helping me complete all University formalities without any hesitation. Dr. H. B. Menon, Professor at Marine Science Department, Goa University, for his valuable support. I wish to express my sincere thanks to Dr. Rahul Sharma, Chief Scientist, Vice-Chancellor's nominee and Project leader of Environmental Impact Assessment of Nodule Mining in the CIB (PMN-EIA), Geological Oceanography Division, National Institute of Oceanography, Goa, without whose help and valuable guidance, it would have been very difficult for me to continue my thesis. He has been always there to listen and give advice. I am deeply grateful to him providing the funding and for the long discussions that helped me sort out the technical details of my work. I am also thankful to him for encouraging the use of correct grammar and consistent notation in my writings and for carefully reading

and commenting on countless revisions of this work. He has also duly assessed the progress of my work and given invaluable suggestions.

I am grateful to Dr. D. V. Borole for his encouragement and practical advice. I am also thankful to him for reading my reports; commenting on my views and helping me understand and enrich my ideas. I also thank him for the radiometric dating.

I also thank all the members of PMN-EIA project at NIO, Drs. A. B Valsangkar, P. A. Lokabharathi, Judith Gonsalves, Mamatha, Mr Jaishankar and project trainees (past and present) Trupti, Sonali, Teena, Poonam, Kazip, Nila, Linsy, Rupali, Sini, Sonali and Dr Anindita Das for help in analysis on board and in laboratory.

I am grateful to Drs. V Balaram, T. G Rao and Sathyanarayana for the ICP-MS analysis carried out at NGRI, Hyderabad, Drs J. N. Pattan and G. Parthiban for the analysis carried out using ICP-MS, Dr V. K Banakar for the analysis carried out using ICP-OES at NIO, Goa and Dr Parameswaran for the Infrared spectroscopic analysis, Drs. V. Ramaswamy and Prakash Babu for help in the size analysis, Dr N. H. Khadge for the porosity data and Dr S. M. Gupta for the biostratigraphic ages.

I am additionally indebted to the following people whose assistance has made the completion of this Ph D possible: Drs. Ala Aldahan, Goran Possnert and T. Ericsson for the ^{10}Be and Mössbauer analysis at Uppsala University, Sweden, Dr S. K. Patil at IIG for the analysis of magnetic properties, Dr Shyam Prasad and Mr Khedekar for assistance with analysis using SEM and EDS instrument, Mr Pawaskar and Mr Uchil for drafting the figures, Dr K. Selvaraj, Dr A. Mudholkar and Mr Ceasar Moraes for the XRF analysis, Mr Girish Prabhu for assistance with XRD analyses, Mr Srinivas for plotting figures for my work, Ms Neetu Singh for help in the mixing calculations, Dr Siby Kurian and Dr Sijin Kumar in the porewater extraction and analysis and Mr R. A. A. Luis for timely help in case of any technical failure,

I appreciate the efforts of the many graduate and undergraduate students who helped me with analysis and completion of many administrative formalities that needed to be completed for this research; my sincere thanks to Mr Jaishankar, Mr Vijayakumar, Domnica, Sampada, Pavan, Ajeesh, Manimaran, Sucharita, Kiranmai, Shamina, Reshma, Arindam, Simontini, Vijay, Chandan, Suraj, Tyson, Renu, Almas, Pooja, Shynu, Lekshmi, Drs. Vineesh, Niyati, Pranab, Mr Santan, Gurudas, Gavin,

Gaonkar D.K. Naik, Sheldon, Ms D. Kundu and Mr A. Mondal for their contributions to the various domains.

I also wish to thank Drs S. D. Iyer, K. A. Kamesh Raju, Dr A. Parthihari and Mr Michael Selvam and not forgetting all my friends: Mr Mani Murali, Dr. M. Kocherla, Ms Vidhya, Mr. B. R. Rao, Mr Durbar Ray, Dr. Aparna Gandhi and Ms. Hilda for their help and support at various stages of this work.

I am grateful to my dear friend Dr. Maria Desa who has been much more than a colleague. Her moral support, advice and motivation have kept me going. Thanks especially to Ms. Ancy Rodrigues, Mrs. Alison Sudhakar for never failing to make time to sit down and discuss any personal or administrative difficulty faced at work with me and being so prompt with advice and feedback.

I have to give a special mention for the support given by late Prof. Orlando Fernandes, Professor, Dhempe College of Arts and Science, Miramar, Goa and my dear Prof. S. M. Borges (Retd.), Smt Parvatibai Chougule College of Arts and Science, Margao, Goa who were the people behind me joining a research career. Their motivation and guidance has helped me to be what I am today. No words can express my gratitude to them. This work would not be completed successfully without their blessings. Late Dr. V.N.Kodagali, formerly with NIO is thanked for providing funds from PMN Project to support by initial tenure at NIO as a Project Assistant.

Most importantly, none of this would have been possible without the love, affection, prayers and patience of my family (Edwin, Simone and Eduardo) to whom this dissertation is dedicated to, has been a constant source of love, concern, support and strength all these years. I would like to express special thanks to my husband. He helped me to concentrate on completing this thesis and supported mentally during the course of this work. Without his help and encouragement, this study would not have been completed.

I would like to express my heart-felt gratitude to my parents, in-laws, brothers and sisters who have aided and encouraged me throughout this endeavor. I love them a lot and dedicate this work to them.

I would like to apologize to all those I have not mentioned by name, and thank them as well.

Last but not the least, the one above all of us, the omnipresent God, for answering my prayers for giving me the strength to plod on despite my constitution wanting to give up and throw in the towel, thank you so much Dear Lord.

Preface

Submarine hydrothermal activity is a widespread feature occurring in all the oceans along the spreading centers at mid oceanic ridges (MOR), at subduction area and at hot spots. Hydrothermal activity at mid ocean ridge vent sites has been the focus of many geochemical and isotopic studies since their discovery in 1977. Besides these three tectonic settings, hydrothermal activity also takes place at the intra-plate seamounts. Although there are several reports on the occurrence of hydrothermal activity at the intra-plate seamounts in the Pacific Ocean such as Macdonald, Loihi, Vailulu'u (Samoan Hotspot related), signatures of hydrothermal mineralization are only found in one intra-plate seamount area in the Indian Ocean. Central Indian Basin (CIB) is known to be dotted with numerous seamounts and a majority of them are located along the well defined fracture zones. This study investigates the sediments around seamounts and fracture zones to find if any hydrothermal activity is occurring in these locations.

Hydrothermal systems are known to play a major role in elemental exchange between ocean and crust through the interaction of circulating seawater with the oceanic crust at various temperatures. In addition to these studies, geochemical investigations of hydrothermally altered crust, which is another product of water-rock interaction at the MOR were carried out to unravel the chemical exchange processes during hydrothermal alteration.

The proposed study focuses on the coarse fraction mineralogy, sedimentology, dating and geochemical studies of porewater, bulk sediments and selective leaches of systematically sampled sediments (~67 short sediment cores) from two sediment types both in the vicinity and away from the seamounts and fracture zones in the CIB to explore the occurrence of submarine volcanic activity and hydrothermalism and also to evaluate the influence of subsurface fluid flow in altering the sediment characteristics and sedimentation history.

Investigation and understanding of volcanogenic and hydrothermal mineralization processes prevailed in the intraplate region concentrating mainly on Pleistocene onwards were carried out. An attempt is made to identify the nature and

variation of the sediment inputs from various sources to the area to understand the sedimentary processes operating in the area. Porewaters studies were carried out on a basinal scale to estimate the benthic fluxes across the sediment-water interface. Geochemical as well as sedimentological investigations were carried out on different sub-environments of a fracture zone environment, in order to understand the role of subsurface fluid circulation if any. To my knowledge, a proposal to integrate such aspects is for the first time in this area.

With a view to fill the gap in our understanding the various aspects of sedimentary processes in the CIB, a geochemical investigation is undertaken with the following objectives.

1. To study the benthic exchange fluxes of nutrients across the sediment water interface in order to understand the source, rate and path of organic matter remineralization, and to link this to regional patterns of productivity.

2. To study the volcanogenic fraction of the sediments derived mainly from the tectonically vulnerable areas

3. To study other coarse fraction components to understand the role of low and high temperature alteration in the areas close to fracture zone and seamount

4. To study the bulk chemistry of the sediments and to develop basinal scale regional distribution maps of the elemental distribution to understand the contributing sediment sources.

5. Study the tracer elements in the surficial sediments to understand the sediment dispersal pattern in the CIB and to predict the sediment dispersal pattern in case of future mining of nodules.

6. To study the variable uptake behavior of various size fractions (at least seven size fractions in the silt and clay fraction) during the hydrothermal precipitation and during the submarine hydrothermal alteration of sediments, if any..

In order to accomplish the above objectives, 26 box cores were collected at every one degree spacing (10° to 16° S Lat and 73.5° to 76.5° E Long) during two cruises in the central Indian Basin. In addition, some of the cores along the north south transect along 75° 30’E in the CIB sampled in different seasons and years provide an ideal opportunity for studying spatial and temporal variability in the digenetic processes

The thesis is divided into eight chapters. A brief discussion of each chapter is given below.

Chapter 1 presents the broad tectonic framework, evolution in time and space and major tectonic features of the Indian Ocean in general and CIB in particular. This chapter also includes a detailed description of the oceanographic setting and physicochemical properties of study area. Also included are aspects related to productivity of surface ocean, benthic biology and microbiology. Following a review of past work in the area, scope and scientific objectives of the present study are presented.

Chapter 2 provides details of the sample collection and description of the methodology and experimental work adopted here. For the present study, morphological characterization of sediment grains was carried out using Scanning Electron Microscopiy (SEM) while major oxides in the mineral grains were analyzed using an Energy dispersive spectrometer (EDS) attachment (OXFORD Link-ISIS EDS) to the SEM at the National Institute of Oceanography, Goa, India. For clay mineral identification, the air dried as well as glycolated clay slides were analyzed on a Philips X-ray diffractometer using Ni-filtered Cu Kα radiation operated at 20 mA and 40 kV from 3° to 15° 2θ at 1.2° 2θ min^{-1} at the National Institute of Oceanography, Goa, India. The grain size analysis of the sediments were studied with the help of MALVERN Laser particle size analyzer (MASTERSIZER 2000) at the National Institute of Oceanography, Goa with a Hydro 2000 MU wet sampling accessory using procedure given in Ramaswamy and Rao (2006). The calcium carbonate content was determined after acidification of the sample with 1N HCl and subsequently measuring the CO_2 using UIC CM 5014 Coulometer. Rare earth elements (REE) and trace metals along with some major elements of the bulk samples, size fractionated sediment samples along with clay samples were analyzed by Inductively Coupled Plasma Optical Emission (ICP-OES) and Flame Atomic Absorption Spectrometry (AAS) at National Institute of Oceanography, Goa ANDInductively Coupled Plasma Mass Spectrometry (ICP–MS) at the National Geophysical Research Institute, Hyderabad and National Institute of Oceanography, Goa. Infrared spectroscopic studies were carried out on the <2 µm size clay fraction pellets (pressed with KBr powder) using a Shimadzu 8201 PC at the National Institute of Oceanography, Goa. For ^{230}Th and ^{210}Pb, alpha activity of the electroplated sample was assayed using ion implanted detector coupled to Octete plus Alpha spectrometer (E G & G ORTEC). ^{10}Be was measured at AMS facility of Uppsala University.

Chapter 3 provides the first report of the occurrence of sediments of metalliferous nature and signatures of hydrothermal alteration of pelagic sediments in an intraplate seamount environment by ascending fluid flow through the sediments. The core was sampled on a flank of a seamount in the CIB, lying in the proximity of the 75° 30'E fracture zone. Multiple geochemical tracers such as isotopic (^{210}Pb, ^{238}U-^{230}Th, ^{10}Be), major, trace and rare-earth elements on the bulk, leach, residue and clay fraction, and infra-red spectroscopy studies of the clay fraction in addition to micromorphological and microchemical analysis helped characterize the hydrothermal nature of the sediments. Selective dissolution carried out using 50% hot HCl has allowed the discrimination between a leach phase (leachable Fe–Mn phase consisting of ferruginous oxides and silicates; Mn-oxides) and a residue phase (refractory fraction containing silicates and sulfides). Mixing calculations were performed on the bulk and leach geochemical data and relative contribution of different source components were estimated. Hydrothermal alteration effects are reflected in the form of 1) the depleted sedimentary organic carbon, 2) dissolution features of radiolarian skeletons, 3) the presence of altered minerals such as smectite and zeolites, and 4) distinctly different magnetic properties in the altered sediments. Rare earth and trace element geochemical data of hydrothermal component in these sediments compared well with previously published geochemical data of hydrothermal material from other major spreading centers (Rainbow, TAG, MAR and EPR).

The part of the results of this chapter were published in the international journal "Marine Chemistry", the paper entitled **"**Selective leaching studies of sediments from a seamount flank in the Central Indian Basin: Resolving hydrothermal, volcanogenic and terrigenous sources using major, trace and rare–earth elements" (**Mascarenhas–Pereira, M. B. L.,** Nath, B. Nagender, 2010, doi: 10.1016/j.marchem.2010.03.004)

Chapter 4 provides new understanding to the origin of glass shards in the CIB and contests earlier findings. Cores collected all along a fracture zone in a north-south transect were examined for glass shard morphology and chemistry. These cores were also dated radiochemically which allowed decipher the timing of deposition of volcanic products in the cores. Morphological features and the chemistry of the shards were used to decipher the origin of this volcanoclastic material. Individual tephra layers were determined by visual estimation using abundance of glass shards. In

addition we have tried to find out if continuous trace and minor element chemistry of raw bulk sediments provide a diagnostic indicator for detecting cryptotephra in the core. We have used the single element (Nb and Cr) normative calculation to quantify the concentration of cryptotephra in the sediments. The estimation of ash in the sediments in the three cores based on both the Nb and Cr normative calculations are in good agreement and perfectly support the visual estimates of ash in the cores.

The sediments in the CIB have shown two independent phases of volcanic activity in the past at ~72-75 kyr corresponding to Toba (YTT) eruption and an older event at 110-120 kyr that does not correspond to any known volcanic eruption in the Indian Ocean. The chemistry of the shards indicates a rhyolitic composition. Insitu origin (phreatomagmatic eruption) is interpreted for the volcanic ash in the deeper layers corresponding to the older event as supported by the presence of large blocky/massive shards with a low degree of vesciculation indicating their formation by hydroclastic fragmentation while the younger event seems to be explosive in nature and the shards transported aerially, as indicated by the abundance of bubble wall shards. Since the cores are located on the flanks of a seamount and in the vicinity of 76° 30' E fracture zone, we assume the possibility of an intraplate volcanism due to reactivation of tectonic activity in the faulted area in the past. Comparison with geochemical data from literature on other volcanic fields in and around the CIB also suggests an in-situ origin. Our data indicate that a caution may be exercised in using major element composition as the only criteria for determining the source of the tephra. Age of the tephra or host sediments is an additional key parameter.

Chapter 5 deals with spatial and seasonal variability in benthic fluxes of nutrients such as silicate, phosphate, nitrite and nitrate over a major part of nodule bearing area of CIB. This study was undertaken to supplement the small geochemical data base currently available in the CIB and to assess the role of early diagenetic processes through diffusive flux calculations of the nutrients. This represents presumably the largest area studied so far in the Indian Ocean for benthic flux estimation. Benthic fluxes were calculated from porewater chemistry data of nitrite, silicate and phosphate in all the 26 cores studied here.

Latitudinal variability in nutrient fluxes is seen in the basin with the northern part of the basin (north of 13°S) acting as a major source of silica to the bottom water compared to the southern part of the study area, while the basin acts as a sink rather than a source of phosphate The high effluxes of silica correlate well with high surface

productivity in the north of the basin, which is probably to a great extent induced by monsoonal forcing suggesting the prevalence of pelagic-benthic coupling in the CIB.

The results of the seasonal variation investigated in cores sampled in austral winter (April 2005; cruise ABP 04) and austral summer (December 2006; ABP 26 cruise) along the north to south transect in the basin are discussed. The diffusive flux patterns of nitrate show remarkable seasonality between winter of 2005 and summer of 2006. Our results show that on an annual basis the sediments were significant exporter of silica to the water column, in contrast, the sediments were a sink for nitrate and phosphate. All these results showed that the net exchanges of nutrients across the sediment-water interface were strongly dominated by a nutrient release.

On comparing the results of the present study with the nutrient fluxes in other parts of the world oceans, it is found that silicate fluxes corroborate well with those found in the Eastern South Atlantic, Central Pacific and Eastern tropical Atlantic for phosphate fluxes.

In addition to responding to pelagic processes and organic matter remineralization in sediments, it was found that the porewater geochemistry of hydrothermally altered sediments was different from the normal pelagic sediments.

Chapter 6 deals with the spatial variation of lithogenic sediment fraction in CIB. Diagnostic elemental associations were used to decipher the dispersal of sediments in the basin and to identify the source of sediments in the area. Different geochemical tracers such as REE, trace and major elements and clays were used.

Mixing calculations of REE data using 4 end members such as biogenic, terrigenous, MORB and metalliferous component helped to estimate the relative proportion of the end members in the sediments. The calculations show that the REE in the sediments of the CIB are a mixture of 0–10% siliceous component, 5–90% terrigenous component, 0–35% MORB component and 0–100% metalliferous component.

In addition elemental geochemistry of different size fractionated surface sediment samples in hydrothermally altered sediments of CIB sediments was studied. These data were compared with size fractions of sediments not influenced by hydrothermalism from Arabian Sea, Equatorial Indian Ocean, Bay of Bengal and siliceous domain of the Indian Ocean. Geochemical study was carried out on nine size fractions (<1, 1-2, 2-4, 4-8, 8-16, 16-32, 32-45, 45-63 and >63 μm). The maximum trace element and REE concentrations were seen in the hydrothermally altered pelagic

clay sediments which were upto 10 times enriched than the cores not influenced by hydrothermal activity. REE's showed fractionation with grain size with the sand size fraction (>63 μm) having the least concentration of trace elements. Further, the controlling factors for the elemental distribution in the different size fractions are discussed.

Major conclusions drawn from this study are summarized in **Chapter 7**. In addition, a brief on the scope for future study in this region is suggested.

Important contributions of this work are: 1) report on the occurrence of metalliferous sediments in an intraplate setting; 2) additional volcanogenic events in the area which were hitherto unknown; 3) pelagic-benthic coupling reflected by benthic biogeochemistry; 4) occurrence of seasonality in deep-seas; 5) quantification of relative contribution of competing sediment sources

List of Tables

List of Figures

Chapter 1

Introduction

1.1. General Introduction

Submarine hydrothermal mineralization is a widespread feature occurring in the modern ocean floor and is found in a variety of tectonic settings along the fast, intermediate and slow spreading centers at mid oceanic ridges, at subduction area, on axial and off-axis volcanoes and seamounts, in sedimented rifts adjacent to continental margins and at hot spots. Hydrothermal activity is most frequent at mid ocean ridge (MOR) vent sites and has been the focus of many geochemical and isotopic studies since their discovery in 1977. Most of the mineralization sites have been discovered in the Pacific (mainly on the East Pacific Rise and along the arc-trench systems and southwestern Pacific) and Atlantic (Lucky strike, Broken spur, Snake pit, Trans Atlantic Geotraverse (TAG) etc. along the Mid-Atlantic ridge). Besides these tectonic settings, hydrothermal activity also takes place at the intra plate tectonic settings. The divergent plate boundaries (MOR) and back-arc are relatively straight and structurally continuous features, making them easier to investigate than the more scattered and dispersed intraplate volcanic provinces within the oceanic basins. Intraplate volcanism and associated hydrothermalism occurs in both submarine and subariel regions of the earth's surface. In ocean basins, hydrothermalism is mostly associated with seamounts. There are several reports on the occurrence of hydrothermal activity at the intraplate seamounts in the Pacific Ocean such as Macdonald, Loihi, Vailulu'u (Samoan Hotspot related). Although, the Central Indian Basin (CIB) is also known to be dotted with numerous seamounts and a majority of them are located along the well defined fracture zones (Kamesh Raju, 1993), signatures of hydrothermal mineralization are only found in one intraplate seamount area in the Indian Ocean. Therefore, it would be interesting to investigate the sediments around seamounts and fracture zones to find if any hydrothermal activity is occurring in these locations.

Direct study of hydrothermal activity and associated mineral formation are possible in modern oceans. Often hydrothermal deposits formed in the geological past have been covered by sediment cover or overlain by lava and have become inaccessible after a time for observation and sampling. Studies of the metalliferous sediments sampled by the gravity and piston cores, and in the cores obtained during the deep-sea drilling programs can be very useful for the reconstruction of the history of hydrothermal activity and mineral formation.

Only a small part of the metal-bearing hydrothermal material contributed to the ocean by high temperature solutions accumulates in massive hydrothermal bodies. A major part of the hydrothermal material accumulates in the vicinity of the hydrothermal vent in the bottom sediments. The distance from hydrothermal vent/field and in the absence of redeposition of sediment material, the accumulation rate of hydrothermal matter in both proximal and distal metalliferous sediments reflect the intensity of the hydrothermal activity and as a consequence the amount of mineral formation and deposition associated with it. The accumulation of coarse grained proximal metalliferous sediments reflects stages of active hydrothermal discharge and the destruction of massive hydrothermal bodies. These properties of the metalliferous sediments enable their use in reconstructing the location and intensity of hydrothermal activity and mineral formation in past geological time, and in determining areas of present location of buried hydrothermal deposits (Gurvich 2006).

1.2. Geology, tectonic framework and history of the Indian Ocean Basin

The Indian Ocean constitutes about one-seventh of the Earth's surface and is the world's third largest water body. This ocean covers an area of 73.6 million km^2, and is separated from the Atlantic and the Pacific Oceans by roughly 20°E and 147°E, respectively. The plate boundaries of various types in the world oceans, such as divergent, convergent, transitional, and diffused can be found in the Indian Ocean.

Central Indian Basin (CIB) covers an area of about 5.7 x $10^6 km^2$ and is bounded by three ridges on the west (Mid Indian Ridge), east (90°E Ridge), north west (Chagos-Laccadive Ridge) and south (South East Indian Ridge-SEIR and the Rodriguez triple junction-RTJ) and opens towards the Bay of Bengal in the north. CIB is the largest and best studied region of the Indian Ocean. CIB seems to have a complex evolutionary pattern from the existence of various structural entities and morphological forms. The detailed structural map of the CIB, bounded between longitudes 72° and 76°E and latitudes 9° and 16°S, reveals the presence of several seamounts, ridge parallel east–west trending abyssal hills, fault scarps and topographic undulations, for instance the trace of triple junction in the Indian Plate (TJT-In) (Kamesh Raju 1990; Dyment 1993), seamounts, abyssal hills, fracture zones (FZ), faults and lineations (Kamesh Raju, 1993, 1990; Mukhopadhyay et al., 2002)

(Fig. 1.1). Around 200 seamounts are reported from CIB (Das et al., 2007 and references therein). These features probably are the manifestation of deformation, reheating and periodic magma eruptions since the geological past (Kamesh Raju et al., 1993; Mukhopadhyay et al., 2002). The CIB can be divided into two distinct regions, the highly deformed north (north of 9°S) and northeastern part and the relatively undeformed southern part (south of 9°S) **(**Fig. 1.2). Morphologically, the southern portion (south of 9°S) of the CIB seems to be complex, due to the presence of a series of north-south trending FZ normal to the SEIR, seamounts, abyssal hills, and valleys (Kodagali 1988; Kamesh Raju 1990, 1993; Kamesh Raju et al., 1993). The sedimentation rate in the CIB is very low (2.7 mm/ka 14°S and 78°E; 3.4 mm/ka 10°S and 82°E; Banakar et al., 1991; Borole 1993). The CIB basement age is reported to be 50–60 Ma (Mukhopadhyay et al., 1995). The Indian Ocean Nodule Field (IONF) is significant from several points of view. Roughly bordered by 10° to 16°30′ S and 72° to 80°E and located within the CIB, the field hosts the world's second largest and second high grade manganese nodule deposit, after the equatorial nodule belt in the north Pacific Ocean.

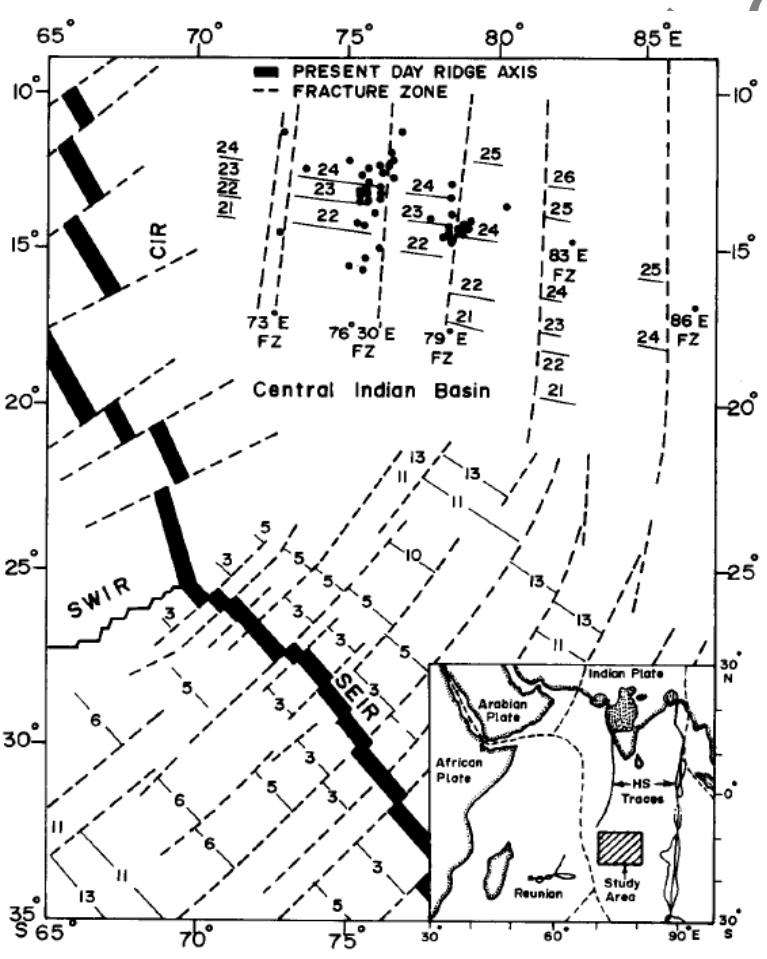

Fig. 1.1: Tectonic fabric map of the northern Indian Ocean showing the identified fracture zones and magnetic lineations and the seamount locations (Kamesh Raju, 1993).

Moreover, the crust underlying this field is characterized by unique morphotectonic signatures owing to its

formation between 60 and 49 Ma under three variable spreading conditions, fast, intermediate and slow, from the Indian Ocean Ridge System (IORS) (Mukhopadhyay et al., 2002 and references therein). The nodule field has been surveyed both extensively (more than 0.4 million km^2 area) and intensively (comprising of a large geophysical data set and geological sample inventory) during the last four decades. Several morphotectonic features, such as seamounts, hills, ridge-normal lineaments and ridge-parallel lineations, have disturbed the apparently smooth topographic gradient (1:7000) of the seafloor. The IONF is surrounded by two prominent north−south trending aseismic ridges: the Chagos–Laccadive Ridge (CLR) to the west and the Ninetyeast Ridge (NER) to the east. The Deformed Boundary Zone (DBZ) is located to the north of the IONF, while the IORS is located to its south. The two aseismic ridges were generated from the Reunion and the Kerguelen hotspot activities, respectively. The WDZ separates the Indian from the Australian plate, and the IORS separates the Australian from the Antarctica plate.

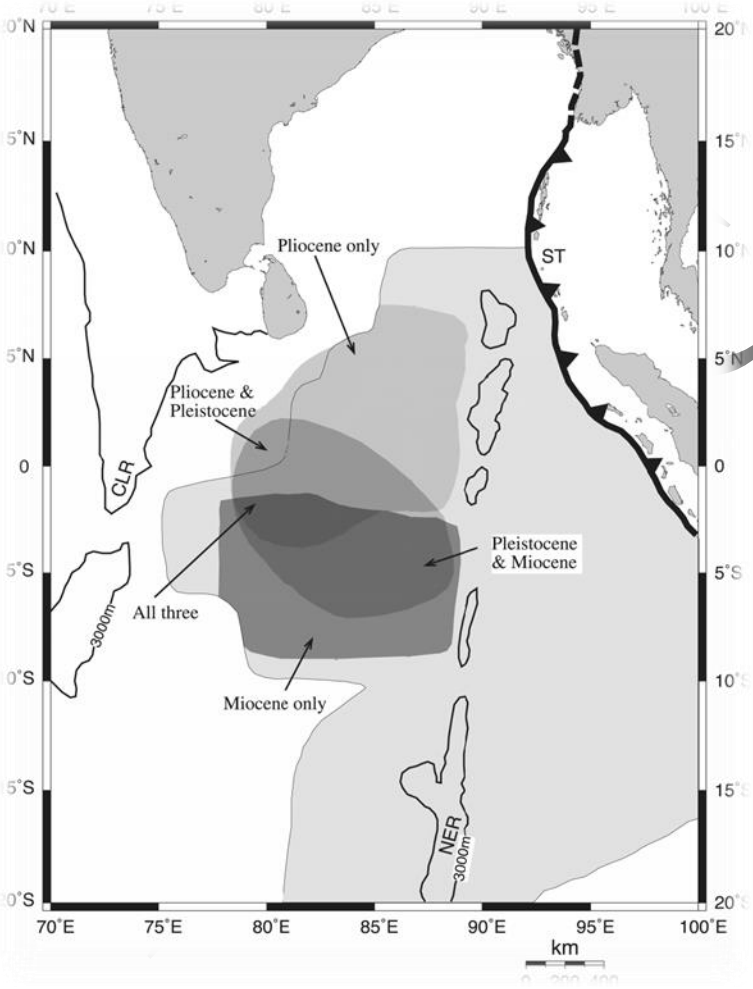

Fig. 1.2: Deformation of oceanic lithosphere in space and time in Central Indian Ocean. Shading shows position of diffuse plate boundary separating Capricorn, Indian, and Australian plates (Royer and Gordon, 1997). Superimposed on this area are approximate spatial extents of long-wavelength folding at three different times (8.0–7.5, 5.0–4.0, 0.8Ma). The earliest folding event is towards south, whereas Pliocene event (5.0–4.0Ma) extends farther northward (Krishna et al., 2001).

Variations in the rate of spreading and formation of new oceanic crust along the ridge crest, during more than one episode of India–Eurasia collision, are imprinted in the IONF. Based on the nature of the ridge-

parallel lineations, which are related to the rate of crustal accretion, the field is divided by latitude into four sectors (Mukhopadhyay et al., 1997): A, B, C, and D, from north to south. Sectors A (north of 10.26°S) and C (between 10.96° and 13.76°S) were formed at a fast rate of spreading (90–95 mm/year, half-rate) and sectors B (between 10.26°S and 10.96°S) and D (south of 13.76°S) were formed at an intermediate (55 mm/year) and slow (26mm/year) rates, respectively. The timing and intensity of the collision of India with Eurasia is constrained by the variable intensity of these flexures caused by tensional stress, suggesting probably a 'soft' touch at ~ 58 Ma and the hard collision at about 51 Ma (Mukhopadhyay et al., 2002 and references therein).

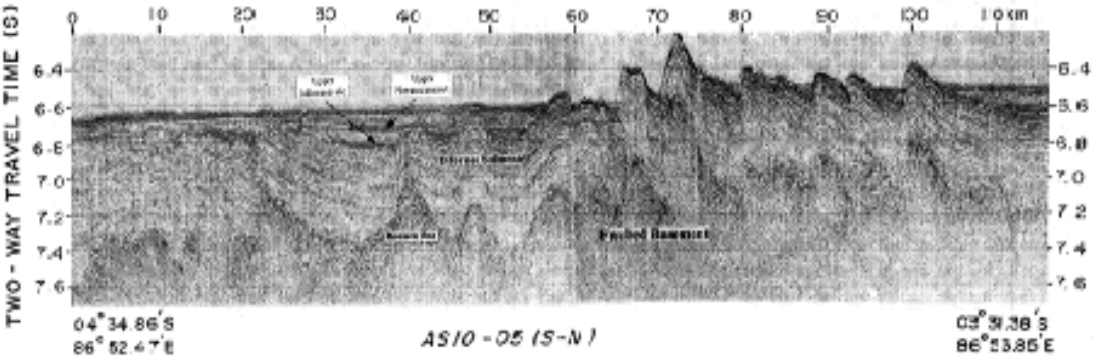

Fig. 1.3: Oceanic basement in CIB and sediment section showing extremely crumpled features in the form of tight folds and high angle faults (Krishna et al., 1998)

Seamounts

Seamounts in the nodule field occur as both isolated entities and in linear chains parallel to flow lines, conforming to the direction of absolute plate motion (also probably the relative motion) of the Indian plate (Mukhopadhyay et al., 2008). Das et al. (2007) identified eight parallel seamount chains in CIB that trend north-south. It is suggested that the occurrence of seamounts in such chained alignments is the result of fast rates of crustal accretion about the divergent plate boundaries (Mukhopadhyay and Batiza, 1994). Around 200 seamounts are reported from the CIB (Mukhopadhyay and Khadge, 1990 and Das et al., 2007 references therein). The majority of these seamounts are ancient, formed between 61 and 52 Ma, and the formation of seamounts have peaked between 56 and 52 Ma (Das et al., 2007) probably emplaced near to or at the ridge axis, along with the generation of new oceanic crust, probably sharing the same melt (Mukhopadhyay et al., 1995). There is

a general increase in seamount population south of 11°S latitude. The average abundance of seamounts in the area is 5897 seamounts/10^6km^2 (Mukhopadhyay 1998). Thus, seamount abundance in the CIB is less than that in the Atlantic Ocean (Batiza et al., 1989; 7000 seamounts/10^6km^2), and the Pacific Ocean (Fornari et al., 1987; 9000 seamount/10^6km^2). The general slope area trends towards the southeastern part of CIB. The flowlines are several broken linear topographically elevated short features and are more prominently arranged perpendicular to the spreading ridge axis.

Mukhopadhyay et al. (2008) summarized that morphologically, these ancient (60Ma) ridge normal north–south trending chains of seamounts appear similar in terms of distribution, petrology and origin to the younger (<10 Ma) seamounts formed at or close to the fast spreading East Pacific Rise (EPR) (Macdonald, 1998; Mukhopadhyay and Batiza, 1994). The occurrence of ridge-normal and flowline-parallel seamount chains suggests that they were largely formed from the fast spreading Indian Ocean Ridge System during Paleocene–Eocene and were later transported from the ridge axis to the basinal region along with the underlying crust. However, many of the seamounts show more than one stage of growth with local intraplate volcanism contributing to the enlargement of the larger ancient seamounts. Subsequently, during its journey away from the ridge crest to the abyssal areas, the crust underlying the nodule field witnessed intraplate volcanism. Intraplate volcanism in the CIB has been of much interest, since this tectonically young and structurally complex basin holds signatures of at least one major plate reorganization at 65±5 Ma; and two major plate boundary structural deformations occurring at 54.5 ±3 Ma (collision of India with Eurasia) and at 7 Ma (intraplate deformation in the Indo-Australian plate). This is evident from the addition of younger rocks at the base of the ancient seamounts, inconsistent growth of volcanoes, eruption of ferrobasalt corresponding to the areas of high amplitude magnetic zones and presence of volcanogenic–hydrothermal materials (vhm) of 10 ka age (Iyer et al., 1997). Varieties of volcanics, such as tholeiitic basalts, spilites, ferrobasalts and pumice, occur within the IONF. The alteration of some of these volcanics has resulted in palagonitisation of the glass and formation of zeolites. These findings collectively hint that the CIB is geodynamically unstable and may have been volcanically active in the recent past.

The study of these seamounts, which are essentially topographically elevated surface manifestations of mantle upwelling, provides a better understanding of crustal and mantle processes. The mode and type of emplacement of seamounts through the

geological ages are generally deduced from the underlying magnetic anomalies, style of disposition, morphology and chemistry. Magnetization of a seamount, normal or reversed, may yield constraints on the timing of seamount volcanism, particularly if a seamount is magnetized in the opposite direction to the underlying crust.

Despite this knowledge, the associated magmatic activity in the intraplate areas of the CIB is not fully understood. However, recent findings such as inconsistent and non-uniform growth of basinal seamounts in the geological past, often influenced by local factors such as magma availability, conduit geometry, and eruption style (Mukhopadhyay and Khadge, 1990), availability of fresh volcanic rocks in and around a number of cratered seamounts (Mukhopadhyay et al., 1995), and abundant volcanogenic hydrothermal materials in a much younger (10,000 years old) sediment section (Iyer et al., 1997), indicate a fairly significant degree of local volcanism in the basin. Additionally, three stages of volcanism in a seamount, located close to Afanasy Nikitin seamount, have been recently identified. For example, the base of this seamount is formed of basic materials, followed up in the middle by a moderately fractionated transitional rock type, while the top is covered with highly fractionated silicic lava (Neprochnov et al., 1998). The reported occurrence of widespread pumice in the abyssal regions in CIB is suggested to be caused by in situ volcanism (Iyer and Sudhakar, 1993), although the formational procedure of pumice, e.g., the thermodynamics of vesicles formation at more than 5000m depth remains unconvincing (Kokelaar, 1986).

Lineations and Fracture zones

Detailed structural maps and section sections of the CIB (Figs. 1.1 and 1.3) reveals a profusely flexured, folded and faulted nature of the seafloor. The ridge-normal structural lineaments in the CIB are largely oriented N-S to NNE-SSW, and lay perpendicular to the present-day southeast Indian ridge (SEIR) (Fig. 1.1). Among the ridge-normal lineaments, the Vishnu FZ (along 73°E), Indrani FZ (along 79°E), Indrani FZ (along 83°E) and Triple Junction trace on the Indian Plate –TJT-In (along 76.5°E) are important (Patriat and Segoufin, 1988, Kamesh Raju and Ramprasad, 1989 and Dyment, 1993; Kamesh Raju, 1993). The average depth of the CIB increases from west to east and the nodule field can be broadly divided longitudinally into three bathymetric areas. Mukhopadhyay et al. (2008) summarized that

bathymetric variations in the CIB is influenced by the rate and direction of spreading at the ridge axis as well as plate reorganization events, stress relating to intra-plate deformation at the plate boundaries between Indian and Australian (IAPB), and Australian and Capricorn (ACPB) sediment thickness, midplate volcanism, and seamount formation. Two types of faults are encountered in the CIB— that is, those having their planes facing northward away from the spreading ridge axis, from which these have been generated, and those having their planes facing southwards towards the ridge axis. The north-facing faults are normal faults.

Vishnu FZ

This fracture zone lies on either side of the CIR (Fig. 1.1), its eastern part is located in the CIB, while the conjugate western part may be traced the southeast of the Reunion Islands on the African plate (Dyment et al., 1999). Detailed multibeam swath bathymetric study (Kessarkar, 1996) of a part of this fracture zone reveals it to be an elevated, wide, NNE–SSW trending feature with very sharply delineated eastern and western boundaries. The average slope along the western boundary (400–500m) is more than that along the eastern boundary (200m). The western boundary is therefore more distinct and pronounced. The elevated central portion of the fracture zone shows many small abyssal hills with ESE–WNW orientation (Mukhopadhyay et al., 2002). The fracture zone widens from about 14km in the north to about 17 km in the south. The fine scale bathymetric variations reveal that the average amplitude and wavelength of the seafloor crenulations within the FZ are 233 m (range 40–530 m) and 22.5 km (range 8.1–38.2 km), respectively (Kessarkar, 1998). The deepest point on the fracture zone encountered in the northern part is about 5230 m. The disposition of magnetic anomalies and the nature of ridge-parallel lineations in the surrounding areas suggest formation of Vishnu FZ from the east–west section of Central Indian Ridge at a half-rate of 80 mm/year between A26 and A23 and at 36 mm/year between A23 and A21. The fracture zone has offset the magnetic lineations of the same age right-laterally by about 70 km, the offset is larger in the eastern side than in the western side (Kamesh Raju, 1990). The northern and central parts of the Vishnu FZ trend N15E (Fig. 1.1), however, its southern part, beyond the southern limit of the CIB changes in trend from N15E to N45E. This change occurred during the second

major plate reorganization event at about 42 Ma (McKenzie and Sclater, 1971; Norton and Sclater, 1979; Tapscott et al., 1980; Patriat and Segoufin, 1988).

Indrani FZ

The Indrani FZ (Fig. 1.1), extending parallel to approximately 79°E longitude, lies on either side of the SEIR, its southern segment extending northward from the eastern edge of Crozet Island on the Antarctic plate. The detailed multibeam swath bathymetric information of this fracture zone (Kamesh Raju et al., 1993) reveals crest-trough topography with an elevation difference of about 300 m. The topography has steep gradients in the south and is gentler in the north. The seafloor along the western flank is shallower than that of the eastern flank. Seamounts along this fracture zone are mostly located in the south. The lithospheric thickness of this fracture zone as deduced from the gravitational edge effect is 100 km and the thermal structure, considering the horizontal heat conduction, indicated the elastic limit of the lithosphere up to 23 km (Kamesh Raju et al., 1993).

Triple junction trace on the Indian plate

Triple junction trace on the Indian plate (Fig. 1.1) shows the trace of the TJT-In which is essentially the paleo-meeting point of three spreading (Kamesh Raju et al., 1993; Mukhopadhyay et al., 2002) ridges, CIR, SEIR and SWIR (present location at 25°S). Like the other major ridge-normal lineaments, the TJT-In is also located between the Vishnu and Indrani FZ's on the Indo–Australian plate, with its conjugate part lying on both sides of the SWIR on the African and Antarctic plates (Patriat and Segoufin, 1988). There have been differences of opinion about the style and nature of evolution of this unique triple junction. On the basis of the then available few data, McKenzie and Sclater (1971) proposed a ridge– ridge–ridge type configuration for the triple junction which subsequently received support from Tapscott et al. (1980). However, Munschy and Schlich (1989) rejected the concept of ridge–ridge–ridge configuration and proposed a ridge–ridge–fault configuration suggesting that both the CIR and SEIR are progressively offset at a rate of 1.4 mm/year mainly because of their different spreading rates. Propagating rifts appear to have played an important role in the evolution of the triple junction, particularly between chrons A28 and A21

(Dyment, 1993), the approximate age of the nodule field. The volcanic and magmatic potential of the TJT-In can be gauged from the occurrence of several volcanic forms

1.3. Age of CIB crust and evolution

Variations in the rate of spreading and formation of new oceanic crust along the ridge crest, during more than one episode of India–Eurasia collision, are imprinted in the CIB. Several authors proposed different plate reconstruction models and explained the tectonic evolution of the Indian Ocean (Desa et al., 2009 and references there in). The breakup of eastern Gondwanaland and the subsequent rifting and drifting of its continents in space and time are responsible for the creation of the present day configuration of the Indian Ocean. Seafloor spreading occurred in three episodes with two major plate reorganizations (Schlich, 1982; Powell et al., 1988; Royer et al., 1988).

The initial breakup during the Early Cretaceous (134Ma), India separated from the contiguous Antarctica-Australia (Desa et al., 2009; Ramana et al., 2001). The first major plate reorganization began around the Middle Cretaceous time and the direction of motion of the Indian plate changed from northwest to north (Powell et al., 1988; Royer and Sandwell 1989; Ramana et al., 1997). A second episode of seafloor spreading occurred from Late Cretaceous to middle Eocene (84-50 Ma) during which the Indian plate moved rapidly northward with an average half-spreading rate of 12cm/yr (Sclater and Fisher 1974). This northward movement was drastically reduced around ~50Ma (Early Eocene) due to the soft collision of Indian plate with the Eurasian plate, which triggered the second major plate reorganization (Powell et al., 1988). The soft collision between India and Asia had paved the way for initial formation of the mighty Himalaya (Mukhopadhyay et al., 1997). This finding is further corroborated by a recent study in the basinal crust which found the anomaly 23 (age 51 Ma) to be indistinct and ill-preserved (Rajendran and Prakasa Rao, 2000). This is probably due to intense flexuring and faulting of the seafloor caused consequent to India–Eurasia collision.

During this reorganization, the direction of the Indian plate motion changed from N-S to NE-SW. During the third phase, the second major plate reorganization commenced during the Oligocene (~30 Ma) in the NE-SW direction due to the hard collision of the Indian plate with the Eurasian plate (Curray et al., 1982) resulted in a

change in the Indian plate motion direction to northeast and the formation of present day Southeast Indian Ridge.

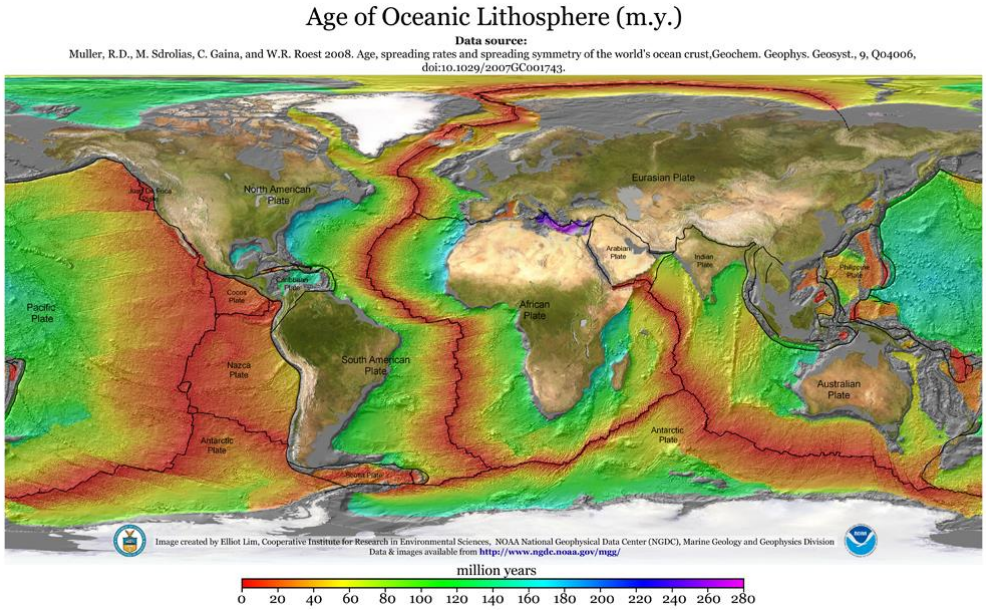

Fig. 1.4: Schematic map showing the ages of the ocean crust in the world ocean (Muller et al., 2008)

Major structural elements evolved in the Central Indian and Crozet Basins during the Late Cretaceous to Middle Eocene (Fig. 1.2). The Afanasy Nikitin seamount chain on the Indian plate and the Conrad Rise on the Antarctica plate are the testimony for excessive volcanism on either side of the spreading ridge between India and Antarctica (McKenzie and Sclater 1971). The Ninety East Ridge, a trace of the Kerguelen mantle plume formed on the Indian plate during Middle Cretaceous to Late Eocene (Pierce 1978; Mahoney et al., 1983; Duncan 1991). The reunion hotspot has created the Deccan flood basalts on the western Indian Shield around 66-68Ma (Fisk et al., 1989). The initiation of seafloor spreading between Australia and Antarctica, and the opening of the Wharton Basin took place during this period (Sclater and Fisher 1974; Crawford 1974; Fedorov et al., 1982; Liu et al., 1983). During the same time the Ninety East Ridge became inactive and the Indian and the Australian plates became single Indo-Australian plate and separation from the Antarctic plate continued to Present (Sclater and Fisher, 1974). The latest event in the history of Indian Ocean is the formation of Red Sea and Gulf of Aden, which separates Arabia from Africa (Fig. 1.4).

Mukhopadhyay et al. (2008) summarizes that the predominance of tensional stress in the northern sectors of the CIB where the seafloor flexed asymmetrically and

the flexures are spaced non-uniformly. By contrast, the seafloor to the south is characterized by closely spaced, long, symmetrical faults, coupled with flexures of high amplitude and large wavelength, as a consequence of the large compressional stress. This is reflected by the increase in local gravity (Stein et al., 1989) and stress values Weissel et al. (1980) and Zoback et al. (1989) indicating an excessively compressed crust. Mukhopadhyay et al. (2008) and Krishna et al. (2001) explained the above situations by taking recourse to episodic collision events between India and Eurasia between the period 60 and 49 Ma.

The events of unification of Indian and Australian plates in the middle Eocene (Liu et al., 1983; Krishna et al., 1995), hard continent-continent collision to the north of the Indian shield (Curray et al., 1982) and continuous generation of new oceanic lithosphere along the Carlsberg-Central Indian-Southeast Indian Ridges have led to the development of instability within the central Indian Ocean lithosphere (Krishna et al., 2002). The compressive stresses that accumulated during the course of the instability process reached the failure stage and triggered seismic activity in the middle of the Indo-Australian plate that deformed the upper lithosphere intensively (Weissel et al., 1980). The imprints of this activity are well documented in both the oceanic basement and the overlying sediments in a wide region in the Central Indian Basin (Fig. 1.3) in the form of long-wavelength anticlinal basement rises and high-angle reverse faults (Fig. 1.3; Krishna et al., 1998, 2001 and references there in). On the basis of ridge earthquake data Royer and Gordon (1997) and Gordon et al. (1998) have demarcated the convergent and divergent diffusive plate boundaries in the central Indian Ocean

Sedimentation in the CIB

The nature of sediments and sedimentation processes operating in the Indian Ocean is complex as a result of the combined effect of an active mid oceanic ridge, 90°E ridge, flexure, folded and faulted nature of the seafloor and uneven supply from the land masses (Goldberg and Griffin, 1970). Many workers have assigned the clay mineral assemblages in the sediments of the Indian Ocean as being detrital (Kolla and Biscaye, 1977, Rao and Nath., 1988).

The distribution of the sediments of the Indian Ocean was mapped by Udintsev (1975) for the International Indian Ocean Expedition Atlas. Different

sediment types are distinguishable in the CIB (Fig. 1.5) grading from the terrigenous sediments on the northern part (up to 5°S latitude) with illite, kaolinite + chlorite making up 90% of the clay minerals mainly derived from the turbiditic currents in the north; from 5° to 14.5°S the major sediment type is siliceous oozes with sporadic calcareous patches present at around 12°–14°S latitude and 82.5°–83.5°E longitudes. The southern part of the basin (south of latitude 14.5°S) is covered with pelagic/red clay (Nath et al., 1989) mainly derived from eolian and volcanogenic sources. Influence of turbiditic currents from the Ganges-Brahmaputra Rivers is noticed up to about 8°S (Rao and Nath, 1988; Nath et al., 1989; Nath et al., 1992; Nath, 2001). The average sediment accumulation rate in CIB varies from 1 to 5 mm/ka (Borole 1993).

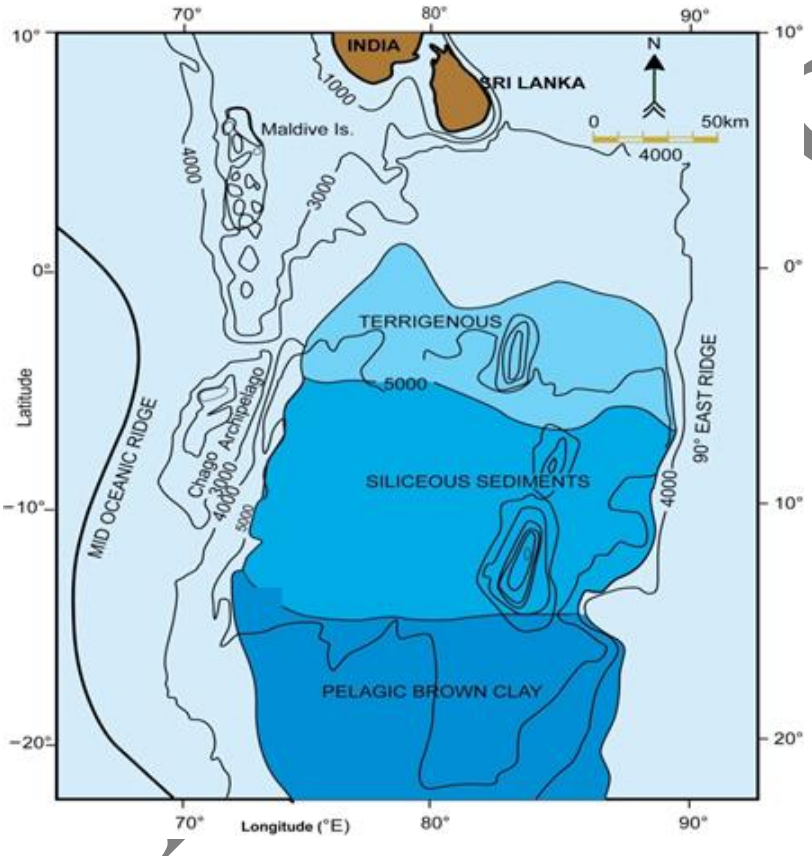

Fig. 1.5: Distributional pattern of different sediment types in the Central Indian Basin (Nath et al., 1989).

Valsangkar (2011) studied the clay mineralogy of the Basin and summarized that the average clay content in the basin increases from 10 to 16°S and also from west to east. He also noted the increase in average clay content along either side of the 76.5°E fracture zone. Similar increase in the clay content was reported along the 73° and 74.5°E fracture zone. The continental source indicators like illite-kaolinite-chlorite abundances were decreasing in abundance from north to south in CIB tracking the dispersal of sediments derived from the turbiditic currents originating from the mouth of the Ganges and Brahmaputra (Nath, 2001). Increase in clay content in the southern part was attributed to additional supply from the south and appeared to be locally supported by volcanic activity. Fine grained smectites-rich sediments derived from

the alteration of in situ submarine basalts and associated volcanic products (Kolla et al., 1976) were also reported. Montmorillonite content was the highest in the red clays of the southern part of the basin and may be derived from basinal ridge rock weathering (Rao and Nath, 1988) containing basic volcanic material. This inference was supported by higher degree of crystallinity in all size fractions of calcareous sediments possibly derived from adjacent ridge rocks. Fe-montmorillonite was also found in the clays fraction of the pelagic and siliceous oozes which was attributed to interaction of Fe-hydroxides and biogenic opal during early diagenesis (Rao and Nath 1988). The sediments of the CIB are organic poor (Nath and Mudholkar, 1989; Nath et al., 2012) typical of well oxygenated areas.

1.4. Oceanography of CIB

The structure of the water masses of the Indian Ocean was first published by Sverdrup, Johnson and Fleming, (1942) which was later modified by Mamayev (1975). An examination at different locations in the Indian Ocean reveals the presence of several water masses, namely Indian Ocean Central water (IOCW), Indian Ocean Equatorial Water (IOEW), Antarctic Intermediate Water (AIW), Red Sea Water (RSW), Persian Gulf Water (PGW), Bottom and Deep Water (BDW), etc.

Detailed studies of the chemical properties of the water column during the Indian Deep Sea Environment Experiment (INDEX) in CIB were carried out by de Sousa et al. (2001). They observed a surface mixed layer about 40m thick, characterized by low salinity (< 34.67 psu), high oxygen (223-245 µM), high pH (>8.2) and low nutrient content (nitrate < 0.02 µM). The low salinity layer was probably due to local excess of precipitation (Warren, 1981) and/or by the influx of low salinity Pacific water as "Indonesian Throughflow" (Warren et al., 1981; Fieux et al., 1996). The isoclines of this low salinity layer shoaled towards the North (de Sousa et al., 2001) consistent with the northward swallowing of the mixed layer. Between 10-11°S a sharp salinity front at 50 m depth separated the low salinity waters (<34.67 psu), marking the influence of "Indonesian Throughflow", from the high salinity waters (>34.70 psu). The top of the thermocline was marked by a rapid increase in nutrient concentrations and decreased pH.

A subsurface salinity maximum (34.74–34.77 psu) associated with a shallow oxygen minimum (67–112 µM) and weak maxima in nutrients (Nitrate: 18–22 µM,

phosphate: 1.4–1.8 µM and silicate: 18–24 µM) and a relatively low pH (7.7–7.9) was observed in the depth range 125–200 m. It was best developed on the eastern side of the Basin. The salinity and dissolved oxygen concentration of this water decreased northwards while the concentrations of nutrients increased in the same direction eroded core of the Subtropical Surface Water (STW), which is formed in latitudes 25–35°S by excess of evaporation over precipitation (Warren, 1981a; Toole and Warren, 1993). de Sousa et al. (2001) had observed water with high salinity (>35.5 psu) associated with high oxygen (245–257 µM) at sea surface at 32°S. Interior circulation carries this water northwards to tropical latitudes (10–15°S) where it is capped by the warm, low-salinity Tropical Surface Water (TSW) formed by excess of precipitation (Toole and Warren, 1993). However, its characteristic properties undergo gradual erosion during its transit, caused by vertical mixing with the low-salinity TSW. Between 9° and 13°S it can be identified by its residual salinity of 34.74–34.77 psu. A shallow oxygen minimum was associated with the subsurface salinity maximum. It was strongest in the north and attenuated towards the south. In this layer, the average concentration of oxygen at 13°S was around 112 µM. This minimum is caused by the in situ consumption of oxygen by sinking detritus (Warren, 1981a, b). The progressive equator-ward decrease of oxygen indicates the progressively increasing transit time of this water from the overturning zone (Lat. 25–35°S).

Below the subsurface salinity maximum there was a layer of deep oxygen maximum in the depth range 250–750 m, where oxygen concentrations reached up to 180 µM. The maximum was intense in the western side of the basin and was associated with weak minima in nutrients (nitrate: 14–22 µM, phosphate: 0.6–2.2 µM and silicate: 12–22 µM and relatively high pH >7.8) (de Souse et al., 2001). This was Sverdrup's Indian Ocean Central Water (Sverdrup et al., 1942), which Warren (1981a) termed as Sub-Antarctic Mode Water (SAMW). It forms at 40–50°S by deep convection during late winter (McCartney, 1977). Toole and Warren (1993) observed this water at 400–600 m depths on the Darwin section at 32°S with high oxygen concentrations of 234–245 µM. It was also observed on the Atlantis II section at 18°S in the depth range 400–500 m with similar concentrations of oxygen (Warren, 1981a). de Souza et al. (2001) suggested that this water enters the Basin from the southwest. Between 32° and 13°S, this water lost little oxygen (~50–60 µM). This suggests that this water, as observed at 13°S, is relatively new, having spent short transit time from the zone of its formation, which means that this water moves faster than the water

above it. The relatively low concentrations of nutrients and higher pH associated with this water also support the above findings.

The salinity minimum corresponding to the Antarctic Intermediate Water (AAIW) was seen as a 400 m thick band in the depth range 800–1200m and between 27.2 and 27.5 density (σ_Θ) levels. Salinity of this water varied within a narrow range of 34.714 and 34.718 psu.

de Sousa et al. (2001) reported a high-salinity band (34.719–34.721 psu) in the density (σ_Θ) range 27.6–27.8 at depths 1500–2200 m. The salinity of this water is highest in the north and attenuates to the south. The intermediate waters of North Indian Ocean are depleted in oxygen and nitrate (Naqvi, 1987), but have higher silicate concentrations. Thus, it appears that the observed changes in the properties of the AAIW between 32° and 13°S are partly due to oxidation of organic matter en route and partly due to mixing with Arabian Sea water. According to de Sousa et al. (2001) the properties of deep waters in this region remained almost constant below 3000 m depth, except phosphate, which showed a gradual decrease from 2.4 to 1.95 µM. The salinity varied within a very narrow range of 34.719–34.720 psu, while the ranges of variation in nitrate and silicate were 34.4–34.6 and 110–120µM, respectively. The deep waters in this region are believed to be of Antarctic origin carried northwards by circumpolar currents. It appears that no major changes have occurred in the properties of this water during its northward transit, as can be seen from the comparison of its properties at 32°S (Toole and Warren, 1993), 18°S (Warren, 1981a, b), and 12°S (Warren, 1982, de Sousa et al., 2001), indicating that at these levels interactions between different water masses are limited.

Chemical parameters of seawater along 20°S in CIB

The Electronic Atlas of WOCE (World Ocean Circulation Experiment) data were used to access on-line plots of the temperature, oxygen and nutrients profiles in the CIB across the transect at 20°S. WOCE was an unprecedented effort during 1990-1997 by scientists from more than 30 nations to study the large-scale circulation of the ocean. The distribution of the chemical parameters in the water column was taken from Profile I03 which is an E-W Profile in the Indian Ocean. This profile is ~4 degrees of latitude south of the study area. From this profile, it can be seen that the temperature (http://www.ewoce.org/gallery/I3_TPOT.gif, Fig. 1.6) variations upto

~500 m are large and reach up to 2.5°C. The warm waters (> 20°C) are restricted to a narrow depth of ~150 m. The deeper levels show the same temperature (1-2°C).

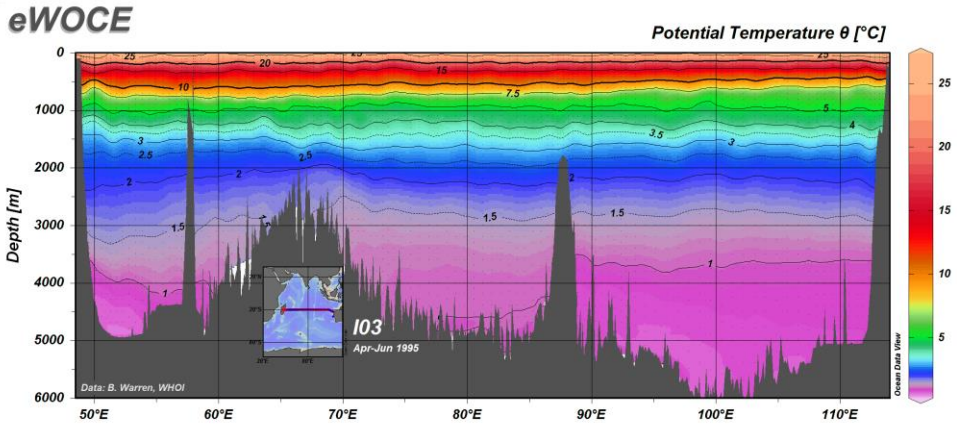

Fig. 1.6: Profile showing the distribution of temperature in seawater on a W-E transect across the Indian Ocean at 20°S latitude (source: www.ewoce.org)

The I03 dissolved oxygen profile (http://www.ewoce.org/gallery/I3_OXYGEN.gif, Fig. 1.7) shows surface oxygenated waters (>200 µmol/kg) upto ~900 m which suddenly decreases to form a subsurface oxygen poor (100 µmol/kg) or oxygen minimum layer at 1000-2000 m depth. The oxygen poor layer is thicker in the western part (Wharton basin) of the transect as compared to the eastern (CIB) part of the transect. The dissolved oxygen content continuously increases with increasing depth. The maximum oxygen concentration is ~180 µmol/kg for most part of the CIB, while in the Wharton basin oxygen reaches a maximum of 200 µmol/kg in the deeper areas. The waters surrounding the Mid Oceanic Ridge exhibit lower dissolved oxygen content (~180 µmol/kg) compared to the abyssal areas.

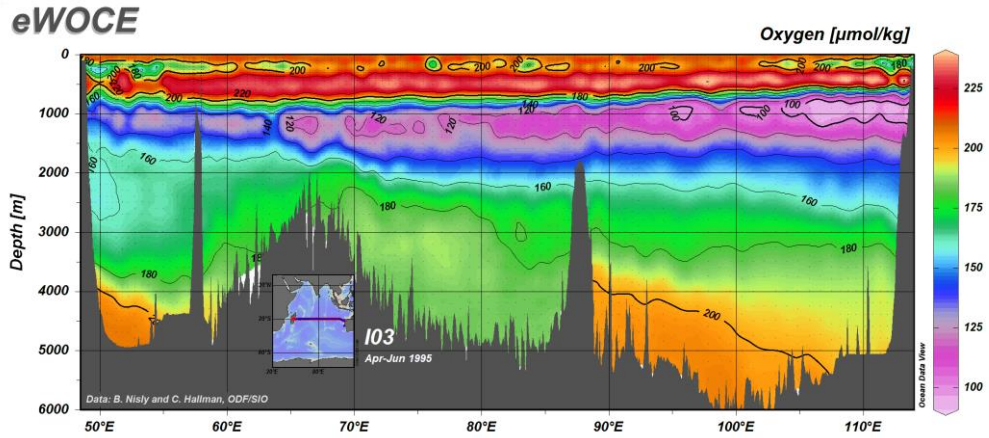

Fig. 1.7: Profile showing the distribution of oxygen in seawater on a W-E transect across the Indian Ocean at 20°S latitude (source: www.ewoce.org)

The dissolved nutrient content in the CIB waters were examined in the vertical profile along 20°S (I03). Low silicate (http://www.ewoce.org/gallery/I3_SILCAT.gif, Fig. 1.8) (0-5 µmol/kg) layer is found all along the transect from surface to ~500 m water depth. There is continous increase in silica content with increasing water depth and silica rich waters (130 µmol/kg) are found below 2500 m water depth. Bottom water layer is rich in silica throughout the transect which thickens towards the eastern side of the CIB (upto 2000 m thick). The high silica content in the benthic layer suggests benthic fluxes of silica to the seawater.

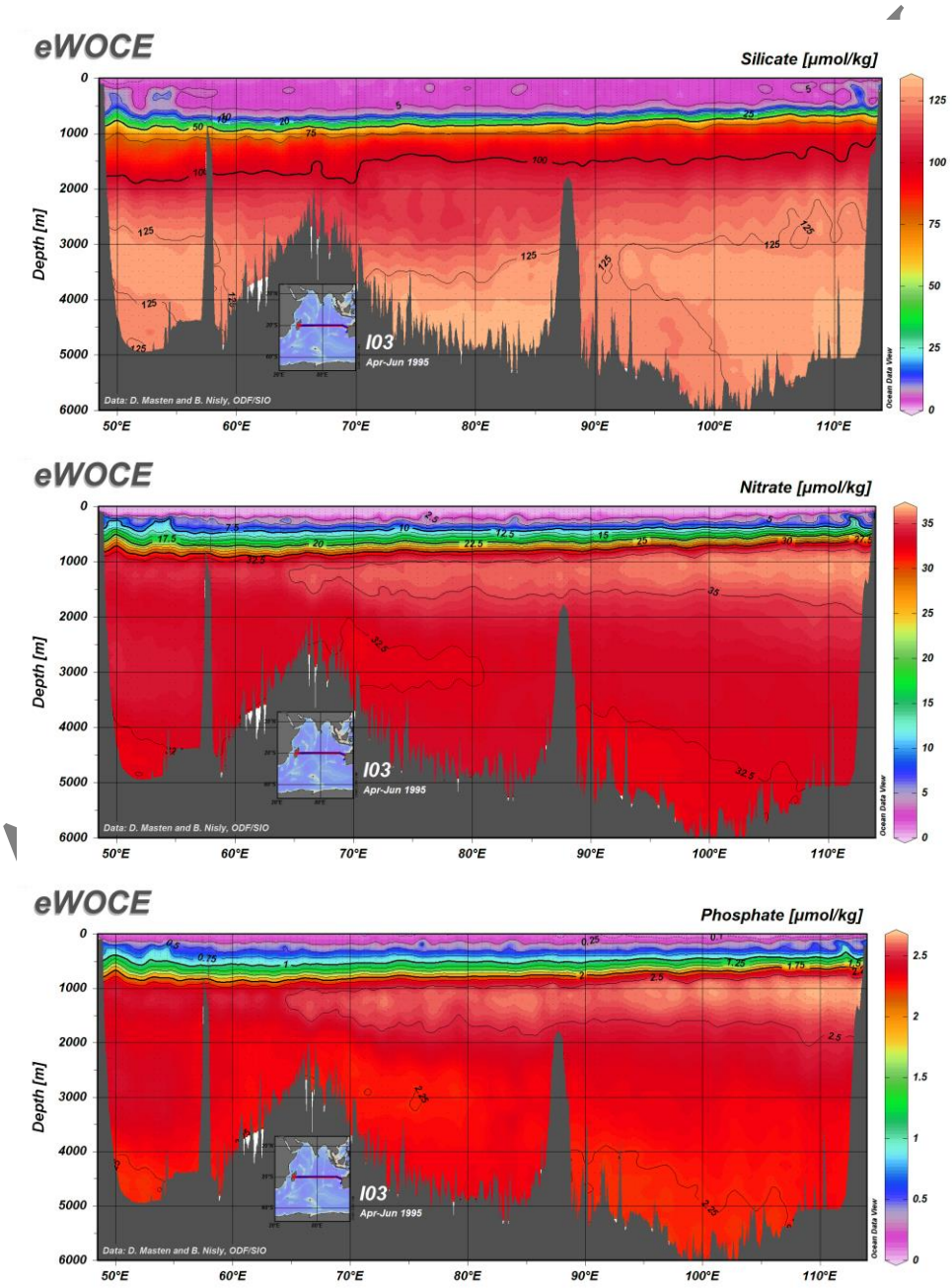

Fig. 1.8: Profile showing the distribution of silicate, nitrate and phosphate (Nutrients, µmol/kg) in seawater on a W-E transect across the Indian Ocean at 20°S latitude (source: www.ewoce.org)

The surface waters are nitrate (http://www.ewoce.org/gallery/I3_NITRAT.gif, Fig. 1.8) poor (0-5 µmol/kg) and form a narrow band (150 m) of waters throughout the basin. There is a drastic increase in the nitrate content (upto 32.5 µmol/kg) in the subsurface waters till about 1000 m water depth. The deeper waters (below 1000 m) are uniformly enriched in nitrate (32.5 µmol/kg) except for a narrow nitrate rich (>35 µmol/kg) layer (~1000 m thick) that forms at 900 to 200 m water depth. This nitrate rich sub surface layer is thicker in the eastern side of the transect compared to the western side.

The dissolved phosphate profile (http://www.ewoce.org/gallery/I3_PHSPHT.gif, Fig. 1.8) also shows a similar trend like that of nitrate profile along 20°S. A shallow (50 m) layer of phosphate poor waters are seen extending throughout the transect. The phosphate content rapidly increases (~2.25 µmol/kg) with increasing depth upto 1000 m. Below 1000 m water depth phosphate concentrations are uniformly distributed throughout the water column. A subsurface phosphate rich (2.5 µmo/kg) layer is seen, whose thickness increases towards the east of the transect.

Studies of chemical properties of the water column in the CIB show three equator-ward-moving water masses (de Sousa et al., 2001). The fastest moving water-mass in the depth range 125–200 m is characterized by high salinity (34.74–34.77 psu) and an oxygen minimum associated with weak maxima in nutrients. The second water-mass with deep oxygen maximum (234–245 m) in the depth range 250–750 m, is associated with minima in nutrients and a relatively high pH. The third water-mass, present at depths 800–1200 m with a low salinity (34.71–34.72 psu) and a density (sigma-theta-σ_t) range of 27.2–27.5 corresponds to the Antarctic Intermediate Water (AAIW) (de Sousa et al., 2001). The bottom is bathed by the North Indian Deep Water (NIDW), which is formed by the mixing of Antarctic Bottom Water (AABW), North Atlantic Deep Water (NADW) and the deep water of the Northern Indian Ocean (Tchernia 1980). The abyssal depths (> 4000 m) are filled with a water-mass of southern origin, mainly the AABW, which has high levels of dissolved oxygen (Tchernia 1980; Warren 1982; Ramesh Babu et al., 2001). These water masses are of great importance for biological productivity in the CIB (Matondkar et al., 2005). de Sousa et al. (2001) concluded that progressive changes in water characteristics to be attributed to mixing with waters above and below, and to oxidation of organic detritus en route. Among the three water masses, the oxygen maximum water showed the

lowest changes in its properties, which may suggest that this water mass is moving the fastest.

Current structure and kinetic energy in the Central Indian Basin

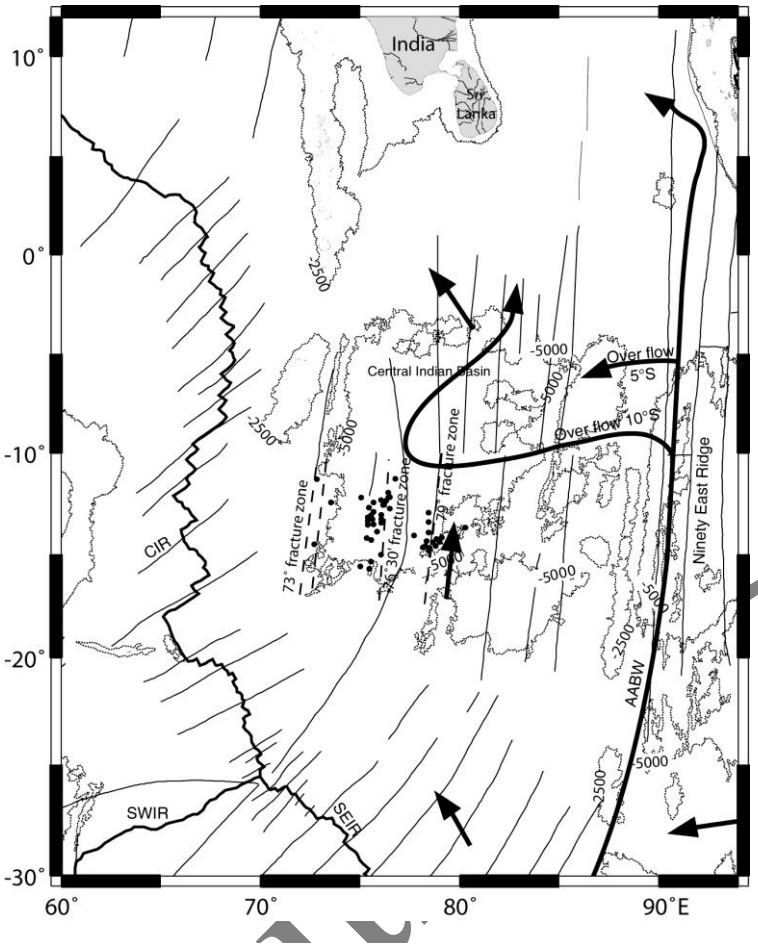

Fig. 1.9: Bathymetry and bottom water circulation patterns of water in the CIB modified from Vineesh et al. (2009) and Pitrowski et al. (2009).

The CIB is protected from circum-polar bottom currents and Antarctic Bottom Water (AABW) currents from the Antarctic Ocean, South Australian basin and West Australian basin by three major ridge systems i.e. South East Indian Ridge on the southern side and the Ninety East Ridge on the eastern side of the basin. Antarctic Bottom Water (AABW) crosses the South-eastern Indian Ridge and flows clockwise around the western margins of the South Australian Basin and Wharton Basin. It continues northwards along the base of the Ninety-East Ridge and enters the CIB (Fig. 1.9) (Johnson and Nigrini, 1982). The AABW enters through deep saddles on the Ninety East Ridge (5° and 10°S) (Fig. 1.9), into the CIB owing to westward movement controlled by the bathymetry and spreads northward (Warren 1982). The Central Indian Ridge acts as a barrier for the bottom-water currents from then Madagascar and Crozet basins entering into this basin. This water becomes mixed with basin waters and thus the bottom water temperatures are enhanced in the central and western parts of the basin. Gordon et al. (2002) clearly demonstrated the entry of AABW currents into the CIB (Fig. 1.9), and argued for its influence

extending up to Bay of Bengal. According to Kolla et al. (1976), the carbonate lysocline and carbonate critical depth (CCrD) along a latitudinal transect of 10°–20°S in the CIB are at 4000 and 5050 m, respectively, and deepen towards the south, whereas Banakar et al. (1998) placed the depth of the lysocline at 4400 m and the CCD at a depth of 4700 m.

Murty et al. (1999) studied the abyssal current structure at 7 levels viz., 4, 8, 15, 30, 50, 100, and 500 mab and kinetic energy in the lower 500 m of the water column at one station at 10°01'S and 76°E in the CIB. Monthly mean currents showed a general SSE flow and suggested seasonal variability in the flow pattern with a reversal in January. The mean flow height is high (2.2cm/sec) at 50mab and decreased above and below 50 mab. The variation of 6 month mean current speed indicates near bottom intensification of the flow at 50mab and the presence of Bottom Ekman Layer (BEL) below 50 mab. Above BEL the total Kinetic energy at each depth was dominated by eddy KE resulted from synoptic scale (12-15 day period) motion. In the BEL, the inertial and tidal (meso-scale) oscillations contributed to the eddy KE. The meso scale oscillations contribution to the variability of the currents in the bottom Ekman layer increased towards seabed.

Under Indian Deep Sea Environment Experiment (INDEX), direct measurements of the ocean currents were carried out in the CIB during 1995–97. The currents were obtained at three mooring stations (10° and 15°S; 2 stations) and 5 depths covering the subsurface, intermediate, deeper and near-bottom depth ranges (Murty et al., 2001). Seasonal variability in the currents at the subsurface (450–670 m), intermediate (1150–1370 m), deeper (3450–3670 m) and near-bottom (4270–5100 m) depths at three mooring stations in the CIB were documented. In the northern basin, seasonal variability in the currents at 500 m and 1200 m depth was attributed to the seasonal north–south shift in the westward-flowing South Equatorial Current (SEC). Low-frequency (30–60 day) oscillation, superimposed on high-frequency (inertial, semi-diurnal and diurnal) fluctuations, were noticed at all the depths including near-bottom depth (5100 m) where the U-component of current was dominant. The variability of the currents at the intermediate depth range (1150–1300 m), encompassing the three stations of 500 km apart, indicated the existence of anticyclonic gyral circulation. The depth variation of kinetic energy (KE) emphasized the bottom intensification of currents with minimum KE at deeper depths followed by relatively higher KE at abyssal depths. In the northern basin, the total KE exhibits

seasonal variation; it was high during southern spring–summer and low during southern fall–winter. The eddy KE constitutes a larger part of the total KE at synoptic scale (12–15 day) fluctuations in the northern basin and meso-scale (inertial, semi-diurnal and diurnal) oscillations in the southern basin (Murty et al., 2001)

1.5. Biological (pelagic and benthic) productivity in the CIB

The first study of primary production of CIB was made during International Indian Ocean Expedition (IIOE) (Krey and Babenerd 1976). Krey and Barbenard (1976) have compiled chlorophyll *a* and primary productivity data for the region where chlorophyll *a* was <0.05 mg m^{-3} at surface and 25 m and 0.05–0.1 mg m^{-3} at 50 m during the November to April season. Matondkar et al. (2005) studied phytoplankton biomass, taxonomy and primary productivity as part of baseline data collection for prospective nodule mining in the CIB in January 1997. The results of Matondkar et al. (2005) showed that the chlorophyll *a* values were low, similar to oligotrophic tropical and subtropical oceanic waters. The average chlorophyll *a* value was 0.775 mg m^{-3} at surface (Fig. 1.10) and 17.75 mg m^{-2} in the average integrated through the water column and was comparable with the value reported from similar environments in the Pacific Ocean (El-Sayed et al., 1979; Malone 1971; Holmes 1961). Similarly, average primary productivity at surface was 3.72 mgC m^{-3} d^{-1} and was 51.23 mgC $m^{-2}d^{-1}$ in column. The chlorophyll *a* maxima at 50 to 80 m was the characteristic feature of the euphotic zones of the area. The high chlorophyll *a* at 75°E and 12°S latitude was found matching with high

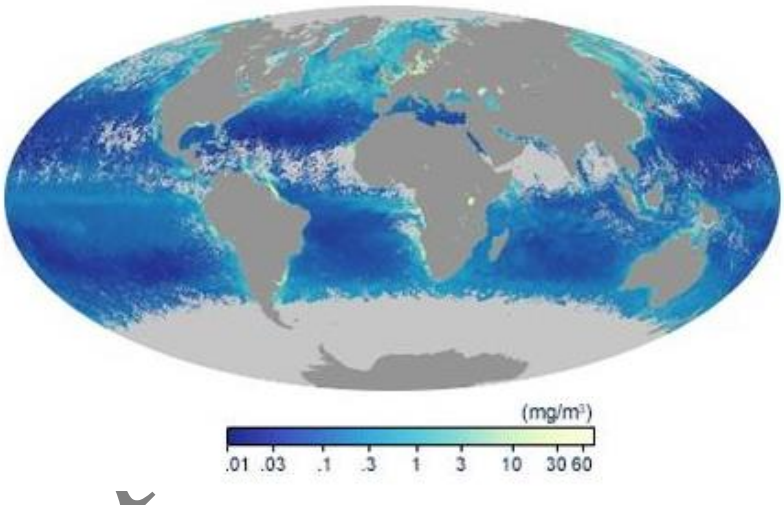

Fig. 1.10: Global map of Chlorophyll in surface waters of the oceans (source: earthobservatory.nasa.gov).

primary productivity, and low chlorophyll *a* at 14°S and 73°E matched with low primary productivity in the same area

The lowest primary productivity at surface was 0.12 mg C m^{-3} d^{-1}, and highest surface production was 9.72 mg C m^{-3} d^{-1}. The integrated column productivity varied from 9.06 mg C m^{-2} d^{-1} to 103.4 mgC m^{-2} d^{-1} in the study area, indicating a relatively high productivity around 10°S and 75°E (Fig. 1.10 and 1.11). The primary productivity of the CIB was very low, the average being 51.23 mg C m^{-2} d^{-1} (Matondkar et al., 2005). It was similar to the range of earlier reported value for the CIB (Krey 1973; Krey and Babenerd 1976) and for the tropical Pacific region (El-Sayed and Taguchi 1979). Similarly, Holmes (1961), Ryther (1969), and Kolbentz–Mishke et al. (1970) reported productivity values of 150 mg C m^{-2} d^{-1} for the deep sea region, where the column chlorophyll a rarely exceeded 25 mg m^{-2} and the maxima were located between 50–150 m depth.

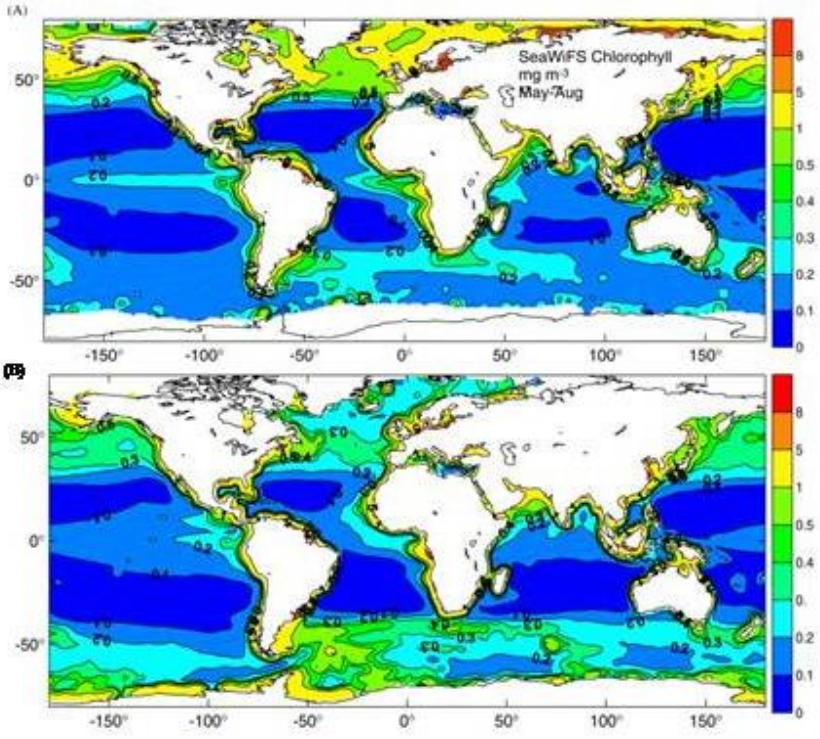

Fig. 1.11: Global distribution for (A) summer season (May–August) and (B) winter season (December–March) 1997–2002, 20 months data of SeaWiFS CHL (mg m^{-3}) (Gardner et al., 2006).

At most of the stations mesozooplankton biomass was maximum in the top 50 m water column, indicating the importance of grazing in the euphotic zone. Appreciable quantities of mesozooplankton were observed below the euphotic zone, where settlement of chlorophyll *a* occurs.

The low iron concentration in the water and its relationship with the water column productivity were correlated. The results show that waters in the CIB have low productivity in the surface as well as subsurface layers.

Diatoms and dinoflagellates were the main groups of organisms in the study area. The phytoplankton cell counts at surface were low, ranging from 0.12 to 1.18 x 10^4/l, where diatoms dominated the population. Average phytoplankton counts at the surface were low (3960 cells/l), compared to those at 25 m (6421 cells/l) and 75 m (5187 cells/l). The high phytoplankton counts were seen in the areas east of 75°E longitude in the northern part of the area and decreased in the southern part. The phytoplankton distribution to the west of 75°E latitude had an opposite trend where counts were higher in the southern stations. The pattern of phytoplankton distribution remained the same at surface, 25m, and 75m depths in all the stations indicating homogeneity of the area (Matondkar et al., 2005). The study showed that the phytoplankton cell counts and chlorophyll a had low biomass level, suggesting low rates of primary productivity in the CIB.

A spatial variation in the integrated value of the Fe in the upper 100 m of the water column studied in the CIB was noticed. Low concentration of Fe (154.74 mg m^{-2}) in the southern stations was found to affect the primary productivity rate, which was 76.26 mg C m^{-2} d^{-1} in the euphotic zone. However, in the northern stations, a high content of Fe (562.75 mg m^{-2}) was found to enhance the primary productivity rate (103.4 mg C $m^{-2}d^{-1}$) (Matondkar et al., 2005). The CIB region is totally isolated from the mainland and the only source of Fe is dust from islands or land masses around the Indian Ocean. Iron is generally required for the growth of the phytoplankton and recently it has been shown that adding iron to the surface waters, stimulates the growth of phytoplankton in the equatorial Pacific where wind-borne dust is negligible as the source (Alten 2002).

Sharma and Rao (1992) from a data of seabed photographs and bathymetry in the CIB, between 10° and 16°S latitudes and between 72° and 84°E longitudes have reported a variety of biogenic activity in the form of lebensspuren, such as the fecal casts and body tubes, fecal pellets, burrow openings, feeding tracks and locomotion trails, as well as mounds and cones in the area. Relation of megabenthic activity to geological features in the CIB was also studied (Sharma and Rao., 1992), and indicated that the sediments were the most preferred substrate, since 88% of the organisms, and 86-100% of the lebensspuren were associated with it as the sediment

provides nutrition as well as shelter to the organisms. This also was reflected by the high regional average of the lebensspuren (8-12 traces/m^2) in the CIB and the presence of sediment in all the locations photographed.

Siliceous ooze is the dominant sediment type in the CIB, with a thin strip of calcareous ooze in the west and red clays to the south (Udintsev, 1975). The various types of organisms and the lebensspuren found in the area had a uniform distribution, irrespective of the sediment type; their density, however, was directly proportional to the area covered by the sediment at each location. Seafloor morphology is the major factor controlling the distribution of the sediments, nodules and rocks (Iyer and Sharma, 1990); which in turn influence the occurrence of megafauna and the lebensspuren (Sharma and Rao., 1992). The summits of the seamounts and abyssal hills, which have large rocky exposures and little sediment, have comparatively less biogenic activity (0-4 traces/m^2, sometimes 4-8 traces/m^2); whereas, the slopes and flanks, which have abundant nodule deposits, generally have 4-12 traces/m^2, and the very gentle slopes and the abyssal plains, which have a thick sediment cover and a few nodules, have as many as 8-16 traces/m^2 average, with a maximum of 33 traces/m^2. Widespread activity can be seen in the areas with more sediment as compared to the areas with nodules and rock exposures. Glasby (1973) also had observed that the occurrence of lebensspuren is particularly marked in the areas of thick sediment cover and not on volcanic outcrops.

The quantitative distribution of benthic fauna in the CIB was studied in detail by Ansari (2000) and found that the CIB abundance is within the density and biomass ranges elsewhere in the Indian Ocean (Thiel, 1966; Parulekar et al., 1992; Ansari et al., 1996) and from similar depths of other oceans (Shirayama, 1984) but on the lower side. Regions with such low abundances are areas having unfavorable feeding conditions, which are usually confined to deep-sea basins. The CIB reportedly has very low organic matter in sediment (Nath and Mudholkar, 1989). According to Sokolova (1972), the CIB falls in the oligotrophic region with respect to benthic production. Low benthic production may result from many environmental factors (Shirayama, 1984) but the rate of decrease of food supply with increasing depth can rightly be considered the most important factor for reduced faunal density in the deep sea (Rowe, 1971). Ansari (2000) compared faunal abundance to the total organic carbon and nitrogen content. The percent distribution of C and N in different sediment layers of the area was very low, varying from 0.21 to 0.57% and 0.02 to 0.08%,

respectively. These values are also a measure of the possibility of meiobenthos meeting organic matter demand. Organic matter is low in CIB sediments (Nath and Mudholkar, 1989) and hence benthic biota has to rely on the particulate organic matter that is produced in the euphotic zone.

Ingole (2003) studied the macrofauna of the CIB, comprising 24 major groups belonging to 15 phyla (Fig. 1.12). The fauna was mainly constituted by Protozoa, Nematoda, Mollusca, Polychaeta, Crustacea and Echinodermata. Polychaeta was the most dominant group in terms of number of individuals, contributing over 33% to the total macrofaunal population the values for the macrobenthic density fluctuated very widely and were considerably higher at some of the stations. The density of macrofauna varied from 30 to 1430 no. m^{-2} and biomass (wet wt) varied from 0.11 to 12.75 g m^{-2}. In general, the density values were higher in the western sector compared to the eastern sector of the CIB. Ingole (2003) attributed the exponential increase in benthic standing stock (density and biomass) from eastern to western region to have a direct relationship between the mid-ocean ridge environment and macrobenthic abundance.

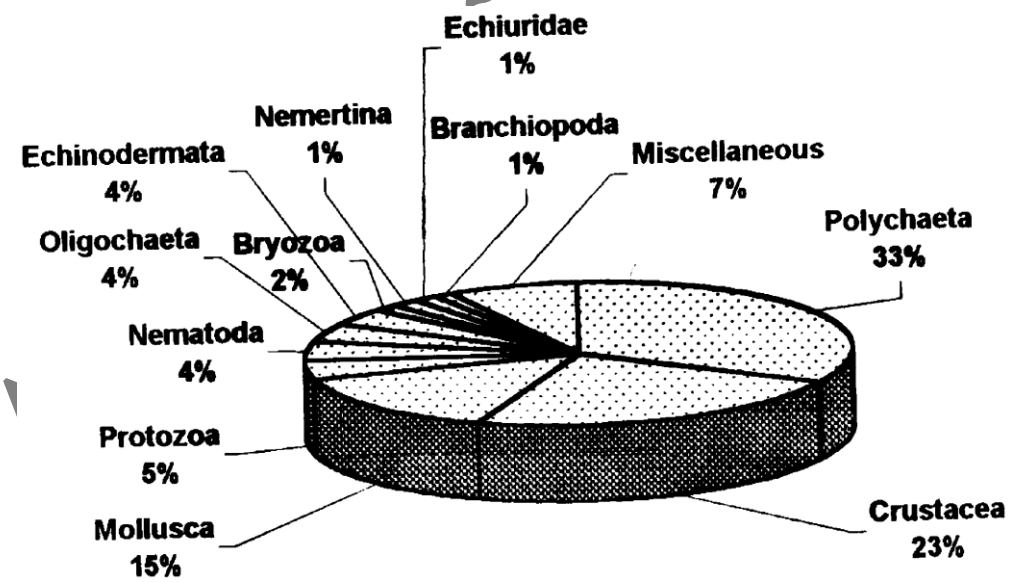

Fig. 1.12: Composition (%) of macrofauna in CIB (Ingole 2003)

Pavithran et al. (2009) concluded that there was reduction in macrobenthic density towards the southern latitudes. CIB is mainly dominated by deposit feeding macrobenthos (polychaetes) and predatory omnivorous nematodes, since the macrobenthic distribution depends on the availability of surface primary production and their abundance is strongly related to sedimentary organic matter. The values for population density were strongly correlated with surface water chl-*a* and sediment

protein, indicating supply of fresh organic matter as a critical factor for maintaining the deep sea benthic diversity and abundance. Vertically, the fauna was distributed down to 30cm depth, with the highest faunal density in the top 2–5 cm sediment section. The presence of fauna at deeper sediment depths could be due to the transport of organic matter by the bioturbators hence facilitating the distribution of fauna in deeper depths.

Parulekar et al. (1982) summarized that quantitative studies of the abyssal benthos (3600 to 5300m) of the CIB show a rich fauna and high standing crops. Density of 3 meiofaunal and 12 maerofaunal taxa are large (2175 to 15233; ~6441m^{-2}). Polychaetes (41.6%), peracarid crustaceans (31.7%), ophiuroids (12.2%), echiuroid-bryozoa (9.7%), molluscs (4.8%), and agglutinating rhizopod protozoans form the macrofanna. Meiofaunal taxa are nematodes (69.4%), harpaetieoid copepods (26.6%), and ostracods (4%). Meiofaunal abundances are positively correlated with distance from shore, whereas the distribution and abundance of macrofauna are independent of variations in depth and distance from the shore. Ratio of macro to meiofauna in the total population is 1 to 31. High benthic biomass and rich fauna are consequences of high organic production in the euphotic zone. The correlation between biomass of the total oxidizable organic matter in the water column and the benthic standing crop is statistically significant ($r = -0.64$) at the $P < 0.05$ level. Rich fauna and high standing crop were associated with the occurrence of polymetallic nodules.

1.6. Past work related to early diagenesis, volcanism and hydrothermalism in the basin.

The Central Indian Basin (CIB) has been extensively studied in the last four decades for the economic viability of exploiting the ferromanganese deposits. Extensive work has been carried out in the country especially at NIO under the national projects such as “Survey and Exploration of Polymetallic Nodules” and “Environmental Impact Assessment” (EIA) of nodule mining sponsored by the Department of Ocean Development (Government of India, presently Ministry of Earth Sciences) and the Council of Scientific and Industrial Research since the early 80’s. Studies such as nodule distribution and seafloor characteristics, benthic cycling of nutrients and sediment characteristics, geotechnical properties of sediments,

distribution of benthos, microbial life and biochemical composition, estimation of particle fluxes, chemical and physical characterization of the water column were carried out during the course of the program.

Most of the research on pore fluid has been undertaken in shallow-water marine environments (Grandel et al., 2000, Woulds et al., 2009a, b). A general lack of reliable information on the interstitial water chemistry from deep-sea sediments is generally acknowledged. This imbalance in knowledge is unfortunate, since pelagic sediments cover more than half of the earth's surface and diagenetic processes in these sediments may be very important in global terms. Immense importance of pore water studies in understanding the ocean biogeochemistry resulted in the extensive research mostly in the Pacific and Atlantic oceans by various workers. A number of studies have been undertaken in recent years in the Eastern Equatorial Atlantic, Eastern Equatorial Pacific, the MANOP sites, on the Madeira abyssal plain, on the Nares abyssal plain, in the South Atlantic and in the North Atlantic (Bender et al., 1977; Grundmanis and Murray, 1977; Sayles, 1979; Emerson et al., 1980; Jahnke et al., 1982; Colley et al., 1984; De Lange, 1986) to understand the role of nutrients in early diagenetic processes. First report on the pore water nutrients of the CIB was published by Nath and Mudholkar (1989). Nath and Mudholkar (1989) reported nitrification with intermediate low nitrate and high organic carbon in the mottled zones of the pelagic cores of CIB. The increasing phosphate values with depth were controlled by the mobilization of iron oxyhydroxides. The silica values were high but below the saturation levels of amorphous silica. The low stability of the bottom water in this region enhanced the dissolution of biogenic silica and thus enhanced the values of interstitial silica (Nath and Mudholkar, 1989) leading to the upward diffusive flux of interstitial silica.

The uplift and erosion of Himalaya has caused an enormous volume of sediment to reach the Bengal fan and subsequently the CIB via the Ganges and the Brahmaputra river system. Workers such as Kolla and Biscaye (1973); Rao and Nath (1988); Nath et al. (1989); Debrabant et al. (1993); Fagel et al. (1994), reported that the northern part of CIB receives detrital material derived from the denudation of Himalayas whereas, the southern part receives siliceous pelagic input associated with equatorial divergence at 10°S (Pattan et al., 1992; Caulet 1992; Banakar et al., 1998). The abundance of this terrigenous material decreases towards the south (Aoki and Sudo 1973; Nath et al., 1989; Bouquillon et al., 1990; Cochran 1990; Debrabant et al.,

1993; France-Lanord and Derry., 1993; Fagel et al., 1994; France-Lanord and Derry, 1996) and could be traced till about 8°S (Nath et al., 1989). Based on the chemical and isotopic studies of clay minerals, France-Lanord et al. (1993); Derry and France-Lanord (1996, 1997) suggested that irrespective of clay mineral variations, the sediments were derived only from the Himalayas and that the change in clay minerals are due to different degrees of weathering in the source rocks.

Isotopic studies were carried out on CIB sediments by Fagel et al. (1997) and Dia et al. (1992). Fagel et al. (1997) studied the Sr-Nd isotopes along with major and trace elements of smectite-rich, clay size (< 2μm) samples, bulk sediments, and leachate residues from the CIB to investigate their geochemical evolution during transport in the water column, sedimentation and diagenesis. The CIB region is of special interest because the sedimentation records the interaction between the detrital supply from the Bengal Fan in the north and the biosiliceous input associated with the equatorial divergence in the south. Fagel et al. (1997) identified three major components that contribute to the pelagic clays of CIB. The first component identified by Fagel et al. (1994), was characterized by a homogeneous geochemical signature and a non-radiogenic Nd isotopic composition which traced a detrital Himalayan-derived origin. The two other components display a seawater-derived isotopic composition with global Sr and regional Indian Ocean Nd signatures.

Dia et al. (1992) used Neodymium isotopic compositions of Quaternary marine sediments from the Indian Ocean collected in different physiographic provinces (abyssal plain, ridge, submarine fan, fracture zone and aseismic ridge environments). Dia et al. (1992) concluded that there are large areas in the Indian Ocean which are isotopically homogeneous, although the results also enforce the idea that in marine sediments the continent-derived material exerts an important control on the Nd budget. The Nd values of the CIB sediments were nearly constant both in the eastern and western parts of the Indian Ocean implying mixing between two major inputs: firstly material coming from the erosion of the Indian shield and secondly from the Indonesian arc. Subsequently all the material was then homogenized by the oceanic circulation. Dia et al. (1992) summarized that Nd isotopic composition of the particles can be used to trace the circulation of water masses from Antarctica to northern parts of the Indian Ocean (which are known for their deep waters). Further, they attributed the Nd isotopic variations in the sediments principally due to the pathways of water circulation, and possibly winds, over the Indian Ocean.

In CIB, a few short sediment cores covering a time span of less than 200 ka have been studied earlier mostly for transition metals (Banakar et al., 1991; Mudholkar et al., 1993; Borole 1993 a and b). U-Th series, geochemistry of sediments and growth layers of ferromanganese crusts have been well known after a detailed study by Nath et al. (2005); Pattan et al. (2005); Gupta (2003); Banakar et al. (2003); Gupta (1996); Borole, (1993); Banakar (1990). Arabian Sea sedimentation patterns and the south Asian monsoon variability is well documented for most part of the Arabian Sea (Clemens et al., 1991, Sirocko and Lange, 1991; Naidu, 2004, Naidu and Malmgren, 1995, 1996, 1999, 2005, etc) and the Bay of Bengal (Cullens 1981; Chauhan et al., 2001, 2004; Burton and Vance, 2000; etc) and the CIB (Borole 1993; Gupta et al., 2006; Nath et al., 2007; Pitrowski et al., 2009, etc)

Volcanogenic components have been significant contributors to Indian Ocean sediments throughout the last 150 million years. These volcanogenic components were derived from mid-ocean-ridge volcanism, hotspot volcanism e.g. from the Reunion and Kerguelen hotspots, subduction related volcanism along the Indonesian Arc and landmass volcanism. At mid-ocean-ridge systems, volcaniclastic sediments are only locally distributed and are recorded, within cores that penetrated basement, as volcaniclastic-rich basal sequences. Tephra generated along the Indonesian Arc has been widely distributed across the northern Indian Ocean (Pattan et al., 1999). Landmass volcanism has contributed volcanic components to the Indian Ocean basins since the early Cretaceous, particularly related to rifting events associated with continental break-up. The Reunion and Kerguelen hotspots have been major contributors of tephra to the Indian Ocean throughout their evolution since the early Cretaceous.

It was Vallier and Kidd (1977), who studied the distribution of volcanogenic sediment in the Indian Ocean using DSDP cores, which lead them to hypothesise that the timing and distribution of the volcanogenic accumulations were controlled by changes in sea-floor spreading rates. However, Sykes and Kidd (1994) reviewed the tectonic development of the Indian Ocean and concluded that the timing of accumulations of volcanic components in the Indian Ocean can be related to rifting of continents, formation of new crust at ridge crests and at hotspots, and to landmass volcanism, linked to subduction along the Indonesian Arc. Their work has shown that hotspots' such as Reunion and Kerguelen, have been the dominant source of volcanogenic sediments to the Indian Ocean basins since the Albian (110Ma), being

far more important than the mid-ocean ridges and variations in their spreading rates which was previously thought to exert a major control.

Volcanogenic sedimentation and evidence of hydrothermal signatures in the CIB were studied in some detail by Iyer et al. (1997, 2007); Iyer and Sudhakar (1993); Pattan et al. (1999); Mascarenhas-Pereira et al. (2006) and Nath et al. (2008). Morphological features and the associated volcanic in the CIB seems to be a vulnerable area for tectonic and magmatic activities (Iyer 2005). The basin has been noted to contain a high incidence of oceanic intraplate earthquake zones wherein the earthquakes can be triggered by magmatism due to their association with pre-existing zones of weakness during a phase of re-activation (Bergman and Solomon, 1980).

1.7. Scientific rationale and scope of the study

Metalliferous sediments, massive sulphide deposits and high-temperature vents occur at the major tectonic boundaries in the oceans (Houghton et al., 2004). Hydrothermal deposits have been discovered along the Central Indian Ridge (Herzig and Plüger, 1998; Plüger et al., 1990). Hydrothermal deposits at intraplate seamounts/regions like the CIB are less common although the seamount morphology, associated fracturing and volcanism could favour hydrothermalism (Alt, 1988). The first actual proof of recent intraplate volcanic-hydrothermal activity (~10ka age) in the CIB was provided by Iyer et al. (1997). Iyer et al. (1997) found high concentrations of volcanogenic-hydrothermal materials (vhm) in sediments located at the base of an intraplate seamount. The vhm consisted of ochrous metalliferous sediments, volcanic spherules and glass shards. The radiolaria associated with the vhm suggest a ~10ka age for the hydrothermal episode. Studies have reported the occurrence of volcanogenic material in the CIB (Gupta, 1988; Iyer et al., 1997, 1999; Pattan et al., 1999; Martin–Barajas et al., 1993; Nath and Rao, 1998; see Nath, 2001 for review; Iyer et al., 1997; Mukhopadhyay et al., 1995). Hydrothermal systems are known to play a major role in elemental exchange between ocean and crust through the interaction of circulating seawater with the oceanic crust at various temperatures. But lack of knowledge of occurrence of hydrothermal mineralization at intraplate regions would probably underestimate the elemental budgets. Thus there is scope for studies on intraplate regions of major oceans. This is one attempt to explore the possibility of one such intraplate region within the CIB.

Volcanogenic components in deep-sea sediments in general are ubiquitous and a widespread occurrence of this component is known in CIB (Gupta, 1988; Iyer et al., 1997, 1999; Pattan et al., 1999; Sukumaran et al., 1999; Martin–Barajas et al., 1993; Nath and Rao, 1998; see Nath, 2001). A major debate is about the contributory sources to this volcanogenic ash. One problem in unambiguous source identification is either the ash or the host sediment is not dated. Source identification is heavily based on compositional similarity. But in a preceding work of this study on a dated core has shown volcanogenic tephra of different ages have near similar composition (Mascarenhas-Pereira et al., 2006) posing a question whether there could be areas and episodes other than 3 major Toba eruptions which are contributing sources. Thus, there is an opportunity to improve our understanding of source if the cores with volcanogenic component/tephra are dated.

In view of the above, sedimentological and geochemical investigations were carried out on the sediment cores and surficial sediments from the Central Indian Basin to understand the volcanogenic and hydrothermal mineralization processes prevalent in the intraplate region concentrating mainly on Pleistocene sediments. Emphasis was also laid on studying the coarse fraction of sediments which consists of volcanic ash, micronodules, palagonites and detrital mineral grains in order to evaluate the volcanogenic and hydrothermal alteration processes operating in the area and their role in authigenic mineral formation.

In general, as compared to Pacific and Atlantic, there is a lack of reliable information on the interstitial water chemistry of deep-sea sediments from the Indian Ocean. This paucity of information has lead to a lack of understanding in the diagenetic processes in these sediments. Role of pore water studies in understanding the ocean biogeochemistry resulted in the extensive research mostly in the Pacific and Atlantic oceans by various workers. Some attempts have been made to understand the pore water nutrients of the Central Indian Ocean (Nath et al., 1989). Little is known about the quantification of fluxes of material across sediment water interface in the abyssal sediments of CIB. Since pore water profiles and benthic fluxes are sensitive indicators of organic matter reminerlization process and dissolution of biogenic silica, an attempt has been made to study the magnitude and regional pattern of benthic fluxes through the water-sediment interface via modeling of pore water profiles of the recovered samples. In addition, an attempt was made to see if the benthic fluxes are controlled by seasonal variation in digenetic processes. In general, deep-sea regions

are not believed to undergo seasonal changes, but here there was an opportunity to work on the sediments collected at different time scales and test this hypothesis. Nutrient exchange between hydrothermally altered sediments and seawater is poorly known. Hydrothermally altered sediments could be poor in organic matter and different set of diagenetic reactions may take place in these sediments and it would be interesting to study the benthic fluxes of these sediments.

Significant work has been carried out so far on the contributory sources of the deep sea sediments of CIB (Kolla and Biscaye, 1973; Rao and Nath, 1988; Nath et al., 1989; 1992; Banakar et al., 1998; Pattan et al., 2005; Mudholkar et al., 1993; Fagel et al., 1994, 1997). This study is an attempt to take this knowledge further to understand the influence of local geology and hydrography on the dispersal and distribution of lithogenic material. In addition, a new approach was adopted by performing the mixing calculations of the REE data to quantitatively assess the relative contribution of competing sources.

In view of the above, a study employing various characteristics of host sediments (coarse fraction mineralogy, sedimentology, dating and geochemical studies of pore water, bulk sediments and selective leaches) from two sediment types both in the vicinity and away from the seamounts and fracture zones in the CIB was undertaken to explore the occurrence of submarine volcanic activity and hydrothermalism and also to evaluate the influence of subsurface fluid flow in altering the sediment characteristics and sedimentation history. The approach of this study is different from published literature as a quantitative approach is adopted here in calculating nutrient fluxes across sediment-water interface and the ternary mixing calculations for source contribution.

While broad target areas for this study are to (i) assess the hydrothermal alteration in an intraplate region; (ii) date the Pleistocene volcanic events in CIB, (iii) quantify the temporal and spatial variability in benthic fluxes of nutrients at sediment-water interface in areas with pelagic sedimentation and compare that with those affected by hydrothermal alteration; and (iv) assess the sediment dispersal pattern using geochemistry of lithogenic fraction and employ mixing calculations to estimate the relative contribution of contributory sources, specific objectives are presented in the preface.

To my knowledge, aspects related to quantification are attempted for the first time in this area.

Chapter 2

Materials Methods

To achieve the scientific objectives underlined in the chapter 1, 64 sediment cores were collected mainly from the Central Indian Basin. For size fraction geochemical studies one sample each from the Equatorial Indian Ocean, Arabian Sea and Bay of Bengal were used from NIO's sample repository.

2.1. Sediment cores

A total of 67 sediment cores were used for the present study, the location and water depth of these cores are presented in Table 2.1 and the sampling locations are shown in Fig. 2.1.

For the elemental variability of the lithogenic fraction in the CIB, sediment cores (AAS 61; BC 1 to 26) were collected at a regular spacing of 1 x 1 degree between latitudes 10° and 16°S and longitudes 73.5° and 76.5°E during the 61st cruise of R.V.A.A. Sidorenko (a Russian Research Vessel hired by Government of India) in the year 2003, while for the porewater studies in the basin, in addition to the above 26 cores (AAS 61), data of 15 box cores collected during the baseline study of the Environmental Impact Assessment of polymetallic nodule mining (PMN–EIA) project, sampled at 10°S in 1997 were used.

Eight cores (Cruise ABP 04 & 26: Box cores 26, 25, 28, 20, 30, 19, 34, 35 and 13) collected from north (10°S) to south (16°S) in the CIB along a meridonial transect along 75.5°E longitude (Fig. 2.1) sampled in two seasons viz., austral winter in April 2005 (cruise ABP 04) and austral summer in December 2006 (ABP 26 cruise) were used to study temporal variation in the nutrients in the basin.

Six cores (cruise ABP 04 & ABP 26; Box core 36, 37 and 38) collected during the 4th and 26th cruise of R.V.A Boris Petrov another Russian research vessel were sampled around a seamount in the vicinity of 76°30'E fracture zone in the CIB to study the nutrient variation around the fracture zone. Core BC#37 was collected from the seamount top, core BC#38 was collected from the valley defining the fracture zone, while BC#36 was collected from the flanks of the seamount at 16°S.

In addition to the cores collected in the CIB, sediment cores from different areas, viz., one each from the Arabian Sea (RVG 167/3923, 7°21.6'N, 76°43.1'E, water depth: 1510 m), Equatorial Indian Ocean (AAS 01/ SPC 14, 0°59.7'S, 77°9.3'E, water depth: 4787 m) and the Bay of Bengal (SK 31/4, 15°N, 84°E) were used.

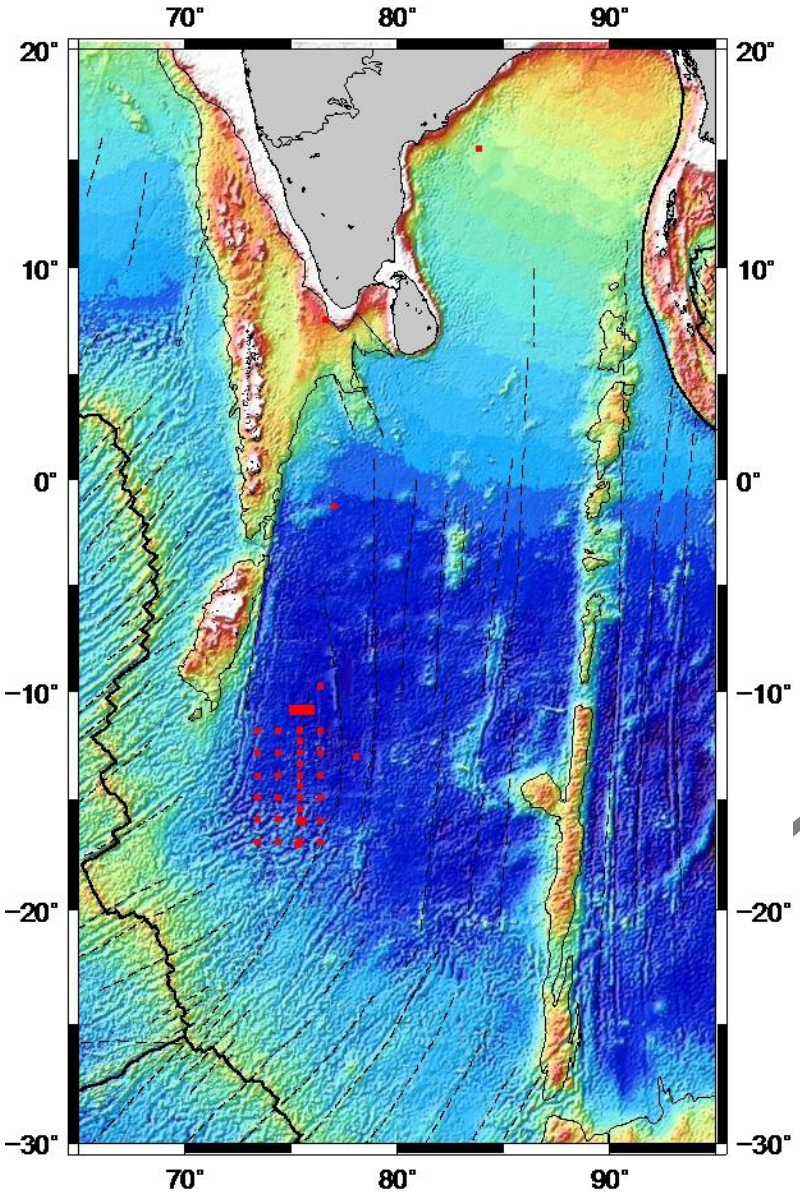

Fig. 2.1: Location map of the cores sampled in the CIB

The sampling station in the Arabian Sea (RVG 167/ 3923) is located between the south of Quilon and the west of Cape Comorin (see Fig. 2.3, Table 2.1). The core collected from the Bay of Bengal (SK 31/4) is located in the middle fan region (Van Der Borch et al., 1974) which has active channels with levees. The area is reported to have been an area of low sedimentation since the beginning of Miocene (Dorrike et al., 1989). The western and the central regions of the bay are characterized by a high sedimentation (20 cm/ky). The core used from the equatorial Indian Ocean was collected during the first cruise of R. V. A. A. Sidorenko (AAS 01/ SPC 14), from a water depth of 4787 m. The area is dominated by calcareous ooze. The core AAS 38/258 represents the siliceous ooze type sediment in the CIB and was collected from a water depth of 5320 m (Table 2.1; Fig. 2.1). The core representing the pelagic clay domain of the CIB (AAS 61/BC 8) was collected during the 61st cruise of R.V.A.A. Sidorenko in the year 2003. The core was recovered from the flanks of a seamount in the vicinity and at the southern end of 76°30′E fracture zone in the CIB from a water depth of 5010 m contain volcanogenic material (Mascarenhas–Pereira et al., 2006) and shows signatures of hydrothermal alteration (Nath et al., 2008).

Fig. 2.2: Photograph of the two sediment sub–samplers (fixed and hand held) used on–board for sub sampling the cores, fixed one designed by Valsangkar (2007).

All the cores collected from the CIB were sampled using a using a box corer (Kastengriefer type) of dimensions 50 x 50 x 50 cm. Colour and lithology of the sediments were noted shortly after the recovery of the core onboard. Careful visual examinations were also made for identifying the presence of turbidites and sediment slumping. For geochemical analysis the entire length of the core was sub-sampled at 2cm interval using manual piston type extrusion (Fig. 2.2.)

2.2. Porewater studies

In order to truly represent the existing sedimentary conditions, all pore fluid analyses must be completed as quickly as possible after sample recovery. Interstitial water values of oxygen may change rapidly when the sediment sample is brought to the surface and exposed to atmospheric conditions. Variations in pressure, pH and the oxidation–reduction potential will in turn cause equilibrium shifts, altering the values of dissolved and solid species. Such changes obscure *in situ* chemical gradients and prevent accurate characterization of the diagenetic processes occurring in pelagic sediments (Setlock, 1979).

A detailed summary of the analytical techniques used in the extraction and analyses of pore fluid parameters is given below:

Porewater extraction

Porewater is extracted using several methods such as hydraulic squeezer (Manheim, 1966, 1968), gas squeezer (Reeburgh, 1967), whole core squeezer (Jahnke, 1988), insitu samplers (Sayles et al., 1975) etc. A refrigerated centrifuge was

used for this work. Sediments for porewater extraction were sub-sectioned from a sub–core from the box core with a dimension of ~12 cm using the subsampling device developed by Valsangkar (2007) (Fig. 2.2). The sub–sampling was carried out at 2cm interval until 10 cm and 5 cm interval from 10 to 20 cm depth. The samples were immediately transferred to the geochemistry laboratory onboard for the extraction of porewater. Sediments were carefully transferred to the centrifuge tubes and were centrifuged at about 5000 rpm in the refrigerated centrifuge at about 2°C. The supernatant water was siphoned off to the plastic bottles. At the end of the separation, the porewaters were filtered with a Millipore filtration unit through 0.42 µm membrane filters. The porewaters were analyzed for nutrients nitrite, phosphate and silicate, mostly on the next day after extraction of porewaters. The basic principle and short description of methods used for analyzing these parameters are mentioned below. Basically, the methods used here are adopted from the standard seawater analyses (Grasshoff et al., 1983).

Pore fluid analysis

pH

Interstitial fluid pH values were measured aboard ship using LABINDIA's µP controlled pH analyzer (PHAN). The electrode potentials were measured with a digital electrometer and standard pH buffers (4, 7 and 9.2 at 25°C) were used to calibrate all measurements. The electrode was flushed with distilled water and porewater sample before taking the subsequent readings. Multiple readings were taken in between the samples to ensure the correctness of the measurements.

Nutrients

Nutrient samples were analyzed on shipboard with manual colorimetric techniques using a spectrophotometer. Nutrients monitored include nitrate, nitrite, phosphate and silica.

- **Nitrate**

Nitrate in seawater is quantitatively reduced to nitrite by heterogeneous reactions involving zinc cadmium or Cu cadmium. Nitrate is quantitatively measured by colorimetry via the formation of an azodye at the wavelength of 543 nm. After

filling the column with cadmium granules, the column was activated by passing 1 liter of NH_4Cl buffer solution with a flow rate of about 25ml for 4minutes. The main standard (potassium nitrate) was prepared by taking 1ml from the standard stock solution (10 µM) diluted to 100ml.

This solution serves as the standard stock for the preparation of working standards. Following this, working standards of 4, 5 and 6 µM concentrations are prepared in 50ml volumetric flask by adding 2ml buffer solutions. Of the 50ml of the standard solution volume, initial 25ml was passed through the column and discarded and the remaining 25ml of the solution was collected into a volumetric flask.

Once the standards have been run, the column was rinsed with 250ml of the buffer solution. Following this, 5ml of porewater was diluted to 25ml with distilled water, added 0.5ml of buffer. This sample solution was passed through the column, discarding the first 10ml and collecting the remaining 10ml of the sample solution. 10–15ml of the buffer solution was passed in between the samples. To the standards and blank solutions, 0.5ml of sulphanilamide was added. After 4 minutes 0.5ml of diamine was added. The absorbance of the colours developed (after 10mins of adding diamine) was measured at 543nm. As the porewater sample volume size was 10 ml, proportional volume of reagents was added (0.25ml).

- **Nitrite:**

The porewater nitrite was estimated on addition of sulphanilamide and diamine to the sample, which form a pink colored azodye complex, and the absorbance of which was measured on a spectrophotometer at 543nm after 15 minutes.

Procedure: To 10 ml of distilled water (blank), working standards (1, 2, 3 µM) and diluted porewater (2 times; 5ml sample + 5ml distilled water) 0.5ml of sulphamilamide was added. After about 4 minutes, 0.5ml diamine was also added to the blanks, standards and samples. The colour of the solution turned pink and the absorbance of this complex was measured after 15 minutes. From these absorbance values, concentration of nitrite in the porewater was calculated.

- **Phosphate:**

The phosphate ions react with acidified molybdate reagent to give phospho–molybdate complex, which is then reduced to a highly colored blue complex by ascorbic acid. The absorbance of the compound is measured using a spectrophotometer.

Procedure: To 10 ml of distilled water (blank), working standards (1, 2, 3 µM) and diluted porewater (2 times; 5ml sample + 5ml distilled water), 0.5ml ascorbic acid (reducing agent) was added. After mixing, 0.5ml of ammonium molybdate reagent was added to the blanks, standards and porewaters. The absorbance of complex was measured at 880nm after 30 minutes. From these absorbance values, concentration of porewater phosphate was calculated.

- **Silicate:**

The determination of silicate ions is based on the formation of yellow silicomolybdic acid, when it is treated with acid molybdate solution. Since this complex is not stable, it is reduced to blue complex by adding oxalic acid and ascorbic acid. Oxalic acid is added to avoid reduction of excess molybdate and to avoid the interference from phosphate ions.

Procedure: 1ml of molybdate reagent was added to 25ml of distilled water (Blank), working standards (5, 10, 15 µM) and porewater (25 times diluted; 1ml sample + 24ml distilled water). After 15 minutes, 1ml of oxalic acid and 0.5ml of ascorbic acid was added and the absorbance was measured spectrophotometrically at 810nm after 30 minutes.

2.3. Sediments

Textural analysis

All the samples were oven dried at a temperature of 60°C. About 10–13g of dried sediment samples were weighed accurately and transferred into a clean 1000 ml beaker. The samples were made salt free by repeated washings using distilled water. Subsequently, the samples were wet sieved through a 63 µm sieve.

Fig. 2.3: Pipette analysis of the studied cores in progress

The sand fraction (>63 µm) retained in the sieve was dried and weighed, while the <63 µm was collected in a 1000ml measuring glass cylinder and subjected to wet sieving again through a 45 µm sieve. The coarse silt fraction (>45 µm) retained on the sieve was dried and weighed, while the mud and silt fraction was collected in a 1000 ml measuring glass cylinder and subjected to pipette analysis (Fig. 2.3; Folk, 1968).

Grain size analysis

Size analyses of <45 µm fraction (silt+clay) were carried out with the help of Laser Particle Analyzer (LPSA) (Fig. 2.4). This technique measures the volume percentage of the different sized particles. The goal of all particle–sizing techniques is to provide a single number that is indicative of the particle size. However, particles are three–dimensional objects for which at least three parameters (length, breadth and height) are required in order to provide a complete description. In case of laser diffraction the diameter of the sphere that yields an equivalent light scattering pattern to the particle being measured is reported. To a good approximation, this corresponds to the sphere of equivalent average cross–sectional area. LPSA provides the volume distribution, showing the volume percentage of particles that have given size. This corresponds to a mass distribution in the case where the particle density is the same for all sizes (www.malvern.com).

The silt+clay component was treated chemically with acetic acid, H_2O_2 and Na_2CO_3 to remove calcium carbonate, organic matter and biogenic silica respectively to represent the lithogenic fraction. 50ml of the samples (<45 µm) from the measuring cylinder was taken in a beaker (after removing the upper 10 cm of <45 µm from the measuring cylinder for clay analysis). To this a total of 100ml of 1:4 acetic acid was added (to remove biogenic carbonate) in part of 50ml each after a

gap of 15 minutes and was left overnight to settle. Next day, these samples were decanted, centrifuged twice to remove the acetic acid present in them. The samples were again centrifuged one more time and washed with minimum of water. 100ml of 3% H_2O_2 was added to the residue and left overnight. This was then decanted; 40ml of Na_2CO_3 was added to dissolve biogenic silica and transferred to 100ml air tight plastic containers that were later kept in a water bath at a temperature of 90°C for 5 hours. The contents were vigorously stirred after intervals of one hour. The suspension was later centrifuged thrice, once with the supernatant and twice with distilled water. These samples were transferred into small plastic bottles and taken for analysis by LPSA. Analyses of different size fraction of <45 µm were determined by using MALVERN Laser particle size analyzer (MASTERSIZER 2000) (Fig. 2.4) at the National Institute of Oceanography, Goa with a Hydro 2000 MU wet sampling accessory using procedure given in Ramaswamy and Rao (2006).

Fig. 2.4: Laser Particle Size Analyzer (LPSA) facility of Geological Oceanography Division, CSIR-National Institute of Oceanography, Goa.

Coarse fraction for volcanic ash studies:

The fractions retained on the 63 and 45 µm sieves were quantified and split into various grain size classes and examined under a binocular microscope. Only glass shards showing no alteration (i.e. coatings of clay minerals) were separated by hand picking. Approximately 0.01gm of the samples were used to represent a particular sample and observed under the high resolution stereoscopic binocular microscope for the identification, quantification and the general description of the coarse fractions. Glass fragments were tested with different liquids of specific gravities (1.492, 1.493, 1.497, 1.512, 1.515 and 1.518) for the determination of refractive index:

Fig. 2.5: Scanning electron Microscope (SEM) at the CSIR-National Institute of Oceanography, Goa

Abundance of shards in the samples was determined in the >63 µm size fraction by visually counting the shards using a binocular microscope. Number of shards v/s depth was plotted to determine the variation of abundance of shards in the core with time. Extensive Scanning Electron Microscopy (SEM) (Fig. 2.5) studies were performed on large (> 150 µm) and small (63–150 µm) grains to examine the grain morphology. SEM studies were carried out using a JEOL JSM–5800LV SEM at the CSIR-National Institute of Oceanography, Goa, India. Operating conditions were 20kV, 55ŋa and were focused (3–5 µm) for accelerating voltage, probe current and beam diameter. Major oxides were analyzed using an Energy dispersive spectrometer (EDS) attachment (OXFORD Link–ISIS EDS) to the SEM. Accuracy of our analytical results is generally better than 7% for K_2O and better than 2% for Al_2O_3 and SiO_2. Errors in accuracy were calculated from the results obtained during repeated analyses of the standard (orthoclase) and on comparison with certified values.

Size fraction separation:

An aspect of study of this thesis is to decipher the size control on mineralogy and geochemistry. For this, the < 45 µm fraction collected in the 1000 ml measuring cylinders was subjected to pipette analysis by which seven size fractions (<1, 1–2, 2–4, 4–8, 8–16, 16–32 and 32–45 µm) were separated using Stoke's law. The finest size fraction was collected first. After each collection of top 10cm of the cylinder, it was made up with water once again, stirred and intended fraction was collected. This was repeated several times until clear water was noticed. After removing the <1 µm fraction, 1–2 µm fraction was recovered. Subsequently, the fractions given in the

above order were recovered. Hence, each fraction could be a true representative of their size.

Organic carbon analysis:

The organic carbon (C_{org}) content of the sediment samples was determined by the wet oxidation method (El Wakeel and Riley, 1957). The principle behind this method is based on the oxidation of organic carbon with chromic acid and titrimetric determination of the oxidant consumed.

About 0.2gm of the powdered salt free sample was accurately weighed out in a boiling tube and 10ml of chromic acid added, using a wide–tipped pipette. The tube was covered with an aluminum foil wrapper and heated in a water bath for 15 minutes. It was allowed to cool and the contents of the tube were transferred into a 250ml conical flask containing 200ml distilled water. About 2–3 drops of ferrous phenanthroline indicator was added and titrated with 0.2N ferrous ammonium sulphate solutions until a pink color just persists. A blank determination was also carried out in the same manner. Then, the concentration of the organic carbon available in the sediment was estimated as: 1ml of 0.2N ferrous ammonium sulphate solutions = 1.15 x 0.6 mg of carbon. The percentage of organic carbon in the sample + 0.6x {(Blank reading – Sample reading)/(Weight of the sample in mg)} x 1.15 x 100. The reproducibility of the organic carbon measurements was checked by running replicates of the sediment samples and it was found to be better than ±5%.

2.4. Elemental analysis

For elemental analyses, Atomic Absorption Spectrometry (AAS), X–Ray Fluorescence Spectrometry (XRF), Inductively Coupled Plasma–Atomic Emission Spectrometry (ICP–AES), and Inductively Coupled Plasma-Mass Spectrometer (ICP-MS) were mainly employed.

Sample digestion for ICP MS, ICP–OES and AAS analysis

Bulk samples, size fractionated sediment samples along with clay samples were decomposed following acid dissolution procedure (Balaram and Rao, 2002) and analyzed for REE and trace metals along with some major elements of the resulting solutions by ICP–MS, ICP–OES, AAS at the National Geophysical Research

Institute, Hyderabad and National Institute of Oceanography, Goa. Geochemical standard (USGS Marine mud standard MAG–1 and Cody shale SCo–1) were used to determine the analytical accuracy. Selective chemical leaching was carried out using hot 50% HCl on 4 sample intervals (following the technique described in Cronan (1976). The residue is expected to contain resistant silicates and aluminosilicates insoluble in HCl (detrital fraction) and sulfides if any. This method is commonly used to assess the hydrothermal component in sediments (Chavagnac et al., 2005) and would allow an easy comparison, however no testing was done using varying concentration of HCl and acetic acid.

Though a large number of leaching techniques are available in the literature, acid based leaching with low pH are found to be suitable for elements like REE (Sholkovitz, 1989; Nath et al., 1994). The leach used here has been adopted elsewhere for assessing the hydrothermal component in sediments (Chavagnac et al., 2005). The leaches were evaporated to dryness and the dried mass was redissolved in ultrapure HNO_3. The bulk, residue, clay sized sediments, size fractionated sediment samples and standards were dissolved using 10 ml of acid mixture containing 6 parts of HF, 3 parts of HNO_3 and 1 part of $HClO_4$ in teflon beakers. The solutions were then evaporated to dryness in a fume hood. Addition of acid mixture was repeated to ensure a complete dissolution of samples. After 10 minutes, 2ml of conc. HCl was added to remove black particles, if present in the sample. A part of this solution was set aside for major element analysis using the AAS and ICP-OES. To the other part of the solution Rh solution was used as an internal standard for analysis by ICP–MS. The bulk standard (MAG–1) was also used to check the accuracy of the leach analyses. Precision and accuracy of the duplicate analyses of USGS reference standard MAG–1 and SCo–1 analyses are presented in Tables 2.2, 2.3 and 2.4. Accuracy was better than 5% for Al, Fe, La, Sm and U, while it was better than 2% for all other elements in case of MAG 1, while SCo–1 analysis showed less accurate readings probably due to sample inhomogeneity. Data shows an excellent precision for most of the elements (better than 6%; Tables 2.2 and 2.3). Since the leaching technique employed here is selective type, the balance between leachates and residues could not be assessed.

XRF

Major elements (SiO_2, TiO_2, Al_2O_3, FeO^T, MgO, CaO, Na_2O, K_2O, P_2O_5) were analyzed by using Axios, PANalaytical X–Ray Fluorescence spectrometer at NIO, Goa. 8gms of wet sample was taken and treated with 1N HCl, followed by several rinsings with distilled water and centrifuging to remove all traces of carbonate solution. The residue was dried in an oven at 60°C. The residue was ground and was once again kept in oven at 110°C. From this, 0.55 mg of this carbonate–free sample was weighed and mixed with 5.5g of dilithium tetraborate and 0.07% Li bromide (Merck) in an agate mortar. The mixture was fused in air on a platinum cell by radio frequency induction heating. The cell was heated to 900°C for 15 seconds to drive off H_2O and CO_2 from the sample, and the temperature was then increased sufficiently above the mixture liquidus to insure complete melting of the sample. Minimum temperatures required for rapid and complete fusion were established by trial and error, and range from 1300° to 1450°C for the studied sediments. A set of 39 Certified Reference Materials (CRN) were used for XRF calibration. The CRM's include twelve sedimentary material of Geological Survey of Japan (GSJ): four sedimentary rocks JCh-1 (chert), JLs-1 (limestone), JSl-1 (clay slate), JSl-2 (clay slate) and eight sediments JLk-1 (lake sediment), JSd-1 (stream sediment), JSd-2 (stream sediment), JSd-3 (stream sediment), JMS-1 (marine sediment), JMS-1 (marine sediment), JSO-1 (soil), JSO-1 (soil). Three United States Geological Survey (USGS) Certified Reference Material QLO-1 (Quartz latite), MAG-1 (marine mud), SGR-1b (green river shale), Chinese stream sediments (GSD 2a -5, 7-23) and Centre national de la recherche scientifique (CNRS) standard Glauconite (Glo).

USGS reference material MAG-1 was used for determining the accuracy. The accuracy was better than 1% for Si, P and Na; 2% for Al and Mn; 5% for Ti, Mg, Ca and K; and 7% for Fe.

Infra-red spectroscopy

Infrared spectroscopic studies were carried out on the <2 µm size clay fraction pellets (pressed with KBr powder) using a Shimadzu 8201 PC at the CSIR-National Institute of Oceanography, Goa.

Mössbauer analyses

The measurements were performed in transmission mode, using a constant acceleration spectrometer (512 cells for unfolded spectra). The source, ^{57}Co in an Rh–matrix was held at room temperature. The absorbers were prepared by mixing the studied material, being in powder form, with BN used as filler. The mixture was gently pressed to a thin disc containing ~ 30mg of the studied sediment per cm^2. All measurements were performed at room temperature. The center shift (CS) is given relative iron metal (–Fe) at room temperature. The measurements were made at Uppsala University, Sweden.

Magnetic studies

Mass specific mineral magnetic parameters such as low and high frequency (0.46 and 4.6 kHz) magnetic susceptibility (χlf and χhf), frequency dependent susceptibility (χfd%=((χlf–χhf)/χlf) x 100), anhysteritic remanent magnetization (χarm), isothermal remanent magnetizations (IRMs of forward and back fields), saturation isothermal remanent magnetization (SIRM) and their ratio parameters (χarm/SIRM, SIRM/χlf, χarm/χlf, SIRM/ARM and S–ratio) were estimated on five sediment samples from core AAS 61/BC 8 at IIG, Alibaug. Low field magnetic susceptibility (χlf), which is measured by Bartinton MS–2B susceptibility meter, shows the concentration of ferromagnetic minerals (such as magnetite and maghaemite) but also sensitive to their grain sizes. Anhysteretic remanent magnetization, which is conventionally expressed as an anhysteretic susceptibility (χarm), is sensitive to the presence of stable single domain ferrimagnetic grains (0.03 – 0.15µm). Anhysteretic remanences were imparted on samples by the application of 100mT alternating field, which is gradually decreased to zero, in the presence of a direct field of 50µT. For imparting anhysteretic remanence, Molspin AF demagnetizer was used and for the remanence measurements Minispin fluxgate spinner magnetometer was used. Isothermal remanent magnetizations (IRMs) were produced in the steps of 20mT, 40mT, 100mT, 300mT and 1000mT (SIRM) by using the pulse magnetizer and the remanences were measured by the Minispin fluxgate magnetometer. SIRM responds to ferromagnetic material in the sample but is not affected by para and diamagnetic minerals unlike magnetic susceptibility. After imparting the 1000mT (SIRM) field, the samples were then subjected to reverse fields

at –20mT , –40mT, –50mT, –60mT, –100mT and –300mT and the corresponding remanences were measured. S–ratio (Bloemendal et al., 1988) indicates relative proportion of magnetite to heamatite component in the samples. Ratio parameters (χarm/SIRM, SIRM/χlf, χarm/χlf) were used to identify the magnetic grain sizes in the samples. Temperature dependent (room temperature to 700°C) magnetic susceptibility experiments for representative samples were carried out by using KLY–2 kappabridge (Azico, Czech Republic).

2.5. Dating and isotopic studies

Biostratigraphy

Age of the sediments was determined using radiolarian assemblages (following Gupta et al., 1996). The >63 μm fraction in each of the 2cm sediment sections was used, and late Quaternary radiolarian index microfossils were identified as described and illustrated in Gupta (1988) and employed for ascertaining the geological ages for the datum levels following Gupta et al. (1996).

Radiometric methods and Isotopic studies:

^{210}Pb and ^{230}Th studies

All the uranium series isotopes reported here were analyzed at CSIR-NIO, Goa. The ^{210}Pb was measured via its daughter nuclide ^{210}Po, using the standard radiochemical procedures. Briefly, about 2 to 3gm of powdered material in the presence of ^{208}Po tracer was brought into complete dissolution by treating with HF, $HClO_4$, HNO_3 and HCl in a teflon vessel. The solution was finally made in 60–70ml of 0.5 to 0.6M HCl, ascorbic acid was added to mask the Fe^{+3} ion in solution. The Polonium isotopes (^{210}Po and ^{208}Po) were then auto-plated onto a 1.5cm diameter silver disc. The plating was carried out for 3–4hrs during which the temperature of the solution was maintained at 65°C. After plating, the silver disc was rinsed with distilled water, dried and alpha activities of Polonium isotopes (^{208}Po and ^{210}Po) were assayed using Silicon surface barrier detector, having sensitive area of 450 mm^2, connected to an EG & G ORTEC Multi–channel analyzer. Uranium–thorium analyses were performed on the same sample solutions, but tracer used was ^{232}U/^{228}Th (Krishnaswami and Sarin, 1976).

^{10}Be studies

^{10}Be was extracted from about 0.5mg sediment through addition of 250 µg Be carrier and subsequent total dissolution in a mixture of HF and H_2SO_4. After an ion exchange column separation, the Be–hydroxide was converted to BeO for accelerator mass spectrometry using the Uppsala 5 MV EN tandem accelerator. Part of the aliquot used for ^{10}Be extraction was used for the analysis of ^{9}Be using ICP–OES at the Department of Analytical Chemistry, Uppsala University, with an instrumental and statistical error of <15%.

Table 2.1: Details of the samples used in the present work

(a) Cores used for surficial variability and porewater studies

Core No	Latitude	Long (°E)	Water depth (m)
Cruise AAS 61			
BC-1	-10	76.49	5355
BC-2RR	-11.00	76.50	5320
BC-3R	-12.00	76.51	5280
BC-4	-13.00	76.50	5360
BC-5	-14.00	76.50	5180
BC-6	-15.00	76.50	4980
BC-7	-16.00	76.50	5070
BC-8	-16.00	75.50	5010
BC-9	-16.00	74.50	5350
BC-10	-16.00	73.50	4900
BC-11	-14.99	73.50	5480
BC-12	-14.99	74.50	5390
BC-13	-15.00	75.50	4840
BC-14	-14.00	75.50	5145
BC-15	-14.00	74.51	5180
BC-16	-14.01	73.51	5120
BC-17	-13.01	73.50	4810
BC-18	-13.00	74.49	5050
BC-19	-13.00	75.49	5070
BC-20	-12.00	75.50	5200
BC-21	-12.00	74.49	5055
BC-22	-12.00	73.50	4900
BC-23	-11.00	73.50	5100
BC-24	-11.00	74.50	5050
BC-25	-11.00	75.50	5300
BC-26	-10.00	75.50	5290

A1/Bc188B	-10.08	76.00	5357
A1/Bc190	-10.17	75.92	5315
A1/Bc193A	-10.17	76.08	5284
A1/Bc194B	-10.00	76.08	5344
A1/Bc197A	-10.01	75.92	5353
T1/Bc159B	-10.00	75.17	5220
T1/Bc181	-10.17	75.17	5280
T1/Bc160A	-10.00	75.34	5291
T1/Bc179A	-10.09	75.26	5180
T1/Bc176B	-10.16	75.34	5236
R1/Bc172	-10.18	75.59	5360
R1/Bc173	-10.01	75.59	5331
R1/Bc166A	-10.09	75.66	5370
R1/Bc169	-10.01	75.75	5384
R1/Bc171	-10.18	75.76	5353
R2/Bc134c	-12.00	76.08	5310
R2/Bc142	-11.92	76.17	5350
R2/Bc145	-12.09	76.00	5252
T2/Bc146	-12.25	75.75	5233
T2/Bc151	-12.33	75.83	5285
T2/Bc153	-12.42	75.92	5290

(b) For seasonal and temporal variability of nutrients in porewaters

Station	**Latitude**	**Long (°E)**	**Water depth (m)**
Cruise ABP 04			
TVBC–26	-9.99	75.50	5338
TVBC–25R3	-10.99	75.49	5292
BC–28	-11.50	75.50	5206
TVBC–20	-11.99	75.50	5120
BC–30	-12.50	75.49	5180
TVBC–19	-13.00	75.50	5089
BC–34	-13.49	75.49	5225
BC–35	-14.50	75.50	5237
TVBC–13	-15.00	75.49	4899
BC–36	-16.03	75.47	5028
BC–37	-16.10	75.43	4252
BC–38	-15.95	75.53	5693
Cruise ABP 26			
SVBC–26	-9.99	75.50	5339
SVBC–25R	-11.00	75.49	5303
SVBC–28	-11.50	75.50	5263
SVBC–20	-11.99	76.49	5223
SVBC–30	-12.50	75.49	5189

SVBC–19	-13.00	76.49	5104
SVBC–34R	-13.50	75.49	5219
SVBC–35	-14.50	75.49	5211
SVBC–13	-14.99	75.49	4894
SVBC–36	-16.03	75.47	5042
SVBC–37	-16.11	75.41	3992
SVBC–38	-15.95	75.53	5642

(c) Elemental geochemistry of size fractions

Station	**Lat**	**Long (°E)**	**Water depth (m)**
AAS 61/BC 8	-16.00	75.50	5010
SK 31/4	15.00	84.00	
AAS 38/258	-12.17	78.20	5320
RVG 167/ 3923	7.35	76.72	1510
AAS 01/ SPC 14	-0.99	77.15	4787

Table 2.2: Accuracy and precision of ICP–OES results

Element (%)	MAG 1	Mean of 2 analysis			Precision %	Accuracy%
Al	8.68	8.22	±	0.137	3.33	5.33
Fe	4.76	4.80	±	0.002	0.08	0.88
Mg	1.81	1.89	±	0.007	0.77	4.61
K	2.95	2.38	±	0.019	1.60	19.20
Na	2.84	3.41	±	0.025	1.51	19.88
Ti	0.45	0.41	±	0.007	3.83	9.03
Ca	1.02	1.03	±	0.048	9.50	1.27
Mn	0.08	0.07	±	0.003	9.44	8.73

Table 2.3: Accuracy and precision of the ICP–MS analysis using geochemical standard MAG 1. All (literature) values (except those marked otherwise) in ppm

Elements	Certified values	This work	Accuracy % (±)	Precision %(±)
Al (%)	8.66 ± 0.16	8.29 ± 0.15	4.28	3.7
Mn (%)	0.076 ± 0.005	0.076 ± 0.0004	0.51	1.03
Fe (%)	4.58 ± 0.42	4.81 ± 0.01	4.89	0.29
V	140 ± 6	136 ± 0.37	2.68	0.54
Cr	97 ± 8	95 ± 0.14	2.52	0.31
Co	20 ± 1.6	20 ± 0.03	1.06	0.29
Ni	53 ± 8	53 ± 0.06	0.71	0.23
Cu	30 ± 3	30 ± 0	0.17	0.01
Zn	130 ± 6	130 ± 1.3	0.36	2.01
Sr	150 ± 15	145 ± 0.8	3.61	1.11
Y	28 ± 3	27.81 ± 0.21	0.67	1.52
Zr	130 ± 6	125 ± 0.17	3.96	0.27
Ba	480 ± 41	473 ± 2.88	1.43	1.22
La	43 ±	41 ± 0.33	4.33	1.62
Ce	88 ± 9	85 ± 0.31	3.62	0.74
Pr	9.3 ±	9.02 ± 0.03	3.04	0.71
Nd	38 ± 5	37 ± 0.2	2.36	1.09
Sm	7.5 ± 0.6	7.81 ± 0.09	4.13	2.43
Eu	1.5 ± 0.14	1.52 ± 0.02	1.37	2.17
Gd	5.8 ± 0.7	5.68 ± 0.06	2.1	2.01
Tb	0.96 ± 0.09	0.97 ± 0	1.2	0.31
Dy	5.2 ± 0.3	5.19 ± 0.11	0.19	4.39
Ho	1.02 ± 0.1	1.03 ± 0.02	0.78	4.67
Er	3 ±	2.94 ± 0.01	2.08	0.58
Tm	0.43 ±	0.43 ± 0.01	0.35	4.9
Yb	2.6 ± 0.3	2.61 ± 0.01	0.31	0.69
Lu	0.4 ± 0.04	0.39 ± 0.01	1.5	4.06
Hf	3.7 ± 0.5	3.81 ± 0.06	2.91	3.13
Pb	24 ± 3	24.05 ± 0.17	0.21	1.44
Th	11.9 ± 1	12.25 ± 0.28	2.98	4.51
U	2.7 ± 0.3	2.83 ± 0.07	4.78	4.81

Table 2.4: Accuracy and precision of analysis done by ICP–MS. Standard reference material used SCo–1. All values (literature) in ppm.

Element	Certified values			Mean of 2 analyses			Accuracy (±)	Precision % (±)
Li	45	±	3	44	±	0.33	2.88	1.49
Be	1.8	±	0.2	1.85	±	0.01	2.56	1.30
Sc	11	±	1	12	±	0.36	9.77	5.88
Ti %	0.38	±	0.039	0.36	±	0.001	5.34	0.28
V	130	±	13	130	±	3.50	0.13	5.38
Cr	68	±	5	58	±	0.57	14.42	1.94
Mn	410	±	30	401	±	4.40	2.16	2.19
Co0	11	±	0.8	10	±	0.01	11.37	0.14
Ni	27	±	4	24	±	0.04	12.80	0.34
Cu	29	±	2	27	±	0.23	5.55	1.68
Zn	100	±	8	77	±	1.71	22.69	4.42
Ga	15	±	3	14	±	0.12	8.23	1.67
Rb	110	±	4	111	±	1.17	0.93	2.11
Sr	170	±	16	173	±	2.95	1.94	3.41
Zr	160	±	30	134	±	7.15	16.50	10.70
Nb	11	±	3	7.38	±	0.75	32.91	20.53
Ba	570	±	30	555	±	2.15	2.71	0.78
La	30	±	1	30	±	0.16	0.88	1.02
Ce	62	±	6	57	±	0.14	7.31	0.47
Pr	6.6	±	0.9	6.31	±	0.04	4.47	1.11
Nd	26	±	2	26	±	0.13	0.12	1.00
Sm	5.3	±	0.3	5.31	±	0.03	0.09	0.98
Eu	1.19	±		1.25	±	0.01	5.34	1.04
Gd	4	±		4.41	±	0.04	10.30	1.63
Tb	0.64	±		0.71	±	0.02	11.25	4.21
Dy	4.2	±	0.5	4.13	±	0.07	1.79	3.49
Ho	0.97	±	0.06	0.83	±	0.01	14.74	3.39
Er	2.5	±	0.4	2.58	±	0.07	3.18	5.47
Tm	0.42	±	0.1	0.38	±	0.01	10.71	2.67
Yb	2.27	±	0.24	2.26	±	0.01	0.66	0.44
Lu	0.34	±	0.03	0.35	±	0.01	4.12	3.39
Pb	31	±	3	14.99	±	1.08	51.65	14.41
Bi	0.37	±	0.07	0.35	±	0.01	4.86	6.25
Th	9.7	±	0.5	9.08	±	0.37	6.35	8.04
U	3	±	0.2	2.806	±	0.10	6.47	7.34

Chapter 3

Metalliferous sediments recovered from the seamount flank in the vicinity of a fracture zone

3.1. Introduction

Hydrothermal mineralization of various types has been frequently found at or near actively spreading mid–ocean ridges (e.g., Rona, 1984). Hydrothermal precipitates are plume derived hydrothermal material which is laid down with detrital material via the water column as deep sea sediment (Marchig et al., 1999). The association of metal–enriched sediments with mid–ocean ridge spreading centers has been established since the 1960's (Boström and Peterson, 1969; Bender et al., 1971). Boström and coworkers (1969) invoked volcanic emanations and deposition of metal–rich phases on ridges to explain the observed distribution of metalliferous sediments. Other evidences support the hypothesis of metal–rich emanations from ridge crests despite the lack of direct observation of hydrothermal venting (Mills and Elderfield, 1995). The dispersion of metalliferous sediments away from the ridge axis could be explained by precipitation of particles within the hydrothermal plumes that formed above the vents, advecting via ambient currents, and settling to the seafloor (see Feely et al., 1987 for example). The sediments near the mid–ocean ridges (e.g., East Pacific Rise, EPR) are strongly enriched in Fe and Mn along with other transition metals in comparison with normal pelagic sediments (e.g., Boström and Peterson, 1966). Lisitzyn and Gurvich (1987) reported the occurrence of metalliferous sediments at Rodriguez Triple Junction, Indian Ocean with Fe and Mn contents reaching to about 25 and 5 % respectively. Metalliferous sediments are also reported from Trans Atlantic Geo–Traverse (TAG) hydrothermal field on Mid–Atlantic Ridge (MAR), Southeast Pacific; from the northern part of the East Pacific Rise; Juan de Fuca Ridge; Indian Ocean; and the best known metalliferous sediments are in the Red Sea (Gurvich, 2006). However occurrence of metalliferous sediments (hydrothermal origin) is rare in abyssal plains or at intraplate volcanic regions.

CIB sediments were studied in the past for several aspects related to provenance, diagenesis and sedimentary processes (Kolla and Biscaye, 1977; Rao and Nath, 1988; Nath and Mudholkar, 1989; Nath et al., 1989, 1992, 2005, 2008, 2013; Banakar et al., 1991, 1998; Dia et al., 1992; Borole, 1993; Debrabrant et al., 1993; Fagel et al., 1994; Fagel et al., 1997; Pattan and Jauhari, 2001; Pattan et al., 2005; Valsangkar, 2011). Also some studies have reported the occurrence of volcanogenic material in the Central Indian Basin (Gupta, 1988; Iyer et al., 1997, 1999; Pattan et al., 1999; Martin–Barajas and Lallier–Verges, 1993; Nath and Rao, 1998; see Nath,

2001 for review), but signatures for hydrothermal component in the CIB sediments were only reported based on the presence of magnetite spherules (Iyer et al., 1997), and aluminium spherules (Iyer et al., 2007) with little effect on bulk chemistry of sediments. Here, we report the occurrence of sediments of metalliferous nature in an intraplate seamount environment. Multiple geochemical tracers have been utilized in this study to characterize the different source components and to estimate their relative contribution to the sediments recovered from the flank of a seamount in the CIB, lying in the proximity of the 75°30'E fracture zone. Presence of volcanogenic glass shards, pumice and palagonitic material possibly of intraplate volcanic origin in the sediments near the same seamount has been reported (Mascarenhas–Pereira et al., 2006).

3.2. Sampling locations

Two short sediment cores AAS 61/BC 8 and S657 were used in the present study. Core AAS 61/BC 8 was collected using a large box corer (50 x 50 x 50cm) at 16°S and 75°30'E from the flanks of a seamount from the CIB along the southern end of the 76° 30'E fracture zone from a water depth of 5010m (Fig. 3.1) during the 61st cruise of R.V.A.A Sidorenko in the year 2003. The core was sampled from pelagic red clay sediment domain (see Nath et al., 1989 for sediment types in CIB). Core S657 was retrieved from the base of a seamount at 14°S and 75.935°E, water depth of 4440 m and ~50 km from the Triple Junction Trace (Fig. 3.1).

3.3. Results and Discussion

Results and discussion mainly pertain to sediments from a seamount flank (Core AAS 61/BC 8), the seamount which is in proximity to 76°30'E fracture zone. Major and minor evidences for the presence of hydrothermal component are presented, quantified using selective leaching technique and mixing model calculations. Geochemical discriminatory ratios and plots were used where necessary. Possible processes responsible for the presence of metalliferous component are also discussed. For the discussion of reporting the presence of aluminium–rich material, material from other locations from within the CIB are also used to argue for a widespread distribution of metalliferous component in this intraplate region. Major, trace and REE data for the bulk sediments are presented in Table 3.1 and those of

leach (hot 50% HCl) and residues are shown in Table 3.2. Lithology of the core is shown in Fig. 3.2, and the downcore variations of some elements are shown in Fig. 3.3.

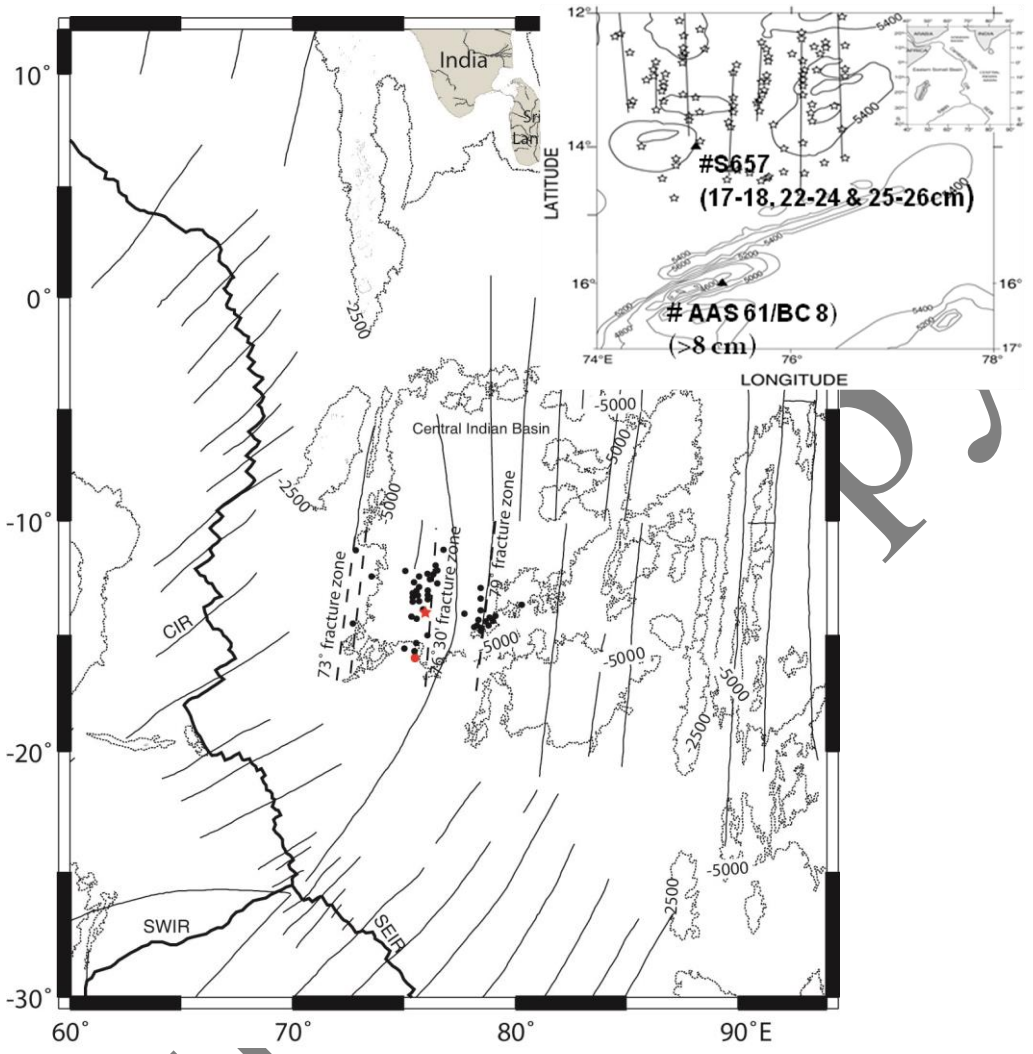

Fig. 3.1: Tectonic map showing the fracture zones and present day ridge axis along with the location of seamounts, which are shown in solid circles. The seamounts (black dots) are mostly aligned along eight chains with some isolated edifices. The studied sediment cores (AAS 61/BC 8 shown as a red dot and core S657 shown as a red star) are marked on the map. The location of the studied cores falls close to the cluster of seamounts in the vicinity of fracture zone. The seamount distribution is from Das et al. (2005).

3.3.1. Depositional change

The sediments in the core show two subsections (units) based on color, while unit 1 (0–6cm bsf) show a light brown color, unit 2 (6–20cm bsf) exhibits a dark brown to black coloration (Fig. 3.2). The coarse fraction (>63 μm) show an abundance of radiolarians in unit 1, which gradually decreases in abundance until 8 cms bsf, leading to complete absence in unit 2 (Fig. 3.2). The transition from pelagic to indurated sediment is marked by the absence of radiolarians and the presence of

ichthyoliths (Fig. 3.2). Glass shards are present throughout the core, but are abundant in unit 2 (Mascarenhas–Pereira et al., 2006). Palagonitic grains were present throughout the core with colors ranging from white, yellow to brown and with a waxy luster. The number of palagonitic grains increase with depth with a concomitant decrease with size. Biostratigraphy and radiometric dating has shown that the unit 1 is younger than 180kyrs (Mascarenhas–Pereira et al., 2006).

The elemental concentrations also show a change with the depositional environment at about 6–10cm bsf (Fig. 3.3; Table 3.1). This steep change in concentration seems to be the transitional zone between the volcanogenic and pelagic sedimentation. Elements such as Th, Ba, Cu and Ni are abundant in the surface layers and decrease in concentration at depths, while other elements such as Hf, Zr and Fe, are low in abundance at the surface and increase in concentration downcore.

Organic carbon also shows a change in depositional environment, with surface organic carbon content of 0.18% (Fig. 3.3) dropping down to below detection concentrations from a depth of 4cm bsf. This suggests that no redox mobilization of Fe and Mn has taken place and the primary depositional signals are preserved (see Kuhn et al., 2000). This is important here as Fe and Mn contents have been used here as diagnostic tools of depositional environment in the following sections of the paper.

3.3.2. Identification of source

3.3.2.1. Bulk chemistry and interpretation of mineral associations

The distribution of Fe, Mn and their ratios in core AAS 61/BC 8 is shown in Fig. 3.3. Boström and Peterson (1969) proposed the index; 100*Al/(Al+Fe+Mn) to differentiate metalliferous sediments from pelagic sediments. According to them, near–field hydrothermal sediments should exhibit metalliferous sediment index (MSI) values of <10%, while background pelagic sediments with no hydrothermal input should exhibit MSI values >50%. All the sediment intervals in AAS 61/BC 8 have MSI <47%, with unit 1 having an average MSI value of 45% and unit 2 having an average MSI value of 41%. This observation is important as it demonstrates that all the sediment intervals in this core have received hydrothermal input which we try to characterize in the following sections.

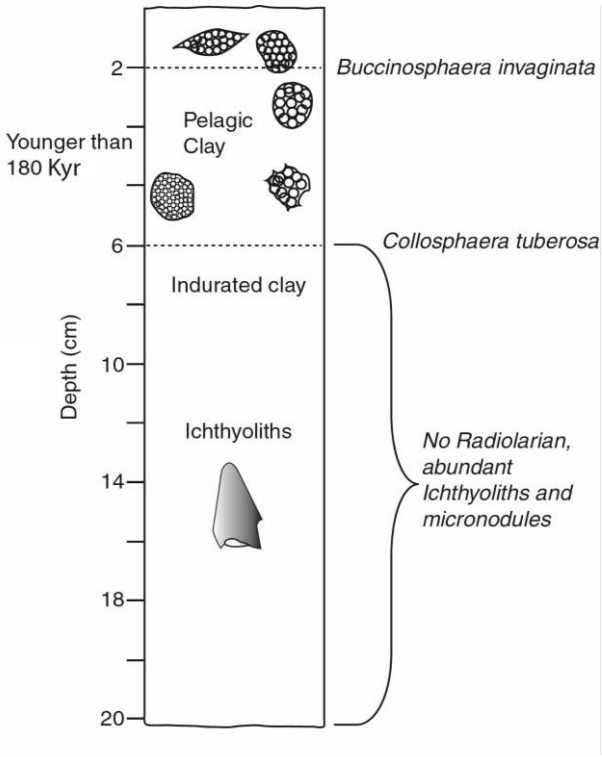

Fig. 3.2: Litholog of AAS 61/BC#8. The top 6cms are pelagic clays with radiolarians and the 6–20cm section is indurated clay with plenty of ichthyoliths.

Although the measured metalliferous sediment index can provide to be a useful tracer of the presence or absence of hydrothermal input to a pelagic sediment core, it does not necessarily provide any sensitive indication of the proximity of the vent site from where the hydrothermal input is received (German, 2003). The Fe/Mn ratio varies from 4.47 at the surface to a maximum of 6.23 downcore (Table 3.3, Fig. 3.4). The possible explanation for this trend could be changes in the type of hydrothermal activity over time, which may have resulted in a higher Fe/Mn ratio due to the abundance of iron rich hydrothermal precipitates. We have used Fe_2O_3/Al_2O_3 ratio as an indicator of amount of hydrothermal material in the core (Marchig et al., 1999). Fe was not remobilized in the analyzed sediments because reduction never reached the level necessary for Fe mobilization. The Fe_2O_3/Al_2O_3 ratio shows an increase in unit 2. Therefore the amount of hydrothermal component is inferred to be greater in older sediments. The Mn concentrations are higher in unit 1 compared to unit 2 and are comparable to hydrothermal sediments associated with off–axis volcanism in Peru basin (Marchig et al., 1999) and metalliferous sediments from DSDP cores 82, 83 and 92 (Donnelly, 1980; Gurvich et al., 1995). This is consistent with decoupling of Fe precipitation and deposition on axis as both sulfides and oxides of Mn precipitation away from the source of venting leading to higher Mn concentration and concomitantly lower Fe/Mn ratios in ridge flank (≤300km off–axis) metalliferous sediments (German et al., 1999). Therefore, if we assume that all Mn is of non–crustal origin and calculate the excess Fe/Mn from its crustal value, then unit 2 (5.31 to 6.23) shows higher values compared to unit 1 (4.47 to 4.71), indicating a higher hydrothermal component in the basal sediments.

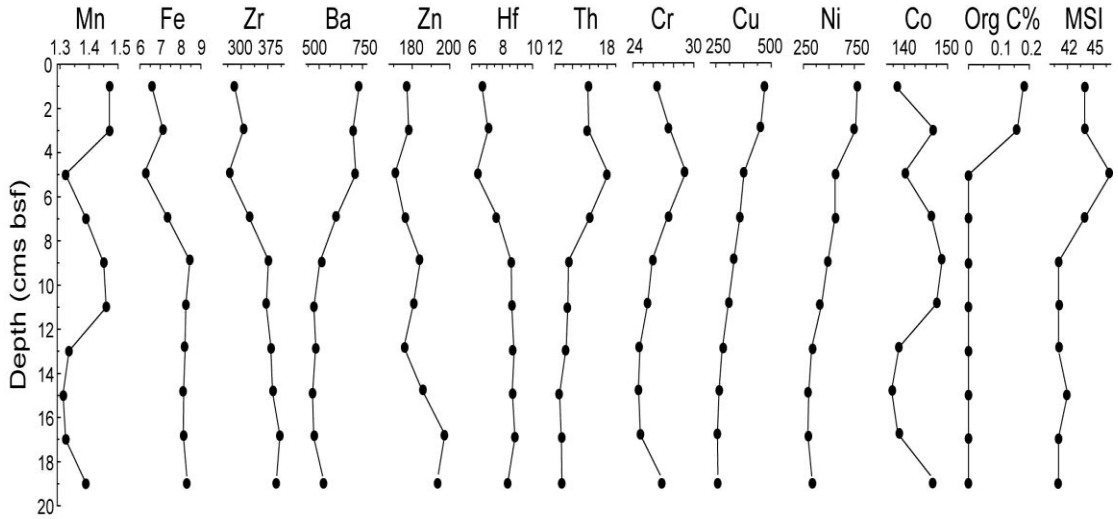

Fig. 3.3: Downcore variation of Fe, Mn, organic carbon and MSI in bulk sediments showing a change in elemental concentration at the boundary from pelagic to volcanogenic hydrothermal sedimentation at 6–10cm. (all values in ppm)

We have also compared the Fe/Mn ratio of our sediments with those of ancient and recent metalliferous sediments (Fig. 3.4). There is a clear difference between the ridge flank and near field metalliferous sediments. The Fe/Mn ratios of the ridge flank have values between 3.4 and 11.6, while the near field metalliferous sediments have values ranging from 17.08 to 1340. Plume particulates however have intermediate values of 8.54 to 40.81. The sediments of AAS 61/BC 8 have Fe/Mn values ranging from 4.47 to 6.23 with an average of 5.52 and correlate with the values found on ridge flank metalliferous sediments. The Fe, Mn contents and Fe/Mn ratios correspond with those found in Central Indian ridge sediments and Fe oxides from the EPR and north Fiji basin of hydrothermal nature (Table 3.3 and 3.4; Fig. 3.4; Walter et al., 1986; McMurtry et al., 1991) implying the presence of a hydrothermal component in our sediments.

Iron is present in a significant amount in the fraction soluble in HCl (~86%). Studies have shown that Fe from minerals like goethite and clay minerals of the smectite group can be stripped by HCl attack. Therefore the relatively high iron content in the HCl soluble phase indicates the high concentration of non–detrital iron bearing minerals. In a ternary plot of Al–Fe–Mn, our bulk data fall in the field of Bauer deep metalliferous sediments (Fig. 3.5).

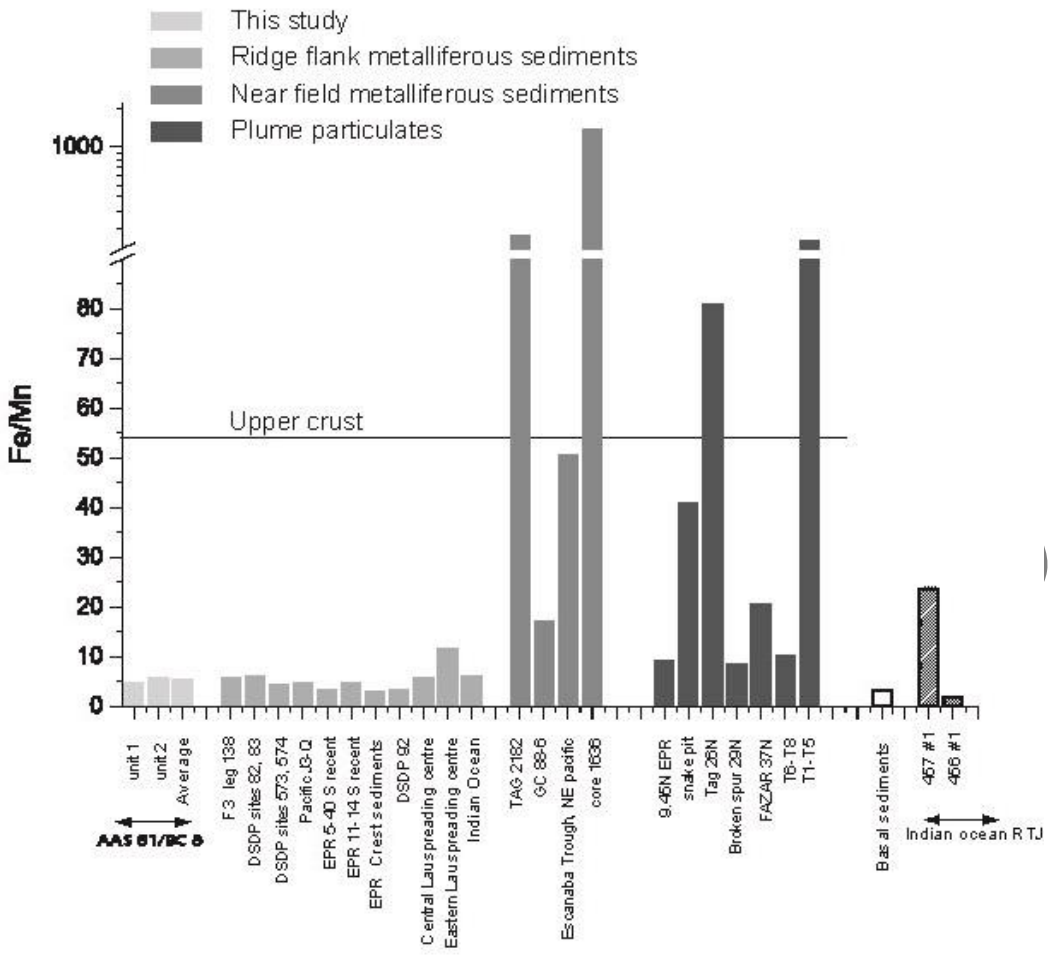

Fig. 3.4: Fe/Mn ratio of AAS 61/BC 8 is compared with metalliferous sediments form ridge flank as well as near field sediments along with plume particulates. (The literature data for Fe/Mn ratios is taken from Gurvich et al., 1995; Donnelly, 1980; Jarvis 1985; Lisitzin et al., 1992; Cherkashev, 1992; Li, 2000; Cronan, 1976; German et al., 1993, 1995, 1997, 1999; Barrett et al., 1987; Hodkinson and Cronan, 1991; James et al., 1995; Boström and Peterson, 1969; Sherrell et al., 1999; Ludford et al., 1996 and Mitra et al., 1994)) Fe/Mn ratios in our sediments are similar to those of ridge flank metalliferous sediments. Conversely, the near field metalliferous sediments and plume particulates have higher Fe/Mn ratios compared to the ridge flank metalliferous sediments.

Discriminating the bulk and residue

Two major features stand out in the elemental composition of bulk and residue data. In general the sediments have low silica compared to CIB sediments (Nath et al., 1989) and high Fe content suggesting a ferruginous nature. Si/Al ratio in bulk sediments is ~2.8, which is less than that reported for typical quartz mineral/biogenic silica (>5, Ziegler et al., 2007), while the residue has a higher ratio of Si/Al (~4). This is consistent with the mineralogy of the core which has low siliceous skeletal remains with dissolution effects seen on some of the radiolarians (Mascarenhas–Pereira et al., 2006; Nath et al., 2008). However Fe/Si ratio of the bulk (0.35–0.48) is comparable to

authigenic Fe rich smectites associated with hydrothermal system in other areas (Central Pacific, Ziegler et al., 2007; DOMES area in North Pacific, Hein et al., 1979). The Na/K ratio in leach residues range between 0.32 and 0.37 and closer to ~0.35 assigned to phillipsite (Kastner, 1979; Ziegler et al., 2007) and is consistent with the volcanogenic–hydrothermal content in unit 2 (Mascarenhas–Pereira et al., 2006; Iyer et al., 2007). Authigenic phillipsite is common in deep sea sediment of every ocean. Commonly associated materials are clinoptilolite, palagonitic glass, smectite, iron and manganese oxides and hydroxides, and locally barite (Boles 1977). Phillipsite has been found in several localities of hydrothermally altered oceanic crust. Alt et al. (1998) show that phillipsite with smectite was produced by low temperature alteration of boninite and andesitic flows and breccia of the upper 700 m of forearcs in the western Pacific.

X–ray diffraction studies have shown that the sediments contain a mixture of quartz, plagioclase feldspars, illite, alteration mineral smectite and authigenic silicate such as zeolites (mainly phillipsite). Earlier studies have shown that the CIB sediments contain illite, chlorite and kaolinite mainly derived from turbiditic currents from Ganges–Brahmaputra through Bengal Fan (Rao and Nath, 1988; Debrabrant et al., 1993), smectite derived from the weathering of basinal basaltic rocks; with presence of both Al–and Fe–rich montmorillonites (Rao and Nath, 1988). Phillipsite and clinoptilolite are major

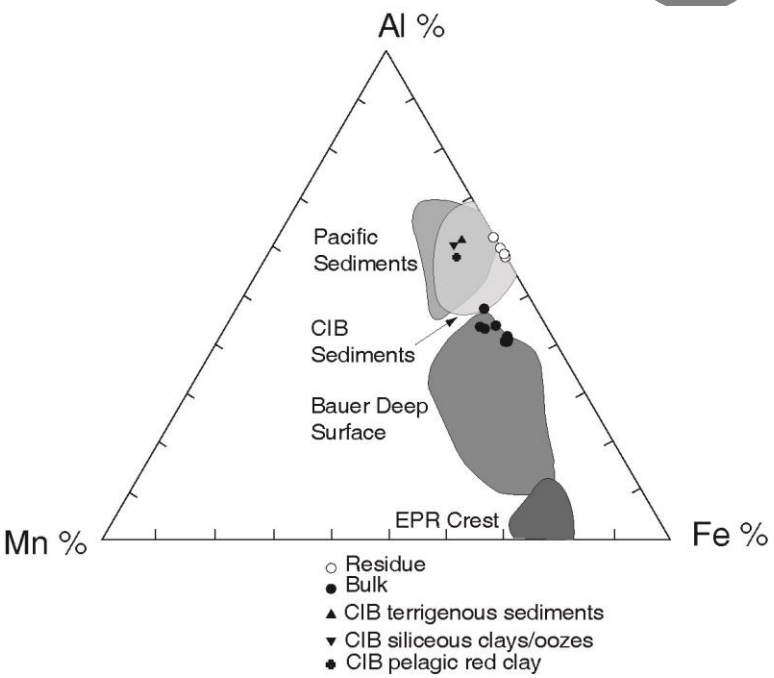

Fig. 3.5: Ternary plot of Al–Fe–Mn illustrating the compositional similarity of bulk sediments to Bauer deep metalliferous sediments. Compositional fields of CIB (Borole, 1993), Pacific and EPR sediments (Plüger et al., 1985 and references therein) along with mean composition of 3 major sediment types in CIB (Nath et al., 1989) are shown.

zeolitic minerals present in CIB sediments (V. P. Rao and B. N. Nath, unpublished data). In the following section on infra–red spectroscopy studies, the presence of nontronite, ferruginous smectites and beidellites in these sediments is also shown.

Two x–y scatter diagrams (Al_2O_3 versus Fe_2O_3 and K_2O versus Al_2O_3), and one ternary diagram (A–CN–K) are plotted to infer the mineralogy (Figs. 3.6a and b). Literature values of chemical composition for clay minerals (kaolinite, smectite, illite and chlorite from Grim, 1968 and references therein), plagioclase, zeolites (Deer et al., 1967 and references therein) in addition to Al–Bediellite and nontronite (Aoki et al., 1996) and authigenic Fe–montmorillonite of hydrothermal origin (McMurtry and Yeh., 1981) are used as possible sources. In addition, chemical data on separated clays from the distal Bengal fan (Aoki et al., 1991) are also included.

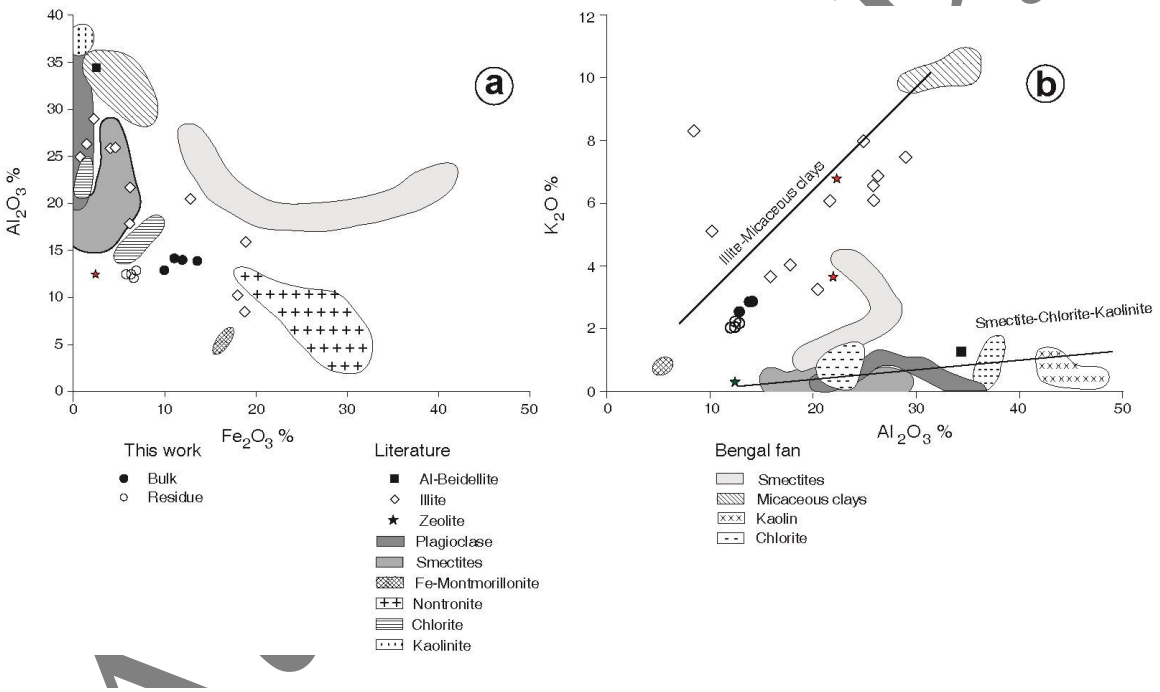

Fig. 3.6: Discriminating source using composition of sediments a) Fe_2O_3 versus Al_2O_3 plot and b) Al_2O_3% versus K_2O%. The plots illustrate that the bulk sediments are a mixture of variable proportions of Fe–rich and Al–rich end members. References of literature data are given in the text.

In the Al_2O_3 vs. Fe_2O_3 plot (Fig. 3.6 a), the bulk sediments fall in between Fe–rich fields of Fe–montmorillonites, nontronites and Bengal fan smectites on one side and Al–rich end–members of smectite, beidellite, micaceous clays from Bengal fan, chlorite, zeolite and plagioclase on other. This could be accounted by the presence of a mixture of variable proportions of Al_2O_3 supplied by illite, plagioclase, smectite and zeolites and Fe_2O_3 contributed by nontronite and Fe–montmorillonite. The residue plot closer to the smectites and micaceous clays of Bengal Fan as compared to the

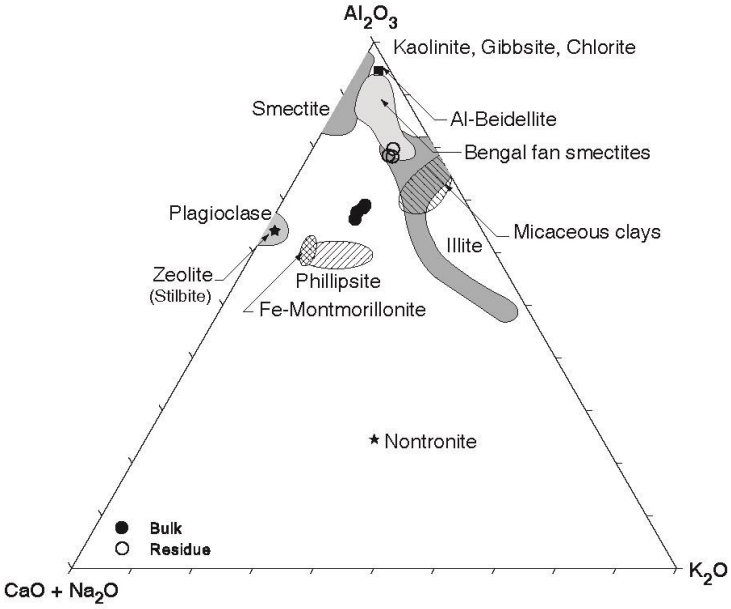

Fig. 3.7: Al_2O_3–($CaO+Na_2O$)–K_2O diagram shows mixing between zeolite, plagioclase and Fe–smectites on one side and illite, Al–rich beidellite, micaceous clays from Bengal Fan, kaolinite and chlorite on other. Residue exhibits reduction of Ca and Na and compositional similarity with micaceous clays and smectites of Bengal Fan and illites

bulk indicating the removal of Fe from the authigenically formed nontronites and Fe–montmorillonite from the bulk sediments. This is also manifested by the Fe/Al ratio of bulk (>1.02) being more than the residue (<0.61). The Fe/Al ratio of residue in the surface sediments approaches the value of PAAS (~0.51). The source composition mainly of aluminosilicate fraction is further constrained from the K_2O and Al_2O_3 plot (Fig. 3.6 b), wherein our sediment data plot between two trend lines, first defining illite, Bengal Fan micaceous clays and the other with overlapping compositional fields of plagioclase, smectite, chlorite, kaolinite, beidellite and zeolites. Thus, the aluminosilicates in these sediments may reflect the mixing of these two groups of mineral sources. The residue data fall close to bulk data with slight reduction in K and Al values

In the ternary diagram of Al_2O_3 – ($CaO+Na_2O$) – K_2O (Fig. 3.7), the bulk sediment data are sandwiched between fields defining zeolite, plagioclase and Fe–smectites on one side and illite, Al–rich beidellite, micaceous clays from Bengal Fan, kaolinite and chlorite on other. The bulk sediments exhibit a loss in $CaO+Na_2O$ on leaching with hot 50% HCl and a concomitant gain in Al_2O_3 content. The bulk sediments are apparently stripped off of CaO and Na_2O from the Fe–montmorillonite, phillipsite and plagioclase with the residue exhibiting compositional similarity with Bengal Fan smectites.

Trace elements

Vanadium along with phosphorus is believed to be incorporated from hydrothermal fluids into hydrothermal iron oxyhydroxides during their formation (Feely et al., 1998; Edmonds and German, 2004 and references therein). V/Fe ratios (Table 3.3) in unit 1 (0–8cms bsf) of BC 8 are lower (0.0020–0.0022) than those of unit 2 (0.0026–0.0029) and close to V/Fe ratios of younger plume particles in the Rainbow hydrothermal field (Edmonds and German, 2004). Relatively higher values in unit 2 sediments suggest the occurrence of past hydrothermal activity through the sorption of V onto Fe–oxyhydroxides

Considering that the Co and Zn in deep–sea marine sediments are mostly derived from particle scavenging in the water column, we have used Co/Zn ratios to discriminate the sources, similar to that adopted for Fe–Mn oxides (e.g., Toth, 1980; Nath et al., 1997). Analytical data on bulk sediments (AAS 61/ BC 8 core) studied here show that Co/Zn ratio (0.70 to 0.83, Table 3.3), fall close to the value for Fe–Mn oxides of mixed hydrothermal hydrogenous origin from the Rodriguez Triple Junction (RTJ) in the Indian Ocean (Nath et al., 1997).

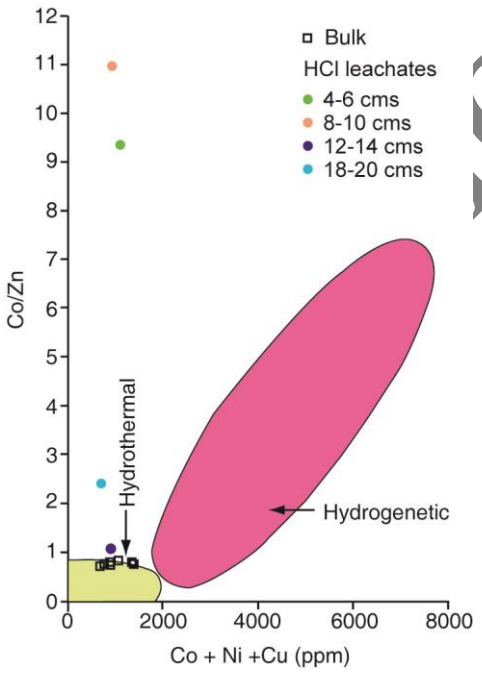

Fig. 3.8: Co/Zn versus Cu+Ni+Co content (Toth, 1980, modified by Nath et al., 1997a). While the data for all bulk sediments fall in the hydrothermal field, leach data for only unit 2 sediments show hydrothermal signatures. Consistent with their pelagic nature, unit 1 sediments fall away from hydrothermal field.

The presence of hydrothermal component is also confirmed from the scatter plot of Co+Ni+Cu versus Co/Zn (Toth, 1980). Co+Ni+Cu values of bulk sediments lie between 500 and 1500 ppm and plot very close to the hydrothermal–hydrogenetic boundary line (Fig. 3.8, modified from Nath et al., 1997). Although the bulk samples show no differentiation with respect to Co/Zn ratio, the HCl soluble leach phase is clearly differentiated with sediment depth.

Data for the HCl leachates of unit 1 (4–6 and 8–10 cm) plot away from the hydrothermal–hydrogenetic fields with Co/Zn values between 9 and 12, while those of unit 2 (12–14 and 18–20 cm) lie closer to the hydrothermal– hydrogenetic

boundary. This is consistent with the variable sources for Co and Zn, while Co is a typical hydrogenous element enriched in hydrogenous precipitates scavenged from seawater, Zn can be derived from a hydrothermal source (Toth, 1980; Nath et al., 1997). Zinc enrichment like the one mentioned here in unit 2 is similar to its occurrence in other hydrothermal clays. The mean Zn/Fe ratio (~0.0024) is comparable to those found in sediments of volcanogenic–hydrothermal origin from RTJ and Fe oxides from the north Fiji basin (Table 3.4, Kuhn et al., 2000; McMurtry et al., 1991) and fall in the range of ERP Fe–Mn oxides (Plüger and Stoffers, 1985), TAG nontronite (Severmann et al., 2004) as well as CIR sediments (Wälter at al., 1986). Extremely high Zn values reported from TAG hydrothermal field (Severmann, 2004) were attributed either to the presence of sphalerite or directly associated with the clays, or alternatively with a remnant amorphous mineral phase (Severmann, 2004).

Cave et al. (2002) have used core top Cu/Fe ratios to demonstrate a decrease down–plume away from the Rainbow hydrothermal field. The sediments sampled ~2 km from the vent site have ratio of 27 x 10^{-3} and the furthest sediment sample at ~25 km having a ratio of 6 x 10^{-3}. This was attributed in the past by Trefry et al. (1985) who conducted a similar study on particulate Cu/Fe of the TAG hydrothermal plume to preferential settling of sulfidic material, relative to lower–density oxyhydroxide material within the dispersing neutrally buoyant plume.

Uranium concentration in these sediments is close to the upper crustal value 2.8 ppm (Taylor and McLennan, 1985). However within the error limits, unit 2 sediments show relative enrichment consistently throughout the section (Table 3.1). U enrichment has been frequently reported for metalliferous sediments from the mid–ocean ridge hydrothermal systems in the past (German et al., 1995 and references therein). Enrichment of U in hydrothermal sediments is either attributed to the quantitative removal of U from the hydrothermal fluids (Michard and Albarède, 1985; German et al., 1998) or the alteration of hydrothermal sulphides (Mills et al., 1993, 1994; German et al., 1998).

REE geochemistry

In this section, we discuss the REE geochemistry of bulk sediments as well as leach and residues of our samples in the light of what is known from published

literature on plume particles and metalliferous sediments. To evaluate the source and various components that contribute to the sediments in CIB, we have compared our sediment data with other metalliferous sediments from different areas as well as hydrothermal fluids (Fig. 3.9).

REEs in bulk sediments

The total REE concentrations range between 526 and 607 ppm with relatively higher concentration in unit 1 compared to unit 2 (Table 3.3). The concentrations reported here are higher than those reported for the ridge–flank metalliferous sediments from the EPR (upto 300 ppm, Owen and Olivarez, 1988) and fall in the range of Leg 92 metalliferous sediments (131–867 ppm, with a cluster between 167 and 529 ppm, Barrett and Jarvis, 1988).

REE concentrations of the bulk sediments have been normalized to the Post Archaen Australian Shale (PAAS) values, which represents an average concentration for continentally derived material (Taylor and McLennan, 1985). The bulk sediments (Fig. 3.9) studied here deviate markedly from a flat pattern, with the REE patterns of all the samples showing light REE (LREE) depletion. Uniformity in the REE patterns suggests either that the sediments are derived from a fairly homogeneous source (or sources) with respect to the REE, or may indicate thorough mixing within the sediments (McLennan, 1989).

$(La/Yb)_n = (La/Yb)_{sample}/(La/Yb)_{PAAS}$, which is an indicator of light to heavy REE fractionation, varies from ~0.46 for unit 1 to as much as 0.55 for unit 2 sediments, which means that there is significant enrichment of HREE downcore. HREE enrichments (e.g. low Nd_n/Yb_n values between 0.56 and 0.59 and La_n/Yb_n values between 0.46 and 0.55) together with low trace element concentration have been indicative of low temperature fluids (Hodkinson et al., 1994; Mills et al., 2001). In contrast high temperature hydrothermal deposits have Nd_n/Yb_n values significantly above 1 (Mills and Elderfield, 1995; Frank et al., 2006). Shale normalized patterns of plume particles at EPR and TAG were indistinguishable when normalized to local seawater (Sherrell et al., 1999). The fractionation can vary with the differences in particulate Fe concentrations, Fe/Mn ratios in plume particles and the style of venting (Sherrell et al., 1999 and references therein).

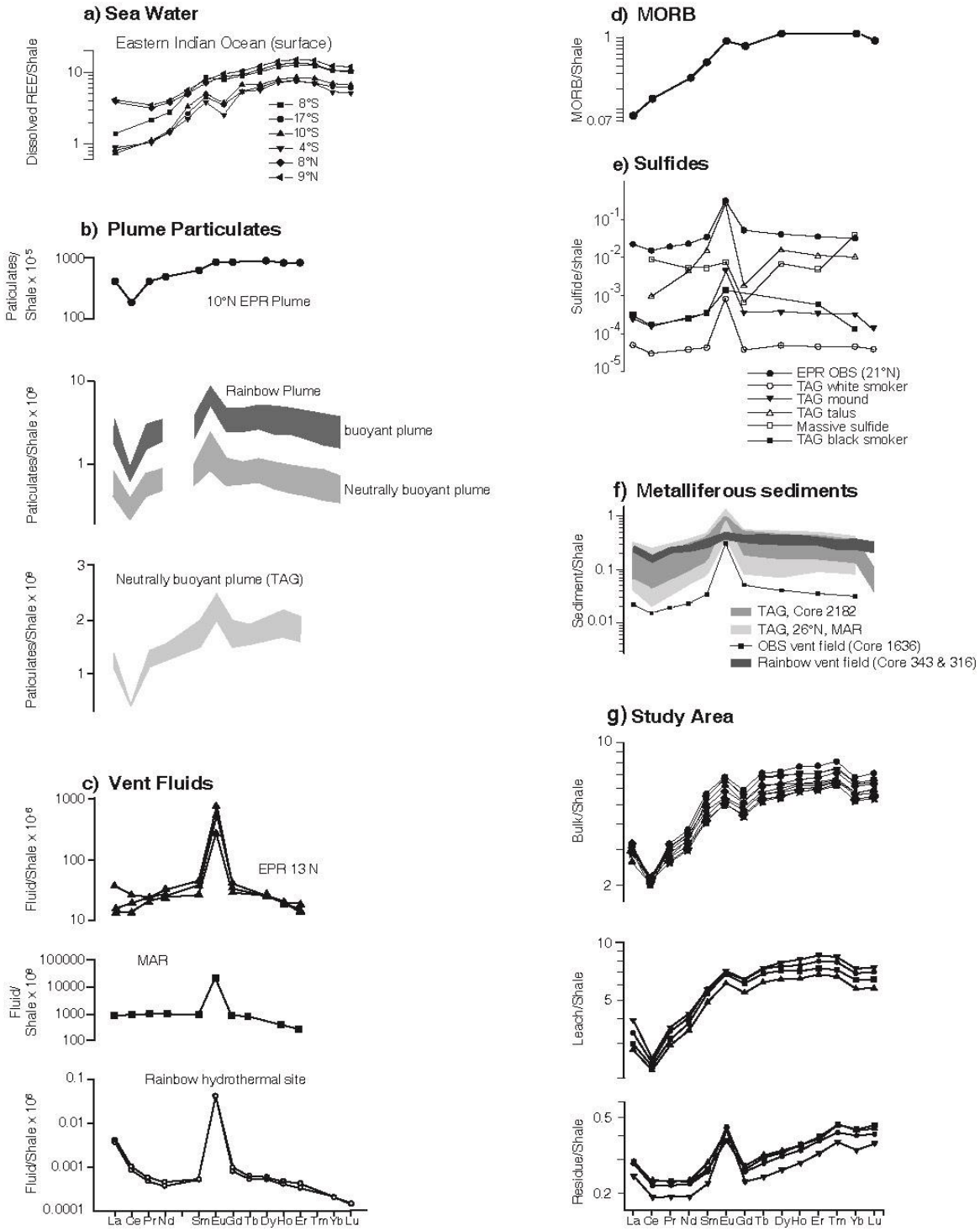

Fig. 3.9: Shale normalized REE distribution patterns for bulk, HCl leachates and residue of AAS 61/BC 8 are shown along with a) seawater (Eastern Indian Ocean–Amakawa et al., 2000); b) plume particulates (Rainbow–Edmonds and German, 2004; TAG–German et al., 1990 and EPR–Sherrell et al., 1999); c) vent fluid (EPR–Klinkhammer et al., 1994; MAR–German et al., 1990; Rainbow hydrothermal site–Douville et al., 2002); d) Indian Ocean MORB–Nath et al., 1992b; e) sulfides–(TAG–Mills and Elderfield, 1995; OBS vent site at 21°N on EPR–German et al., 1999; West Tasmania, Australia–Whitford et al., 1988) and f) metalliferous sediments–(German et al., 1993; 1999; Chavagnac et al., 2005 and Mills et al., 1993). While the patterns for bulk as well as leach closely resemble the plume particulate data, those for residue seem to be a contribution from sulfides and MORB.

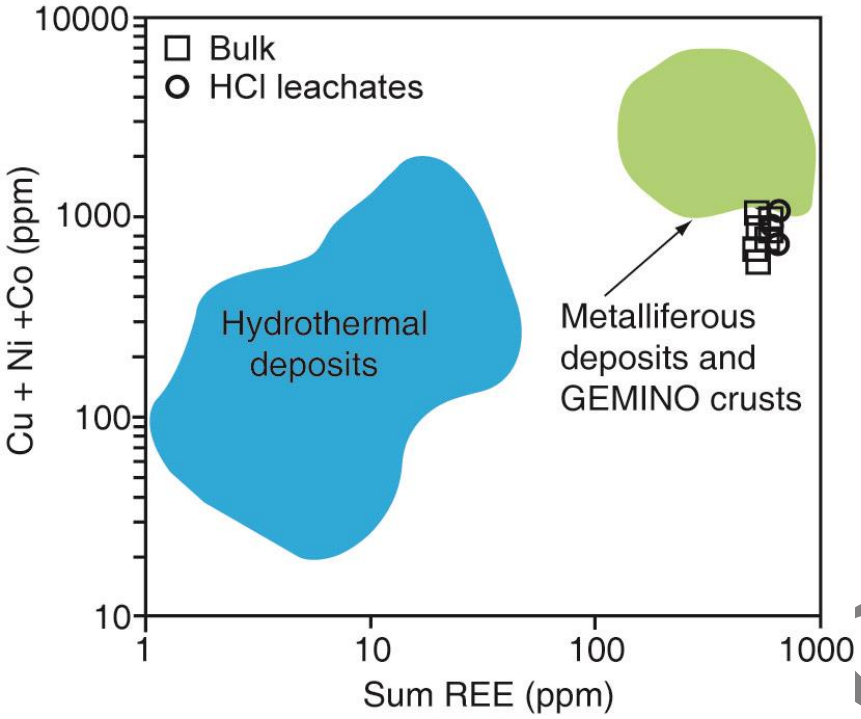

Fig. 3.10: A plot of ΣREE versus Cu+Ni+Co content (both for bulk and leach) in comparison with literature data for hydrothermal deposits and metalliferous deposits (Clauer et al., 1984, modified by Nath et al., 1997a).

Further corroboration of a largely metalliferous nature of the sediments comes from a binary plot of Cu+Ni+Co concentrations v/s ΣREE (Clauer et al., 1984), with the bulk and the HCl leach, representing the non–lithogenic component falling in the same field defined as metalliferous sediments (Fig. 3.10), suggesting that the sediments are predominantly metalliferous in nature

Cerium anomaly

A significant feature of the shale normalized REE patterns is the presence of negative Ce anomalies (Fig. 3.9), with Ce/Ce* (Ce* is being obtained by linear interpolation between shale normalized La and Pr) values ranging from 0.66 to 0.79 with an average of 0.73 (Table 3.3), in contrast to the sediments overlain by nodules (Nath et al., 1992a) and typical hydrogenetic Fe–Mn oxides from the basinal parts of the Indian Ocean which all have positive Ce anomalies (Nath et al., 1992a, 1994; Nath, 1993). A negative Ce anomaly strongly suggests a seawater source for the REEs, scavenged largely by Fe–oxyhydroxides consistent with the plume chemistry literature (German et al., 1990; Sherrell et al., 1999). REE distribution patterns with HREE enrichment and pronounced Ce anomalies are characteristic of seawater (German et al., 1999). Thus, the plume particles from several areas have shown negative Ce–anomaly (Fig. 3.9). Previous work on metalliferous sediments has revealed shale–normalized patterns similar to our sediments with negative Ce

anomaly and HREE enrichment (Fig. 3.9, Marchig et al., 1982). Seawater REE patterns are also acquired by the metalliferous sediments on the ridge crest (Olivarez and Owen, 1989), which is explained by the extensive scavenging of REEs from seawater by hydrothermal Fe–Mn oxyhydroxides as they are dispersed off–axis (German et al., 1990; Sherrell et al., 1999), either prior to sedimentation or post–deposition during early diagenesis.

Microbial oxidation is also reported in hydrothermal systems (Mandernack and Tebo, 1993), leading to the possible Ce anomaly of plume particles relative to ambient seawater (Sherrell et al., 1999) but this process is probably insufficient to overcome the marked negative Ce anomaly of ambient seawater. The metalliferous sediments are unlikely to have positive Ce anomalies, as long as they have a substantial hydrothermal component in them.

Eu anomaly

PAAS normalized REE patterns of the bulk sediments reveal another significant feature (Fig. 3.9), viz., a positive Eu anomaly compared to its neighboring lanthanides. The Eu anomaly is denoted by (Eu_{sample}/Eu_{shale}) /Eu*, with Eu* being obtained by linear interpolation between shale normalized Sm and Gd values. Positive Eu anomalies reflect a large hydrothermal component in the sediments as hydrothermal fluids, as well as other hydrothermal phases show a large positive Eu anomaly (German et al., 1993; Mills et al., 1993; Klinkhammer et al., 1994; Mills and Elderfield, 1995; Hrischeva and Scott, 2007). Fractionation of Eu from other REEs and reduction of Eu^{+3} to Eu^{+2} can occur at temperatures above 200–250°C (e.g., Bau, 1991). REE fractionation controlled by redox equilibrium at high temperatures can lead to LREE enrichment and strong positive Eu anomalies in reduced metalliferous fluids at active spreading centers (e.g., Bau, 1991). Metalliferous sediments from TAG (German et al., 1993) also have similar REE patterns with respect to LREE depletion and positive Eu anomaly. The degree of Eu anomaly is the result of mixing which indicates a small component of REE sourced from the hydrothermal fluids mixed into the major source of REE from ambient seawater (Chavagnac et al., 2005).

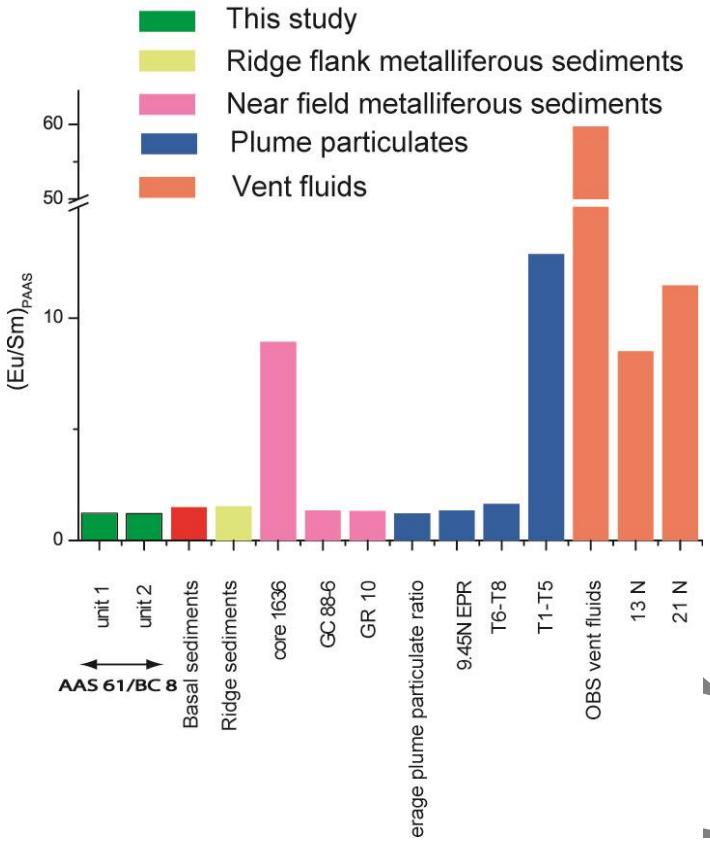

Fig. 3.11: PAAS normalized Eu/Sm ratios of our sediments (AAS 61/8) are compared with metalliferous sediments from ridge flank as well as near field sediments along with plume particulates and vent fluids. The data are from Jarvis (1985); Bender et al. (1971); German et al. (1990, 1995, 1997, 1999, 2002); Klinkhammer et al. (1994) and Sherrell et al. (1999).

In order to determine whether the degree of Eu anomaly indicates the proximity to hydrothermal source, we plotted Eu/Sm ratios of our sediments along with other ridge flank sediments (Bender et al., 1971), near vent sediments (German et al., 1995, 1997, 1999) along with plume particulates (German et al., 1990, 2002; Sherrell et al., 1999) and vent fluids (Klinkhammer et al., 1994; Michard and Albarède, 1986) (Fig. 3.9). Eu/Sm ratios of our sediments are more similar to those of ridge flank metalliferous sediments, average plume particulates and near field plume particulates ratios (Fig. 3.11, and references therein).

Mixing calculations using major elemental data of bulk sediments

Based on the possible source components interpreted from above discussion, relative proportion of each end member contributing to the bulk is assessed using ternary mixing equation with mass balance equation (Albarède, 1995; Chavagnac et al., 2005) shown below.

$$\int_{terrigenous} + \int_{metalliferous} + \int_{MORB} = 1$$

$$C^{i}_{mix} = \left(\int_{terrigenous} \times C^{i}_{terrigenous}\right) + \left(\int_{metalliferous} \times C^{i}_{metalliferous}\right) + \left(\int_{MORB} \times C^{i}_{MORB}\right)$$

where ∫ represents the proportion of each end–member contributing to the bulk sediments and C^{i}_{mix} is the concentration of element i in the mixture of 3 end members. Three end members which are considered to have contributed to these sediments are used in this mixing calculations, viz., metalliferous sediments from Bauer depression (Sayles and Bischoff, 1973), Indian MORB (Sun, 1979) and terrigenous sediments (Nath et al., 1989) from northern Indian Ocean; (i.e. metalliferous sediments, MORB and terrigenous material). This assumption of 3–end members is presumably valid as other components in these sediments such as biogenic silica/opal are poor carriers of REEs and trace elements. Though scavenging and adsorption REEs on Fe and Mn–oxides is a dominant process during low temperature processes, hydrogenic oxides may not be responsible for the REE geochemistry as shown in next section. The mixing calculations show that 35–45 % metalliferous sediments could reproduce Fe and Mn values of our sediments. Mixing calculations for other major elements such as Na and Mg also show affinity towards composition of metalliferous sediments, while the MORB contribution is apparently higher for Ti and Al.

3.3.2.2. Leaching Studies

Different approaches were required to characterize the hydrothermal component in the leach and residual fraction, which essentially contains oxides and REE adsorbed on to hydrogenous and hydrothermal Fe oxyhydroxides in the leachates and crystalline iron oxides and sulphides in the residue.

HCl soluble data

Shale normalized REE patterns of bulk, HCl leachates and residue are plotted along with data from the literature for various possible sources such as i) seawater, ii) plume particulates iii) vent fluids, iv) MORB, v) sulphides and vi) metalliferous sediments in Fig. 3.9. The REE concentrations and the shale normalized patterns of HCl leachates are remarkably similar to that of bulk sediments (Fig. 3.9g) indicating that most of the REEs in the bulk sediment are dominated by REEs in the leach fraction. Leachates seem to account for >90 % of total REEs to the sediments (Table 3.2) suggesting that they are dominantly oxide–bound. The REE patterns of the leachates show a positive Eu anomaly, a negative Ce anomaly and LREE depletion compared to MREE.

The negative Ce anomaly and the HREE enrichment in the sediments (both bulk and leach) are similar to seawater data, and plume particles from the EPR, TAG and Rainbow hydrothermal sites as plume particles essentially scavenge REE from ambient seawater. The patterns are also similar to the metalliferous sediments of other areas (Fig. 3.9). Higher REE concentration in our sediments compared to other metalliferous sediments is probably due to the extensive scavenging of dissolved REE from seawater onto hydrothermally derived Fe–Mn oxyhydroxide colloidal particles, either in the water column or after the particles have settled on the seafloor over a longer period of time (Barrett and Jarvis, 1988; Olivarez and Owen, 1989; German et al., 1990; Edmonds and German, 2004). REE patterns of hydrothermal fluids display positive Eu anomaly with LREE enrichment (Douville et al., 2002). The negative Ce anomaly and positive europium anomaly in bulk and the leach sediments are also exhibited by metalliferous sediments from TAG and OBS vent field. Hydrothermal particles collected from TAG are essentially Fe oxyhydroxides (German et al., 2002), and show REE patterns typical of mixed contributions from both seawater and hydrothermal fluids. HREE enrichment in our sediments compared to other metalliferous sediments is probably due to higher seawater derived component.

We have normalized REE to Fe in leach in our sediments and compared with that of plume particles as Fe oxides/hydroxides are the host phase in both situations. The surface sample has high REE/Fe (1.29×10^{-2}) while the mid sections (8–10 cm and 12–14 cm) have the lowest REE/Fe (0.86×10^{-2}) with the mean REE/Fe ratio in core studied being 0.96×10^{-2}. In a similar study by Chavagnac et al. (2005), the mean REE/Fe ratios (2×10^{-3}) are an order lower than our values and upto two orders lower than the corresponding REE/Fe ratios of plume particles of Rainbow vent field (1.6×10^{-4}). Particulate REE/Fe ratios in neutrally buoyant plumes of TAG (German et al., 1990) have enrichment greater than 10 fold relative to end member vent fluids. This is consistent with what is already known from the study of both plumes and ridge flank hydrothermal sediments that uptake of dissolved REE from seawater causes the REE content of Fe–oxyhydroxides material to evolve continuously within a dispersing hydrothermal plume, leading to progressive higher REE/Fe ratios being observed at increasing distance from the initial vent source (Mitra et al., 1994; German et al., 2002; Edmonds and German, 2004).

HCl–insoluble residue data

The shale normalized REE patterns for the residues show LREE depletion, HREE enrichment and a pronounced Eu anomaly (Fig. 3.9g). The residue left after HCl leach would contain detrital phases like silicates, sulphides and resistant minerals. In the following section, nature and possible source of the residue material are assessed. According to the published literature, aluminosilicate fraction to the basin is possibly contributed as i) turbiditic sediments from the terrestrial source (Nath et al., 1989, 1992b; Kolla et al., 1976), ii) dust from the distal sources such as Australia or African or Indian subcontinent (e.g., Kolla and Biscaye, 1977; Fagel et al., 1994; Nath et al., 2013), and iii) local rocks and mid oceanic ridge basalts (Rao and Nath, 1988; Nath et al., 1989, 1992a).

We will now compare the literature data for these probable silicate sources. Terrigenous sediments from the northern part of the CIB are characterized by flat REE patterns, without Ce fractionation (Nath et al., 1992a). The residue patterns seen in our sediments are therefore not comparable to those of terrigenous sediments of CIB as the terrigenous input to the core location at 16°S in CIB would be minimal. It was envisaged in the past that the influx of terrigenous sedimentation is limited to 8–10° S (Nath et al., 1989, 1992b; Fagel et al., 1994; Nath, 2001). There must therefore be an additional source contributing to the HCl–insoluble fraction.

Slight La enrichment in combination with positive Eu anomaly (Fig. 3.9) is distinctly similar to the REE patterns of vent fluids from Rainbow hydrothermal site as well as sulphides from OBS vent field on EPR (German et al., 1999). As there are no reports on REE data of sulphides from the Indian Ocean, we have used OBS sulphides from the 21°N EPR for comparison. TAG massive sulphides are not considered as they are weathered compared to the OBS of EPR. A major component of the residue could be sulphidic-type hydrothermal material. The elements that form sulphides such as Fe, V, Cr, Cu, Zn and Pb are in fact enriched in the HCl insoluble fraction over that of La (Table 3.2). HREE fractionation over MREE in the HCl–insoluble residue suggests a contribution of MORB like source (Fig. 3.9, Nath et al., 1992b). We consider that the residue contains a mixture of three components namely

i) sulphide type hydrothermal material, ii) MORB derived weathered detritus and iii) clastic silicates from distal sources.

The importance of the relative proportion these potential sources contributing to the residue (i.e. sulfides, MORB and terrigenous material) is assessed by modeling the REE data using ternary mixing equations as was done for major elements.

$$\int_{MORB} + \int_{terrigenous} + \int_{sulfides} = 1$$

$$C^{i}_{mix} = (f_{MORB} * C^{i}_{MORB}) + (f_{terrigenous} * C^{i}_{terrigenous}) + (f_{sulphide} * C^{i}_{sulphide})$$

Three end members used here are terrigenous sediments from northern Indian Ocean, sulfides and MORB. The results of these calculations are presented as shale normalized REE patterns in Fig. 3.12. To avoid a bias, the mixing calculations were repeated using composition of sulfides from different locations viz., TAG, EPR, and west Tasmania, Australia (Fig. 3.13).

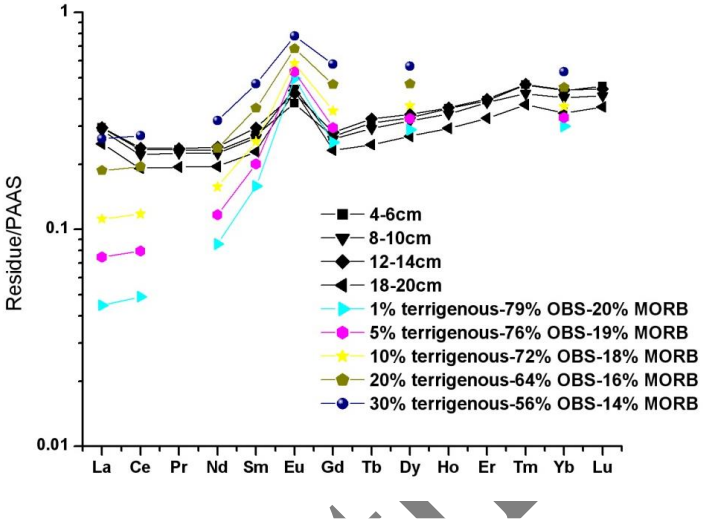

Fig. 3.12: REE mixing calculation using 3 end members viz., Terrigenous sediments in the CIB; OBS sulphides from EPR; and the Indian Ocean MORB (References for these values are given in text) in the residue fractions.

The results of sulfidic contribution has varied only marginally (between 64 and 72%) when any of the sulfidic end member from different areas was used. Relative proportions of terrigenous component (10–20 %), sulfides (64–72%) and MORB (16–18 %) reproduce the REE patterns shown for the acid–insoluble residue, clearly suggesting that the terrigenous and MORB source contribution to the REEs in the residue is lower than that of sulfidic–type material. However, these calculations should be considered as indicative and may not represent the proportion in which they are incorporated during the sediment formation (see Chavagnac et al., 2005 for discussion).

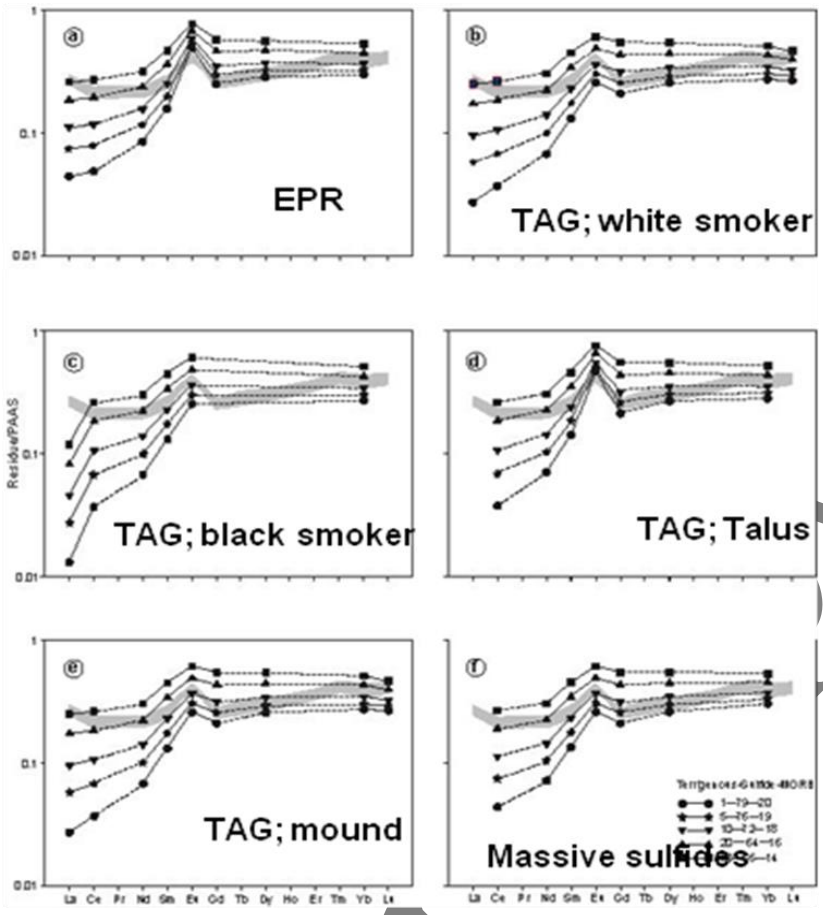

Fig. 3.13: Ternary REE mixing calculation results using 3 endmembers (Terrigenous, sulfides and MORB) are presented in PAAS–normalized REE patterns for the residue fraction. Relative contribution to the sulfides in the residue was estimated using sulfides from 3 different areas, a) EPR (OBS); b–e) TAG (white smoker, black smoker, talus and mound); f) massive sulfides from west Tasmania, Australia. Calculations with varying sulfides have yielded nearly similar contribution (64–72%) of sulfides to residues.

3.3.3. Other evidences for a hydrothermal component

3.3.3.1. Infra-red spectroscopic studies

SEM–EDAX studies of some of the lithic grains recovered from the core were dense, massive and highly porous, and were similar to some of the lithic grains found in the hydrothermal system on the Juan de Fuca Ridge (Murnane and Clague, 1983). The grains contained Fe and Al (averaging 24% Fe_2O_3 and 14% Al_2O_3) and the calculated formula (based on 24 O atoms) and the composition is close to those of ferruginous smectites (Newman, 1987; Schöps et al., 1993). The Fe_2O_3/SiO_2 ratio is close to 0.51 and fall within the previously reported values for nontronites (McMurtry et al., 1983; Murnane and Clague, 1983; Alt, 1988; Severmann et al., 2004). To identify if any ferruginous smectites of hydrothermal origin are present in the

sediments studied here, infrared spectroscopy and ICP–MS analyses were carried out on the clay–sized sediment fraction (<2 μm).

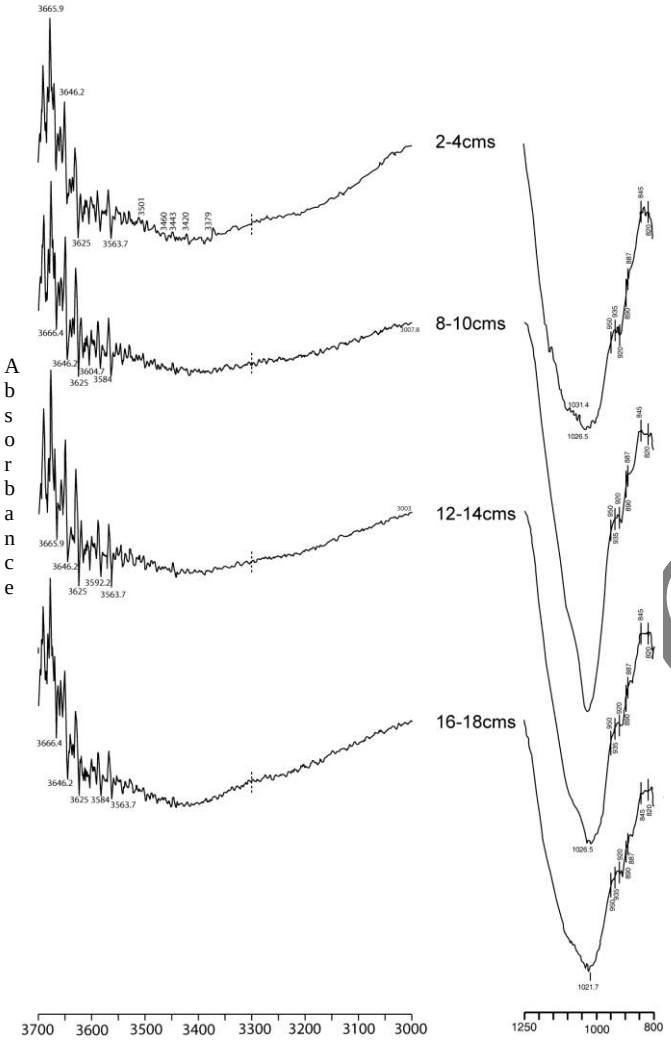

sections (untreated, 2 μm size fractions). Left: OH–stretching region at 3700–3000 cm^{-1} with absorption bands representing ferruginous smectite and nontronite. Right: Si–O stretching region with absorption band at 1020 cm^{-1} corresponding to low Fe content in tetrahedral position of smectite. Absorption bands between 920–820 cm^{-1} represent increasing Fe content in octahedral sites and the presence of nontronite, ferruginous smectite and beidellite.

IR studies show an intense SiO_2 stretching absorption at ~1020 cm^{-1} for all the four samples studied (Fig. 3.14), which corresponds to a very low tetrahedral Fe^{3+} content in the sample (e.g., Goodman et al., 1976; Cole, 1985; Schöps et al., 1993). OH bending vibration between 920 and 820 cm^{-1} results from a variable substitution of Al by Fe. Smaller absorption bands occur at 820, ~887 and 935 cm^{-1}, the first two bands suggesting Al–OH deformation in nontronite (Farmer and Russel, 1967), and the third band may suggest the presence of beidellite (White, 1971). The absorption band at ~880 cm^{-1} is attributed to the substitution of octahedral Fe by Al in the smectites (Cole, 1985), or to the Fe–Al–OH substitution in ferruginous smectites (Russel, 1979) and also to the Al–OH deformation in nontronites (Frost et al., 2002, and references therein). The OH–bending vibration at 920 cm^{-1} in this study is similar to that seen in nontronites studied by Farmer and Russell (1967).

Absorption bands are seen at 3625, 3592 and 3563 cm^{-1} in the OH–stretching region which can represent Al–Fe–OH stretching either in ferruginous smectites (Russell, 1979) or in nontronites (Frost et al., 2002, and references therein). This

equivalent band at 3564 cm^{-1} is indicative of Fe–FeOH stretching vibration in nontronites (Van der Marcel and Beutel Spacher, 1976). IR studies, therefore, suggest that the clay sized sediments studied here contain smectites of dioctahedral series of monmorillonite–beidellite–nontronite with a dominance of nontronites and ferruginous smectites.

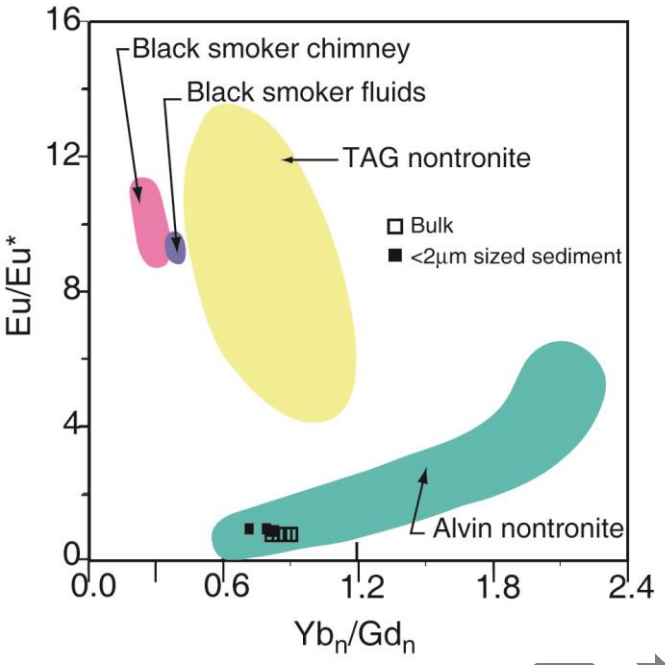

Fig. 3.15: Chondrite normalized Yb/Gd v/s. Eu/Eu* in the bulk and <2 µm sized sediments compared to the composition of nontronites and other hydrothermal precipitates from various areas (modified from Severmann et al., 2004). Samples from this study plot in the Alvin nontronite field.

While the earlier studies have attributed the presence of Fe–rich montmorillonite in the CIB to the diagenetic origin (Rao and Nath, 1988), occurrence of both the ferruginous smectites and the nontronitic clays in these sediments would probably suggest hydrothermal origin (e.g., McMurtry and Yeh, 1981). Iyer et al. (1997) have recovered volcanogenic–hydrothermal material (vhm), and sediments with a composition close to nontronite at 14°S and 75°56.1'E which is ~45 km from the 76°30'E fracture zone in the CIB and suggested that they form through submarine exhalations and deposition in the surrounding siliceous sediments. Hydrothermal nontronites commonly are very low in Al (Singer et al., 1984), while the higher Al (Al_2O_3 ~14wt%) present in these samples apparently indicates that the clays may not have formed from high temperature hydrothermal sources (Schöps et al., 1993). It has been suggested that nontronites characterized by distinctly elevated Al and Ti content have been described to be formed at low temperatures (32–48°C) in the Central Pacific seamounts (Schöps et al., 1993). Compositionally, bulk sediments as well as the <2 µm sized clay fraction studied here, fall in the field of Alvin nontronites (Fig. 3.15), which were calculated to form at 59+/–5°C (Severmann et al., 2004). Interaction of low temperature (up to 50°C) hydrothermal fluids with basalts can be responsible for the production of Al–rich

clays such as those found in DSDP Hole 417 (Scheidegger and Stakes, 1980; Alt and Honnorez, 1984). Lack of a well crystallized iron mineral such as hematite in our samples indicate the dominance of amorphous Fe–oxides/oxyhydroxides which may form at temperatures of ~100°C (McMurtry and Yeh, 1981). The sediments studied here must therefore, have been influenced by temperatures ranging between 50 and 100° C.

3.3.3.2. Mössbauer studies

All sediment samples showed nearly identical Mössbauer spectra. Very weak (less than few %) magnetic phases were detected in some samples, the main contribution was a quadrupole doublet with CS = 0.36(1) mm/s and the separation of the doublet peaks (= |QS|) being 0.55(2) mm/s. Thus all iron in the samples was in ferric (Fe^{3+}) form. This was principally due to the high contents of authigenic ferric oxides in the sediments. There was no significant difference between Mössbauer spectra recorded on bulk samples and on the leached residues, nor between measurements on samples picked from different depths of the sediment. As no typical magnetic signal (a sextet) was detected, the magnetic domains, if at all present, have to be very small (<100 Å).

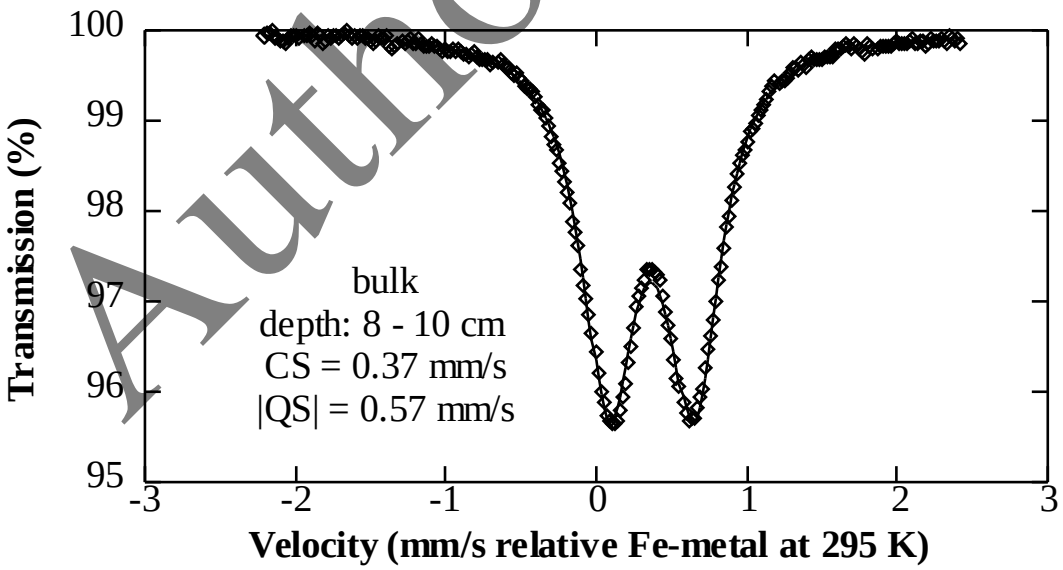

Fig. 3.16: Typical Mössbauer spectra obtained for the sediments studied shows that most of the Fe is present in ferric state. Spectrum of 8–10cm sediment section shown as an example. The dots are the data points, the straight line is the fitted function, assuming Lorentzian shaped peaks with no thickness correction.

Mössbauer spectrum of a bulk sample picked from a depth of 8–10cm is shown in Fig. 3.16. The dots are the data points, the straight line is the fitted function, using a locally developed program at Uppsala, assuming Lorentzian shaped peaks with no thickness correction.

3.3.3.3. Magnetic studies

Hydrothermal alteration is also evidenced from the obtained mineral magnetic data (Fig. 3.17). Hydrothermally altered samples (BC#8) showed relatively higher χlf, SIRM, χarm, SIRM/χlf, SIRM/ARM and S–ratio values indicating higher ferrimagnetic content of stable single domain (0.03–0.15μm) magnetite in the samples. Conversely, the unaltered samples from a sediment core in the adjoining area have exhibited relatively lower χlf, χarm/SIRM, Xarm/χlf, S–ratio values and higher χfd%, χARM/SIRM and χARM/χlf values indicating magnetite of super–paramagnetic (<0.03 μm) size as the major magnetic component in the samples.

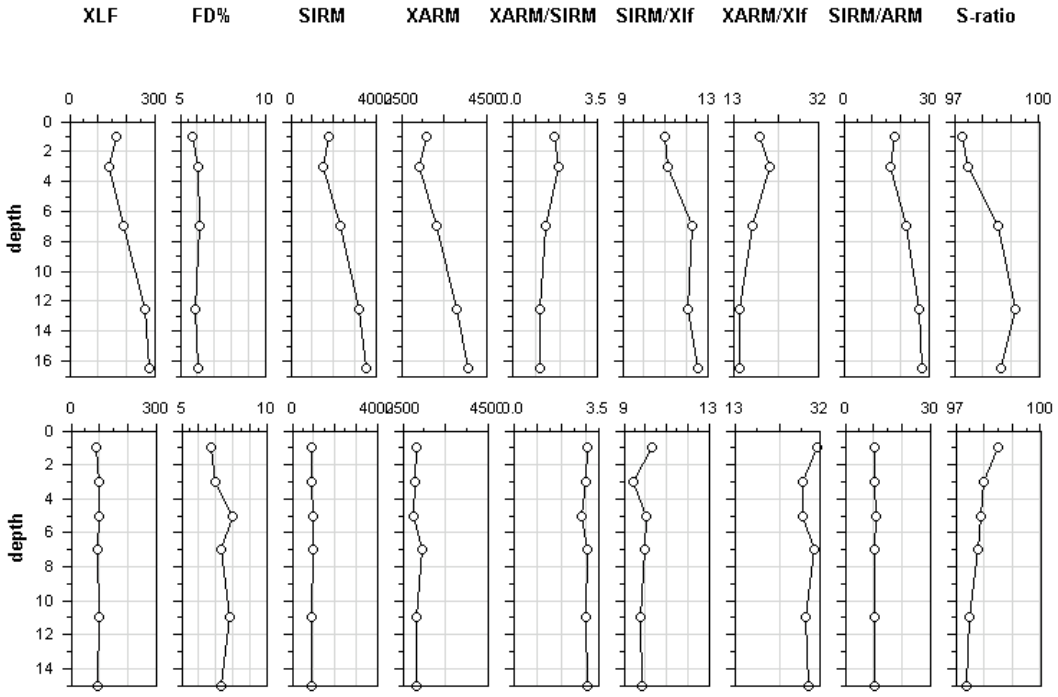

Fig. 3.17: Downcore variations of magnetic susceptibility (Xlf), frequency dependent susceptibility (fd), saturation isothermal remanent magnetization (SIRM), anhysteretic remanent magnetization (XARM) and other ratio–parameters (AXARM/SIRM, SIRM/Xlf, XARM/Xlf, SIRM/ARM and S–ratio). Units for magnetic parameters– Xlf: 10^{-8} m^3/kg; fd: %; SIRM: 10^{-5} Am^2/kg; XARM: 10^{-8} m^3/kg; XARM/SIRM: 10^{-3} m/A; SIRM/Xlf: 10^3 A/m; XARM/Xlf: dimensionless; SIRM/ARM: dimensionless; S–ratio: %

Binary plots (Fig. 3.18) of χlf v/s χarm and χarm v/s χarm/SIRM parameters further compliment these inferences. Isothermal remanence magnetization experiments (Fig. 3.17) along with temperature dependent magnetic susceptibility variations unambiguously suggest 'magnetite' as the dominant magnetic mineral in the altered and unaltered samples. However, the altered and unaltered samples displayed difference in the relative quantity of magnetic mineral and their grain sizes.

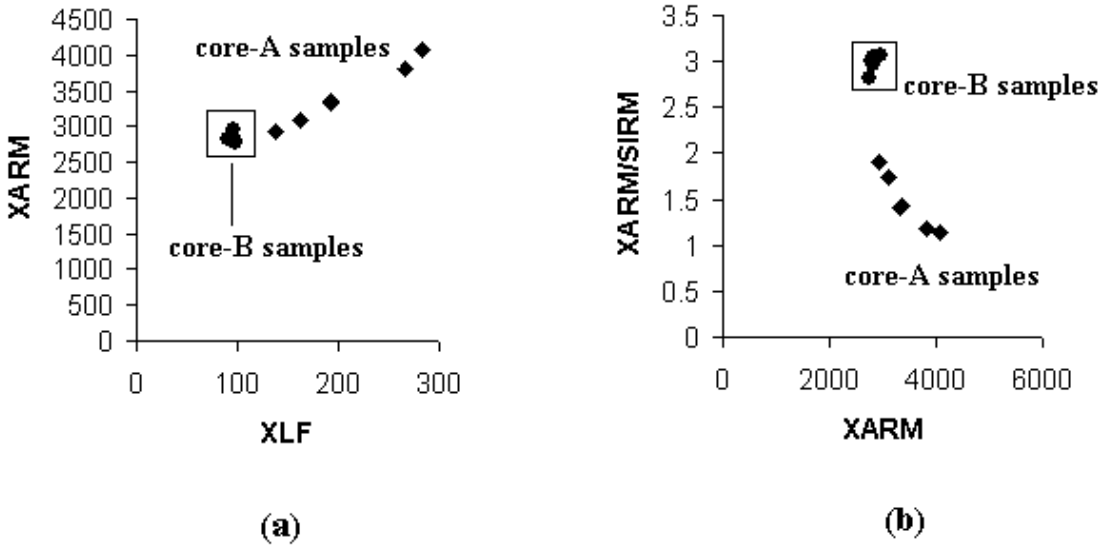

Fig. 3.18: Scatter plots of magnetic parameters (a) Xlf v/s XARM and (b) XARM v/s XARM/SIRM indicative of magnetic concentration and grain sizes in the Core – A (hydrothermally altered) and Core – B (not altered) samples.

Altered sediments enriched by secondary magnetite of SSD size (0.03 – 0.15 μm) apparently resulted during the hydrothermal alteration. Whereas, the relatively lower ferrimagnetic (magnetite) component of SP grain sizes (<0.03 μm) in the unaltered sediments is characteristic of pelagic deep sea sediments.

3.3.3.4. Volatile content

To gain information about the possible source of the hydrothermal fluids, we have analyzed the S and Cl concentrations in some spheroidal aggregates separated from the sediments (Fig. 3.19). Relatively high S and Cl concentrations together with low S/Cl values (0.09 to 0.54) found in some of the individual grains suggest that they can be derived from neutral type hydrothermal fluids with temperatures at nearly 200 to 350 ºC in areas of abundant water supply with upwelling of chloride rich fluids

above an active magmatic source (Newsom et al., 1999). However, grains with relatively high S content (12%) and near absence of chlorine were also found in our sediments likely reflecting influence of acid–sulfate type hydrothermal solutions. The influence of latter type of fluids may be limited in view of abundance water supply in the oceanic areas, as the acid sulfate hydrothermal system is dominant in water starved areas (Newsom et al., 1999). Both through ascent and advection, the magmatic fluids would have altered the primary signal of the sediments imparting hydrothermal signatures.

3.3.3.5. Presence of Aluminum rich grains

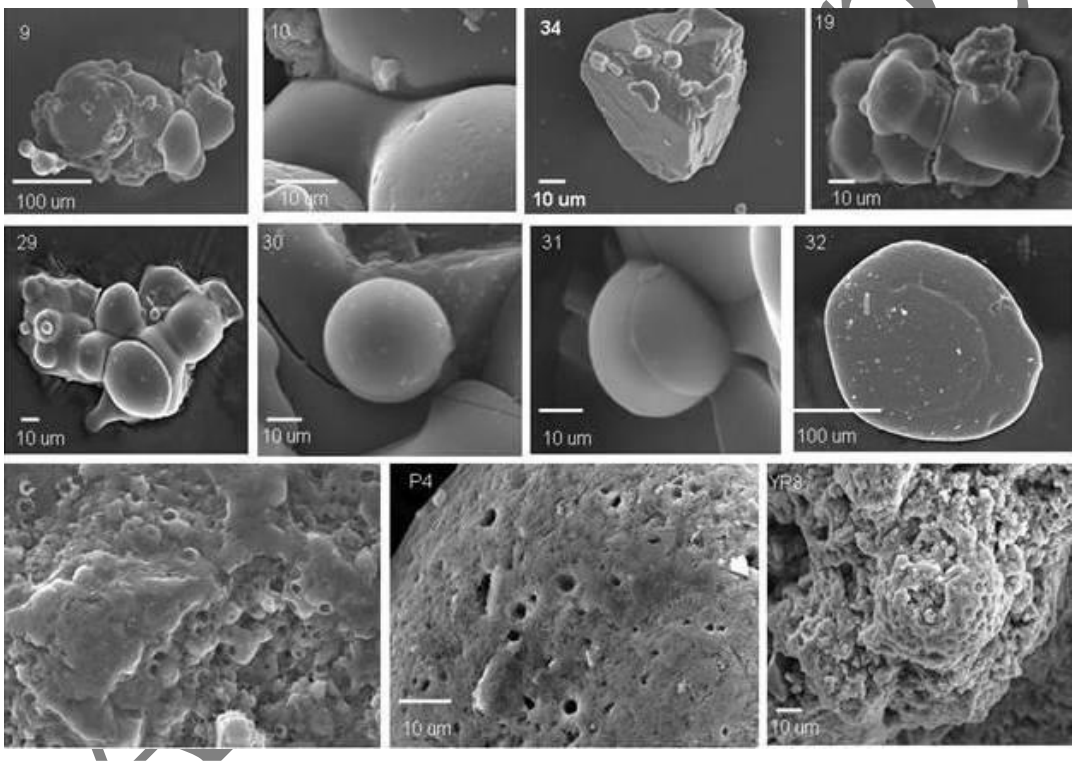

Fig. 3.19: SEM photographs; 1) Top two rows show the morphological types of lithic grains have high Cl, S, Cu, Zn, Al (also Ag) (photo no 9: S: 2.33%, Cl: 1.51%; photo no 34: S: 1.96%, Cl: 22.77%); bubble and spherical shapes resembling melt droplets. 2) Bottom row presents the close up of highly deformed radiolarian shell indicating features of wear away of skeletal features.

Aluminium rich grains have been observed in AAS 61/BC 8 as well as an additional core (S657 which is 37 cm long) from the CIB (Fig. 3.1). In this core the vhm is concentrated within the upper 6 cm of the core and the Al rich particles were observed at depths of 17–18, 22–24 and 25–26 cm, while in the AAS 61/BC8 core, the Al rich particles were observed at depths >8 cm .

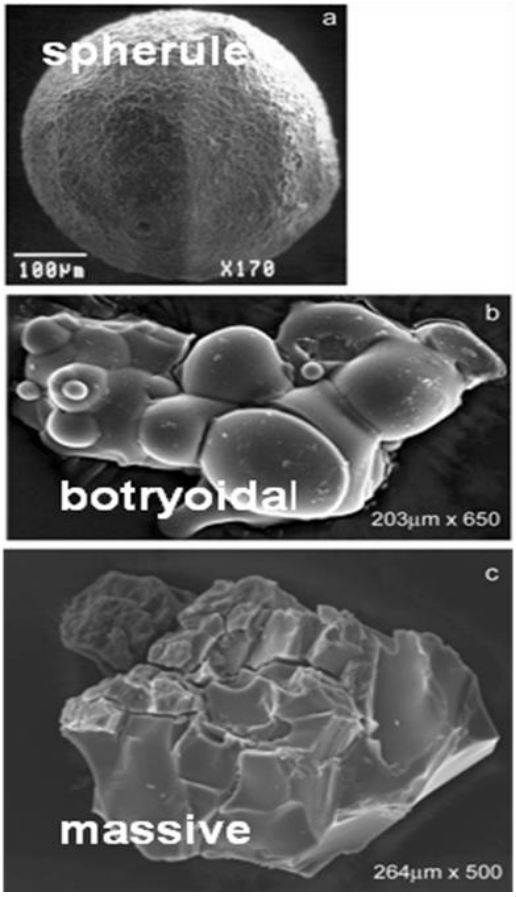

Fig. 3.20: Scanning electron micro-graphs of Al rich grains in the CIB. (a). Typical aluminium rich spherule (S657, 17–18cm). (b). Large, irregular particle with hydration cracks (AAS 61/BC 8, 8–20cm bsf). (c) Bulbous or nodular structure with hydration cracks seen at edges of the globule (AAS 61/BC 8, 8–20cm bsf). This kind of feature probably represents a later detachment of spherules as seen in (a).

A total of 25 specimens were examined of which 21 are spherules while the remaining are grains. The spherules range in size from 40 to 200 µm and generally had a brownish coating probably due to the adhering siliceous sediment. In core BC 8, the particles can be basically classified in to 2 types, 1) Massive, with irregular shape and sharp edges (Fig. 3.20). These are mostly elongated along one axis. Hydration cracks are seen on the surface. Size range from 230 µm to as small as 60 µm, 2) the other type of particles show smooth surface, with a botyriodal structure. Cracks are seen at the joints of the globules to the main particle. It appears that the globules (range from oval to elongate) protrude from the main particle. Their edges are mostly rounded with an even fracture. Size range from 250 µm to as small as 125 µm.

The globular shape and cracks at the globule boundaries may suggest that the spheroids seen in SS 657 could have been derived from the dislocation or breaking from the globular grains. In addition to the spherules and grains, three irregular moss–like growths over a glass shard (?) were also noticed in S657 samples. The studied specimens predominantly have aluminium (85–99%) while Si, Mg, Ca, Na, K and P contents contribute the rest (Table 3.6). Trace concentrations of Ti and Fe are present whereas Cu, Zn and Ag are lower and SO_3 is rare. In one grain of AAS 61/ BC 8, sulphur is enhanced (~2.33%) and in another Cu and Zn are high (3.65 and 5.5%, respectively) (Table 3.6). This is interesting because in core S657, sulphur content in the metalliferous sediment range from 0.21 to 4.65% (one specimen had ~10% S) while sulphur in the magnetite

spherules range between 0.21 and 1.55% (Iyer et al., 1997a). There are several instances of occurrence of native metals in the East Pacific Rise and Mid Atlantic Rise regions. Native copper has been noted in the sediments from the EPR black smoker at 18.5°S (Marchig et al., 1986) while at 21°N wurtzite (zinc sulphide), chalcopyrite, pyrite and native sulphur are common (Oudin, 1983). Sediment traps retrieved close to hydrothermal vents at 13°N EPR (Jedwab and Boulegue, 1984) recovered graphite crystals (5–100 μm size), with antimonide overgrowths, were considered to be of hydrothermal origin and this is attested by the presence of metallic iron associated with (deposited on) silica, as found in the sediment trap.

In comparison to the EPR, there are only a few reports of native minerals from the Mid–Atlantic Ridge (MAR). The particles of native metals (Fe, Al) discovered in basalts from the San Paulo fault in South Atlantic were assigned to an origin during the pre–crystallisation stage of basaltic melt evolution while Zn aggregates were related possibly to hydrothermal processes (Shterenberg, 1993). Mozgova et al. (1996) detailed the first report of cobalt pentlandite from a MAR hydrothermal deposit (14°45'N) that occurs as small (<20 μm), round to irregular grains and aggregates together with chalcopyrite, bornite, isocubanite, chalcocite, digenite, with minor pyrite and marcasite and with rare covellite and Au–bearing zincian copper.

Dekov et al. (1999) reported strands and elongated grains (up to 300 μm in length) of native copper and alpha–copper–zinc collected from the sediments from the Mir zone, Trans–Atlantic Geotraverse hydrothermal field of the MAR (26°N). Subsequent findings from the same area revealed a number of small, irregular–shaped and spherical shiny metallic particles of metallic tin, tin–rich lead and tin–copper phases (Dekov et al., 2001). In general, native metallic particles could have been formed as accessory minerals disseminated in the ridge crest basic rocks and/or massive sulfide mounds.

Besides the above native metals, the presence of native aluminium and/or aluminium–rich materials has been detailed by a few workers. Cole (1985) found Al–rich authigenic smectites in the brine pools of the Atlantis II Deep, Red Sea that formed under high temperatures (150–200°C) close to the hydrothermal input to the brine pool. At 21°N EPR, Al – Si gels occur, sometimes with opal that also forms a thin film on the outer wall of an inactive wurtzite chimney. Mineralogical studies supported the transport and deposition of Al as Al–Si gels very close to high temperature vent sites (Oudin, 1983). Shterenberg et al. (1986) discovered native

aluminium (94.6 and 95.3%) coupled with ZnO and $ZnCl_2$ in the sediments at Site 647, North Eastern Pacific Ocean and suggested segregation of Al particles from hydrothermal fluids that effused at 350°C.

Haymon and Kastner (1986) found mixtures of beidellitic smectite and Al–rich chlorite/smectite formed from altered basalt. They opined the products to be of high–temperature interaction between basalt glass + plagioclase and Mg – poor, acidic hydrothermal fluids, with some possible contribution of Mg from bottom seawater. Haymon and Kastner (1986) reported high–temperature Al–rich clays from the EPR (21°N) that occur within 2km of a black smoker vent field while Howard and Fisk (1988) reported Al–rich clays and boehmite (AlO(OH)) from the Gorda Ridge.

Exsolution of metal–rich fluid present in the magma (Yang and Scott, 1996) and degassing of magmatic vapours during submarine eruptions (Rubin, 1997) could also result in the deposition of certain metals. But degassing inputs to the ocean are probably highly episodic, occurring almost entirely during eruptions; and involve enhanced and abnormal hydrothermalism as well. The mean hydrothermal effluent concentrations of Al, Zn, Fe, Mn, Au and Ir are predicted to be ~$10–10^3$ times greater than in a degassed effluent (Rubin, 1997). According to Howard and Fisk (1988), the extreme acidity (pH 3–3.5) of the hydrothermal solutions (350°C) not only results in an intense alteration of the basalts but also leads to mobilisation of Al, until it is enriched 1000 times in vent fluids over normal seawater concentrations (Michard et al., 1984; Von Damm et al., 1985).

The presence of native Al in basic and ultrabasic rocks, according to Oleynikov et al. (1978), is evidence that during the pre–chamber evolution of the magmatic systems, under high P–T and low oxygen fugacity (fO_2, (Nekrassov and Gorbachov, 1977) conditions, a stage exists of metallisation of the silicate melt. Degassing signatures are also evident from other tracers described in subsequent section.

Age of the two sediment cores

Biostratigraphic dating, using Buccinosphaera invaginata and Collosphaera tuberosa, of S657 depicted three distinct peaks at 28, 16 and 6cm (dominant vhm) core depth. These peaks correspond to 130, 70 and 10 kyr age, respectively (Iyer et al., 1997a). The presence of Stylatractus universus (extinction at ~425kyr) and

Collosphaera Orthoconus (First Appearance Datum level ~650 ka) helps to bracket the age of another sample, S94 to the south, between 425–650 ka (Iyer et al., 1999). Therefore, we postulate that the vhm were produced quite recently (~10ka ago) while the Al specimens are of ~70 kyr. The sediments of BC 8 comprised of two lithic units (Fig. 3.2), a) a short sediment surface (~6cm) of radiolarians ooze underlain by b) grayish–brown colored indurated pelagic clays section (6 –20cm). Only the top 6 cm section was datable biostratigraphically, since the deeper section was devoid of radiolarians. This section contained two late Quaternary radiolarian index fossils (1) Buccinosphaera invaginata (Haeckel) and (2) Collosphaera tuberosa (Haeckel). Among them, B. invaginata had a shorter time range and is the youngest radiolarian index fossil (Gupta et al., 1996) with the first appearance datum found at ~180,000yrs (Johnson et al., 1989). Therefore, the sediments deeper than 6 cm bsf can be identified as older than 180kyr (Mascarenhas–Pereira et al., 2006).

3.3.3.6. Isotopic studies

Isotopic studies were carried out on the AAS 61/BC 8 sediments. The systematics of $^{230}Th_{excess}$ (portion of total ^{230}Th not supported by the decay of ^{234}U in the sediment) exponentially decreases with depth down to about 12 cm which is underlain by sediments with variable $^{230}Th_{excess}$ values (Fig. 3.21). Bioturbation cannot be responsible for this variation as the sediment sections with higher $^{230}Th_{excess}$ lack benthic biota and depleted in organic matter. Furthermore, sedimentation rate in the top 6cm, estimated from $^{230}Th_{excess}$ least square line regression (^{230}Th $t_{1/2}$ = 75.2 kyr), is 0.32mm/kyr corresponding to an age span of about 175kyr which is in agreement with the biostratigraphy (Mascarenhas–Pereira et al., 2006). Lack of linearity in $^{230}Th_{excess}$ profile (Fig. 3.21) may be attributed to emanation of magmatic fluids, probably through both vertical ascent and lateral advection. Additionally, the deeper than 6 cm section also shows higher ^{210}Pb activity over both ^{238}U and ^{230}Th (Fig. 3.21) indicating a likely magmatic origin (e.g. Krishnaswami et al., 1984). $^{238}U/^{210}Pb$ values are also markedly lower in these sediments suggesting a magmatically influenced fractionation. $^{210}Pb/^{230}Th$ values below unity in the top 6 cm, and values between 1.19 and 3.84 in the deeper part point to a significant enrichment of $^{210}Pb_{excess}$ relative to its parent ^{230}Th. Further, unsupported ^{210}Pb is only found in the deeper sediments, which suggests a recent (about a century old) hydrothermal

emanation considering the relatively short (22.3yr) half life of ^{210}Pb. ^{210}Pb excesses indicate the presence of a deeper degassing reservoir supplying volatiles to shallow stalled magma (Berlo et al., 2004). A radioactive disequilibrium between ^{210}Pb and ^{210}Po (half life=138.4days) was noticed in several hydrothermal areas such as Macdonald Seamount, EPR, Gorda Ridge and Loihi Seamount and was related to nearly complete removal or degassing of the more volatile Po (Rubin,1997).

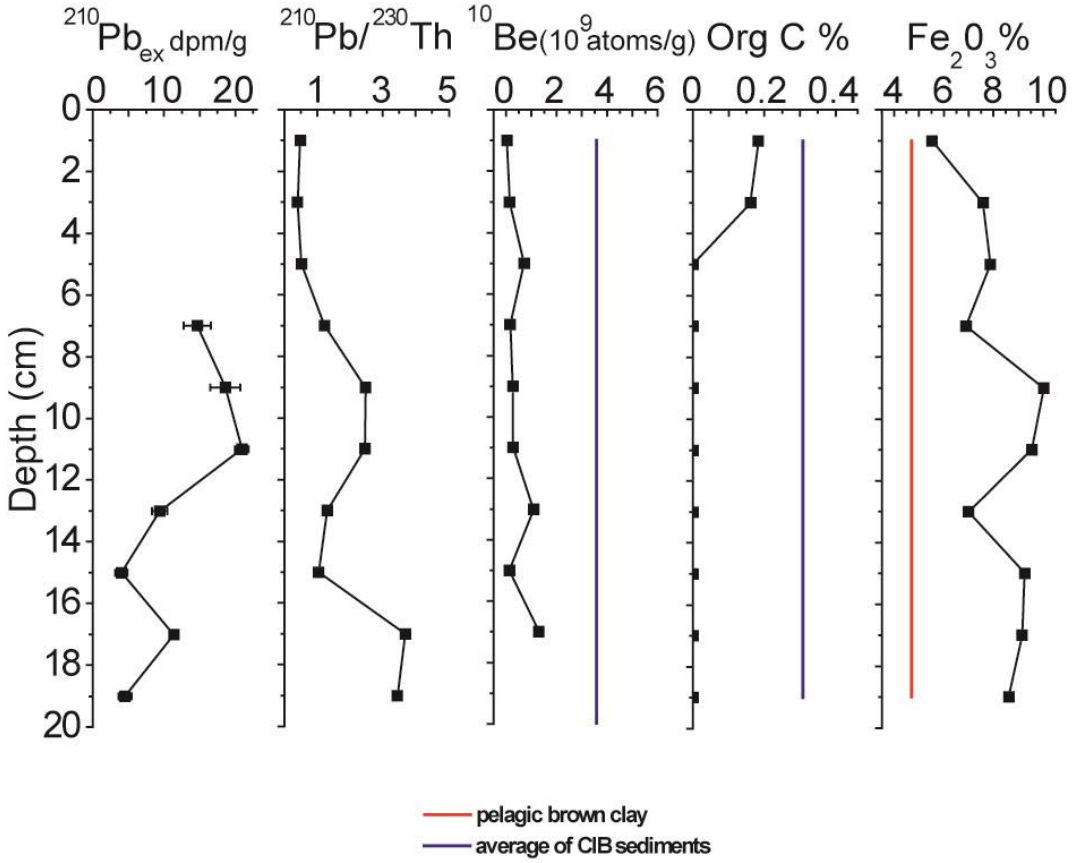

Fig. 3.21: Isotopic variation in the core AAS 61/BC 8 along with organic carbon and iron. The elemental iron composition is compared with the average composition of 3 types of sediments occurring in CIB while ^{10}Be is compared with the 3 types of sediments occurring in the CIB. Exponential decay is seen in $^{230}Th_{excess}$ profile only down to 12cm. $^{210}Pb_{excess}$ is only seen in the sediments deeper than 6 cm. ^{10}Be and C_{org} content in this core are very low compared to other CIB sediments. C_{org} is below detection in sediments deeper than 4cm.

^{10}Be concentrations are extremely low (0.4 to 1.3 x10^9atoms/g; Fig. 3.21) compared to several surficial sediments from the CIB (^{10}Be up to 5 x 10^9atoms/g; Nath et al., 2007). The low ^{10}Be (half life 1.5myr) values of the sediment suggest that leaching by emanating hydrothermal fluids can be the reason for the relatively low ^{10}Be. Observation of selectively leached by hydrothermal fluids ^{10}Be was documented

in sediment covered hydrothermal systems in the Guaymas Basin and Escanaba Trough (Bourles et al., 1991).

3.4. Conclusion

Detailed geochemical investigations of CIB sediments have shown the presence of significant metalliferous component in two areas close to two seamounts which are found along the 76°30'E fracture zone, which traces the movement of the Rodriguez triple junction. Detailed analyses of major, trace and rare earth elements (REE) on the bulk, leach, residue and clay fraction, magnetic and infra red spectroscopy studies of the clay fraction helped characterize the hydrothermal nature of the sediments.

- The sediments are iron–rich, majority of Fe, Mn is in leachable fraction and are compositionally comparable to ridge–crest metalliferous sediments. Elemental ratios and geochemical discrimination plots of major element data reveal that the sediments are a mixture of Fe–rich mineral phases on one hand apparently from hydrothermal sources and aluminosilicates such as illite, zeolites, micaceous clays and smectites contributed from the Bengal fan, weathering of basinal basalts and authigenic processes. Ternary mixing calculations of bulk sediment major element data show that 35–45% metalliferous sediments could reproduce Fe and Mn values of our sediments.
- The shale normalized REE patterns of the bulk sediments are remarkably similar to those of the HCl soluble leach fraction, implying that the REEs in the HCl soluble leach fraction dominate the bulk fraction. HCl leacheates exhibit characteristics of vent fluids as well as seawater with pronounced Eu anomaly with HREE enrichment and negative Ce anomaly. The residue on the other hand has a high concentration of Fe, V, Zn, and Pb indicating a sulfidic input to the sediments. Ternary mixing calculations of REEs carried out on the residual fraction indicate that the sulfide–like material dominates (64–72%) over terrigenous (10–20%) and MORB derived (16–18%) components in the acid–insoluble residue.
- Infrared spectroscopic studies indicate the presence of a dioctahedral smectites of monmorillonite–beidellite–nontronite series, with dominance of nontronite and ferruginous smectite suggesting a hydrothermal nature. Moreover, the composition of clay sized fraction is similar to known hydrothermal nontronitic clays from the Alvin

site. The temperature of formation for these smectites is estimated to range from 50° to 100°C. The presence of metalliferous sediments near the fracture zone suggests that the fracture zones may provide an easy conduit for in–situ volcanic activity in the area. While the earlier reports have shown spherules and lithic grains of metalliferous nature, this is the first study to report hydrothermal features in the bulk sediments of the CIB. The intraplate volcanoes located along the fracture zones, have therefore not only induced hydrothermal activity but also contributed nuclei and metals for the formation of the manganese nodules which are widespread in the CIB.

- The presence of aluminium rich particles in two sediment cores from the CIB, although geographically separated but are located at the base of two seamounts reaffirms their association with volcanogenic–hydrothermal material. These particles occur as grains and spherules and have an average Al content of ~95%. Morphologically and compositionally, the specimens are similar to those reported from the East Pacific Rise. It is hypothesized that during progressive melting of magma, a basaltic magma is produced which has high contents of reducants such as methane and hydrogen, and a low oxygen fugacity. During the upward migration of such magma, reduction to metallic aluminium and formation of Al rich particles tales place.
- Isotopic (^{210}Pb, ^{238}U–^{230}Th, ^{10}Be), major and trace elements, micromorphological and microchemical data, show evidence of recent (~100yrs) and contemporaneous hydrothermal alteration and degassing altering the >200kyr sedimentary record from this area. Alteration effects are also reflected in the depleted sedimentary organic carbon, 2) dissolution features of radiolarian skeletons; 3) the presence of altered minerals such as smectite and zeolites and 4) distinctly different magnetic properties in the altered sediments.
- The presence of hydrothermal sediments and subsequent alteration by circulating fluids may be widely prevalent in the CIB, than what is known presently, in view of the favorable sites of fluid ascent in the seamount flanks and along the conduits in the faulted areas of the well defined fracture zones. This is probably induced by reactivation of tectonic forces along the fracture zones.

Table 3.1: Major, rare earth and trace element concentrations in bulk sediments of AAS 61/BC 8. All values except those mentioned otherwise are in ppm.

Element/ Depth (cm)	0–2	2–4	4–6	6–8	8–10	10–12	12–14	14–16	16–18	18–20
Al (%)	6.43	6.75	6.74	6.82	6.74	6.65	6.61	6.74	6.55	6.63
Mn %)	1.47	1.47	1.32	1.39	1.45	1.46	1.33	1.31	1.32	1.39
Fe (%)	6.58	7.13	6.20	7.36	8.46	8.26	8.22	8.16	8.14	8.32
V	152	164	125	163	221	221	222	234	231	230
Cr	26	28	29	27	26	25	25	25	25	27
Co	138	147	140	146	149	148	139	137	139	146
Ni	782	761	562	562	490	428	333	300	294	336
Cu	473	452	378	359	332	307	279	264	258	260
Zn	177	178	171	175	184	180	176	185	197	194
Sr	187	195	179	200	224	228	231	233	234	233
Y	257	241	198	221	218	201	191	184	182	192
Zr	281	307	265	322	377	370	384	388	408	399
Ba	732	693	712	598	507	470	480	463	469	525
La	113	121	100	117	123	117	113	110	110	115
Ce	158	169	163	170	177	178	171	168	172	172
Pr	27.15	28.43	24.75	27.26	26.41	25.46	24.29	23.21	22.97	24.18
Nd	121	128	112	123	119	114	108	104	101	107
Sm	29.84	31.22	28.28	29.73	26.88	25.87	24.46	23.17	22.63	24.24
Eu	7.16	7.33	6.71	7.19	6.27	5.84	5.81	5.46	5.42	5.73
Gd	25.70	27.25	23.87	25.69	23.80	22.58	21.92	20.77	20.44	21.80
Tb	5.25	5.50	4.86	5.23	4.75	4.44	4.35	4.11	4.01	4.34
Dy	32.62	33.97	29.54	32.18	29.56	28.20	26.79	25.62	25.35	27.11
Ho	7.03	7.62	6.33	7.00	6.59	6.25	5.93	5.78	5.75	6.17
Er	20.23	22.00	18.02	20.29	19.33	18.41	17.38	16.79	16.87	17.69
Tm	3.06	3.27	2.68	3.02	2.91	2.71	2.64	2.51	2.55	2.64
Yb	17.99	19.24	16.09	17.89	17.41	16.18	15.57	14.83	14.83	15.69
Lu	2.87	3.10	2.58	2.78	2.75	2.58	2.45	2.40	2.33	2.49
Hf	6.65	7.08	6.30	7.71	8.60	8.63	8.79	8.67	8.85	8.37
Pb	19.22	19.82	19.27	19.22	19.05	18.39	18.11	17.78	17.59	17.69
Th	15.79	15.89	18.14	15.95	13.55	13.49	13.28	12.52	12.76	12.79
U	2.27	2.52	2.28	2.67	3.21	3.35	3.34	3.16	3.11	3.27

Table 3.2: Relative proportion (%) in HCl leachates and residue fraction in AAS 61/BC 8.

Sample ID:	4–6 cm		8–10 cm		12–14 cm		18–20 cm	
Analyte (%)	residue	leach	residue	leach	residue	leach	residue	leach
Al	66	34	59	41	59	41	57	43
Fe	15	85	13	87	13	87	14	86
V	19	81	14	86	15	85	10	90
Cr	55	45	58	42	45	55	43	57
Co	3	97	3	97	2	98	3	97
Ni	7	93	7	93	8	92	9	91
Cu	8	92	7	93	7	93	6	94
Zn	71	29	80	20	31	69	56	44
Sr	27	73	27	73	24	77	39	61
Y	4	96	4	96	5	95	3	97
La	8	92	8	92	9	91	6	94
Ce	9	91	8	92	7	93	7	93
Pr	6	94	7	93	8	92	5	95
Nd	5	95	6	94	7	93	5	95
Sm	4	96	5	95	7	93	4	96
Eu	5	95	7	93	7	93	6	94
Gd	4	96	4	96	5	95	4	96
Tb	4	96	4	96	6	94	3	97
Dy	4	96	5	96	6	94	4	96
Ho	4	96	4	96	6	94	4	96
Er	4	96	5	95	6	94	4	96
Tm	5	95	5	95	7	93	5	95
Yb	6	94	6	94	8	92	5	95
Lu	6	94	6	94	8	92	5	95
Pb	23	77	25	75	15	85	22	78
Th	34	66	25	75	30	70	19	81
U	38	62	28	72	24	76	26	74

Table 3.3: Important elemental ratios of the sediments of AAS 61/ BC 8

Ratios/Depth (cms)	0–2	2–4	4–6	6–8	8–10	10–12	12–14	14–16	16–18	18–20
Co+Ni+Cu*	1393	1360	1080	1068	971	882	751	701	690	743
Co/Zn	0.78	0.83	0.82	0.83	0.81	0.82	0.79	0.74	0.70	0.76
∑REE *	572	607	539	588	585	567	543	526	527	546
Eu/Eu*	1.22	1.18	1.22	1.22	1.17	1.14	1.18	1.17	1.19	1.17
Ce/Ce*	0.66	0.66	0.75	0.70	0.71	0.75	0.76	0.77	0.79	0.75
La/Ce	0.72	0.72	0.61	0.69	0.69	0.66	0.66	0.65	0.64	0.67
V/Fe x 10^{-4}	0.0023	0.0023	0.0020	0.0022	0.0026	0.0027	0.0027	0.0029	0.0028	0.0028
$(La/Yb)_{PAAS}$	0.46	0.47	0.46	0.48	0.52	0.53	0.53	0.55	0.55	0.54
Fe/Mn	4.47	4.85	4.71	5.31	5.84	5.67	6.17	6.23	6.18	6.00
Fe_2O_3/Al_2O_3	0.78	0.80	0.70	0.82	0.95	0.94	0.94	0.92	0.94	0.95
∑REE/Fe	0.0087	0.0085	0.0087	0.0080	0.0069	0.0069	0.0065	0.0061	0.0056	0.0052
Nd/Fe	0.0018	0.0018	0.0018	0.0017	0.0014	0.0014	0.0013	0.0012	0.0011	0.0010
MSI	44.38	43.97	47.25	43.81	40.50	40.64	40.90	41.58	40.92	40.58
∑REE/Fe(leach)	NA	129.5	NA	86	NA	86	NA	NA	NA	93

NA: not analyzed
*ppm

Table 3.4: Fe normalized element concentrations of the bulk sediments of this study compared with literature data.

Element	this study	RTJ sediments (cfb)[a]	CIR sediments [b]	EPR 10°S Fe–Mn oxides[c]	Fe oxides[d]	TAG Nontronite[e]
Mn/Fe	0.1829	0.077	0.107	0.22	0.15	no data
Zn/Fe	0.0024	0.001	0.002	0.003	0.002	0.004

[a] RTJ sediments (Kuhn et al., 2000).
[b] CIR sediments containing 48.5 % hydrothermal Fe–Mn oxides from 21° 34' S (Plüger et al., 1986)
[c] East Pacific Rise (10°S) sediments mainly consisting of Fe–Mn oxides (Walter and Stoffers, 1985)
[d] Hydrothermal Fe oxides from the North Fiji basin (McMurtry et al., 1991)
[e] Hydrothermal clays from TAG zone associated with sulphide debris and Fe oxides (Severmann et al., 2004)
cfb: carbonate free basis

Table 3.5: Microprobe and EDS analyses of aluminium rich specimens recovered from two sediment cores in the CIB. The specimens have been classified as G = Grain, S = Spherule, O = Oval, I = Irregular, M = Massive. (All values in wt%, nd– not detected).

	SiO_2	TiO_2	Al_2O_3	Fe_2O_3	MgO	CaO	Na_2O	K_2O	P_2O_5	SO_3	CuO	ZnO	Ag_2O
Northern area (#S657)													
17–18 cm													
1	1.91	nd	96.77	0.09	nd	0.84	0.07	0.12	0.21	nd	nd	nd	nd
2	0.66	nd	98.4	nd	nd	0.88	0.03	0.02	nd	nd	nd	nd	nd
3	0.23	nd	98.76	nd	nd	0.76	nd	nd	0.23	nd	nd	nd	nd
4	0.3	nd	98.68	nd	nd	0.81	0.02	nd	0.17	nd	nd	nd	nd
5	0.46	nd	98.52	nd	nd	0.88	nd	nd	0.13	nd	nd	nd	nd
6	0.32	nd	98.55	nd	nd	0.82	nd	0.04	0.28	nd	nd	nd	nd
7	0.56	nd	98.08	0.1	nd	0.94	0.19	0.09	0.27	nd	nd	nd	nd
8	0.45	nd	98.59	nd	nd	0.85	nd	nd	0.12	nd	nd	nd	nd
9	0.46	nd	98.61	nd	nd	0.74	0.03	0.03	0.12	nd	nd	nd	nd
10	0.24	nd	98.61	nd	nd	0.76	nd	nd	0.16	nd	nd	nd	nd
22–24 cm													
11	0.3	nd	98.84	nd	nd	0.83	0.02	0.02	nd	nd	nd	nd	nd
12	0.28	0.02	98.77	nd	nd	0.78	nd	nd	0.13	nd	nd	nd	nd
13	0.52	nd	98.36	nd	nd	0.9	0.03	0.03	0.14	nd	nd	nd	nd
14	0.13	0.03	99.11	nd	nd	0.62	nd	nd	0.11	nd	nd	nd	nd
15	0.24	nd	98.69	0.12	nd	0.74	0.06	nd	0.17	nd	nd	nd	nd
16	0.53	nd	98.25	nd	nd	0.82	0.05	nd	0.33	nd	nd	nd	nd
17	0.99	nd	97.98	nd	nd	0.9	nd	nd	0.11	nd	nd	nd	nd
18	0.35	nd	98.42	nd	nd	0.89	0.06	nd	0.29	nd	nd	nd	nd
19	0.34	nd	98.68	0.07	nd	0.77	nd	nd	0.15	nd	nd	nd	nd
20	0.3	nd	98.91	nd	nd	0.62	nd	0.03	0.15	nd	nd	nd	nd
25–26 cm													
21	0.32	nd	96.73	nd	2.01	0.8	nd	nd	0.15	nd	nd	nd	nd
Southern area (#AAS 61/BC 8)													
22	1.57	nd	94.48	nd	0.24	nd	nd	nd	nd	1.97	0.68	0.88	0.17
23	1.44	nd	96.65	nd	0.51	nd	nd	nd	nd	nd	0.43	0.53	0.53
24	nd	nd	84.65	nd	nd	nd	nd	nd	nd	nd	6.14	9.19	nd
25	3.28	nd	96.72	nd	nd	nd	nd	nd	nd	nd	nd	nd	nd

Chapter 4

Volcanogenic sedimentation along a fracture zone

4.1. Introduction

The occurrence of ash in marine sediments has long been recognized to be an important component of the global sedimentary system (Scudder et al., 2009). Tephra layers in marine sediments provide a high–resolution and temporally precise record of volcanic activity (Paterne et al., 1988; Arculus and Bloomfield, 1992; Bednarz and Schmincke, 1994). Submarine tephra studies have become increasingly important because distal tephra deposits are often the only indicators for reconstructing the petrogenetic evolution of volcanic terrains that have been eroded or buried under younger sediments (Fisher and Schmincke, 1984; Straub, 1997). Tephra also provide a link to past volcanism, climate, arc evolution, biological productivity and other geological processes (e.g. Kennett et al., 1977; Straub, 1995, 2003; Carey, 1997; Ziegler et al., 2007). The petrogenetic significance of submarine tephra layers, however, is not always easy to interpret. Marine tephra layers, mostly characterized by their glass shard fraction are known to be compositionally heterogeneous, thus enhancing the problem of compositional contrast. This may reflect pre–eruptive zoning of the magma chamber, syn– or post-depositional mixing, or mixing of material produced from different contemporaneous eruptions. Moreover, glass shard composition likely represents derivative liquids of less evolved source area magmas, the evolved composition of which obscures essential information about the magma source and their evolution (Straub, 1997).

Recently, several papers have been published which have attempted to summarize and collect details on the techniques involved in tephrochronology and the information on the tephra layers. These include Haflidason et al. (2000), Turney et al. (2004), Dugmore et al. (2004) and Hunt and Hill (1993, 2001). Chemically fingerprinting the deposit of a volcanic eruption is invaluable for identifying these chronostratigraphic markers over wide areas, and correlating them to particular eruptions. Typically, the chemistry of glass shards, is unique and allows different eruptions to be distinguished. Eruptions from the same volcano are, however, generally compositionally similar and glass chemistry of successive eruptions is commonly not distinctive (Smith et al., 2005, 2011).

Tephra layers have been reported in a number of areas, for example on the Vityaz Fracture zone on the Indian Ocean ridge flank (Nath and Iyer, 1989), in

Iceland, New Zealand and Kamchatka (Braitseva et al., 1997; Larsen et al., 1999; Lowe et al., 2000), CIB (Mascarenhas–Pereira et al., 2006, Pattan et al., 1999) but invisible (and often microscopic) cryptotephra layers (Basile et al., 2001; Turney et al., 2004; Peters et al., 2000; Scudder et al., 2009) have been found in many more areas of the world at a distance from volcanic sources (e.g. Scudder et al., 2009; Von Rad et al., 2002; Wastegard 2005). However no cryptotephra tephra have been reported in the CIB sediments till date. Some historic tephras can be assigned a known calendar date such as the eruptions of Toba in Indonesia at 840,000 ± 30,000, 500,000 ± 5,000 and at 73,000 ± 4,000yrs ($^{40}Ar/ ^{39}Ar$ ages reported by Diehl et al., 1987; Chesner et al., 1991).

There are many possible sources that could contribute to the volcanogenic material to the Indian Ocean such as the Reunion hotspot (Upton and Wadsworth, 1966; Fretzdorff and Haase, 2002), the Kerguelen plume (Wallace, 2002), Broken ridge (Mahoney et al., 1995), Indian Ocean Ridge volcanics (Price et al., 1986), Afro-Arabian flood volcanism (Ukstins Peate et al., 2003) and the Taupo volcanic center (New Zealand) (Sutton et al., 1995; Wilson, 1993). Earlier studies on volcanogenic sediments from other locations in the Central Indian Basin by Gupta (1988); Sukumaran et al. (1999); Iyer et al. (1993, 1997); Pattan et al. (1999) and Martin–Barajas and Lallier–Vergas (1993) have proposed insitu volcanic source, distal fallout from Toba or Indonesian volcanic arc, respectively. In an extension to the work done by Mascarenhas–Pereira et al. (2006), on a sediment core from a flank of a seamount along the 76° 30'E fracture zone, four additional cores collected all along the same fracture zone from north to south were examined for glass shard morphology and chemistry for a regional coverage and to test the hypothesis of widespread dispersal of Youngest Toba Tuff (YTT; Pattan et al., 1999). Often, source is assigned based on compositional similarity without considering the age of the tephra or tephra bearing sediments. Thus, these cores were also dated radiochemically to decipher the precise timing of the volcanic history of the cores. We then discuss the relationship between the morphology and chemistry of the shards in order to decipher the origin of this volcanoclastic material and the extent of this activity. For the first time, an attempt is made here to identify cryptotephra in the CIB sediments. The terms tephra,

glass or shards as used in this chapter mean the same and all the three terms represent the volcanoclastic grains studied here.

4.2. Sample details and lithology of cores

Five short sediment cores i.e. BC 8, BC 13, BC 14, BC 20 and BC 25 of cruise AAS 61 of R.V.A.A. Sidorenko were used for this study (Fig. 4.1a). In addition, 4 cores (BC 36, 37, 38 and TVBC 08R), representing a flank of a seamount, top of a seamount, and a valley adjacent to the seamount all from the 76° 30'E fracture zone complex in CIB, collected during 4th cruise of R.V. Akademik Boris Petrov (ABP-04) were selected for this study to assess the regional variability of dispersal of volcanogenic sediments. Detailed topography of the fracture zone and the locations of sampled stations are shown in Fig. 4.1b. All these sediment cores were collected as a part of the project on "Environmental Impact Assessment for Nodule Mining" (PMN-EIA).

4.3. Results

In this section, results of textural analyses of silt and clay fraction, ash counts in sand fraction, morphological and chemical characteristics of separated glass shards/ash grains, dating of sediments, bulk sediment chemical data are presented (Figs. 4.2 to 4.7; Tables 4.1 to 4.3).

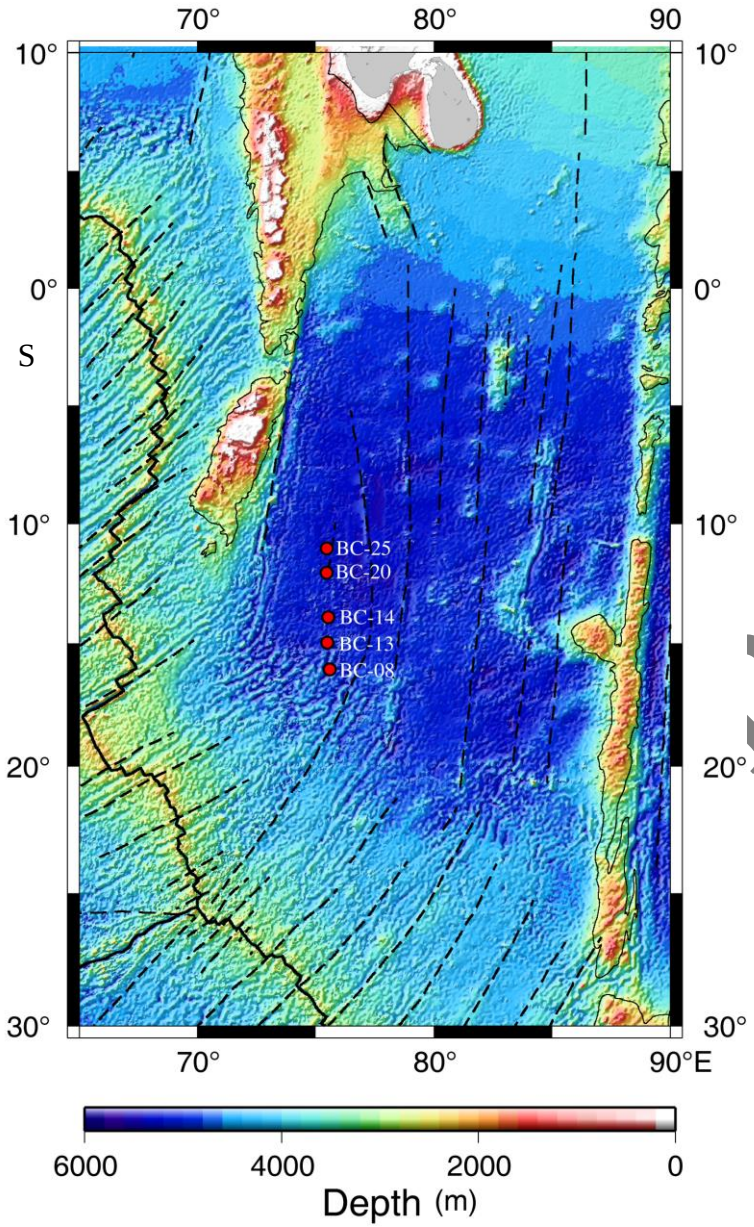

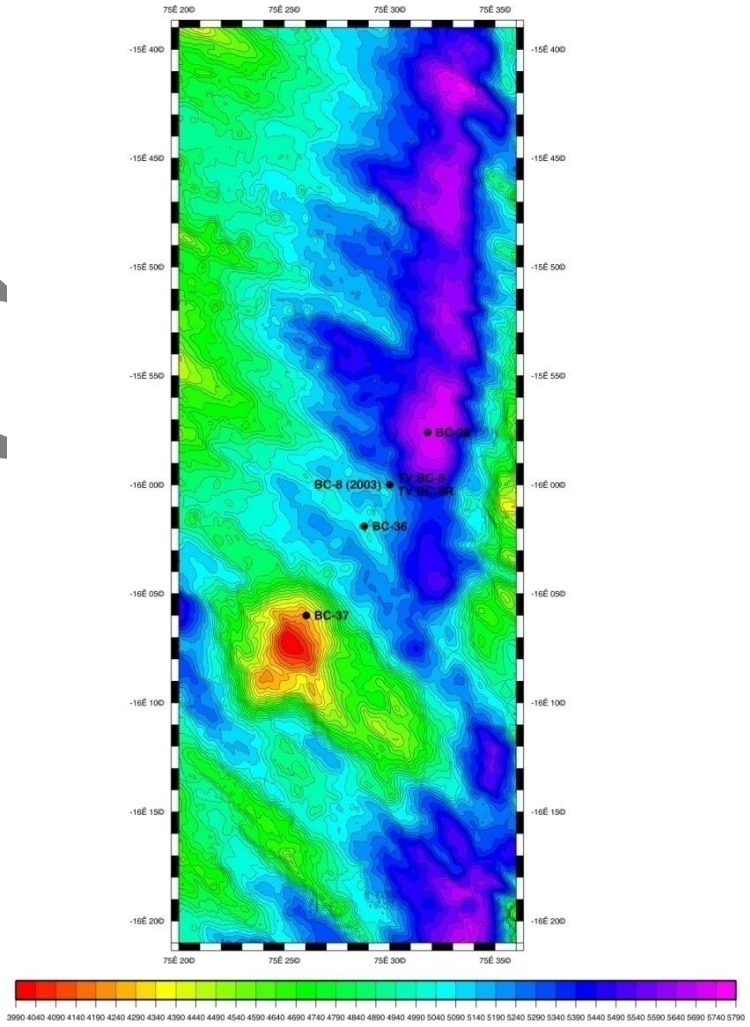

Fig. 4.1: (a) Major physiographic features of the Indian Ocean along with the location of the cores studied. Dashed lines indicate the fracture zones (from Kamesh Raju et al., 1993); (b) Detailed multibeam map of a part of fracture zone. Four sediment cores from different depth domains are marked in the figure

4.3.1. Textural data

Laser particle size analyses (LPSA) were carried out on size fraction <63 µm in all the sections of the cores (Fig. 4.2). While the mean grain size of the samples ranges from ~13 to 34 µm, the median grain size varies between ~5 and 30 µm. The size spectra reveal a distinct bimodal distribution of sizes in all the sediment sections studied. The higher volume percentage is seen in two size ranges, one between 20 and 50 µm which is coarse and the second between 2 and 5 µm which is fine. In these two size ranges, there is an inverse relationship between the maximum volume percentage and size of the particles. Those samples having higher volume in the size range 20-50 µm have lesser volume % in 2-5 µm. Significantly, however AAS 61/BC 13 which is the southernmost core show a high volume % in the range of 2-5 µm and less in 20-50 µm. It is observed that the northern most part of the study area (AAS 61/BC 25, 11°S) had coarser sediments of size >20 µm, while the southern part of study area (AAS 61/BC 13, 15°S) had median grain size more than 13 µm.

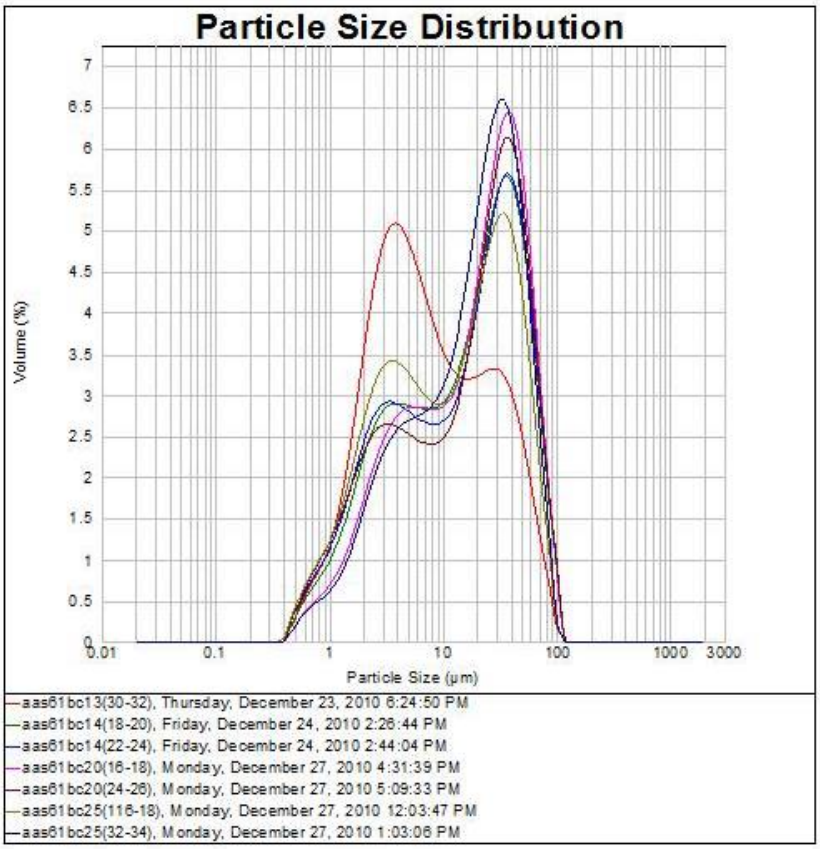

Fig. 4.2: Histograms of particle size distribution of the two volcanic horizons in the four cores studied using Laser particle size analyser.

4.3.2. Volcanic glass count and morphological description

The coarse fraction (>45 and 63 µm) was studied under the microscope. All the sediments with bimodal distributions have volcanic ash in the coarser size fraction. A known quantity of coarse fraction obtained after coning and quartering was weighed and the number of glass shards were counted under the microscope and subsequently calculated on per gram basis to demarcate the depths at which the glass shards were abundant. The abundance of glass shards in the cores studied is shown in Fig. 4.2. The data have shown that volcanic glass was prominently abundant at two horizons in cores AAS 61/BC 14 at 18-20 cm and 22-24 cm, in AAS 61/BC 20 at 16-18 and 24-26 cm and AAS 61/BC 25 at 16-18 cm and 32-34 cm; at one horizon in AAS 61/BC 13 at 30-32 cm and below 8 cm bsf in AAS 61/BC 8 core (Table 4.1).

The microscopic investigations indicated the glass shards to be fresh, shining and colourless and indicative of a silicic composition (Horn et al., 1969) with different sizes (45–250 µm) and shapes with no signs of alteration. Colorless volcanic glass shards were found dispersed through most of the core length. Scanning Electron Microscopy images allowed us to describe the morphological features of the tephra. Representative photos of shards recovered from both the depths are presented in Fig. 4.3. The tephra comprised of four different types of shards (Fig. 4.3) that were easily distinguished microscopically in all the cores studied, 1) blocky with a few vesicles, 2) platy, 3) bubble walled or Y-shaped with smooth and slightly curved surfaces and 4) angular, moderately vesicular shards with tubular vesicles that extend the length of the shard. In addition, the layers contained micronodules, lithics (e.g. quartz, palagonites) and bioclast fragments.

AAS 61/BC 20, 16–18 cm

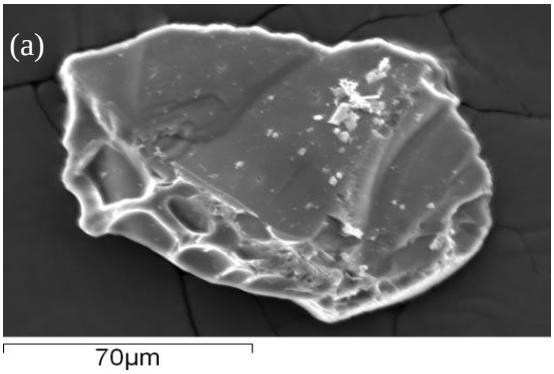

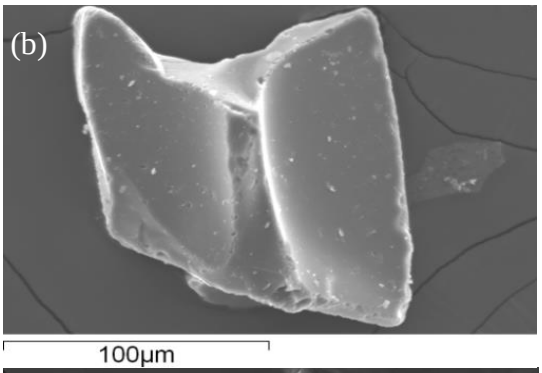

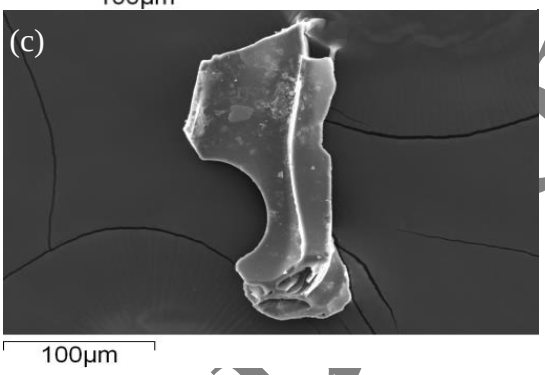

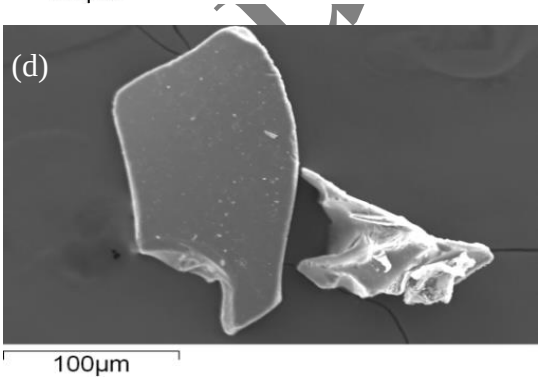

24–26 cm

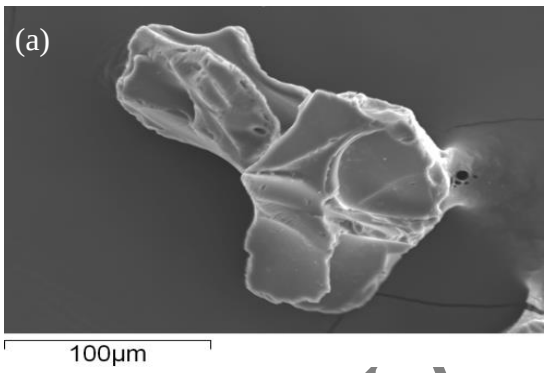

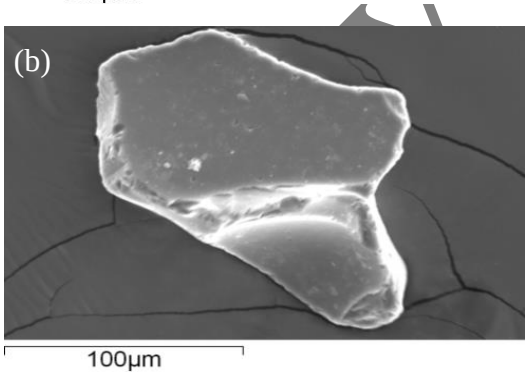

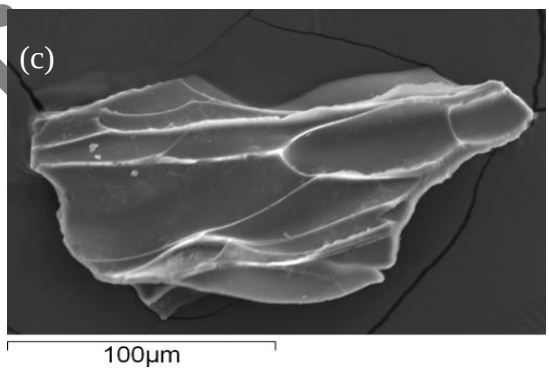

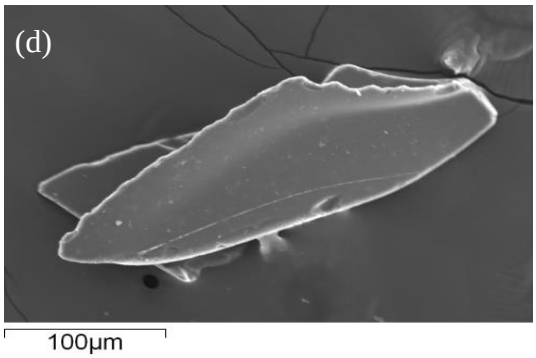

AS 61/BC 25, 16–18 cm

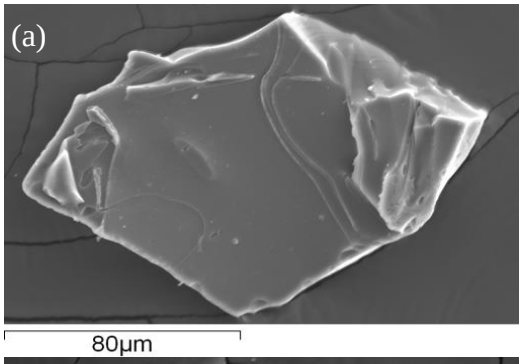

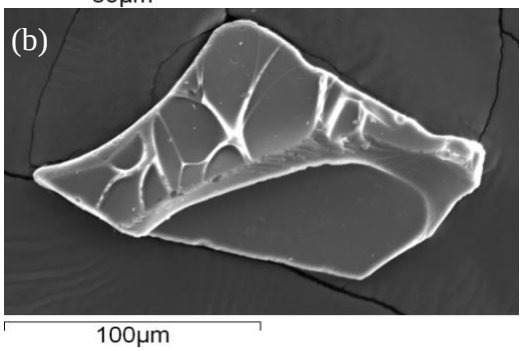

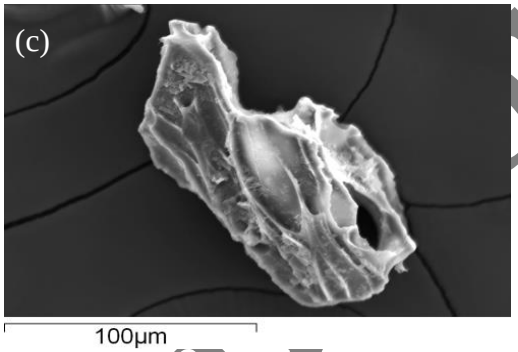

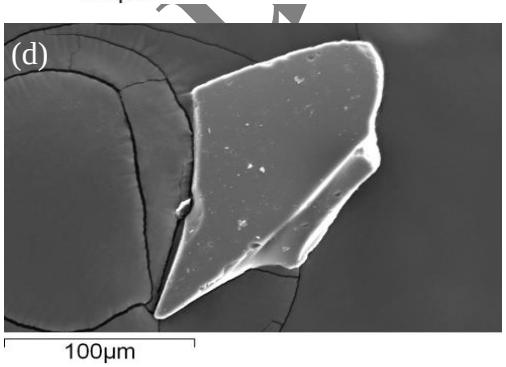

32–34 cm

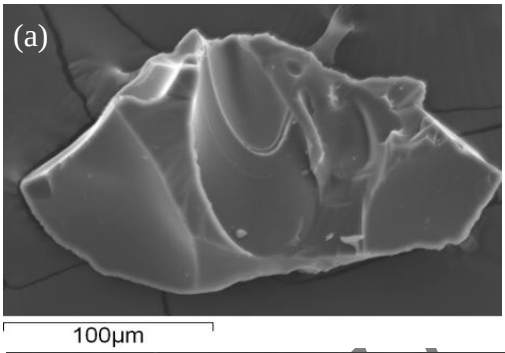

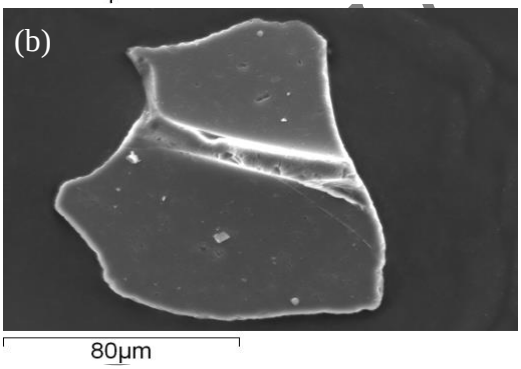

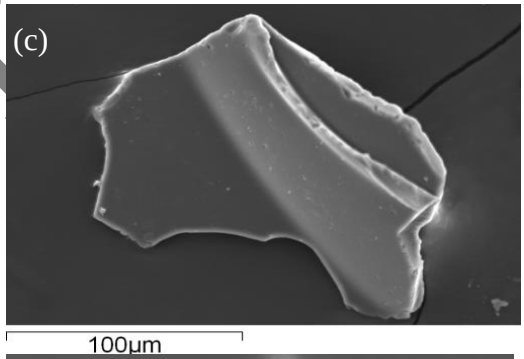

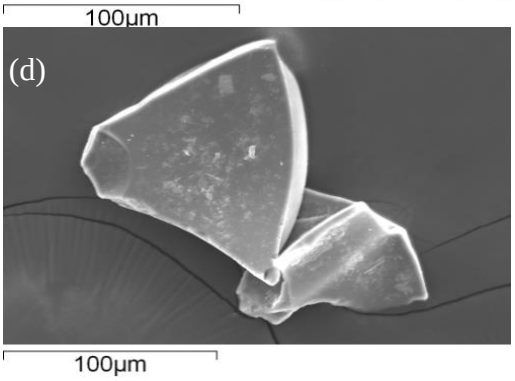

AAS 61/BC 14, 18–20 cm

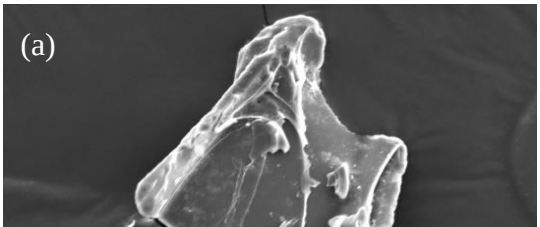

22–24 cm

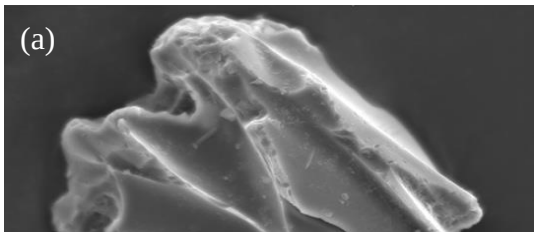

Fig. 4.3: Scanning electron microscope photographs of glasses investigated (scale and magnification at the bottom of the Figures). The left hand panel shows the glass shards recovered from a shallow depth while the right hand panel shows the photographs of glass shards from deeper depth. The glass morphologies recovered from both the depths in the three cores studied are similar. (a) massive shards with sharp edges; (b) bubble wall shards with smooth and slightly curved surfaces; (c) Massive shards with vescicles extending the length of the shard; (d) platy shard with angular and sharp edges.

4.3.3. Refractive Index

Different morphological types of glass (platy, bubble wall, vesicular and massive) were separated from the sediment cores (ABP 04/BC-37, ABP 04/BC-36, ABP 04/TVBC-08R, ABP 04/BC-38) sampled from different sub-environments (valley: ABP 04/BC 38; flank of a seamount: ABP 04/BC 36 and ABP 04/TVBC 08R and seamount top: ABP 04/BC 37) within the fracture zone complex in the CIB (Fig. 4.1b). Glass fragments, which were picked, were tested with liquids of different specific gravity (1.492, 1.493, 1.497, 1.512, 1.515, 1.518) for the determination of refractive index (RI) for both the size fractions (>45 and >63 μm). The table 4.2 shows the refractive index of volcanic glass shards from four cores.

RI of different morphological glass types in all the sediments of the 4 cores studied ranged between 1.493 and 1.518 (Table 4.2). The maximum RI (1.518) was seen in ABP 04/BC 36 and BC 38 which are located on the flank of seamount and valley respectively, while the lowest RI (1.493) (Table 4.2) was restricted to platy type of glass shards. Most of the glass fragments are colorless and transparent indicating possibly a felsic source. Previous studies in the area also have revealed siliceous tephra. RI was found to vary with the composition (George 1924) and there is a close correlation between RI and silica content (Williams et al., 1954). Therefore RI of volcanic glasses is an important parameter for determination of magmatic source and magmatic composition. Further, the mean RI is a very good indicator to determine the bulk chemistry in terms of concentration of major as well as trace element composition of natural volcanic glasses (Langford, 1984). The refractive index of 1.500 ± 0.005 for the colorless glass corresponds to a silica percentage of about 70–74%, which possibly indicates rhyolitic composition. The RI of all the glass shards studied fall in a narrow range of 1.493–1.518 (Table 4.2), which may indicate that, they have a common source.

4.3.4. Radiometric dating and age of tephra layers.

The sediments of the cores AAS 61: BC 14, 20 and 25 were radiometrically dated using excess ^{230}Th method ($^{230}Th_{excess}$ portion of the ^{230}Th that is not supported by the decay of ^{234}U in the sediments). The ages were obtained from the down core

distribution of $^{230}Th_{excess}$ activity (Borole, 1993), assuming constant sediment accumulation and rain rate of ^{230}Th to the core sites. The measured $^{230}Th_{excess}$ activity is a function of depth for AAS 61/BC 14, 20 and 25. The decay curve of $^{230}Th_{excess}$ for sediment section between the surface (0 cm) and the bottom of the cores (26 cm for AAS 61/BC 14; 34 cm for AAS 61/BC 20 and 25 and 36 cm for AAS 61/BC 13) is linear with depth and involved a single slope averaged over the entire core depth (Table 4.1; Fig. 4.4). The estimated sedimentation rates are 0.269 cm kyr^{-1} and corresponds to an age of ~92 kyr for the sediments at 26 cm for AAS 61/BC 14 (^{230}Th half life = ~75 kyr), 0.229 cm kyr^{-1} and corresponds to an age of 146 kyr for the sediments at 34 cm for AAS 61/BC 20 and the sedimentation rate of 0.233 cm kyr^{-1} for AAS 61/BC 25 gives a maximum age of ~141 kyr at the base of 34 cm. These rates of low sedimentation rate are not uncommon in the CIB and were also reported on the flank of a seamount in CIB, which is the southernmost end of the study area (0.032 cm kyr^{-1}, Mascarenhas–Pereira et al., 2006; 0.062 cm/kyr, Nath et al., 2013). These ages are plotted as a function of depth to estimate the depositional ages of the ash layers. Sediments of cores AAS 61/BC 25 and 20 record a longer age span (141 and 146 kyr respectively) compared to AAS 61/BC 13 and 14 which

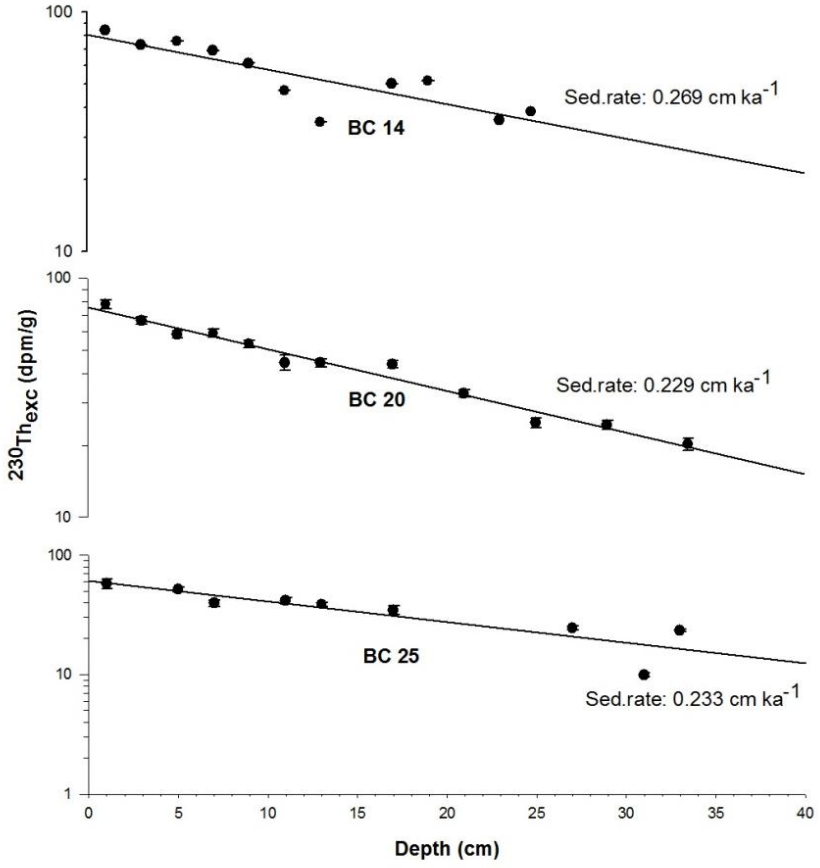

Fig. 4.4: $^{230}Th_{excess}$ profile in cores showing sedimentation rates of 0.269 cm/kyr for AAS 61/BC 14, 0.229 cm/kyr for AAS 61/BC 20, of 0.233 cm/kyr for AAS 61/BC 25.

extends to ~85 and 92 kyr respectively. The shallower ash layers in all the cores displayed a maximum age of ~74 kyr, while the deeper ash layer exhibited an age of >180 kyr. The age of the deeper tephra layer increases southwards from ~85 kyr in AAS 61/BC 20 (12°S), 109 kyr in AAS 61/BC 14 (14°S), 141 kyr in AAS 61/BC 13 (15°S) and >180 kyr in AAS 61/BC 8 (16°S) (Mascarenhas–Pereira et al., 2006).

4.3.5. Glass chemistry

We obtained EDS data on individual, fresh glass shards (Table 4.3). All the four morphological types were analyzed for their major constituents. These analyses were comparable to those of fresh glasses elsewhere (Fisher and Schmincke, 1984). No significant change in major oxide composition was seen as a function of glass morphology.

The glass shards have the composition of high silica with a large range of SiO_2 (73 – 79%), K_2O (3.9 – 7.17%), Na_2O (1.71 – 6.35%) and low TiO_2 (0.01 – 0.27%). High silica content suggests that the glass shards studied here can be classified to be of rhyolitic in composition (following the classification of Marsh, 1976), as andesites (57 ± 3% SiO_2) and dacites (63 ± 3% SiO_2) have less silica than rhyolites. Low TiO_2 (0.01 – 0.27%) of the glass is consistent with high SiO_2 concentration (73 – 79%). The analyzed samples display a range in chemical composition of total alkalies (Na_2O+K_2O) from 7.63 to 10.52%.

4.4. Discussion

The grain morphological studies of the shards in all the cores indicate two shard populations at two different depths; shallower tephra layer dominated by bubble wall shards, while the deeper tephra layer is dominated with massive and blocky shards (Fig. 4.3). The shape of individual fragmented clast is usually related to its mode of interaction with water (Wohletz, 1983). The blocky shards with a few vesicles, showing spherical to oval shape are typically formed in hydroclastic processes, while bubble walled or Y–shaped with smooth and slightly curved surfaces, represent the remnants of three bubble junctions, or double concave plates that formed the wall between adjoining bubbles (Fisher and Schmincke, 1984) probably formed sub-aerially. Platy shards probably formed from the glass walls

separating large flattened vesicles and angular shards which are moderately vesicular with tubular vesicles that extend the entire length of the shard were also present in the cores. Shards range from highly vesicular to poorly vesiculated and block/massive. The vesicles coalesce to give rise to a tubular morphology (Fig. 4.3). The glass shards have conchoidal to (irregular) angular fractures that likely record rapid quench fragmentation during interaction between magma and water. Bubble wall shards are typical of explosive volcanism and aerial transport while massive/block shards typically indicate a submarine source.

These morphological features suggest that the glass shards in the younger sediments are of magmatic origin and very similar to glass shards in some other cores from the Indian Ocean and in the Bay of Bengal (Rose and Chesner., 1987; Gasparatto et al., 2000; Liu et al., 2006).

Additionally, the particle size studies show a bimodal size distribution for all the cores studied. The first peak which is between 2 and 5 μm size can be considered to be representative of the clay component in the sample and the second peak which is silt-sized between 20 and 50. There was a distinct regional pattern (latitudinal) seen in the two size fractions (2–5 and 20–50 μm) as revealed by the LPSA data (Fig. 4.2). A prominent increase in the volume % is seen in the 20–50 μm in AAS 61/BC 25 core which also happens to be the northern most core (11°S), while the least volume % is seen in the finer fraction (2–5 μm) in the southern core (AAS 61/BC 14, 14°S). The volume % of clay-sized dominant peak in these samples is less than the volume % of peak representing silt size. The peaks probably represent clay minerals and other minerals of weathered nature. Clay minerals in CIB are contributed from three sources, viz., through turbidity current from north in the Bay of Bengal mainly contributed by Ganges-Brahmaputra rivers (Rao and Nath, 1988), aeolian transport from distal areas such as South Africa and Australia (Fagel 2007 and references therein; Nath et al., 2013) and the alteration of basinal volcanic sources. On the other hand, the peak at medium coarse-silt range would either represent biogenic silica or volcanic ash, both of which are abundantly present in the basin. However, the samples were treated with sodium carbonate which has removed opaline silica.

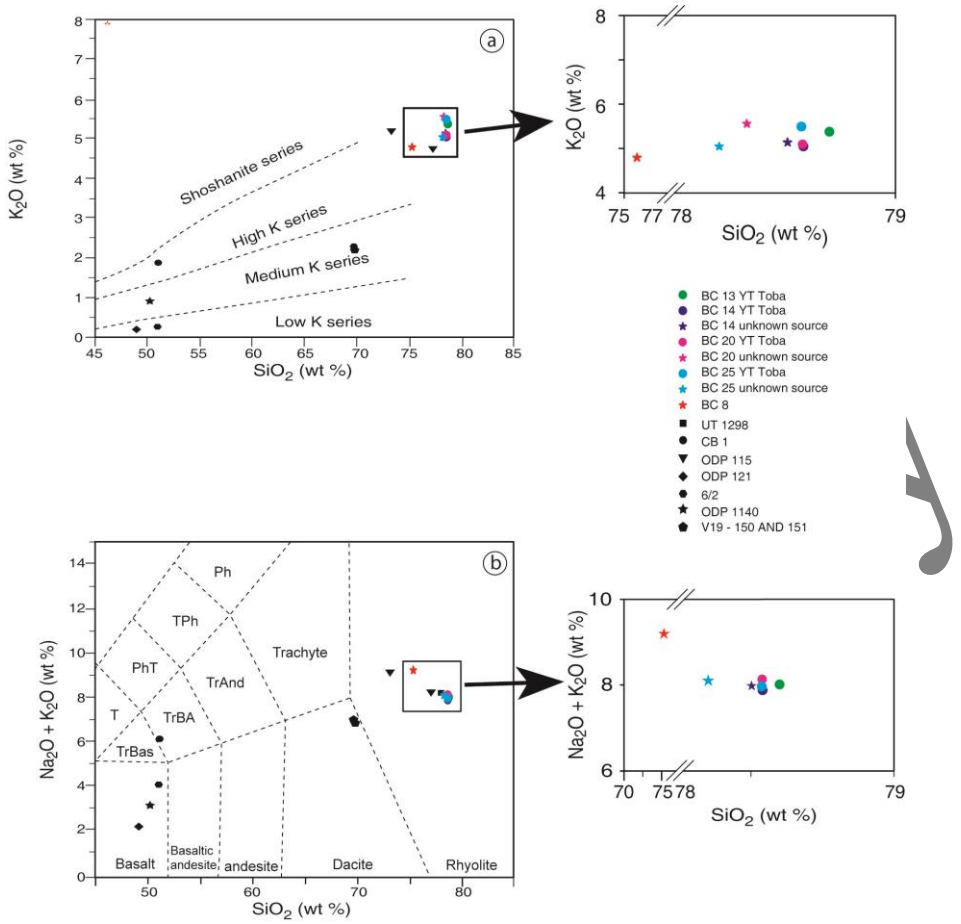

Fig. 4.5: (a) $Na_2O + K_2O$ vs. SiO_2 plot (TAS diagram). Nomenclature fields after Le Bas at al., (1986), with abbreviations: Tr, trachytic; T, tephrite; PhT, phonotephrite; TPh, tephri–phonolite; Ph, phonolite. The shards of the present study plot in the rhyolitic field.
(b) K_2O vs. SiO_2 plot of the shards, which shows all glasses with high SiO_2 plot in the high K series, while those of Kerguelen plateau, Broken ridge, Indian Ocean triple junction, including glass reported by Ninkovitch (1979), for the Toba caldera plot in the middle to low K series. Series boundaries after Rickwood (1989). Symbols for different volcanic field are same as in Fig 4.5a.

In order to be able to chemically distinguish the source of the tephra in these sediments Total Alkalis vs. Silica (TAS) diagram (Fig. 4.5) was plotted. Initial and limited data for Toba units (e.g. Westgate et al., 1998; Shane et al., 1995) did not show much variation, however later studies on Toba units (Smith et al., 2011) comprising of a larger data set showed much more compositional variation. This was attributed to similarity of the composition of deposits of the Toba eruption. In the present study, major oxides (wt %) of the glass shards from AAS 61/BC 14, 20 and 25 tephra layers were plotted (Fig. 4.6). The compositional ranges of the elements in both

the layers (Toba and Non Toba) overlap in all the three cores (Fig. 4.7, Table 4.3) probably due to similar composition of the glass shards. The distal tephra deposits found in the deeper layer identified by visual studies reveal an age of deposition of ~100 kyrs (AAS 61/BC 20 and 25). The morphology of the shards found in these older sediments (massive and block type; Fig. 4.3) indicate a submarine source.

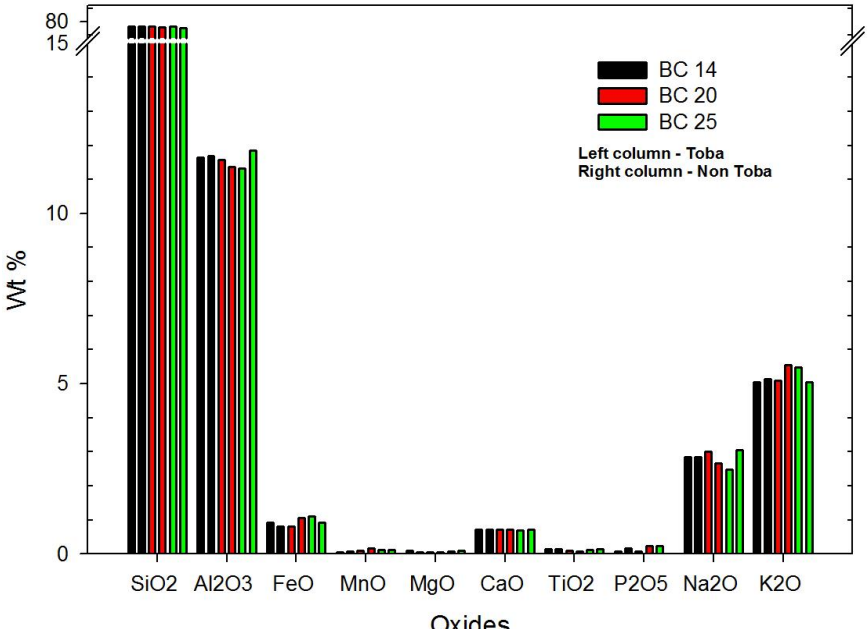

Fig. 4.6: Comparison of major oxides (average of shards in each layer) in three cores (Black columns: AAS 61/BC 14, red columns: AAS 61/BC 20 and green columns AAS 61/BC 25). The oxide wt % in both the ash layers in all the cores is similar and therefore cannot be differentiated chemically.

One of the possible source of volcanic ash to the study area is the rhyolitic emissions that occurred in the Toba region identified as Oldest Toba Tuff at 840,000 ± 30,000, Middle Toba Tuff: 500,000 ± 5,000 and Youngest Toba Tuff at 73,000 ± 4,000yrs (Diehl et al., 1987; Chesner et al., 1991). The age of this older layer does not correspond to any of the three Toba eruptions (YTT, MTT and OTT). Similar glass chemistries and morphologies were also found in the southern most core (AAS 61/BC 8, 16°S) which is reported to have been derived from insitu volcanism (>180 kys) (Mascarenhas–Pereira et al., 2006).

4.4.1. Determining cryptotephra in sediments

To confirm the ash layers found in the cores using abundance of glass shards, an attempt is made here to see if trace and minor element chemistry of bulk sediments could provide a diagnostic indicator for detecting cryptotephra in the core. Visual techniques such as microscopic observations are commonly employed to estimate the

abundance of discrete ash in sediments. Cryptotephra, is invisible to the naked eye and thus difficult to identify on account of their very fine grain size and of low abundance and alteration of ash grains to authigenic clays (Scudder et al., 2009). Such features (cryptotephra) are the result of small to moderate eruptions, long distance from the source volcano, or bioturbation (Lowe and Turney, 1997). Cryptotephra may be distributed hundreds of kilometers from the source (Pollard et al., 2006) and are dominated by glass shards finer than 80 μm in diameter (Basile et al., 2001; Turney et al., 2004). Many methods such as Cr, Al and Nb based normative calculations (Peters et al., 2000; Scudder et al., 2009), are used to quantify the concentration of cryptotephra in the sediments. We have used the single element normative calculation based on Scudder et al. (2009) and Urbat and Pletsch (2003). Urbat and Pletsch, (2003) used normative calculations on the basis of Al and Cr contents to discriminate between the major sediment components (terrigenous, volcanogenic, biogenic, and diagenetic). A few assumptions are made for both the methods. Accordingly, first-order estimates of the amount of dispersed ash was estimated by normalizing the Al concentration in each sample to average shale to estimate the total amount of "terrigenous clay and ash" (Plank et al., 2000), on the premise that the Al concentration in the ash and terrigenous material are approximately equal. Concentrations of Nb and Cr were then used to calculate the amount of terrigenous material, with dispersed volcanic ash being subsequently determined by its difference. In case of Cr based normative calculations, we assumed that all Cr is in the terrigenous components and that the volcanic components do not contain any Cr. Secondly, we assumed that the Al and Cr concentrations in the respective components correspond to the concentrations of these elements in the average shale. The latter assumption is warranted because the purest discrete ash layers contain only very low concentrations of Cr (17-38 ppm) compared to Cr concentration of average shale (110 ppm) (Taylor and McLennan, 1985).

Assumption 1: all Al is in Ter and Vol
Step 1: $\%TerVol = (Al_{sample}/Al_{shale}) \times 100$.
Assumption 2: Vol contains no Cr
Step 2: $\%Vol = \%TerVol - (Cr_{sample}/Cr_{shale}) \times 100$.
Assumption 3: All Cr is in terrigenous component.
Step 3: %Ter = 100% – %Vol.

In the present cores, however, the mixed compositional nature of the sediments requires use of another element, because Cr is mostly enriched in the lithogenic fraction (Taylor and Nesbitt., 1998). Basalts may have significant Cr (Taylor and McLennan, 1985). Accordingly, we used Nb-based normative calculations to determine the ash layers. In case of Nb-based normative calculations, we assume that all Nb is in the volcanic component. Nb is enriched in average shale (19 ppm; Taylor and McLennan, 1985) and commonly depleted in ashes (0.5-6 ppm; Taylor and Nesbitt, 1998) and rhyolites (~3.09 ppm; Scudder et al., 2009) similar to the concentration found in the sediments of the study area. Nb-based normative calculations suggest that 19–29 % of the sediments are comprised of ash (Fig. 4.7), while Cr-based normative calculations suggest that 26–31wt% of the sediments is comprised of ash (Fig. 4.7). The estimation of ash in the sediments in the three cores based on both the Nb and Cr normative calculations are in good agreement and perfectly support the visual estimates of ash in the cores. However none of these methods (Cr- and Nb-based calculations) are able to distinguish compositional variation within the total bulk composition, nor can they identify the source of these ashes in the sediments (Scudder et al., 2009).

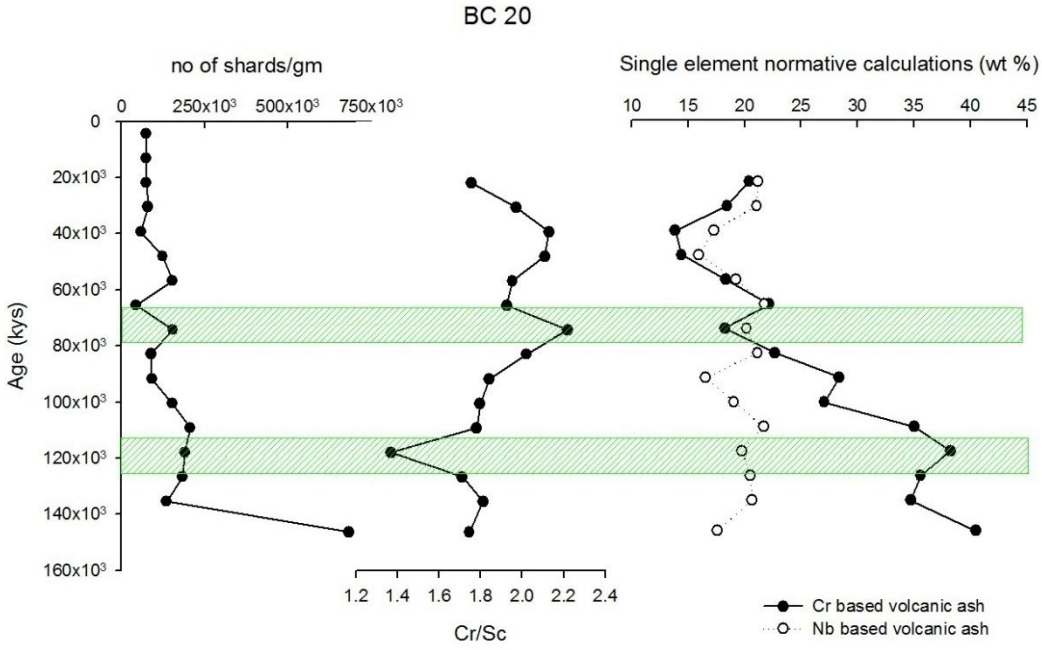

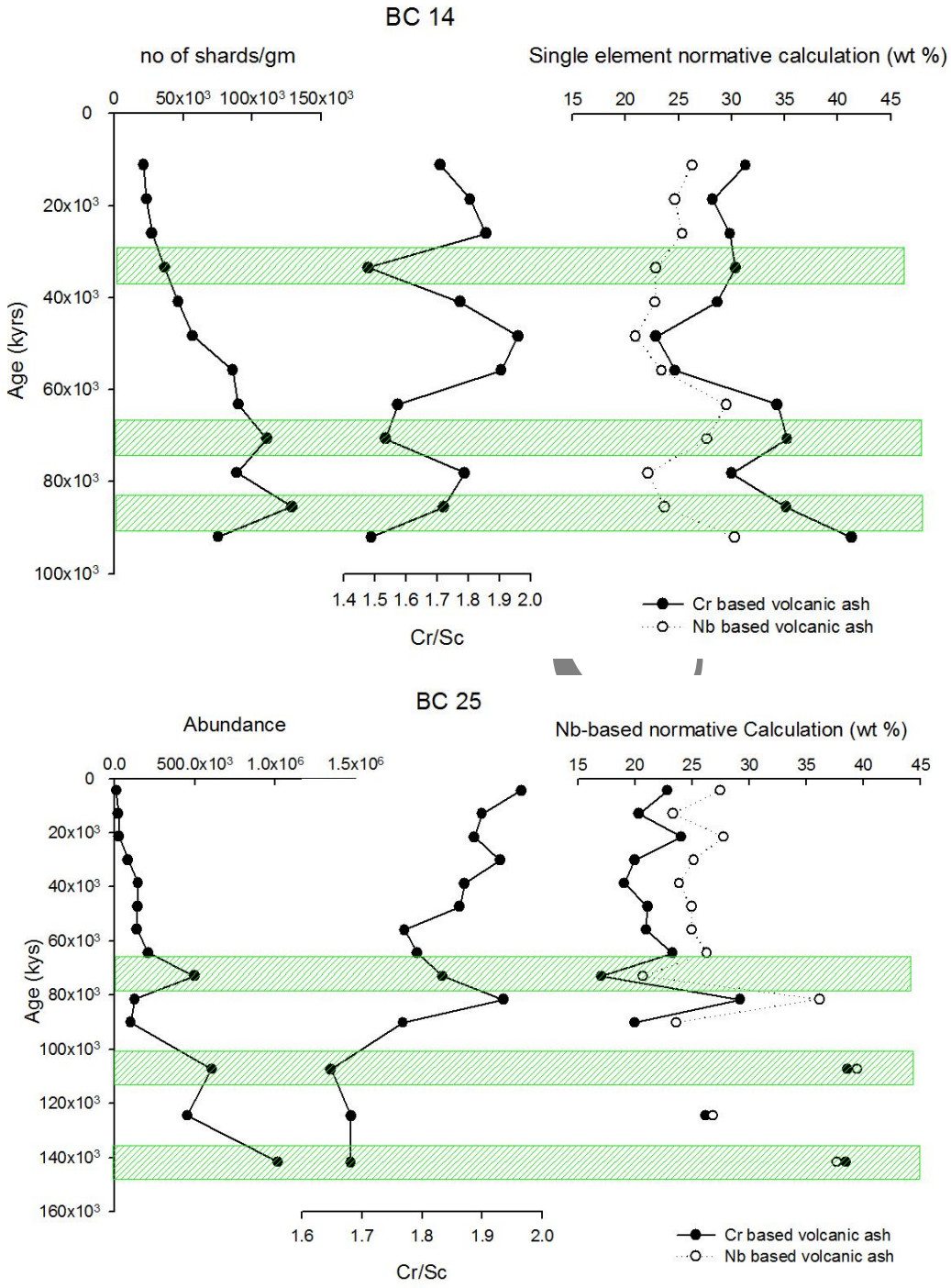

Fig. 4.7: Correlation of abundance of glass shards (no of shards gm^{-1} of sediment) in AAS 61/BC 14, 20 and 25 with respect to age of the cores, with Cr/Sc ratio of bulk sediments and ash wt % based on Cr and Nb concentration Normative calculations. Note the presence of volcanic activity indicated by abundance of glass shards, Cr/Sc ratio and single element normative calculations and excellent correlation in all the ash layers in all the three cores.

The concentration of many immobile elements in fine grained sediments are relatively same as a result of thorough mixing and repeated cycles of weathering and erosion so that the "normal" pelagic sediments should in general have similar composition to PAAS (Lim et al., 2008). Elements such as Sc are relatively immobile during sedimentation and diagenetic processes. Lim et al. (2008) found that Cr in glass is depleted by one order magnitude compared to the corresponding bulk sediments. The Cr and Sc data obtained by ICP–MS of the bulk sediments including the layers that showed high abundance of glass shards are shown in Table 4.1. In the present study, we have used Cr/Sc as a tool to detect invisible tephra and as a means of detecting the probable positions of distal/proximal cryptotephras in the pelagic sediments in CIB. A comparison of the Cr/Sc ratio and the abundance of glass shards (no of shards gm^{-1}) in the bulk sediments (Fig. 4.7) show a similar pattern between the two in terms of timing and overlying trend. There are three notable features of this comparison. First, the "dips" in the ratio coincide with the high abundance of shards in the cores. Second, the ~74 kyr and the ~110–120 kyr volcanic events are clearly captured by increased abundance of glass shards as well as the low Cr/Sc ratio. Thirdly, we are also able to decipher another crypotephra within the AAS 61/BC 14 core which did not show as a visible tephra. This volcanic event is much younger than 74 kyr i.e. ~34 kyr is depicted by the Cr/Sc ratio which is not seen by the rise in abundance of glass shards in core AAS 61/BC 14. We can therefore suggest that the low Cr/Sc ratios at the positions coinciding with high abundance of shards indicate the likely presence of tephra in the core. A comparison of the record of all the sites and the accumulation rate of the ash shows a similar pattern in terms of timing and the general trend. The abundance of shards, accumulation rates as well as the Cr/Sc ratio which indicates the cryptotephra layers synchronize well and indicate an increase in accumulation rates around ~72–75 kyr and another peak at >100 kyr. This is the first time that cryptotephra is being determined in deep sea sediments of CIB.

In fact, before starting the present study, we wanted to distinguish the tephra layer using major and trace element geochemical analyses and statistical methods. Furthermore, any possible differentiation between the Toba and insitu tephra layers was our first hope. However, most of the major and trace element geochemical results

(Table 4.3) could not be useful to identify substantial differences between the two tephra layers as both of the tephra layers have almost similar geochemistry.

4.4.2. Comparison with previous studies on ash

The chemistry of the volcanic glass shards usually enables distal volcanic ash units to be correlated to a known eruption. Analysis of glass composition of tephra throughout the Indian subcontinent provided evidence for direct correlation with Younger Toba Tuff (Westgate et al., 1998; Dehn et al., 1991; Schulz et al., 1998; Mathews et al., 2012; Smith et al., 2011). However, many magmatic systems over time systematically produce distally dispersed tephras with very similar (often indistinguishable) major element chemistries such as Katla, Iceland (Haflidason et al., 2000; Davis et al., 2004), Mount St Helens (Busacca et al., 1992) and Campanian province (Wulf et al., 2004; Smith et al., 2011). A similar case is seen in case of magmas that drove the three largest Toba eruptions (OTT, MTT and YTT) which were compositionally similar (Smith et al., 2011) and the glass chemistry normally used to distinguish individual glass layers of different eruption units cannot be solely relied upon to identify chronostratigraphic markers in their distal deposits (Smith et al., 2011). Glass composition of proximal YTT ranges from 76.5–78.4wt% SiO_2, 4.8–5.6wt% K_2O, 2.6–3.5wt% Na_2O, 0.5–1.0wt% CaO, 0.6–1.2wt% FeO^T. The similarities in major and trace element glass chemistry for most of the Toba eruptions (Smith et al., 2011) suggest that the tephra horizons in deep sea cores may have been miscorrelated in the past, particularly in sequences which do not have independent chronological control (Mathews et al., 2012). Trace element data however may provide an additional tool which can be used to distinguish products from the same volcanic centre (Albert et al., 2012)

Potential counterparts of the marine tephra are presented in Table 4.4, listing the major eruptions that have occurred in and around the CIB during the last 150 kyr along with the composition of our shards and all the above mentioned sources.

Possible sources that could have contributed to the volcanogenic material at the site are: (1) the Reunion hotspot; (2) the Kerguelen plume; (3) Broken ridge; (4) Indian Ocean ridge volcanics; (5) Afro–Arabian flood volcanism, or (6) the Taupo volcanic center (New Zealand). A comparison of the age of the sediments containing

the shards is made with all the above mentioned sources (Table 4.4). Volcanic products of the Reunion and Kerguelen hotspots tracts are dominantly of effusive basaltic volcanism type (Upton and Wadsworth., 1966; Wallace 2002). Same is the case with the volcanic products found at the Indian Ocean ridge system and at Broken ridge (Price et al., 1986; Mahoney et al., 1995), and therefore cannot be a potential source for our tephras. Though the Afro–Arabian flood volcanism and the Taupo volcanic center have a similar range of silica as in our tephras but the depositional ages are around the time of the Oi2 cooling anomaly for Afro–Arabian volcanism at ~30 Ma and late Pleistocene time scale of 26.5 kyr for Taupo (Ukstins Peate et al., 2003).

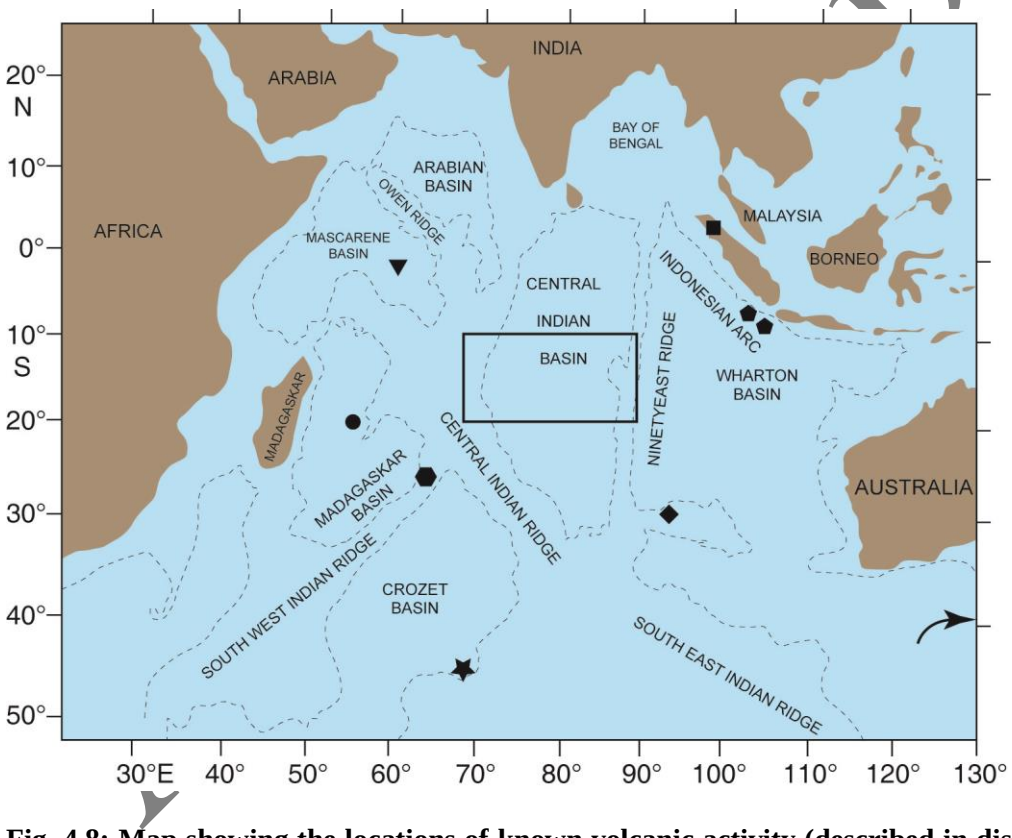

Fig. 4.8: Map showing the locations of known volcanic activity (described in discussion) in the Indian Ocean region with respect to our sampling location. Symbols denote: ■, Toba caldera (Westgate et al 1998)., ⬟, Toba volcanics (Ninkovitch, 1979)., ●, Reunion volcanics (Upton et al., 2000)., ▼, Afro–Arabian tephra (Ukstins Peate et al., 2003)., ◆, Broken Ridge (ODP site 121, site 752A: Mahoney et al., 1995)., ⬣, Indian Ocean Triple junction representing Central Indian Ridge volcanics (Price et al., 1986)., ★, Kerguelen plateau (ODP site 1140: Wallace, 2002); and. arrow in the extreme right points to the Taupo volcanic site in New Zealand, which is essentially a rhyolite dominated zone. The box denotes our sampling location in the CIB.

Many tephra beds, silicic pumice clasts and dispersed glass shards have been found in the Pliocene and Quaternary deep-sea sediments of CIB, south of the equator (Iyer and Sudhakar, 1993; Martin–Barajas and Lallier–Vergas, 1993; Pattan et al., 1999). They have been assigned to various sources like intraplate volcanism (Iyer and Sudhakar, 1993; Mascarenhas–Pereira at al., 2006), distal fallout from the Indonesian volcanic arc (Martin-Barajas and Lallier-Vergas, 1993), Youngest Toba Tuffs of Sumatra (Pattan et al., 1999; see Nath, 2001 for a review), Krakatau volcano (Iyer and Karisiddaiah., 1990; Mudholkar and Fiji, 1995). Although Martin–Barajas and Lallier–Vergas, (1993) suggest an Indonesian arc source for CIB tephra and pumice, the low alkalis they report did not permit a direct Indonesian source.

In the present study, the first ash layer gives an age of ~74 kyr which correlates well to previously established age of Youngest Toba Tuff. At least 3 major episodes of rhyolitic emissions have occurred in the Toba region in the past, which are identified as Oldest Toba Tuff at 840,000 ±30,000, Middle Toba Tuff: 500,000 ± 5,000 and Youngest Toba Tuff at 73,000 ± 4,000yrs (^{40}Ar/ ^{39}Ar ages reported by Diehl et al., 1987; Chesner et al., 1991), the latter episode of YTT has been found to spread to large distances such as the northern and Central Indian Ocean (Dehn et al., 1991; Schulz et al., 1998; Pattan et al., 1999; von Rad et al., 2002). Many studies in the CIB reported Toba tephra, with the ODP 758 core which is within the 1000 km radius off Sumatra containing deposits of all the three of the large Toba eruptions (Dehn et al., 1991; Westgate et al., 1998). The chronology suggests Unit A correlates to YTT, C to MTT and D to OTT (Dehn et al., 1991; Westgate et al., 1998; Lee et al., 2004). However the OTT and YTT show similar major element glass chemistry (Lee et al., 2004). The YTT and OTT are the largest of the Toba eruptions; therefore most of the distal tephra are likely to be correlated to these events. Unfortunately, the glass chemistries are indistinguishable and therefore make the correlation of distal tephra to a particular eruption unreliable.

The ages of deeper depth of our cores constrain a local source or sources other than Toba have contributed these ash layers. The ages of deeper depth of core do not correspond to the eruptions of all 3 major Toba eruptions.

4.4.3. Implications of the study

Two tephra layers have been identified within the cores studied spanning a time to 140 kyr. The study highlights the importance of supplementing major elemental data with trace elemental data of glass shards as well as bulk sediments and dating the sediments, in order to precisely validate the event of formation of the tephra layer. Although past work has shown that major and minor element data suggest a reliable match between proximal and distal tephras (Pattan et al., 1999; Shultz et al., 2002), it is well known that many magmatic systems systematically over time produce distally dispersed tephras with very similar (often indistinguishable) major element chemistries For example, Smith et al. (2011) show that some volcanic events from the same magma source can produce identical chemistry in the shards. Therefore, it is evident that major element correlation does not necessarily provide robust proximal–distal correlations (Albert et al., 2012).

4.5. Conclusion

Laser particle size analyses of sand fraction show a distinct bimodal size distribution in all the sections of the sediment cores from a N-S transect (10° to 16°S, along 75.5°E longitude) parallel to the 76.5°E fracture zone from the CIB. Of the two peaks (2–5 and 20–50 μm), clay sized fraction are interpreted to represent the clay minerals and the silt size fraction is volcanic ash which is abundant in the cores studied here. Morphological and geochemical studies carried out on volcanic glass shards have allowed us to conclude the following:

- Two distinct ash layers were found in 3 of the cores studied. The youngest event is dated to (~72–75 kyr) which corresponds to Younger Toba eruption (YTT), while the older event (85–109 kyr) is a new event hitherto unknown which does not correspond to any known volcanic eruption in the Indian Ocean. The chemistry of the shards indicates a rhyolitic composition of the magma.

- Insitu origin (phreatomagmatic eruption) is interpreted for the volcanic ash in the deeper layers corresponding to the older event as supported by the presence of large blocky/massive shards with a low degree of vesciculation

indicating their formation by hydroclastic fragmentation while the younger event seems to have explosive in nature and the shards transported aerially, as indicated by the abundance of bubble wall shards,.

- Since the cores are located on the flanks of a seamount and in the vicinity of 76°30ˈE fracture zone, we assume the possibility of an intraplate volcanism due to reactivation of tectonic activity in the faulted area in the past.
- Major element composition of all the siliceous tephra in the possible source areas irrespective of their ages are nearly similar and therefore suggest that a caution may be exercised in using major element composition as the only criterion for determining the source of the tephras.

Table 4.1: Abundance of glass shards (no of shards gm^{-1}), age (kyr) and Cr/Sc ratios (estimated in bulk sediments).

Core No	**BC 13**		**BC 14**			**BC 20**			**BC 25**			**BC 8**	
sed. rate	**0.413**		**0.269**			**0.229**			**0.233**			**0.032**	
Depth (cm)	abundance	Age	abundance	Age	Cr/Sc	abundance	Age	Cr/Sc	abundance	Age	Cr/Sc	abundance	Age
0-2	NA	2.4	NA	3.7	Na	73232	4.4	NA	10726	4.3	1.96		
2-4	16417	7.3	21319	11.2	1.71	73972	13.1	NA	21621	12.9	1.9		
4-6	32500	12.1	23497	18.6	1.81	74566	21.8	1.76	26811	21.5	1.89		
6-8	33333	16.9	27325	26.0	1.86	79338	30.6	1.97	83333	30.0	1.93		
8-10	31944	21.8	36633	33.5	1.48	58385	39.3	2.13	145405	38.6	1.87	>180	abundant
10-12	34751	26.6	46341	40.9	1.77	123333	48.0	2.11	141637	47.2	1.86		below
12-14	29166	31.5	56994	48.3	1.96	153500	56.8	1.95	139261	55.8	1.77		8cm
14-16	27439	36.3	85964	55.8	1.91	44078	65.5	1.93	208837	64.4	1.79		
16-18	24460	41.2	89887	63.2	1.57	153846	74.2	2.22	85465	73.0	1.83		
18-20	31932	46.0	110747	70.6	1.53	88108	83.0	2.02	125112	81.5	1.94		
20-22	32748	50.8	88957	78.1	1.79	91596	91.7	1.84	99315	90.1	1.77		
22-24	27167	55.7	129007	85.5	1.72	151875	100.4	1.8		98.7	1.65		
24-26	31292	60.5	75268	92.0	1.49	206787	109.2	1.78	604000	107.3	1.68		
26-28	28947	65.4				190513	117.9	1.37		115.9	1.68		
28-30	32214	70.2				183505	126.6	1.71	85024	124.5	1.66		
30-32	35000	75.1				135365	135.4	1.81		133.1	1.67		
32-34	10447	79.9				683152	146.3	1.75	192537	141.6	1.75		
34-36	9248	84.7											

Table 4.2: Refractive index of volcanic ash grains in two size fractions of four morphological types.

Type of glass	BC–37		BC–36		TVBC–08R		BC–38	
	>63 μm	>45 μm	>63 μm	>45 μm	>63 μm	>45 μm	>63 μm	>45 μm
Platy	1.493	1.493	1.497	1.512	1.493	1.493	1.512	1.493
Bubble–wall	1.512	1.512	1.512	1.512	1.512–15	1.512–15	1.518	1.512–15
Pipe vesicles	1.512–15	1.512	1.512	1.512	1.512	1.512–15	1.512	1.515
Massive	1.515	1.515	1.515–18	1.515	1.515	1.515	1.515	1.512–15

Table 4.3: EDS analysis obtained on the individual glass shards in the 5 cores studied. (Elemental oxides in %).

Core No.	Depth	Grain	SiO_2	Al_2O_3	Fe_2O_3	MnO	MgO	CaO	TiO_2	P_2O_5	Na_2O	K_2O	$Na_2O+ K_2O$
BC 13	30-32 cm	1	78.67	11.22	1.01	0.18	0	0.85	0.08	nd	2.13	5.86	7.99
		2	78.49	11.57	1.09	0.01	nd	0.81	0.07	nd	2.92	5.04	7.96
		3	78.89	11.2	1	0.1	nd	0.74	nd	0.1	2.46	5.52	7.98
		4	78.68	11.54	0.94	nd	0.1	0.54	0.01	0.09	2.84	5.26	8.1
		5	78.83	11.02	0.94	0.23	0.07	0.75	0.16	0.26	2.25	5.5	7.75
		6	78.65	11.8	0.76	nd	nd	0.52	0.01	nd	3.2	5.06	8.26
		average	78.70	11.39	0.96	0.13	0.06	0.70	0.07	0.15	2.63	5.37	8.01
BC 14	18-20 cm	1	78.65	11.55	1.01	0.02	0.04	0.69	0.06	0.16	2.74	5.07	7.81
		2	78.88	11.3	1.03	0.06	0.1	0.8	0.19	nd	2.19	5.44	7.63
		3	78.31	11.67	1.01	0.12	0.17	0.77	0.12	nd	2.61	5.22	7.83
		4	78.4	11.84	0.81	0.01	0.03	0.59	0.16	nd	3.27	4.88	8.15
		5	78.83	11.42	0.76	0.04	0.22	0.55	0.16	nd	3	5.03	8.03
		6	78.78	11.8	0.9	0.03	0	0.74	nd	nd	2.97	4.79	7.76
		7	78.24	11.87	0.86	nd	nd	0.85	0.13	0	3.16	4.89	8.05
		average	78.58	11.64	0.91	0.05	0.09	0.71	0.14	0.08	2.85	5.05	7.89
	22-24 cm	1	78.37	11.89	0.67	0.03	nd	0.74	nd	0.26	3.14	4.9	8.04
		2	78.45	11.7	0.86	0.03	nd	0.77	nd	0.14	2.96	5.09	8.05
		3	78.71	11.23	0.94	nd	0.08	0.81	0.16	nd	2.55	5.54	8.09
		4	78.59	11.9	0.76	nd	0.03	0.65	0.09	nd	2.77	5.21	7.98
		5	77.7	12.09	0.92	0.08	0.07	0.83	0.19	nd	3.2	4.92	8.12
		6	78.56	11.44	0.82	0.07	0.08	0.69	0.1	0.4	2.75	5.09	7.84
		7	78.79	11.49	0.86	0.15	0.06	0.7	nd	0.06	2.53	5.35	7.88
		8	78.93	11.82	0.7	0.12	nd	0.53	nd	0.02	2.92	4.96	7.88
		average	78.51	11.70	0.82	0.08	0.06	0.72	0.14	0.18	2.85	5.13	7.99

Core No.	Depth	Grain	SiO_2	Al_2O_3	Fe_2O_3	MnO	MgO	CaO	TiO_2	P_2O_5	Na_2O	K_2O	$Na_2O+ K_2O$
BC 20	16-18 cm	1	78.37	11.83	0.68	0.01	nd	0.7	0.07	nd	3.42	4.91	8.33
		2	78.61	11.69	0.69	nd	0.01	0.67	0.18	nd	3.08	5.07	8.15
		3	78.51	11.66	0.98	0.2	nd	0.77	0.05	nd	2.84	5	7.84
		4	78.68	11.55	0.74	0.1	0.1	0.75	0.15	nd	2.93	5	7.93
		5	78.73	11.17	1.01	nd	0.04	0.67	0.01	0.07	2.82	5.47	8.29
		average	78.58	11.58	0.82	0.10	0.05	0.71	0.09	0.07	3.02	5.09	8.11
	24-26cm	1	76.26	10.46	2.06	0.38		1.18	0.19	0.3	2.01	7.17	9.18
		2	78.64	11.56	0.67	0.16	0.14	0.52	nd	0.15	3.12	5.06	8.18
		3	78.76	11.76	0.78	0.05	0	0.46	0.02	nd	3.51	4.66	8.17
		4	78.83	11.26	1.07	0.11	0.05	0.61	nd	nd	2.33	5.74	8.07
		5	78.71	11.29	1.06	0.11	0.04	0.8	0.03	nd	2.27	5.69	7.96
		6	78.77	11.87	0.79	nd	0.04	0.76	0.05	nd	2.69	5.02	7.71
		average	78.33	11.37	1.07	0.16	0.05	0.72	0.07	0.23	2.66	5.56	8.21
BC 25	16-18 cm	1	78.86	11.37	0.93	0.17	nd	0.59	nd	nd	2.98	5.12	8.1
		2	77.39	11.9	1.37	0.12	0.13	0.73	0.12	0.33	2.72	5.2	7.92
		3	78.55	11.78	0.75	0.05	0.05	0.66	0.11	nd	3.1	4.96	8.06
		4	79.35	10.47	1.4	0.2	0.04	0.67	0.16	nd	1.71	6	7.71
		5	79.07	11.19	1.02	0.05	0.1	0.78	0.02	nd	2.06	5.71	7.77
		6	78.23	11.23	1.17	nd	nd	0.74	0.21	0.16	2.32	5.95	8.27
		average	78.58	11.32	1.11	0.12	0.08	0.70	0.12	0.25	2.48	5.49	7.97
	32-34 cm	1	78.76	11.75	0.75	0.12	nd	0.78	nd	nd	2.81	5.02	7.83
		2	77.94	12.19	0.96	nd	0.1	0.55	0.04	nd	3.41	4.8	8.21
		3	78.08	11.68	1.03	0.11	0.16	0.83	0.24	-0.42	2.98	5.31	8.29
		4	77.98	11.86	0.97	0.15	nd	0.65	0.12	nd	3.2	5.06	8.26
		5	78.38	11.57	1.13	nd	0.04	0.77	0.27	0.11	2.36	5.37	7.73
		6	78.08	12.04	0.66	0.09	nd	0.71	0.07	0.1	3.56	4.69	8.25
		average	78.20	11.85	0.92	0.12	0.10	0.72	0.15	-0.07	3.05	5.04	8.10

Core No	Depth	Grain	SiO_2	Al_2O_3	Fe_2O_3	MnO	MgO	CaO	TiO_2	P_2O_5	Na_2O	K_2O	Na_2O+K_2O
BC 8	6-20cm	1	75.3	12.3	0.9	nd	nd	0.64	0.07	nd	4.45	4.47	8.92
		2	75.4	12.7	0.65	nd	nd	0.55	0.09	nd	5.55	3.9	9.45
		3	76	12	0.93	nd	nd	0.68	0.07	nd	3.86	4.76	8.62
		4	76.3	12.2	0.91	nd	nd	0.66	0.05	nd	3.37	4.61	7.98
		5	75.3	12.5	0.7	nd	nd	0.57	nd	nd	4.76	4.33	9.09
		6	76.3	11.8	0.8	nd	nd	0.6	0.1	nd	3.7	4.7	8.4
		7	74.7	11.8	0.85	0.07	nd	0.53	0.1	nd	5.75	4.46	10.21
		8	73.9	12.4	0.72	0.09	nd	0.62	0.04	nd	6.35	4.17	10.52
		9	75.6	11.2	1.26	nd	nd	0.78	0.13	nd	2.36	6	8.36
		10	74.8	12.1	0.9	0.05	nd	0.74	0.07	nd	5.01	4.52	9.53
		11	75.1	11.6	0.89	0.08	nd	0.64	0.05	nd	4.63	5.01	9.64
		12	74.8	12	0.81	0.07	nd	0.55	0.07	nd	5.57	4.6	10.17
		13	75	11.1	1.2	0.1	nd	0.8	nd	nd	3.6	5.6	9.2
		14	74.3	12.3	0.7	0.07	nd	0.62	0.12	nd	6.13	4.38	10.51
		average	75.2	12	0.87	0.08	nd	0.64	0.08	nd	4.65	4.68	9.33

Table 4.4: Comparison of elemental data (in wt%) of glass shards from possible sources in the Indian Ocean.

Sample No.	Area	SiO_2	Al_2O_3	Fe_2O_3	FeO	MnO	MgO	CaO	Na_2O	K_2O	H_2O	P_2O_5	TiO_2	Na_2O+K_2O	Reference
UT1298	Toba Caldera	78	12		0.8	0.09	0.04	0.71	3.18	5.03			0.06	8.21	Westgate et al., 1998
CB1	Reunion	51	15		11	0.2	3.76	7.65	4.32	1.86			3.35	6.18	Upton et al., 2000
ODP 115,site 711A	Indian Ocean (Afro–Arabian)	73	14	2.42		0.18	0.28	0.47	3.92	5.23			0.53	9.15	Ukstins Peate et al., 2003
ODP 115,site 711A	Indian Ocean (Afro–Arabian)	77	12	2.27		0.11	0.13	0.21	3.54	4.77			0.38	8.31	Ukstins Peate et al., 2003
ODP 121,site 752A	Broken Ridge	49	14		11	0.18	7.66	12.2	2.1	0.18		0.13	1.6	2.28	Mahoney et al., 1995
6/2	Indian Ocean triple junction	51	17		7.8	0.2	8.73	10	3.91	0.25			1.08	4.16	Price et al., 1986
ODP 1140	Kerguleun	50.1	13	14.6		0.23	4.67	9.14	2.32	0.89	0.69	0.42	3.52	3.21	Wallace 2002
V19–151	Sunda Strait	69.6	14.2	0.7	2.2	0.12	1.4	2.5	4.7	2.3	1.5	0.12	0.49	7	Ninkovitch 1979
V19–150	Sunda Strait	69.7	13.8	0.8	1.9	0.12	1.3	1.8	4.7	2.2	2.8	0.12	0.45	6.9	Ninkovitch 1980
P915	Taupo, New Zealand	71.8	14.7	3.03		0.09	0.66	2.47	4.22	2.5			0.41	6.72	Sutton et al., 1995

Chapter 5

Porewater chemistry and Benthic fluxes of nutrients

5.1.Introduction

The studies of interstitial water chemistry are concerned with establishing causal relationships between depositional environments, diagenetic reactions and chemistry of sedimentary pore fluids. Porewater studies play an important role in understanding the diagenesis process operatingboth at the sediment–water interface and in subsurface sediments.

The driving mechanism of diagenetic reactions is the decomposition of organic matter, which is mainly mediated biologically and consists of oxidation processes. When free oxygen approaches depletion and is therefore no longer available as principal oxidizing agents, oxidizing species of N, Mn, Fe, S and C are used as terminal electron acceptors following the sequence of highest Gibb's free energy yield (e.g., Barbani et al., 1995). All these reactions release the formerly solid–associated nutrients to porewater, where nutrients can either diffuse towards areas with low nutrient concentration or be scavenged through adsorption and re-precipitation process. High nutrient concentrations in the porewater result in diffusional fluxes through the water sediment interface towards the water column. Determination of nutrients in the porewater helps in understanding the nature of oxidation, behavior of oxidants and their importance in the organic matter diagenesis. In addition, detailed porewater studies are also critical for accurate geochemical mass balance calculations. Porewater nutrient studies also help understand the sediment–biota related processes such as bioturbation, bioirrigation, diffusion, advection and chemical reactions occurring at the sediment–water interface. Porewater also plays a major role in formation of authigenic minerals. One of the most important mineral resources in the ocean, manganese nodules are considered to receive a major source of metals through porewater for their formation.

One of the most effective ways to describe the intertwined chemical and biological processes co–existing in marine sediments is through the study of chemical gradients present in the interstitial waters. Because of the large ratio of solid surface area to interstitial water volume existing in fine–grained deep–sea sediments, any chemical reaction leading to the changes in the mineral–seawater–organic matter mixture tends to significantly affect porewater composition. Determination of fluxes of dissolved constituents between marine sediments and the overlying sea water has often been attempted by geochemists (e.g., Berelson et al., 1990; Grunwald et al.,

2010) for making mass balance calculations for sediment/ocean systems. Chemical gradients are produced in pore fluids either by diagenetic reactions occurring within the sediments in a steady state or by non–steady state. In fine-grained oceanic sediments, these diffusive fluxes can be calculated directly from interstitial water concentration gradients or by measuring the fluxes directly, either in situ, on shipboard or in the laboratory using carefully obtained sediment cores (Setlock 1979).

The bulk of pore fluid research previously undertaken has been conducted in shallow–water marine environments (Grandel et al., 2000;Woulds et al., 2009a andb). A general lack of reliable information on the interstitial water chemistry from deep–sea sediments is generally acknowledged.This imbalance in knowledge is unfortunate, since pelagic sediments cover more than half of the earth's surface and diagenetic processes in these sediments may be very important in global terms. Immense importance of porewater studies in understanding the ocean biogeochemistry resulted in the extensive research mostly in the Pacific and Atlantic Oceans by various workers (e.g., Jahnke et al., 1982; Schulz et al., 1994; Hensen et al., 1998). Some attempts have been made to understand the porewater nutrients of the Central Indian Basin(Nath and Mudholkar, 1989). Consequently little is known about the organic matter or silica cycle operating in the pelagic sediments of CIB. Since porewater profiles and benthic fluxes are sensitive indicators of the preservation of organic matter and biogenic silica, we investigated the porewater profiles of nitrite, nitrate, silicate and phosphate in the sediments of the region. The magnitude and regional pattern of benthic fluxes of nutrients silicate and phosphate through the water–sediment interface are quantified from porewater profiles. Estimates of benthic fluxes in general for the Indian Ocean deep–seas are rare (e.g., Van Beueskom et al., 1997; van der Weijden et al., 2002). Thus, this study will supplement the small geochemical data base currently available in the CIB (Nath and Mudholkar, 1989; Das et al., 2011) and to assess the role of early diagenetic processes through diffusive flux calculations of the nutrients. In addition, an attempt is made to see if any seasonal changes occur in benthic fluxes in the deep–sea. It is usually considered that the seasonality seen in surface water characteristics is not imparted to deep–sea but, some of the studies have shown the possibility of occurrence of seasonality in the deep–sea (e.g., Billett et al., 1982; Lampitt et al., 1985) induced by the seasonality in export fluxes from surface ocean. While this work presents first regional distribution maps of benthic fluxes of nutrients in the CIB, an attempt is made to understand the local variability in a

fracture zone environment where metalliferous sediments occur in one of its sub-environments (Chapter 3).

Estimation of diffusive fluxes

Among the major objectives of interstitial water studies is the documentation of specific diagenetic reactions occurring within the sediments and the overall understanding of the diagenetic process itself. Regular concentration changes with depth for specific chemical species indicate the consumption/production of specie within the region. The concentration gradient with depth can be compared for different core samples and also for different chemical species (nutrients in this case). The detailed study of diffusive fluxes and concentrations of nutrientsaccording to depth candecipher the direction of transport and assess the relative importance of sediments or overlying waters in controlling the diagenetic process

The major factors governing the distribution of a dissolved constituent in marine porewaters include

A. Diffusion
B. Vertical advection
C. Chemical Reactions

Aqueous diffusion obeys the first law of diffusion formulated by Fick (1955):For steady state diffusion, diffusive flux remains constant for a fixed layer (fixed depth) with respect to time i.e. fluxes and hence concentration gradient does not change with time.It assumes a homogeneous and continuous process.

Fick's first law of diffusion states:

When the concentration within the diffusion volume does not change with respect to time $(J_{\text{in}} = J_{\text{out}})$. In one (spatial) dimension, this is

$$J = -D\frac{\partial \phi}{\partial x} \quad (1)$$

Where

- J is the diffusion flux in dimensions of ((amount of substance) length^{-2} time^{-1}), example $\left(\frac{\text{mol}}{m^2 \cdot s}\right)$

- D is the diffusion coefficient or diffusivity in dimensions of (length^2 time^{-1}), example $\left(\frac{m^2}{s}\right)$
- ϕ is the concentration of diffusing species in solution in dimensions of ((amount of substance) length^{-3}), example $\left(\frac{\text{mol}}{m^3}\right)$
- x is the distance over which diffusion occurs (length), example m

Fick's 2nd law of diffusion is for the non–steady state process where the flux varies with time.

$$\frac{\partial \phi}{\partial t} = D \frac{\partial^2 \phi}{\partial x^2} \quad (2)$$

where

- ϕ is the concentration diffusing species in solution in dimensions of ((amount of substance) length^{-3}), (mol m^{-3})
- t is time (s)
- D is the diffusion coefficient in dimensions of (length^2 time^{-1}), (m^2 s^{-})
- x is the distance over which diffusion occurs (length), (m)

In addition to the major factors in Fickian diffusion, such as mean velocity of the diffusant and mean free path, three other factors govern diffusion in porous sediments (1) tortuosity, (2) porosity, and (3) electrostatic attraction between diffusant and sediment phase surfaces (Setlock 1979). Tortuosity and porosity are important because the diffusing species must pass through narrow channels between clay particles. The porosity governs the amount of diffusant passing through a unit cross section in unit time while tortuosity produces an effective lengthening of the path over which diffusion occurs. Together these terms make the interstitial fluid diffusion coefficients a fraction (one–fifth to one–twentieth) of the aqueous coefficients. A one dimensional model of diffusion in marine sediments is generally employed since lateral gradients in porewater composition and porosity are much smaller than the existing vertical gradient for these parameters(Setlock 1979).

A steady state diagenetic process is considered and fluxes are calculated using the following equations given in Schulz and Zabel (2000)

The diffusive flux in the sediment (J_{sed}) is calculated as:

$J_{sed} = -\Phi * D_{sed} * \partial C/\partial x$ (3)

where,

Φ = porosity

D_{sed} = diffusion coefficient of the specie in the sediments

$\partial C/\partial x$ = concentration gradient with respect to depth taken from sediment–water interface

The diffusion coefficient in the sediments (D_{sed}) can be calculated on the basis of a dimensionless tortuosity (Θ) and the diffusion coefficient in free solutions of sea–water (D^{sw}). The nutrient diffusivities were obtained from Schulz and Zabel, (2000) and corrected for the bottom–water temperature (Boudreau, 1997). On this basis, we calculated D^{sw}values of 1.039 x 10^{-9} m^2 s^{-1} for NO_3^-, 1.0545 x 10^{-9} m^2 s^{-1} for NO_2^-, 3.432 x 10^{-10} m^2 s^{-1} for $PO_4^{3-}$and 5.02233 x 10^{-10} m^2 s^{-1} for SiO_4^{4-} assuming a bottom water temperature of 2°C. While the nutrients in porewaters are analysed for this work, bottom water concentrations of the nutrients were extracted from the WOCE data base.A linear gradient ($\partial C/\partial x$) between the uppermost interstitial water sample and the bottom water concentration was constructed. The flux of the nutrient species out of the sediment was estimated using this gradient. The factors that can influence the fluxes of chemical constituents include biological activity, especially of macrobenthic organisms (Glud et al., 1994).

The diffusion coefficient in the porewater volume of sediments differs from the diffusion coefficient of free solutions in such a manner that diffusion in the porewater volume cannot follow a straight course, but has to deviate the direction at sediment grains. The degree of deviation around particles is called tortuosity (θ). It describes the mean ratio between the real length of the pathway and the straight–line distance. Tortuosity can be quantified either using by measuring the electrical resistivity (R) or indirectly through the porosity values (Schulz, 2000).

The diffusion coefficient in sediments is expressed as:

$$D_{sed} = D^{sw} / \Theta^2 \quad (4)$$

The tortuosity (Θ) can be calculated by the following equation using porosity (Φ) as given by Boudreau(1997).

$$\Theta^2 = 1 - \ln(\Phi^2) \quad (5)$$

This relation (Boudreau's law) is widely used for various porosity calculations for marine sediments.

5.2. Results and Discussion

5.2.1. Downcore profiles of porewater nutrients in the basin

Degradation of organic matter causes the liberation of inorganic forms of elements such as nitrogen, phosphorus, silicon, carbon etc., bound in the organic matter. The sediments (AAS 61; BC 1 to 26)were sampled in the siliceous and pelagic red clay domain (Fig. 2.1) of the CIB (Nath et al., 1989). The porosity in the basin ranges from 0.73 to 0.95 (Khadge, unpublished data). Data comprising of NO_2^-, PO_4^{3-}, SiO_4 and organic carbon concentration profiles up to a sediment depth of 20cm are presented in Figs.5.1 to 5.4 and Tables 5.1 and 5.2. Measurements of nutrients in the porewaters at each of the twenty six stations revealed that the phosphate concentrations in the sediments were usually lower than in the overlying seawater while silicate concentration in the overlying waterswaslowercompared to the sediments (Fig. 5.2). Whether or not exchange of these solutes between the sediment and the overlying water will occur is controlled by the redox conditions near the sediment/water interface, and the microbial processes which occur there. For example, nitrification in the aerobic surface layer may prevent efflux of ammonium to the water (Nedwell et al., 1983); while release of phosphate from the sediment may be prevented by the presence of a surface oxidized layer (Mortimer, 1941; Van Raaphorst et al., 1988). The porewaters at the nine stations (Table 5.3)(north to south of the study area) were collected on two occasions for two successive yearsrepresenting Austral winter(April; ABP 04 cruise) of 2005 and austral summer (December, ABP 26 cruise) of 2006 onboard*RVAA Boris Petrov* allowing the assessment of seasonal nutrient benthic fluxes for the whole basin.

A general rapid and often exponential downward increase of porewater concentrations near the sediment surface was observed. Several peaks were seen at intermediate depths in some of the porewater PO_4^{3-} and SiO_4 profiles. Subsurface increase of porewater PO_4^{3-} and SiO_4 could be attributed to mineralization, while decrease at depths may be due to several reasons. One of the most plausible explanations is macrobenthic irrigation which dilutes the solutes (Zabel et al., 1998).

Porewater nitrite

Nitrite concentrations were generally low, rarely exceeding 1μM (Figs.5.1a and b). Relatively, higher values were noticed only in one station (BC#22 in the west) and

moderately high in one station in north (BC#26) and two stations in the east (BC#3 and 5). In remaining stations, values less than 0.7μM were noticed in the surficial sediments (0–2cm; Fig.5.1a). Downcore profiles at several stations showed intermediate high values. Nitrite is an intermediate product both during nitrification and denitrification. Nath and Mudholkar (1989) have reported similar results of detectable levels of nitrite in intermediate sediment intervals which has showed mottling or bioturbation features. Fall in nitrate values along with increased levels of organic carbon in the solid phase suggested the effect of bioturbation and oxygen consumption on porewater nitrite (Nath and Mudholkar, 1989).

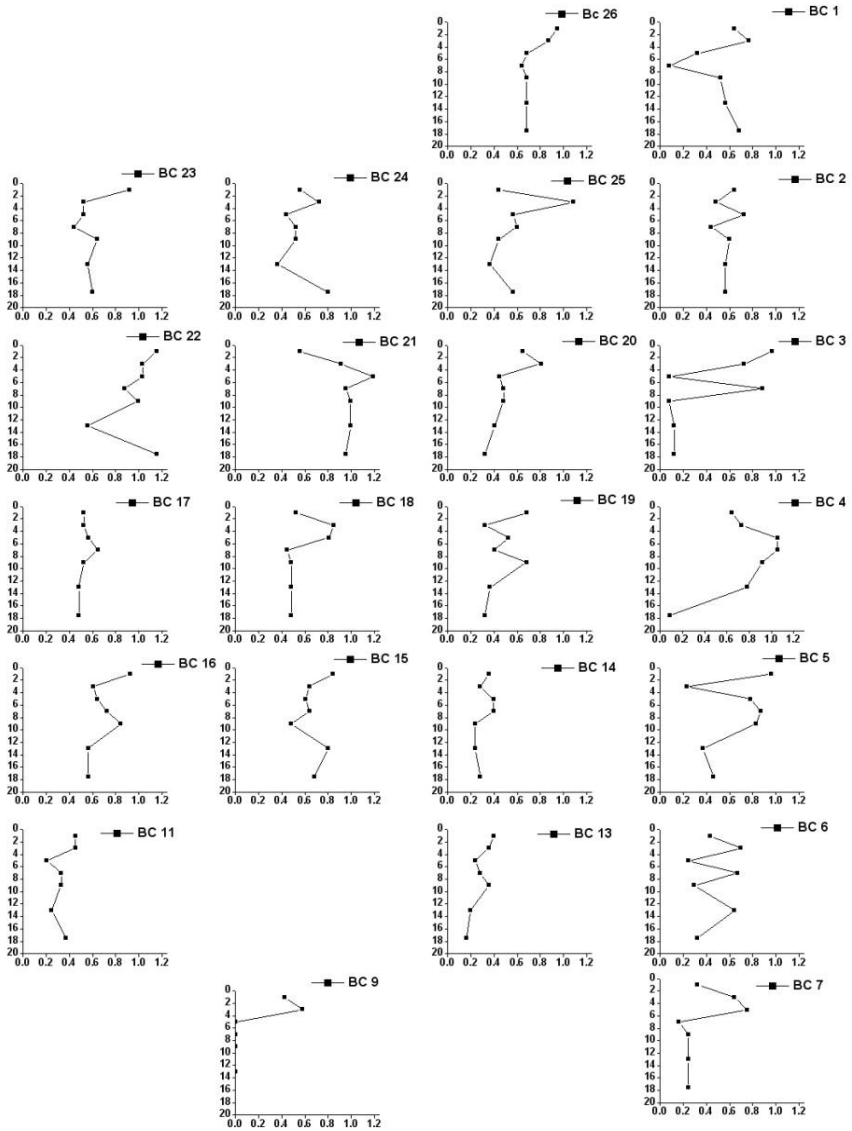

Fig. 5.1a: Regional variation in downcore nitrite concentration (μM) in the porewaters of the CIB. Depth profiles are placed according to their geographic coordinates. Top mostrow represents northernmost latitude (10°S) and the spacing between each sampled row is 1° latitude.

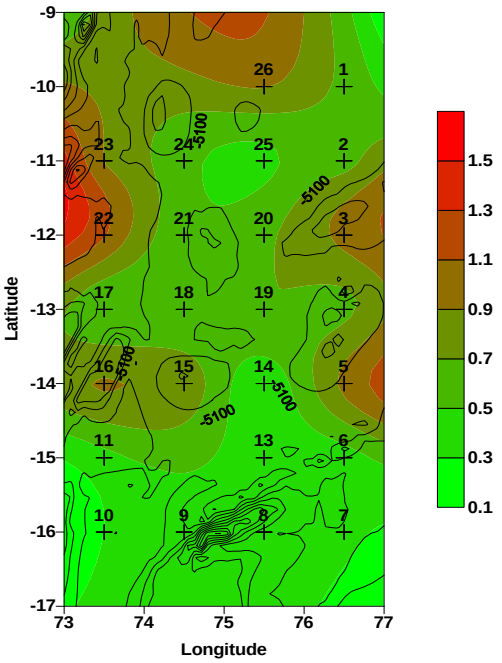

Intense nitrification seems to be taking place in the southern latitudes with the NO_2^- concentration south of 14°S (Fig. 5.1 a) being relatively low compared to the northern latitudes. Decrease of $NO_2^-$was accompanied by a low to complete absence of NH^{4+} in those locations. CIB sediments were found to harbor high nitrifying bacteria and involved in nitrification of NH_4 to NO_2 (Ram et al., 2001).

Fig. 5.1b: Regional variation of dissolved nitrite (µM) in the core top sediments (0-2cm) of the CIB.

Porewater silica

Porewater silica concentrations in all the cores except two cores in the east and one in the south were higher than the bottom water values of 130µM reaching a maximum value of > 600µM mostly at the deeper depth of 10–15cm below the interface (Figs. 5.2aandb).

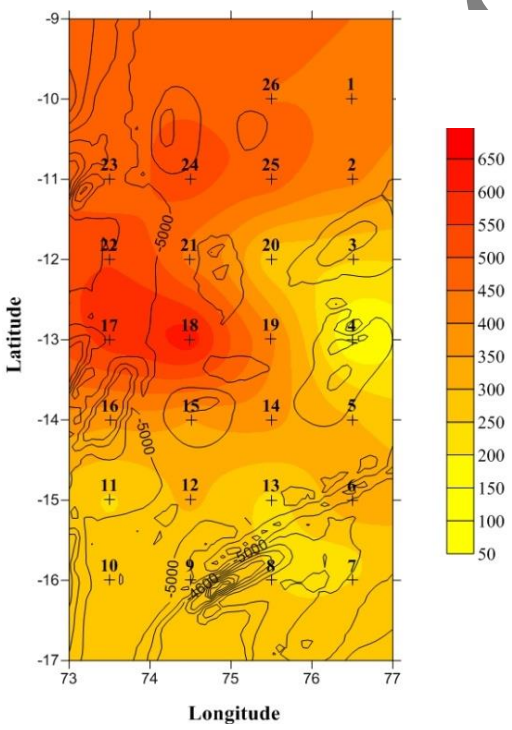

Fig. 5.2a: Regional variation of porewater silica (µM) in the surface sediments (0-2cm) of the CIB.

When the porewater silica concentrations in the surficial sediments were considered (0–2cm), a distinct trend of high values in the northern (10 to 12°S) and central western (between 12° and 13°S latitudes and 73° and 75°E longitudes) areas of the study area (Fig. 5.2a) was noticed. Porewater silica values, considered for all the cases ranged from a minimum of 90µM to a maximum of 790µM, with intracore variation fallingin the range of 200 to 250µM. Consistently high silica values (although less than the super saturation limits of amorphous silica) and gradual decrease in

silica values towards sediment–water interface was observed in all the porewater profiles.This is consistent with the high bottom water silica values overlying opaline sediments worldwide (Edmond etal., 1979) diffused out from sediment porewaters in these areas (see Nath and Mudholkar, 1989 for porewater silica behavior in CIB).Schink et al. (1975) attributed the high interstitial values of SiO_4 to productivity of the overlying waters, which was later contradicted by Sayles (1979) whose study indicated the silicate mineral equilibrium as the controlling factor.

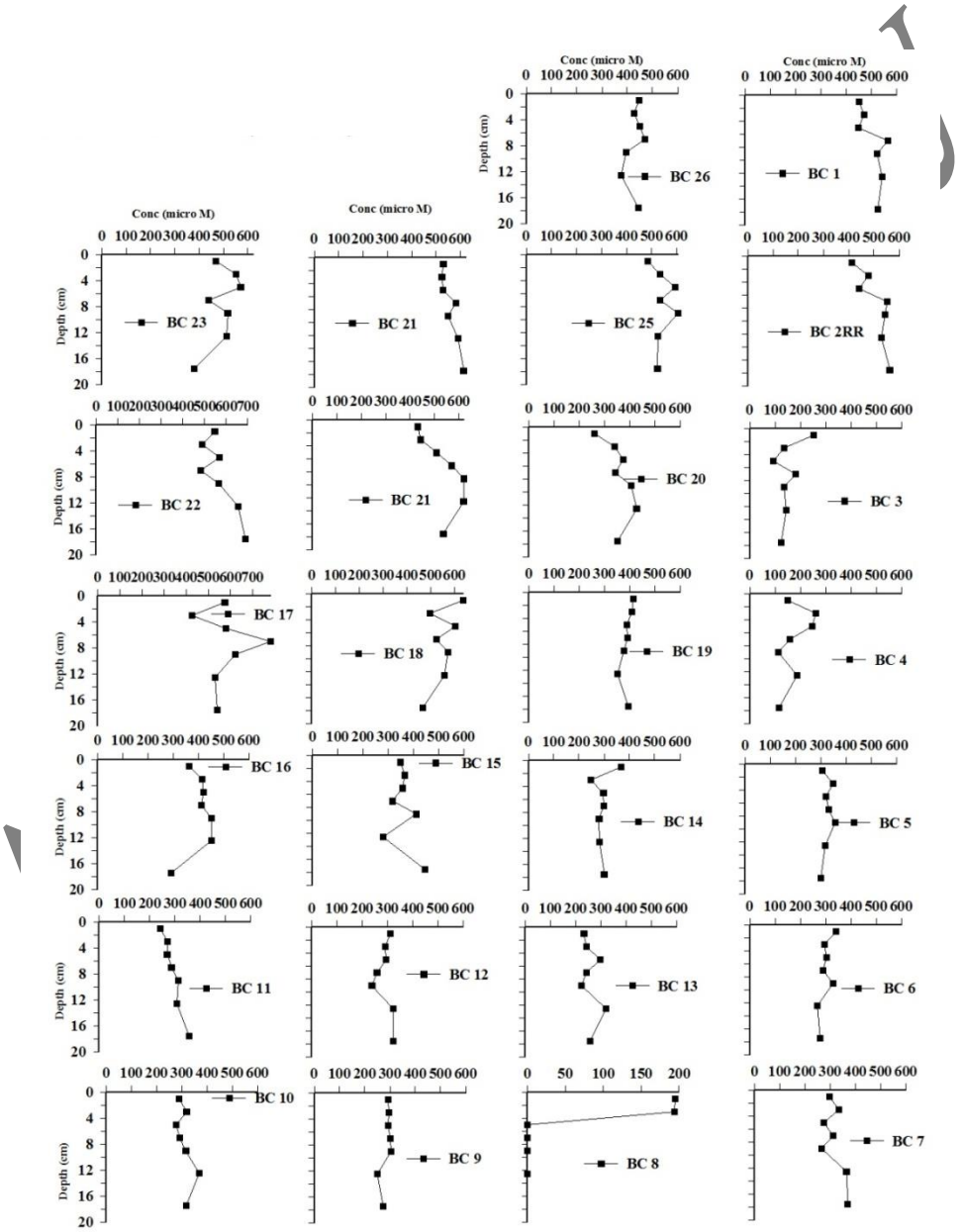

Fig. 5.2b: Regional variation in downcoresilicate concentration (µM) in the porewaters of the CIB. Depth profiles are placed according to their geographic coordinates as in Fig 5.1a.

Porewater phosphate

Unlike porewater profiles for SiO_4 wherein most of the stations indicate release into bottom waters, profiles of porewaterPO_4^{3-} behave in anopposite manner. The porewater phosphate concentrations mostly hover between 1.5 and 2.5µM (Figs. 5.3aandb) and some values were below detection limits. Compared to overlying water (between 2.3 and 2.4µM), the porewater concentrations were lower especially in the surface sediments. The downcore profile of porewaterPO_4^{3-}concentration in the basin showed distinct trends with lowest values in the eastern most cores i.e., along the 76.5°E latitude (Fig. 5.3b). Most of the cores showed sub–surface variation, either with no discernible gradient or with lower values at the surface. LowerporewaterPO_4^{3-} contents in the surficial layers compared to the deeper section indicate an efflux to the surface sediments while higher bottom waterconcentration compared to surface sediments suggest influx of phosphate at water sediment interface.

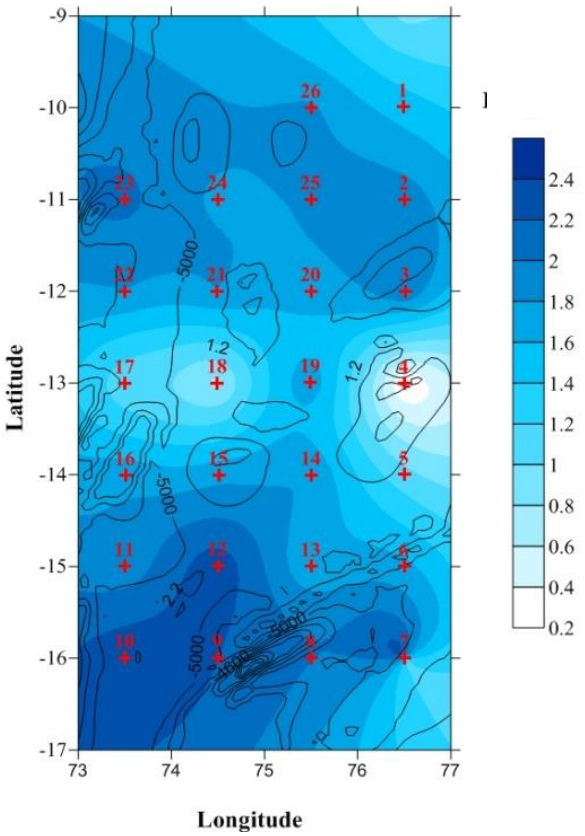

Fig. 5.3a:Regional variation of porewater phosphate (µM) in the surface sediments of the CIB.

Phosphorus (P) is, like nitrogen (N), a redox–sensitive nutrient. Phosphate is reported to be readily associated with particulate Fe and Mn (Van Raaphorst and Kloosterhuis, 1994). The capacity of this process is determined by the supply of Fe (III) in the sediment. In addition, enhanced oxygen penetration depth through macrofaunal activities may increase the volume of sediment possible for P accumulation. While high PO_4^{3-} concentration in the porewater at depths may be associated with PO_4^{3-} release upon the microbially mediated reductive dissolution of Fe and Mn oxyhydroxidesand Fe–bound P is released into porewater (Heggie et al.,1990), i.e., mobilization of P to the porewater and subsequent

transport across the sediment–water interface; the low concentration of PO_4^{3-} seen at the water sediment interface (relative more oxic) may be due to increased sorption of dissolved PO_4^{3-} on to metal oxides (Woulds et al., 2009). Thus, the activities of benthic fauna and the oxygen conditions of the bottom water may have significant effects on the form and amount of nutrients that are mobilized to the porewater and subsequently released to the overlying water.

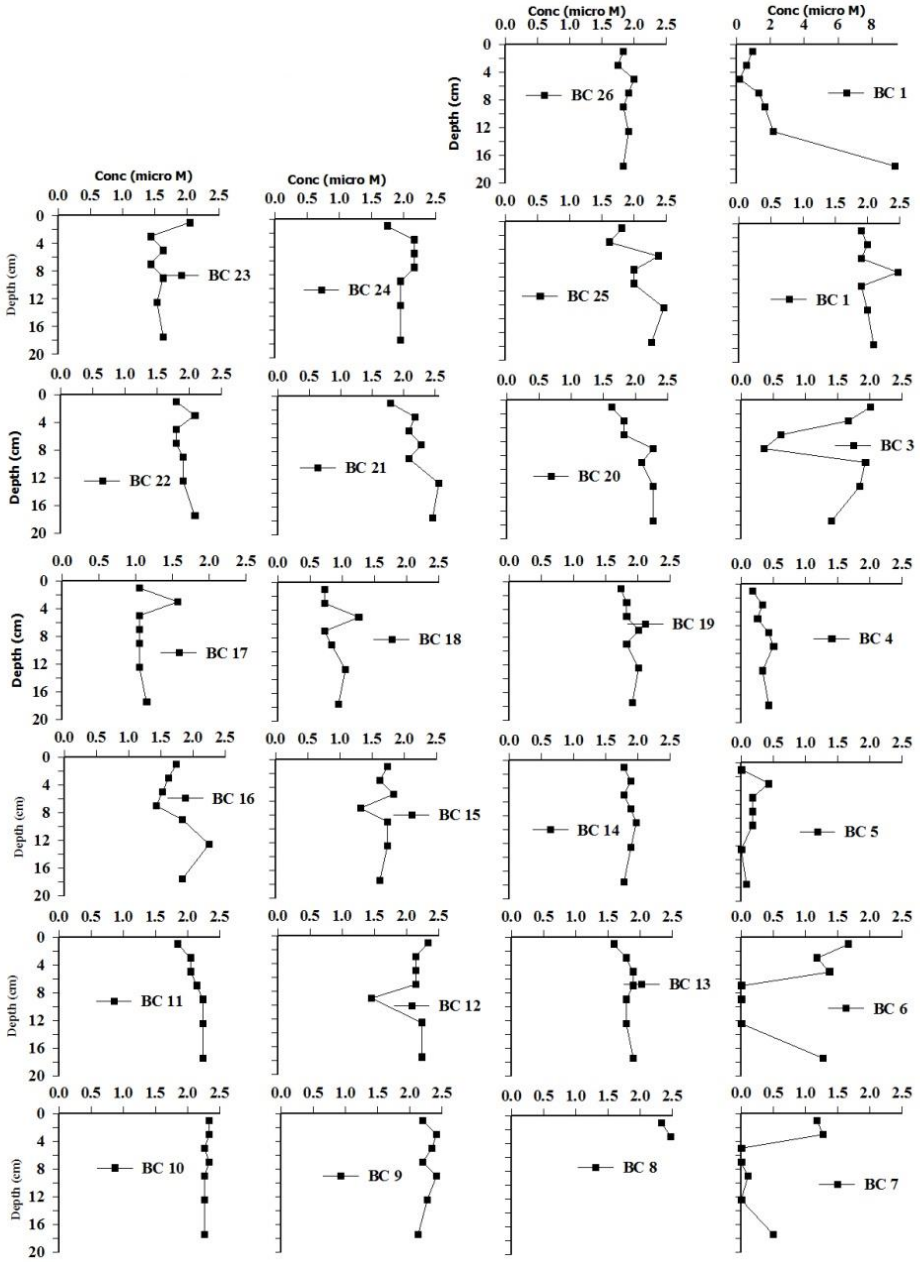

Fig. 5.3b: Regional variation in downcore phosphate concentration (µM) in the porewaters of the CIB. Depth profiles are placed according to their geographic coordinates as in Fig 5.1a.

Sedimentary organic carbon

Sedimentary organic carbon has been analyzed for the entire core length of all the cores collected during the AAS 61 cruise at an interval of 2cm (Figs. 5.4a and b). The organic carbon values are less than 0.57% in all the cores studied here (Table 5.2). When the surficial values are concerned, three patches of high values were seen in the northeast, west and east of the basin (Fig. 5.4a). High values were mostly associated with topographic highs (abyssal hills) in the east and west of the basin while low values were seen in the vicinity of large seamounts in the south (Fig. 5.4a). The association of organic matter to the topographic highs indicates bathymetric control on the organic carbon. Incidentally, these areas were influenced by rugged topography and a different sediment type. Areas floored by rugged topography probably have some influence on the preservation of organic matter.

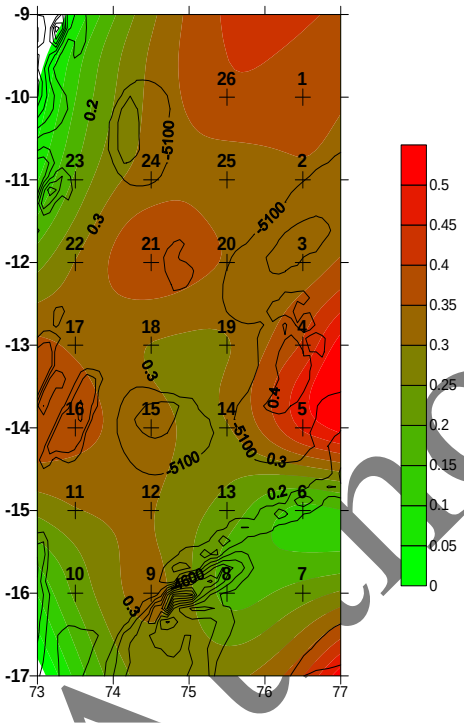

Fig. 5.4a:Sedimentary organic carbon content (%) variation in the core tops (0-2 cm) of CIB.

In most of the cores, a surface enrichment was seen with a change in gradient at about 5 to 8cm (Fig. 5.3b). The gradient was relatively smooth in the surface 8cm in some of the cores. Relatively smoother profiles in the surficial layers were seen in some cores, which probably may indicate mixing depth. The range in the variability of organic matter content in surface was relatively large in the south.

The northern stations (10–12°S) seems to have similar surficial as well as downcore profiles of organic carbon indicating some sort of relation to the sediment type. The southern stations had similar downcore pattern but different magnitude. When the downcore profiles were considered, subsurface peaks were seen more in the northern areas compared to the southern areas (Figs. 5.4a and b). When downcore profiles of all the cores were plotted, there seems to be a regional trend of subsurface enrichment, which must be driven by lateral advection of porewaters in the intermediate depths. A color change from

sediments with dark yellowish brown homogenous nature underlain by sediments with intercalations and mottling indicating the influence of bioturbation and mixing features was seen in all the cores. This color change would probably limit the base of enriched organic C whichmay act as a boundary between preservation and decomposition. Thesediment color change may probably be due to the influence of surface and subsurface feeders and bioturbation activity (e.g., Nath and Mudholkar, 1989). Intermediate lows could also indicate the change in community structure with varying ratios in population of surface and suspension feeders to the burrowing organisms

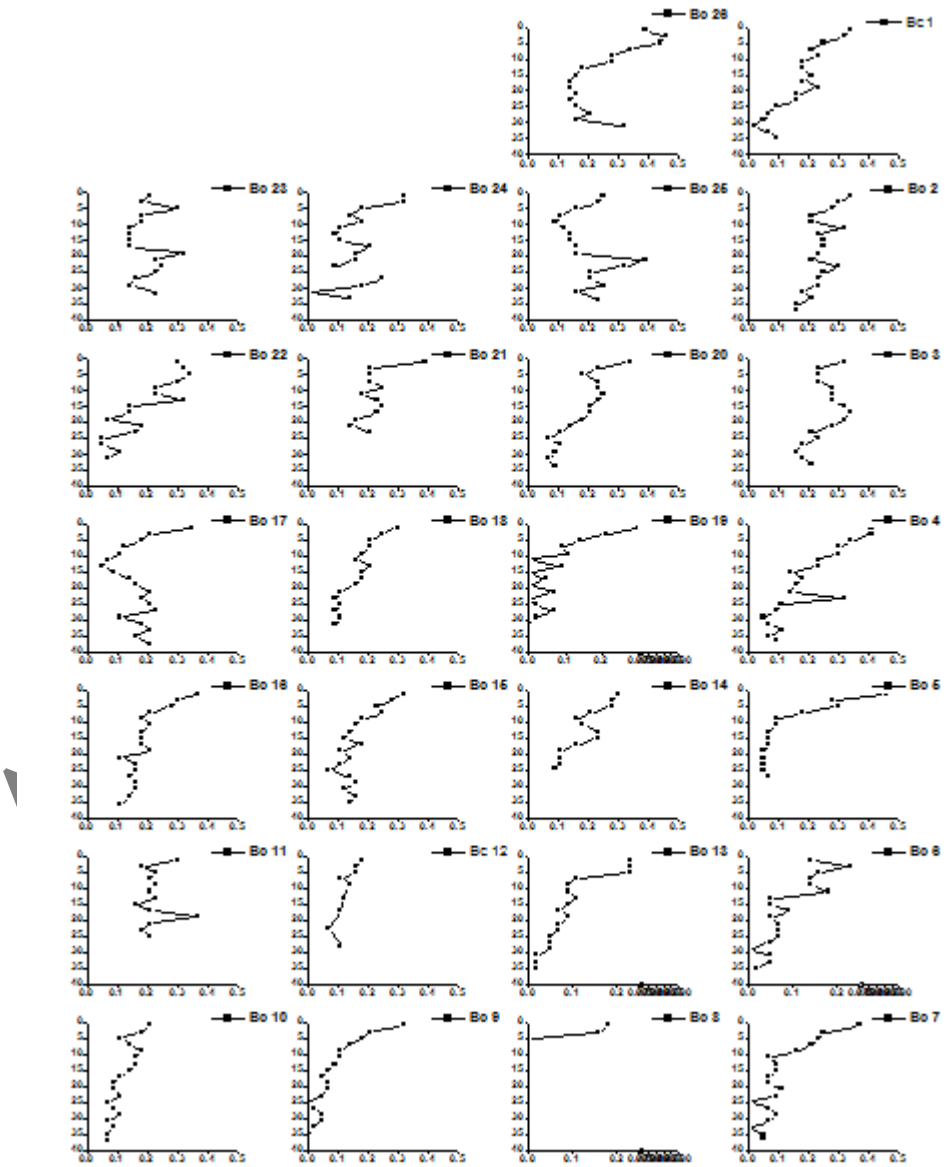

Fig. 5.4b: Regional variation in downcore sedimentary organic carbon (%) in the CIB. Depth profiles are placed according to their geographic coordinates as in Fig 5.1a.

5.2.2. Regional distribution patterns of silicate and phosphate fluxes

The CIB is bounded by ridges and has pronounced differences in topography (Kodagali et al., 1992) and sediment deposition rates (Borole, 1993). Some areas act as depocenters while others are dominated by erosional bottoms (Banakar et al., 1991; Borole, 1993). One of the aims of this study was to investigate whether the spatial variability could be correlated to sediment deposition pattern of the basin. In order to fulfill this objective a systematic sampling coveringthe entirebasin with stations located both on seamount tops with low accumulation rates as well as in the deep basins with high accumulation rates was carried out.

In addition toporewater nutrient data from 26 stations sampled at every 1 degree covering two sediment types (siliceous and pelagic clays), nutrient data (0-2cm; water sediment interface) from 21 stations (Table 5.4) sampled between 10° and 12°S recovered during the baseline study of the PMN-EIA project were also used to make a comprehensive benthic flux distribution map of nutrients (silica and phosphate) of the CIB. The resulting distribution maps of diffusive benthic fluxes at the water–sediment interface of silicate and phosphate calculated from linear gradients from concentration profiles of respective nutrients at 26 stations (AAS 61 cruise) and 21 stations (baseline study of PMN EIA project) are presented in Figs.5.5and5.6, respectively (Table 5.5).

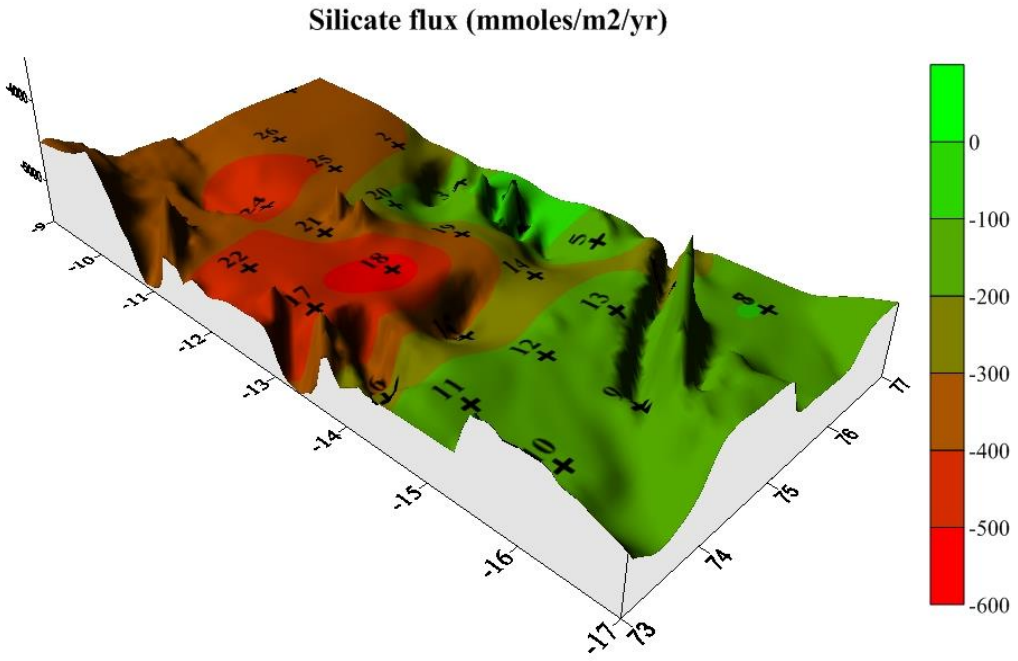

Fig.5.5:Regional distribution of silica flux at the sediment–water interface in the Central Indian Basin

The porewater composition and fluxes of dissolved nutrients through the sediments water interface showed a distinct regional distribution in the CIB. Silica fluxes ranged from –12 to –597mmol $m^{-2}yr^{-1}$ (negative numbers denotes fluxes out of sediment) (Table. 5.5, Fig. 5.5). Silica flux map showed latitudinal variability at ~12°S. The highest silica flux was found in the north and southwest of the basin with values of ~-500mmol $m^{-2}yr^{-1}$. The diffusive flux was also calculated from a gradient between bottom water to sediments depth of 6 and 10cm. The resulting maps (flux: 4–6cm to bottom waters) showed similar pattern of diffusive fluxes calculated between the surface (flux: 0–2cm to bottom waters) sediments and overlying water with only minor changes in magnitude of flux. The most striking feature of all maps was the relatively large area north of 12°S with high efflux which acts as a source of silica to bottom waters (Fig. 5.5). Sediment distribution maps of the CIB showed siliceous ooze domain north of 12°S which is exactly the region with high efflux. Distinct latitudinal changes in the porewater data (Fig. 5.5) also follow the variation in sediment type suggesting a possible control on benthic biogeochemical processes. Areas with high silica fluxes coincide with the most productive areas in the CIB in the north of the basin (up to 12°S; PP > 6686mmol $m^{2-}yr^{-1}$; Source: global maps of primary productivity of Antoine et al., 1996), suggesting a response of benthic ecosystem to pelagic processes.

Pelagic–Benthic coupling – Silica evidence

The benthic silicate fluxes in the CIB reveal a very prominent pattern. The benthic silicate fluxes in the CIBcoincide with flow path of the Antarctic bottom waters which enter the basin through the saddles at 10°S (Gordon et al., 2002). Workers like Nelson and Smith (1986) and Wilson et al. (1986) reported a strong dominance of diatoms among the phytoplanktonic assemblage in the surface waters of the Southern Ocean and thereforewererich in silica (Dileep Kumar and Yuan–Hui., 1996). Export production of the Antarctica waters expressed as silicate is regularly higher than export production measured as carbon flux, and results in a large flux of silica in diatom frustules to the bottom (Dugdale and Wilkerson, 1989). It is estimated that two–thirds of the world ocean biogenic silica accumulation occurs on the sea–floor of the Southern Ocean (DeMaster, 1981; Ledford–Hoffman et al., 1986). However in CIB, radiolarian dissolution may account for the influx of the silica in the southern

stations and contribute significantly to the benthic release of silicate in the CIB, particularly at 10°S.

Benthic fluxes-surface water productivity relationship was studied by comparing the variations of benthic fluxes to those of primary productivity along a meridional transect along 75.5°E (Fig. 5.5). An almost linear increase of silicawas observed from north to south except for the southern-most stations 35 and 13. This coincides with the trend in primary production deduced by remote sensing data (Antoine et al., 1996). The primary productivity in winter is slightly higher than the summer, but the general north to south increase with a decrease south of 14°S (Fig. 5.5) corresponding to changes in surface production reflect the distinct coupling between pelagic and benthic processes in the CIB. Such changes were also reported in the Arabian Sea which were attributed to a change in the production regime and consequently in the transfer of biogenic components from non–siliceous primary producers to siliceous algae (Rixen et al., 1996).

Calculations done on mass balance of silica in the CIB reveal that 19% of biogenic silica produced in the surface waters at 10°S reach the water sediment interface, which is also reflected by concomitant high in diffusive flux (~-376mmol $m^{-2}yr^{-1}$) while at the southern stations the benthic sediments receive ~9%, less than half of what is produced in the surface waters with a concomitant decrease in DSi (~-106.7mmol $m^{-2}yr^{-1}$; Chauhan et al., 2010, unpublished). The high silica in the porewaters and fluxes in the north thus result from a larger input of biogenic opal from the surface in this region compared to the other southern stations.

Although the change in primary production is small above both sediments types (siliceous and pelagic clays), the northern stations receive greater input of terrigenous material in terms of aeolian dust from the northern hemisphere. This in turn enhances the sinking velocity of particulate organic matter as the biogenic material, aggregate with biogenic particles. Therefore the regional differences in the amount and composition of biogenic material, and the transport conditions in the northern stations favor an input of more liable and less mineralized organic matter due to rapid sinking through the water column. Therefore, in addition to the distinct coupling between pelagic and benthic processes in the CIB, there seems to be decoupling between organic carbon and biogenic opal cycles (Grandel et al., 2000).

Chauhan et al. (2010, unpublished data) measured ~8 fold gradient in silica accumulation rates in sediments from north to south in CIB (10° to 15°S). They also

found that 99% biogenic silica reaching the near bottom (7m above seafloor) is dissolved at the water– sediment interface, which emphasizes the impact of near bottom mineralization process on degradation of organic material.

Phosphate fluxes

Phosphate fluxes range from 0.44 to 1.65mmol $m^{-2}yr^{-1}$ (Table. 5.5, Fig. 5.6). Benthic fluxes of phosphate also display a high rate of uptake at 12°S (>0.28mmol $m^{-2}yr^{-1}$, upto 1.39mmol $m^{-2}yr^{-1}$, Table 5.5). Generally the basin seems to act as a sink than a source of phosphate. Low benthic fluxes in the south of the basin could be related to higher nutrient recycling in the surface waters, resulting in a lower export flux or a generally higher remineralization within the water column (Hensen et al., 1998).

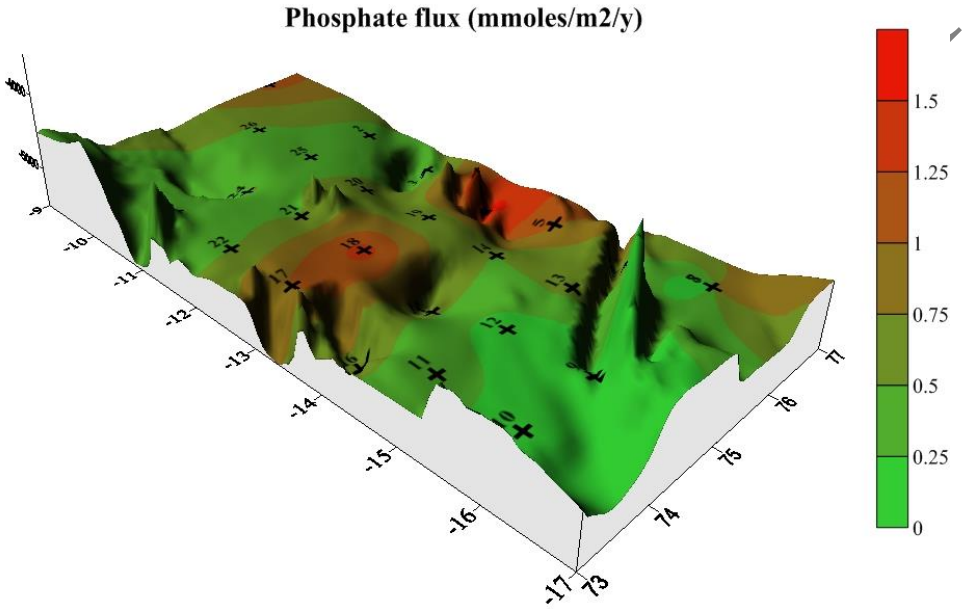

Fig. 5.6: Regional pattern in benthic flux of phosphate at the sediment-water interface in the Central Indian Basin

5.2.3. Seasonal variation of porewater nutrients and sedimentary organic carbon

In the following section, seasonal variation as interpreted from several geochemical parameters (nutrients and organic carbon) studied from nine selected stations sampled in north–south transect of the basin along longitude 75°E are presented (Tables5.3, 5.6 and 5.7;Figs. 5.7 to 5.12). Each station was sampled consecutively for two years in different seasons (Austral winter and summers). Seasonal variation of all the parameters analyzed were plotted to see if there has been any variation between these two seasons (Austral winter (ABP 04) of 2005 and

Austral summer of 2006 (ABP 26) (Figs. 5.7 to 5.12). The stations were superimposed on the local bathymetry to study the influence of topography on these parameters.

PorewaterpH

The porewater pH shows a wider range in concentration at station 19 (~0.5 pH units) at 13°S and the southern stations compared to northern stations (Fig. 5.7). South of station 19, both the winter and summer porewater pH showed identical trend, while the change in pH in northern stations was minimal for both seasons. The narrow range of variation in downcore pH values especially in the northern cores (North of 13°S) indicate near neutral conditions in the area. However the pH seemed to increase gradually since 2005 (ABP 04) (Fig. 5.7). Most of the cores displayed gradual increase in pH values downcore. This increase in pH downcore could be related to reduced activity of burrowing animals. The summer pH was higher in most of the samples in the transect with maximum pH of >7.5 pH units seen in the southern station (pelagic clays) compared to the northern station containing siliceous ooze. Higher summer time pH also coincided with higher summer time porewater silica concentration in these cores indicating that an increased alkalinity had induced higher biogenic silica dissolution. The high pH particularly in the southern stations (BC 35 and 13) may be associated with hydrothermal fluids in the area (Nath et al., 2008). The high pH in the southern cores may have induced the dissolution of biogenic silica, which is evidenced by intense dissolution features observed in opaline skeletons in the south (Chapter 3; Nath etal., 2008).

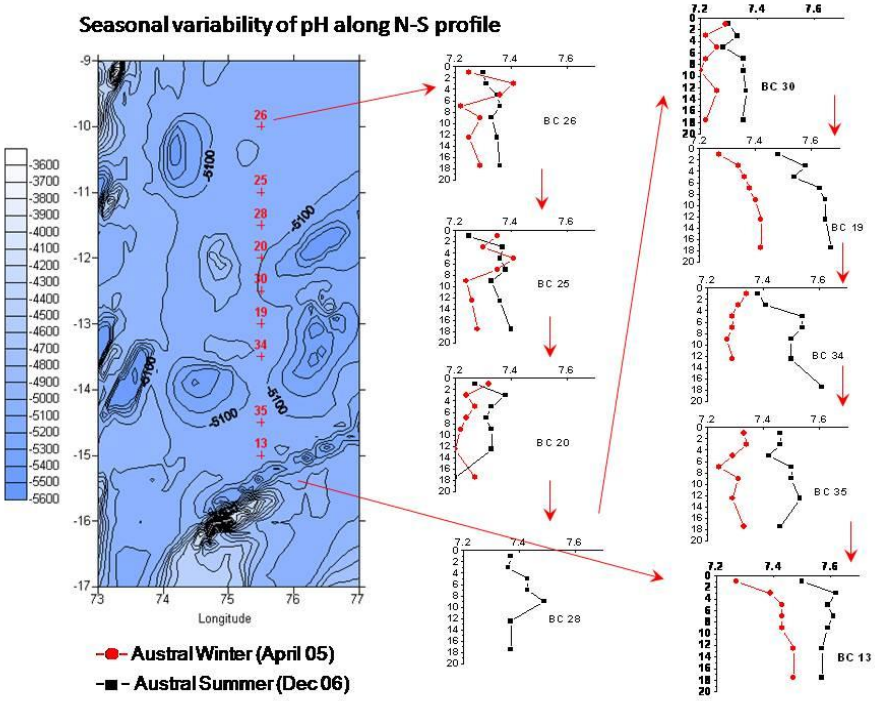

Fig. 5.7: Seasonal variation of porewaterpH along the north-south transect in the CIB

Porewater phosphate

A systematic shift from low phosphate concentration in the ABP–04 (austral winter) in the north to high phosphate concentration towards south was seen (Fig. 5.8). A shift from low to high phosphate concentration in the ABP–04 cores is seen at 13°S (BC 19). The phosphate concentrations were in the range of 1–3µM except at station 20 and station 19 (<5µM).

All the cores showed a subsurface decrease in concentration at about 6–8cm bsf. The highest difference in phosphate values (~5µM) between austral summer and austral winter was seen at 13°S (i.e. BC 19) (Fig. 5.8) while all the other stations to the north as well as south showed similar pattern for both the seasons. The seasonal difference in phosphate seems to be profound in mid–latitudes of the study area considered.

The winter profiles of the year represent profiles having minimum biological contribution. Phosphate concentration decrease with a concave up form (Fig. 5.8) indicative of consumption, probably as a result of increased adsorption or reaction with Fe–oxides as the interface is approached (Li et al., 1973). This was especially seen in the southern most core BC 13. The most peculiar feature was seen in the BC

20 profile at 12°S, thisis probably due to the production of phosphate during the summer time that was consumed by the biological community during the winter time.

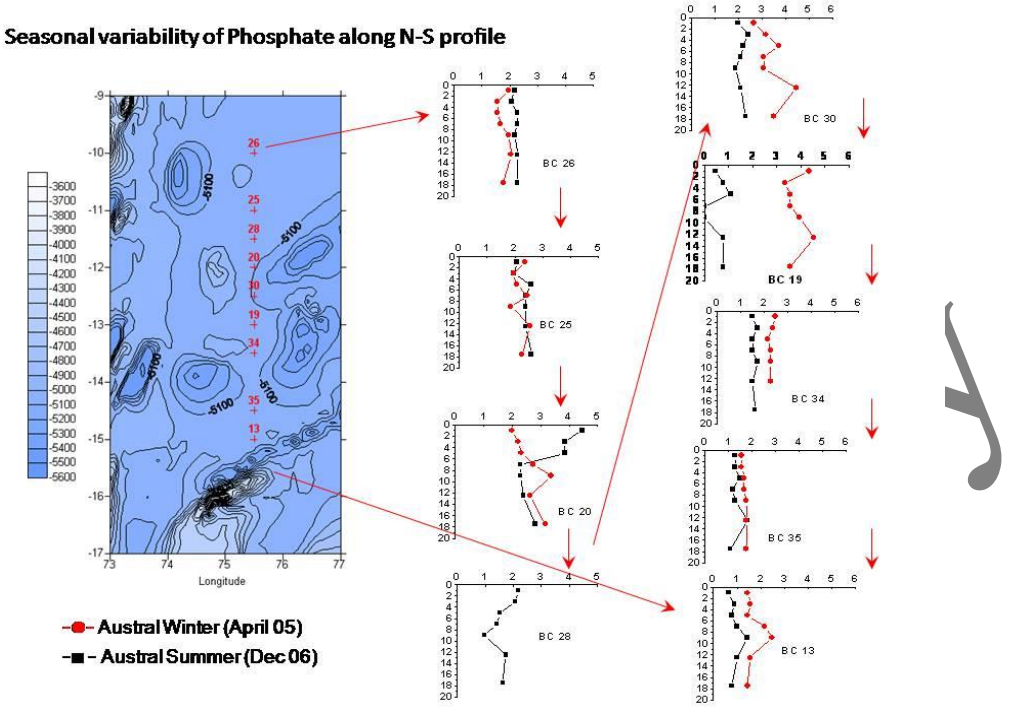

Fig. 5.8: Seasonal variation of porewater phosphate (µM) along the north-south transect in the CIB.

Nitrite

In general ABP–04 (austral winter) had lower nitrite concentrations in the northern stations as compared to the southern stations (Fig. 5.9). The same situation is found in sediments collected during summer too.The northern station, i.e. BC 26 and BC 25 austral summer samples, had high nitrite concentration in the surface layers and nitrite goes below detection limit in the subsurface sediments, while in the austral winter a reverse trend was seen, with the core surfaces having low concentration and subsurface sediments being high (Fig.5.9). During winter, the nitrite is consumed at 2cm bsf while in the summer the depth of consumption is increased to 4–6cm bsf.

The maximum surface nitrite concentration is seen in BC 19 (~0.4µM), while the maximum subsurface nitrite concentration is seen in the austral winter sample at BC 34 (~0.6µM).

Nitrite in porewater indicates an intermediate product between ammonia and nitrate. Presence of nitrite in the southern stations indicates either the nitrification or ammonification is more prevalent in the southern areas. Seasonal variations in the

nitrite values would thus indicate changes in nitrogen cycle in the benthic sedimentary environment on shorter time scales too.

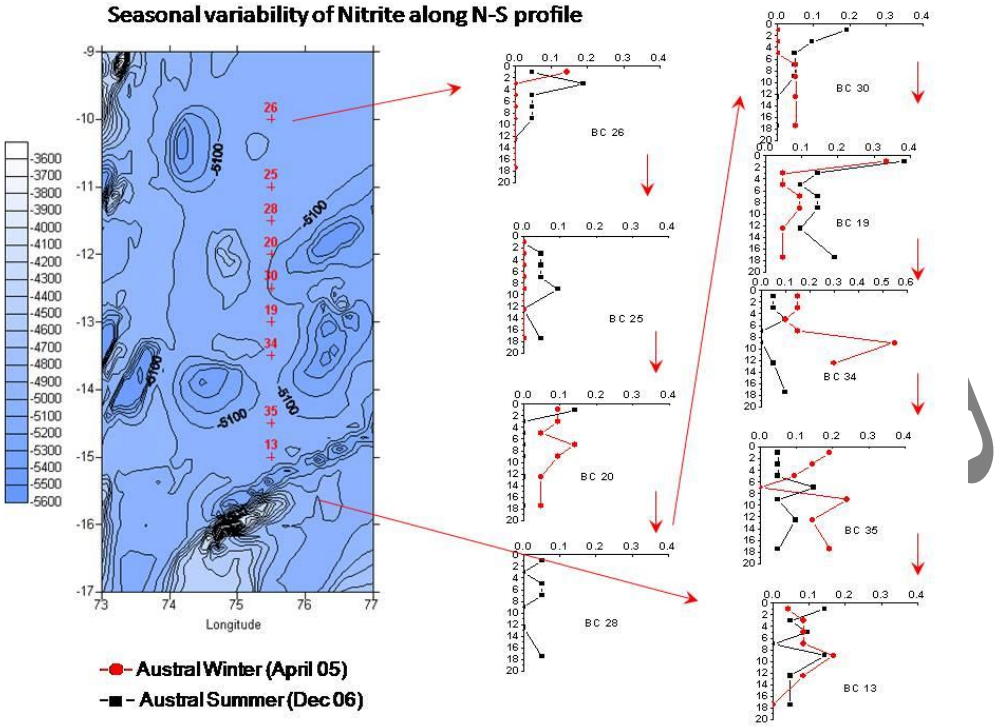

Fig. 5.9: Seasonal variation of porewaternitrite(µM) along the north-south transect in the CIB.

Nitrate

In the top10cm of the sediment, nitrate accumulates in porewater (Fig.5.10) from decomposition of organic matter producing ammonium and primary amines that are then oxidized to nitrite, and from nitrate produced by nitrifying bacteria (Billen 1982; Suess et al., 1980).The concentration of nitrate of winter and summer is nearly similar in many stations from north to south except those in stations 19 and 20 (Fig.5.10). Difference in nitrate concentration between austral summer and austral winter at the surface is the minimum in the southern part of the study area i.e. from 12°S onwards, while the nitrate concentration (>40µM) is highest in the austral winter at BC 20 station. Significantly, only the surficial sediments (top 2cms) show an increase in porewater nitrate concentrations probably related to fresh supplies of organic matter.

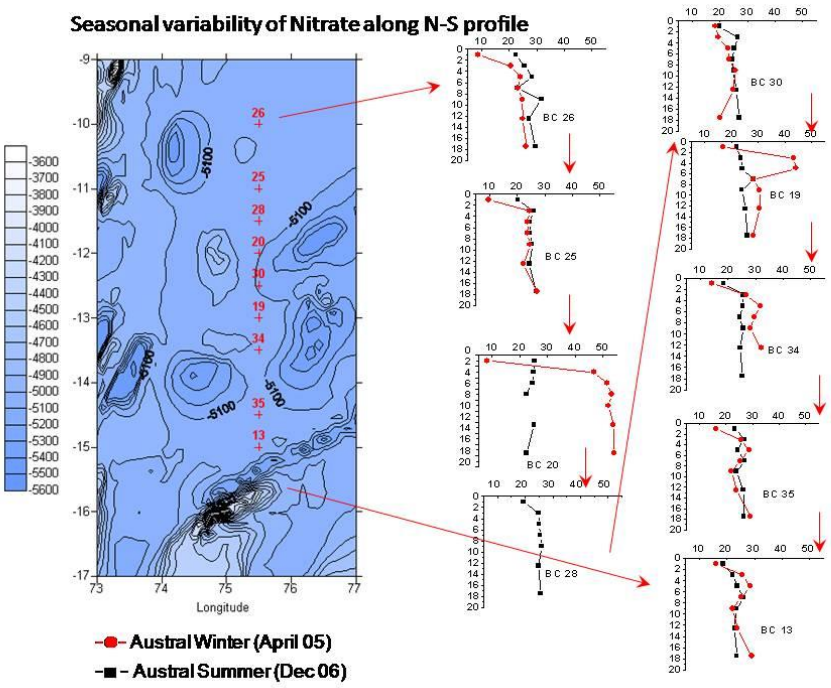

Fig. 5.10: Seasonal variation of porewaternitrate (µM) along the north-south transect in the CIB.

Silicate

In general, cores collected during winter season have lower silicate concentration than those collected during summer in all stations (Fig. 5.11), except some variations at stations 19 and 13. However, the downcore profile of the silicate concentration in the winter and summer samples parallel each other in most of the cores. Many of the records show a gradual decrease towards the surface suggesting a diffusive silica flux from the sediments to the sediment–water interface is typical of CIB siliceous clays. Silica responds to opal dissolution and increase in porewater silica during summer would probably indicate an increasing dissolution influenced by intensified AABW.

A latitudinal variation in the silica concentration is seen in the basin, with the northern stations having a generally higher silicate concentration compared to the southern stations. This is seen in the austral winter as well as summer samples. The higher silica concentration, north of 12°S is probably due to the sediment type (siliceous ooze) in the basin.

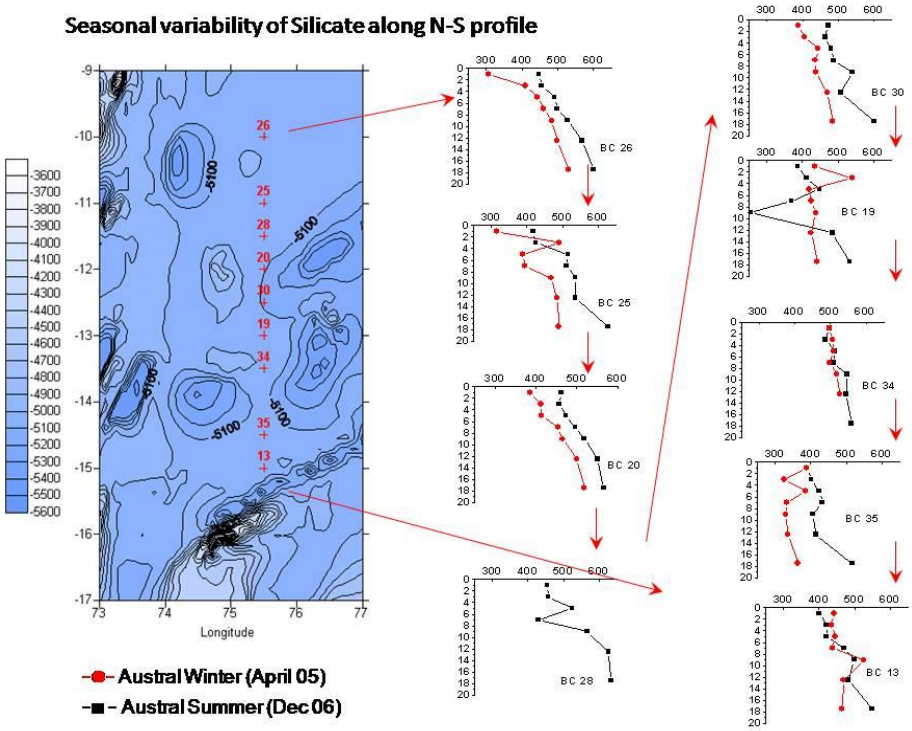

Fig. 5.11: Seasonal variation of porewatersilica (µM) along the north-south transect in the CIB.

Sedimentary organic carbon

Organic carbon has been analyzed in sediments at every 2cm interval for a maximum core length of 42cm and a minimum of 24cm core length. All the cores (ABP 26, summer) have a surface concentration of about 0.3% (Fig. 5.12) except in 2 cores i.e. at 10° and 13°S. The sediments representing summer (ABP 26) have a surface concentration of ~0.2% except at BC 20 (0.39%), BC 13 and BC 34 (0.16%). The downcore profiles of all the cores follow the same trend with the surface having higher concentration followed by a gradual subsurface decrease in concentrations. In the northern two cores (BC 26 and 25), and as also in other cores in the area, summer values are distinctly higher in the surface, except in BC 20 at 12°S where in the winter sample has higher C_{org}content (0.39%) in the surface compared to summer samples.

The downcore distribution of sedimentary C_{org} did not vary significantly between the seasons. However, pronounced differences are seen in the upper 10cm between winter and summer. This might indicate the fresh supplies of organic carbon or an affect of seasonal contribution. Higher C_{org} in summer is possibly due to relatively higher sedimentation of primary productivity detritus during the preceding productive months (October to March). Earlier studies concentrating on the temporal

time scales have shown that the lower C_{org} in the surface layers has remained unchanged after two years, which was interpreted as there is no change in the overall community structure of the feeding community and that surface and suspension feeders dominate over burrowing organisms (Nath, unpublished data). In some cores, subsurface peaks are seen indicating burrowing activity in those areas. The subsurface lows and highs in organic carbon are ascribed to benthic burrowing and bioturbation activity, which seems to become shallower with time. Higher oxidation rate of C_{org}in oxic conditions can be the probable reason for relatively lower C_{org}in the winter in surface sediments.

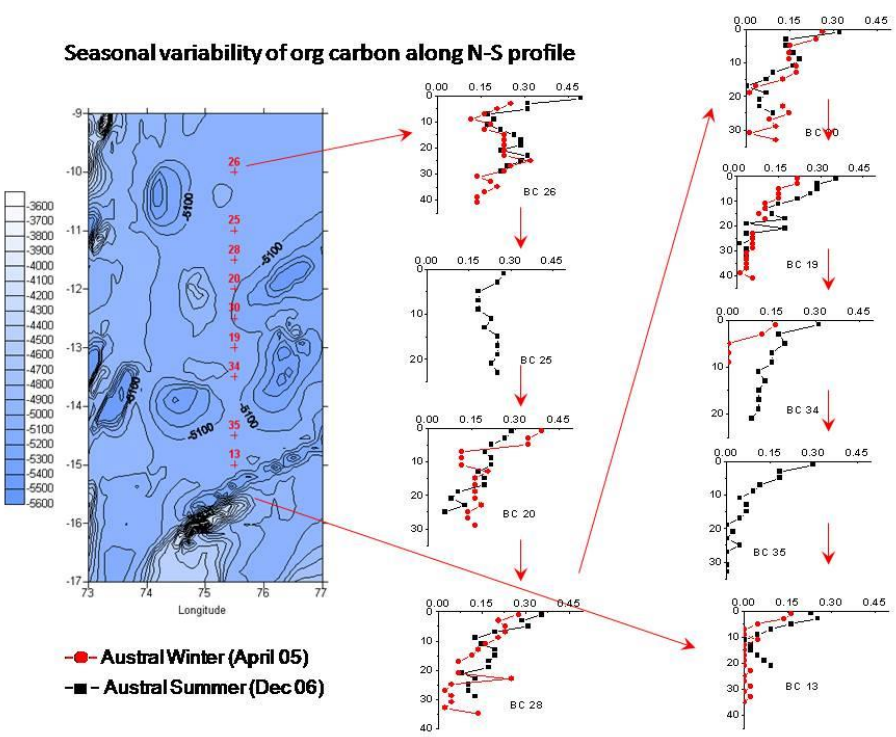

Fig. 5.12: Seasonal variation of sedimentary organic carbon (%) along the north-south transect in the CIB.

Intermediate peaks are seen in some cores at about 20–25cm bsf, which is typical of subsurface diagenesis induced by the benthic burrowing activity. In two of the cores, the subsurface peaks seen during the winter are not seen during the summer. This might suggest a shift in diagenetic fronts related to benthic burrowing activity has taken place. Two southern stations (BC 34 and 13) sampled during the winter time have the lowest C_{org} (0.16%) in the entire north to south transect. In addition, winter samples of the BC 13 core, the C_{org} concentration in the subsurface sediments were below detection limit. This core is in close proximity to the Rodriguez triple Junction wherein the recent (<100yrs) hydrothermal alteration has been found to have been reported to be responsible for depleted C_{org} (Nath et al., 2008). Organic matter

degradation were found to be widespread in ridge–flank hydrothermal systems compared to non–hydrothermal settings (Wheat and McDuff, 1994) suggesting an intense hydrothermal effect.

Seasonal variation of nutrient fluxes

Discussion on the tropic level of the aquatic ecosystem is often approached using porewater gradients. In oligotrophic ecosystems, the nutrient profiles are vertical, i.e. the concentrations remain at the same level throughout the water column and the sediments. In contrast, in eutrophic ecosystems nutrients profiles exhibit sharp gradients near the sediment–water interface. One of the primary goals of this project was to evaluate the seasonality of benthic processes in the CIB. The seasonal supply of carbon to the seafloor might lead to the assumption that sediment microbial metabolism is also highly seasonal in the nature.

The diffusive flux patterns of nitrate show remarkable seasonality between winter of 2005 and summer of 2006 (Table 5.8). The nitrate fluxes are predominantly positive (i.e. into the sediment) across the sediment–water interfaces for both seasons, indicating that there is net denitrification in the sediments in both seasons. A higher influx of nitrate to the sediments in winter suggests that there was a higher abundance of "labile" organic matter in the upper sediment layers to support denitrification. Maximum rates of influx of nitrate from water to sediments were seen during the winter(April 2005), with rates of ca. ~72mmol$m^{-2}yr^{-1}$) at the stations 20 indicating that the winter time rates are higher than summer rates by approximately a factor of > 1.5. The lowest winter rate of the nitrate input to sediments was ca. 45mmol $m^{-2}yr^{-1}$at station 30, which was the maximum influx in summer time.Low nitrate concentration in winter probably due to consumption by benthic organisms leads to greater influx of nitrate from overlying waters to the sediments, while in summerproduction in the top sediment layer causes the influx of nitrate to be lowered significantly by nearly 1.5 times (Table 5.8). The low concentration in the summer denotes the direct coupling to primary productivity which is supported by the decrease of nitrate levels. Studies have shown that the nitrate is not only affected by phytoplankton assimilation but by the nitrogen recycling process as well, which occurs in the water column (Grunwald et al., 2010, Patsch and Kuhn, 2008) and in the sediments (Murray et al., 2006). Decomposition of organic materials in winter leads to enhanced oxygen demand in the

sediment leading to denitification(Van Beusehom et al., 2008). This may be the probable reason for low nitrate concentration in the winter due to enhanced assimilation and denitrification.

Nitrite is an intermediate in both nitrification and denitrification and therefore fluxes are difficult to interpret, particularly since these processes are often closely coupled in marine sediments (Jenkins and Jemp, 1984). For instance, high nitrite in fluxes associated with high nitrate effluxes are indicative of net nitrite consumption by nitrification, whereas high nitrite in fluxes associated with high nitrate influxes reflect net nitrite consumption by denitification(Hall etal., 1996).

Fluxes of silicate are normally assumed to be straightforward, with release due to dissolution of siliceous material, controlled by temperature (e.g. Hammond et al., 1985), and limited uptake by phytoplankton. The seasonal patterns of silica fluxes in year 2006 show opposite trend with that of nitrate fluxes in the northern latitudes. Higher effluxes are seen in the summer. This may be due to dominance of siliceous remains in the preceding months (September to December). This trend is however reversed south of 13°S with silica patterns comparable to those of nitrate. Studies in the surface ocean have shown seasonality in phytoplankton community as a result of silica limitation (Egge, 1998; Dippner, 1998).In the Indian Ocean, higher productivity is seen in the summer at ~ 10–12°S compared to the winter. The seasonal difference in silicate flux is maximum in the northern part of the basin (N of 13°S; Table 5.8). It can be seen that on an annual basis, the sediments were significant exporter of silica to the water column. In contrast, the sediments were a sink for nitrate and phosphate. The net fluxes of phosphate being very small compared to nitrate, probably because of the low solubility of iron phosphates in the oxidized environment near the sediment–water interface. Phosphate fluxes are also controlled by the interplay of various processes such as degradation of organic matter and by the buffering mechanism involving adsorption to iron oxides formed from reduced iron that enters the ocean via hydrothermal vents (Berner 1973), also co–precipitation with ferric minerals (Krom and Berner, 1981), precipitation of iron and manganese rich coatings of foraminiferal carbonate ooze (Sherwood et al., 1987) and the formation of authigenic carbonate flourapatite (Ruttenberg and Berner, 1993). Phosphorus may also be scavenged by windblown, iron rich detritus (Berner et al., 1973). Phosphate fluxes are positive in both seasons indicating benthic PO_4^{3-} regeneration rate is always lower than the rate of its

adsorption and precipitation in these oxic rich sediments, but the net gain of nitrate into the sediment in the winter was much more than the summer.

Phosphate fluxes increase significantly during winter in most of the cores. Reduction of FeOOH causes dissolution of the mineral, apparently releasing PO_4^{3-} (Slomp et al., 1998) from the Fe–rich minerals into the sediments which add up to porewater PO_4^{3-} pool and ultimately result in higher PO_4^{3-} fluxes. Average PO_4^{3-}fluxes in winter was 0.837mmol $m^{-2}yr^{-1}$which was more than 2 fold higher than PO_4^{3-}flux rate (Table 5.8) observed in summer. Low PO_4^{3-} in the surficial layers in winter could be due to the presence of oxidizing surface layer resulting in PO_4^{3-}adsorption to Fe and Mn oxides. Higher bioturbation during winter could be the probable reason for relatively lower diffusive fluxes compared to summer when benthic activity is low.

The porosity in the surface layers did not vary much between December and April but overall the porosity was higher in winter in the subsurface. The concentration gradient between the two seasons may be due to the changing biogeochemical condition in the bottom waters and sediments. Higher diffusive fluxes observed in summer were induced by higher concentration gradients across water–sediment interface compared to winter.

These results showed that the net exchanges of nutrients across the sediment–water interface can vary seasonally possibly in relation in variation in incoming organic matter in case of nitrite and nitrate, oxidation changes driven variability in surface adsorption processes may affect phosphate fluxes and the alkalinity changes may affect the dissolution of opaline silica.

5.2.4. Diagenetic changes in hydrothermally influenced and non hydrothermal areas in the CIB

To understand the diagenetic changes on a local scale, the nutrient variation in an area with large variations in topography and that influenced by vulnerable tectonics, a fracture zone environment was investigated. The data presented in this study are mainly focused on porewater composition (Table 5.9), sedimentary organic carbon (Table 5.10) and benthic fluxes measured (cruise ABP 04 data, Table 5.11) at three different stations with varying geological setting around this (76.5°S) fracture zone in CIB, i.e., on the top of seamount (ABP 04/BC 37), flanks of the seamount (ABP 04/BC 36 and BC 8) and in a valley (ABP 04/BC 38) defining the fracture zone. Incidentally, sediments from the flank of the seamount (AAS 61/BC 8) have revealed evidences of

volcanogenic input (Mascarenhas–Pereira etal., 2006), hydrothermal alteration (Nath etal., 2008) and had significant metalliferous component (Chapter 3; Masarenhas–Pereira and Nath, 2010).

Porewater chemistry

We have compared sediments from hydrothermally influenced areas (AAS 61/BC 8) to other areas in the CIB not influenced by hydrothermalism (Figs. 5.13, 5.14 and 5.15). A representative sample (core AAS 61/BC 1R) is used to represent the siliceous ooze domain while BC 15 core is used to represent the pelagic clays in the area. We have also compared sub-environments (valley, seamount top and flank) within the fracture zone to study the diagenetic changes in the sediments due to hydrothermalism. The following differences are seen between the hydrothermally influenced sediments and other sediments in CIB.

Sedimentary C_{org} on the flanks of the seamount AAS 61/BC 8 and ABP 04/BC 36) is low (upto 0.18%) in the surface sediments (Fig. 5.13). It is interesting to note the downcore (below 2–4cm) concentration of the flank samples where C_{org} values go below detection limit for the entire length of the core. The valley (ABP 04/BC 38) sediments show subsurface enrichment probably due to burrowing animals (Nath and Mudholkar 1989). Other CIB sediments, however, are twice enriched in C_{org} (upto 4%) as compared to the hydrothermally influenced core (Fig. 5.13) followed by gradual decrease in the subsurface. Depletion of C_{org} content was also found to be widespread in other hydrothermal systems similar to our study area compared to non-hydrothermal sediments (Wheat and McDuff, 1994) suggesting an intense hydrothermal effect.

Dissolved silica in the porewaters in the seamount flank (hydrothermally influenced) is enriched (~400µM) (Fig. 5.13) in the surface sediments (only down to 4 cm). Below 4 cm, the silica is undetectable in the porewaters. The valley and seamount top show similar subsurface profile but show large difference in magnitude (~200µM). The seamount top sediments (ABP 04/BC 37) show low silica (283–394 µM) in the porewaters. This core has high carbonate content ($CaCO_3$, 48–76%) (Nath et al., 2008; 2013) compared to non-carbonate sediments (<1%) on the seamount flank. The hydrothermally influenced core exhibit the least efflux (-67mmol $m^{-2}yr^{-1}$) (Fig. 5.15) compared to normal pelagic clays (-238mmol $m^{-2}yr^{-1}$) and siliceous ooze (-

354mmol $m^{-2}yr^{-1}$) in the area. The hydrothermally influenced core (AAS 61/BC 8) has abundant radiolarian only down to 6 cm, below which intense dissolution features were seen in the scanning electron microscope (see Chapter 3). Compared to other pelagic clays in the area, distinct enrichment of Fe, P and depletion of Si and Mg were reported in these sediments (Nath et al., 2008). The observed changes in the porewater may have resulted from the hydrothermal alteration in the sediments.

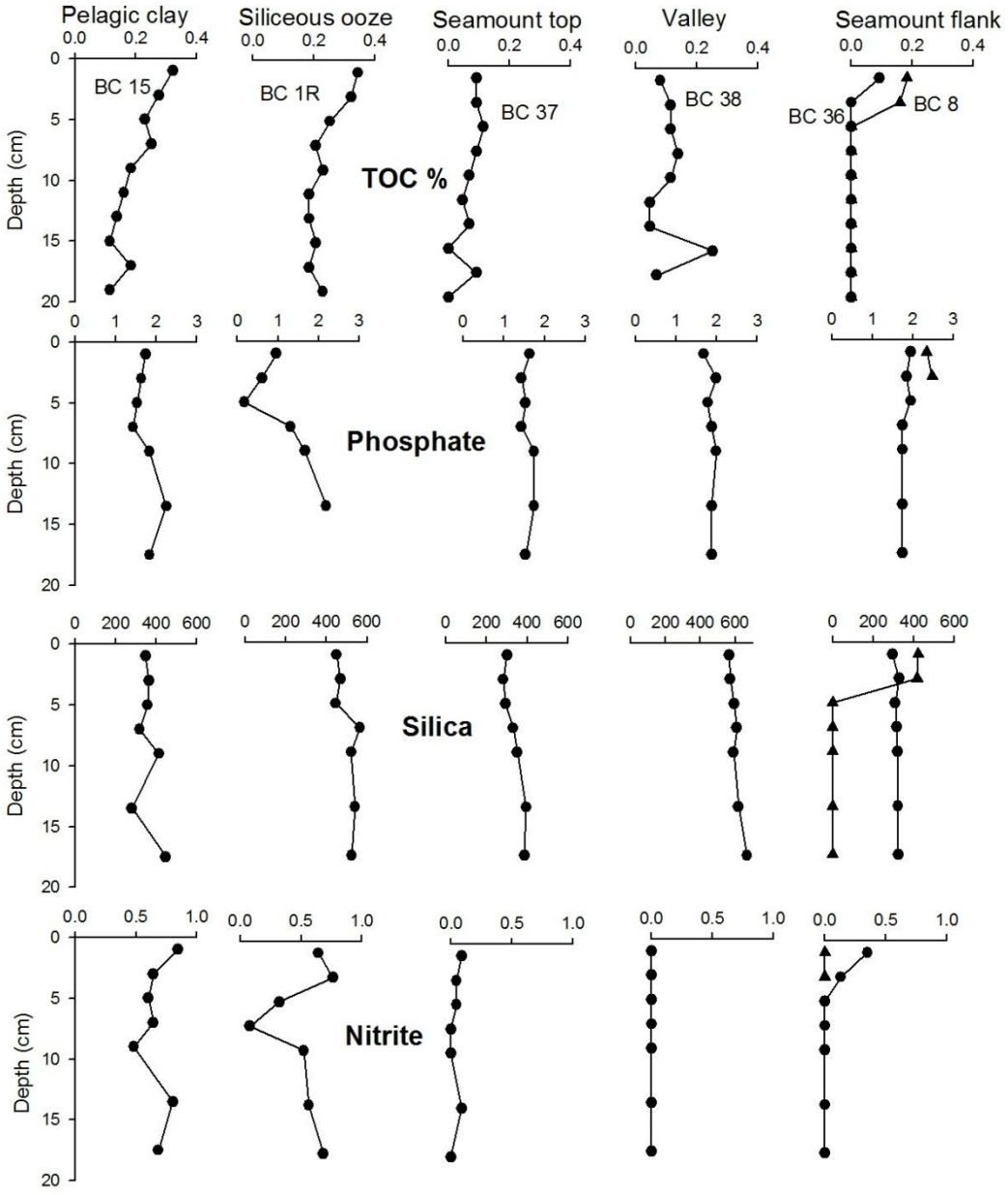

Fig. 5.13: Sedimentary organic carbon and porewater nutrients in the fracture zone environment (valley: ABP 04/BC 38; seamount top: ABP 04/BC 37 and seamount flank: ABP 04/BC 36 and BC 8). Hydrothermally influenced sediments (AAS 61/BC 8) are compared to non-hydrothermal areas (siliceous ooze: AAS 61/BC 1R; pelagic clays: AAS 61/BC 15) in the CIB.

The phosphate content in the hydrothermally influenced core is nearly equal (2.34µM) to the overlying bottom water in the area (2.39µM) (Fig. 5.13) and therefore is in equilibrium. The flux of phosphate to the sediments is therefore minimal (0.04mmol $m^{-2}yr^{-1}$) (Table 5.11; Fig. 5.14) compared to other areas (siliceous ooze: 1.09mmol $m^{-2}yr^{-1}$; pelagic clays: 0.54mmol $m^{-2}yr^{-1}$) in the CIB. The other sub-environments around the fracture zone have low phosphate content (0.85 to 1.71µM) (Table 5.11) compared to the overlying waters (2.40µM). The highest flux to the sediment is found in the valley sediments (ABP 04/BC 38, 0.65mmol $m^{-2}yr^{-1}$) followed by seamount top (ABP 04/BC 37, 0.47mmol $m^{-2}yr^{-1}$) and flank (ABP 04/BC 36, 0.39mmol $m^{-2}yr^{-1}$) (Table 5.11, Fig. 5.14). The hydrothermally influenced sediments are distinct in having the least influx of phosphate (0.04mmol $m^{-2}yr^{-1}$). Incidentally, this core (AAS 61/BC 8) has high Fe and P content in the sediments (Nath et al., 2008). AAS 61/BC 8 core which lies in close proximity to a fracture zone has shown evidence of past hydrothermal activity with degassing and circulation of migrating hydrothermal fluids in the last 100yrs (Nath et al., 2008). This is also reflected in the PO_4^{3-} concentration of the interstitial fluids. Adsorption of P onto hydrous ferric oxides or precipitation of iron phosphate phase (Nath et al., 1989) could possibly be the reason for PO_4^{3-} enrichment of bottom seawater relative to interstitial PO_4^{3-} concentration.

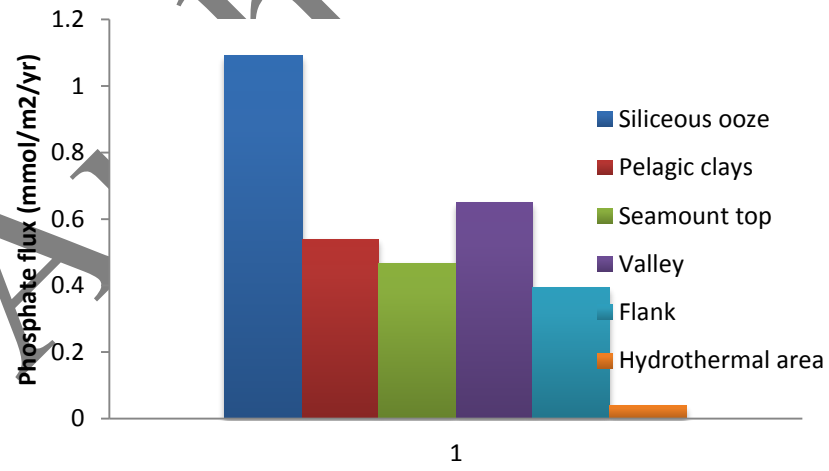

Fig. 5.14: Comparison of phosphate influx in the hydrothermally influenced sediments (BC 8) recovered from the flanks of a seamount with fluxes from the sub-environment of the fracture zone and normal pelagic clays and siliceous ooze in the CIB.

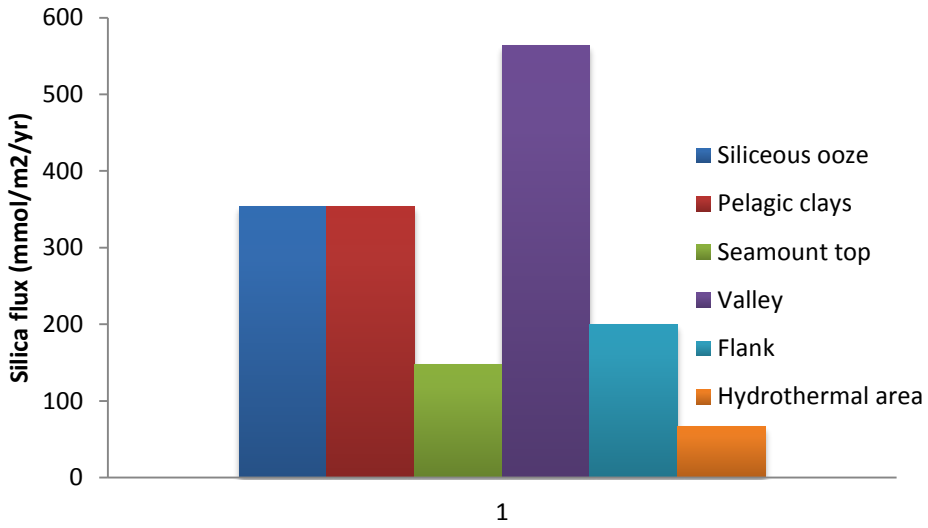

Fig. 5.15: Comparison of silica efflux in the hydrothermally influenced sediments (BC 8) recovered from the flanks of a seamount with fluxes from the sub-environment of the fracture zone and normal pelagic clays and siliceous ooze in the CIB. Lowest fluxes are seen in hydrothermally influenced area

The nitrite levels in the interstitial waters of the hydrothermally influenced sediments are below detection at the surface, while the other flank sediments have a surface enrichment (0.3 to 0.4µM; till 6cm) below which nitrite is undetectable (Fig. 5.13). The valley sediments also show complete absence of nitrite in the entire core. The extremely low levels of NO_2^- (Fig. 5.13) or the total absence in some of the cores suggest lack of denitrification and oxic conditions prevailing in the sediment. In the valley (BC 38), the NO_2^- is entirely consumed by microbial processes in the entire length of the core while on the flanks (BC 36) it is within the top 5cms indicated by concentrations that are below detection in the core retrieved from the valley and flanks of a seamount. The siliceous ooze and pelagic clay sediments in the CIB have higher nitrite content in the surface sediments (0.96 and 1.73µM respectively; Table 5.13).

5.2.5. Comparison with other basins

Benthic fluxes for SiO_4 in the CIB range between -12 and -597mmol $m^{-2}yr^{-1}$; Table 5.12) and are similar to those of the southern (<-650mmol $m^{-2}yr^{-1}$, Hensen et al., 1998) and eastern south Atlantic (>-400mmol $m^{-2}yr^{-1}$, Zabel et al., 1998) (Table 5.12). The CIB has high flux values of silica (max -597mmol $m^{-2}yr^{-1}$) due to the siliceous ooze that is spread throughout the northern part of the basin. Similar values of diffusive

fluxes of silica are seen in the southern ocean and the inner Ross Sea, where diffusive fluxes exceed -700mmol $m^{-2}yr^{-1}$ (Rangueneauet al., 2001).

Phosphate influxes in the CIB range between 0.04 and 1.65mmol $m^{-2}yr^{-1}$ for PO_4^{3-}(Table 5.12).Data collected in the eastern equatorial Atlantic show phosphate fluxes to vary between -0.07 and -0.2mmol $m^{-2}yr^{-1}$ (Froelich et al., 1979) (Table 5.12) while in the eastern tropical Atlantic phosphate fluxes vary between 1.6 and -5.51mmol $m^{-2}yr^{-1}$ (Jahnkeet al., 1989) (Table 5.12) while slightly higher values of PO_4^{3-} fluxes were found in the Eastern south Atlantic (0 – >-4mmol $m^{-2}yr^{-1}$, Zabel et al., 1998) and lower values in the Southern and Central Atlantic (2 to -11mmol $m^{-2}yr^{-1}$, Hensen et al., 1998)(Table 5.12). The phosphate fluxes in the Eastern tropical Atlantic (Jahnkeet al., 1989) are comparable to those inCIB.

5.2.6. Ecological significance of sediment nutrient fluxes

Seasonality of pelagic processes, coupled to rapid delivery of largely unaltered particulate organic matter, and episodic events like benthic storms and turbidity currents generated by downslope transport were identified as potential driving forces of deep–sea temporal variability (Smith et al., 1992; Sayles et al., 1994). Resulting dramatic depositional events have been documented in the past (Lampitt 1985; Gross et al., 1988; Smith et al., 1994), but because of the ephemeral nature of the perturbations and logistical constraints, little is known of the geochemical response of surface sediments. Pulsed delivery of organic matter inputs have been shown to be correlated with benthic remineralization rates (Nixon 1981; Nixon and Pilson 1983; Hopkinson and Vallino 2005). Benthic nutrient regeneration contributes to the seasonal cycle as well as the seasonal cycle of primary production in shallow coastal areas (Nixon et al., 1976). Release of nutrients from the sediments can supply a substantial fraction of the nutrient requirements for primary producers in coastal waters (e.g. Dollar et al., 1991;Giblin et al., 1997). However there is little evidence to substantiate this in the deep seas.

To estimate the extent of this support by sediments as a nutrient source for primary production, nitrogen (NO^{3-} + NO^{2-}) and phosphate (PO_4^{3-}) sediment release were compared to calculate the nutrient (nitrogen and phosphorus) demand based on Redfield composition ratios (C:N:P of 106:16:1). Primary productivity in the basin ranged from 10950 to 7300mmol $m^{-2}yr^{-1}$ (Antonieet al., 1996) in October –December

(Austral Summer) and 7300 to 4558mmol $m^{-2}yr^{-1}$ in April–June (Austral Winter). There is a latitudinal variation seen in the primary productivity with higher productivity (7300 and 10950mmol $m^{-2}yr^{-1}$ in austral winter and summer respectively) seen in the northern part (north of 12°S) of the basin. This transition in primary productivity coincides with the sediment type in the basin, with the siliceous oozes seen in areas with higher primary productivity compared to the pelagic clay domain in the southern part of the basin. Phosphate requirement may be estimated to 69 to103mmol $m^{-2}yr^{-1}$ in summer and 43 to 69mmol $m^{-2}yr^{-1}$ in winter, while nitrogen demand may be estimated to 1654 to1103mmol $m^{-2}yr^{-1}$ in summer and 689 to 1103mmol $m^{-2}yr^{-1}$ in winter. Lowest nutrient demand was observed in April (australwinter) and benthic nutrient fluxes supplies 0.3 and 1.48% in the siliceous and pelagic domain respectively. Interestingly, the contribution of benthic flux to primary productivity shows an opposite trend to the nutrient demand, with higher contribution of benthic fluxes in the austral winter.

Some work on deep–sea sediment and porewater dynamics suggested that benthic response will be confined to the sediment–water interface, variation of input fluxes would be damped out, producing little variation in the porewater composition and solute fluxes (Martin and Bender 1988; Sayles et al., 1994). The principal reason for this constancy is the assumption that bioturbation rates are too slow to bury newly deposited organic carbon to depth where porewater profiles would be affected, implying that only low reactive carbon is present at depth. This contrasts with the recent observation of rapid bioturbation rates associated with freshly deposited particles (Smith et al., 1993) suggesting that fresh organic particles could be rapidly incorporated in the sediment and influence porewater composition. Direct observations of large changes in deep–sea porewater composition on seasonal timescales have also been made (Gehlen et al., 1997). Studies in the deep-sea Antarctic sediments (Rabouille et al., 1998) suggest that the link between production and benthic processes is very strong in this region.

5.3. Conclusions

Porewater profiles of pH, NO_2^-, PO_4^{3-}, SiO_4 and sedimentary organic carbon in the sediment differ radically in different depositional environments of the CIB. The

porewater composition of dissolved nutrients through the sediments water interface shows a distinct regional distribution in the CIB.

- Diffusive benthic fluxes of phosphate and silicate calculated from porewater data of sediments at 47 locations in the abyssal CIB show that the phosphate fluxes vary between 1.65 and 0.04mmol $m^{-2}yr^{-1}$ and silicate: -12 and-597mmol $m^{-2}yr^{-1}$. The most striking feature is the relatively large area north of 12°S with high silica efflux, which is dominated by siliceous ooze acts as a source of silica to bottom waters. Generally the basin acts as a sink than a source of phosphate. Low benthic fluxes in the southern portion of the basin could be related to higher nutrients recycling in the surface waters, resulting in a lower export flux or a generally higher remineralization within the water column. The benthic silicate fluxes in the CIB also coincide with flow path of the Antarctic bottom waters (AABW) which enter the basin through the saddles at 10°S. AABW are rich in silica and may account for the influx of the silica in the southern stations.
- Mass balance calculations of silica in the CIB reveal that 19% of biogenic silica produced in the surface waters at 10°S reach the water sediment interface, which is also reflected by concomitant high in diffusive flux (~-376mmol $m^{-2}yr^{-1}$) while at the southern station the benthic sediments receive (~9%) less than half of what is produced in the surface waters with a concomitant decrease in DSi (~-106.7mmol $m^{-2}yr^{-1}$). The high silicic acid in the porewaters and fluxes in the north thus result from a larger input of biogenic opal from the surface in this region compared to the southern stations.
- Seasonal variation studied along the north–south along 75.5°E longitude show a distinct change at ~13°S in the geochemical parameters studied here which are probably influenced by the sediment type and local bathymetric changes. A seasonal pattern is seen in nutrient profile along the N-S transect. Phosphate fluxes are high during summer in the north, while winter fluxes are higher in the south. Silica fluxes also show seasonal variability. The corrosiveness of the Antarctic bottom waters seem to more intense during the summer season, leading to variation in opal dissolution.
- The benthic environment seems to be responding to the surface water productivity in the CIB. During the summer, microbial activity results in high production of phosphate throughout the sediment column but particularly near the interface. Decomposition rates often decrease exponentially with depth below the interface, therefore seasonally high production often results in porewater concentration

maxima few centimeters below the sediment surface. In the winter, physical processes such as biogenic reworking, fluid transport associated with solute diffusion into burrows, result in extensive exchange of sediment porewater with the bottom waters and causes a general lowering of phosphate values from the earlier summer levels. This mechanism can be used to explain the seasonal variation in the downcore nutrient profiles in the basin.

- Organic carbon concentrations are higher in the surface in many of the cores suggesting either the fresh supplies over the period of study or may be responding to seasonal variation with summer favoring higher productivity and export fluxes. Subsurface changes were also noticed in organic carbon concentrations which might suggest the changes in burrowing intensity with season.
- Global maps of primary productivity display the most productive areas in the CIB are in the north of the basin (up to 12°S; PP > 6686mmolm^{2-}yr^{-1}). Our results reveal a distinct coupling between the general pelagic regional distribution pattern of primary production and the response of benthic processes as indicated by the flux of remineralized nutrients, through a spatially differing degree of decoupling during transport and remineralization of particulate organic matter and biogenic silica
- Distinct changes in porewater nutrient profiles and fluxes were seen in hydrothermally influenced sediments compared to sediments not influenced by hydrothermalism. Local changes were also seen in nutrient profiles of sediment cores sampled in different sub-environmentsaround a fracture zone.

Table 5.1: Station numbers, water depth and concentration of nutrients in 26 cores sampled at every 1 degree spacing from 10° to 16°S during the AAS 61 cruise in the CIB.

CRUISE AAS 61				
Core No.	**Depth (cm)**	**Nutrients (µM)**		
		Phosphate	**Nitrite**	**Silicate**
BC01R	0–2	0.96	0.64	450
	2–4	0.61	0.76	470
	4–6	0.18	0.32	447
	6–8	1.31	0.08	565
	8–10	1.66	0.52	523
	10–15	2.19	0.56	541
	15–20	9.37	0.68	525
BC 02	0–2	1.90	0.64	413
	2–4	2.00	0.48	478
	4–6	1.90	0.72	441
	6–8	2.47	0.44	553
	8–10	1.90	0.60	544
	10–15	2.00	0.56	531
	15–20	2.09	0.56	563
BC 03	0–2	2.01	0.97	253
	2–4	1.66	0.72	136
	4–6	0.61	0.08	92
	6–8	0.35	0.88	181
	8–10	1.93	0.08	135
	10–15	1.84	0.12	144
	15–20	1.40	0.12	124
BC 04	0–2	0.17	0.64	149
	2–4	0.33	0.73	261
	4–6	0.25	1.05	248
	6–8	0.42	1.05	158
	8–10	0.50	0.92	112
	10–15	0.33	0.78	186
	15–20	0.42	0.09	115
BC 05	0–2	ND	0.96	305
	2–4	0.42	0.23	349
	4–6	0.17	0.78	320
	6–8	0.17	0.87	330
	8–10	0.17	0.82	357
	10–15	ND	0.37	317
	15–20	0.08	0.46	299
BC 06	0–2	1.66	0.43	341
	2–4	1.17	0.70	296
	4–6	1.37	0.24	305
	6–8	ND	0.67	289
	8–10	ND	0.30	330

	10–15	ND	0.64	266
	15–20	1.27	0.32	278
BC 07	0–2	1.17	0.32	296
	2–4	1.27	0.64	333
	4–6	ND	0.75	275
	6–8	ND	0.16	311
	8–10	0.10	0.24	265
	10–15		0.24	364
	15–20	0.49	0.24	367
BC 08	0–2	2.34	ND	420
	2–4	2.48	ND	417
	4–6	NA	NA	ND
	6–8	NA	NA	ND
	8–10	NA	NA	ND
	10–15	NA	NA	ND
	15–20	NA	NA	ND
BC 09	0–2	2.20	0.42	632
	2–4	2.41	0.58	638
	4–6	2.34	ND	632
	6–8	2.20	ND	651
	8–10	2.41	ND	654
	10–15	2.27	ND	535
	15–20	2.13	ND	585
BC 10	0–2	2.34	ND	619
	2–4	2.34	ND	685
	4–6	2.27	ND	598
	6–8	2.34	ND	626
	8–10	2.27	ND	679
	10–15	2.27	ND	791
	15–20	2.27	ND	682
BC 11	0–2	1.85	0.45	241
	2–4	2.05	0.45	271
	4–6	2.05	0.21	269
	6–8	2.15	0.33	286
	8–10	2.24	0.33	312
	10–15	2.24	0.25	306
	15–20	2.24	0.37	356
BC 12	0–2	2.34	0.58	311
	2–4	2.15	0.45	290
	4–6	2.15	0.29	293
	6–8	2.15	0.21	258
	8–10	1.46	0.25	238
	10–15	2.24	0.21	322
	15–20	2.24	0.33	322
	0–2	1.60	0.40	233
	2–4	1.79	0.36	242

	4–6	1.89	0.24	297
BC 13	6–8	1.89	0.28	242
	8–10	1.79	0.36	224
	10–15	1.79	0.20	321
	15–20	1.89	0.16	258
	0–2	1.74	0.36	366
	2–4	1.63	0.28	247
	4–6	1.84	0.40	297
BC 14	6–8	1.33	0.40	298
	8–10	1.74	0.24	280
	10–15	1.74	0.24	282
	15–20	1.63	0.28	300
	0–2	1.74	0.84	348
	2–4	1.63	0.64	365
	4–6	1.53	0.60	358
BC 15	6–8	1.43	0.64	318
	8–10	1.84	0.48	413
	10–15	2.25	0.80	280
	15–20	1.84	0.68	447
	0–2	1.79	0.92	363
	2–4	1.89	0.60	415
	4–6	1.79	0.64	420
BC 16	6–8	1.89	0.72	412
	8–10	1.98	0.84	452
	10–15	1.89	0.56	452
	15–20	1.79	0.56	292
	0–2	1.05	0.52	575
	2–4	1.57	0.52	426
	4–6	1.05	0.57	579
BC 17	6–8	1.05	0.65	783
	8–10	1.05	0.52	622
	10–15	1.05	0.48	531
	15–20	1.15	0.48	540
	0–2	0.73	0.52	636
	2–4	0.73	0.85	497
	4–6	1.26	0.81	603
BC 18	6–8	0.73	0.44	524
	8–10	0.84	0.48	572
	10–15	1.05	0.48	557
	15–20	0.94	0.48	467
	0–2	1.74	0.68	415
	2–4	1.83	0.32	408
	4–6	1.83	0.52	390
BC 19	6–8	2.01	0.40	393
	8–10	1.83	0.68	378
	10–15	2.01	0.36	353

	15–20	1.92	0.32	394
BC 20	0–2	1.64	0.64	261
	2–4	1.83	0.81	340
	4–6	1.83	0.44	375
	6–8	2.28	0.48	343
	8–10	2.10	0.48	406
	10–15	2.28	0.40	428
	15–20	2.28	0.32	351
BC 21	0–2	1.80	0.56	433
	2–4	2.18	0.91	444
	4–6	2.09	1.19	510
	6–8	2.28	0.95	570
	8–10	2.09	0.99	622
	10–15	2.56	0.99	620
	15–20	2.47	0.95	537
BC 22	0–2	1.80	1.15	547
	2–4	2.09	1.03	489
	4–6	1.80	1.03	568
	6–8	1.80	0.87	481
	8–10	1.90	0.99	564
	10–15	1.90	0.56	655
	15–20	2.09	1.15	690
BC 23	0–2	2.05	0.92	468
	2–4	1.44	0.52	552
	4–6	1.64	0.52	571
	6–8	1.44	0.44	439
	8–10	1.64	0.64	518
	10–15	1.54	0.56	512
	15–20	1.64	0.60	381
BC 24	0–2	1.75	0.56	530
	2–4	2.16	0.72	524
	4–6	2.16	0.44	528
	6–8	2.16	0.52	581
	8–10	1.95	0.52	548
	10–15	1.95	0.36	591
	15–20	1.95	0.80	613
BC 25	0–2	1.81	0.44	484
	2–4	1.62	1.08	534
	4–6	2.38	0.56	594
	6–8	2.00	0.60	533
	10–15	2.47	0.36	525
	15–20	2.28	0.56	523
BC 26	0–2	1.83	0.95	448
	2–4	1.75	0.87	428
	4–6	2.00	0.68	450
	6–8	1.92	0.64	469

	8–10	1.83	0.68	396
	10–15	1.92	0.68	375
	15–20	1.83	0.68	444

Table 5.2: Organic carbon content (wt%) in the CIB sediments.

Core No	Depth (cm)									
	0–2	**2–4**	**4–6**	**6–8**	**8–10**	**10–12**	**12–14**	**14–16**	**16–18**	**18–20**
BC 01	0.34	0.32	0.25	0.21	0.23	0.18	0.18	0.21	0.18	0.23
BC 02	0.34	0.3	0.28	0.21	0.21	0.32	0.23	0.25	0.25	0.23
BC 03	0.18	0.23	0.23	0.18	0.18	0.09	0.11	0.07	0.14	0.07
BC 04	0.41	0.41	0.34	0.30	0.30	0.23	0.23	0.14	0.18	0.16
BC 05	0.46	0.28	0.30	0.18	0.09	0.09	0.07	0.07	0.07	0.05
BC 06	0.14	0.23	0.16	0.14	0.14	0.18	0.05	0.05	0.09	0.05
BC 07	0.25	0.23	0.16	0.11	0.09	0.12	0.14	0.14	0.16	0.16
BC 08	0.18	0.16	BD	BD	BD	BD	BD	BD	BD	BD
BC 09	0.32	0.21	0.18	0.14	0.11	0.11	0.09	0.07	0.05	0.07
BC 10	0.21	0.18	0.11	0.14	0.18	0.16	0.16	0.14	0.11	0.09
BC 11	0.30	0.18	0.23	0.21	0.23	0.21	0.23	0.16	0.21	0.37
BC 12	0.09	0.09	0.09	0.05	0.28	0.12	0.11	0.07	0.07	
BC 13	0.23	0.23	0.23	0.11	0.09	0.09	0.11	0.09	0.07	0.09
BC 14	0.30	0.28	0.28	0.21	0.16	0.18	0.23	0.23	0.16	0.11
BC 15	0.32	0.28	0.23	0.25	0.18	0.16	0.14	0.12	0.18	0.11
BC 16	0.37	0.30	0.28	0.21	0.18	0.21	0.18	0.18	0.18	0.21
BC 17	0.34	0.23	0.18	0.23	0.23	0.25	0.23	0.21	0.21	0.18
BC 18	0.30	0.25	0.21	0.21	0.18	0.16	0.21	0.18	0.18	0.16
BC 19	0.30	0.21	0.14	0.09	0.11	BD	0.09	0.00	0.05	BD
BC 20	0.37	0.28	0.16	0.18	0.21	0.23	0.16	0.23	0.18	0.18
BC 21	0.39	0.21	0.21	0.21	0.25	0.18	0.23	0.25	0.23	0.16
BC 22	0.30	0.32	0.34	0.30	0.23	0.23	0.32	0.14	0.14	0.07
BC 23	0.46	0.39	0.32	0.16	0.16	0.14	0.18	0.16	0.18	0.18
BC 24	0.32	0.32	0.18	0.14	0.18	0.11	0.09	0.11	0.21	0.16
BC 25	0.30	0.39	0.18	0.23	0.25	0.23	0.32	0.32	0.39	0.41
BC 26	0.39	0.46	0.44	0.34	0.28	0.28	0.18	0.16	0.14	0.14

Table 5.3: Seasonal variation in nutrient concentration of phosphate and silicate in porewatersin cores sampled in austral winter and summer along a north-south transect along the fracture zone in CIB.

	Season Month/Year Cruise No	Austral Winter April–05 ABP 04 /TVBC		Austral Summer December–06 ABP 26/SVBC	
Core No	Nutrient	Silicate (µM)	Phosphate (µM)	Silicate (µM)	Phosphate (µM)
BC 26	0–2cm	306	1.96	447	2.17
	2–4 cm	410	1.57	455	2.07
	4–6 cm	444	1.57	492	2.28
	6–8 cm	461	1.66	498	2.28
	8–10 cm	483	1.96	528	2.17
	10–15 cm	499	2.06	568	2.28
	15–20 cm	531	1.76	600	2.28
BC 25	0–2cm	315	2.35	418	2.07
	2–4 cm	490	1.96	424	1.97
	4–6 cm	388	2.06	516	2.59
	6–8 cm	393	2.45	510	2.38
	8–10 cm	469	1.86	536	2.38
	10–15 cm	484	2.55	536	2.38
	15–20 cm	489	2.25	629	2.59
BC 28	0–2cm	na	na	454	2.18
	2–4 cm	na	na	457	2.07
	4–6 cm	na	na	525	1.52
	6–8 cm	na	na	430	1.41
	8–10 cm	na	na	567	0.98
	10–15 cm	na	na	626	1.74
	15–20 cm	na	na	634	1.63
BC 20	0–2cm	385	2.00	461	4.47
	2–4 cm	412	2.21	457	3.85
	4–6 cm	413	2.32	473	3.85
	6–8 cm	454	2.74	496	2.29
	8–10 cm	466	3.37	519	2.29
	10–15 cm	500	2.64	551	2.39
	15–20 cm	519	3.16	566	2.81
BC 30	0–2cm	388	2.65	472	1.98
	2–4 cm	405	3.18	463	2.42
	4–6 cm	445	3.71	480	2.20
	6–8 cm	436	3.07	488	2.09
	8–10 cm	438	3.07	540	1.87
	10–15 cm	469	4.45	507	2.09
	15–20 cm	484	3.50	600	2.31
BC 19	0–2cm	435	4.34	387	0.44
	2–4 cm	540	3.35	412	0.77
	4–6 cm	418	3.55	448	1.10
	6–8 cm	425	3.55	369	0.00
	8–10 cm	438	3.95	254	0.00
	10–15 cm	425	4.54	484	0.77
	15–20 cm	442	3.55	533	0.77
BC 34	0–2cm	498	2.47	497	1.49
	2–4 cm	505	2.36	486	1.71
	4–6 cm	508	2.15	512	1.49
	6–8 cm	498	2.26	508	1.49
	8–10 cm	518	2.26	546	1.71
	10–15 cm	527	2.26	545	1.49
	15–20 cm	na	na	559	1.60
BC 35	0–2cm	388	1.55	389	1.28
	2–4 cm	325	1.55	402	1.28

	4–6 cm	386	1.66	424	1.49
	6–8 cm	333	1.66	433	1.17
	8–10 cm	330	1.76	405	1.28
	10–15 cm	335	1.76	414	1.81
	15–20 cm	364	1.76	517	1.07
BC 13	0–2cm	442	1.45	400	0.66
	2–4 cm	435	1.55	421	0.88
	4–6 cm	445	1.45	421	0.77
	6–8 cm	438	2.17	470	0.99
	8–10 cm	526	2.48	499	1.43
	10–15 cm	469	1.55	482	0.99
	15–20 cm	465	1.45	550	0.77

na: not analyzed

Table 5.4: Porewater nutrient concentration in surface (0–2cm) sediments sampled during the base line study of the PMN–EIA project

Core No.	Nutrients in µM			
	Phosphate	Nitrite	Nitrate	Silicate
A1/Bc188B	2.1	0.95	45	430
A1/Bc190	1.33	0.34	43	370
A1/Bc193A	2.17	0	43	370
A1/Bc194B	2.24	0	46	360
A1/Bc197A	1.61	0.31	45	370
T1/Bc159B	1.51	0.11	41	280
T1/Bc181	2.43	0.25	46	350
T1/Bc160A	2.64	0.4	39	410
T1/Bc179A	2.36	0.49	41	320
T1/Bc176B	2.86	0.46	39	360
R1/Bc172	3.5	0.35	52	340
R1/Bc173	1	0.49	43	390
R1/Bc166A	0.51	0.77	43	400
R1/Bc169	2.96	0.35	37	510
R1/Bc171	2.78	0.49	42	370
R2/Bc134c	3.26	0.55	39	480
R2/Bc142	1.99	0.4	39	360
R2/Bc145	2.6	0.35	32	400
T2/Bc146	3.26	0.31	33	340
T2/Bc151	2.3	0.2	33	540
T2/Bc153	2.35	0.35	33	430

Table 5.5: Benthic diffusive flux (mmol/m^2/yr) at sediment-water interface.

AAS 61	Phosphate	Silicate		Baseline	Phosphate	Silicate
BC 01	1.09	–354		A1/Bc188B	0.23	–349
BC 2	0.38	–317		A1/Bc190	0.85	–274
BC 03	0.28	–126		A1/Bc193A	0.17	–270
BC 04	1.65	–12		A1/Bc194B	0.12	–266
BC 05	nd	–178		A1/Bc197A	0.61	–270
BC 06	0.6	–241		T1/Bc159B	0.73	–172
BC 07	0.89	–170		T1/Bc181	–0.03	–263
BC 08	0.04	–67		T1/Bc160A	–0.2	–319
BC 09	0.16	–174		T1/Bc179A	0.03	–212
BC 10	0.07	–168		T1/Bc176B	–0.39	–274
BC 11	0.47	–121		R1/Bc172	–0.88	–233
BC 12	0.07	–197		R1/Bc173	1.09	–290
BC 13	0.61	–107		R1/Bc166A	1.51	–310
BC 14	0.49	–264		R1/Bc169	–0.47	–447
BC 15	0.54	–238		R1/Bc171	–0.32	–277
BC 16	0.58	–268		R2/Bc134c	–0.7	–408
BC 17	1.03	–472		R2/Bc142	0.34	–268
BC 18	1.39	–597		R2/Bc145	–0.16	–303
BC 19	0.52	–314		T2/Bc146	–0.69	–237
BC 20	0.6	–142		T2/Bc151	0.08	–488
BC 21	0.5	–352		T2/Bc153	0.04	–357
BC 22	0.48	–451		min	–0.88	–488
BC 23	0.25	–341		max	1.51	–172
BC 24	0.51	–444				
BC 25	0.46	–395		min of all	–0.88	–597
BC 26	0.46	–376		max of all	1.65	–12
min	0.04	–597				
max	1.65	–12				

Table 5.6: Organic carbon content (wt%) in cores sampled in the Austral summer of 2006 (December) in the CIB during the ABP 26 cruise.

ABP 26/SVBC											
Depth (cm)	**26**	**25**	**28**	**20**	**19**	**30**	**35**	**13**	**34**	**35**	**13**
0–2	0.49	0.28	0.36	0.29	0.36	0.32	0.30	0.23	0.31	0.30	0.23
2–4	0.31	0.25	0.29	0.26	0.29	0.14	0.18	0.25	0.17	0.18	0.25
4–6	0.31	0.18	0.31	0.22	0.29	0.14	0.18	0.16	0.20	0.18	0.16
6–8	0.17	0.18	0.20	0.20	0.26	0.16	0.11	0.09	0.15	0.11	0.09
8–10	0.20	0.18	0.13	0.22	0.22	0.18	0.09	0.05	0.15	0.09	0.05
10–12	0.17	0.23	0.15	0.22	0.15	0.16	0.05	0.00	0.10	0.05	BD
12–14	0.22	0.21	0.19	0.17	0.10	0.09	0.07	0.02	0.13	0.07	0.02
14–16	0.26	0.25	0.20	0.20	0.13	0.07	0.07	0.02	0.10	0.07	0.02
16–18	0.29	0.25	0.17	0.20	0.17	BD	0.05	0.05	0.10	0.05	0.05
18–20	0.29	0.25	0.17	0.10	0.03	0.07	0.00	0.07	0.10	BD	0.07
20–22	0.22	0.23	0.08	0.08	0.17	0.05	0.02	0.09	0.08	0.02	0.09
22–24	0.31	0.25	0.13	0.13	0.03	0.05	BD			BD	
24–26	0.29		0.10	0.06	0.06	0.09	0.05			0.05	
26–28	0.24		0.10		0.01		BD			BD	
28–30	0.22		0.13		0.03		BD			BD	
30–32					0.03		BD			BD	
32–34					0.03		BD			BD	

BD: below detection

Table 5.7: Organic carbon content (wt%) in cores sampled in the Austral winter of 2005 (April) in the CIB during the ABP 04 cruise. (BD: below detection)

ABP 04/TVBC							
Depth (cm)	**26**	**28**	**20**	**19**	**30**	**13**	**34**
0–2		0.28	0.39	0.22	0.26	0.16	0.16
2–4	0.25	0.21	0.34	0.22	0.24	0.14	0.11
4–6	0.21	0.23	0.34	0.15	0.15	0.05	BD
6–8	0.16	0.23	0.11	0.15	0.15	BD	BD
8–10	0.11	0.21	0.11	0.15	0.15	BD	BD
10–12	0.18	0.16	0.11	0.10	0.17	0.05	
12–14	0.16	0.14	0.21	0.10	0.17	BD	
14–16	0.23	0.12	0.16	0.08	0.13	BD	
16–18	0.23	0.07	0.16	0.10	0.03	BD	
18–20	0.23		0.16		0.01	BD	
20–22	0.23	0.07	0.16			BD	
22–24	0.23	0.25	0.18	0.06	0.13	0.02	
24–26	0.32	0.05	0.14	0.06	0.15	BD	
26–28	0.25	0.02	0.14	0.06	0.08	BD	
28–30	0.23	0.05	0.16	0.06	0.10	0.02	
30–32	0.14	0.05		0.03	0.01	BD	
32–34	0.18	0.02		0.03	0.10	0.02	
34–36	0.21	0.14		0.03		BD	
36–38	0.16			0.03			
38–40	0.14			0.01			
40–42	0.14			0.06			

Table 5.8: Seasonal variation in diffusive nutrient fluxes at water–sediment interface of N-Stransect in CIB

Season Month/Year Cruise No	A. Winter Apr–05 ABP 04	A. Summer Dec–06 ABP 26	A. Winter Apr–05 ABP 04	A. Summer Dec–06 ABP 26	A. Winter Apr–05 ABP 04	A. Summer Dec–06 ABP 26
	diffusive flux (mmol/m^2/yr)					
	Nitrate		**Silicate**		**Phosphate**	
BC 26	67	28	–212	–349	0.39	0.18
BC 25	64	37	–220	–353	0.04	0.28
BC 28	na	37	na	–378	na	0.18
BC 20	72	24	–326	–408	0.36	–1.79
BC 30	45	37	–331	–408	–0.22	0.36
BC 19	45	32	–358	–296	–1.59	1.60
BC 34	50	40	–426	–426	–0.05	0.75
BC 35	49	30	–317	–322	0.75	0.99
BC 13	47	39	–373	–310	0.81	1.41

Table 5.9: Nutrient concentration in porewaters of cores sampled in fracture zone complex in CIB.

Cruise ABP 04		**Nutrients in µM**			
Station No.	**Depth (cm)**	**Phosphate**	**Nitrite**	**Nitrate**	**Silicate**
BC 36	0–2	1.95	0.35	14.5	294
	2–4	1.84	0.13	27.5	327
	4–6	1.95	BD	26.9	309
	6–8	1.74	BD	26.9	316
	8–10	1.74	BD	28.3	320
	10–15	1.74	BD	28.0	321
	15–20	1.74	BD	27.7	324
BC 37	0–2	1.64	0.09	15.6	301
	2–4	1.43	0.04	26.1	283
	4–6	1.54	0.04	25.0	294
	6–8	1.43	BD	24.4	331
	8–10	1.74	BD	26.7	351
	10–15	1.74	0.09	25.4	394
	15–20	1.54	BD	25.9	387
BC 38	0–2	1.68	BD	16.1	566
	2–4	2.00	BD	26.5	572
	4–6	1.79	BD	29.5	594
	6–8	1.89	BD	30.3	610
	8–10	2.00	BD	29.1	591
	10–15	1.89	BD	31.5	619
	15–20	1.89	BD	31.1	669

BD: below detection

Table 5.10: Organic carbon content (wt%) in cores sampled in the fracture zone complex in the CIB.

Depth (cm)	BC 36	BC 37	BC 38
0–2	0.092	0.092	0.080
2–4	0.000	0.092	0.115
4–6	0.000	0.115	0.115
6–8	0.000	0.092	0.138
8–10	0.000	0.069	0.115
10–12	0.000	0.046	0.046
12–14	0.000	0.069	0.046
14–16	0.000	0.000	0.253
16–18	0.000	0.092	0.069
18–20	0.000	0.000	

Table 5.11: Comparison of fluxes at the water–sediment interface (0–2cm) in hydrothermally influenced areas and non-hydrothermally influenced areas in the in the CIB.

Nutrient diffusive flux (mmol/m^2/yr)						
	Siliceous ooze	Pelagic clay	Seamount top	Valley	flank	flank
Station No	AAS 61BC 01R	AAS 61BC 15	ABP 04BC 37	ABP 04BC 38	ABP 04BC 36	AAS 61BC 08
Phosphate	1.09	0.54	0.47	0.65	0.39	0.04
Silicate	–354	–238	–148	–564	–199	–67

Table 5.12: Comparison of phosphate and silicate fluxes of the CIB with the Atlantic and Pacific Ocean and the Ross Sea (flux: mmol/m^2/yr)

+ve flux: eflux: sediments to bottom waters
-ve flux: influx: bottom waters to sediments

Diffusive Flux (mmol/m^2/yr)		Depth (m)	Specific area	Phosphate range	Silicate range	Reference
Atlantic	NE				-33 -113 (insitu)	Ragueneau et al., 2001
					-37 -120 (porewater)	
	ES	1000-3000	Off Nambia	0>-4	>-400	Zabel et al., 1998
	East Equatorial			-0.07 - 0.2		Froelich et al., 1979
	East Tropical			1.6 -5.51	-40 -160	Jahnke et al., 1989
	South and Central	>1000		2 -11	0 - 650	Hensen et al., 1998
Outer Ross Sea					-367	Table 5 in Ragueneau et al., 2001
Pacific	WN		Coast of Japan		-77 - 389	Shibamoto and Harada, 2010
	CEN	4500–5700	0–2		-153 - 343	Berelson et al., 1990
			Siliceous ooze		-8 -68	Setlock, 1979, thesis
			Calcareous ooze		-49 -102	
	C		0–4cm		-150±18 - 270±22	Jahnke et al., 1982
			0–10cm		-62.5±7.3 - 241±14.6	
Indian		>4000	Somali Margin		-280 (porewater)	Koning et al., 1997
					-260 (incubation)	
	CIB	>5000	0–2	-0.88 1.65 0.04 1.65	-12 to -597	Baseline and AAS 61 AAS 61

Chapter 6

Assessing the contributory sources to CIB sediments

6.1. Introduction

Significant work has been carried out so far on the contributory sources of the deep sea sediments of CIB (Kolla and Biscaye, 1973; Rao and Nath, 1988; Nath et al., 1989; 1992; Ben Othman et al., 1989; Mudholkar et al., 1993; Banakar et al., 1998; Pattan et al., 2005; Fagel et al., 1994; 1997). The uplift and erosion of Himalayas has caused an enormous volume of sediment to reach the Bengal fan and subsequently the CIB (mainly to the northern part) (Nath et al., 1989; France-Lanord et al., 1993; Derry and France-Lanord 1996, 1997; Debrabant et al., 1993; Fagel et al., 1994) via the Ganges and the Brahmaputra river system, the southern part however has siliceous planktonic skeletons associated with equatorial divergence at 10°S (Pattan et al., 1992; Caulet 1992; Banakar et al., 1998) and pelagic clays (see Nath et.al., 2013). The transportation of the detrital sediments from the Indian subcontinent to the CIB has been influenced by turbiditic currents for which the Ninety East Ridge acts as a barrier (Kolla and Biscaye, 1973) while Kolla and Biscaye (1973) showed a tongue of kaolinite-rich sediment extending westwards from the Northwest Cape (Australia) into the Indian Ocean, which has been suggested to be blown into the eastern Indian Ocean as a result of the prevailing easterly winds which increase the overall kaolinite content of the pelagic sediments (McTainsh 1989; Gingele et al., 2001; Nath et al., 2013).

Based on isotopic studies along with major and trace elements of smectite-rich, clay size (<2 μm) samples, bulk sediments and leachate residues carried out on CIB sediments, Fagel et al. (1997) identified three major components that contribute to the pelagic clays of CIB. The first component was characterized by a homogeneous geochemical signature and a non-radiogenic Nd isotopic composition which traced a detrital Himalayan-derived origin. The two other components displayed a seawater-derived isotopic composition with global Sr and regional Indian Ocean Nd signatures. Neodymium isotopic compositions of Quaternary marine sediments from the Indian Ocean (Dia et al., 1992) sampled from different physiographic provinces (abyssal plain, ridge, submarine fan, fracture zone and aseismic ridge environments) revealed that large areas in the Indian Ocean were isotopically homogeneous by the oceanic circulation, although the results also enforce the idea that in marine sediments the

continent-derived material exerts an important control on the Nd budget. The Nd values of the CIB sediments were nearly constant both in the eastern and western parts of the Indian Ocean implying mixing between two major inputs: material coming from the erosion of the Indian shield and the Indonesian arc (Dia et al., 1992). The western Indian Ocean values were more variable perhaps due to the proximity of old continental terrains (i.e. southern Africa) and the influence of Atlantic waters. Dia et al. (1992) attributed the Nd isotopic variations in the sediments principally due to the pathways of water circulation, and possibly winds, over the Indian Ocean.

Biogenic component is also abundant in the CIB sediments. Pattan et al. (1992) reported a gradual increase in biogenic silica (BSi) from north (equator) to south of the basin. High radiolarian abundance and BSi content in this area was suggested to reflect the surface primary productivity and better preservation of radiolarian tests. Lower BSi in the southern part of the basin was attributed to change in sediment type from siliceous ooze in the north to pelagic clays in the south which is probably related to the distance from the equatorial productivity belt.

Volcanogenic sources have been significant contributors to Indian Ocean sediments throughout the last 150 million years (e.g., Kidd et al., 1992). These volcanogenic components were derived from mid-ocean-ridge volcanism, hotspot volcanism e.g. from the Reunion and Kerguelen hotspots, subduction related volcanism along the Indonesian Arc and landmass volcanism. At mid-ocean-ridge systems, volcaniclastic sediments are only locally distributed and are recorded, within cores that penetrated basement, as volcaniclastic-rich basal sequences (Price et al., 1986). Tephra generated along the Indonesian Arc has been widely distributed across the northern Indian Ocean (Pattan et al., 1999). Landmass volcanism has contributed volcanic components to the Indian Ocean basins since the early Cretaceous, particularly related to rifting events associated with continental break-up. The Reunion and Kerguelen hotspots have been major contributors of tephra to the Indian Ocean throughout their evolution since the early Cretaceous (Upton and Wadsworth., 1966; Wallace 2002). The distribution of volcanogenic sediment in the Indian Ocean was studied by Vallier and Kidd (1977) using DSDP cores, which lead them to hypothesise that the timing and distribution of the volcanogenic accumulations were controlled by changes in sea-floor spreading rates. However, Sykes and Kidd (1994)

reviewed the tectonic development of the Indian Ocean and concluded that the timing of accumulations of volcanic components in the Indian Ocean can be related to rifting of continents, formation of new crust at ridge crests and at hotspots, and to landmass volcanism, linked to subduction along the Indonesian Arc. Their work has shown that hotspots such as Reunion and Kerguelen, have been the dominant source of volcanogenic sediments to the Indian Ocean basins since the Albian (110 Ma), being far more important than the mid-ocean ridges and variations in their spreading rates which was previously thought to exert a major control. Volcanogenic sedimentation and evidence of hydrothermal signatures in the CIB were studied in some detail by Iyer and Sudhakar (1993), Martin–Barajas et al. (1993), Mukhopadhyay et al. (1995), Iyer et al. (1997, 2007), Nath and Rao (1998), Pattan et al. (1999), see Nath (2001) for review, Mascarenhas-Pereira et al. (2006), Nath et al. (2008). Metalliferous sediments along with hydrothermal alteration products have been reported in only few papers by Iyer et al. (2007); Nath et al. (2008) and Mascarenhas-Pereira and Nath (2010), in the CIB. Morphological features and the associated volcanics in the CIB suggest that this is a vulnerable area for tectonic and magmatic activities (Iyer 2005).

While the sources for CIB sediments are well constrained as shown above, relative contribution from each of the contributing sources is not known. An attempt is made to quantitatively assess the contribution of these sources to CIB sediments. For this, a new approach was adopted by performing the mixing calculations of the rare-earth element (REE) geochemical data to quantity the relative contribution of competing sources using four end members such as biogenic, terrigenous, MORB and metalliferous components. Using the computed data, regional distributional maps of these components are presented.

One of the objectives of the Environmental Impact assessment of manganese nodule mining Project (PMN-EIA) was to map the natural dispersal patterns of sediments in order to predict the probable plume generation and dispersal pattern in case of future commercial nodule mining in the CIB. To this end, diagnostic elemental associations are used here to decipher the natural dispersal pattern of sediments in the basin and also to identify the source of sediments in the area. Different geochemical tracers such as REE, trace and major elements were used. The

influence of local geology and hydrography on the dispersal and distribution of lithogenic material was also studied.

The southern area of the study is reported to be hydrothermally active with signatures of degassing as recent as ~100 yrs (Nath et al., 2008). Geochemical studies of the hydrothermally altered pelagic clay sediments reveal enrichment of trace element and REE concentrations which were upto 10 times than the cores not influenced by hydrothermal activity (Mascarenhas-Pereira and Nath, 2010). While Nath et al. (1992) and Banakar and Jauhari (1993) have reported the REE in bulk sediments from CIB, little research has been carried out on the geochemistry and distribution of major, trace and REEs of different size fractions in marine sediments from the CIB except for the work done by Tlig and Steinberg (1982) with no literature on the role of sediment size fractions in acquiring the hydrothermal signature. Elemental geochemistry of different size fractionated surface sediment samples in hydrothermally altered sediments of CIB was studied to understand the uptake of elements in the various fractions during hydrothermal alteration. These data were compared with the geochemistry of different size fractions of sediments not influenced by hydrothermalism from Arabian Sea, Equatorial Indian Ocean, Bay of Bengal, siliceous domain of the Indian Ocean. Various geochemical discriminants are used to distinguish depositional and tectonic setting of ancient sedimentary formations. Size fraction geochemistry data were used to test some of these discriminants.

6.2. Results and Discussion

6.3.1. Elemental distribution in the surface sediments from CIB

The elemental data obtained by AAS, ICP–OES and ICP–MS (Tables 6.1 to 6.4 and 6.6) were entered in excel spread sheet for calculations and plotting. Accuracy and precision of the analyses are presented elsewhere (Tables 2.2, 2.3, 2.4). The elemental variations of all surface samples (Figs. 6.1 to 6.4) were plotted using sigma plot. Topographic influence on the elemental variation was studied by superimposing elemental variation data on a bathymetric map (Figs. 6.1 to 6.4). Diagnostic elements

for different geochemical processes were studied to interpret the spatial resolution of these parameters within the basin.

Elemental data of marine sediments can be used as indicators for both spatial and temporal trends in dispersal patterns in the marine environment. Despite the generally recognized usefulness of sediment chemistry data, its assessment is not always simple, because of the uncertainties associated with sampling, analyses, grain–size effects, provenance differences, types of diluents (carbonate etc.). For this study, though a number of major and trace elements have been analyzed in all the 26 surficial sediments (Tables 6.1, 6.2 and 6.3), data for selected elements are presented here which are useful in process description. Trace element distributions in surface sediments across the basin are shown and described in section 6.3.2. Studying elemental composition of surface sediments has a potential to be used as diagnostic tool to understand the fate of the terrestrial materials transported into the basins, provenance, diagenesis, assessment of crustal sources, depositional environment as well as the factors controlling the distribution and geochemistry of sediments (Keil et al., 1994; Hedges and Keil, 1995; Nath et al., 2001 and references therein; Bianchi et al., 2002;).

6.3.2. Sources and natural dispersal patterns of sediments in the CIB

Terrigenous contribution to the sediments:

In order to trace the dispersal of terrigenous material in the study area regional distributional plots of elements such as Al, Zr, Nb, Rb and Ti contents which are refractory in nature were plotted (Figs. 6.1a and b). Al, Ti and Zr, in marine sediments are primarily derived from aluminosilicate minerals from terrigenous sources, however they could also be derived from alteration of oceanic volcanic rocks, hydrothermal exalations and authigenic process (Kolla et al., 1976; Cronan, 1980). However, these elements have been widely used to trace the terrigenous input to marine sediments. Aluminium or titanium normalizations are generally used to correct for the terrestrial influences in marine sediments (Nath et al., 1989, 1992; Murray et al., 1992, 1993; Murray and Leinen, 1993). Zirconium (Zr) is another lithogenic element resistant to weathering and alteration processes (e.g., Taylor and McLennan, 1985; Feng and Kerrich, 1990). The sources of zirconium are the zirconium silicate

mineral, zircon and beddeleyite. Zircon is present in rhyolite and trachyte dikes present in peninsular India. Zircons derived from Himalayan Rivers were also reported in turbiditic sediments in the northern part of basin (Nath et al., 2005).

The elemental distributional plots show a similar trend in the study area with higher content in the northern and southern part of the basin (Fig. 6.1a and b). The similarity in the distributional patterns of these elements indicates a common source of derivation (Pattan et al., 2005). Al content in the study area ranges from 4.18 to 7.31%, (avg 5.43%); Zr content ranges from 99 to 409 ppm with an average of 142 ppm, while Ti content ranges from 0.19 to 0.43% (avg 0.23%). Rubidium content in the sediments showed an average value of 60 ppm (Tables 6.1 and 6.3). Zr, Nb and Ti contents show high concentration in the southern part of the study area (BC–8) (Table 6.3; Fig. 6.1a) where volcanic and hydrothermal alteration of sediments have been reported (Iyer et al., 2007; Nath et al., 2008) compared to the other sediments in the area (Table 6.3, Fig. 6.1a and b). The lowest concentration of Nb (4.59 ppm) and Ti (0.21%) (Table 6.3) are found in central part of the study area, which is underlain by siliceous ooze. The high content of these detrital elements in the north of the basin (north of 13°S) supports the major detrital input to northern part of the CIB. Sr and Nd isotopic studies of sediments from ODP Leg 116 near the equator (1°S) in CIB suggest that the area receives sediments mostly from two sources, a major component is derived from the meta-sedimentary rocks of High Himalayan Crystalline (HHC) and a small portion from Lesser Himalayas (LH) and Tibetan Sedimentary Series (TSS) (Bouquillon et al., 1990; Derry and France-Lanord 1996, 1997). The source of sediment to the CIB however has remained unchanged since 17 Ma despite changes in sedimentation rate, tectonics and climate (France-Lanord et al., 1993). Banakar et al. (1998) reported terrigenous

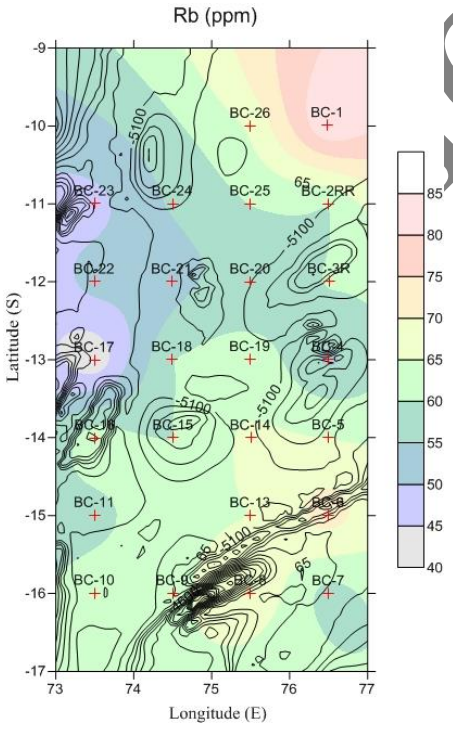

Fig. 6.1a: Regional distribution pattern of Rb content (ppm) in the CIB sediments.

influence to the CIB sediments north of 3°S indicated by the dominance of detrital clays. Before these reports, Kolla and Biscaye (1973) have argued that the sediments derived from the Himalaya could reach south of Bengal Fan by the turbidity currents (Kolla and Biscaye, 1973). Further, robust mineralogical and geochemical data and shale normalised REE pattern data indicated the extent of terrigenous sedimentation in CIB (Nath et al., 1989; 1992, 2008; Fagel et al., 1993). Occurrence of detrital silicate material derived from HHC in a ferromanganese crust from CIB (Banakar et al., 2003) is also reported. Terrigenous influence upto 14°S was reported by Mudholkar et al. (1993) and Borole (1993).

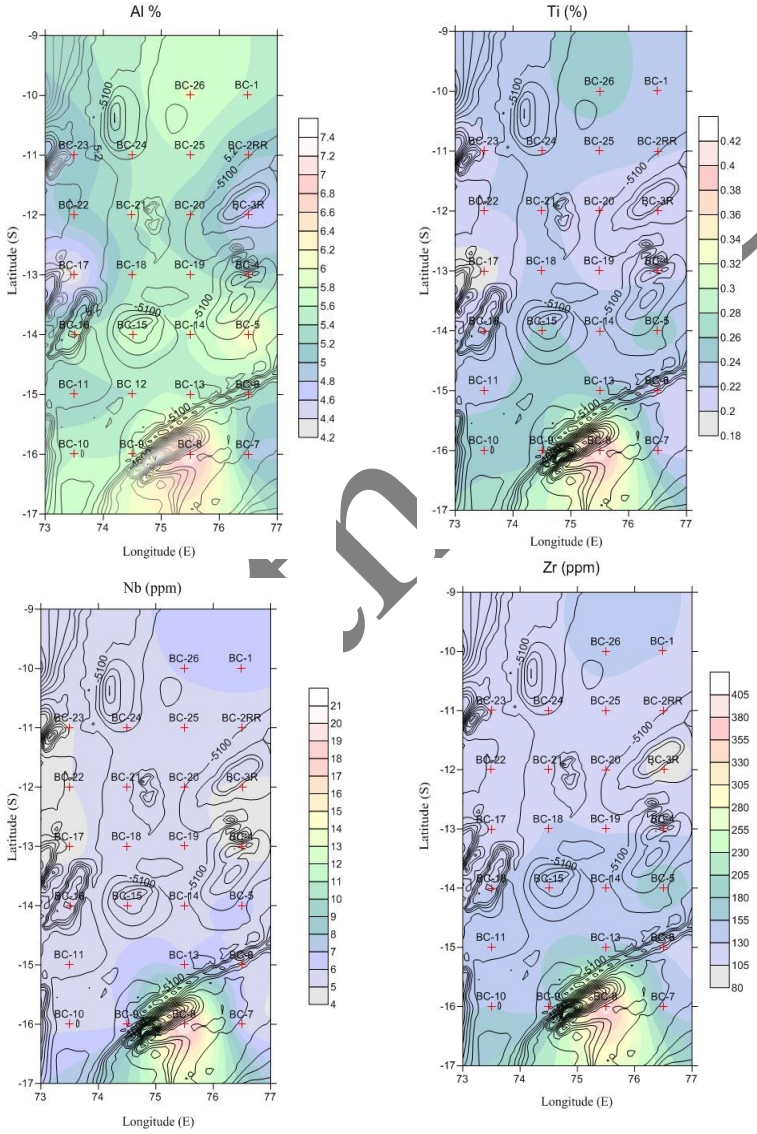

Fig. 6.1b: Regional distribution pattern of Al, Ti (%), Nb and Zr content (ppm) in the CIB sediments.

Rb gets accumulated into clay minerals (Faure, 1986) and therefore its distributional pattern in marine sediments could be used as an indicator of transportation pathways of fine–grained fraction of sediments along the bottom. Mechanical sorting of minerals that have tendency to get concentrated in finer fraction (eg. Biotite) during transport greatly increases Rb/Sr ratio of clays relative to source rock but Rb may be leached from biotite during weathering,

sediment reworking or exchange with saline solutions (Odin and Rex, 1982; Clauer, 1982). Rb content (85 ppm) in the sediments is found to be highest in the northern area (BC–1) and decreases towards the west of the basin which reflects the terrigenous input to the basin, while relatively low concentration found in the southern part of the area (BC–8) may reflect local weathering of basinal rocks (Nath et al., 2008).

Biogenic sedimentation.

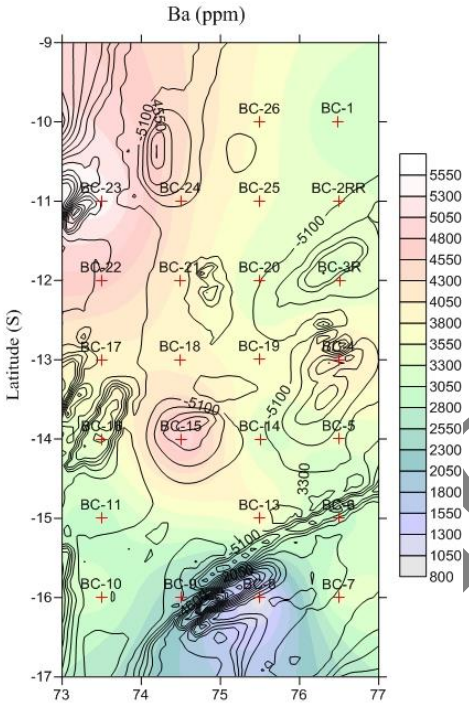

Fig. 6.2: Regional distribution pattern of Ba content (ppm) in the CIB sediments.

In deep-sea sediments below the carbonate compensation depth (CCD), indicators of biogenic sedimentation are organic carbon, opal, Ba, P and sometimes Cu and Zn contents. Strontium could also be a good indicator as it would have replaced Ca in $CaCO_3$ before the carbonate dissolution. BSi content in the sediments of the CIB varied from 1.8 to 35% with the maximum between 11° and 13°S (Pattan et al., 1992). Here, mainly Ba and Sr data are presented. The Ba concentration in the CIB varied from 859 (BC 8) to 5493 ppm (BC 23) with an average of 3506 ppm (Table 6.3; Fig 6.2). The highest concentrations were found in the northwestern and central part of the study area (Fig. 6.2). The source of Ba in the sediments is mainly barite. Barite occurs in different depositional environments, deposited through processes including biogenic, hydrothermal, and evaporation, among others. Barite forms from hydrothermal processes where Ba–rich hydrothermal fluids vent onto the seafloor (Lydon et al., 1985; Poole, 1988). Enrichment of barite in seafloor sediment by biogenic processes may occur in some areas where upwelling, nutrient–rich currents result in high biological productivity in surface waters. The Ba enrichment can be a result of sequestration of Ba from solution and by selected sediment components such as $CaCO_3$. The highest Ba contents are found in sediments

rich in biogenic opal as diatom frustules can contain up to 30,000 ppm of Ba (Collier and Edmond 1984). This Ba is removed from the water column by adsorption or by the formation of $BaSO_4$ crystals in reducing micro–environments of sinking organic particles (Bishop et al., 1977). High Ba content in CIB sediments was attributed to dissolution residue (Nath et al., 1989) or to the incorporation along with Mn-oxides (Banakar et al., 1998). Tiny barite crystals in CIB sediments were found by Fagel et al. (1997). Barite is known to be the principal carrier of Ba in deep-sea sediments (Goldberg and Arrbenius, 1958; Bishop, 1988; Dymond et al., 1992; Pattan et al., 1993). As barite is particularly concentrated in sediments formed below the equatorial zones of high biological productivity (Goldberg and Arrhenius, 1958; Dehairs et al., 1980; Sawlan and Murray, 1983; Schmitz, 1987), its occurrence is attributed to chemical precipitation in productive areas. Jauhari and Pattan (2001) reported high Ba content in the siliceous sediments (avg 3056 ppm), followed by red clays (avg 2483 ppm) and least in calcareous oozes (avg 1500 ppm). Support for biological role in Ba enrichment in CIB sediments also comes from the geochemical data. In the area influenced by hydrothermalism (Mascarenhas-Pereira et al., 2010), Ba concentration (859 ppm) are very less compared to the rest of the study area (Fig. 6.2).

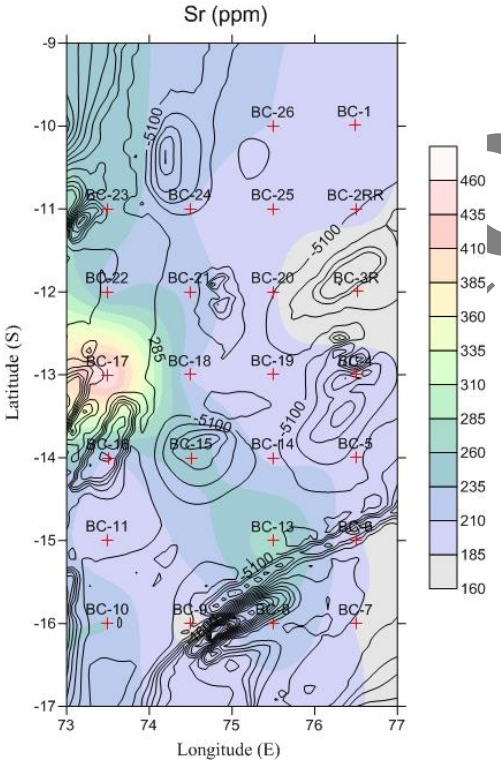

Fig. 6.3: Regional distribution pattern of Sr content (ppm) in the CIB sediments.

Sr content in the CIB sediments varies from 165 to 483 ppm (Table 6.3). Highest concentration of Sr is found in the central part of the study area (Fig. 6.3) with concentration upto 483 ppm. Strontium commonly occurs in nature and is found chiefly in the form of the sulfate mineral celestite ($SrSO_4$) and the carbonate strontianite ($SrCO_3$). Of the two, celestite occurs much more frequently in sedimentary deposits (Ober 2008). Sr in marine sediments is mainly present in

calcareous tests of organism with foraminifera and cocoliths containing upto 1750 ppm Sr, part of which may be diagenitically added (Turekian, 1964). Acantharid skeletons made up of celesite ($SrSO_4$) are also important contributors of Sr to marine sediments (Turekian, 1977). Distributional maps of Ba and Sr are plotted (Fig. 6.2 and 6.3) show similar trend with the northwestern part of the study area having enrichment of these elements and depletion in the southern areas and these maps likely reflect the trend of biogenic sedimentation in the area.

Hydrogenous and diagenetic contribution:

The metals like Co, Ni, Cu, Zn and Fe have affinity for biota and have nutrient like distribution in the oceans. Some metals like Fe and Mn are enriched in marine sediments due to their direct precipitation from seawater as hydroxides (Landing and Bruland, 1987) and elements like Cu, Ni, Co and Zn are scavenged by their incorporation and/or adsorption to authigenic mineral phases (Altschuler, 1980). Lithogenous fractions introduced by the rivers are the major source of Fe supply to the oceans, with additional contribution from aeolian dust (Duce and Tindale 1991). Iron in sediments is normally fractionated between pelagic clay, hydrogenous metals, and metalliferous components (Nath et al., 1989). Iron–rich basal deposits are found in oxidizing environments on the crests and flanks of actively spreading ocean ridges.

In the present study area on CIB sediments, Mn content varies from 0.62 to 2.03% (avg: 0.93%) (Table 6.1). Northern part of the basin has the least Mn content (Fig. 6.4) while Mn content was highest in the southeast and southern areas of the basin (BC–5: 1.8% and BC–8: 1.9%; Table 6.1). Fe and Mn can also be associated with hydrothermal sediments. Fe and Mn contents reaching to about 25% and 5% respectively were reported in metalliferous sediments at Rodriguez Triple Junction (Lisitzyn and Gurvich 1987). High Fe content (8.16%) along with Mn (2.03%) (Table 6.1) in the southern area may be attributed to hydrothermal influence in the sediments (Mascarenhas-Pereira and Nath., 2010). Manganese is a redox sensitive element which, in an oxic environment, precipitates as Mn^{4+}, whereas under reducing environment Mn dissolves into pore water as Mn^{2+} and diffuses upwards to precipitate as Mn^{4+} once an oxic environment is encountered (Lynn and Bonatti, 1965). Mn enrichment is also reported in many hydrothermal systems such as in the Manus

basin, where Fe-Si-Mn oxyhdroxides precipitate from hydrothermal fluids (Zeng et al., 2012) and Lau basin Fe-Mn-Si oxides and nontronite were reported (Sun et al., 2012). The Mn-oxide phase in the CIB sediments might also be in the form of oxide coatings on biogenic components or manganese micronodules which are abundant in the coarse fraction in these sediments. Higher abundance of micronodules occurs in the pelagic red clays compared to the siliceous ooze (Suresh Raj, personal communication). This pattern is similar to the surface distributional plot of Mn content in CIB (Fig. 6.4) sediments implying a control of micronodules on the Mn content of the sediments.

Ni content shows large variability in the basin with values ranging from 186 to 1005 ppm (avg 326 ppm), while Cu content ranges from 277 to 801 ppm (avg 385 ppm). Zn (range: 65 to 289 ppm; avg 130 ppm) and Co content (range: 47 to 162 ppm; avg 72 ppm) (Table 6.3) however show less variability in the area. The distributional maps of Cu, Ni, Cu and Zn (Fig. 6.4) show a similar trend in the study area with gradual increase from north to south of the basin. Mn, Ni, Cu, Zn and Co have their excess or noncrustal supply of around 90% of their bulk composition (Pattan and Jauhari., 2001) suggesting that supply of elemental excess to the seafloor is independent of biogenic or terrigenous input into the basin. The degree of variation of the incorporation of Ni, Cu, and Co with Mn in the Mn oxide phases is probably due to the combined effects of the hydrogenesis and the early diagenesis. It is also reported that due to a) high negative surface charge b) high cation adsorption capacity and c) large specific surface area, manganese oxides are important scavengers of trace metals in the marine environment. Thus the trace metal concentration in the surface sediments is at least partially dependent on the abundances of manganese oxides (Banerjee, 1998). Pattan (1993) reported high Mn concentration in red clay (1.9%), relatively low concentration in the siliceous ooze (0.11–0.95%) and lowest in calcareous ooze (0.26%) and showed a strong positive correlation (r=0.8) with Cu, Ni and Zn. This was attributed due to the presence of Fe–Mn oxide phase probably in the form of Mn–micronodules.

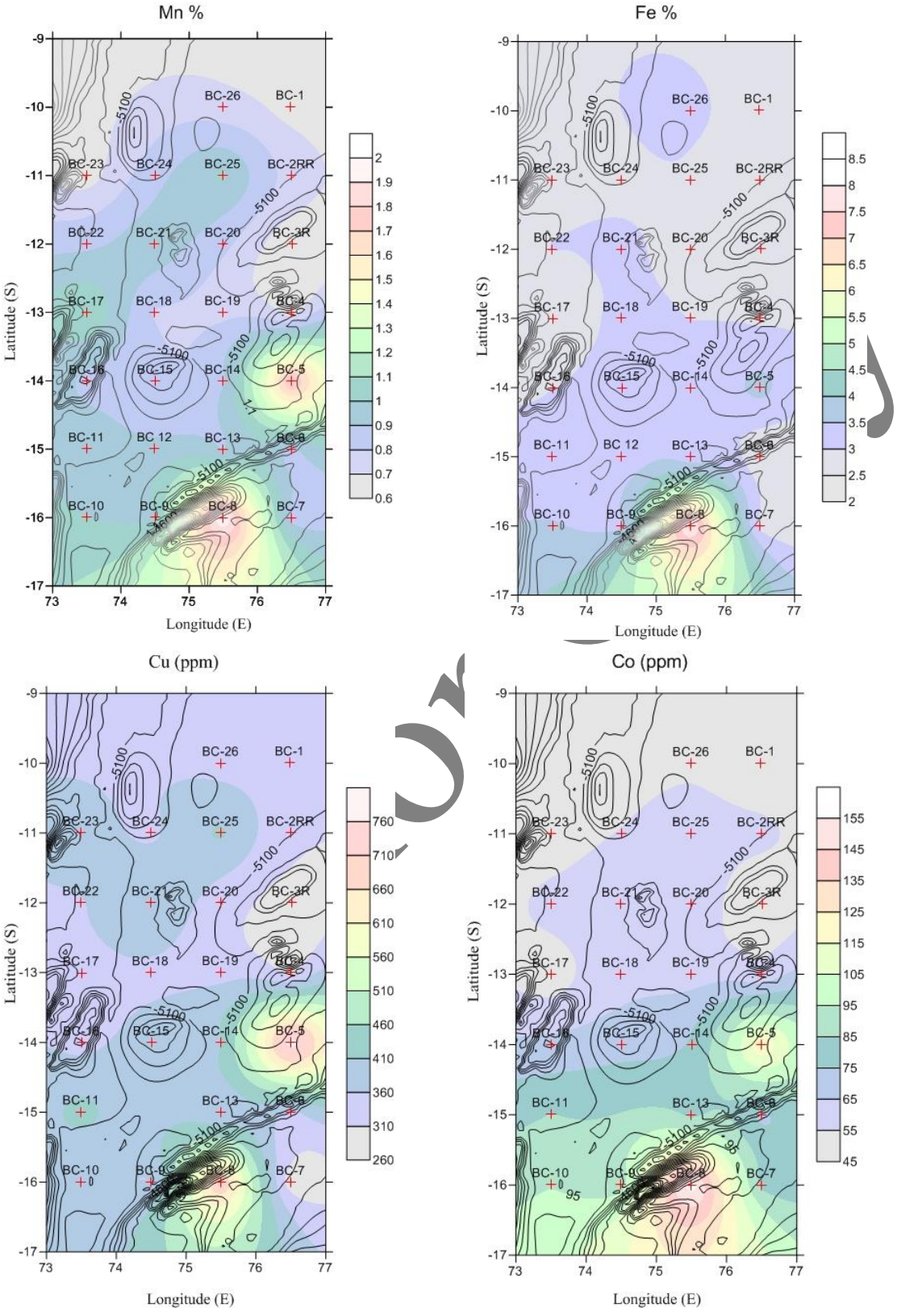
Mn %
Fe %
Cu (ppm)
Co (ppm)
Latitude (S)
Longitude (E)
BC-1
BC-2RR
BC-3R
BC-4
BC-5
BC-6
BC-7
BC-8
BC-9
BC-10
BC-11
BC 12
BC-13
BC-14
BC-15
BC-16
BC-17
BC-18
BC-19
BC-20
BC-21
BC-22
BC-23
BC-24
BC-25
BC-26
-5100

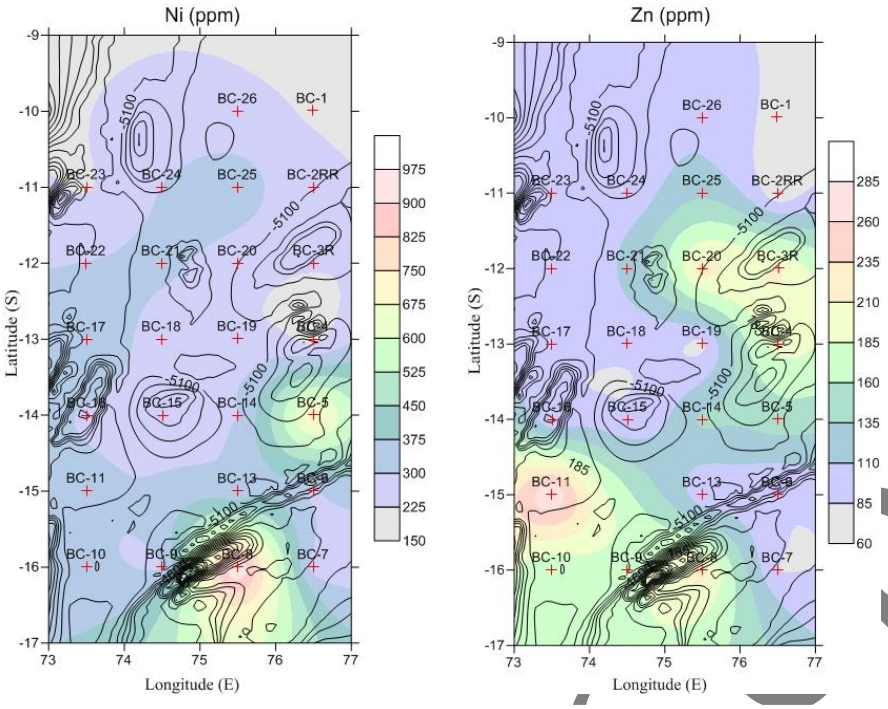

Fig. 6.4: Regional distribution pattern of Mn, Fe (%), Cu, Co, Ni and Zn contents (ppm) in the CIB sediments.

Hydrothermal contribution

Many of the elemental distributional maps (Fig. 6.4) clearly reflect a change in pattern in the southern portion of the study area. For example, this area has high concentration of Fe (8.16%), Mn (1.87%), Cu (721 ppm), Ni (1005 ppm), Co (162 ppm), Zn (222 ppm) compared to the other siliceous and pelagic clay sediments in the area probably reflecting the hydrothermal component in the sediments (Mascarenhas-Pereira and Nath, 2010)

Signatures for hydrothermal component in the CIB sediments were reported based on volcanogenic-hydrothermal material such as microscopic magnetite and titanium spherules (Iyer et al., 1997) and suggested that they formed through submarine exhalations and deposition in the surrounding siliceous sediments. Later studies by Iyer et al. (2007) reported aluminum rich grains in the sediments at two locations: core AAS 61/BC 8 (16°S and 75.5°E) and S657 (14°S and 75.935°E) both sampled from a seamount complex (located at the flank and base of a seamount) lying in close proximity to a fracture zone (76.5°E; ~ 50 km from the TJT–In). They assigned an age of ~10 ka to the hydrothermal activity based on radiolarian assemblages. Signatures of degassing of hydrothermal emanations have been reported

to be much younger as recent as 100 yrs (Nath et al., 2007). Dominance of amorphous Fe–oxides/oxyhydroxides (Mascarenhas-Pereira and Nath., 2010) in the sediments along with nontronite similar to Alvin nontronites which were calculated to form at 59±5°C (Severmann et al., 2004) indicated that the sediments in the area may have been influenced by temperatures ranging between 50° and 100°C. Presence of ferruginous smectites and nontronitic clays in these sediments (Mascarenhas-Pereira and Nath., 2008) suggested a hydrothermal origin (e.g., McMurtry and Yeh, 1981). Such low temperature hydrothermally-formed ferromanganese crusts in the CIB were repoted by Iyer (1991).

6.3.3. Rare-earth element geochemistry and mixing calculations of REE data to determine the 4 end member proportions in CIB

Rare-earth elements have been determined by Nath et al. (1992) for terrigenous, siliceous oozes/clays (nodule bearing and nodule free), pelagic red clays and calcareous clays from the CIB. The REE fractionations within a single depositional environment were found to be characteristic for each sediment type, with flat shale-normalized patterns associated with terrigenous sediments, positive Ce anomalies with siliceous sediments, negative Ce and positive Eu anomalies with calcareous sediments, and LREE depleted patterns with pelagic red clays. This observation suggests a strong lithological control. REEs are robust indicators of provenance and coherent as a group and the changes they undergo during the sedimentary processes are generally subtle. REEs (including the lanthanides and Y) have analogous chemical properties and low solubility, and they are not easy to transfer and take inter–element fractionation during geological processes such as weathering, disintegration, transportation, deposition and early diagenesis related to the formation of marine sediments.

As shown in previous sections, and previous studies based on sedimentological, mineralogical, geochemical data, this work suggests that there could be four potential sources for CIB sediments. The possible contribution of sediments to the basin are in the form of, i) turbiditic sediments from the terrestrial source (Kolla et al., 1976; Nath et al., 1989, 1992b); ii) siliceous productivity,

especially in the northern part of the study area; iii) weathering of locally occurring seamount and mid oceanic ridge basalts (Nath et al., 1989, 1992a) and, finally, iv) metalliferous source (Mascarenhas–Pereira and Nath., 2010). Therefore, an attempt is made to quantify the relative contribution of sources using mixing calculations of REE data.

REE data of surface samples (BC 1 to 26) from 26 locations in the CIB were used in the mixing calculations to find the relative proportions of end members to the sediments in the basin (Fig. 6.7). Relative proportion of each end member contributing to the sediments is assessed using mixing equation with mass balance equation (Albarède, 1995; Mascarenhas–Pereira and Nath 2010) shown below.

$$\int_{Siliceous} + \int_{terrigenous} + \int_{MORB} + \int_{metalliferous} = 1$$

$$C^{i}_{mix} = (\int_{Siliceous} \times C^{i}_{Siliceous}) + (\int_{terrigenous} \times C^{i}_{terrigenous}) + (\int_{MORB} \times C^{i}_{MORB}) + (\int_{metalliferous} \times C^{i}_{metalliferous})$$

where $\int$ represents the proportion of each end–member contributing to the bulk sediments and C^{i}_{mix} is the concentration of element i in the mixture of 4 end members. The end members used are terrigenous sediments (SK 31/4) as representing the sediments from Bay of Bengal, metalliferous sediments from EPR, (Barrett, 1988; carbonate free), Indian MORB (Sun, 1979) and siliceous productivity especially in the northern part of the study area. We have used data by Akagi et al. (2011) to represent the REE content in the siliceous tests.

The surface samples were grouped based on their location and sediment type. Accordingly we have made 3 groups as siliceous type, pelagic type and transition (between siliceous and pelagic) type. Based on literature data, a range was specified for each end member. For siliceous type 20–30% siliceous component was considered, and

50–80% for terrigenous component,

5–20% for MORB/basalt weathered component and

5–20% for metalliferous component.

Pelagic red clays of CIB have lesser biogenic silica and siliceous test components (Nath et al., 1989; Pattan et al., 1992), so for this type 5-20% siliceous component was considered, as these are in the southern part of basin,

10–30% of MORB component was considered and

40–90% of metalliferous component was considered as they are close to the metalliferous sediments in the south.

And for sediments in the transition zone, the range of end member proportion was set between the siliceous and pelagic types.

Iterations were run for end members between the proportions specified for the core top data of all the 26 sediment samples. This was repeated for each core so that the resultant values obtained was the best fit end member proportion which matched the original sediment composition.

The mixing calculations have shown that the siliceous component between 5 and 30%, 10–80% terrigenous component, 5 and 30% MORB component and 0 and 70% metalliferous component could reproduce the REE values of the sediments in the basin (Fig. 6.5).

On the other hand, when iterations were run without any predetermined values (which we call UNFORCED, Fig. 6.6), the mixing calculations show that about 0 and 10% siliceous component, 5 and 90% terrigenous component, 0 and 35% MORB component and 0 and 100% metalliferous component could reproduce the REE values of the sediments in the basin.

Relative proportion of these contributing components calculated for all the cores are plotted in regional distributional maps (Figs. 6.5 and 6.6). Both the forced and unforced regional distribution maps of the 4 end member show a similar distribution trend. The siliceous ooze component is enriched in the entire northern part of the basin (upto about 14°S), but with pockets in north eastern part of the basin, while the terrigenous component is enriched in the western and central part of the basin with BC 15 exhibiting the maximum proportion (upto 80%, Figs. 6.5 and 6.6). This is consistent with previous findings. While Rao and Nath (1988) and Nath et al. (1989) have shown the terrigenous influence upto 8°S, their data having a gap between 8° and 10°S, Borole (1993) and Mudholkar et al. (1993) felt that the terrigenous matter could reach as south as 14°S. The contributions from the basaltic weathering is maximum in the north-western part of the basin with cores 23 and 24 displaying the maximum REE contribution from the MORB end member. Based on clay mineralogical and geochemical evidences (Rao and Nath, 1988; Nath et al.,

1989; 1992), contribution of weathering from basinal volcanic rocks to the sediments was interpreted. Seamount basalts in the region have shown the composition of MORB (Mukhopadhyay et al., 1995), which supports the results obtained here. The REE contributed from the metalliferous end member is maximum in the southern station (BC 8) which is upto 75% in both forced and unforced distribution maps which is consistent with the results presented in Chapter 3 and previous publications (Nath et al., 2008; Iyer et al., 2008; Mascarenhas-Pereira and Nath, 2010; Das et al., 2011).

The REE data obtained by the mixing calculations (forced and unforced) was shale normalized and plotted in Fig. 6.7. The shale normalized REE data of the surface sediments is also plotted for reference. Both the plots (forced and unforced) of shale normalized REE data are identical to the bulk sediments shale normalized plots indicating that the mixing calculations were able to extract the probable proportion of end member composition to the sediments of the CIB.

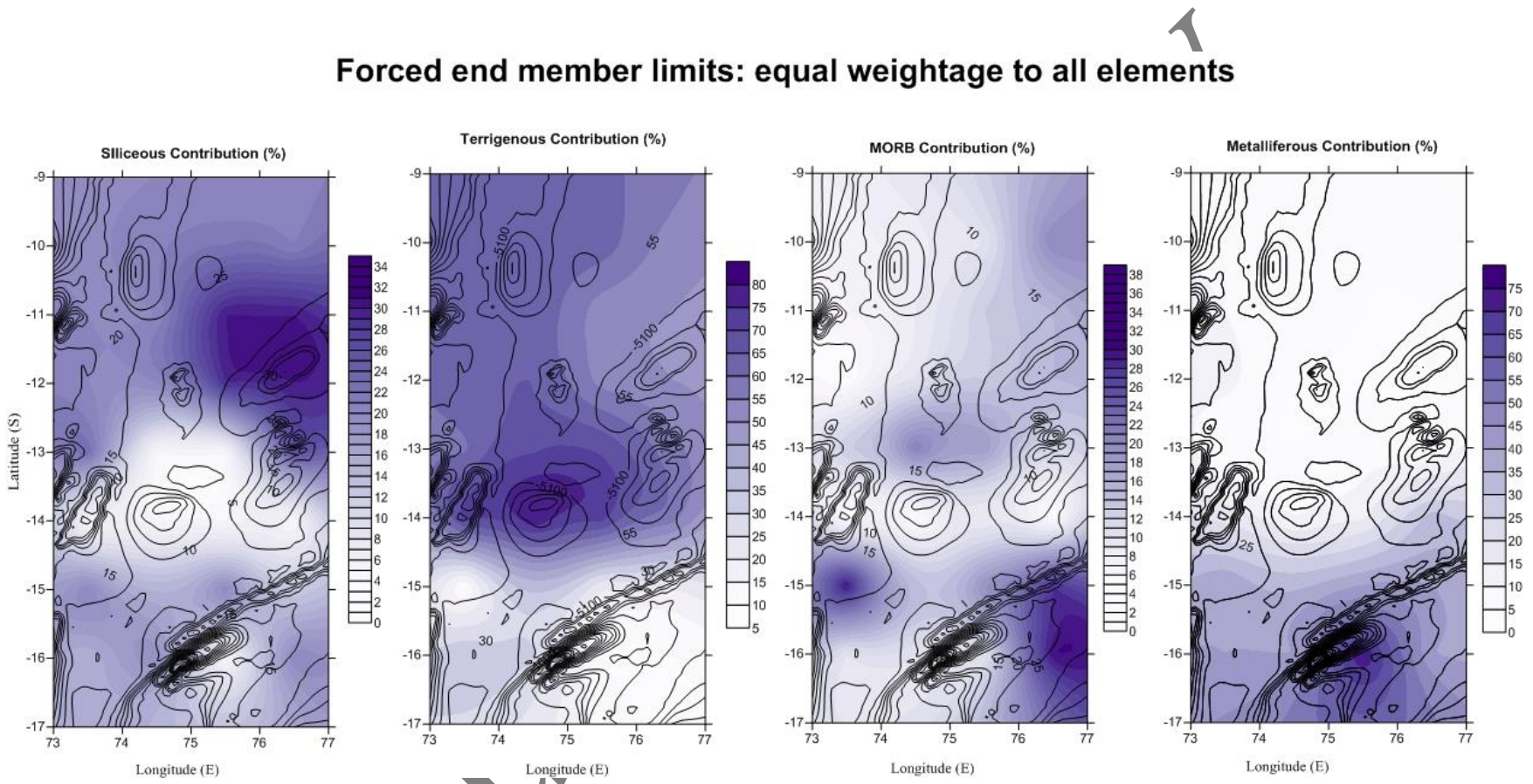

Fig. 6.5: Distribution and relative endmember (siliceous, terrigenous, MORB and metalliferous) contribution to the CIB sediments obtained using ternary mixing calculations for 26 surface samples. The range of values for each endmember was set based on past literature.

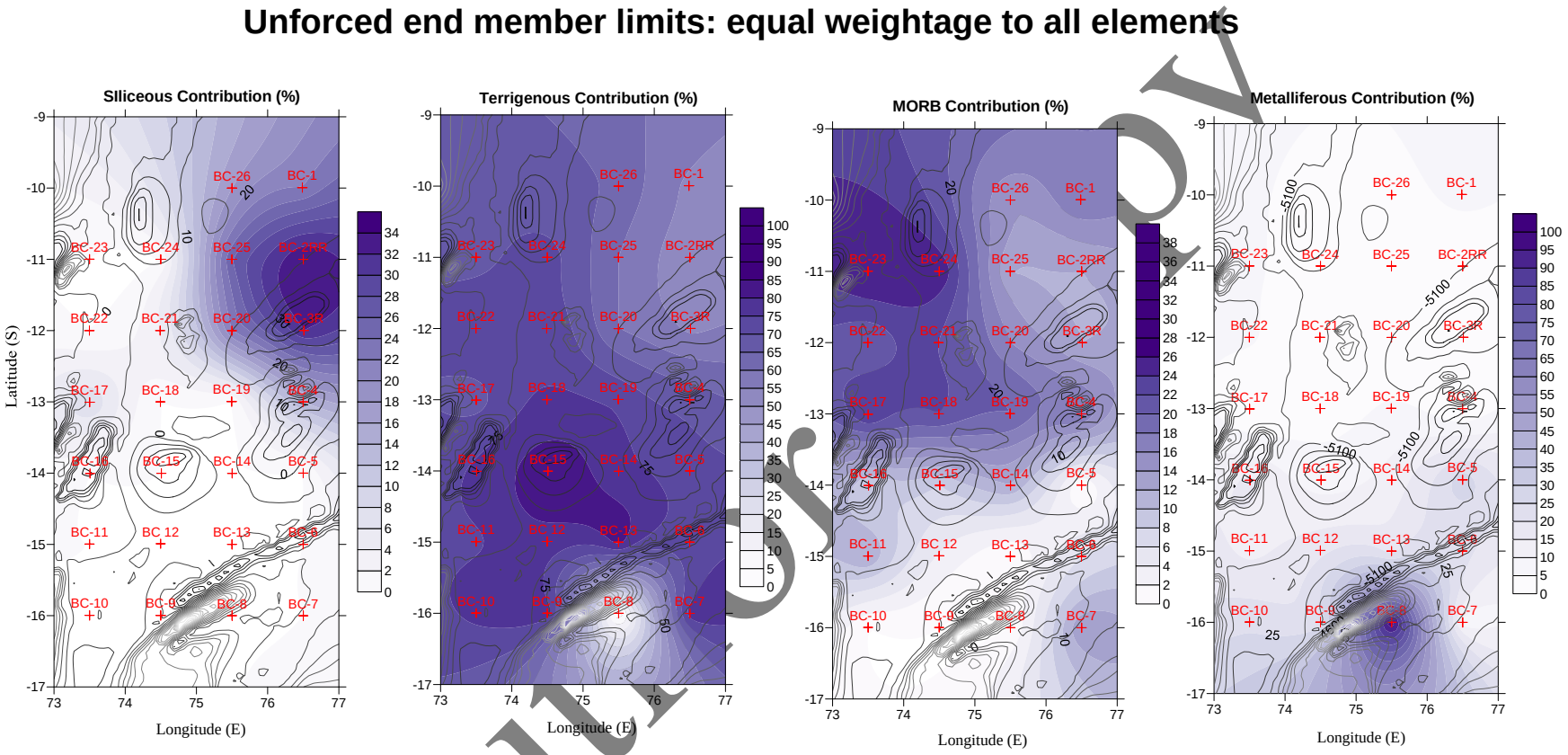

Fig. 6.6: Distribution and relative endmember (siliceous, terrigenous, MORB and metalliferous) contribution to the CIB sediments obtained using ternary mixing calculations for 26 surface samples. The relative % of each endmember was determined by repeated iteration (changing the 4 end member proportions) till the errors between the obtained and original values were negligible.

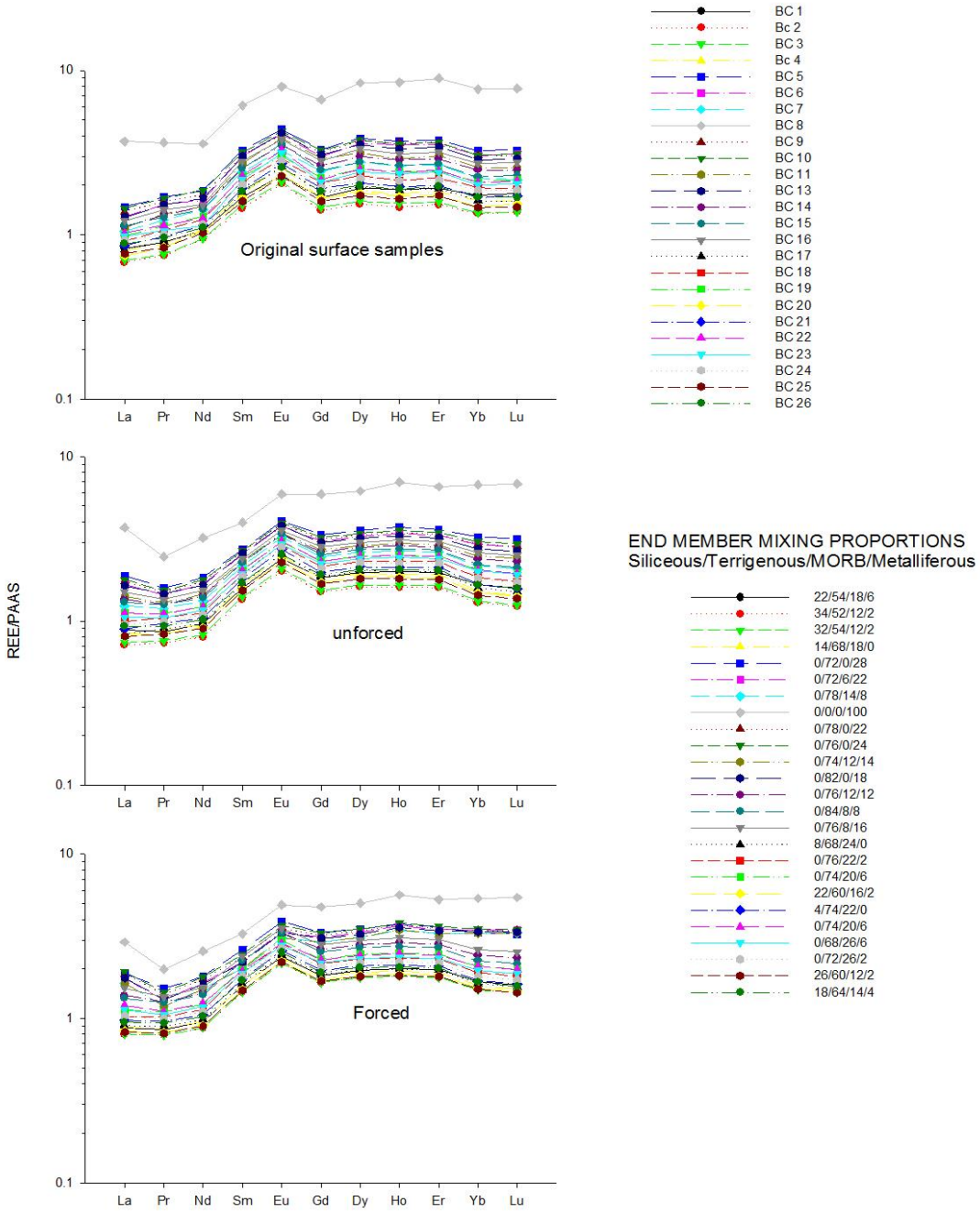

Fig. 6.7: Shale normalized REE patterns of the (a) surface sediments, (b) unforced and (c) forced proportion of the four end members. Endmembers (siliceous, terrigenous, MORB and metalliferous) used for the mixing calculation to simulate the proportion of endmembers in the surface sediments of the CIB.

6.3.4. Size fractionation influence on elemental geochemistry of metalliferous sediments.

While a large database dealing with the partitioning of REE during petrogenesis exists in literature, less is known about subsequent fractionation of these elements during alteration of igneous rocks, and further less during is known hydrothermal alteration of sediments. Some studies (e.g., Klinkhammer et al., 1994) have provided clues to the behavior of REEs during high temperature alteration of mid-oceanic basalts. From a study on REE geochemistry of vent fluids from sediment-hosted and bare-rock hydrothermal systems, they have found the fluids to have REE patterns different from seawater and MORB and suggested that the occurrence of partitioning of the REE between fluid and rock during high-temperature hydrothermal alteration of MORB, which is dominated by crystochemical exchange during dissolution and recrystallization reactions at the exposed surfaces of plagioclase phenocrysts. The LREE enrichment and positive Eu anomaly in fluids were attributed to the chemical substitution for Ca^{+2} and Sr^{+2}, respectively and predicted that the total +3REE content of vent fluid varies in a systematic way during the transition from anorthite-rich MORB plagioclase to albite-rich hydrothermal plagioclase during the hydrothermal alteration. As far as the alteration of sediments in the hydrothermal systems, ^{10}Be was found to have been stripped off from the sediments (Bourles et al., 1991; Nath et al., 2008); significant enrichment of Mg and U are observed in Escanaba Trough sediments and has been attributed to extensive seawater-metasomatism (German et al., 1995). In mass-wasted sediments from the sulphide mound at TAG, enrichment of U due to oxidation of sulfides is reported (German et al., 1993). While the scavenging of REE by hydrothermal Fe-oxide particulates is considered as a main mechanism in controlling the geochemical cycles at hydrothermal systems (e.g., German et al., 1990), REE uptake by various sediment size fractions during the hydrothermal alteration is not known. Therefore, we have analyzed the nine size fractions in a sediment core (AAS 61/BC#8), which has shown pronounced signatures of hydrothermal alteration (Chapter 3, Nath et al., 2008; Iyer et al., 2007; Mascarenhas-Pereira and Nath, 2010; Das et al., 2011), for elemental geochemistry. As a comparison, sediments from different non-hydrothermal areas

from the Central and Northern Indian Ocean (including those in Bay of Bengal and Arabian Sea) were also analyzed.

Hydrothermally influenced sediments.

REE concentrations of the bulk and size fractions of the hydrothermally altered sediments have been normalized to the Post Archaen Australian Shale (PAAS) values, which represent an average concentration for continentally derived material (Taylor and McLennan, 1985). The bulk and the size fractions of the sediments (Figs. 6.8 and 6.9) from the hydrothermally altered area deviate markedly from a flat pattern, with the REE patterns of all the samples showing light REE (LREE) depletion and heavy REE (HREE) enrichment.

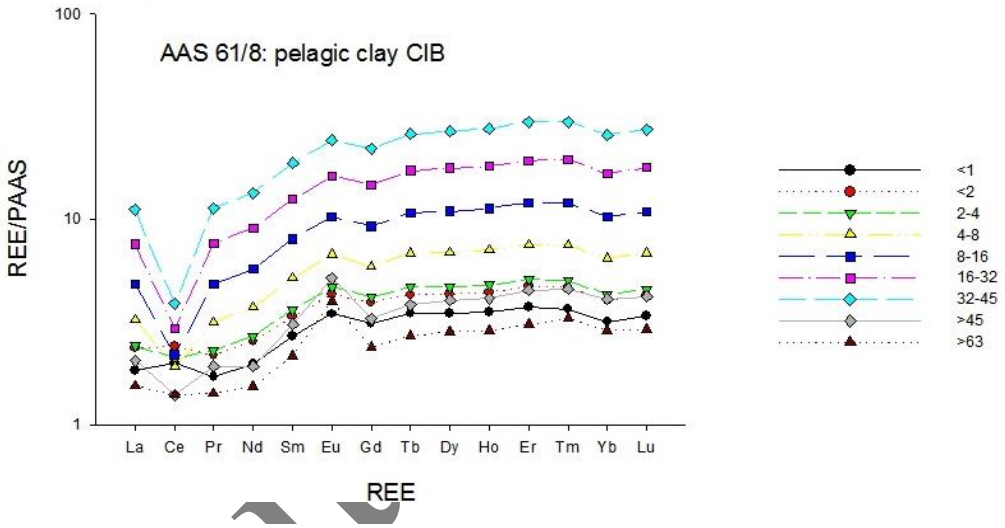

Fig. 6.8: Shale normalized patterns of the size fractions of the hydrothermally altered sediments in the Central Indian Basin.

Shale-normalised patterns of the size fractions of the hydrothermally influenced sediments show a distinct trend. There is a continuous enrichment in the REE content with increasing size, i.e. from <1 to < 45 µm size fraction (Table 6.4a). The >45 and 63 µm fractions are however depleted in REE content compared to the finer fraction. The REE content in the bulk sediments of the hydrothermally altered sediments (Table 6.4a, Fig. 6.9) is upto 10 times enriched than shale indicating scavenging of REE by hydrothermal Fe-Mn oxyhydroxides (German et al., 1990; Edmonds and German, 2004; Mascarenhas-Pereira and Nath, 2010)

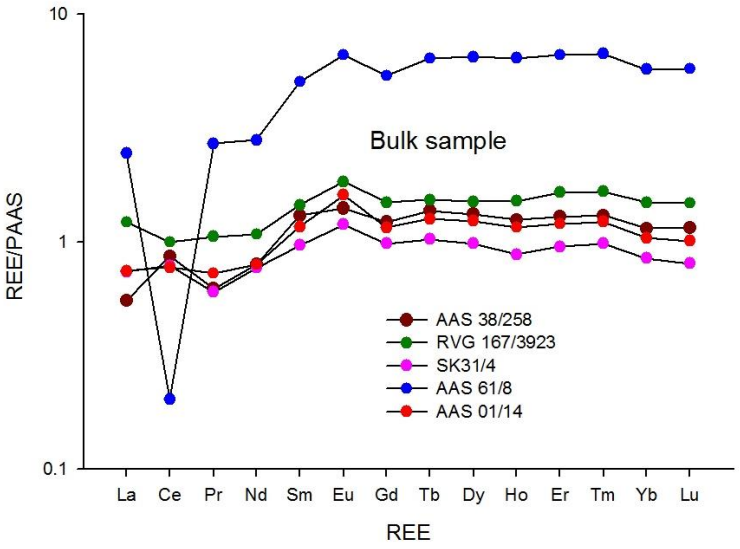

Fig. 6.9: Shale normalized patterns of the bulk samples (carbonate free basis) from the hydrothermally altered sediments in the Central Indian Basin and the Arabian Sea, Bay of Bengal, Central and Northern Indian Ocean.

Another distinct feature of the shale normalized REE patterns of the sediments is the presence of negative Ce anomalies with depletion of Ce being more pronounced in the size fractions less than 32 μm (Fig. 6.8). Ce/Ce* anomaly values range from 1.12 to 0.35 (Table 6.5). The clay size fraction (<1 μm) however shows positive Ce anomaly (Fig. 6.8) similar to the sediments overlain by nodules (Nath et al., 1992a) and typical hydrogenetic Fe–Mn oxides from the basinal parts of the Indian Ocean (Nath et al., 1992a, 1994; Nath, 1993). A negative Ce anomaly with HREE enrichment in the coarser fraction strongly suggests a seawater source for the REEs, scavenged largely by Fe–oxyhydroxides consistent with the plume chemistry literature (German et al., 1990; Sherrell et al., 1999). Nearly all the size fractions show a distinct positive Eu anomaly. Eu anomaly to sediments can be due to presence of plagioclase feldspar or eolian component. However, Eu anomaly can occur at high P-T conditions and be typical of hydrothermal fluids (e.g., Bau, 1991) and metalliferous sediments. Previous work on metalliferous sediments has revealed shale–normalized patterns similar to our sediments with negative Ce anomaly and HREE enrichment (Fig. 6.8, Marchig et al., 1982). Seawater REE patterns are also acquired by the metalliferous sediments on the ridge crest (Olivarez and Owen, 1989), which is explained by the extensive scavenging of REEs from seawater by hydrothermal Fe–Mn oxyhydroxides as they are dispersed off–axis (German et al., 1990; Sherrell et al., 1999; Barrett and Jarvis, 1988; Olivarez and Owen, 1989), either prior to sedimentation or post–deposition during early diagenesis. Sediments with size between 32 and 45 μm have the highest REE, strong negative Ce anomaly and

presumably the highest metalliferous component. Of this size could be micronodules or the fish debris. Both micronodules and fish debris in the areas influenced by hydrothermal activity can acquire the geochemical signatures prevailing in the area (Oudin and Cocherie, 1988; Dekov et al., 2003). Fe–Mn micronodules formed in the sediments around hydrothermal fields in the East Pacific Rise are diagenetic formations with their metalliferous part being a primary hydrothermal precipitate (Dekov et al., 2003). REE distribution patterns, positive Eu and Ce anomalies of TAG micronodules were attributed to high hydrothermal influence and diagenetic remobilization (Dekov et al., 2003). Fish debris from Atlantis-II metalliferous sediments were found to record hydrothermal activity (Oudin and Cocherie, 1988).

Non-hydrothermal areas

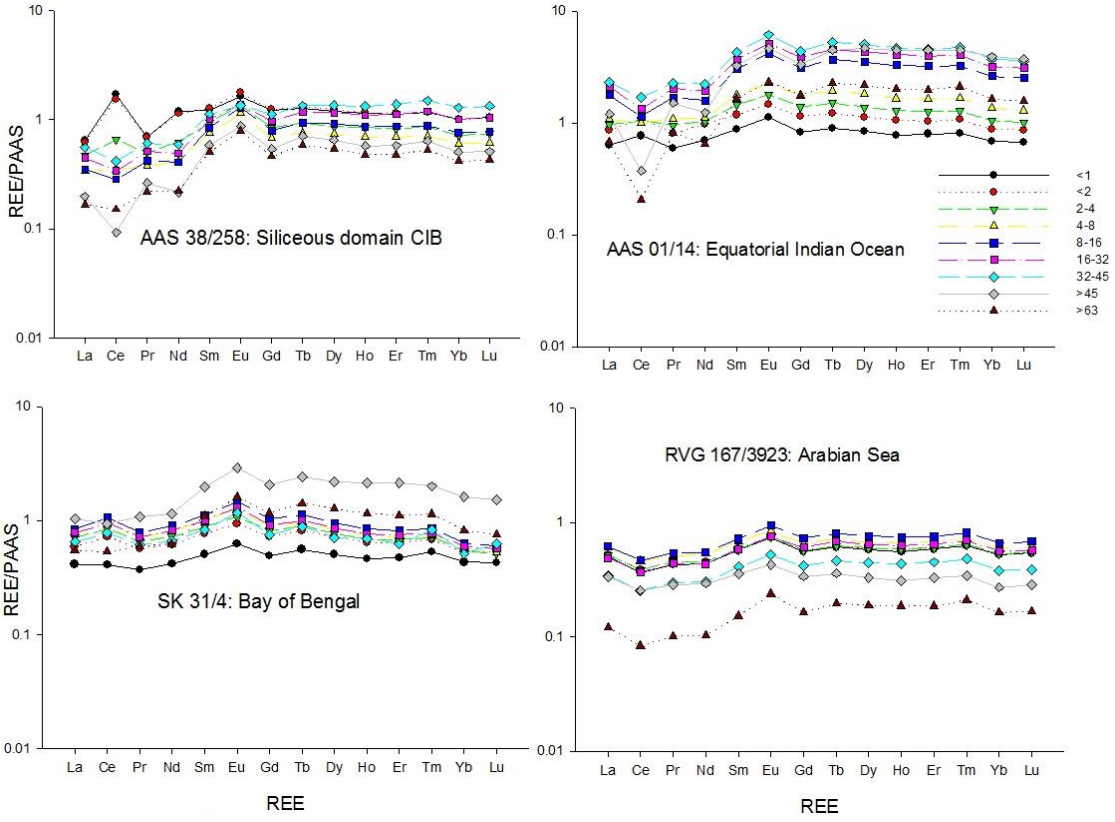

Fig. 6.10: Shale normalised REE patterns of the different size fractions in the non hydrothermal sediments (Arabian Sea, Bay of Bengal, Equatorial and Central Indian Basin.

The shale normalised REE patterns of the sediments from the Arabian Sea, Bay of Bengal and northern Indian Ocean are nearly flat (Fig. 6.10) indicating a terrigenous or a homogenous source to the sediments. The sediments of the Bay of Bengal, Arabian Sea and siliceous clay of the CIB as well as the equatorial Indian Ocean are depleted in REE compared to PAAS. The hydrothermally altered sediments are however enriched in the REE (Fig. 6.10). In general, REE show clear fractionation with grain size (Fig. 6.10). The transition between one type of REE pattern (enrichment) to the other in the Arabian Sea, Bay of Bengal and siliceous oozes sediments in the CIB is less pronounced compared to the progressive uptake of REE with increasing grain size in the hydrothermally altered sediments (Fig. 6.8). Comparing the grain size fractions, the >63 μm fraction in the Arabian Sea , equatorial Indian Ocean, siliceous and hydrothermally altered sediments of the CIB have the lowest REE abundances while in the Bay of Bengal size fractions, the finest fraction (<1 μm) has lowest REE content. A slight enrichment of REE compared to shale is seen from < 1 to about 2-4 μm (Fig. 6.10) in the sediments of Arabian Sea and Bay of Bengal. The equatorial sediments however show progressive enrichment of REE with size till <45 μm. The patterns of coarser fractions (>45 and 63 μm) and the <45 μm are nearly similar. The >63 μm fraction can be composed of quartz, siliceous radiolarians with very low REE content (McLennan, 1989).

All the size fractionated shale normalised patterns are rather flat except for the slight negative Ce anomaly and weak positive Eu anomaly (Fig. 6.9 and 6.10). The finer sediment size fractions (<1 to 32 μm) exhibit an enrichment in REE content compared to the coarser fractions (>45 and >63 μm). The sediment may be composed of terrigenous material and the flat pattern is thus inherited. In general, as the grain size decreases, the Ce anomaly increases (Table 6.5). This may be attributed to two reasons: the coarsest grain sizes contain large amounts of biogenic components which are depleted in Ce, the finest grain sizes contain larger amounts of clay and traces of oxyhydroxides adsorbed on them which can be enriched in Ce (Goldberg et al., 1963). Intermediate grain sizes tend to be neither enriched nor depleted in Ce because the biogenic and clay components balance each other. In a similar study, Tlig and Steinberg (1982) report a positive Ce anomaly in finer fractions and associated this

due to the smectite present in the clay fraction. However, this could not be true but may alternatively be due to presence of Fe-Mn oxyhydroxides.

The finer fraction, usually <1–4 µm in the siliceous ooze, equatorial Indian Ocean, and the Bay of Bengal exhibit a positive Ce anomaly (Table 6.5) which is also reported by Tlig and Steinberg (1982) for siliceous oozes in the Indian Ocean. However the positive Ce anomaly exists in sediments from calcareous, siliceous and pelagic domains of CIB. Therefore Ce enrichment seems to be independent of both location and lithology.

Positive Eu anomaly exists in almost all samples and size fractions. It may be due to feldspars which concentrate Eu during magmatic processes by the reduction of Eu^{+3} to Eu^{+2} (Philpotte 1970).

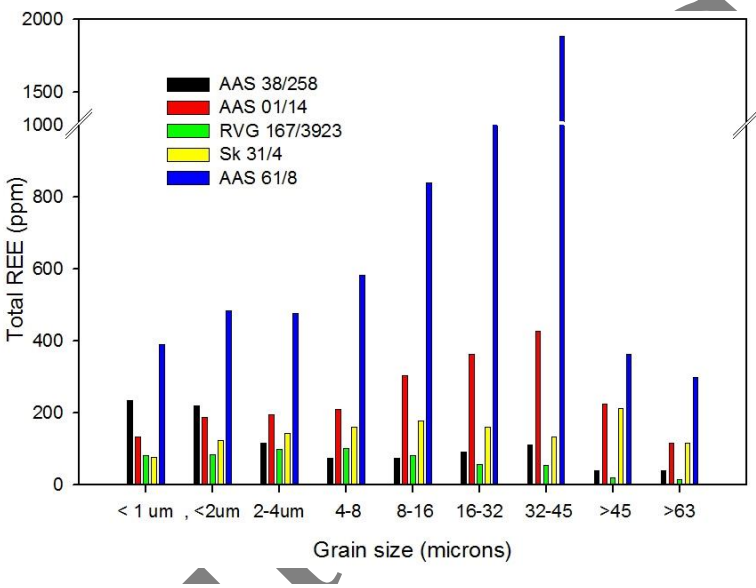

Fig. 6.11: Variation in total REE content in different size fractions of hydrothermally altered sediments and those from the nonhydrothermally influenced areas (Arabian Sea, Bay of Bengal, Equatorial Indian Ocean and siliceous domain).

Our observation of REE in different sediment populations, i.e., sand, silt and clay fraction of the sediments, and the inferred mineralogical control suggests that fluvial processes of sorting affect REE distribution in the sediments. Similar observations have also been reported by McLennan (1989), Morey and Setterholm (1997) and Vital and Stattegger (2000). This distribution is likely affected by differential concentration of various REE holding minerals and diluting minerals in different size fractions and the variation in the percentage of different size fractions in the bulk sediments.

Textural fractionation of major and trace elements in hydrothermal and non hydrothermal sediments

Results for the study area in siliceous ooze (AAS 38/258) domain in the CIB show that Al, Fe, K, Mg, Sr, Ti and Rb concentration are higher in the finer fraction, while Mn, Ca, Na are higher in the coarser fraction (Fig. 6.12, Table 6.4a to e). Fe and Mg show a similar behaviour in distribution in all the studied area. The concentration continually increases with a decrease in size. The relation between Fe and Mg is however different in the hydrothermally altered sediments of the CIB. The highest concentration of Fe% (~15%) (Table 6.6) in the finer fraction (1–4 μm) is seen in the sediments influenced by hydrothermal alteration in CIB with Mg% exhibiting the lowest values for the same size fractions. Fe variation seen in the fine fraction indicated increase in iron oxides, while anincrease in Mg% indicates presence of chlorite. This is corroborated by the XRD studies of the size fraction, in which chlorite is abundant (avg 20%). This is seen in all the cores studied, particularly the core sampled in the hydrothermal altered sediments in CIB. Abundance of clay minerals (illite, kaolinite, smectite and chlorite) in the clay sized fraction (<2 μm) are responsible for the high concentration of Al, Fe, Mg, K and Na in that size fraction.

Concentrations of the following elements including Rb, Th, U, Nb, La, Ce, Pb, Pr, Sr, Nd, Zr, Hf, Sm, Eu, Gd, Tb, Dy, Y, Ho, Er, Yb, Lu, Sc, V, Cr, Co and Ni in the isolated size fractions of all the 5 surface samples were normalized to corresponding upper continental crust and plotted (Fig. 6.13). Fig. 6.13 indicates that the elements Sr to Y show overall parallel to upper continental crust (UCC) normalized concentrations in most of the samples. Ba, Th, Ce, Nd, Yb, Tb and Y are enriched in the equatorial and siliceous sediments of the CIB while most of the elements are enriched in the hydrothermally altered sediments (AAS 61/8 core) (Mascarenhas–Pereira and Nath, 2010) except for Rb, Ta and Hf.

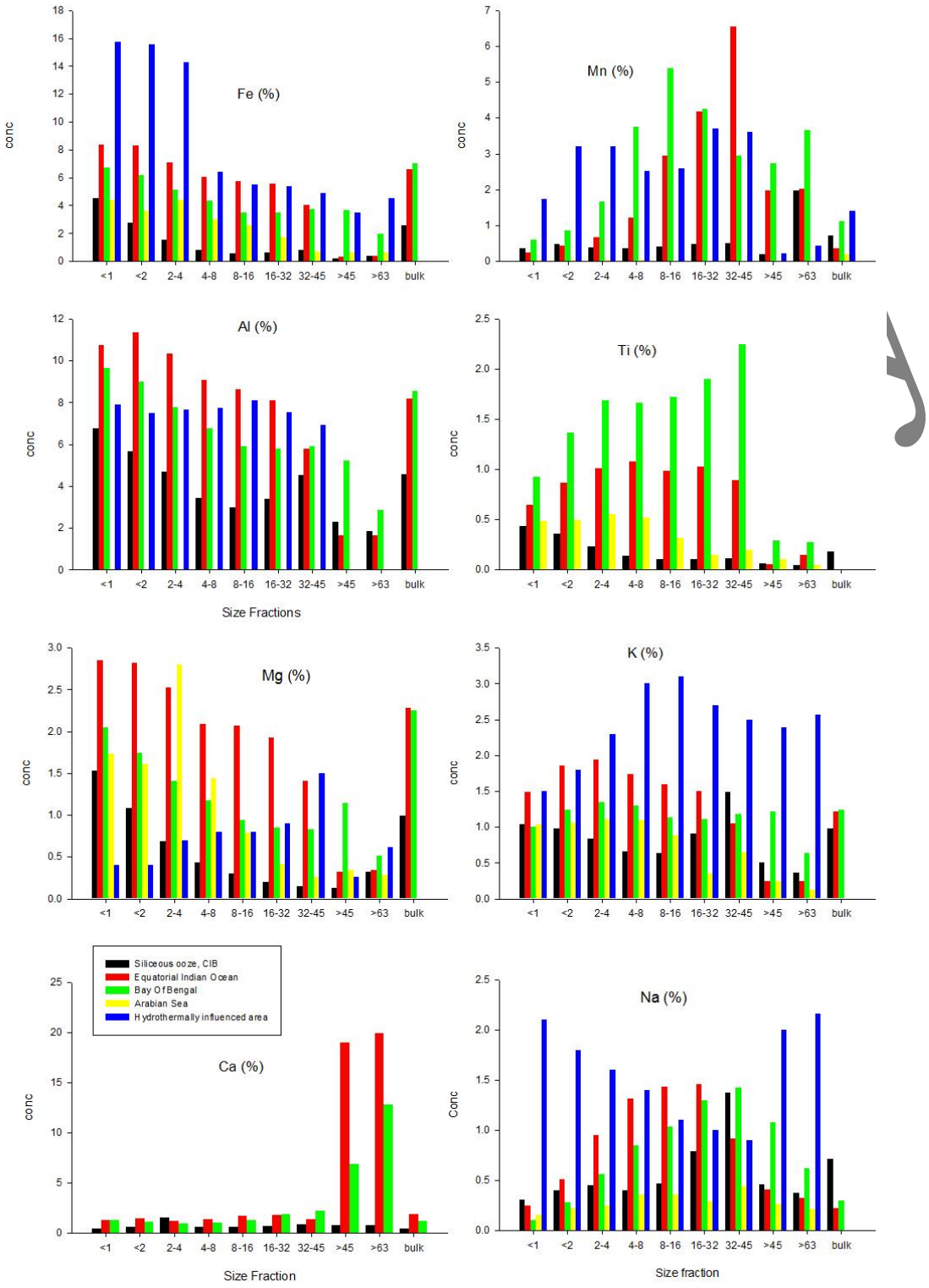

Fig. 6.12: Major elemental distribution in 9 different size fractions and bulk samples of hydrothermally altered sediments, Bay of Bengal, Arabian Sea, Northern and Central Indian Basin.

Elemental ratios such as Ni/Co, V/Cr and V/(V+Cr) have been used to define paleoredox conditions of deposition (Rimmer, 2004). These ratios in the present study in the Indian Ocean seem to suggest deposition in changing bottom water conditions or conditions modified by the process of weathering and alteration of sediments. The ratio of Ni/Cr (3.46 to 8.02) varies in the bulk samples in all the 5 surface samples studied (Table 6.6). This ratio is relatively higher in Arabian Sea bulk samples compared to the rest of the Indian Ocean sediments. The Bay of Bengal sediments show minor variation of Ni/Cr (2.4 to 3.4) within the grain sizes, while maximum variation (5.34 to 18.56) is seen in the size fraction of the equatorial sediments (Table 6.6) and warrants caution in using them for interpreting paleoredox. V/Cr ratios show little variation in all the samples studied with an average ratio varying between 0.67 and 4.64. Most of the V/Cr ratios of the size fraction in all the samples studied are less than 2 which represent an oxic environment of deposition (Jones and Manning, 1994), except for the hydrothermally influenced clays which show V/Cr ratio > 2.

Elements Sc, Nb, Ta, Th and REE provide an approximation of upper continental crust abundances in sedimentary rocks (Taylor and McLennan, 1985). La/Th ratios of the grain sizes range from 0.8 to 10.5 (Table 6.6). However each core exhibits a narrow range of values. The maximum La/Th ration is seen in the hydrothermally influenced sediments (max: 10.5, min: 6.3; avg: 8.3) while minimum values are seen in the Arabian Sea (max: 2.5, min: 2; avg: 2.3) and siliceous sediments (max: 2.12, min: 0.8; avg: 1.5). The constant distribution of this ratio in the sediments suggest that these two elements behave coherently during weathering cycle, so that the average of this ratio reflect the average continental sources of these deposits. The hydrothermally altered sediments are highly enriched in La/Th ratio (6.3) compared to UCC while those in non-hydrothermal areas are either similar (2.3 in Arabian Sea, 3 in Equatorial Indian Ocean) or lower (1.8 in Bay of Bengal and 1.5 in siliceous oozes from CIB) average values than UCC (2.8; Taylor and McLennan, 1985).

Geochemical compositions: implications for sediment provenance and grain size sorting

Trace elements such as Th, Zr, Hf and REE as well as Th/Sc and Cr/Th elemental ratios have proven to be useful tools for determining the composition of the source–area of sediments (Taylor and McLennan, 1985; Basu et al., 1990; Condie and Wronkiewicz, 1990; McLennan et al., 1993; Fedo et al., 1996; Cullers, 2000; Condie et al., 2001; among many others) as they are least effected by processes such as weathering, transport and sorting. In particular the commonly immobile elements Al, Fe, Ti, Th, Sc, Co, Cr, REE and their ratios have been found to be useful (Taylor and McLennan, 1985). These elements even if mobilised have short residence time in water and hence are almost quantitatively transferred into the sediments. However, before drawing conclusions on the provenance of sediments, the influence of sedimentary processes on the chemical composition of sediments must be carefully evaluated. In this discussion, we first evaluate the compositional features that may have resulted from weathering of the source material and processes of sorting. Then, we discuss the provenance of the analyzed sediments and their possible sources.

Selected trace elemental distribution within the surface samples is presented in Fig. 6.13 as spider diagrams. The selected trace elements correspond to low field strength elements (LFSE) or large ion lithophile elements (LILE–Rb, Sr, Th and U) and higher field strength elements (HFSE– Th, U, Zr, Hf, Y and Nb). The multi elemental spider diagrams for each of the five surface samples normalised to chondrite demonstrate the increasing trace element concentration with increasing grain size till about 32–45 µm size fraction (Fig. 6.13). The maximum trace element concentration is seen in the hydrothermally altered sediments which are 10 times enriched than the cores from Arabian Sea, Bay of Bengal and Indian Ocean with each core, the sand size fraction (>63 µm) has the least concentration of trace elements. All the trace elements in all the surface samples of the Indian Ocean are enriched compared to the primitive chondrite. The highest trace element concentration is seen in the hydrothermally altered sediments which is ~100 times enriched compared to chondrite, followed by AAS 38/258. The bulk samples of all the cores except for hydrothermally altered sediments exhibit similar concentration of trace elements.

High field strength elements (HFSE)

Increase of HFSE concentration with the clays is seen with Nb (25–124 ppm in >1 µm) and Zr (10–24 ppm in 1–2 µm) enrichment compared to the coarser size fraction. Generally, the enrichment of Y, Zr, Hf, Th and U with the fine grain lithologies is due to the association with heavy minerals often present as inclusions in clay minerals (Descourvieres et al., 2011). Zr, Hf and Nb are similar in concentration to the chondrite in the sand fraction of the Arabian Sea and gradually become enriched with decreasing grain size. The average Th/U ratio in all the lithologies is from 2–24, with the average Th/U ratio for clays (>1 and 1–2 µm) is from 1 to 20. Average Th/U ratio of 3 and 6 is seen in Arabian Sea and Pelagic clay sediments being similar to average UCC ratio of 3.8. A higher Th/U ratio than the UCC value is thought to be the product of intense weathering (McLennan et al., 1993). The average Zr concentration for the 9 size classes is enriched in decreasing size from 23 times in >63 µm to 68 times in 2 µm, while zircon in UCC is 190 ppm. An increase in Zr concentration within the fine grained lithologies suggest that zircon mineral was selectively concentrated by grain size fractionation of the sediments

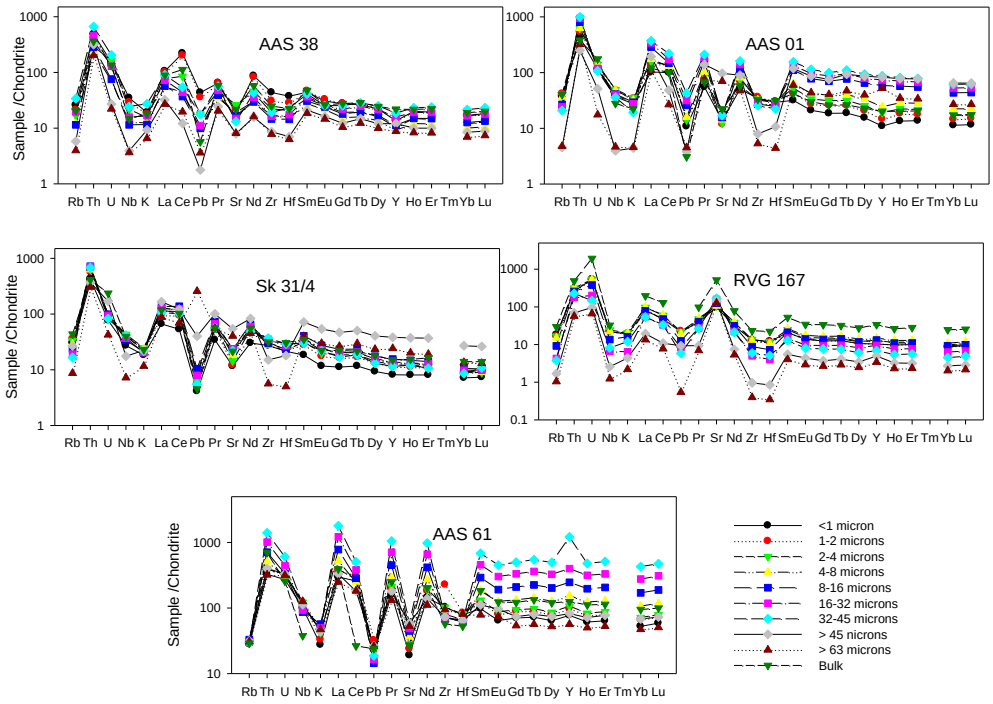

Fig. 6.13: Trace elements suites (LILE and HFSE) normalized to the composition of primitive chondrite. The LILE and HFSE are arranged according to decreasing ionic potential.

To constrain the provenance and tectonic settings for the deposition of the five samples from the Indian Ocean, ternary diagrams have been used (Bhatia and Crook, 1986). The elements Th, Hf, Co, Zr, La and Sc are compared in Th–Co–Zr/10 and La–Th–Sc ternary diagrams (Figs. 6.14 and 6.15). Both strongly incompatible elements Th and strongly and compatible elements Sc and Co as well as those related to dense–minerals Hf and Zr are represented.

The Th–Hf–Co plot for bulk sediments (Figs. 6.14 and 6.15) shows a cluster of sands near the PAAS composition, from which a trend towards progressive Co enrichment is seen in the siliceous ooze domain and the pelagic clays of the CIB. A considerable amount of variability is seen in the Th–Hf–Co plot. A distinct trend is seen in the size fractions of the sediments (Figs. 6.14 and 6.15). The size fractions chemistry of the Bay of Bengal, equatorial Indian Ocean, CIB siliceous and hydrothermally altered sediments plot parallel to the Th–Co apexes and away from the Hf apex. The sediments of the Arabian Sea, on the other hand, show Th enrichment and a strong depletion of Co. The pelagic clays of the CIB show affinity towards the Co apex, clearly reflecting the effect of hydrothermalism in the area (Mascarenhas–Pereira and Nath., 2010).

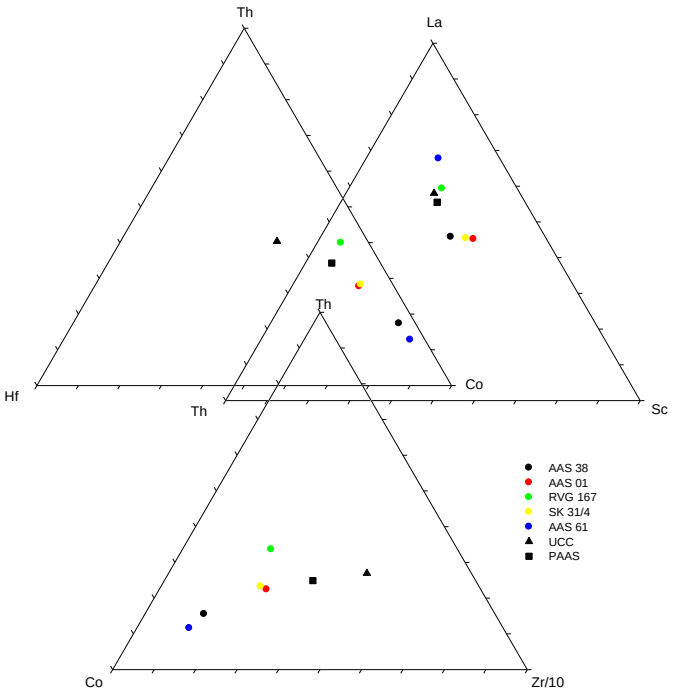

Fig. 6.14: Zr/10–Th–Co ternary plot of 9 different size fraction and bulk elemental composition of Bay of Bengal, Arabian Sea, Equatorial Indian Ocean and Central Indian Basin (siliceous and pelagic clays). Data for PAAS and UCC are included for comparison. (Modified from Abanda and Hannigan, 2006).

The Th–Co–Zr/10 diagram for bulk sediment is displayed in Fig. 6.14. The scaling factor has been used to bring the fields more to the centre of the diagram (Bhatia and Crook, 1986). On this plot, the sediments plot parallel to the Co–Th axis with a clear differentiation between the hydrothermally altered sediments and sediments from BOB, AS, EQ and CIB. The hydrothermally altered sediments are clustered near the Co pole and away from the UCC and PAAS. The pelagic clays also have a higher Zr content, tending to plot towards this pole as heavy mineral contents increase during the volcanic process. The sediments of the AS have the highest Th content and the lowest Co content. Sediments from the Bay of Bengal, Arabian Sea, equatorial Indian Ocean and the siliceous sediments from CIB show a similar trend with the coarser fraction plotting within the active and passive continental margins while the finer fraction including the bulk plotting in the continental Island arcs due to relative Sc enrichment, while a relative enrichment of Th cause the sand fraction of the siliceous sediments of CIB to plot outside the defined tectonic boundaries.

Bulk sediment distribution plotted on the La–Th–Sc diagram (Fig. 6.15) shows dispersion, with sediments of AS, BOB, and siliceous oozes of CIB plotting close to UCC and PAAS. Only the hydrothermally altered sediments of CIB sediments show a trend away from UCC and PAAS compositions, displaying enrichment in La.

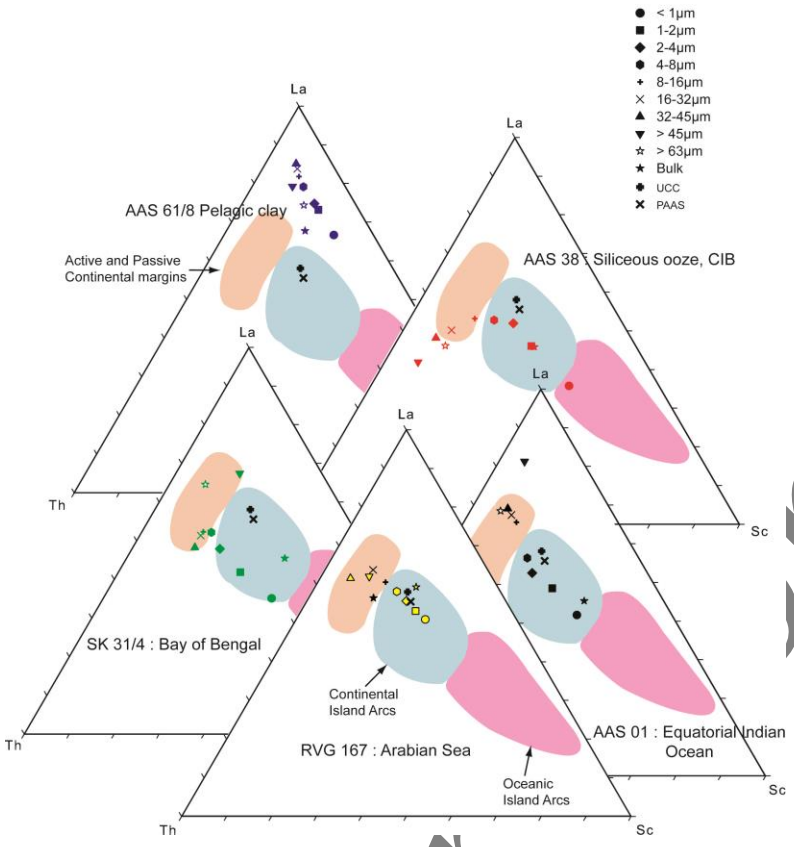

Fig. 6.15: Trace element (La–Th–Sc) ternary plot of 9 different size fraction and bulk elemental composition of hydrothermally altered sediments and sediments from Bay of Bengal, Arabian Sea, Northern and Central Indian Basin. The representation of light REE (La), incompatible element (Th) and compatible element (Sc) is shown in the Fig. 6.15. Data for PAAS and UCC are included for comparison. (Modified from Descourvieres et al., 2011).

The Th/Sc ratio is widely used as an index to discriminate between felsic and basic sources. Both elements have a very low water/rock partition coefficient and they are not affected by changes in the oxidation states inducing changes in solubility (Nyakairu and Koeberl., 2002). The Th/Sc ratio of all the size fractions show a wide variability (0.3 to 4.6) (Fig. 6.16 and 6.17) either much higher or lower than the reported values of PAAS and UCC (~0.91 and 0.97 respectively; Taylor and McLennan 1985). The size fractions of all the samples studied show a clear size discrimination with the finer size fraction exhibiting a lower Th/Sc while the coarser fraction have relatively higher Th/Sc ratio. The Th distribution may be affected by the occurrence of accessory phases such as monazite, which strongly control Th/Sc ratio with grain size. Like Th/Sc ratio, Cr/Th ratio has been proposed to discriminate between felsic and basic sources. Chromium can occur under oxidizing conditions as

Cr^{6+}, which is soluble in the form CrO_4^{2-} species (Middleburg et al., 1988). Changes in the oxidation states of Cr may, thus affect the provenance record of the metal/Th ratios (Middleburg et al., 1988). The Cr/Th ratio is relatively higher in the finer fraction compared to the coarser fraction (Fig 6.17). A low Th/Sc ratio (<1) indicates a mafic source which is usually enriched in compatible elements such as Sc, while higher concentration of incompatible element such as Th is generally found in well differentiated felsic rocks (Taylor and McLennan, 1985; Cullers 2002). Using this ratio, the sediments seem to have two sources with the finer fraction having a mafic source while the finer fraction is derived from a felsic source. In the present study, enrichment of Th relative to Sc in coarser fractions (Fig. 6.16) likely results from mineral sorting, which concentrates felsic and Th rich phases in the coarser fractions (Liu et al., 1994). A mixing model used to constrain the sources (mafic or felsic) using Th/Sc and Cr/Th ratios (Condie and Wronkiewicz, 1990) show that the sediments show differentiation in composition as a function of grain size (Figs. 6.16 and 6.17). Also sand has Th/Sc ratios between 2 and 5.2 (Fig. 6.17), within average Archean crustal granite composition (3.75 to 10) (Condie, 1993). In addition, low Cr/Ni ratio (0.01 to 1.5) are very less or close to the UCC (1.75) although higher than felsic Archean end member composition (3.0; Taylor and McLennan, 1985) and point to a relatively enrichment of ferromangnesian minerals within the clays rather than originating from a mafic source (Cr/Ni=8.25; Descourvieres et al., 2011).

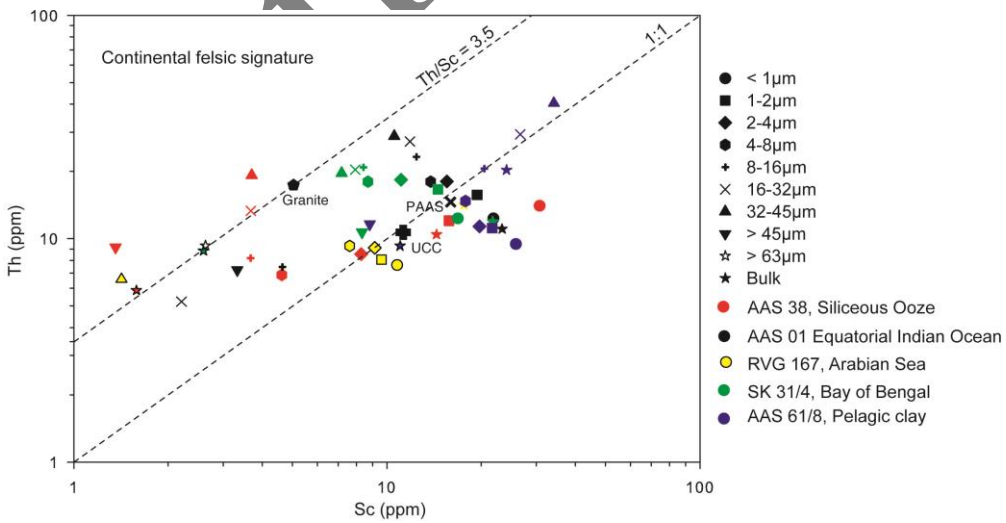

Fig. 6.16: Provenance and source signature diagrams for hydrothermally altered sediments and sediments from Bay of Bengal, Arabian Sea, Northern and Central Indian Basin. Data for PAAS, UCC and Archean granite are included for comparison.

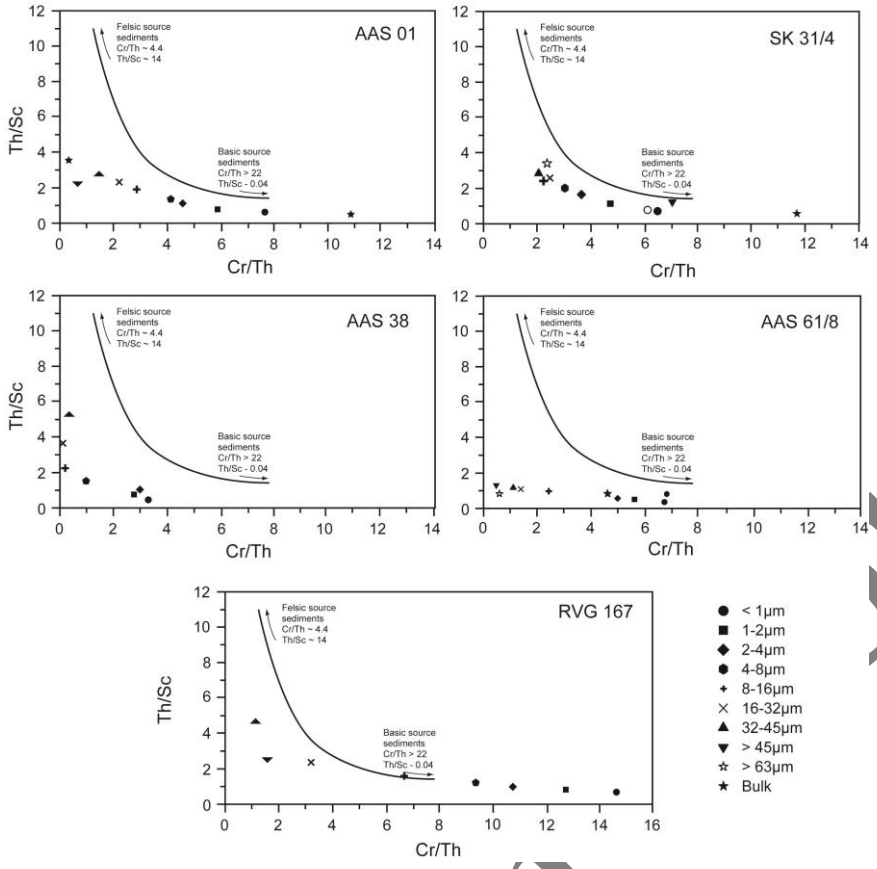

Fig. 6.17: Provenance and source signature diagram for sediments of Bay of Bengal, Arabian Sea, Equatorial Indian Ocean and Central Indian Basin (siliceous and pelagic clay.

6.4. Conclusions

Regional elemental distribution maps of the lithogenic fraction of the sediments of the CIB have facilitated to evaluate the role of local geology and bathymetry in the sediment distribution and dispersal pattern in the area. Geochemical tracers such as major, trace and rare earth elements were used as indicators of geological processes, provenance, and tectonic settings of basin. Studying composition of surface sediments allowed us to understand the fate of the terrestrial materials transported into the basins as well as the factors controlling the distribution and geochemistry of sediments. Al, Ti, Nb and Zr were useful to trace the detrital signature in the basin. Distribution patterns of these elements showed low concentration in the central part, while northern and southern parts were enriched in these elements. In marine sediments, these elements are primarily derived from aluminosilicate minerals which are generally detrital. High concentration in the north

of the study area indicated a terrigenous influence mainly by the Ganges–Brahmaputra and rivers draining Deccan basalts. High concentration in the southern part of the basin indicated an additional source such as MORB and local volcanic rocks. Distributional pattern of Rb/Sr were useful as an indicator of transportation pathways of fine–grained fraction of sediments along the bottom.

A new approach was adopted to quantitatively assess the relative contribution of competing sources in the CIB by performing the mixing calculations of the REE data of 26 surface samples. Mixing calculations using 4 end members such as biogenic, terrigenous, MORB and metalliferous component helped to estimate the relative proportion of the end members in the sediments. The calculations showed that the REE in the sediments of the CIB were a mixture of 0–10% siliceous component, 5–90% terrigenous component, 0–35% MORB component and 0–100% metalliferous component.

Elemental geochemistry of different size fractionated surface sediment samples in hydrothermally altered sediments of CIB sediments was studied and compared with size fractions of sediments not influenced by hydrothermalism from Arabian Sea, Equatorial Indian Ocean, Bay of Bengal and siliceous domain of the Indian Ocean. Geochemical study was carried out on nine size fractions (<1, 1–2, 2–4, 4–8, 8–16, 16–32, 32–45, 45–63 and >63 μm). The maximum trace element and REE concentrations were seen in the hydrothermally altered pelagic clay sediments which were upto 10 times enriched than the cores not influenced by hydrothermal activity. REE showed fractionation with grain size with the sand size fraction (>63 μm) having the least concentration of trace elements, probably due to enrichment of quartz, and biogenic material.

Table 6.1: Major elemental data of surface sediments from the CIB.

Core No (AAS 61)	Al%	Fe%	Mn%	Mg%	K%	Na%	Ca%	Ti %	P%
BC 1	5.56	2.67	0.65	1.12	1.46	1.7	0.69	0.22	0.08
BC 2	5.03	2.54	0.77	1.13	1.18	1.51	0.55	0.21	0.08
BC 3	4.67	2.65	0.62	1.08	1.19	1.57	0.44	0.19	0.07
BC 4	5.18	2.92	0.64	1.2	1.17	1.7	0.52	0.20	0.08
BC 5	6.26	3.7	1.85	1.64	1.32	1.82	0.73	0.25	0.14
BC 6	5.27	2.63	0.86	1.09	1.35	1.66	0.76	0.21	0.08
BC 7	4.95	2.8	0.85	1.14	1.14	1.54	0.6	0.21	0.07
BC 8	7.31	8.16	2.03	1.87	1.75	2.24	1.45	0.40	0.44
BC 9	5.63	3.4	0.98	1.31	1.3	1.72	0.64	0.24	0.08
BC 10	5.6	3.55	1	1.17	1.14	1.34	2.04	0.24	0.08
BC 11	5.23	3.2	0.99	1.26	1.2	1.72	0.64	0.22	0.08
BC 12	5.39	3	0.92	1.07	1.17	0.94	3.37	0.22	0.08
BC 13	5.51	3.18	0.89	1.24	1.23	1.4	2.7	0.23	0.08
BC 14	5.6	3.1	0.88	1.26	1.31	1.62	0.71	0.22	0.08
BC 15	5.71	3.36	0.82	1.36	1.26	1.55	0.85	0.23	0.08
BC 16	5.55	3	0.87	1.26	1.28	1.56	0.7	0.22	0.08
BC 17	4.18	2.45	1.11	0.94	0.86	1.23	8.58	0.18	0.08
BC 18	5.4	3.15	0.79	1.32	1.26	1.62	0.63	0.23	0.08
BC 19	5.46	2.99	0.78	1.2	1.31	1.73	0.6	0.21	0.08
BC 20	5.28	2.77	0.83	1.17	1.19	1.56	0.6	0.21	0.08
BC 21	5.43	3.11	0.97	1.37	1.18	1.63	0.82	0.23	0.09
BC 22	5.17	3.01	0.88	1.21	1.08	1.33	1.45	0.23	0.08
BC 23	4.98	2.85	0.65	1.28	1.03	1.32	2.15	0.22	0.08
BC 24	5.41	2.9	0.87	1.3	1.19	1.5	0.85	0.23	0.08
BC 25	5.59	2.96	1.03	1.26	1.28	1.71	0.59	0.23	0.09
BC 26	5.84	3.14	0.74	1.39	1.33	1.7	0.7	0.24	0.08

Table 6.2: REE elemental data of surface sediments from the CIB (in ppm).

Core No (AAS 61)	La	Ce	Pr	Nd	Sm	Eu	Gd	Tb	Dy	Ho	Er	Tm	Yb	Lu	∑REE
BC 1	31.66	83.76	7.97	36.06	9.47	2.47	7.79	1.49	9.00	1.87	5.45	0.81	4.92	0.77	203
BC 2	25.96	82.54	6.56	32.01	8.01	2.22	6.56	1.19	7.19	1.45	4.34	0.61	3.76	0.59	183
BC 3	26.65	81.48	6.71	31.95	8.43	2.25	6.81	1.25	7.48	1.54	4.49	0.64	3.81	0.60	184
BC 4	30.50	87.98	7.77	36.19	9.81	2.79	7.81	1.47	8.66	1.75	5.19	0.74	4.53	0.69	206
BC 5	56.53	128	14.95	63.03	18.14	4.72	15.36	2.93	18.05	3.67	10.73	1.56	9.18	1.42	349
BC 6	49.45	105	13.47	54.92	16.67	4.43	13.89	2.76	16.80	3.49	10.09	1.40	8.54	1.34	303
BC 7	40.30	108	10.79	48.18	13.37	3.52	11.29	2.12	12.97	2.59	7.56	1.05	6.21	0.94	269
BC 8	141	216	32	121	33.91	8.62	30.83	6.29	39.18	8.39	25.57	3.65	21.70	3.35	693
BC 9	52.90	124	14.00	59.46	16.92	4.37	14.74	2.94	17.43	3.57	10.41	1.48	8.59	1.31	332
BC 10	55.29	131	14.62	62.84	17.64	4.59	15.13	2.91	17.64	3.53	10.36	1.42	8.59	1.34	347
BC 11	42.24	109	11.75	50.47	15.00	4.17	13.60	2.43	14.66	2.86	8.63	1.19	7.20	1.10	284
BC 13	48.87	114	13.40	56.41	16.64	4.49	14.24	2.73	16.50	3.29	9.75	1.36	8.04	1.25	311
BC 14	42.65	108	11.66	50.41	14.14	3.77	12.20	2.32	13.95	2.83	8.24	1.18	6.97	1.07	280
BC 15	43.19	105	11.22	48.52	14.00	3.85	11.52	2.17	12.92	2.61	7.68	1.07	6.32	0.99	271
BC 16	46.26	101	12.48	51.44	15.55	4.09	13.10	2.57	15.56	3.07	9.08	1.29	7.66	1.19	285
BC 17	30.94	77.10	7.95	35.24	10.03	2.81	8.36	1.53	9.14	1.85	5.44	0.74	4.54	0.69	196
BC 18	35.08	97.10	9.33	42.30	11.60	3.12	9.65	1.80	10.69	2.12	6.32	0.88	5.44	0.83	236
BC 19	37.62	95.17	9.95	43.79	12.51	3.26	10.34	1.96	11.77	2.39	6.94	1.00	5.91	0.93	244
BC 20	28.39	86.03	7.41	35.70	9.18	2.48	7.81	1.41	8.38	1.70	4.96	0.71	4.14	0.67	199
BC 21	32.87	91.15	8.61	38.66	10.57	2.93	8.89	1.64	9.68	1.94	5.67	0.82	4.78	0.75	219
BC 22	38.92	84.99	10.07	42.44	12.71	3.53	10.05	1.93	11.72	2.39	7.02	1.00	5.84	0.92	234
BC 23	37.43	76.18	9.32	38.27	11.97	3.40	9.72	1.85	11.27	2.33	6.83	0.94	5.69	0.89	216
BC 24	35.24	84.42	8.84	39.14	11.17	3.06	8.99	1.71	10.32	2.11	6.14	0.88	5.25	0.81	218
BC 25	29.21	84.85	7.31	34.81	8.84	2.45	7.43	1.36	8.08	1.63	4.91	0.69	4.11	0.64	196
BC 26	33.59	87.57	8.44	37.56	10.17	2.77	8.53	1.57	9.29	1.88	5.60	0.81	4.74	0.73	213

Table 6.3: Trace elemental data of surface sediments from the CIB. (in ppm).

Core No	Li	Be	Sc	V	Cr	Co	Ni	Cu	Zn	Ga	Rb	Sr	Y	Zr	Nb	Mo	Ba	Hf	Pb	Th	U
BC–1	29.81	1.41	14.96	60.74	33.58	49.02	215	326	77.92	13.49	85.18	189	56.03	131	6.53	3.83	3050	3.41	36.94	15.63	1.80
BC–2	25.16	1.24	14.81	60.36	32.26	56.87	241	322	65.08	12.71	59.95	191	44.04	111	5.27	5.01	3432	2.89	37.24	11.27	1.27
BC–3	28.28	1.22	17.16	60.14	18.18	48.39	232	285	213	12.50	60.64	165	43.93	98.60	4.98	5.30	3268	2.79	34.85	12.95	1.22
BC–04	29.09	1.29	18.12	62.32	29.01	57.04	186	289	197	13.23	53.80	198	52.20	124	4.59	2.91	4194	3.21	34.93	12.88	1.16
BC–5	60.07	1.66	22.09	81.86	23.13	124	744	801	149	16.48	64.91	206	111	178	6.40	30.07	3344	4.41	69.42	17.65	1.53
BC–6	30.01	1.21	16.79	56.81	22.44	72.58	288	340	85.74	13.03	72.57	186	104	125	5.66	6.80	2936	3.61	41.77	18.47	1.61
BC–7	28.68	1.08	17.02	59.14	25.62	81.90	260	277	84.07	12.95	57.65	183	77.45	148	5.36	3.88	3415	3.78	41.13	13.82	1.34
BC–8	52.11	2.09	26.44	179	23.16	162	1005	721	222	18.37	69.10	238	294	409	21.22	30.91	859	8.77	84.00	16.54	2.53
BC–9	36.12	1.36	21.18	71.44	30.19	90.27	288	358	174	14.11	63.68	172	108	148	5.97	5.66	2286	3.86	49.67	17.22	1.49
BC–10	33.93	1.33	20.83	69.92	24.96	94.72	323	365	161	14.52	62.20	237	108	155	5.83	5.50	3164	4.12	54.27	16.51	1.39
BC–11	35.83	1.46	20.33	75.44	33.43	85.24	326	428	289	15.24	58.24	188	82.95	137	5.31	9.89	2910	3.82	46.13	14.69	1.36
BC–13	34.19	1.44	21.22	69.31	27.41	82.41	317	362	92.80	14.84	64.96	280	97.14	150	6.25	5.84	3887	4.24	49.10	17.09	1.42
BC–14	34.41	1.52	21.02	66.37	30.88	75.80	299	408	142	14.87	66.05	203	82.85	143	5.98	7.56	3183	3.86	43.40	16.35	1.45
BC–15	33.61	1.38	21.26	69.89	29.19	72.23	266	379	88.00	14.68	59.87	248	78.80	144	5.64	4.19	5109	3.77	40.89	14.37	1.24
BC–16	31.55	1.32	18.25	61.96	27.01	67.89	291	345	89.00	13.57	63.37	201	93.64	132	5.78	6.12	3382	3.72	41.17	15.99	1.44
BC–17	23.75	0.99	15.52	50.87	14.47	48.93	369	348	99.24	10.21	40.72	483	54.91	110	4.69	9.38	3885	2.95	30.98	10.02	0.98
BC–18	30.58	1.46	19.23	70.64	33.19	62.24	261	355	90.47	13.81	59.93	207	63.35	131	5.66	4.56	3923	3.69	39.72	13.80	1.32
BC–19	30.31	1.33	18.40	60.87	27.51	60.30	238	342	75.62	13.09	63.53	190	69.27	128	5.43	5.37	3600	3.67	40.14	15.05	1.44
BC–20	25.42	1.30	16.16	58.24	29.14	60.84	265	334	223	12.28	55.59	186	49.30	117	5.09	7.13	3338	2.95	36.82	11.50	1.21
BC–21	27.95	1.41	18.44	69.34	33.42	65.40	320	402	115	13.46	53.30	229	58.36	130	5.29	5.01	4005	3.32	39.40	12.09	1.22
BC–22	27.29	1.50	16.75	61.30	31.24	58.30	301	358	99.70	12.97	52.04	226	74.07	111	4.98	5.66	4658	2.95	38.53	12.46	1.35
BC–23	26.71	1.14	16.18	64.54	34.98	47.53	216	373	95.91	12.11	48.32	255	73.82	113	4.96	3.31	5493	2.93	31.16	10.90	1.58
BC–24	26.43	1.30	16.36	63.43	27.53	55.57	302	350	84.13	12.48	55.71	210	62.23	117	5.48	5.84	4181	3.12	35.53	12.60	1.37
BC–25	29.05	1.26	16.19	68.45	34.99	58.56	344	420	131	12.93	60.19	191	48.57	123	5.48	13.57	3624	3.23	39.11	11.87	1.35
BC–26	32.18	1.47	18.46	76.11	40.31	54.08	247	344	110	13.86	65.70	210	58.03	138	6.10	4.89	3728	3.35	35.26	12.95	1.51

Table 6.4a: Distribution of REE in different grain size fractions of the Central Indian Basin sediments: Hydrothermally altered sediments (in ppm).

Elements	Central Indian Basin– AAS 61/BC 8								
Size (μm)	< 1	<2	2–4	4–8	8–16	16–32	32–45	>45	>63
La	70	90	92	123	185	289	426	78	59
Ce	159	191	168	152	175	234	310	111	112
Pr	15.12	19.14	20	28	43	67	100	17	13
Nd	67	86	91	127	195	308	456	65	52
Sm	14.94	18.66	20.16	28.68	44.59	70	104	17.01	12.05
Eu	3.74	4.66	5.07	7.30	11.08	17.52	26.18	5.59	4.31
Gd	14.53	18.36	19.40	27.50	43	68	103	15.22	11.10
Tb	2.69	3.32	3.61	5.29	8.31	13.36	20.13	2.97	2.09
Dy	16.27	20.24	21.89	32.19	51.31	83.01	126	18.83	13.26
Ho	3.48	4.37	4.75	7.03	11.24	17.96	27.30	4.08	2.85
Er	10.60	13.47	14.56	21.40	34.24	54.93	84.91	12.87	8.74
Tm	1.48	1.88	2.02	3.04	4.87	7.92	12.08	1.86	1.34
Yb	8.94	11.32	12.17	18.21	28.99	47.03	73	11.56	8.05
Lu	1.47	1.84	1.97	2.95	4.72	7.73	11.84	1.82	1.27
∑REE	389	485	477	584	839	1285	1880	363	300

***Elemental concentration in ppm**

Table 6.4b: Distribution of REE in different grain size fractions of the Arabian Sea sediments (in ppm).

Elements	Arabian Sea–RVG 167/3923								
Size (μm)	<1	<2	2–4	4–8	8–16	16–32	32–45	>45	>63
La	19.08	19.98	22.95	23.49	18.63	13.08	12.82	4.60	3.20
Ce	29.22	30.66	36.51	37.11	29.19	20.29	20.38	6.65	4.73
Pr	3.77	4.01	4.52	4.78	3.86	2.61	2.53	0.89	0.66
Nd	14.72	15.38	17.96	18.46	14.73	10.31	9.95	3.48	2.50
Sm	3.18	3.23	3.80	4.01	3.26	2.27	1.97	0.84	0.61
Eu	0.80	0.81	0.90	1.02	0.82	0.56	0.46	0.26	0.17
Gd	2.58	2.64	3.05	3.41	2.81	1.93	1.58	0.76	0.55
Tb	0.47	0.48	0.56	0.62	0.53	0.36	0.28	0.15	0.11
Dy	2.71	2.78	3.11	3.55	2.99	2.07	1.53	0.88	0.63
Ho	0.56	0.57	0.66	0.74	0.62	0.43	0.31	0.19	0.13
Er	1.66	1.71	1.93	2.14	1.83	1.28	0.93	0.53	0.39
Tm	0.25	0.26	0.29	0.33	0.28	0.19	0.14	0.09	0.06
Yb	1.48	1.50	1.67	1.85	1.58	1.08	0.76	0.46	0.34
Lu	0.23	0.24	0.26	0.30	0.25	0.17	0.12	0.07	0.05
∑REE	81	84	98	102	81	57	54	20	14

Table 6.4c: Distribution of REE in different grain size fractions of the Equatorial Indian Ocean sediments (in ppm).

Elements	Equatorial Indian Ocean–AAS 01/SPC 14								
Size (μm)	<1	<2	2–4	4–8	8–16	16–32	32–45	>45	>63
La	24.30	33.08	37.06	40.99	67.76	80.73	87.86	45.81	25.91
Ce	61.01	86.91	82.89	79.30	90.68	106	134	29.46	16.26
Pr	5.24	7.15	8.39	9.57	14.94	17.84	20.00	13.29	7.23
Nd	23.57	33.14	35.09	37.78	53.70	65.39	74.89	41.87	22.08
Sm	4.86	6.54	8.06	9.75	16.90	20.46	23.77	18.06	9.14
Eu	1.22	1.58	1.94	2.45	4.50	5.55	6.62	4.99	2.52
Gd	3.82	5.32	6.44	8.06	14.40	17.93	20.41	15.53	8.30
Tb	0.69	0.94	1.17	1.49	2.85	3.52	4.08	3.46	1.75
Dy	3.93	5.27	6.44	8.43	16.47	20.12	23.68	21.89	10.12
Ho	0.77	1.05	1.28	1.64	3.25	4.03	4.64	4.44	1.99
Er	2.27	2.94	3.61	4.65	9.15	11.17	13.04	12.77	5.62
Tm	0.33	0.43	0.52	0.67	1.32	1.63	1.92	1.82	0.86
Yb	1.93	2.47	2.94	3.79	7.36	8.95	10.49	11.03	4.60
Lu	0.29	0.37	0.44	0.56	1.09	1.34	1.55	1.62	0.68
∑REE	134	187	196	209	304	365	427	226	117

Table 6.4d: Distribution of REE in different grain size fractions of the Bay of Bengal sediments (in ppm).

Elements	Bay of Bengal– SK 31/4								
Size (μm)	< 1	<2	2–4	4–8	8–16	16–32	32–45	>45	>63
La	15.74	22.46	27.11	29.14	32.09	29.89	25.02	39.30	20.82
Ce	32.59	57.67	67.35	76.28	84.53	75.81	61.79	74.45	42.39
Pr	3.27	5.04	5.78	6.29	6.93	6.34	5.39	9.54	5.29
Nd	14.11	21.09	24.53	27.39	30.50	27.66	22.58	38.76	21.14
Sm	2.81	4.26	4.85	5.55	6.19	5.57	4.59	10.96	6.05
Eu	0.68	1.02	1.16	1.35	1.59	1.41	1.27	3.12	1.73
Gd	2.30	3.36	3.79	4.18	4.77	4.24	3.48	9.63	5.43
Tb	0.43	0.63	0.69	0.75	0.87	0.77	0.69	1.86	1.10
Dy	2.37	3.39	3.62	3.99	4.45	4.02	3.33	10.30	5.94
Ho	0.46	0.64	0.68	0.74	0.84	0.75	0.69	2.13	1.15
Er	1.34	1.83	1.91	2.05	2.33	2.13	1.77	6.12	3.16
Tm	0.22	0.27	0.29	0.30	0.35	0.32	0.34	0.81	0.46
Yb	1.22	1.50	1.53	1.61	1.80	1.66	1.45	4.58	2.30
Lu	0.18	0.23	0.22	0.23	0.26	0.25	0.27	0.65	0.33
∑REE	78	123	144	160	177	161	133	212	117

Table 6.4e: Distribution of REE in different grain size fractions of the siliceous ooze/clays in the CIB (in ppm).

Elements	Central Indian Basin–AAS 38/258								
Size (μm)	<1	<2	2–4	4–8	8–16	16–32	32–45	>45	>63
La	24.91	23.76	18.12	12.84	13.48	17.15	21.32	7.59	6.39
Ce	135	123	52.08	27.51	22.62	26.99	33.14	7.40	12.01
Pr	6.15	6.11	4.38	3.32	3.71	4.55	5.35	2.31	1.94
Nd	40.53	38.36	21.20	14.16	13.77	16.62	19.98	7.34	7.54
Sm	6.74	7.11	5.19	4.16	4.69	5.56	6.26	3.23	2.82
Eu	1.78	1.91	1.46	1.24	1.39	1.49	1.47	0.94	0.85
Gd	5.62	5.75	3.96	3.16	3.70	4.50	5.22	2.51	2.15
Tb	0.98	1.03	0.72	0.59	0.72	0.92	1.04	0.55	0.45
Dy	5.58	5.82	4.05	3.43	4.28	5.42	6.34	3.04	2.53
Ho	1.14	1.15	0.84	0.69	0.85	1.09	1.32	0.57	0.47
Er	3.22	3.25	2.38	1.97	2.47	3.17	3.95	1.66	1.37
Tm	0.47	0.48	0.35	0.29	0.36	0.48	0.61	0.26	0.22
Yb	2.86	2.84	2.03	1.70	2.15	2.82	3.64	1.43	1.18
Lu	0.46	0.45	0.32	0.26	0.34	0.45	0.58	0.22	0.18
∑REE	235	221	117	75	75	91	110	39	40

Table 6.5: Diagnostic elemental ratios for the size fractionated sediment samples.

Core number	size	Ce/Ce*	Eu/Eu*	Yb/Gd	Eu/Sm	La/Yb	Gd/Yb	La/Sm
AAS 38/258	<1 µm	2.51	1.36	0.84	1.36	0.64	1.19	0.54
	<2 µm	2.35	1.40	0.82	1.38	0.62	1.22	0.50
	2–4 µm	1.35	1.51	0.85	1.44	0.66	1.18	0.56
	4–8 µm	0.97	1.61	0.89	1.54	0.56	1.13	0.49
	8–16 µm	0.73	1.57	0.96	1.53	0.46	1.04	0.44
	16–32 µm	0.70	1.40	1.04	1.38	0.45	0.97	0.46
	32–45 µm	0.72	1.21	1.15	1.20	0.43	0.87	0.50
	>45 µm	0.40	1.55	0.94	1.50	0.39	1.06	0.37
	>63 µm	0.78	1.62	0.91	1.54	0.40	1.10	0.36
RVG 167/3923	<1 µm	0.79	1.31	0.95	1.29	0.95	1.06	0.90
	<2 µm	0.79	1.30	0.94	1.29	0.98	1.07	0.92
	2–4 µm	0.82	1.25	0.91	1.22	1.01	1.10	0.92
	4–8 µm	0.81	1.30	0.90	1.30	0.94	1.11	0.84
	8–16 µm	0.79	1.27	0.93	1.29	0.87	1.08	0.81
	16–32 µm	0.80	1.26	0.92	1.27	0.90	1.09	0.83
	32–45 µm	0.82	1.24	0.80	1.21	1.24	1.25	0.99
	>45 µm	0.75	1.50	1.00	1.56	0.74	1.00	0.74
	>63 µm	0.75	1.37	1.03	1.42	0.69	0.97	0.71
AAS 61/BC 8	<1 µm	1.12	1.19	1.02	1.29	0.58	0.98	0.59
	<2 µm	1.07	1.18	1.02	1.28	0.59	0.98	0.60
	2–4 µm	0.90	1.20	1.04	1.29	0.56	0.96	0.58
	4–8 µm	0.60	1.22	1.09	1.31	0.50	0.91	0.55
	8–16 µm	0.45	1.19	1.11	1.28	0.47	0.90	0.52
	16–32 µm	0.39	1.19	1.14	1.29	0.45	0.88	0.51
	32–45 µm	0.35	1.18	1.17	1.29	0.43	0.86	0.50
	>45 µm	0.70	1.64	1.26	1.69	0.50	0.80	0.63
	>63 µm	0.95	1.75	1.20	1.84	0.54	0.83	0.65
AAS 01/SPC 14	<1 µm	1.25	1.33	0.83	1.29	0.93	1.20	0.78
	<2 µm	1.30	1.26	0.77	1.24	0.99	1.30	0.76
	2–4 µm	1.08	1.27	0.76	1.24	0.93	1.32	0.70
	4–8 µm	0.92	1.30	0.78	1.29	0.80	1.29	0.62
	8–16 µm	0.66	1.36	0.84	1.37	0.68	1.18	0.57
	16–32 µm	0.64	1.36	0.83	1.39	0.67	1.21	0.55
	32–45 µm	0.74	1.41	0.85	1.43	0.62	1.18	0.53
	>45 µm	0.69	0.17	1.17	1.42	0.08	0.85	0.10
	>63 µm	0.27	1.36	0.92	1.42	0.42	1.09	0.38

	size	Ce/Ce*	Eu/Eu*	Yb/Gd	Eu/Sm	La/Yb	Gd/Yb	La/Sm
	< 1 µm	1.05	1.26	0.88	1.24	0.95	1.14	0.84
	<2µm	1.25	1.26	0.74	1.22	1.10	1.35	0.81
	2–4µm	1.24	1.27	0.67	1.23	1.31	1.50	0.87
SK 31/4	4–8 µm	1.30	1.32	0.63	1.25	1.34	1.58	0.85
	8–16 µm	1.31	1.38	0.62	1.32	1.32	1.61	0.82
	16–32 µm	1.27	1.37	0.65	1.30	1.33	1.54	0.86
	32–45 µm	1.23	1.50	0.69	1.42	1.27	1.45	0.88
	>45 µm	1.72	1.43	0.79	1.46	0.63	1.27	0.50
	>63 µm	0.93	1.42	0.70	1.47	0.67	1.43	0.47

Table 6.6: Major and trace elemental data of size fractionated sediments (trace element values in ppm)

	ICP-OES (%)						ICP–MS																	
RVG 167/3923	Fe%	K%	Mg%	Na%	Al%	Ca%	Ti%	Mn%	Sc	V	Cr	Co	Ni	Cu	Zn	Rb	Sr	Y	Zr	Nb	Mo	Hf	Pb	Th	U
1µm	4.4	1.04	1.73	0.16	NA	NA	0.49	0.02	10.8	50	112	9.9	78	65	106	44	711	16	51.3	5.4	0.4	1	53.7	7.6	4.3
2µm	3.6	1.06	1.61	0.23	NA	NA	0.49	0.02	9.6	44	103	8.9	79	87	100	40	749	17	50.6	5.5	0.3	1	56.5	8.1	4.3
2–4µm	4.4	1.11	2.8	0.24	NA	NA	0.55	0.02	9.1	43	98	9.0	84	114	123	40	784	20	52.9	6.0	0.3	1	54.4	9.1	4.3
4–8µm	3.0	1.1	1.44	0.36	NA	NA	0.52	0.02	7.6	36	87	7.6	81	130	121	36	765	23	49.8	5.5	0.3	1	48.3	9.3	4.2
8–16µm	2.6	0.88	0.78	0.36	NA	NA	0.32	0.01	4.6	24	50	4.7	52	84	70	22	915	21	33.9	3.4	0.2	1	30.8	7.5	3.1
16–32µm	1.7	0.35	0.42	0.29	NA	NA	0.14	0.01	2.2	11.3	17	2.4	21	41	23	10	1150	15	19.4	1.6	0.3	0	20.5	5.2	1.6
32–45µm	0.7	0.65	0.26	0.44	NA	NA	0.19	0.01	1.4	11.6	7.36	1.7	10	24	9	9.16	1225	11	23.0	2.0	0.1	1	14.5	6.6	1.2
>45µm	0.6	0.24	0.35	0.27	NA	NA	0.1	0.01	0.8	5.0	3.18	1.3	50	52	52	4.08	1034	7.79	3.7	0.6	0.3	0	23.0	2.0	0.8
>63µm	0.6	0.12	0.28	0.21	NA	NA	0.04	0	0.8	4.3		1.3	7	ND	ND	2.51	927	5.36	1.5	0.3	1.9	0	1.3	1.7	0.5
Bulk	NA	NA	NA	NA	NA	NA	NA	0.2	17.6	NA	64	18.9	152	82	61	71	3753	53	90.0	8.0	0.6	2	0.0	14.2	15.5
AAS 61/8	Fe%	K%	Mg%	Na%	Al%	Ca%	Ti%	Mn%	Sc	V	Cr	Co	Ni	Cu	Zn	Rb	Sr	Y	Zr	Nb	Mo	Hf	Pb	Th	U
1µm	15.7	1.5	0.4	2.1	7.9	NA	NA	1.7	25.9	216	64	104	199	332	151	68	138	121	399	25	12.4	8.4	57	9.5	2.2
2µm	15.5	1.8	0.4	1.8	7.5	NA	NA	3.2	21.7	224	63	192	379	413	191	75	173	154	880	30	11.7	9.0	79	11.2	2.6
2–4µm	14.2	2.3	0.7	1.6	7.64	NA	NA	3.2	19.8	201	57	178	465	438	179	76	205	168	397	30	11.4	8.7	56	11.3	2.6
4–8µm	6.4	3	0.8	1.4	7.72	NA	NA	2.5	17.9	147	101	125	447	381	165	77	263	243	309	24	10.7	7.1	41	14.7	2.4
8–16µm	5.5	3.1	0.8	1.1	8.09	NA	NA	2.6	20.5	124	50	118	528	391	161	79	325	387	280	21	11.9	6.6	36	20.6	2.7
16–32µm	5.4	2.7	0.9	1	7.51	NA	NA	3.7	26.7	124	41	158	845	485	201	72	355	625	279	23	17.0	6.5	41	29.3	3.6
32–45µm	4.9	2.5	1.5	0.9	6.93	NA	NA	3.6	34.2	116	45	144	860	462	179	71	425	1904	282	28	18.0	6.9	46	40.5	4.9
>45µm	3.5	2.39	0.26	2	NA	NA	0.47	0.2	8.8	56	5.57	19	64	486	609	76	418	129	281	28	7.1	7	65	11.6	2.7
>63µm	4.5	2.57	0.62	2.16	NA	NA	0.38	0.4	11.0	91	5.57	39	126	627	523	74	385	89	366	31	50.7	9	64	9.3	2.5

ICP–OES (%)							ICP–MS																		
AAS 38/258	Fe%	K%	Mg%	Na%	Al%	Ca%	Ti%	Mn%	Sc	V	Cr	Co	Ni	Cu	Zn	Rb	Sr	Y	Zr	Nb	Mo	Hf	Pb	Th	U
1µm	4.53	1.04	1.53	0.30	6.76	0.43	0.43	0.37	31	87	46	57	130	292	165	62	136	21	169	8.54	2.52	4	107	14.05	1.22
2µm	2.74	0.98	1.08	0.40	5.65	0.57	0.36	0.48	16	55	33	55	125	280	153	51	158	21	120	7.15	1.78	3	88	12.04	1.07
2–4µm	1.52	0.84	0.69	0.45	4.68	1.56	0.23	0.38	8.28	35	25	34	113	214	104	41	191	16	85	5.33	1.56	2	44	8.52	1.30
4–8µm	0.79	0.66	0.43	0.40	3.43	0.58	0.14	0.35	4.62	20	6.73	25	108	205	103	29	138	14	65	3.23	2.00	2	23	6.88	0.56
8–16µm	0.57	0.63	0.30	0.46	2.97	0.59	0.10	0.41	3.67	16	1.63	24	141	245	110	28	122	18	56	2.82	3.47	2	24	8.20	0.61
16–32µm	0.62	0.90	0.19	0.79	3.37	0.68	0.10	0.48	3.68	14	1.52	23	164	284	127	47	108	25	63	3.86	4.93	2	28	13.35	1.03
32–45µm	0.80	1.49	0.15	1.37	4.50	0.87	0.11	0.50	3.70	15	6.71	21	156	285	120	82	95	29	74	5.99	6.12	2	43	19.24	1.64
>45µm	0.21	0.51	0.13	0.46	2.29	0.80	0.06	0.19	1.36	4	ND	6.07	33	78	151	14	57	19	33	0.96	0.82	1	4.38	9.15	0.22
>63µm	0.39	0.36	0.32	0.38	1.83	0.79	0.05	1.98	1.59	11	ND	29	392	544	203	9.56	59	14	30	0.90	15.94	1	8.91	5.87	0.18
Bulk	2.57	0.98	0.99	0.71	4.56	0.43	0.18	0.72	14.40	ND	50	47	262	384	62	50	157	34	96	3.60	12.69	2	13.95	10.45	1.06
AAS 01/SPC 14	Fe%	K%	Mg%	Na%	Al%	Ca%	Ti%	Mn%	Sc	V	Cr	Co	Ni	Cu	Zn	Rb	Sr	Y	Zr	Nb	Mo	Hf	Pb	Th	U
1µm	8.37	1.49	2.85	0.25	10.72	1.27	0.64	0.23	21.88	96	94	20	110	128	61	91	100	17	134	9.13	1.10	3	27	12.34	0.92
2µm	8.32	1.85	2.82	0.51	11.37	1.41	0.87	0.42	19.44	99	93	29	155	168	86	101	87	23	141	11.87	1.14	3	35	15.75	1.15
2–4µm	7.07	1.94	2.52	0.95	10.33	1.24	1.01	0.67	15.56	95	83	33	213	210	115	98	90	30	130	12.23	1.64	3	35	18.09	1.12
4–8µm	6.04	1.74	2.09	1.31	9.08	1.35	1.07	1.21	13.83	95	75	37	356	330	138	87	103	38	125	12.00	3.74	3	39	18.01	1.11
8–16µm	5.76	1.60	2.07	1.43	8.61	1.69	0.99	2.94	12.42	85	66	53	736	702	252	65	113	92	105	10.10	11.06	3	64	23.25	0.93
16–32µm	5.57	1.49	1.92	1.46	8.08	1.79	1.02	4.18	11.86	82	60	59	941	991	287	59	119	115	110	9.90	15.85	3	78	27.19	0.95
32–45µm	4.06	1.05	1.41	0.92	5.80	1.41	0.89	6.53	10.56	74	42	66	1224	1384	372	50	123	137	99	8.84	27	2	105	28.81	0.86
>45µm	0.33	0.24	0.32	0.40	1.63	18.94	0.05	1.96	3.33	19	4.83	10.54	180	355	139	11	704	129	31	0.97	20	1	9.40	7.25	0.41
>63µm	0.35	0.25	0.34	0.32	1.66	19.86	0.15	2.01	2.64	16	2.89	6.52	79	146	85	11	508	82	21	1.14	4.98	0	11.12	9.31	0.14
Bulk	6.60	1.21	2.28	0.22	8.16	1.89		0.36	23.32	NA	120	25.44	159	214	112	96	161	32	128	6.85	2.04	3	7.57	11.05	1.40
SK 31/4	Fe%	K%	Mg%	Na%	Al%	Ca%	Ti%	Mn%	Sc	V	Cr	Co	Ni	Cu	Zn	Rb	Sr	Y	Zr	Nb	Mo	Hf	Pb	Th	U
1µm	6.70	1.00	2.04	0.10	9.62	1.25	0.93	0.60	16.83	89	80	17.11	58	58	61	73	84	13	105	6.68	1.61	2	10.17	12.31	0.62
2µm	6.14	1.24	1.74	0.28	8.99	1.07	1.37	0.84	14.56	98	79	19.37	63	85	81	86	88	18	123	9.85	1.92	2	13.50	16.63	0.78
2–4µm	5.11	1.34	1.40	0.56	7.78	0.92	1.68	1.65	11.11	98	67	21.60	62	95	112	81	104	19	121	10.61	3.71	2	14.97	18.39	0.78
4–8µm	4.32	1.30	1.17	0.85	6.74	1.05	1.66	3.75	8.70	96	56	27.96	78	107	120	69	134	20	107	10.13	10.88	2	21.96	18.05	0.74
8–16µm	3.50	1.14	0.94	1.03	5.88	1.28	1.72	5.39	8.43	77	49	31.54	91	114	201	57	172	24	116	8.30	6.45	2	25.80	20.89	0.79
16–32µm	3.49	1.11	0.85	1.30	5.80	1.91	1.90	4.25	7.93	90	51	23.81	63	87	181	46	171	22	136	9.07	12.74	3	19.57	20.41	0.75
32–45µm	3.72	1.17	0.82	1.42	5.92	2.20	2.25	2.93	7.17	95	43	18.61	46	69	122	40	159	18	143	10.17	8.50	3	13.60	19.67	0.66
>45µm	3.67	1.21	1.15	1.08	5.20	6.88	0.29	2.72	8.33	79	76	30.18	93	162	516	64	394	60	58	4.30	20.48	2	99	10.70	1.36
>63µm	1.98	0.63	0.51	0.62	2.84	12.78	0.27	3.65	2.60	29	21	12.74	31	41	386	21	293	38	22	1.77	7.64	1	635	8.84	0.34
Bulk	7.01	1.24	2.25	0.30	8.54	1.17	NA	1.11	21.80	NA	140	27.00	93	94	158	105	155	24	124	9.70	9.29	3	11.17	11.93	1.89

Chapter 7
Summary and conclusions

Central Indian Basin, an intraplate abyssal plain region is dotted by several seamounts and other tectonic features such as fracture zones which are remnants of past tectonic activity. Numerous studies were carried out in the past in this region, which are related to manganese nodule occurrence, genesis, depositional environment aspects comprising of sediment sources and their components. However, a regional and quantitative approach was lacking. A systematic approach was adopted here and a variety of sedimentological and geochemical studies were carried out on 67 sediment cores collected from the CIB. Multiple geological proxies are integrated to improve our understanding of volcanogenic and hydrothermal mineralization processes prevailing in this intraplate region. Porewater studies were carried out on a basinal scale to estimate the benthic fluxes of nutrients across the sediment-water interface. New in this work is an attempt to study the seasonal variability in benthic fluxes. The time frame these sediments cover is Pleistocene onwards. While the regional approach is to quantify the sediment components and benthic fluxes comprised of systematically sampling in a grid of 1 degree spacing, detailed investigations were carried out on different sub-environments of a fracture zone environment, in order to understand the role of subsurface fluid circulation if any. Influence of size fractionation on elemental uptake in hydrothermally altered sediments was investigated. For comparison, sediments (Bay of Bengal, Arabian Sea, Equatorial Indian Ocean, siliceous ooze domain in CIB) which are not influenced by hydrothermal processes were also studied. A summary of the work carried out and salient findings of this study are described below:

- Geochemical studies of the bulk as well as the HCl soluble fraction of sediments collected from the flanks of a seamount near the 76°30’E fracture zone complex in the CIB indicate that they are ferruginous in nature and Fe/Mn ratios were comparable to ridge crest sediments elsewhere influenced by hydrothermal processes.
- Shale–normalized REE patterns were indistinguishable from metalliferous sediments and plume particulates from the EPR, TAG and Rainbow hydrothermal sites. The sediments studied were estimated to contain ~50–80% and 90–95% hydrothermal component in the bulk and leach fraction, respectively. While the ternary mixing calculations on bulk sediments indicated 35-45% metalliferous sediments could reproduce Fe and Mn values of the studied sediments, the HCl insoluble fraction indicated that the sulfide–like material dominates (~65%) over

terrigenous (20%) and MORB derived (15%) components the residue. Occurrence of both Fe-Mn oxides and sulfides was similar to those occurring in Red Sea.

- Infrared spectroscopic studies indicated the presence of dioctahedral smectites of monmorillonite–beidellite–nontronite series, with dominance of nontronite and ferruginous smectite suggesting a hydrothermal nature. Moreover, the composition of clay size fraction was similar to known hydrothermal nontronitic clays from the Alvin site. The temperature of formation for these smectites was estimated to range from 50° to 100°C.

- The presence of metalliferous sediments near the fracture zone suggests that the fracture zones may provide an easy conduit for mineralization processes in the area. While the earlier reports have shown spherules and lithic grains of metalliferous nature, this is the first study to report hydrothermal features in the bulk sediments of the CIB. The intraplate volcanoes located along the fracture zones, have therefore not only induced hydrothermal activity but also contributed nuclei and metals for the formation of the manganese nodules which are widespread in the CIB.

- Size analyses of carbonate, organic carbon and opal-free and <63µm size using laser particle size analyzer showed a distinct bimodal size distribution in all the sections of the cores studied. The two peaks occur mainly at 2-5 and 20-50µm size domains and represent the clay and silt fractions in the sediments. The clay fraction would mainly represent the clay minerals, microscopic observation of silt size fraction revealed abundant volcanic ash.

- Morphological and geochemical studies carried out on volcanic glass shards recovered from a north-south transect (75.5°E) from 10° to 16°S in the CIB have revealed their presence in all the sections of the cores studied. Two distinct ash abundant layers were found in 3 of the 5 cores studied. The youngest event was dated (~72-75 kyr) which corresponds to the well known Toba eruption (75 kyr) while the older event (85-109 kyr) does not correspond to any known volcanic eruption in the Indian Ocean. The chemistry of the shards indicated a rhyolitic composition of the magma.

- Insitu origin (phreatomagmatic eruption) was interpreted for the volcanic ash in the deeper layers corresponding to the older event as supported by the presence of large blocky/massive shards with a low degree of vesciculation indicating their formation by hydroclastic fragmentation while the younger event seemed to have

been explosive in nature and the shards transported aerially, as indicated by the abundance of bubble wall shards.

- Since the cores were located on the flanks of a seamount and in the vicinity of 76° 30' E fracture zone, we assume the possibility of an intraplate volcanism due to reactivation of tectonic activity in the faulted area in the past. Comparison with geochemical data from literature on other volcanic fields in and around the Central Indian Basin also suggests a possible in-situ origin.

- Major element composition of all the siliceous tephra in the possible source areas irrespective of their ages were nearly similar and therefore it is suggested that a caution may be exercised in using major element composition as the only criterion for determining the source of the tephras.

- Sedimentary organic carbon and porewater profiles of pH, NO_2^-, PO_4^{3-}, SiO_4 (covering the top 45 cm) differ with different depositional environments of the CIB. The porewater composition of dissolved nutrients through the sediment water interface shows a distinct regional distribution in the CIB.

- Porewater data from surface sediments at 47 locations were used to generate distribution maps of diffusive benthic fluxes of phosphate and silicate in the CIB for water depth > 5000 m. The phosphate fluxes vary between 1.65 and 0.04 mmol m^{-2} yr^{-1} and silicate: –12 and –597 mmol m^{-2} yr^{-1}. The most striking feature is the relatively large area north of 12°S with high silica efflux, which is dominated by siliceous ooze acts as a source of silica to bottom waters. Generally the basin acts as a sink than a source of phosphate. Low benthic fluxes in the southern part of the basin could be related to higher nutrients recycling in the surface waters, resulting in a lower export flux or a generally higher remineralization within the water column. The benthic silicate fluxes in the CIB also coincided with flow path of the Antarctic bottom waters (AABW) which enter the basin through the saddles at 10°S.

- Mass balance calculations of silica in the CIB reveal 19% of biogenic silica produced in the surface waters at 10°S reach the water sediment interface , which is also reflected by concomitant high in diffusive flux (~-376 mmol m^{-2} yr^{-1}) while at the southern station the bottom sediments receive (~9%) less than half of what is produced in the surface waters with a concomitant decrease in DSi (~-106.7 mmol m^{-2} yr^{-1}; Chauhan et al., 2010, unpublished). The high silica in the porewaters and fluxes in the

north thus result from a larger input of biogenic opal from the surface in this region compared to the southern stations.

- Seasonal variation studied in a north–south transect along 75.5°E longitude show a distinct change at ~13°S in the geochemical parameters which were probably influenced by the sediment type changes and local bathymetric changes. Seasonal pattern was seen in nutrient profile along the N S transect. Both the nutrients phosphate and silicate have shown seasonal variability in benthic fluxes. Phosphate fluxes were high during summer in the north, while winter fluxes were higher in the south. Changes in the silica fluxes with season is probably related to the intensity of the Antarctic bottom waters which seem to be more intense during the summer season, leading to variation in opal dissolution.

- The benthic environment seems to be responding to the surface water productivity in the CIB. During the summer, microbial activity results in high production of phosphate throughout the sediment column but particularly near the interface. Decomposition rates often decrease exponentially with depth below the interface, therefore seasonally high production often results in porewater concentration maxima a few centimeters below the sediment surface. In the winter, physical processes such as biogenic reworking, fluid transport associated with solute diffusion into burrows, result in extensive exchange of sediment porewater with the bottom waters and causes a general lowering of phosphate values from the earlier summer levels. This mechanism can be used to explain the changes seen in the northern part of the basin (north of 12°S). However the southern part of the basin responds differently to surface productivity.

- Organic carbon concentrations were higher in the surface in many of the cores suggesting either the fresh supplies over the period of study or increased surface productivity and export fluxes in recent times. Global maps of primary productivity display the most productive areas in the CIB are in the north of the basin (up to 12°S; PP > 6686 mmoles m^{2-} yr^{-1}). There is a good agreement between our porewater fluxes with that of primary productivity pattern in the overlying waters. Subsurface changes were also noticed in organic carbon concentrations which might suggest the changes in burrowing intensity with season.

- Seasonal changes noticed seem to be more distinct in areas with variable topography. Therefore, any benthic ecosystem model should include topography as

one of the important parameter in deciphering the dispersal patterns as well as in process control responding to seasonal climatic changes.

- The data presented here reveal a distinct coupling between the general pelagic regional distribution pattern of primary production and the response of benthic processes as indicated by the flux of remineralized nutrients, through a spatially differing degree of decoupling during transport and remineralization of particulate organic matter and biogenic silica observed in the CIB.

- Geochemical data of core top sediments has helped construct the regional elemental distribution maps of the lithogenic fraction of CIB sediments and has facilitated to evaluate the provenance, role of local geology and bathymetry in the sediment distribution and dispersal pattern in the area. Studying composition of surface sediments allowed us to understand the fate of the terrestrial materials transported into the basins as well as the factors controlling the distribution and geochemistry of sediments. Al, Ti, Nb and Zr were useful to trace the detrital signature in the basin. Distributional pattern of Rb/Sr were useful as an indicator of transportation pathways of fine-grained fraction of sediments along the bottom. Distribution patterns of these elements showed low concentration in the central part, while northern and southern part were enriched in these elements. High concentration in the northern part of the study area indicated a terrigenous influence mainly by the Ganges-Brahmaputra and rivers draining Deccan basalts. High concentration in the south of the basin indicated an additional source such as MORB and local volcanic rocks.

- A new approach was adopted to quantitatively assess the relative contribution of competing sources in the CIB by performing the mixing calculations of the REE data of top sediments. Mixing calculations using 4 endmembers such as biogenic, terrigenous, MORB and metalliferous components helped to estimate the relative proportion of contribution of each endmember to the sediments. The calculations showed that the REE in the sediments of the CIB were a mixture of 0–10% siliceous component, 5–90% terrigenous component, 0–35% MORB component and 0–100% metalliferous component.

- Elemental geochemistry of different size fractionated hydrothermally altered sediments of CIB were studied and compared with those not influenced by hydrothermalism from Arabian Sea, Equatorial Indian Ocean, Bay of Bengal,

siliceous domain of the Indian Ocean. Geochemical study carried out on nine size fractions (<1, 1-2, 2-4, 4-8, 8-16, 16-32, 32-45, 45-63 and >63 µm)) has shown that the maximum trace element and REE concentrations were seen in the hydrothermally altered pelagic clay sediments which were upto 10 times enriched than the sediments not influenced by hydrothermal activity. REE showed fractionation with grain size with the sand size fraction (>63 µm) having the least concentration of trace elements, probably due to enrichment of quartz, and biogenic material.

Future studies:

- While the comprehensive data set presented here has allowed to decipher the natural dispersal pathways and to quantify the modern day sources of sediments to the basin, on geological time scales, the tectonic uplift and climate changes in the source area would affect the provenance signatures. Therefore there is a need to quantify the changes in different contributory sources in the geological past. Detailed isotopic studies of elements such as Sr, Nd, Pb and Hf would allow us to study the change in provenance and climate change in the area.
- Geochemical investigations on the hydrothermally altered sediments have shown enrichment of certain elements such as Fe, Cu, Pb, Zn etc compared to normal sediments of the CIB. Fractionation of these elements into different chemically operational phases during hydrothermal alteration would add to the knowledge on the carrier phase for these elements during hydrothermal alteration.
- Detailed investigation along a fracture zone in the CIB revealed past volcanic activity whose source could not be ascertained. Further investigations along other fracture zones in the CIB would be needed to constrain the source, mechanism of intraplate volcanism and extent of volcanic activity in the area.
- While the regional distributional patterns of benthic fluxes of nutrient fluxes are presented here, porewater oxygen and elements such as lanthanides, Mn, Fe would help contribute to the geochemical balance. The data presented here would help to generate a benthic ecosystem model for the CIB.
- The hydrothermally altered sediments have shown signatures of degassing through upward migrating solutions which will definitely alter the chemical constitution of the porewater in these sediments. Therefore a complete understanding of the processes responsible for the chemical changes in the composition of the

interstitial waters is necessary. It is necessary to study the inorganic chemical composition of the fluids and also stable isotopes, in particular $^{87}Sr/^{86}Sr$, $^{6}Li/^{7}Li$, Zn and the oxygen isotopic composition of the fluids and associated rocks in the hydrothermal system. Isotopic studies of elements sensitive to redox conditions such as molybdenum would be needed to trace the provenance and redox conditions operating during the uptake of metals in the different size fractions.

Bibliography

Akagi, T., Fu, F. –F., Hongo, Y., Takahashi, K., 2011. Composition of rare earth elements in settling particles collected in the highly productive North Pacific Ocean and Bering Sea: Implications for siliceous–matter dissolution kinetics and formation of two REE–enriched phases Geochim. Cosmochim. Acta 75, 4857–4876.

Albarède, F., 1995. Introduction to Geochemical Modeling, 543 pp, Cambridge Univ. Press, New York.

Albert, P. G., Tomlinson, E. L., Smith, V. C., Di Roberto, A., Todman, A., Rosi, M., Marani, M., Muller, W., Menzies M. A., 2012. Marine–continental tephra correlations: Volcanic glass geochemistry from the Marsili Basin and the Aeolian Islands, Southern Tyrrhenian Sea, Italy. J. Volcanol. Geothermal Res., 229–230, 71–94.

Alt, J. C., 1988. Hydrothermal oxide and nontronite deposits on seamount in the Eastern Pacific. Mar. Geol., 81, 227–239.

Alt, J. C., Honnorez, J., 1984. Alteration of upper oceanic crust DSDP site 417: Mineralogy and chemistry. Contrib. Mineral. Petrol., 87, 149–169.

Alt, J. C., Teagle, D. A. H., Brewer, T., Shanks, W. C. III., Halliday, A., 1998. Alteration and mineralization of an oceanic forearc and the ophiolite–ocean crust analogy. J. Geophy. Res., 103, 12365–12380.

Altschuler, Z. S., 1980. The geochemistry of trace elements in marine phosphorites. Part I: Characteristic abundances and enrichment. In: Bentor, K. K. (Ed.), Marine Phosphorites. Society of Economic Paleontologists and Mineralogists. Special Publication, 29, 19–30.

Amakawa, H., Alibo, D. S., Nozaki, Y., 2000. Nd isotopic composition and REE pattern in the surface waters of the eastern Indian Ocean and its adjacent seas. Geochim. Cosmochim. Acta., 64, 1715–1727.

Amano, K., Taira, A., 1992, Two–phase uplift of Higher Himalayas since 17 Ma: Geol., 20, 391–394.

Ansari, Z. A., 2000. Distribution of deep–sea benthos in the proposed mining area of Central Indian Ocean. Mar. Geo. Geotech., 18, 201–207.

Ansari, Z. A., Ingole, B. S., Parulekar, A. H., 1996. Benthos of the EEZ of India. In: Qasim, S. Z., Roonwal, G. S. (Eds.), India's exclusive economic zone—resources, exploitation, management. Omega Scientific Publishers, New Delhi, pp. 74–86.

Antonie, D., Andre, J. M., Morel, A., 1996. Oceanic primary production. Estimation at global scale from satellite (coastal zone color scanner) chlorophyll. Global Biochem. Cycles 10, 1, 57–69.

Aoki, S., Kohyama, N., Hotta, H., 1996. Hydrothermal clay minerals found in sediment containing yellowish–brown material from the Japan Basin. Mar. Geol., 129, 3–4, 331–336.

Aoki, S., Kohyama, N., Ishizuka, T., 1991. Sedimentary history and chemical characteristics of clay minerals in cores from the distal part of the Bengal Fan (ODP 116). Mar. Geol., 99(1–2), 175–185.

Aoki, S., Sudo, T., 1973. Mineralogical study of the core samples from the Indian Ocean, with special reference to the vertical distribution of clay minerals. J. Oceanogr. Soc. Japan, 29, 87–93.

Arculus, R. J., Bloomfield, A. L., 1992. Major–element chemistry of ashes from sites 782, 784 and 786 in the Bonin Forearc. In: Fryer, P., Pearce, J. A., Stokking,

L. B et al. (Eds.), Proc ODP Sci Results 125. College Station TX (Ocean Drilling Program) 125, 277–292.

Balaram, V., Rao, T. G., 2002. Rapid multi–elemental determination in geological samples by microwave acid digestion and ICP–MS. Proc. 3rd ISMAS (BC) Bangalore, India, pp. 22–27.

Banakar, V. K., 1990. Uranium–Throium isotopes and transition metal fluxes in two oriented manganese nodules from the Central Indian Basin: implications for nodule turnover. Mar. Geol., 95, 71–76.

Banakar, V. K., Galy, A., Sukumaran, N. P., Parthiban, G., Volvaiker, A. Y., 2003. Himalayan sedimentary pulses recorded by silicate detritus within a ferromanganese crust from the Central Indian Ocean. Earth Planet. Sci. Lett., 205, 337–348.

Banakar, V. K., Gupta, S. M., Padmavati, V. K., 1991. Abyssal sediment erosion from the Central Indian Basin: Evidence from radiochemical and radiolarian studies. Mar. Geol., 96, 167–173.

Banakar, V. K., Parthiban, G., Pattan, J. N., Jauhari, P., 1998. Chemistry of surface sediment along a north–south transect across the equator in the Central Indian Basin: An assessment of biogenic and detrital influences on elemental burial on the seafloor. Chem. Geol., 147, 217–232.

Banerjee, R., 1998. Mineralogical and geochemical characters of surface sediments from the central Indian Basin. Curr. Sci., 75(12), 1364–1371.

Barbanti, A., Bergamini, M. C., Frascari, F., Miserocchi, S., Ratta, M., Rosso, G., 1995. Diagenetic processes and nutrient fluxes at the sediment–water interface, Northern Adriatic Sea Italy. Interactions between sediments and water. Aust. J. Mar. Freshwater Res., 46, 55–67.

Barksdale, J., 1968. Titanium. In: Clifford A. H. (Ed.). The Encyclopedia of the Chemical Elements. New York: Reinhold Book Corporation. pp.732–738. LCCN68–29938.

Barrett, T. J., Jarvis, I., 1988. Rare earth element geochemistry of metalliferous sediments from DSDP Leg 92, the East Pacific Rise transect. Chem. Geol., 67, 243–259.

Barrett, T. J., Taylor, P. N., Lugowski, J., 1987. Metalliferous sediments from DSDP Leg 92: the East Pacific Rise Transect. Geochim. Cosmochim. Acta., 51, 2241–2253.

Basile, I., Petit, J. R., Touron, S., Grousset, F. E., Barkov, N., 2001. Volcanic layers in Antarctic (Vostok) ice cores: Source identification and atmospheric implications: J. Geophy. Res., 106, 31915–31931.

Basu, A. R., Sharma, M., DeCelles, P. G., 1990. Nd, Sr isotopic provenance and trace element geochemistry of Amazonian Foreland Basin Fluvial Sands, Bolivia and Peru: implications for Ensialic Andean Orogeny. Earth Planet. Sci. Lett., 105, 149–169.

Batiza, R., Fox, P. J., Vogt, P. R., Cande, S. C., Grindlay, N. R., 1989. Abundant Pacific type near–ridge seamounts in the vicinity of the Mid–Atlantic Ridge, 26 °S. J. Geol., 97, 209–220.

Bau, M., 1991. Rare–earth element mobility during hydrothermal and metamorphic fluid–rock interaction and the significance of the oxidation state of europium. Chem. Geol., 93, 219–230.

Bednarz, U., Schmincke, H. –U., 1994. Composition and origin of volcaniclastic sediments in the Lau Basin (SW–Pacific), ODP Leg 135 (sites 834–893). In:

Hawkins, J., Parson, L., Allan, J., et al., (Eds.), Proc ODP Sci Results 135. College Station TX (Ocean Drilling Program) 135, 51–74.

Ben Othman, D., White, W. M., Patchett, J., 1989. The geochemistry of marine sediments, island arc magma genesis, and crust–mantle recycling. Earth Planet. Sci. Lett., 94, 1–21.

Bender, M. L., Fanning, K. A., Froelich, P. N., Heath, G. R., Maynard, V., 1977. Interstitial nitrate profiles and oxidation of sedimentary organic matter in the Eastern Equatorial Atlantic. Sci., 198, 605–609.

Bender, M., Broeker, W. S., Gornitz, V., Middel, U., Day, R., Sun, S. S., Biscaye, P., 1971. Geochemistry of three cores from the East Pacific Rise. Earth Planet. Sci. Lett., 12, 425–433.

Berelson, W. M., Hammond, D. E., ÕNeil, D., Xu, X. –M., Chin, C., Zukin, J., 1990. Benthic fluxes and porewater studies from sediments of the central equatorial north Pacific: Nutrient diagenesis. Geochim. Cosmochim. Acta., 54, 3001–3012.

Berlo, K., Blundy, J., Turner, S., Cashman, K., Hawkesworth, C., Black, S., 2004. Geochemical Precursors to Volcanic Activity at Mount St. Helens, USA. Sci., 306, 1167–1169.

Bernat, M., 1973. Les terres rares dans le milieu marin. Ph.D. thesis, Paris, Univ. Paris, 112p.

Berner, R. A., 1973. Phosphate removal from sea water by adsorption on volcanogenic ferric oxides. Earth Planet. Sci. Lett., 18, 77–86.

Berner, R. A., 1980. Early diagenesis–A theoretical approach. Prinston University Press.

Bhatia, M. R., Crook, K. A. W., 1986. Trace element characteristics of greywackes and tectonic setting discrimination of sedimentary basins. Contrib. Mineral. Petrol., 92, 181–193.

Bhuiyan, M. A. H., Rahman, M. J. J., Dampare, S. B., Suzuki, S., 2011. Provenance, tectonics and source weathering of modern fluvial sediments of the Brahmaputra–Jamuna River, Bangladesh: Inference from geochemistry. J. Geochem. Explor., 111, 113–137.

Bianchi, T. S., Mitra S., McKee, B. A., 2002. Sources of terrestrially–derived organic carbon in lower Mississippi River and Louisiana shelf sediments: implications for differential sedimentation and transport at the coastal margin. Mar. Chem., 77, 211–223.

Billen, G., 1982. An idealized model of nitrogen recycling in marine sediments. Am. J. Sci., 282, 512–541.

Biscaye, P. E., 1965. Mineralogy and sedimentation of recent deep–sea clay in the Atlantic Ocean and adjacent seas and ocean. Geol. Soc. Am. Bull., 76, 803–832.

Bishop, J. K. B., Edmond, J. M., Ketten, D. R., Bacon, M. P., Silker, W. B., 1977. The chemistry, biology, and vertical flux of particulate matter from the upper 400 m of the equatorial Atlantic Ocean Deep–sea Research Part II–topical Studies in Oceanography – Deep Sea Res. II, 24, 6, 511–520.

Bloemendal, J., Lamb, B., King, J. W., 1988. Paleoenvironmental implications of rock–magnetic properties of Late Quaternary sediment cores from the eastern equatorial Atlantic. Paleoceanography 3, 61–87.

Boles, J. R., 1977. Zeolites in deep–sea sediments. In: Mineralogy and Geology of Natural Zeolites, Miner. Soc. Amer., Short Course Notes, 4, 137–163.

Bölke, J. K., Honnorez, J., Honnorez–Guerstein, B. –M., 1980. Alteration of basalts from Site 396–B, DSDP: petrographic and mineralogic studies. Contr. Mineral. Petrol., 73, 341–364.

Borole, D. V., 1993. Late Pleistocene sedimentation: A case study in the Central Indian Ocean Basin. Deep Sea Res., 40, 761–775.

Boström, K., Peterson, M. N. A., 1966. Precipitates from hydrothermal exhalations on the East Pacific Rise. Econ. Geol., 61, 1258–1265.

Boström, K., Peterson, M. N. A., 1969. The origin of aluminium–poor ferromanganoan sediments in areas of high heat flow on the East Pacific Rise. Mar. Geol., 7, 427–447.

Boudreau, B. P., 1997. Diagenetic models and their implementation. Springer–Verlag, New York.

Bouquillon, A., France–Lanord, C., Michard, A., Tiercelin, J. J., 1990. Sedimentology and isotopic chemistry of the Bengal fan sediments: the denudation of the Himalaya. Proc. ODP Sci. Results., 116, 43–57.

Bourlès, D. L., Raisbeck, G. M., Brown, E. T., Yiou, F., Edmond, J. M., 1991. Beryllium isotope systematics of submarine hydrothermal systems. Earth Planet. Sci. Lett., 105, 534–542.

Braitseva, O. A., Ponomareva, V. V., Sulerzhitsky, L. D., Melekestsev, I. V., Bailey, J., 1997. Holocene key-marker tephra layers in Kamchatka, Russia. Quat. Res., 47, 125–139.

Burton, K. W., Vance, D., 2000. Glacial–interglacial variations in the neodymium isotope composition of seawater in the Bay of Bengal recorded by planktonic foraminifera. Earth Planet. Sci. Lett., 176, 425–441.

Busacca, A. J., Marksb, H. M., Rossi, R., 2001. Volcanic Glass in Soils of the Columbia Plateau, Pacific Northwest, USA. Soil Sci. Soc. Am. J., 65, 161–168.

Carey S., 1997. Influence of convective sedimentation on the formation of widespread tephra fall layers in the deep sea. Geol., 25, 9:839–842.

Caulet, J. P., 1992. Les rapports des campagnes a la mer a bord du Marion–Dufresne, D65/SHIVA du 17 aout au 14 September 1990. TAAF–MNHN. Paris, p. 53.

Cave, R. R., German, C. R., Thomson, J., Nesbitt, R. W., 2002. Fluxes to sediments from the Rainbow Hydrothermal plume, 36° 14’ N on the MAR. Geochim. Cosmochim. Acta., 66, 1905–1923.

Chauhan, O. S., Gujar, A. R., 1996. Surficial clay mineral distribution on the southwestern continental margin of India: Evidence of input from the Bay of Bengal Cont. Shelf Res., 16(3), 321–33.

Chauhan, O. S., Gujar, A. R., Rao, C. M., 1994. On the occurrence of ferromanganese mcronodules from the sediments of the Bengal Fan; a high terrigenous sediment input region. Earth Plant. Sci. Lett., 128, 563–573.

Chauhan, O. S., Patil, S. K., Suneethi, J., 2004. Fluvial influx and weathering history of the Himalayas since Last Glacial Maxima – Isotopic, sedimentological and magnetic records from the Bay of Bengal. Curr. Sci., 87(4), 509–515.

Chauhan, O. S., Suneethi, J., 2001. 18 Ka BP records of climatic changes, Bay of Bengal: Isotopic and sedimentological evidences. Curr. Sci., 81(9), 1231–1234.

Chavagnac, V., German, C. R., Milton, J. A., Palmer, M. R., 2005. Sources of REE in sediment cores from the Rainbow vent site (36° 14’ N, MAR). Chem. Geol., 216, 329–352.

Cherkashev, G. A., 1992. Geochemistry of metalliferous sediments from ore–forming areas in the ocean. In: Gramberg, I. S., Ainemer, A. I. (Eds.), Hydrothermal Sulfide Ores and Metalliferous Sediments of the Ocean. St. Petersburg (Nedra), pp. 138–152 (in Russian).

Chesner, C. A., Rose, W. I., Deino, A., Drake, R., Westgate, J. A., 1991. Eruptive history of the Earth's largest Quaternary caldera Toba, Indonesia clarified. Geol., 19, 200–203.

Clauer, N., 1982. The rubidium–strontium method applied to sediments: Certitudes and uncertainties. In: Odin, G. S. (Ed.), Numerical dating in stratigraphy. New York, John Wiley & Sons, pp. 245–276.

Clauer, N., Stille, P., Bonnot–Courtois, C., Moore, W. S., 1984. Nd–Sr isotopic and REE constraints on the genesis of hydrothermal manganese crusts in the Galapagos. Nature 311, 743–745.

Clemens, S. C., Prell, W. L., Murray, D. W., Shimmield, G. B., Weedon, G. P., 1991. Forcing mechanisms of the Indian monsoon. Nature 353, 720–725.

Cochran, J. R., 1990. Himalayan uplift, sea level, and the record of Bengal Fan sedimentation at the ODP Leg 116 sites, in Cochran, J. R., et al., Proceedings of the Ocean Drilling Program, Scientific results, vol 116: College Station, Texas, Ocean Drilling Program, pp. 397–414.

Cole, T. G., 1985. Composition, oxygen isotope geochemistry, and the origin of smectite in the metalliferous sediments of the Bauer Deep, southeast Pacific. Geochim. Cosmochim. Acta., 49, 221–235.

Colley, S., Thomson, J., Wilson, T. R. S., Higgs, N. C., 1984. Post depostional migration of elements during diagenesis in brown clay and turbidite sequences in the northeast Atlantic. Geochim. Cosmochim. Acta., 48, 1223–1234.

Collier, R. W., Edmond, J. M., 1984. The trace element geochemistry of marine biogenic particulate matter. Prog. Oceanogr., 13, 113–199.

Condie, K. C., 1993. Chemical composition and evolution of the upper continental crust: contrasting results from surface samples and shales. Chem. Geol., 104, 1–37.

Condie, K. C., Lee, D., Farmer, G. L., 2001. Tectonic setting and provenance of the Neoproterozoic Uinta Mountain and Big Vottonwood groups, northern Utah: constraints from geochemistry, Nd isotopes, and detrital modes. Sed. Geol., 141–142, 443–464.

Condie, K. C., Wronkiewicz, D. J., 1990. The Cr/Th ratio in Precambrian pelites from the Kaapvaal Craton as an index of craton evolution. Earth Planet. Sci. Lett., 97, 256–267

Crawford, A. R., 1974. Indo–Antarctica, Gondwanaland, and the distortion of a granulite belt. Tectonophysics 22, 141–157

Cronan, D. S., 1976. Basal metalliferous sediments from the eastern Pacific. Geol. Soc. Am. Bull., 87, 928–934.

Cronan, D. S., 1980. Underwater Minerals. Academic Press, London, 362 pp

Cullen, J. L., 1981. Microfossil evidence for changing salinity patterns in the Bay of Bengal over the last 20000 years. Palaeogeogr. Palaeoclimatol. Palaeoecol., 35, 315–356, doi: 10.1016/0031–0182(81)90101–2.

Cullers, R. L, Basu, A., Suttner, L. J., 1988. Geochemical signature of provenance in sand–size material in soils and stream sediments near the Tobacco Root batholith, Montana, U.S.A. Chem. Geol., 70, 335–348.

Cullers, R. L., 1994a. The chemical signature of source rocks in size fractions of Holocene stream sediment derived from metamorphic rocks in the wet mountains region, Colorado, USA. Chem. Geol., 113, 327–343.

Cullers, R. L., 1994b. The controls on the major and trace element variation of shales, siltstones and sandstones of Pennsylvanian–Permian age from uplifted continental blocks in Colorado to platform sediment in Kansas, USA. Geochim. Cosmochim. Acta., 58, 4955–4972.

Cullers, R. L., 2000. The geochemistry of shales, siltstones and sandstones of Pennsylvian–Permian age, Colorado, USA: implications for provenance and metamorphic studies. Lithos 51, 181–203.

Cullers, R. L., 2002, Implication of elemental concentrations for provenance, redox conditions, and metamorphic studies of shales and limestones bear Pueblo, CO, USA. Chem. Geol., 191, 305–327.

Cullers, R. L., Podkovyrov, V. N., 2000. Geochemistry of the Mesoproterozoic Lakhanda shales in southeastern Yakutia, Russia: implications for mineralogical and provenance control, and recycling. Precambrian Res., 104, 77–93.

Curray, J. R., Emmel, F. J., Moore, D. G., Russel, W. R., 1982. Structure, tectonics, and geological history of the northeastern Indian Ocean, In: Nairn, A. E., Stheli, F. G. (Eds.), The Ocean Basins and Margins: The Indian Ocean. vol 6, New York, Plenum, pp. 399–450.

Das, A., Fernandes, C. E. G., Naik, Sonali., Nath, B. N., Suresh, I., Mascarenhas-Pereira, M. B. L., Gupta, S. M., Khadge, N. H., PrakashBabu, C., Borole, D. V., Sujith, P. P., Valsangkar, A. B., Mourya, B. S., Biche, S. U., Sharma, R., LokaBharathi, P. A., 2011. Bacterial response to contrasting sediment geochemistry in the central Indian Basin. Sedimentology 58(3), 756-784.

Das, P., Iyer, S. D., Kodagali, V. N., 2007. Morphological characteristics and emplacement mechanism of the seamounts in the Central Indian Ocean Basin. Tectonophysics 443, 1–18.

Das, P., Iyer, S. D., Kodagali, V. N., Krishna, K. S., 2005. A new insight into the distribution and origin of seamounts in the Central Indian Ocean Basin. Mar. Geod., 28, 259–269.

Davies, S. M., Wohlfarth, B., Wastegard, S., Andersson, M., Blockley, S., Possnert, G., 2004. Were there two Borrobol Tephras during the early Late–glacial period: implications for tephrochronology? Quat. Sci. Rev., 23, 581–589.

De Lange, G. J., 1986. Chemical composition of interstitial water in cores from the Nares abyssal plain (western North Atlantic). Oceanol. Acta., 9, 159 168.

Debrabant, P., Fagel, N., Chamley, H., Bout, V., Caulet, J. P., 1993. Neogene to Quaternary clay mineral fluxes in the Central Indian basin. Palaeogeogr. Palaeoclimatol. Palaeoecol., 103 (3–4), 117–131.

Deer, W., Howie, R., Zussman, J., 1967. Rock–Forming Minerals. Pearson Education Ltd publishing. 2nd edition.

Dehn, J., Farrel, J. W., Schmincke, H. –U., 1991. Neogene tephrochronology from site 758 on Ninety East Ridge: Indonesian arc volcanism of the past 5 Ma. Proc. ODP, Sci. Results., 121, 273–295.

Dekov, V. M, Marching, V., Rajta, I., Uzony, I., 2003. Fe-Mn micronodules born in metalliferous sediments of two spreading centers, the East Pacific Rise and Mid-Atlantic Ridge. Mar. Geol., 199, 101–121.

Dekov, V. M., Damyanov, Z. K., Kamenov, G. D., Bonev, I. K., Bogdanov, K. B, 1999. Native copper and α–copper–zinc in sediments from the TAG

hydrothermal field (Mid–Atlantic Ridge, 26° N): nature and origin. Mar. Geol., 161, 229–245.

Dekov, V. M., Damyanov, Z. K., Kamenov, G. D., Bonev, I. K., Rajta, I., Grime, G. W., 2001. Sorosite (ŋ–Cu_6Sn_5)–bearing native tin and lead assemblage from the Mir zone (Mid–Atlantic Ridge, 26° N). Oceanol. Acta., 24, 205–220.

DeMaster, D. J., 1979. The marine budget of silica and ^{32}Si. Ph.d. Thesis, Univ. Yale, Connecticut, 308 pp.

DeMaster, D. J., 1981. The supply and accumulation of silica in the marine environment. Geochim. Cosmochim. Acta., 45, 1715–1732.

Derry, L. A, France–Lanord, C., 1997. Himalayan weathering and erosion fluxes: climate and tectonic controls. In: Ruddiman, W. F. (Ed.), Tectonic uplift and climate change. New York, Plenum Press, pp. 289–311.

Derry, L. A., France–Lanord, C., 1996. Neogene Himalayan weathering history and river $^{87}Sr/^{86}Sr$: impact on the marine record. Earth Planet. Sci. Lett., 142, 59–74.

Desa, M., Ramana, M. V., Ramprasad, T., 2009. Evolution of the Late Cretaceous crust in the equatorial region of the Northern Indian Ocean and its implication in understanding the plate kinematics. Geophys. J. Int., 177, 1265–1278.

Descourvieres, C., Douglas, G., Leyland, L., Hartog, N., Prommer, H., 2011. Geochemical reconstruction of the provenance, weathering and deposition of detrital–dominated sediments in the Perth Basin: The Cretaceous Leederville Formation, south–west Australia. Sediment. Geol., 236, 62–76.

deSousa, S. N., Sardessai, S. D., Rameshbabu, V., Murty, V. S. N., Gupta, G. V. M., 2001. Chemical characteristics of Central Indian Basin waters during the southern summer. Deep Sea Res. Part II., 48, 3343–3352.

Dia, A., Dupré, B., Allègre, C. J., 1992. Nd isotopes in Indian Ocean sediments used as a tracer of supply to the ocean and circulation paths. Mar. Geol., 103, 349–359.

Dickson, R. R., Brown, J., 1994. The production of North Atlantic Deep Water: sources, rates, and pathways. J. Geophys. Res., 99, 12 319–12 341.

Diehl, J. F., Onstott, T. C., Chesner, C. A., Knight, M. D., 1987. No short reversals of Brunhes age recorded in the Toba Tuffs, north Sumatra, Indonesia. Geophys. Res. Lett., 14, 753 – 756.

Dileep Kumar, M., Yuan–Hui, Li., 1996. Spreading of water masses and regeneration of silica and 226Ra in the Indian Ocean. Deep–Sea Res. II., 43(1), 83–110.

Dippner, J. W., 1998. Competition between different groups of phytoplankton for nutrients in the southern North Sea. J. Mar. Syst., 14, 181–198.

Dollar, S., Smith, S., Vink, S., Obresbski, S., Hollibaugh, J., 1991. Annual cycle of benthic nutrient fluxes in Tomales Bay, California and contribution of the benthos to total ecosystem metabolism. Mar. Ecol. Prog. Ser., 79, 115–125.

Donnelly, T. W., 1980. Chemical composition of deep sea sediments–Sites 9 through 425, Legs 2 through 54. In: Rosendahl, B. R., Hékinian, R., et al., (Eds.), Initial. Rep. Deep Sea Drill. Proj., 54, Washington, D.C: Government Printing Office, pp. 899–949.

Dorrike, A. V. S., Cochran, J. R., and ODP Leg 116 shipboard scientific party., 1989. The Bengal Fan: some preliminary results from ODP drilling. Geo–Mar. Lett., 9, 1–10.

Douville, E., Charlou, J. L., Oelkers, E. H., Bienvenu, P., Jove Colon, C. F., Donval, J. P., Fouquet, Y., Prieur, D., Appriou, P., 2002. The Rainbow vent fluids (36° 14' N, MAR): the influence of ultramafic rocks and phase separation on trace

metal content in Mid–Atlantic Ridge hydrothermal fluids. Chem. Geol., 184, 37–48.

Duce, R. A., Tindale, N. W., 1991. Atmospheric transport of iron and its deposition in the ocean. Limnol. Oceanogr., 36, 1715–1726.

Dugdale R. C., Wilkerson F. P., 1989. Regional perspectives in global new production. In: Denis, M. M. (Ed.), Oceanologie Actualite et Prospective, Proceedings of the Centennial of Station d'Endoume, Marseille, pp. 289–309.

Dugmore, A. J., Larsen, L., Newton, A. J., 2000. Tephrochronology and its application to Late Quaternary Environmental Reconstruction, with Special Reference to the North Atlantic Islands. In: Buck, C. E., Millard, A. R. (Eds.), Tools for Constructing Chronologies, Springer-Verlag, London, pp. 173-188.

Duncan, R. A., 1991. Age distribution of volcanism along aseismic ridges in the eastern Indian Ocean, In: Weissel, J. K., Peirce, J. et al., (Eds.), Proceedings of ODP, Scientific Results, College Drilling Program, College Station, vol.121, pp. 507–517.

Dyment, J., 1993. Evolution of the Indian Ocean Triple Junction between 65 and 49 Ma (anomalies 28 to 21). J. Geophys. Res., 98, 13863–13878.

Dyment, J., Gallet, Y., 1999. The Magofond 2 cruise: a surface and deep tow survey on the past and present Central Indian Ridge. InterRidge News 8, 25–31.

Edmond, J. M., Jacobs, S. S., Gordon, A. L., Mantyla, A. W., Weiss, R. F., 1979. Water column anomalies in dissolved silica over opaline pelagic sediments and the origin of the deep silica maximum. J. Geophys. Res., 84.

Edmonds, H. N., German, C. R. 2004. Particle geochemistry in the Rainbow hydrothermal plume, Mid–Atlantic Ridge. Geochim. Cosmochim. Acta., 68 (4), 759–772.

Egge, J. K., 1998. Are diatoms poor competitors at low phosphate concentrations? J. Mar. Syst., 16, 191–198.

El Wakeel, S. K., Riley, J. P., 1961. Chemical and mineralogical studies of deep–sea sediments. Geochim. Cosmochim. Acta., 25(2), 110–146.

El–Sayed, S. Z., Taguchi, S., 1979. Phytoplankton standing crop and primary productivity in the Tropical Pacific. In: Marine Geology and Oceanography of Pacific Manganese Nodule Province. New York and London: Prenum Press. pp. 241–286.

Emerson, S., Jahnke, R., Bender, M., Froelich, P., Klinkhammer, G., Bowser, C. J., Setlock, G., 1980. Early diagenesis in sediments from the Eastern Equatorial Pacific. I. Porewater nutrient and carbonate results. Earth Planet. Sci. Lett., 49, 57-80.

Emsley, J., 1980. The phosphorus cycle. In: The handbook of organic chemistry, (Ed.), Hutzinger, O., Springer Verlag, Berlin.

Emsley, J., 2001. Nature's Building Blocks: An A–Z Guide to the Elements. Oxford, England: Oxford University Press

Fagel, N., 2007. Clay minerals, deep circulation, and climate marine clay minerals, deep circulation and climate. In: Hillaire–Marcel, C., de Vernal, A. (Eds.), Paleoceanography of the Late Cenozoic, Methods. vol 1, Elsevier, Amsterdam, pp. 139–184.

Fagel, N., André, L., Debrabant, P., 1997. Multiple seawater derived geochemical signatures in Indian oceanic pelagic clays. Geochim. Cosmochim. Acta., 61, 989–1008.

Fagel, N., Debrabant, P., André, L., 1994. Clay supplies in the Central Indian Basin since the Late Miocene: climatic or tectonic control? Mar. Geol., 122, 151–172.

Farmer, V. C., Russell, J. D., 1967. Infra–red absorption spectrometry in clay studies. Proc. 15th Natl. Conf. on Clays and Clay Minerals, pp. 121–142.

Faure, G., 1986. Principles of Isotope Geology. John Wiley & Sons, New York, 587 pp

Fedo, C. M., Eriksson, K. A., Krogstad, E. J., 1996. Geochemistry of shales from the Archean (≈3.0 Ga) Buhwa Greenstone belt, Zimbabwe: Implication for provenance and source area weathering. Geochim. Cosmochim. Acta., 60, 1751–1763.

Fedo, C. M., Nesbitt, H. W., Young, G. M., 1995. Unraveling the effect of potassium metasomatism in sedimentary rocks and paleosols, with implications for paleoweathering conditions and provenance. Geol., 23, 921–924.

Fedorov, L. V., Grikurov, G. E., Kurinin, R. G., and Masolov, V. N., 1982. Crustal structure of the Lambert Glacier Area from geophysical data, In: Craddock, C., Loveless, J. K., Vierima, T. L., Crawford, K., (Eds.), Antarctica Geoscience, University of Wisconsin Press, Madison, WI. pp. 931–936.

Feely, R. A., Lewison, M., Massoth, G. J., Robert–Baldo, G., Lavelle, J. W., Byrne, R. H., Von Damm, K. L., Curl Jr, H. C., 1987. Composition and dissolution of black smoker particles from active vents on the Juan de Fuca Ridge. J. Geophys. Res., 92, 11,347–11,363.

Feely, R. A., Trefry, J. H., Lebon, G. T., German, C. R., 1998. The relationship between P/Fe and V/Fe ratios in hydrothermal precipitates and dissolved phosphate in seawater. Geophys. Res. Lett., 25 (13), 2253–2256.

Feng, R., Kerrich, R., 1990. Geochemistry of fine–grained clastic sediments in the Archean Abitibi greenstone belt, Canada, Implications for provenance and tectonic setting. Geochim. Cosmochim. Acta., 54, 1061–1081.

Fick, A., 1955. Über diffusion. Ann. Phys. Leipzig 94, pp. 59–68.

Fieux, M., Andrié, C., Charriaud, E., Ilahude, A. G., Metzl, N., Molcard, R., Swallow, J. C., 1996. Hydrological and chlorofluoromethane measurements of the Indonesian throughflow entering the Indian Ocean. J. Geophys. Res., 101 (C5), 12433–12454.

Fisher, R. V., Schmincke, H. –U., 1984. Pyroclastic rocks. Springer, Verlag, Berlin.

Fisk, M. R., Duncan, R. A., Baxter, A. N., Greenough, J. D., Hargraves, R. B., Tatsumi, Y., Shipboard Scientific Party., 1989. Reunion hotspot magma chemistry over the past 65 m.y.: Results from Leg 115 of the Ocean Drilling Program. Geol., 17, 934–937.

Folk, R. L., 1966. A review of grain size parameters. Sedimentology 6, 73–93.

Fornari, D. J., Batiza, R., Allan, J. F., 1987. Irregularly shaped seamounts near the East Pacific Rise: Implications for seamount origin and Rise axis processes. In: Keating, B. H., et al., (Eds.), Seamounts, islands and atolls. Geophys. Monogr., Am. Geophys. Union, 43, pp. 13–21.

France–Lanord, C, Derry, L. A., 1997. Organic carbon burial forcing of the carbon cycle from Himalayan erosion. Nature 390 65–67.

France–Lanord, C., Derry, L., Michard, A., 1993. Evolution of the Himalaya since Miocene time: isotopic and sedimentologic evidence from Bengal Fan. In: Treolar, P. J., Searles, M., (Eds.), Himalayan Tectonics. Geol. Soc. London Spec. Publ., 74, pp. 603–621.

Frank, M., Marbler, H., Koschinsky, A., van de Flierdt, T., Klemm, V., Gutjahr, M., Halliday, A. N., Kubik, P. W., Halbach, P., 2006. Submarine hydrothermal venting related to volcanism in the Lesser Antilles: Evidence from ferromanganese precipitates. Geochem. Geophys. Geosyst., 7, Q04010, doi: 10.1029/2005GC001140.

Fretzdorff, S., Haase, K. M., 2002. Geochemistry and petrology of lavas from the submarine flanks of Réunion Island (western Indian Ocean): implication for magma genesis and the magma source. Mineral. Petrol., 75, 153–184.

Froelich, P. N., Klinkhammer, G. P., Bender, M. L., Luedtke, N. A., Heath, G. R., Cullen, D., Dauphin, P., Hammond, D., Hartman, B., Maynard, V., 1979. Early oxidation of organic matter in pelagic sediments of the eastern equatorial Atlantic: suboxic diagenesis. Geochim. Cosmochim. Acta., 43, 1075–1090.

Frost, R. L., Kloprogge, J. T., Ding, Z., 2002. Near–infrared spectroscopic study of nontronites and ferruginous smectite. Spectrochim Acta., Part A, 58, 1657–1668.

Gardner, W. D., Mishonov, A. V., Richardson, M. J., 2006. Global POC concentrations from in–situ and satellite data Deep–Sea Res. II 53, 718–740

Gasparotto, G., Spadafora, E., Summa, V., Tateo, F., 2000. Contribution of grain size and compositional data from the Bengal Fan sediment to the understanding of Toba volcanic event. Mar. Geol., 162, 561–572.

Gehlen, M., Rabouille, C., Ezat, U., Guidi–Guilvard, L. D., 1997. Drastic changes in deep–sea sediment porewater composition induced by episodic input of organic matter. Limnol. Oceanogr., 42, 980–986.

German, C. R., 2003. Hydrothermal activity on the eastern SWIR (50° – 70°E): Evidence from core–top geochemistry, 1887 and 1998. Geochem. Geophys. Geosyst., 4(7), 9102.

German, C. R., Barreiro, B. A., Higgs, N. C., Nelsen, T. A., Ludford, E. M., Palmer, M. R., 1995. Seawater–metasomatism in hydrothermal sediments (Escanaba Trough, northeast Pacific). Chem. Geol., 1119, 175–190.

German, C. R., Bourlés, D. L., Brown, E. T., Hergt, J., Colley, S., Higgs, N. C., Ludford, E. M., Nelsen, T. A., Feely, R. A., Raisbeck, G., Yiou, F., 1997. Hydrothermal scavenging on the Juan de Fuca Ridge: $^{230}Th_{xs}$, ^{10}Be, and REEs in ridge–flank sediments. Geochim. Cosmochim. Acta., 61(19), 4067–4078.

German, C. R., Colley, S., Palmer, M. R., Khripounoff, A., Klinkhammer, G. P., 2002. Hydrothermal plume–particle fluxes at 13°N on the East Pacific Rise. Deep Sea Res., Part I, 49, 1921–1940.

German, C. R., Hergt, J., Palmer, M. R., Edmond, J. M., 1999. Geochemistry of a hydrothermal sediment core from the OBS vent–field, 21° N East Pacific Rise. Chem. Geol., 155, 65–75.

German, C. R., Higgs, N. C., Thompson, J., Mills, R., Elderfield, H., Blusztajn, J., Fleet, A. P., Bacon, M. P., 1993. A geochemical study of metalliferous sediments from the TAG hydrothermal mound, 26° 08' N, Mid Atlantic Ridge. J. Geophys. Res., 98, 9683–9692.

German, C. R., Klinkhammer, G. P., Edmond, J. M., Mitra, A., Elderfield, H., 1990. Hydrothermal scavenging of rare earth elements in the ocean. Nature 345, 516–518.

German, C. R., Richards, K. J., Rudnicki, M. D., Lam, M. M., Charlou. J. L., and the FLAME Scientific Party. 1998. Topographic control of a dispersing hydrothermal plume. Earth Planet. Sci. Lett., 156, 267–273.

Giblin, A., Hopkinson, C., Tucker, J., 1997. Benthic metabolism and nutrient cycling in Boston Harbor, Massachusetts. Estuaries 20, 346–364.

Gingele, F. X., Deckker, P. D., Hillenbrand, C. D., 2001. Clay mineral distribution in surface sediments between Indonesia and NW Australia – Source and transport by ocean currents. Mar. Geol., 179, 135–146.

Glasby, G. P., 1973. Role of sub–marine volcanism in controlling the genesis of marine manganese nodules. Oceanogr. Mar. Bio. Annu. Rev., 11, 27.

Glud, R. N., Gundersen, J. K., Jorgensen, B. B., Revsbech, N. P., Schulz, H. D., 1994. Diffusive and total oxygen uptake of deep–sea sediments in the southeast Atlantic Ocean. Deep–Sea Res. (I), 41, 1767–1788.

Goldberg, E. D., Koide, M., Schmitt, R. A., Smith, R. H., 1963. Rare Earth distributions in the marine environment. J. Geophys. Res., 68, 4209–4217.

Goodman, B. A., Russell, J. D., Fraser, A. R., Woodhams, F. W. D., 1976. A Mössbauer and IR spectroscopic study of the structure of nontronite. Clays Clay Miner., 24, 53–59.

Gordon, A. L., Claudia, F., Giulivi, T. T., Stewart, S., John, M., Donald, O., 2002. Bay of Bengal nutrient–rich benthic layer. Deep–Sea Res. II., 49, 1411–1421.

Gordon, R. G., DeMets, C., Royer, J. –Y., 1998. Evidence for long–term diffuse deformation of the lithosphere of the equatorial Indian Ocean. Nature 395, 370–374, doi: 10.1038/26463.

Grandel, S., Rickert, D., Schluter, M., Wallmann, K., 2000. Pore water distinct quantification of diffusive benthic fluxes of silicic acid, nitrate and phosphate in surface sediments of the deep Arabian Sea. Deep–Sea Res. II., 47, 2707–2734.

Grasshoff, K., Ehrhardt, M., Kremling, K., 1983. Methods of Sea water Analysis, 2nd edtn, Verlag Chemie, Weinheim.

Grim, R. E., 1968. Clay Mineralogy. McGraw–Hill, Inc., New York, 596 pp.

Gross, T. F., Williams III, A. J., Nowell, A. R. M., 1988. A deep–sea sediment transport storm. Nature 331, 518–521.

Grundmanis, V., Murray, J. W., 1977. Nitrification and denitrification in marine sediments from Puget Sound. Limnol. Oceanogr., 22, 804–813.

Grunwald, M., Dellwig, O., Kohlmeier, C., Kowalski, N., Beck, M., Badewei, T. H., Kotzur, S., Liebezeit, G., Brumsack, H. –J., 2010. Nutrients dynamics in a back barrier tidal basin of the Southern North Sea: Time–series, model simulations, and budget estimates. J. Sea Res., 64, 199–212.

Gupta, A. K., Das, M., Bhaskar, K., 2006. South Equatorial Current (SEC) driven changes at DSDP Site 237, Central Indian Ocean, during the Plio–Pleistocene: evidence from benthic foraminifera and stable isotopes. J. Asian Earth Sci., 28, 276–290.

Gupta, S. M., 1988. Radiolarian zonation and volcanic ash layers in two Quaternary sediment cores from the central Indian Ocean basin. J. Palaeontol. Soc. India., 33, 59–71.

Gupta, S. M., 1996. Quantitative radiolarian distribution in the surface sediment from the central Indian Ocean and their paleomonsoonal significance. J. Geol. Soc. India., 47, 339–354.

Gupta, S. M., 2003. Orbital frequencies in radiolarian assemblages of the central Indian Ocean: implications on the Indian summer monsoon. Palaeogeogr. Palaeoclimatol., Palaeoecol., 97, 97–112.

Gupta, S. M., Fernandes, A. A., Mohan, R., 1996. Tropical sea surface temperatures and the Earth's Eccentricity cycles. Geophy. Res. Lett., 23, 3159–3162.

Gurvich, E. G., 2006. Metalliferous Sediments of the World Ocean—Fundamental Theory of Deep–Sea Hydrothermal Sedimentation. Springer–Verlag, 17, Heidelberg, 416pp.

Gurvich, E. G., Levitan, M. A., Zuzmina, T. G., 1995. Chemical composition of leg 138 sediments and history of hydrothermal activity, Proc. Ocean Drill, Program Sci. Results, 138, 769–778.

Haflidason, H., Eiriksson, J., Kreveld, S. V., 2000. The tephrochronology of Iceland and the North Atlantic region during the Middle and Late Quaternary: a review. J. Quat. Sci., 15, 3–22.

Hall, P. O. J., Hulth, S., Hulthe, G., Landen, A., Tengberg, A., 1996. Benthic nutrient fluxes on a basin–wide scale in the Skagerrak (North–Eastern North Sea). J. Sea Res., 35, 123–137.

Hammond, D. E., Fuller, C., Harmon, D., Hartman, B., Korosec, M., Mileer, L. G., Rea, R., Warren, S., Berelson, W., Hager, S., 1985. Benthic fluxes in San Francisco Bay. Hydrobiolobigia 129, 69–90.

Haymon , R. M., Kastner, M., 1986. The formation of high temperature clay minerals from basalt altered during hydrothermal discharge on the east Pacific Rise axis at 21° N. Geochim. Cosmochim. Acta., 50, 1933–l 939.

Hedges, J. I., Keil, R. G., 1995. Sedimentary organic matter preservation: an assessment and speculative synthesis. Mar. Chem., 49, 81–115.

Heggie, D. T., Skyring, G. W., O'Brien, G. W., Reimers, C., Herczeg, A., Moriarty, D. J. W., Burnett, W .C., Milnes, A. R., 1990. Organic carbon cycling and modern phosphorite formation on the east Australia continental margin: An overview, In: Notholt, A. J. G., Jarvis, I. (Eds.), Phosphorite research and development, Geological Society, London Special Publication 52, pp. 87–117.

Heier, K.S. and Billings, G.K., 1970. Rubidium. In: Wedepohl, K. H. (Ed.), Handbook of Geochemistry. Springer, Berlin, pp. 37B 1–37N I.

Hein, J., Yeh, H., Alexander, E., 1979. Origin of iron–rich montmorillonite from the manganese nodule belt of the North equatorial Pacific. Clays Clay Miner., 27, 185–194.

Hensen, C., Landenberger, H., Zabel, M., Schulz, H. D., 1998. Quantification of diffusive benthic fluxes of nitrate, phosphate, and silicate in the southern Atlantic Ocean. Global Biochem. Cycles 12, 193–210.

Herzig, P. M., Plüger, W. L., 1998. Explorations for hydrothermal activity near the Rodriguez Triple Junction, Indian Ocean. Can. Mineral., 26, 721–736.

Hodkinson, R. A., Cronan, D. S., 1991. Regional and depth variability in the composition of cobalt–rich ferromanganese crusts from the SOPAC area and adjacent parts of the central equatorial Pacific. Mar. Geol., 98, 437–44.

Hodkinson, R. A., Stoffers, P., Scholten, J., Cronan, D. S., Jeschke, G., Rogers, T. D. S., 1994. Geochemistry of hydrothermal manganese deposits from the Pitcairn Island hotspot, southeastern Pacific. Geochim. Cosmochim. Acta., 58, 5011–5029.

Holmes, R. W., 1961. Summary of productivity measurements in the southeastern Pacific ocean. In: Doty, M. S. (Eds.), Primary Productivity Measurement: Marine and Freshwater. Washington, DC, IGY World data center, Natl. Acad. Sci., pp. 18–57.

Hopkinson, C. S., Vallino, J., 2005. Efficient export of carbon to the deep ocean through dissolved organic matter. Nature 433, 142–145.

Horn, D. R., Delach, M. N., Horn, B. M., 1969. Distribution of volcanic ash layers and turbidites in the North Pacific. Geol. Soc. Am. Bull., 81, 1715–1724.

Howard, K. J., Fisk, M. R., 1988. Hydrothermal alumina–rich clays and boehmite on the Gorda Ridge. Geochim. Cosmochim. Acta., 52, 2269–2279.

Hrischeva, E., Scott, S. D., 2007. Geochemistry and morphology of metalliferous sediments and oxyhydroxides from the Endeavour segment, Juan de Fuca Ridge. Geochim. Cosmochim. Acta., 71, 3476–3497.

Hunt, J. B., Hill, P. G., 2001. Tephrological implications of beam size-sample-size effects in electron microprobe analysis of glass shards. J. Quat. Sci., 16, 105–117.

Hunt, J. B., Hill, P.G., 1993. Tephra geochemistry: a discussion of some persistent analytical problems. The Holocene 3, 271–278.

Ingole, B. S., 2003. Macrobenthic abundance in the vicinity of spreading ridge environment in Central Indian Ocean. Curr. Sci., 85(3), 328–333.

Iyer, S. D. 1991 Comparison of internal features and microchemistry of ferromanganese crusts from the Central Indian Basin. Geo-Mar. Lett., 11, 44–50.

Iyer, S. D., 2005. Evidences for incipient hydrothermal event(s) in the Central Indian Basin: A review. Acta Geol. Sin., 79, 77–86.

Iyer, S. D., Gupta, S. M., Charan, S. N., Mills, O. P., 1999. Volcanogenic hydrothermal iron–rich materials from the southern part of the Central Indian Ocean Basin. Mar. Geol., 158, 15–25.

Iyer, S. D., Karisiddaiah, S. M., 1990. Petrology of ocean floor rocks from Central Indian Ocean basin. Indian J. Mar. Sci., 19, 13-16

Iyer, S. D., Mascarenhas–Pereira, M. B. L., Nath, B. N. 2007. Native aluminium (spherules and particles) in the central Indian Basin sediments: Implications on the occurrence of hydrothermal events. Mar. Geol., 240, 177–184.

Iyer, S. D., Prasad, S. M., Gupta, S. M., Charan, S. N., Mukherjee, A. D., 1997b. Hydrovolcanic activity in the Central Indian Ocean Basin. Does nature mimic laboratory experiments? J. Volcano. Geotherm. Res., 78, 209–220.

Iyer, S. D., Prasad, S. M., Gupta, S. M., Charan, S.N., 1997a. Evidence for recent hydrothermal activity in the Central Indian Ocean Basin. Deep–Sea Res., 44, 1167–1184.

Iyer, S. D., Sharma, S., 1990. Correlation between occurrence of manganese nodules and rocks in part of the Central Indian Ocean Basin. Mar. Geol. 92, 127–138.

Iyer, S. D., Sudhakar, M., 1993. A new report on the occurance of zeolitites in the abyssal depth of the Central Indian Ocean Basin. Sediment. Geol., 84, 169–178.

Izett, G. A., 1981. Volcanic ash beds: recorders of Upper Cenozoic silicic pyroclastic volcanism in the western United States. J. Geophys. Res., 86, 10200–10222.

Jahnke, R. A., 1988. A simple, reliable and inexpensive pore water sampler. Limnol. Oceanogr., 33 (3), 483–487.

Jahnke, R. A., Emerson, S. R., Grundmanis, V., 1982. Porewaters of the central Pacific Oceans: nutrient results. Earth Planet. Sci. Lett., 61, 233–256.

Jahnke, R. A., Emerson, S. R., Reimers, C. E., Schuffert, J., Ruttenberg, K., Archer, D., 1989. Benthic recycling of biogenic debris in the eastern tropical Atlantic Ocean. Geochim. Cosmochim. Acta., 53, 2947–2960.

James, R. H., Elderfield, H., Palmer, M. R., 1995. The chemistry of hydrothermal fluids from the Broken Spur site, 29° N Mid–Atlantic Ridge. Geochim. Cosmochim. Acta., 59, 651–659.

Jarvis, I., 1985. Geochemistry and origin of Eocene–Oligocene metalliferous sediments from the central equatorial Pacific: Deep Sea Drilling Project sites

573 and 574. In: Mayer, L., Theyer, F., et al., (Eds.), Initial. Rep. Deep Sea Drill. Proj. vol. 85, Washington, D.C, U. S. Government Printing Office, pp. 781–804.

Jedwab, J., Boulegue, J., 1984. Graphite crystals in hydrothermal vents. Nature 310, 41–43.

Jenkins, M. C., Kemp, W. M., 1984. The coupling of nitrification and denitrification in two estuarine sediments. Limnol. Oceanogr., 29, 609–619.

Johnson, D. A., Nigrini, C., 1982. Radiolarian biogeography in surface sediments of the Eastern Indian Ocean. Mar. Micropaleontology 7, 237–287.

Johnson, D. A., Schneider, D. A., Nigrini, C., Caulet, J. P., Kent, D. V., 1989. Pliocene–Pleistocene radiolarian events and magnetostratigraphic calibrations for the tropical Indian Ocean. Marine Micropaleontol., 14, 33–66.

Kamesh Raju, K. A., 1990. Magnetic and bathymetric studies in the vicinity of the 73^{o}E fracture zone, Central Indian Basin. Mar. Geol., 95, 147–153.

Kamesh Raju, K. A., 1993. Magnetic lineation, fracture zones and seamounts in the Central Indian Ocean Basin. Mar. Geol., 109, 195–201.

Kamesh Raju, K. A., Ramprasad, T., 1989. Magnetic lineation in the Central Indian Basin for the period A24–A21: A study in relation to the Indian Ocean Triple Junction. Earth Planet. Sci. Lett., 95, 395–402.

Kamesh Raju, K. A., Ramprasad, T., Kodagali, V. N., Nair, R. R., 1993. Multibeam bathymetric, gravity and magnetic studies over 79 degrees E fracture zone, central Indian basin. J. Geophy. Res. (B: Solid Earth), 98, 9605–9618.

Kastner, M., 1979. Zeolites. In: Burns, R. G. (Eds.), Marine Minerals. Reviews in mineralogy. vol. 6, Mineralogical Society of America, Washington, DC, pp. 111–122.

Keil, R. G., Tsamakis, E., Bor Fuh, C., Giddings, J. C., Hedges, J. I., 1994. Mineralogical and textural controls on the organic composition of coastal marine sediments: Hydrodynamic separation using SPLITT–fractionation. Geochim. Cosmochim. Acta., 58, 879–893.

Kennett, J. P., McBirney, A. R., Thunell, R. C., 1977. Episodes of Cenozoic volcanism in the Circum–Pacific Region. J. Volcanol. Geothermal Res., 2, 145–163.

Kessarkar, P. M., 1996. Geological studies of a typical characteristics in a part of sSeafloor generated by two spreading ridges in the Central Indian Ocean Basin. MSc Dissertation, Goa University, 99 pp.

Kessarkar, P. M., 1998. Tectonic reorganization in the Indian Ocean: Evidences from seafloor crenulations. Curr. Sci., 74, 472–476.

Klinkhammer, G. P., Elderfield, H., Edmonds, J. M., Mitra, A., 1994. Geochemical implications of rare earth element patterns in hydrothermal fluids from mid–ocean ridges. Geochim. Cosmochim. Acta., 58, 5105–5113.

Kodagali, V. N., 1988. Influence of regional and local topography on the distribution of polymetallic nodules in Central Indian Ocean Basin. Geo–Mar. Lett., 8, 173–178.

Kodagali, V. N., KameshRaju, K. A., Ramprasad, T., George, P., Jaisankar, S., 1992. Detailed bathymetric surveys in the central Indian Basin. Int. Hydrogr. Rev., 69, 143–150.

Kokelaar, P., 1986. Magma–water interactions in subaqueous and emergent basaltic volcanism. Bull. Volcanol., 48, 275–289.

Kolbentz–Mishke, O. J., Volkovinsky, V. V., Kabanova, J. O., 1970. Plankton primary productivity of the world ocean. In: Wooster, W. S. (Ed.), Scientific

Exploration of the South Pacific. Washington, DC: Natl. Acad. Sci., pp. 183–191.

Kolla, V., Biscaye, P. E., 1977. Distribution and Origin of Quartz in the Sediments of the Indian Ocean. J. Sed. Res., 47, 642–649.

Kolla, V., Henderson, L., Biscaye, P. E., 1976. Clay mineralogy and sedimentation in the western Indian Ocean. Deep Sea Res., 23, 949–961.

Kolla, V., Kidd, R. B., 1982. Sedimentation and sedimentary process in the Indian Ocean. In: Nairn, A. E. M., Stehli, F. G. (Eds.), The Ocean Basins and Margins: The Indian Ocean. Plenum, New York, vol. 6, pp. 1–45.

Koning, E., Brummer, G. –J, Van Raaphorst, W., Van Bennekom, A. J., Helder, W., Van Iperen, J., 1997. Settling, dissolution and burial of biogenic silica in the sediments off Somalia (northwestern Indian Ocean). Deep–Sea Res. II., 44 (6/7), 1341–1360.

Krey, J., 1973. Primary production in the Indian Ocean. In: Eitzschel, B. (Eds.), The Biology of the Indian Ocean. Springer–Verlag, Berlin, pp. 115–126.

Krey, J., Babenerd, B., 1976. Phytoplankton production atlas of the International Indian Ocean Expedition: Institüt für Meereskunde University of Kiel, Germany, p. 70.

Krishna, K. S., Bull, J. M., Scrutton, R. A., 2001. Evidence for multiphase folding of the central Indian Ocean lithosphere. Geol., 29, 715–718.

Krishna, K. S., Ramana, M. V., Gopala Rao, D., Murthy, K. S. R., Malleswara Rao, M. M., Subrahmanyam, V., Sarma, K. V. L. N. S., 1998. Periodic deformation of oceanic crust in the central Indian Ocean. J. Geophy. Res., 103, 17,859–17,875.

Krishna, K. S., Rao, D. G., Neprochnov, Y. P., 2002. Formation of diapiric structure in the deformation zone, central Indian Ocean: A model from gravity and seismic reflection data. Proceedings of Indian Academy of Science (Earth and Planetary Science), 111, 17–28.

Krishna, K. S., Rao, D. G., Ramana, M. V., Subrahmanyam, V., Sarma, K. V. L. N. S., Pilipenko, A. I., Shcherbakov, V. S., Murthy, I. V. R., 1995. Tectonic model for the evolution of oceanic crust in the northeastern Indian Ocean from the Late Cretaceous to the Early Tertiary. J. Geophys. Res. (B: Solid Earth), 100(B10), 20011–20024.

Krishnaswami, S., Sarin, M. M., 1976. The simultaneous determination of Th, Pu, Ra isotopes, ^{210}Pb, ^{55}Fe, ^{32}Si and ^{14}C in marine suspended phases. Acta Geol. Sin., 83, 143–156.

Krishnaswami, S., Turekian, K. K., Bennett, J. T., 1984. The behavior of ^{232}Th and the ^{238}U decay chain nuclides during magma formation and volcanism. Geochim. Cosmochim. Acta., 48, 505–511 .

Krom, M. D., Berner, R. A., 1981. The diagenesis of phosphorus in a nearshore sediment. Geochim. Cosmochim. Acta., 45, 207–216.

Kuhn, T., Burger, H., Castradori, D., Halbach, P., 2000. Volcanic and hydrothermal history of ridge segments near the Rodriguez Triple Junction (Central Indian Ocean) deduced from sediment geochemistry. Mar. Geol., 169, 391–409.

Lampitt, R. S., 1985. Evidence for the seasonal deposition of detritus to the deep–sea floor and its subsequent resuspension. Deep–Sea Res., 32, 885–897.

Lampitt, R. S., Raine, R. C. T., Billete, D. S. M., Rice, A. L., 1995. Material supply to the European continental slope: a budget based on benthic oxygen demand and organic supply. Deep–Sea Res. I., 42, 1865–1870.

Landing, W. M., Bruland, K. W., 1987. The contrasting biogeochemistry of iron and manganese in the Pacific Ocean. Geochim. Cosmochim. Acta., 51, 29–43.

Langford, S. A., 1984. Refractive index– a geochemical indicator in natural, volcanic glasses. J Non–Crystalline Solids Proceedings of the International Conference on Glass in Planetary and Geological Phenomena. vol. 67, p. 192.

Larsen, G., Dugmore, A., Newton, A., 1999. Geochemistry of historical-age silicic tephras in Iceland. The Holocene 9, 463–471.

Ledford–Hoffman, P. A., DeMaster, D. J., Nittrouer, C. A., 1986. Biogenic silica accumulation in the Ross Sea and the importance of Antarctic continental–shelf deposits in the marine silica budget. Geochim. Cosmochim. Acta., 50, 2099–2110.

Lee, C. H., Lee, S. –R., 1998. Authigenic phillipsite in deep–sea manganese nodules from the Clarion–Clipperton area, NE Equatorial Pacific. Mar. Geol., 148**,** 125–133.

Lee, M. Y., Chen, C. –H., Wei, K. –Y., Iizuka, Y., Carey, S., 2004. First Toba supereruption revival. Geology 32, 61–64.

Li, Y. H., 2000. A Compendium of Geochemistry: from Solar Nebula to the Human Brain. Princeton Uni. Press, Princeton, NJ.

Lim, C., Ikehara, K., Toyoda, K., 2008. Cryptotephra detection using high–resolution trace–element analysis of Holocene marine sediments, southwest Japan. Geochim. Cosmochim. Acta., 72, 5022–5036.

Lisitzin, A. P., Crook, K. A. W., Bogdanov, Yu. A., Zonenshain, L. P., Murav'ev, K. G., Tufar, W., Gurvich, E. G., Gordeev, V. V., Ivanov, G. V., 1992. Hydrothermal fields of the Manus basin rift zone. Int. Geol. Rev., 35, 105–126.

Lisitzyn, A. P., Gurvich, E. G. (Eds.) 1987. Metalliferous sediments in the Indian Ocean (In Russian). Nauka, Moscow.

Liu, C. –Q., Masuda, A., Okada, A., Yabuki, S., J., Fan, Z. L., 1994. Isotope geochemistry of Quaternary deposits from the arid lands in northern China. Earth Planet. Sci. Lett., 127, 25–38.

Liu, C. –Q., Masuda, A., Okada, A., Yabuki, S., Zhang, J., Fan, Z. L., 1993. A geochemical study of loess and desert sand in northern China: Implications for continental crust weathering and composition. Chem. Geol., 106, 359–374.

Liu, C. S., Curray, J. R., McDonald, J. M., 1983. New constraints on the tectonic evolution of eastern Indian Ocean. Earth Planet. Sci. Lett., 65, 331–342.

Liu, Z., Colin, C., Trentesaux, A., 2006. Major element geochemistry of glass shards and minerals of the Youngest Toba Tephra in the southwestern South China Sea. J. Asian Earth Sci., 27, 99–107.

Lonsdale, P., 1977. Clustering of suspension–feeding macrobenthos near abyssal hydrothermal vents at oceanic spreading centers. Deep–Sea Res., 24, 857–863.

Lowe J. J., Turney, C. S. M., 1997. Vedde Ash layer discovered in a small lake basin on the Scottish mainland. J. Geol. Soc., 154, 605–612.

Lowe, D. J., Newnham, R. M., McFadgen, B. G., Higham, T. F. G., 2000. Tephras and New Zealand archaeology. J. Archaeolog. Sci., 27, 859–870.

Ludford, E. M., Palmer, M. R., German, C. R., Klinkhammer, G. P., 1996. The geochemistry of Atlantic hydrothermal particles. Geophys. Res. Lett., 23(23), 3503–3506.

Lydon, J. W., Goodfellow, W. D., Jonasson, I. R., 1985. A general model for straiform baritic deposits of the Selwyn Basin, Yukon Territory an District of

MacKenzie. In: Current Research, Part A: Ottawa, Geologic; Survey of Canada, Paper 85–lA, 11, 651–660.

Lynn, D. C., Bonatti, E., 1965. Mobility of manganese in diagenesis of deep–sea sediments. Mar. Geol., 3, 457–474.

Macdonald, K. C., 1998. Linkages between faulting, volcanism, hydrothermal activity and segmentation on fast spreading centers. In: Buck, W. G., Delaney, P. T., Karson, J. A., Lagabrielle, Y. (Eds.), Faulting and Magmatism at Mid–Ocean Ridges. Am. Geophys. Union, Washington, DC, pp. 27–58.

Mahoney, J. J., Jones, W. B., Frey, F. A., Salters, V. J. M., Pyle, D. G., Davies, H. L., 1995. Geochemical characteristics of lavas from Broken Ridge, the Naturaliste Plateau and southernmost Kerguelen Plateau: Cretaceous plateau volcanism in the southeast Indian Ocean. Chem. Geol. 120, 315–345.

Mahoney, J. J., Macdougall, J. D., Lugmair, G. W., Gopalan, K., 1983. Kergulen hotspot source for Rajmahal Traps and Ninetyeast Ridge? Nature 303, 385–389.

Malone, T. C., 1971. The relative importance of netplankton and nanoplankton as primary production in neric and oceanic tropical waters. Limnol. Oceanogr., 26, 633–639.

Mamayev, O. I., 1975. Temerature–salinity analysis of world ocean waters. Elsevier Oceanography Series 11, 374pp.

Mandernack, K. W., Tebo, B. M., 1993. Manganese scavenging and oxidation at hydrothermal vents and in vent plumes. Geochim. Cosmochim. Acta., 57(16), 3907–3923.

Manheim, F. T., 1966. A hydraulic squeezer for obtaining interstitial water from unconsolidated sediments. Pro. Paper U.S. Geol. Sur., 550C, 256–261.

Manheim, F. T., 1968. Disposable syringe techniques for obtaining small quantities of pore water from unconsolidated sediments. J. Sediment. Petrol., 38, 666–668.

Marchig, V., Erzinger, J., Heinze, P. –M., 1986. Sediment in the black smoker area of the East Pacific Rise (18.5°S). Earth Planet. Sci Lett., 79, 93–106.

Marchig, V., Gundlach, H., Möller, P., Schley, F., 1982. Some geochemical indicators for discrimination between diagenetic and hydrothermal metalliferous sediments. Mar. Geol., 50, 241–256.

Marchig, V., von Stackelberg, U., Wiedicke, M., Durn, G., Milovanovic, D., 1999. Hydrothermal activity associated with off–axis volcanism in the Peru Basin. Mar. Geol., 159, 1–4, 179–203.

Marsh, B. D., 1976. Some Aleutian andersites: their nature and source. J. Geol., 84, 27–45.

Martin, W. R., Bender, M. L., 1988. The variability of benthic fluxes and sedimentary remineralization rates in response to seasonally variable organic carbon rain rates in the deep sea: a modelling study. Amer. J. Sci., 288, 561–574.

Martin–Barajas, A., Lallieri–Verges, E., 1993. Ash layers and pumice in the central Indian Basin: relationship from the formation of manganese nodules. Mar. Geol., 115, 307–329.

Mascarenhas–Pereira, M. B. L., Nath, B. N., Borole, D. V., Gupta, S. M., 2006. Nature, source and composition of volcanic ash in sediments from a fracture zone trace of Rodriguez Triple Junction in the Central Indian Basin. Mar. Geol., 229, 79–90.

Mathews, N. E., Smith, V. C., Costa, A., Durant, A. J., Pyle, D. M., Pearce, N. J. G., 2012. Ultra–distal tephra deposits from super–eruptions: Examples from Toba, Indonesia and Taupo Volcanic Zone, New Zealand. Quat. Int., 258, 54–79.

Matondkar, S. G. P., Nair, K. K. C., Ansari, Z. A., 2005. Biological characteristics of Central Indian Basin waters during the southern summer. Mar. Georesource. Geotechnol., 23, 299–314.

McCartney, M. S., 1977. Subantarctic mode water. In: Angel, M. V. (Ed.), A voyage of Discovery. George Deacon 70 Anniversary Volume, supplement to Deep Sea Research. Pergamon Press, Oxford, pp. 103–119.

McKenzie, D. P., Sclater, J. G., 1971. Evolution of Indian Ocean since Late Cretaceous. Geophy. J. R. Astron. Soc., 25, 437–528.

McLennan, S. M., 1989. Rare earth elements in sedimentary rocks, Influence of provenance and sedimentary processes. In: Lipin, B. R., McKay, G. A. (Eds.), Geochemistry and Mineralogy of the Rare Earth Elements. Rev. Mineral., 21, pp 169–200.

McLennan, S. M., 1993. Weathering and global denudation. J. Geol., 101, 295–303.

McLennan, S. M., Hemming, S., McDaniel, D. K., Hanson, G. N., 1993. Geochemical approaches to sedimentation, provenance, and tectonics. In: Johnsson, M. J., Basu, A. (Eds.), Processes controlling the composition of clastic sediments. Geol. Soc. Am. Spec. Pub. 284, 21–40.

McLennan, S. M., Taylor, S. R., Kroner, A., 1983. Geochemical evolution of Archean shales from South Africa: I. The Swaziland and Pongola Supergroups. Precamb. Res., 22, 93–124.

McManus, J., Berelson, W. M., Hammond, D. E., Kilgore, T. E., DeMaster D. J., Ragueneau, O. G., Collier, R. W., 1995. Early diagenesis of biogenic silica: dissolution rates, kinetics, and paleoceanographic implications. Deep–Sea Res. II., 42, 871–903.

McMurtry, G. M., de Carlo, E. H., Kim, K. H., 1991. Accumulation rates, chemical partitioning, and Q–mode factor analysis of metalliferous sediments from the North Fiji Basin. Mar. Geol., 98, 271–295.

McMurtry, G. M., Wang, C. –H., Yeh, H. –W., 1983. Chemical and isotopic investigations into the origin of clay minerals from the Galapagos hydrothermal mound field. Geochim. Cosmochim. Acta., 47, 475–489.

McMurtry, G. M., Yeh, H. –W., 1981. Hydrothermal clay mineral formation of East Pacific Rise Bauer Basin sediments. Chem. Geol., 32, 189–205.

McTainsh, G. H. 1989. Quaternary Aeolian dust processes and sediments in the Australian region. Quaternary Science Reviews 8, 235–253.

Michard, A., Albarède, F., 1986. The REE content of some hydrothermal fluids. Chem. Geol., 55, 51–60.

Michard, G., Albarède, F., Michard, A., Minister, J. –F., Charlou, J. –L, Tan, N., 1984. Chemistry of solutions from the 13°N East Pacific Rise hydrothermal site. Earth Planet. Sci. Lett., 67, 297–307.

Middelburg, J. J., Van Der Weijden, C. H., Woittiez, J. R. W., 1988. Chemical processes affecting the mobility of major, minor and trace elements during weathering of granitic rocks. Chem. Geol., 68, 253–273.

Mills, R. A., Elderfield, H., 1995. Rare earth element geochemistry of hydrothermal deposits from the active TAG Mound, 26 °N Mid–Atlantic Ridge. Geochim. Cosmochim. Acta., 59, 3511–3524.

Mills, R. A., Elderfield, H., Thomson, J., 1993. A dual origin for the hydrothermal component in a metalliferous sediment core from the Mid–Atlantic Ridge. J. Geophys. Res., 98, 9671–9678.

Mills, R. A., Wells, D. M., Roberts, S., 2001. Genesis of ferromanganese crusts from the TAG hydrothermal field. Chem. Geol., 176, 283–293.

Mitra, A., Elderfield, H., Greaves, M. J., 1994. Rare earth elements in submarine hydrothermal fluids and plumes from the Mid–Atlantic Ridge. Mar. Chem., 46, 217–235.

Morey, G. B., Setterholm D. R., 1997. Rare earth elements in weathering profiles and sediments of Minnesota: Implications for provenance studies. J. Sed. Res., 67, 105–115.

Mortimer, C. H., 1941. The exchange of dissolved substances between mud and water in lakes. I. J. Ecol., 29, 280–329.

Mozgova, N. N., Krasnov, S. G., Batuyev, B. N., Borodaev, Y. S., Efimov, A. V., Markov, V. F., Stepanova, T. V., 1996. The first report of cobalt pentlandite from a Mid–Atlantic Ridge hydrothermal deposit. Cand. Mineral., 34, 23–28.

Mudholkar, A. V., Pattan, J. N., Parthiban, G., 1993. Geochemistry of deep sea sediment cores from the Central Indian Ocean Basin. Indian J. Mar. Sci., 22, 241–246.

Mudholkar, A., Fiji, T., 1995. Fresh pumice from the central Indian Basin: a Krakatau 1883 signature. Mar. Geol., 125, 143–151.

Mukhopadhyay, R., 1998. Post–Cretaceous intraplate volcanism in the Central Indian Ocean Basin. Mar. Geol., 151, 135–142.

Mukhopadhyay, R., Batiza, R., 1994. Basinal seamounts and seamount chains of the Central Indian Ocean: probable near axis origin from a fast spreading ridge. Mar. Geophys. Res., 16, 303–314.

Mukhopadhyay, R., Batiza, R., lyer, S. D., 1995. Petrology of seamounts in the Central Indian Ocean Basin: Evidence for near–axis origin. Geo–Mar. Lett., 15, 106–110.

Mukhopadhyay, R., George, P., Ranade, G., 1997. Spreading rate dependent seafloor deformation in response to India–Eurasia collision: results of a hydrosweep survey in the Central Indian Ocean Basin. Mar. Geol., 140, 219–229.

Mukhopadhyay, R., Ghosh, A. K., Iyer, S. D., 2008. The Indian Ocean nodule field: Geology and resource potential. Handbook Exploration Environmental Geochemistry, Hale, M. (Eds.). Elsevier, Amsterdam, The Netherlands, 292.

Mukhopadhyay, R., Iyer, S. D., Ghosh, A. K., 2002. The Indian Ocean Nodule Field: Petrotectonic evolution and ferromanganese deposits. Earth Sci. Rev., 60, 67–130.

Mukhopadhyay, R., Khadge, N. H., 1990. Seamounts in the Central Indian Ocean Basin: indicators of the Indian plate movement. Proc. Indian Acad. Sci. (Earth Planet. Sci.) 99, 357–365.

Munschy, M., Schlich, R., 1989. The Rodriguez Triple Junction (Indian Ocean): Structure and evolution for the past one million years. Mar. Geophys. Res., 11, 1–14.

Murnane, R., Clague, D. A., 1983. Nontronite from a low temperature hydrothermal system on the Juan de Fuca Ridge. Earth Planet. Sci. Lett., 65, 343–352.

Murray, J., Renard, A. F., 1891. Report on deep–sea deposits. Report on the Scientific Results of the Voyage of "H.M.S. Challenger" during the years 1873–1876, Neill and Co., Edinburgh, 520 pp.

Murray, L. G., Mudge, S. M., Newton, A., Icely, J. D., 2006. The effect of benthic sediments on dissolved nutrient concentrations and fluxes. Biogeochemistry 81, 159–178.

Murray, R. W., Buchholtz Ten Brink, M. R., Gerlach, D. C., Russ, G. P., III, Jones, D. L., 1992. Interoceanic variation in the rare–earth, major, and trace element

depositional chemistry of chert. Perspectives gained from the DSDP and ODP record. Geochim. Cosmochim. Acta., 56, 1897–1913.

Murray, R. W., Leinen, M., 1993. Chemical transport to the seafloor of the equatorial Pacific Ocean across a Latitudinal transect at 135 °W, Tracking sedimentary major, trace, and rare earth element fluxes at the Equator and the Intertropical Convergence Zone. Geochim. Cosmochim. Acta., 57, 4141–4163.

Murray, R. W., Leinen, M., Isern, A. R., 1993. Biogenic flux of Al to sediment in the central equatorial Pacific Ocean: Evidence for increased productivity during glacial periods, Paleoceanography, 8, 651– 670.

Murty, V. S. N., Babu, V. R., Rao, A. S., Beena, B. S., 1999. Current structure and kinetic energy of the abyssal waters in the central Indian Ocean basin. Proceedings of the Third 1999 Ocean Mining Symposium, Goa, India, November 8–10, pp. 216–223.

Murty, V. S. N., Savin, M., RameshBabu, V., Suryanarayana, A., 2001. Seasonal variability in the vertical current structure and kinetic energy in the Central Indian Ocean Basin. Deep–Sea Res., (II) 48(16), 3309–3326

Naidu P. D., Malmgren B. A., 2005. Seasonal sea surface temperature contrast between the Holocene and last glacial period in the western Arabian Sea (ODP Site 723A) modulated by monsoon upwelling. Paleoceanography 20, PA1004.

Naidu, P. D., 2004. Isotopic evidences of past upwelling intensity in the Arabian Sea. Global Planet. Change., 40, 285– 293.

Naidu, P. D., Malmgren, B. A., 1996. A high–resolution record of late Quaternary upwelling along the Oman Margin, Arabian Sea based on planktonic foraminifera, Paleoceanography 11, 129–140.

Naidu, P. D., Malmgren, B. A., 1999. Quaternary carbonate record from the equatorial Indian Ocean and its relationship with productivity changes. Mar. Geol., 161(1), 49–62.

Naqvi, S. W. A., 1987. Some aspects of oxygen deficient conditions and denitrification in the Arabian Sea. J. Mar. Res., 45, 1049–1072.

Nath, B. N., 1993. Rare earth element geochemistry of the sediments, ferromanganese nodule and crusts from the Indian Ocean, Ph.D. thesis. Goa Uni., India.

Nath, B. N., 2001. Geochemistry of sediments. In: Sen Gupta, R., Desa, E. (Eds.), The Indian Ocean–A perspective. 2, pp. 645–690.

Nath, B. N., Aldahan, A., Possnert, G., Selvaraj, K., Mascarenhas–Pereira, M. B. L., Chen C. T. A., 2007. ^{10}Be variation in surficial sediments of the Central Indian Basin. Nucl. Instrum. Methods Phys. Res., Sect. B, 259(1), 610–615.

Nath, B. N., Balaram, V., Sudhakar, M., Plüger, W. L., 1992. Rare earth element geochemistry of ferromanganese deposits of the Indian Ocean. Mar. Chem., 38, 185–208.

Nath, B. N., Bau, M., Rao, B. R., Rao, Ch. M., 1997b. Trace and rare earth elemental variation in Arabian Sea sediments through a transect across the oxygen minimum zone. Geochim. Cosmochim. Acta., 61, 2375–2388.

Nath, B. N., Borole, D. V., Aldahan, A., Patil, S. K., Mascarenhas–Pereira, M. B. L., Possnert, G., Ericsson, T., Ramaswamy, V., Gupta, S. M., 2008. ^{210}Pb, ^{230}Th, and ^{10}Be in Central Indian Basin seamount sediments: Signatures of degassing and hydrothermal alteration of recent origin, Geophys. Res. Lett., 35, L09603, doi:10.1029/2008GL033849.

Nath, B. N., Gupta, S. M., Mislankar, P. G., Rao, B. R., Parthiban, G., Roelandts, I., Patil, S. K., 2005. Evidence of Himalayan erosional event at approx. 0.5 Ma

from a sediment core from the equatorial Indian Ocean in the vicinity of ODP Leg 116 sites. Deep–Sea Res. II., 52, 2061–2077.

Nath, B. N., Iyer, S. D., 1989. Basalt microlapilli in deep sea sediments of Indian Ocean in the vicinity of Vityaz fracture zone J. Geol. Soc. India., 34; 303-309.

Nath, B. N., Khadge, N. H., Nabar, S., Raghukumar, C., Ingole, B. S., Valsangkar, A. B., Sharma, R., Srinivas, K., 2012. Monitoring the sedimentary carbon in an artificially disturbed deep–sea sedimentary environment. Environmental Monitoring Assessment 184, 2829–2844.

Nath, B. N., Mudholkar, A. V., 1989. Early diagenetic processes affecting nutrients in the pore waters of Central Indian Ocean cores. Mar. Geol., 86, 57–66.

Nath, B. N., Plüger, W. L., Roelandts, I., 1997a. Geochemical constraints on the hydrothermal origin of ferromanganese encrustations from the Rodriguez Triple Junction, Indian Ocean. In: Nicholson, K., Hein, J. R., Bühn, B., Dasgupta, S. (Eds.), Manganese Mineralization: Geochemistry and Mineralogy of Terrestrial and Marine Deposits. vol. 119, Geol. Soc. Spec. Publ., pp. 192–221.

Nath, B. N., Rao, B. R., 1998. Late Pliocene–Pleistocene sedimentation and episodic volcanism recorded by a sediment core of the central Indian Basin, paper presented at 6th International Conference on Palaeoceanography, Lisbon, Portugal.

Nath, B. N., Rao, V. P. C., Becker, K. P., 1989. Geochemical evidence of terrigenous influence in deep–sea sediments up to 8° S in the Central Indian Basin. Mar. Geol., 87, 301–313.

Nath, B. N., Roelandts, I., Sudhakar, M., Plüger, W. L., 1992. Rare Earth element patterns of the Central Indian Basin sediments related to their lithology. Geophy. Res. Lett., 19, 1197–1200.

Nath, B. N., Roelandts, I., Sudhakar, M., Plüger, W. L., Balaram, V., 1994. Cerium anomaly variation in ferromanganese nodules and crusts from the Indian Ocean. Mar. Geol., 120, 385–400.

Nath, B. N., Sijinkumar, A. V., Borole, D. V., Gupta, S. M., Mergulhao, L. P., Mascarenhas-Pereira, M. B. L., Ramaswamy, V., Guptha, M. V. S., Possnert, G., Aldahan, A., Khadge, N.H., Sharma, R., 2013. Record of carbonate preservation and the Mid-Brunhes climatic shift from a seamount top with low sedimentation rates in the Central Indian Basin. Boreas 42(3), 762-778.

Nedwell, D. B., Hall, S. –E., Anderson, A., Hagstrom, A. F., Lindstrom, E. B., 1983. Seasonal changes in the distribution and exchange of inorganic nitrogen between sediment and water in the Northern Baltic (Gulf of Bothnia). Estuarine. Coastal Shelf Sci., 17, 169–179.

Nekrossov, I. Ya., Gorbachov, N. S., 1977. Study of the Cu–Fe–Sn–S–H_20 system at 300°–500°C and the origin of cassiterite–sulphide ores. In: Articles in Physico–chemical Petrology. Nauka, Moscow, 7, 176–199. (in Russian).

Nelson, B. K., DePaolo, D. J., 1988. Comparison of isotopic and petrographic provenance indicators in sediments from Tertiary continental basins of New Mexico. J. Sed. Petrol., 58, 348–357.

Nelson, D. M., Smith, W. O., 1986. Phytoplankton bloom dynamics of the western Ross Sea ice edge – 11. Mesoscale cycling of nitrogen and silicon. Deep Sea Res., 33, 1389–1412.

Neprochnov, Yu. P., Gopala Rao, D., Subrahmanyam, C., Murthy, K. S. R., 1998. Intraplate deformation in the Central Indian Ocean Basin. Geol. Soc. Ind. Monogr. 39, 250 pp.

Nesbitt, H. W., Mackovics, G., Price, R. C., 1980. Chemical processes affecting alkalis and alkaline Earth during continental weathering. Geochim. Cosmochim. Acta., 44, 1659–1666.

Nesbitt, H. W., Young, G. M., 1982. Early Proterozoic climates and plate motions inferred from major element chemistry of lutites. Nature 299, 715–717.

Nesbitt, H.W., Young, G.M., 1984. Prediction of some weathering trends of plutonic and volcanic–rocks based on thermodynamic and kinetic considerations. Geochim. Cosmochim. Acta., 48 (7), 1523–1534.

Newman, A. C. D., 1987. Chemistry of clays and clay minerals. Longman Scientific and Technical, Harlow.

Newsom, H. E., Hagerty, J. J., Goff, F., 1999. Mixed hydrothermal fluids and the origin of the martian soil. J. Geophys. Res., 104, 8717–8728.

Ninkovitch, D., 1979. Distribution, age and chemical composition of tephra layers in the deep-sea sediments off western Indonesia. J. Volcanol. Geotherm. Res., 5, 67–86.

Nixon, S. W, Pilson, M. E. Q., 1983. Nitrogen in estuarine and coastal marine ecosystems. In: Carpenter, E. D., Carpenter, D. G. (Eds.), Nitrogen in the marine environment. Academic Press, New York, pp. 565–648.

Nixon, S. W., 1981. Remineralization and nutrient cycling in coastal marine ecosystem. In: Neilson. B. J., Cronin, L. E. (Eds.), Estuaries and nutrients. Hurnana Press, pp. 111–138.

Nixon, S. W., Kelly, J. R., Oviatt, C. A., Hale, S. S., 1976. Nitrogen regeneration and the metabolism of coastal marine bottom communities. In: Anderson, J. M., MacFadden, A. (Eds.), The role of terrestrial and aquatic organisms. 17th Symposium of the British Ecological Society. Blackwell. Oxford, pp. 269–283.

Norton, I. O., Sclater, J. G., 1979. A model for the evolution of the Indian Ocean and the breakup of Gondwanaland. J. Geophys. Res., 84, 6803–6830.

Nyakairu, G.W.A., Koeberl, C., 2002. Variation of mineral, chemical, and rare earth element composition in size fractions of clay–rich sediments from the Kajjansi and Ntawo clay deposits, Central Uganda. Chemie der Erde–Geochemistry 62, 73–86.

Ober, J. A., 2008. Mineral commodity Summaries. Strontium, USGS Report., 2010–05–14.

Odin, G. S., Rex, D. C., 1982. Potassium–argon dating of washed, leached, weathered and reworked glauconies. In: Odin, G. S. (Ed.), Numerical dating in stratigraphy, Part I: New York, John Wiley & Sons, pp. 363–385.

Oleynikov, B. V., Okrugin, A. V., Leskova, N. V., 1978. Petrological significance of native aluminium finds in basites. Dokl. Acad. Sci. USSR, 243, 191–194. (in Russian).

Olivarez, A. M., Owen, R. M., 1989. REE/Fe variation in hydrothermal sediments: implication for the REE content of seawater. Geochim. Cosmochim. Acta., 53, 757–762.

Oudin, E., 1983. Hydrothermal sulphide deposits of the East Pacific Rise (21°N), Part I, Descriptive mineralogy. Mar. Min., 4, 39–72.

Oudin, E., Cocherie, A., 1988 Fish debris record the hydrothermal activity in the Atlantis II Deep sediments (Red Sea). Geochim. Cosmochim. Acta., 52, 177–184.

Owen, R. M., Olivarez, A. M., 1988. Geochemistry of rare earth elements in pacific hydrothermal sediments. Mar. Chem., 25(2), 183–196.

Parulekar, A. H., Harkantra, S. N., Ansari, Z. A., Matondkar, S. G. P., 1982. Abyssal benthos of the Central Indian Ocean. Deep–Sea Res., 29, 1531–1537.

Parulekar, A. H., Ingole, B. S., Harkantra, S. N., Ansari, Z. A., 1992. Deep–sea benthos of the western and central Indian Ocean. In: Desai, B. N. (Ed.), Oceanography of the Indian Ocean. New Delhi, Oxford and IBM Publishing Co., pp. 261–267.

Paterne, M., Guichard, F., Labeyrie, J., 1988. Explosive activity of the south Italian volcanoes during the past 80,000 years as determined by marine tephrochronology. J. Volcanol. Geotherm. Res., 34, 153–172.

Patriat, P., Stgoufin, J., 1988, Reconstruction of the Central Indian Ocean. In: Scotese, C. R., Sager, W. W. (Eds.), Mesozoic and Cenozoic Plate Reconstructions. Tectonophysics, 155, pp. 211–234.

Patsch, J., Kuhn, W., 2008. Nitrogen and carbon cycling in the North Sea and exchange with the North Atlantic– A model study. Part I. Nitrogen budget and fluxes. Continent. Shelf Res., 28, 767–787.

Pattan, J. N., 1993. Manganese micronodules: A possible indicator of sedimentary environment. Mar. Geol., 113(3–4), 331–44.

Pattan, J. N., Banakar, V. K., 1997. Diagenetic remobilization of rare earth elements in sediment core from the Central Indian Basin. Indian J. Mar. Sci., 26, 341–344.

Pattan, J. N., Jauhari, P., 2001. Major, trace, and rare earth elements in the sediments of the Central Indian Ocean Basin: Their source and distribution. Mar. Georesour. Geotechnol., 19, 85–106.

Pattan, J. N., Masuzawa, T., Borole, D. V., Parthiban, G., Jauhari, P., Yamamoto, M., 2005. Biological productivity, terrigenous influence and non crustal elements supply to the Central Indian Ocean Basin: paleoceanography during the past ~ 1 Ma. J. Earth Syst. Sci., 114, 63–74.

Pattan, J. N., Shane, P., Banakar, V. K., 1999. New occurrence of youngest Toba Tuff in abyssal sediments of the Central Indian Basin. Mar. Geol., 155, 243–248.

Pavithran, S., Ingole, B. S., Nanajkar, M., Raghukumar, C., Nath, B. N., Valsangkar, A. B., 2009. Composition of macrobenthos from the central Indian Ocean Basin. J. Earth Syst. Sci., 118(6), 689–700.

Peirce, J. W., 1978. The northward motion of India since the Late Cretaceous. Geophys. J. R. Astron. Soc., 52, 277–311.

Peters, J. L., Murray, R. W., Sparks, J. W., Coleman, D. S., 2000. Terrigenous matter and dispersed ash in sediment from the Caribbean Sea; results from Leg 165. Proceedings of the Ocean Drilling Program, Scientific Results, Leg 165, pp. 115–124.

Philpotts, J. A., 1970. Redox estimation from a calculation of Eu^{2+} and Eu^{3+} concentrations in natural phases. Earth Planet. Sci. Lett., 9, 257, 268.

Piotrowski, A. M., Banakar, V. K., Scrivner, A. E., Elderfield, H., Galy, A., Dennis, A., 2009. Indian Ocean circulation and productivity during the last glacial cycle. Earth Planet. Sci. Lett., 285(1–2), 179–189.

Piper, D. Z., 1974a. Rare earth elements in the sedimentary cycle: a summary. Chem. Geol., 14, 285–304.

Plank, T., Ludden, J. N., Escutia, C., et al., 2000. Proceedings of the Ocean Drilling Program, initial reports, Izu–Mariana Margin; Proceedings of the Ocean Drilling Program, Part A, Initial Reports, 185.

Plüger, W. L. et al., 1990. Discovery of hydrothermal fields at the Central Indian Ridge. Mar. Min., 9, 73–86.

Plüger, W. L., Friedrich, G., Stoffers, P., 1985. Environmental controls on the formation of deep–sea ferromanganese concretions: Monograph Series on Mineral Deposits. 25, 31–52.

Plüger, W., Schwarz, P., Scholten, J., Stoffers, P., 1986. Geochemie und Mineralogie der Sedimente des Mittelindischen Rückens zwischen 21°S und der Rodriguez Triple Junction (SO 43)., In: GEMINO 2: Geothermale Metallogenese Indischer Ozean., 1–38, Aachen, RWTH, Aachen.

Poole, F. G., 1988, Stratiform barite in Paleozoic rocks of the western United States, 7th 1nternational Association on the Genesis of Ore Deposits Symposium Proceedings, pp. 309–319

Powell, C. M., Roots, S. R., Veevers, J. J., 1988. Pre–breakup continental extension in East Gondwanaland and the early opening of the eastern Indian Ocean. Tectonophysics 155, 261–283.

Price, R. C., Kennedy, A. K., Riggs–Sneeringer, M., Frey, F. A., 1986. Geochemistry of basalts from the Indian Ocean triple junction: implications for the generation and evolution of Indian Ocean ridge basalts. Earth Planet. Sci. Lett., 78, 379–396.

Puchelt, H., 1972. Barium. In: Wedepohl, K. H. (Ed.), Handbook of Geochemistry. Springer, Berlin, pp. 56BI–5602.

Rabouille, C., Gaillard, J. –F., Tréguer, P., Vincendeau, M. –A., 1997. Biogenic silica recycling in surficial sediments across the Polar Front of the Southern Ocean (Indian sector). Deep–Sea Res. II., 44 (5), 1151–1176.

Ragueneau, O., Gallinari, M., Corrin, L., Grandel, S., Hall, P., Hauvespre, A., Lampitt, R. S., Rickert, D., Stahl, H., Tengberg, A., Witbaard R., 2001. The benthic silica cycle in the northeast Atlantic: annual mass balance, seasonality, and importance of non–steady–state processes for the early diagenesis of biogenic opal in deep–sea sediments. Prog. Oceanogr., 50, 171–200.

Ragueneau, O., Treguer, P., Leymaert, A., Anderson, R.F., Brzezinski, M. A., DeMaster, D. J., Dugdale, R., Dymond, J. R., Fischer, G., Francois, R., Heinze, C., Maier–Reimer, E., Martin– Jezequel, V., Nelson, D. M., Queguiner, B., 2000. A review of the Si cycle in the modern ocean: recent progress and missing gaps in the application of biogenic opal as a paleoproductivity proxy. Global Planet. Change 26(4), 317–365.

Rajendran, S., Prakasa Rao, T. K. S., 2000. Analysis of a north – south magnetic profiles over the Central Indian Ocean. Curr. Sci., 78, 1378– 1381.

Ram, A. S. P., LokaBharathi, P.A., Nair, S., Chandramohan, D., 2001. A deep–sea bacterium with unique nitrifying property. Curr. Sci., 80, 1222–1224.

Ramana, M. V., Ramprasad, T., Desa, M., 2001. Seafloor spreading magnetic anomalies in the Enderby basin, East Antarctica. Earth Planet. Sci. Lett., 191, 241–255.

Ramana, M. V., Subrahmanyam, V., Chaubey, A. K., Ramprasad, T., Sarma, K. V. L. N. S., Krishna, K. S., Desa, M., Murty, G. P. S., 1997. Structure and origin of the 85°E Ridge. J. Geophys. Res., 102, 17995–18012.

Ramaswamy, V., Rao, P. S., 2006. Grain size analysis of sediments from the northern Andaman Sea: Comparison of laser diffraction and sieve–pipette techniques. J. Coast. Res., 22, 1000–1009.

Ramesh Babu, V., Suryanarayana, A., Murthy, V. S. N., 2001. Thermohaline circulation in the central Indian basin (CIB) during austral summer and winter periods of 1997. Deep–Sea Res., I 48, 3327–3342.

Rao, V. P., Nath, B. N., 1988. Nature, distribution and origin of clay minerals in grain size fractions of sediments from manganese nodule field, Central Indian Ocean Basin. Indian J. Mar. Sci., 17, 202-207.

Reeburgh, W. S., 1967. An improved interstitial water sampler. Limnol. Oceanogr., 12, 140–141.

Rickwood, P., 1989. Boundary lines within petrologic diagrams which use oxides of major and minor elements. Lithos., 22, 247-263.

Rimmer, S.M., 2004. Geochemical paleoredox indicators in Devonian–Mississippian black shales, central Appalachian basin (USA). Chem. Geol., 206, 373–391.

Rixen, T., Haake, B., Ittekkot, V., Guptha, M. V. S., Nair, R. R., Schlüssel, P., 1996. Coupling between SW monsoon–related surface and deep ocean processes as discerned from continuous particle flux measurements and correlated satellite data. J. Geophys. Res., 101, 28569–528582.

Rollinson, H. R., 1993. Using geochemical data: Evaluation, presentation, interpretation. Longman 352.

Rona, P.A., 1984. Hydrothermal mineralization at seafloor spreading centers. Earth Sci. Rev., 20, 1–104.

Rose, W. I., Chesner, C. A., 1987. Dispersal of ash in the great Toba eruption, 75 ka. Geol., 15, 913–917.

Roser, B. P., Coombs, D. S., Korsch, R. J., Campbell, J. D., Mortimer, N., Grapes, R., 2000. Whole–rock analyses of sandstones, silt–stones, and tuffs from the Murihiku Terrane, New Zealand. Res. Rep.–Vic. Univ. Wellingt., Sch. Earth Sci., 7, 26 pp.

Rowe, G. T., 1971. Benthic biomass and surface productivity. In: Costlow, J. D. (Ed.), Fertility of the sea. vol. 2, New York, Gordon and Breach, pp. 441–454.

Royer, J. Y., Patriat, P., Bergh, H. W., Scotese, C. R., 1988. Evolution of the Southwest Indian Ridge from the Late Cretaceous (anomaly 34) to the Middle Eocene (anomaly 20). Tectonophysics 155, 235–260.

Royer, J. Y., Sandwell, D. T., 1989. Evolution of the Eastern Indian Ocean since Late Cretaceous: Constraints from Geosat altimetry. J. Geophys. Res., 94, 13755–13782.

Royer, J.–Y., Gordon, R. G., 1997. The motion and boundary between the Capricorn and Australian plates. Science 277, 1268–1274.

Rubin, K., 1997. Degassing of metals and metalloids from erupting seamount and mid–ocean ridge volcanoes: observations and predictions. Geochim. Cosmochim. Acta., 61, 3525–3542.

Russell, J. D., 1979. An Infrared spectroscopic study of the interaction of nontronite and ferruginous montmorillonite with alkali metal hydroxides. Clay Miner., 14, 127.

Ruttenberg, K. C., 1992. Development of a sequential extraction method for different forms of phosphorus in marine sediments. Limnol. Oceanogr., 37, 1460–1482.

Ruttenberg, K. C., Berner, R. A., 1993. Authigenic apatite formation and burial in sediments from non-upwelling, continental margin environment. Geochim. Cosmochim. Acta., 57, 991-1007.

Ryther, J. H., 1969. Photosynthesis and fish production in the sea. Science 166, 72–76.

Sayles, F L., Martin, W. R., Deuser W. G., 1994. Response of benthic oxygen demand to particulate organic carbon supply in the deep sea near Bermuda. Nature 371, 686–689.

Sayles, F, L., 1981. The composition and diagenesis of interstitial solutions – II. Fluxes and diagenesis at the water–sediment interface in the high latitude North and South Atlantic. Geochim. Cosmochim. Acta., 45, 1061–1086.

Sayles, F. L., 1979. The composition and diagenesis of interstitial solutions–I Fluxes across the seawater– sediment interface in the Atlantic Ocean. Geochim Cosmochim. Acta., 43, 527–545.

Sayles, F. L., Bischoff, J. L., 1973. Ferromanganoan sediments in the equatorial East Pacific. Earth Planet. Sci. Lett., 19 (3), 330–336.

Schink, D. R., Guinasso Jr. N. L., Fanning K. A., 1975. Processes affecting the concentration of silica at the sediment–water interface of the Atlantic Ocean. J Geophys Res., 80, 3013–3031.

Schlich, R., 1982, The Indian Ocean: aseismic ridges, spreading centers, and oceanic basins, In: Nairn, A. E. M., Stehli, F. G. (Eds.), The Ocean Basins and Margins. 6, Plenum, New York, pp. 51–147.

Schneider, R. R., Price, B., Muller, P. J., Kroon, D., Alexander, I., 1997. Monsoon related variations in Zaire (Congo) sediment load and influence of fluvial silicate supply on marine productivity in the east equatorial Atlantic during the last 200,000 years. Paleoceanography 12, 463–481.

Schnetger, B., Brumsack, H. –J., Schale, H., Hinrichs, J., Dittert, L., 2000. Geochemical characteristics of deep–sea sediments from the Arabian Sea: a high–resolution study Deep–Sea Res. II., 47, 2735–2768.

Schöps, D., Herzig, P. M.., Halbach, P., Friedrich, G., Blum, N., 1993. Mineralogy, chemistry and oxygen isotope thermometry of nontronitic smectites from Central Pacific seamounts. Chem. Geol., 106, 331–343.

Schuller, P., Ellies, A., Castillo, A., Salazar, I., 2003. Use of ^{137}Cs to estimate tillage– and water–induced soil redistribution rates on agricultural land under different use and management in central–south Chile. Soil Tillage Res., 69, 69– 83.

Schulz, H. D., Dahmke, A., Schinzel, U., Wallmann, K., Zabel, M., 1994. Early diagenetic processes, fluxes and reaction rates in sediments of the South Atlantic. Geochim. Cosmochim. Acta., 58, 2041–2060.

Schulz, H. D., Zabel, M., 2000. Marine Geochemistry. Springer, Heidelberg.

Schulz, H., von Rad, U., Erienkeuser, H., 1998. Correlation between Arabian Sea and Greenland climate oscillations of the past 110,000 years. Nature 393, 54–57.

Sclater, J. G., Fisher, R. L., 1974. The evolution of the East Central Indian Ocean with emphasis on the tectonic setting of the Ninety East Ridge. Geol. Soc. Am. Bull., 85, 681–702.

Scudder, R. P., Murray, R., Plank, T., 2009. Dispersed ash in deeply buried sediment from the northwest Pacific Ocean: An example from the Izu–Bonin arc (ODP Site 1149). Earth Planet. Sci. Lett., 284, 639–648.

Setlock, G. H., 1979. Dissolved oxygen and nutrient distributions in interstitial waters of abyssal marine sediments. Early diagenetic in manganese nodule localities. Ph.D. Thesis. Uni. Wisconsin, Madison. 486 pp.

Severmann, S., Mills, R. A., Palmer, M. R., Fallick, A. E., 2004. The origin of clay minerals in active and relict hydrothermal deposits. Geochim. Cosmochim. Acta., 68(1), 73–88.

Sharma, R., Rao, A., 1992. Geological factors associated with megabenthic activity in the Central Indian Ocean Basin. Deep–Sea Res., 39, 705–713.

Shaw, T. J., Gieskes, J. M., Jahnke, R. A., 1990. Early diagenesis in di!ering depositional environments: the response of transition metals in pore water. Geochim. Cosmochim. Acta., 54, 1233–1246.

Sherrell, R. M., Field, M. P., Ravizza, G., 1999. Uptake and fractionation of rare earth elements on hydrothermal plume particles at 9° 45' N, East Pacific Rise. Geochim. Cosmochim. Acta., 52, 669–677.

Sherwood, B. A., Sager, S. L., Holland, H. D., 1987. Phosphorus in foraminiferal sediments from North Atlantic Ridge cores and in pure limestones. Geochim. Cosmochim. Acta., 51, 1861–1866.

Shibamoto, Y., Harada, K., 2010. Silicon flux and distribution of biogenic silica in deep sea sediments in the western North Pacific Ocean. Deep–Sea Res. I., 57, 163–174.

Shimmield, G. B., 1992. Can sediment geochemistry record changes in coastal upwelling palaeoproductivity? Evidence from northwest Africa and the Arabian Sea. In: Summerhayes, C. P., Prell, E. L., Emeis, K. –C. (Eds.), Upwelling Systems: Evolution Since the Early Miocene, Geological Society London, Special Publication, 64, 29–46.

Shimmield, G. B., Mowbray, S. R., Weedon, G. P., 1990. A 350 ka history of the Indian Southwest Monsoon–evidence from deep–sea cores, northwest Arabian Sea. Trans. Royal Society Edinburg, Earth Sci., 81, 289–299.

Shirayama, Y., 1984. The abundance of deep–sea meiobenthos in the western Pacific in relation to environmental factors. Oceanologia Acta 7, 113–121.

Sholkovitz, E. R., 1989. Artifacts associated with the chemical leaching of sediments for rare–earth elements. Chem. Geol., 77, 47–51.

Shterenberg, L. E., Kuzmina, O. V., Laputina, I. P., Tzepin, A. I., 1986. On the find of native aluminium in association with ZnO and $ZnCI_2$ in the sediments of site 647 (North–Eastern Pacific Ocean. Lith. Ore Dep., 1, 137–140. (in Russian).

Singer, A., Stoffers, P., Heller–Kallai, L., Szafranek, D., 1984. Nontronite in a deep–sea core from the south Pacific. Clays Clay Miner., 32, 375–383.

Singh, P., 2009. Major, trace and REE geochemistry of the Ganga River sediments: influence of provenance and sedimentary processes. Chem. Geol., 266, 251–264.

Sirocko, F., Lange, H., 1991. Clay mineral accumulation rates in the Arabian Sea during the Late Quaternary. Mar. Geol., 97, 105–119.

Skyes, T. J. S., Kidd, R. B., 1994. Volcanogenic sediment distribution in the Indian Ocean through the Cretaceous and Cenozoic and their paleoenvironmental implications. Mar. Geol., 116, 267–291.

Slomp, C. P., Malschaert, J. F. P., Van Raaphorst W., 1998. The role of adsorption in sediment–water exchange of phosphate in North Sea continental margin sediments. Limnol. Oceanogr., 43, 832–846.

Smith, C. R., Pope, R. H., De Master, D. J., Magaard, L., 1993. Age–dependent mixing of deep–sea sediments. Geochim. Cosmochim. Acta., 57, 1473–1488.

Smith, K. L., Jr., Baldwin, R. J., Williams, P. M., 1992. Reconciling particulate organic carbon flux and sediment community oxygen consumption in the deep North Pacific. Nature 359, 313–316.

Smith, K. L., Kaufmann R. S., Baldwin R. J., 1994. Coupling of near–bottom pelagic and benthic processes at abyssal depths in the eastern North Pacific. Limnol. Oceanogr., 39, 1101–1118.

Smith, V. C., Pearce, N. J. G., Matthews, N. E., Westgate, J. A., Petraglia, M. D., Haslam, M., Lane, C. S., Korisettar, R., Pal, J. N., 2011. Geochemical fingerprinting of the widespread Toba tephra using biotite compositions. Quat. Int., 246, 97–104.

Smith, V. C., Shane, P., Nairn, I. A., 2005. Trends in rhyolite geochemistry, mineralogy, and magma storage during the last 50 kyr at Okataina and Taupo volcanic centres, Taupo volcanic zone, New Zealand. J. Volc. Geotherm. Res., 148, 372–406.

Sokolova, M. N., 1972. Trophic structure of deep–sea macrobenthos. Mar. Biol., 16, 1–12.

Stein, C. A., Cloetingh, S., Wortel, R., 1989. Seasat derived gravity data constraints on stress and deformation in the northeastern Indian Ocean. Geophys. Res. Lett., 16, 823–826.

Straub, S. M., 1995. Contrasting compositions of Mariana Trough fallout tephra and Mariana island arc volcanics: a fractional crystallization link. Bull. Volcanol., 57 (6), 403–421.

Straub, S. M., 1997. Multiple sources of Quaternary tephra layers in the Mariana Trough. J. Volcanol. Geotherm. Res., 76, 251–276.

Straub, S. M., Layne, G. D., 2003. The systematics of chlorine, fluorine and water in Izu arc front volcanic rocks. Implications for volatile recycling in subduction zones. Geochim. Cosmochim. Acta., 67, 4179–4203.

Suess, E., 1980. Particulate organic carbon flux in the oceans surface productivity and oxygen utilization. Nature 288, 260–263.

Sukumaran, N. P., Banerjee, R., Borole, D. V., Gupta, S. M., 1999. Some aspects of volcanic ash layers in the Central Indian Basin. Geo–Mar. Lett., 18, 203–298.

Sun, S. S., Nesbitt, R. W., Sharaskin, A. Y., 1979. Geochemical characteristics of mid–ocean ridge basalts. Earth Planet. Sci. Lett., 44(119), 138.

Sun, Z., Zhou, H., Glasby, G. P., Yang, Q., Yin, X., Li, J., Chen, Z., 2012. Formation of Fe–Mn–Si oxide and nontronite deposits in hydrothermal fields on the Valu Fa Ridge, Lau Basin. J. Asian Earth Sci., 43, 1, 64–76.

Sutton, A. N., Blake, S., Wilson, C. J. N., 1995. An outline geochemistry of rhyolitic eruptives from Taupo volcanic centre, New Zealand. J. Volcanol. Geotherm. Res., 68, 153–175.

Sverdrup, H. U., Johnson, M. W., Flemig, R. H., 1942. The Oceans: Their Physics, Chemistry and general Biology. Prentice–Hall, pp. 1087.

Tapscott, C., Patriat, P., Fisher, R. L., Sclater, J. G., Hoskins, H., Parsons, B., 1980. The lndian Ocean Triple Junction. J. Geophys. Res., 85, 4723–4739.

Taylor, S. R., McLennan, S. M., 1985. The Continental Crust: Its Composition and Evolution, Blackwell, Malden, Mass, 312 pp.

Tchernia, P., 1980. Descriptive Regional Oceanography. 253 pp. Pergamon, New York.

Thiel, H., 1966. Quantitative Untersuchungen iiber die Meiofauna des Tiefseebodens. Veroff. Inst. Meeresforsch. Bremerh., Vol. 2, 131-147.

Tlig, S., Steinberg, M., 1982. Distribution of rare–earth elements (REE) in size fractions of recent sediments of the Indian Ocean. Chem. Geol., 37, 317–333.

Toole, J. M., Warren, B. A., 1993. A hydrographic section across the subtropical South Indian Ocean. Deep–Sea Res. I., 40, 1973–2019.

Toth, J. R., 1980. Deposition of submarine crusts rich in manganese and iron. Geol. Soc. Am. Bull., 91, 44–54.

Trefry, J. H., Trocine, R. P., Klinkhammer, G. P., Rona, P. A., 1985. Iron and copper enrichment of suspended particles in dispersed hydrothermal plumes along the Mid Atlantic Ridge. Geophy. Res. Lett., 12, 506–509.

Turekian, K. K., 1964. The marine geochemistry of strontium.Geochim. Cosmochim. Acta., 28, 1479–1496.

Turekian, K. K., 1965. Some aspects of the geochemistry of marine sediments. In: Riley, J., Skirron, G. (Eds.), Chemical Oceanography. Academic Press, London, pp. 81–126.

Turekian, K. K., 1977. The fate of metals in the oceans. Geochim. Cosmochim. Acta., 1, 1139– 1144.

Turekian, K. K., Katz, A., Chan, L., 1973. Trace element trapping in pteropod tests. Limnol. Oceanogr., 18, 240–249.

Turekian, K. K., Wedepohl, K. H., 1961. Distribution of elements in some major units of the earths crust. Bull. Geol. Soc. Am., 72, 175–192.

Turney, C. S. M., Lowe, J. J., Davies, S. M., Hall, V. A., Lowe, D. J., Wastegard, S., Hoek, W. Z., Alloway, B., SCOTAV and INTIMATE groups. 2004. Tephrochronology of Last Termination sequences in Europe: a protocol for improved analytical precision and robust correlation procedures (a joint SCOTAV–INTIMATE proposal). J. Quat. Sci., 19, 111–120.

Udintsev, G. B., 1975. Geological and Geophysical Atlas of the Indian Ocean. Udintsev, G. B. (Ed.), Academy Science, USSR, Moscow, 23.

Ukstins Peate, I., Baker, J. A., Kent, A. J. R., Al–Kadasi, M., Al–Subbary, A., Ayalew, D., Menzies, M., 2003. Correlation of Indian Ocean tephra to individual Oligocene silicic eruptions from Afro–Arabian flood volcanism. Earth Planet. Sci. Lett., 211, 311–327.

Upton, B. G. J., Wadsworth, W. J., 1966. The basalts of Reunion Island, Indian Ocean. Bull. Volcanol., 29, 7–23.

Urbat, M., Pletsch, T., 2003. Pleistocene deep-sea sediment in ODP Hole 1149A, Nadezhda Basin; sources, alteration, and age controls (0–800 ka). Proc. Ocean Drill. Program, Sci. Results 185, 21.

Vallier, T. L., Kidd, R. B., 1977. Volcanic sediments in the Indian Ocean. In: Heirtler, J. R., Bolli, H. M., Davies, T. A., Saunders, J. B., Sclater, J. G. (Eds.), Indian Ocean Geology and Biostratigraphy. Am. Geophys. Union, Geophys. Monogr., pp. 87–118.

Valsangkar, A. B., 2007. A device for finer–scale sub–sectioning of aqueous sediments. Curr. Sci., 92(4), 428–431.

Valsangkar, A. B., 2011. Spatial distribution and longitudinal variation of clay minerals in the Central Indian Basin. Acta. Geol. Sin., 85, 814–825.

Van Bennekom, A. J., Berger, G. W., Van der Gaast, S. J., De Vries, R. T. P., 1988. Primary productivity and the silica cycle in the Southern Ocean (Atlantic Sector). Palaeogeogr. Palaeoclimatol. Palaeoecol., 67, 19–30.

Van Beusekom, J. E. E., Weigelt–Krenz, S., Martens, P., 2008. Long term variability of winter nitrate concentrations in the Northern Wadden Sea driven by fresh water discharge, decreasing denitrification. Helgoland Marine Research 62, 49–57.

Van der Borch, C. C., Sclater, J. G., and others 1974. Site 218 initial report deep sea drilling project, (Washington DC: Govt. Printing Office) 22, 325–348.

Van der Marcel, H. W., Beutel Spacher, H., 1976. Atlas of the infrared spectra of clay minerals and their admixtures. Elsevier, Amsterdam, pp. 146–148.

Van Raaphorst, W., Kloosterhuis, H. T., 1994. Phosphate sorption in superficial intertidal sediments. Mar. Chem., 48, 1, 1–16.

Van Raaphorst, W., Ruardij, P., Brinkman, A. G., 1988. The assessment of benthic phosphorus regeneration in an estuarine ecosystem model. J. Sea Res., 22, 1, 23–36.

Vineesh, T. C., Nath B. N., Banerjee, R., Jaishankar, S., Lekshmi, V., 2009. Manganese nodule morphology as indicators for oceanic processes in the Central Indian Basin. Int. Geol. Rev., 51, 27–44.

Vital, H., Stattegger, K., 2000. Major and trace elements of stream sediments from the lowermost Amazon River. Chem. Geol., 168, 151–168.

Von Damm, K. L., Edmond, J. M., Grant, B., Measures, C. I., Walden, B., Weiss, R. F., 1985. Chemistry of submarine hydrothermal solutions at 21°N, East Pacific Rise. Geochim. Cosmochim. Acta., 49, 2197–2220.

von Eynatten, H., Barceló–Vidal, C., Pawlowsky–Glahn, V., 2003. Modeling compositional change: the example of chemical weathering of granitoid rocks. Math. Geol., 35, 231–251.

von Rad, U., Burgath, K. –P., Pervaz, M., Schulz, H., 2002. Discovery of the Toba Ash (c. 70 ka) in a high–resolution core recovering millennial monsoonal variability off Pakistan. In: Clift, P. D. et al. (Eds.). The tectonic and climatic evolution of the Arabian Sea region. Geol. Soc. Sp. Pub., London, 195, 445–461.

Wakefield, S. J., 1982. Silica distribution in interstitial waters and sediments from the south–eastern Pacific. Sediment. Geol., 31, 13–31.

Wallace, P.J., 2002. Volatiles in submarine basaltic glasses from the northern Kerguelen Plateau (ODP Site 1140): implications for source region compositions, magmatic processes, and plateau subsidence. J. Petrol., 43 (7), 1311–1326.

Walling, D. E., Collins, A. L., Sichingabula, H. M., 2003. Using unsupported lead–210 measurements to investigate soil erosion and sediment delivery in a small Zambian catchment. Geomorphology 52, 193–213.

Walter, P., Schwarz, P., Scholten, J., Stoffer, P., 1986. Geochemie und Mineralogie der Sedimente des Mittelindischen Rückens zwischen 21°S und der Rodriguez Triple Junction (SO 43). In: GEMINO 2: Geothermale Metallogenese Indischer Ozean, 1–38, Aachen, RWTH, Aachen.

Walter, P., Stoffers, P., 1985. Chemical characteristics of metalliferous sediments from eight areas on the Galapagos rift and East Pacific Rise between 2°N and 42°S, Mar. Geol., 65, 271–287.

Warren, B. A., 1981a. Trans–Indian hydrographic section at latitude 18°S: property distributions and circulations in the South Indian Ocean. Deep–Sea Res., 28, 759–788.

Warren, B. A., 1981b. The shallow oxygen minimum of the South Indian Ocean. Deep–Sea Res., 28, 859–864.

Warren, B. A., 1982. The deep water of the Central Indian Basin. J. Mar. Res., 40 (Supplement), 823–860.

Wastegård, S., 2005. Late Quaternary tephrochronology of Sweden: a review. Quat. Int., 130, 49–62.

Wehausen, R., Brumsack, H. –J., 1999. Cyclic variations in the chemical composition of eastern Mediterranean Pliocene sediments: a key for understanding sapropel formation. Mar. Geol., 153, 161–176.

Wei, S., Puling, L., Mingyi, Y., Yazhou, X., 2003. Using REE tracers to measure sheet erosion changing to rill erosion. J. Rare Earths., 21, 587–590.

Weissel, J. K., Anderson, R. N., Geller, C. A., 1980. Deformation of the Indo–Australian plate. Nature 287, 284–291.

Westgate, J., Shane, P. A. R., Pearce, N. J. G., Perkins, W. T., Korisettar, R., Chesner, C., Williams, M. A. J., Acharyya, S. K., 1998. All Toba tephra occurrences

across peninsular Indiabelong to the 75,000 yr BP eruption. Quat. Res., 50, 107–112.

Wheat, C. G., McDuff, R. E. 1994. Hydrothermal flow through the Mariana Mounds: Dissolution of amorphous silica and degradation of organic matter on a mid-ocean ridge flank, Geochim. Cosmochim. Acta, 58, 2461–2475.

White, J. L., 1971. Interpretation of infrared spectra of soil minerals. Soil Sci., 112, 22–31.

Whitfield, M., Turner, D. R., 1979. Water–rock partition coefficients and the composition of seawater and river water. Nature (London), 278, 132–137.

Whitford, D. J., Korsch, M. J., Porritt, P. M., Craven, S. J., 1988. Rare–earth element mobility around the volcanogenic polymetallic massive sulfide deposit at Que River, Tasmania, Australia. Chem. Geol., 68 (1–2), 105–119.

Wilson, C.J.N., 1993. Stratigraphy, chronology, styles and dynamics of late Quaternary eruptions from Taupo volcano, New Zealand. Philos. Trans. R. Soc. Lond. A 343, 205–306.

Wilson, D. L., Smith, W. O. Jr., Nelson, D. M., 1986. Phytoplankton bloom dynamics of the western Ross Sea ice edge. I. Primary productivity and species–specific production. Deep–Sea Res., 33, 1375–1387.

Wohletz, K. H., 1983. Mechanisms of hydrovolcanic pyroclast formation: Size, shape, and experimental studies. J. Volcanol. Geotherm. Res., 17, 31–63.

Woulds, C., Anderson, J. H., Cowie, G. L., Middelburg, J. J., Levin, L. A., 2009. The short–term fate of organic carbon in marine sediments: Comparing the Pakistan margin to other regions. Deep–Sea Res II., 56, 393–402.

Woulds, C., Schwartz, M. C., Brand, T., Cowie, G. L., Law, G., Mowbray, S. R., 2009. Porewater nutrients concentrations and benthic nutrient fluxes across the Pakistan margin OMZ. Deep–Sea Res. II., 56, 333–346.

Wronkiewicz, D. J., Condie, K. C., 1989. Geochemistry and provenance of sediments from the Pongola Supergroup, South Africa: evidence for a 3.0–Ga–old continental craton. Geochim. Cosmochim. Acta., 53, 1537–1549.

Wulf, S., Kraml, M., Brauer, A., Keller, J., Negendank, J. F. W. 2004. Tephrochronology of the 100 ka lacustrine sediment record of Lago Grande di Monticchio (southern Italy). Quaternary International 122, 7–30.

Yang, K., Scott, S. D., 1996. Possible contribution of a metal–rich magmatic fluid to a sea–floor hydrothermal system. Nature, 383, 420–423.

Zabel, M., Dahmke, A., Schulz, H. D., 1998. Regional distribution of diffusive phosphate and silicate fluxes through the sediment–water interface: the eastern South Atlantic. Deep–Sea Res. I., 45, 277–300.

Zeng, Z., Ouyang, H., Yin, X., Chen, S., Wang, X., Wu, L., 2012. Formation of Fe–Si–Mn oxyhydroxides at the PACMANUS hydrothermal field, Eastern Manus Basin: Mineralogical and geochemical evidence. J. Asian Earth Sci., 60, 22, 130–146.

Zhang, X. C., Nearing, M. A., Polyakov, V. O., Friedrich, J. M., 2003. Using rare–earth oxide tracers for studying soil erosion dynamics. Soil Sci. Soc. Am. J., 67, 279–288.

Ziegler, C. L., Murray, R. W., Hovan, S. A., Rea, D. K., 2007. Resolving eolian, volcanogenic, and authigenic components in pelagic sediment from the Pacific Ocean. Earth Planet. Sci. Lett., 254, 3–4, 416–432 .

Zoback, M. L., et al., 1989. Global patterns of tectonic stress. Nature 341, 291–298.

Publications

- Singh, P., Raghukumar, C., Parvatkar, R. R., **Mascarenhas-Pereira, M. B. L.,** 2013. Heavy metal tolerance in the psychrotolerant Cryptococcus sp. isolated from deep-sea sediments of the Central Indian Basin. Yeast 30; 2013; 93-101**.**

- Nath, B. N., Sijinkumar, A. V., Borole, D. V., Gupta, S. M., Mergulhao, L. P., **Mascarenhas-Pereira, M. B. L.,** Ramaswamy, V., Guptha, M. V. S., Possnert, G., Aldahan, A., Khadge, N. H., Sharma, R., 2013. Record of carbonate preservation and the Mid-Brunhes climatic shift from a seamount top with low sedimentation rates in the Central Indian Basin. Boreas, doi: 10.1111/j.1502-3885.2012.00304.x. ISSN 0300-9483.

- Biche, S., Pandey, S., Gonsalves, M. J. B. D., Das, A., **Mascarenhas-Pereira, M. B. L.,** LokaBharathi, P. A., 2012. Phosphate solubilizing bacteria: comparison between coastal and deep sea sediments. J. Coast. Environ., 3(2), 153-164.

- Das, A., Fernandes, C. E. G., Naik, S. S., Nath, B. N., Suresh, I., **Mascarenhas-Pereira, M. B. L.,** Gupta, S. M., Khadge, N. H., Prakash Babu, C., Borole, D. V., Sujith, P. P., Valsangkar, A. B., Mourya, B. S., Biche, S. U., Sharma, R., Loka Bharathi, P A., (2011). Bacterial response to contrasting sediment geochemistry in the Central Indian Basin. Sedimentology. doi: 10.1111/j.1365-3091.2010.01183.x

- **Mascarenhas–Pereira, M. B. L.,** Nath, B. N., 2010. Selective leaching studies of sediments from a seamount flank in the Central Indian Basin: Resolving hydrothermal, volcanogenic and terrigenous sources using major, trace and rare–earth elements. Marine Chemistry doi: 10.1016/j.marchem.2010.03.004.

- Nath, B. N., Borole, D. V., Aldahan, A., Patil, S. K., **Mascarenhas-Pereira, M. B. L.,** Possnert, G., Ericsson, T., Ramaswamy, V., Gupta, S. M., 2008. ^{210}Pb, ^{230}Th and ^{10}Be in Central Indian Basin seamount sediments: Signatures of degassing and hydrothermal alteration of recent origin. Geophysical Research Letters. 35; L09603, doi:10.1029/2008GL033849.

- Iyer, S .D., **Mascarenhas-Pereira,** M. B. L., Nath, B. N., 2007. Native aluminium (spherules and particles) in the Central Indian Basin sediments: Implications on the occurrence of hydrothermal events. Marine Geology 240, 77-184.

- Nath, B. N., Aldahan, A., Possnert, G., Selvaraj, K., **Mascarenhas-Pereira, M. B. L.,** Chen, C. T. A., 2007. ^{10}Be variation in surficial sediments of the Central Indian Basin. Nuclear Instruments and Methods in Physics Research Section B: Beam Interactions with Materials and Atoms 259, 610-615.
- **Mascarenhas-Pereira**, **M. B. L.,** Nath, B. N., Borole, D. V., Gupta, S. M., 2006. Nature, source and composition of volcanic ash in sediments from a fracture zone trace of Rodriguez Triple Junction in the Central Indian Basin. Marine Geology 229, 79-90.

Workshops/Conferences

1. Benthic pelagic coupling in the Central Indian Basin. 2011. **Mascarenhas-Pereira**, **M. B. L.,** Nath, B. N., Kurian, S., Khadge, N. H., Paper presented during the Seventh International Conference on Asian Marine Geology, NIO Goa held during 11 to 14th Oct 2011.
2. Age and nature of ferromanganese coated pumices from the Central Indian Ocean Basin. 2011. Kalangutkar, N., Iyer, S. D., **Mascarenhas-Pereira, M. B. L.,** Nath, B. N., Paper presented during the AOGS, August, 8-12, 2011 at Taipei, Taiwan.
3. Biogenic Silica: An important proxy for paleo-climate reconstruction: A case of orbital forcing on paleoproductivity in the Central Indian Basin. 2011. Chauhan T., **Mascarenhas-Pereira, M. B. L.,** Nath, B. N., Borole, D. V., Kurian, S., Paper presented during the AOGS August, 8-12, 2011 at Taipei, Taiwan.
4. Was Mid-Brunhes Climate Shift (MBCS) a response to eccentricity minimum repeated at every 400-ka in the last ~3 Million years? Gupta, S.M., Nath, B.N., **Mascarenhas-Pereira, M.B.L.,** 2011. Paper presented during the National conference on Science of Climate Change and Earth's Sustainability, ESI-Lucknow
5. Silica budget at the sediment-water interface in the Central Indian Basin. 2010. Teena Chauhan, **Mascarenhas-Pereira, M. B. L.,** Nath, B. N., Borole, D. V., Kurian, S., Paper presented during the 8th International Sedimentological Congress, Mendoza, Argentina during 26th Sept to 1st Oct 2010
6. Sink pathways and transformation of Phosphorus in Andaman Back-arc Basin sediments with hydrothermal signatures. 2008. Nath, B. N., Naman, D., Kurian, S., **Mascarenhas-Pereira, M.B.L.,** Kumar, M., Kamesh Raju, K.A., Paper presented during the AOGS at Busan, Korea.

7. On the variability of ^{10}Be in Central Indian Basin sediments in a fracture zone setting. 2008. Nath, B.N, Aldahan, A, Borole, D.V, **Mascarenhas-Pereira, M.B.L**, Possnert, G, Naik, T. Paper presented during the 11th International Conference on Accelerator Mass Spectrometry on 14-19th Sep, at Rome.

8. Tectonic and climatic forcing on the 3 million year record from the central Indian Basin. 2006. Nath, B. N., Rao, B. R., Aldahan, A., Gupta, S. M., Borole, D. V., Possnert, G., **Mascarenhas-Pereira, M. B. L.,** Paper presented during the CSIR-NSFC workshop on Global change: Ocean-Atmosphere-Land interactions driven by Monsoon held at N.I.O, Goa during December 4 to 6, 2006.

9. ^{10}Be variation in surficial sediments of the Central Indian Basin. 2005. Nath, B. N., Aldahan, A., Selvaraj, K., **Mascarenhas-Pereira**, **M. B. L.,** Possnert, G., Paper presented during the 10th International Conference on Accelerator Mass Spectrometry, Berkeley, California during September 5 to 10, 2005.

10. Evidence for hydrothermal signatures in the Central Indian Basin sediments recovered from a seamount flank. 2004. **Mascarenhas-Pereira**, **M. B. L.,** Nath, B. N., Gupta S. M., Paper presented during National symposium on application of Marine Geosciences, held at N.I.O during February 19-20, 2004.

11. Variable orbital forcing on biogenic and lithogenic fractions in a sediment core from the Central Indian Basin responding to monsoonal and tectonic controls. 2003 Nath, B. N., **Mascarenhas**, **M. B. L.,** Gupta, S. M., Sarkar, S., Naman, D., Paper presented during International workshop on Monsoon evolution and Tectonic-climate Linkage in Asia held at Tokyo Metropolitan University, Japan during November 21-23, 2003.

In Review

1. Study of copper-sediment interactions in deep sea sediments influenced by hydrothermal activity from the Central Indian Basin: A multi-method approach. Chakraborty, P., Saranya Jayachandran., Nath, B. N., Lathika N., Nagaraju G., Kartheek C., Krushna V., **Mascarenhas-Pereira, M. B. L.,** (communicated to Environmental Pollution)

2. Alkaline phosphatase activity is widely prevalent in deep sea sediments of Central Indian Basin. Biche, S., Das, A., **Mascarenhas-Pereira, M. B. L**., Nath, B.,

Naik, S., Helekar, S., Sharma, R., LokaBharathi, P. A., (communicated to Extremophiles).

3. Age and nature of ferromanganese coated pumices from the Central Indian Ocean Basin Kalangutkar, N., Iyer, S. D., **Mascarenhas-Pereira, M. B. L.,** Nath, B. N., (communicated to Quaternary International)

4. Volcanogenic sedimentation along a fracture zone in the Central Indian Basin **Mascarenhas-Pereira, M. B. L.,** Nath, B. N., Borole, D. V., (submitted to Marine Geology).

5. Silica budget at the sediment-water interface in the Central Indian Basin. Chauhan, T., **M. B. L.Mascarenhas-Pereira**, Nath, B. N., Borole, D. V., Kurian, S., (ready for submission to Geochimica et Cosmochimica Acta)

BOREAS An international journal of Quaternary research

Record of carbonate preservation and the Mid-Brunhes climatic shift from a seamount top with low sedimentation rates in the Central Indian Basin

BEJUGAM NAGENDER NATH, ADUKKAM V. SIJINKUMAR, DNYANDEV V. BOROLE, SHYAM M. GUPTA, LINA P. MERGULHAO, MARIA B. L. MASCARENHAS-PEREIRA, VENKITASUBRAMANI RAMASWAMY, MEDIMI V. S. GUPTHA, GÖRAN POSSNERT, ALA ALDAHAN, NANDKUMAR H. KHADGE AND RAHUL SHARMA

BOREAS

Nagender Nath, B., Sijinkumar, A. V., Borole, D. V., Gupta, S. M., Mergulhao, L. P., Mascarenhas-Pereira, M. B. L., Ramaswamy, V., Guptha, M. V. S., Possnert, G., Aldahan, A., Khadge, N. H. & Sharma, R. 2013 (July): Record of carbonate preservation and the Mid-Brunhes climatic shift from a seamount top with low sedimentation rates in the Central Indian Basin. *Boreas*, Vol. 42, pp. 762–778. doi: 10.1111/j.1502-3885.2012.00304.x. ISSN 0300-9483.

In the present investigation, an age model of carbonate-rich cores from a seamount top in the Central Indian Basin (CIB) was constructed using both isotopic ($^{230}Th_{excess}$, AMS ^{14}C, oxygen isotopes) and biostratigraphic methods. The chronologies using the two methods are in good agreement, yielding a record of the late Middle Pleistocene to the Pleistocene–Holocene transition (550 to 11.5 ka). The first appearance datum (FAD) of the radiolarian *Buccinosphaera invaginata* (180 ka) and coccolith *Emiliania huxleyi* (268 ka) and the last appearance datum (LAD) of the radiolarian *Stylatractus universus* (425 ka) were used. A monsoon-induced productivity increase was inferred from carbonate, organic carbon and $\delta^{13}C$ records in response to the Mid-Brunhes Climatic Shift (MBCS), consistent with an increased global productivity. While the coccolith diversity increased, a decrease in coccolith productivity was found during the MBCS. At nearly the same time period, earlier records from the equatorial Indian Ocean, western Indian Ocean and eastern Africa have shown an increased productivity in response to the influence of westerlies and increased monsoon. The influence of easterlies from Australia and the intensification of aridity are evidenced by increased kaolinite content and clay-sized sediments in response to the MBCS. An increased abundance of *Globorotalia menardii* and other resistant species beginning from marine isotope stage (MIS) 11 and the proliferation of coccolith *Gephyrocapsa* spp. indicate increased dissolution, which is consistent with the widespread global carbonate dissolution during this period. The relatively high carbonate dissolution during the transition period of MIS 3/2 and glacial to interglacial periods (MIS 6, 7 and 8) may be due to the enhanced flow of corrosive Antarctic Bottom Water (AABW) into the CIB.

Bejugam Nagender Nath (nagender@nio.org), Adukkam V. Sijinkumar (sijingeo@gmail.com; present address: Department of Post Graduate Studies & Research in Geology, Govt. College Kasaragod, Kerala 671123, India), Dnyandev V. Borole (dnyanb@gmail.com), Shyam M. Gupta (smgupta@nio.org), Lina P. Mergulhao (mlina@rediffmail.com), Maria B. L. Mascarenhas-Pereira (mariab@nio.org), Venkitasubramani Ramaswamy (rams@nio.org), Medimi V. S. Guptha (medimi.guptha@googlemail.com; present address: 62, Sagar Society, Dona Paula, Goa 403004, India), Nandkumar H. Khadge (khadge@nio.org) and Rahul Sharma (rsharma@nio.org), Geological Oceanography Division, National Institute of Oceanography (CSIR), Dona Paula, Goa-403 004, India; Göran Possnert (goran.possnert@teknik.uu.se), Tandem Laboratory, Uppsala University, Regementsvägen 1, SE-752 37 Uppsala, Sweden; Ala Aldahan (ala.aldahan@geo.uu.se), Department of Earth Sciences, Uppsala University, Villavägen 16 B, 752 36 Uppsala, Sweden and Department of Geology, United Arab Emirates University, P.O. Box 17551, Al Ain, UAE; *received 4th March 2012, accepted 5th September 2012.*

While studies of the past monsoon, upwelling and productivity in South and East Asia have received widespread attention, the palaeomonsoonal variation in areas south of the southern limit of the Intertropical Convergence Zone (ITCZ) in the Indian Ocean is poorly known. Studies of the Central Indian Basin (CIB) provide an opportunity to remedy this. It is expected that the summer monsoon can have a greater effect than the winter monsoon, owing to weak and variable dry winds from the land towards the sea. Studies related to the reconstruction of monsoon and related productivity variations from the CIB for the Quaternary are much rarer (e.g. Gupta 2003, 2009; Gupta *et al*. 2006) than studies of the northwestern and northeastern Indian Ocean. The Pleistocene palaeoceanographic changes of the CIB have been studied by various workers based on micropalaeontological and geochemical variations (Pattan *et al*. 1992, 2005; Gupta 1996; Banakar *et al*. 1997, 2003; Gupta *et al*. 2006). Based on the distribution of modern monsoonal radiolarian assemblages (Gupta 1996) and their late Quaternary variations (Gupta & Fernandes 1997), Gupta *et al*. (1996) reconstructed tropical sea-surface temperatures (SSTs) using the transfer function technique, and found the influence of the Earth's orbital eccentricity cycles on monsoonal SSTs for the last ~1.4 Ma in the CIB.

Studies based on planktic foraminifera are lacking mainly because of the lack of well-preserved carbonate records. Because many of the sediments of the CIB are below the CCD (Carbonate Compensation Depth), carbonate dissolution limits their use for the reconstruction of palaeotemperature and palaeoceanographic conditions from foraminifera and their oxygen isotope analysis. Thus, palaeoceanographic studies in the CIB so far have relied on radiolarian-based

DOI 10.1111/j.1502-3885.2012.00304.x

biostratigraphic and $^{230}Th_{excess}$-based radiometric dating methods (Banakar *et al.* 1991; Gupta 2002; Mascarenhas-Pereira *et al.* 2006; Nath *et al.* 2008). Here we present the first carbonate-based palaeoceanographic record from the CIB, which was made possible by sampling of the seamount top, which is situated close to the lysocline. We have studied the late Quaternary carbonate preservation and productivity changes based on planktic foraminifera, coccolithophores and geochemical proxies. We also present a record of regional response to the Mid-Brunhes Climatic Shift (MBCS). The MBCS occurs from 430 to 300 ka, with the amplitude of glacial–interglacial climate cycles increasing substantially from early MIS 11 (Jansen *et al.* 1986). The chronological framework is constructed using radiolarian and coccolith biostratigraphy and radiochemical ($^{230}Th_{excess}$ and ^{14}C) methods, and the glacial–interglacial stages are identified using the oxygen isotope data.

Oceanographic settings

Studies of chemical properties of the water column in the CIB show three equator-ward-moving water-masses (de Sousa *et al.* 2001). The fastest moving water-mass in the depth range 125–200 m is characterized by high salinity (34.74–34.77 psu) and an oxygen minimum associated with weak maxima in nutrients. The second water-mass with deep oxygen maximum (234–245 μm) in the depth range 250–750 m, is associated with minima in nutrients and a relatively high pH. The third water-mass, present at depths 800–1200 m with a low salinity (34.71–34.72 psu) and a density (sigma-theta-σ_t) range of 27.2–27.5, corresponds to the Antarctic Intermediate Water (AAIW) (de Sousa *et al.* 2001). The bottom is bathed by the North Indian Deep Water (NIDW), which is formed by the mixing of Antarctic Bottom Water (AABW), North Atlantic Deep Water (NADW) and the deep water of the Northern Indian Ocean (Tchernia 1980). The abyssal depths (>4000 m) are filled with a water-mass of southern origin, mainly the AABW, which has high levels of dissolved oxygen (Tchernia 1980; Warren 1982; Ramesh Babu *et al.* 2001). The AABW is blocked by the South East Indian Ridge on the southern side and by Ninety East Ridge (except for a few openings) on the eastern side of the basin. The Central Indian Ridge acts as a barrier for the bottom-water currents from the Madagascar and Crozet basins entering into this basin. According to Kolla *et al.* (1976), the carbonate lysocline and carbonate critical depth (CCrD) along a latitudinal transect of 10–20°S in the CIB are at 4000 and 5050 m, respectively, and deepen towards the south, whereas Banakar *et al.* (1998) placed the depth of the lysocline at 4400 m and the CCD at a depth of 4700 m.

Materials and methods

Sampling

Two box cores, namely BC 37 (16°06.031′S, 75°26.04′E, water depth: 4252 m, core length: 0.40 m) and SVBC 37 (16°06.943′S, 75°25.083′E, water depth: 3992 m, core length: 0.25 m), collected from the top of a seamount during the 4th and 26th expeditions of RV 'Akademik Boris Petrov' (Fig. 1) were used in the present study. The seamount at the point where the two

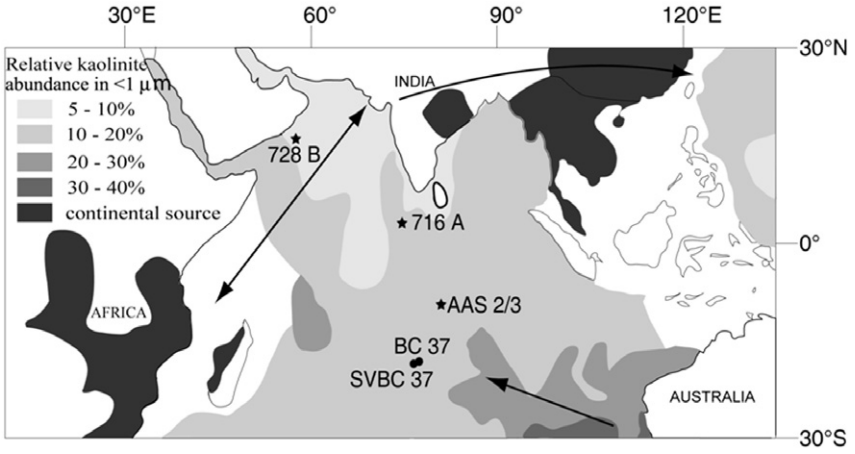

Fig. 1. Location map of seamount cores BC 37 and SVBC 37, and relative percentage of kaolinite in the <1-μm clay size fraction in sediments of the Indian Ocean and surrounding seas (Griffin *et al.* 1968; Fagel 2007). The continental source of kaolinite for marine sediments is also shown. Arrows depict jet stream transport pathways in the Asian subcontinent, and the tropospheric transport path is shown from the Australian continent to the Central Indian Basin and between Arabia and Africa (Lisitzin 1996). Locations of cores considered for discussion are shown. AAS 2/3 (7°48′S, 80°E; Gupta 2009); 716A represents ODP Hole 716A located in the equatorial Indian Ocean (4°56′N, 73°17′E); and 728B represents ODP Hole 728B in the NW Arabian Sea (17°40.790′N, 57°49.553′E) (Gupta *et al.* 2010).

sediment cores were collected is ~1200 m high, rising from a sea-floor depth of ~5100 m (Fig. 2). The seamount is located on the flanks of the 76°30′E fracture zone (Fig. 2). Core BC 37 was subsampled at 2-cm intervals, and SVBC 37 at 1-cm intervals for the present investigation. Core BC 37 is characterized by two distinct sediment layers: the top 0–16 cm is composed of foraminifera-rich homogenous greyish orange pink sediments, and the bottom mixed layer comprises moderate brown to moderate yellowish brown sediments with dark yellowish orange intercalations. SVBC 37 comprises brown to white foraminiferal ooze. The location of the cores in relation to the seamount top provides an opportunity to study the palaeoceanography of carbonate sediments in a predominantly siliceous ooze domain.

Foraminiferal analysis

About 10 g of each dried sample was soaked in Milli-Q water overnight and washed through a 63-μm-mesh sieve. Later, the dried filtrate was sieved through a 125-μm-mesh sieve. The coarse fraction (>125 μm) was used for quantitative and qualitative analysis of planktic foraminifera assemblages under a stereo-zoom binocular microscope. The same fraction was used for counting total benthic foraminifera. The samples were split into several aliquots to reduce the total number of planktic foraminifera to a minimum of 300 individuals. The taxonomic identification at the species level is from Kennett & Srinivasan (1983). For radiolarian biostratigraphy, the >63-μm fraction was used, and late Quaternary radiolarian index microfossils are identified as described and illustrated in Gupta (1988) and employed for ascertaining the geological ages for the datum levels following Gupta *et al.* (1996). The ranking of the various planktic foraminiferal species was based on their susceptibility to dissolution (based on a combination of rankings established by Bé (1977), Thunell & Honjo (1981) and Berger *et al.* (1982); Table 1). Resistant species are *Globorotalia menardii*, *Neogloboquadrina dutertrei*, *Pulleniatina obliquiloculata*, *Globorotalia tumida*, *Globorotalia crassaformis*, *Globorotalia truncatulinoides*, *Candeina nitida* and *Sphaeroidinella dehiscens.*

Determination of grain size and clay mineralogy

Salt-free sediments were sieved to separate the less than 63-μm (silt and clay) fraction using deionized water (Milli-Q system). This silt and clay fraction was treated with 1:4 acetic acid to remove biogenic carbonate. Subsequently, the carbonate-free sediments were washed thoroughly with deionized water and centrifuged. The residue was further treated with 3% H_2O_2 to remove organic matter. After washing and centrifuging, 40 mL of Na_2CO_3 was added to dissolve biogenic silica/opal, and the treated sediments were transferred to 100-mL air-tight plastic containers that were kept in a water bath at a temperature of 90°C for 5 h. The content of the containers was vigorously stirred at regular intervals of 1 h. The suspension was later centrifuged and rinsed three times with distilled water. The grain size distributions of the treated sediments, now free from biogenic components, were measured with a Malvern laser particle size analyser (Mastersizer 2000) with a Hydro 2000 MU wet-sampling accessory using procedures given in Ramaswamy & Rao (2006).

For clay mineral analysis, the clay fraction (<2 μm) was separated by the settling technique according to Stokes' law (Folk 1968) from the silt and clay lithogenic fraction. The salt and organic carbon-free sediment samples were prepared as thick slurry, pipetted onto glass slides, glycolated overnight at 60°C, and kept in the desiccators. The clay slides were analysed on a Philips X-ray diffractometer using Ni-filtered Cu Kα radiation operated at 20 mA and 40 kV from 3 to 32°2θ min^{-1}. The relative abundance of the clay minerals was determined according to the method described in Biscaye (1965) using weighted peak areas (4×illite, 2×kaolinite and chlorite; and 3.33×quartz).

AMS ^{14}C dating, oxygen isotope, $CaCO_3$ and organic carbon measurement

Approximately 10 to 16 tests of *Globigerinoides ruber* in the size range 250–315 μm were used for oxygen isotope analysis. The shells were placed in thimbles and crushed using a thin needle; a few drops of methanol were added and the samples were then cleaned in an ultrasonic bath for 8–10 s. The cleaned tests were analysed using an Isotope Ratio Mass Spectrometer at NIO, Goa. For AMS ^{14}C dating, nearly 5 mg of *G. menardii* was picked from each of the five depth intervals, and the dating was carried out at the Uppsala University Tandem Accelerator Facility, Sweden (BC 37) and the Poznan Radiocarbon Laboratory, Poland (SVBC 37). Calendar age calibration was based on the CalPal 2007 program (Weninger *et al.* 2007; http://www.calpal.de). Total carbon was determined using a carbon–nitrogen elemental analyser, and the carbonate carbon (TIC) was determined with a coulometer at NIO, Goa after acid evolution of CO_2. Organic carbon was estimated from the difference between total carbon and carbonate carbon. The mass accumulation rate (MAR) of $CaCO_3$ was calculated using its concentration, linear sedimentation rate (LSR) and dry bulk density (DBD).

Coccolithophore studies

A small amount of sediment was suspended in water to which a few drops of hydrogen peroxide were added. The sample was kept overnight and ultrasonically treated to disaggregate the sediments. A drop of highly diluted solution was put on a glass slide, which was

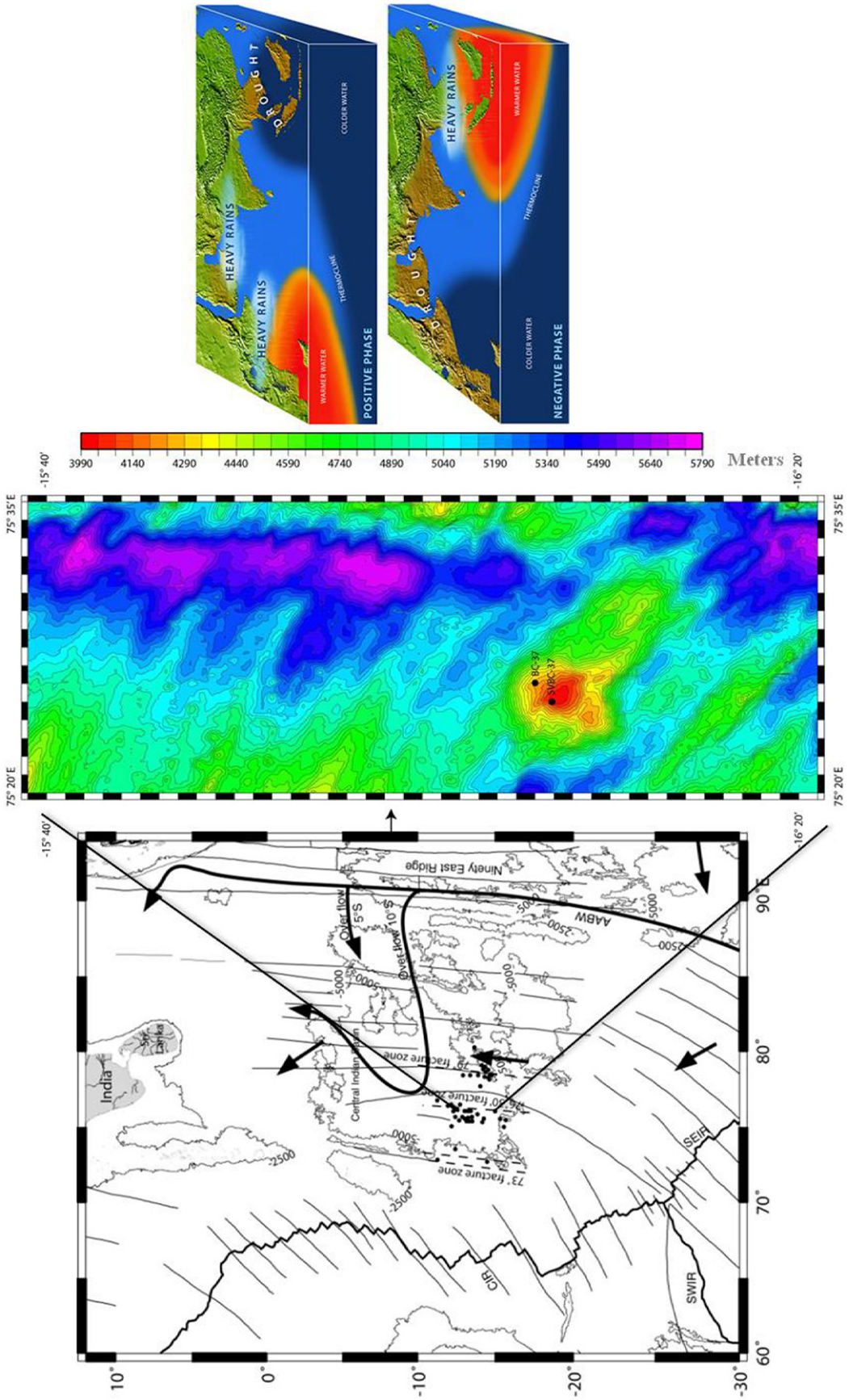

Fig. 2. Detailed multibeam bathymetry of the Central Indian Ocean with core locations BC 37 and SVBC 37. Left panel shows a larger view of the study area with the Indian Ocean Ridge system, the Rodriguez Triple Junction and fracture zones; dots denote the seamounts. Arrows represent the entry of AABW currents into the CIB through deep saddles (5 and 10°S) of the Ninety East Ridge System and their movement (adapted from Gordon *et al.* 2002). Right panel shows the influence of the Indian Ocean Dipole (IOD) positive and negative phases (source: www2.ucar.edu).

Table 1. Ranking of planktic foraminifera species in order of decreasing susceptibility to dissolution in columns (a) and (b); planktic foraminifera abundance decreasing order in columns (c) to (f) in cores BC 37 and SVBC 37.

(a) Rank	(b) Species name	BC 37 (W.D. 4252 m)		SVBC 37 (W.D. 3990 m)	
		(c) Species name	(d) Average %	(e) Species	(f) Average %
1	*GIobigerinoides ruber*	*G. menardii*	62.64	*G. menardii*	25.70
2	*Orbulina universa*	*P. obliquiloculata*	8.01	*G. ruber*	13.60
3	*Globigerinella siphonifera*	*N. dutertrei*	6.60	*G. sacculifer*	12.07
4	*Globigerina rubescens*	*G. sacculifer*	5.70	*N. dutertrei*	9.64
5	*Globigerinoides sacculifer*	*G. tumida*	3.02	*P. obliquiloculata*	8.51
6	*Globigerinella aequilateralis*	*G. inflata*	2.75	*G. tumida*	5.90
7	*Globigerinoides tenellus*	*G. conglobatus*	2.74	*G. conglobatus*	5.45
8	*GIobigerinoides conglobatus*	*G. ruber*	1.80	*G. aequilateralis*	3.77
9	*Globigerina bulloides*	*G. aequilateralis*	1.72	*G. truncatulinoides*	3.47
10	*Globigerinoides quadrilobatus*	*G. truncatulinoides*	1.63	*G. bulloides*	2.42
11	*Globigerinita glutinata*	*S. dehiscens*	0.64	*G. glutinata*	1.96
12	*Candeina nitida*	*G. crassaformis*	0.62	*S. dehiscens*	1.84
13	*Globorotalia theyeri*	*G. quadrilobatus*	0.60	*G. inflata*	1.69
14	*Globorotalia truncatulinoides*	*G. bulloides*	0.39	*N. pachyderma*	1.50
15	*Globigerina inflata*	*O. universa*	0.36	*O. universa*	1.26
16	*GIoborotalia menardii*	*G. hexagonus*	0.33	*G. crassaformis*	0.45
17	*Neogloboquadrina dutertrei*	*N. pachyderma*	0.13	*G. theyeri*	0.21
18	*Neogloboquadrina pachyderma*	*G. glutinata*	0.08	*G. tenellus*	0.19
19	*Pulleniatina obliquiloculata*	*G. tenellus*	0.08	*G. rubescens*	0.15
20	*Globorotalia crassaformis*	*G. rubescens*	0.07	*G. hexagonus*	0.13
21	*Sphaeroidinella dehiscens*	*G. siphonifera*	0.04	*G. siphonifera*	0.04
22	*Globorotalia tumida*	*G. theyeri*	0.02	*C. nitida*	0.02
		C. nitida	0.02	*G. quadrilobatus*	0.02

then dried using infrared light and coated with Gold-Palladium at 100 Å in a sputter coater. This gold-coated sample stub was scanned using JSM-5800 LV SEM at 15 kV. Species composition and abundances were determined by identifying and counting the species of coccolith randomly at a magnification of 3500× for 20 fields of view. Identification of various taxa of coccolithophorids was performed following the references of Winter *et al.* (1994) and Kleijne (1993). Diversity was expressed as Shannon-Wiener diversity index (H′), measuring a combination of species richness and evenness of distribution on specimens over species, and was carried out using the PRIMER software (Clarke & Gorley 2001).

Radiochemical analyses

Radiochemical analyses were carried out on samples taken at 2-cm intervals within the core. About 1–2 g of dried bulk sediments was brought into solution by HF-$HClO_4$-HNO_3-HCl digestion in the presence of ^{208}Po and ^{232}U/^{228}Th spike. The ^{210}Pb was measured via its daughter nuclide ^{210}Po, using standard radiochemical procedures after auto-deposition (for details see Flynn 1968 and Anderson & Fleer 1982). After the auto-deposition of Po, the solution was dried and the residue was digested with HNO_3 and dissolved in 9 M HCl. U-Th radiochemical separations and purification were carried out following the standard procedure of Krishnaswami & Sarin (1976). The alpha activity of the electroplated sample was assayed using an ion implanted detector coupled to an Octete plus Alpha spectrometer (EG & G ORTEC). The values for $^{230}Th_{excess}$ were calculated by subtracting the ^{234}U activity from the total ^{230}Th activities.

Results

Biostratigraphy, $^{230}Th_{excess}$, AMS ^{14}C, oxygen and carbon isotopes

The age models for the cores are based on multiple dating techniques. While we used dating tools such as $^{230}Th_{excess}$, AMS ^{14}C, oxygen isotope and biostratigraphy (radiolarian and coccolith) for establishing the age model for core BC 37 (Table 2; Fig. 3A, B), the age model for SVBC 37 was constructed using mainly biostratigraphy, AMS ^{14}C and correlation with the nearby BC 37 (Table 3; Fig. 3B). The first appearance of *Buccinosphaera invaginata* (180 ka) is seen in the 4–6 cm interval (5–6 cm in SVBC 37), and the last appearance of *Stylatractus universus* (425 ka) at 32–34 cm (20–21 cm in SVBC 37). For core SVBC 37, the younger age marker of the radiolarian (*B. invaginata*) and *Emiliania huxleyi* is used for the final age model. *E. huxleyi*, an age-diagnostic nannofossil, occurs from the top section (0–2 cm) to a depth of 18–20 cm in core BC 37 and at 18–19 cm in SVBC 37 (Fig. 3A, B; Tables 2 and 3), representing the age of first occurrence.

Table 2. Chronology of core BC 37 based on biostratigraphy, radiochemical and oxygen isotope tuning (ages are in ka). A = absent; P = present; FAD = first appearance datum; LAD = last appearance datum.

Depth (cm)	*E. huxleyi*	*C. invaginata*	*S. universus*	*C. tuberosa*	Age (*E. huxleyi* based)[1]	Age (Radiolarian based)	Age (^{230}Th method)	Age (^{14}C cal.)	Oxygen isotope boundaries
0–2	P	P	A	P	14.11		16.13	13.82±163	
2–4	P	P	A	P	42		48		
4–6	P	P	A	P	70	<180	80		MIS 4/5, 75 ka
FAD of *C. invaginata* 180 ka									
6–8	P	A	A	P	98	>180	112		
8–10	P	A	A	P	126	215	145		MIS 5/6, 130 ka
10–12	P	A	A	P	155	232	177		
12–14	P	A	A	P	183	250	209		
14–16	P	A	A	P	211	267	241		
16–18	P	A	A	P	239	285	274		
18–20	P	A	A	P	268	302	306		
FAD of *E. huxleyi* 268 ka									
20–22	A	A	A	P	296	320	338	>45	
22–24	A	A	A	P	324	337	370		
24–26	A	A	A	P	352	355	403		MIS 10/11, 362 ka
26–28	A	A	A	P	380	372	435		
28–30	A	A	A	P	409	390	467		MIS 11/12, 422 ka
30–32	A	A	A	P	437	407	500		
32–34	A	A	A	P	465	<425	532		
LAD of *S. universus* 425 ka									
34–36	A	A	P	P	493	>425	564		
36–38	A	A	P	P	521		596		
38–40	A	A	P	P	550		629	>45	

[1]Considering that sediment deposition of 20 cm has taken 268 ka (FAD of *E. huxleyi*).

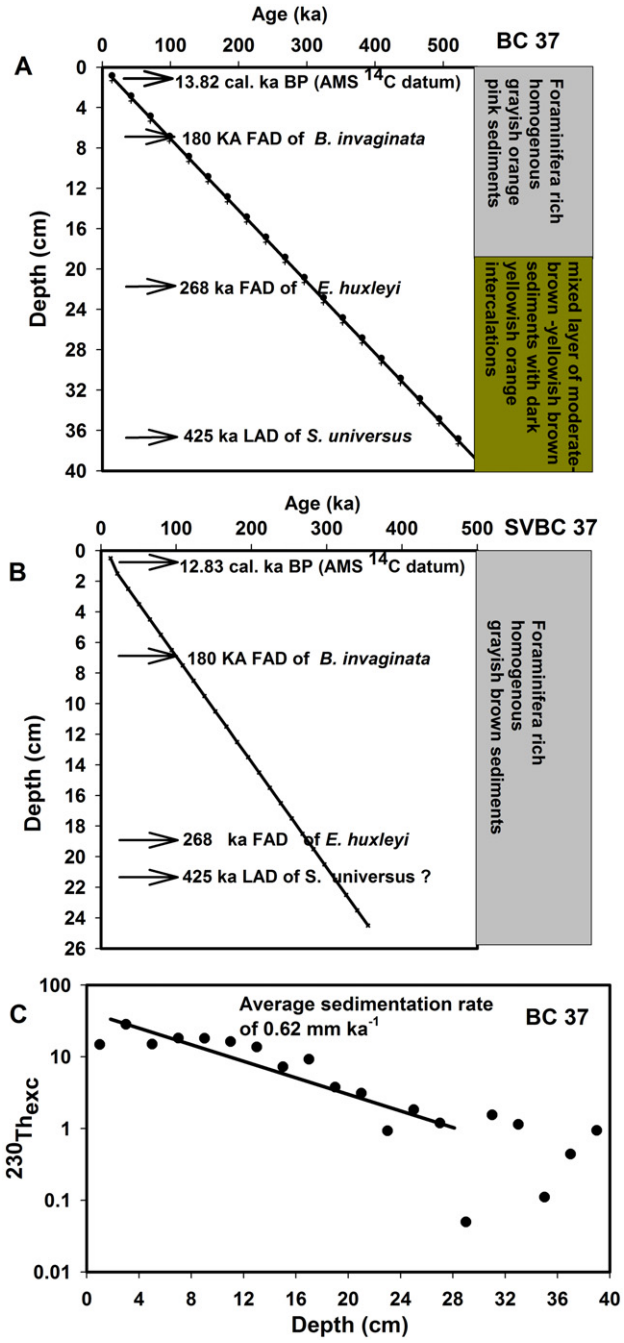

Fig. 3. Biostratigraphy, sedimentation rates and core description. A. Various biostratigraphic and AMS ^{14}C datum levels as a function of depth and age (BC 37). B. Biostratigraphic zones and AMS ^{14}C datum of core SVBC 37. C. $^{230}Th_{excess}$ profile in core BC 37 showing an average sedimentation rate of 0.62 mm ka^{-1}. This figure is available in colour at http://www.boreas.dk.

The decay curve of $^{230}Th_{excess}$ for the sediment section between 0 and 26 cm is linear with depth (Fig. 3C), and the estimated sedimentation rate is 0.62 mm ka^{-1}, giving an age of ~420 ka for sediments at 26 cm (this estimate is close to the dating limit of the $^{230}Th_{excess}$ method, half-life≈75 ka). Although the $^{230}Th_{excess}$ values in sediments deeper than 26 cm are not exactly linear, we have extrapolated the sedimentation rate to assign an age for the base of the core. Five sediment sections from both cores were used for AMS ^{14}C dating. Among them, only the surface sections (0–2 cm) gave an age, namely 13.82±163 cal. ka BP for core BC 37 (Table 2) and 12.83±86 cal. ka BP for SVBC 37 (Table 3); the deeper sections (2–3, 20–22 and 38–40 cm) were beyond the dating limit of radiocarbon and hence represent an age older than ~45 ka (Tables 2 and 3). The *G. ruber* oxygen isotope stratigraphy of core BC 37 was plotted and found to have a continuous record since MIS 14 (Fig. 4A). Very low sedimentation rates preclude sample representation from MIS 1 and lead to fewer sample points in other stages, limiting the derivation of a smooth oxygen isotope curve (Fig. 4A). However, glacial to interglacial boundaries identified from oxygen isotope data match with the chronology developed by other methods (Table 2). The $\delta^{13}C$ values for BC 37 show positive and high values in the latest Pleistocene (*c.* 300 to 14 ka) and low values between 550 and 300 ka (Fig. 4B; Table 4).

Organic carbon, $CaCO_3$*, grain size and clay mineralogy*

The C_{org} content is significantly low in both cores, ranging from below detection to 0.21% (Table 4). Relatively higher C_{org} values are observed during the last 300 ka compared with the low values during 300 to 550 ka (Fig. 4C, F). $CaCO_3$ content in SVBC 37 is higher than in BC 37, and the values range between 77 and 92% and between 48 and 78%, respectively (Table 4; Fig. 4D, E). Variations in the $CaCO_3$ and C_{org} values follow each other, and both show higher values during the last 300 ka (Fig. 4). The MAR of $CaCO_3$ for both cores is similar to the down-core variation of $CaCO_3$% (Fig. 4D–G). Records of down-core variation of clay minerals (kaolinite+chlorite %) and grain size class (<2 μm and 8–16 μm) are shown in Fig. 5. A distinct increase in the kaolinite% along with chlorite% is noticed at about 270 ka (Fig. 5A). At the termination of MIS 11, another distinct increase in the clay-sized lithogenic material (<2 μm) is concomitant with a decreasing trend of coarser fine silt (8–16 μm; Fig. 5B, C).

Coccolithophore record and ranking of planktic foraminiferal dissolution indices

The down-core variation of *Gephyrocapsa oceanica*, *Gephyrocapsa caribbeanica*, *Gephyrocapsa* spp. and *E. huxleyi* along with the Shannon–Wiener diversity index of coccolithophores are shown in Fig. 6A–E. *Gephyrocapsa* spp. show a major increase from MIS 14 to 8, whereas the Shannon–Wiener diversity index of coccolithophores shows a conspicuous decrease during the global Mid-Brunhes Dissolution Interval (MBDI).

Table 3. Chronology of core SVBC 37 based mainly on biostratigraphy and AMS ^{14}C dates (ages are in ka). A = absent; P = present; FAD = first appearance datum; LAD = last appearance datum.

Depth (cm)	*E. huxleyi*	*C. invaginata*	*S. universus*	Age (*E. huxleyi* based)	Age (radiolarian-based)	^{14}C (calibrated)
0–1	P	P	A	7.24	15	12.83 ± 86
1–2	P	P	A	22	45	
2–3	P	P	A	36	75	>45
3–4	P	P	A	51	105	
4–5	P	P	A	65	135	
5–6	P	P	A	80	<180	
FAD of *C. invaginata* 180 ka						
6–7	P	A	A	94	188	
7–8	P	A	A	109	204	
8–9	P	A	A	123	221	
9–10	P	A	A	138	237	
10–11	P	A	A	152	253	
11–12	P	A	A	167	270	
12–13	P	A	A	181	286	
13–14	P	A	A	196	302	
14–15				210	319	
15–16	P	A	A	225	335	
16–17	P	A	A	239	351	
17–18	P	A	A	254	368	
18–19	P	A	A	268	384	
FAD of *E. huxleyi* 268 ka						
19–20	A	A	A	282	400	
20–21	A	A	A	297	<425	
LAD of *S. universus* 425 ka						
21–22	A	A	P	311	>425	
22–23	A	A	P	326		
23–24	A	A	P	340		
24–25	A	A	P	355		

A sudden increase in the diversity of cocolithophores is seen from 300 ka onwards. Planktic foraminiferal assemblages of both sediment cores yielded 23 species, with *G. menardii* being the most abundant species in both cores (Figs 7H, 8A; Table 1). Furthermore, differences in foraminiferal assemblages are very conspicuous, which is reflected in their susceptibility to dissolution (Figs 7A–F, 8A–G). Based on the ranking scheme of species prone to dissolution employed here (a combination of the schemes proposed by Bé 1977, Thunell & Honjo 1981 and Berger *et al*. 1982 for planktic foraminifera), we find that about 60% in core SVBC 37 (3992 m) and about 80% in BC 37 (4252 m) are resistant species (Table 1).

Discussion

Chronology

The carbonate sediments of our samples provided an opportunity to date the sediments by several methods. The biostratigraphy used in this work is based on the Quaternary index fossils of radiolaria and coccolithophores (mainly *E. huxleyi*). The radiolarian index events were calibrated to an 'absolute' time scale based on the palaeomagnetic polarity time scale by Johnson *et al*. (1989). Two synchronous radiolarian biostratigraphic datum levels, namely the first appearance datum (FAD) of *B. invaginata* (~180 ka) and the last appearance datum (LAD) of *S. universus* (~425 ka), were used (Johnson *et al*. 1989; Gupta 2002) (Fig. 3A). These two synchronous radiolarian biostratigraphic datum levels have been widely used in reconstructing the chronology of late Quaternary sediments of the CIB (Gupta 1988, 2002, 2003; Nath *et al*. 2008). *B. invaginata* is the index species of the very first and topmost zone of the Neogene radiolarian biostratigraphy. The accuracy of the age model based on the two biostratigraphic events in a sediment section from the equatorial Indian Ocean was found to be ±2 ka at tilt and ±1 ka at precession bands (4% error) (Gupta 2002). *Collosphaera tuberosa* (FAD 650 ka) is present throughout core BC 37, suggesting that the cored sediment section is not older than 650 ka (Gupta 2002) (Table 2). The nannofossil index fossil, such as the FAD of *E. huxleyi*, is commonly used to assign the age of 268 ka BP. This corresponds closely to the ages estimated for the same depth using $^{230}Th_{excess}$ and radiolarian index fossil chronology (306 and 302 ka respectively; Table 2). The FAD of *E. huxleyi* is synchronous worldwide in the

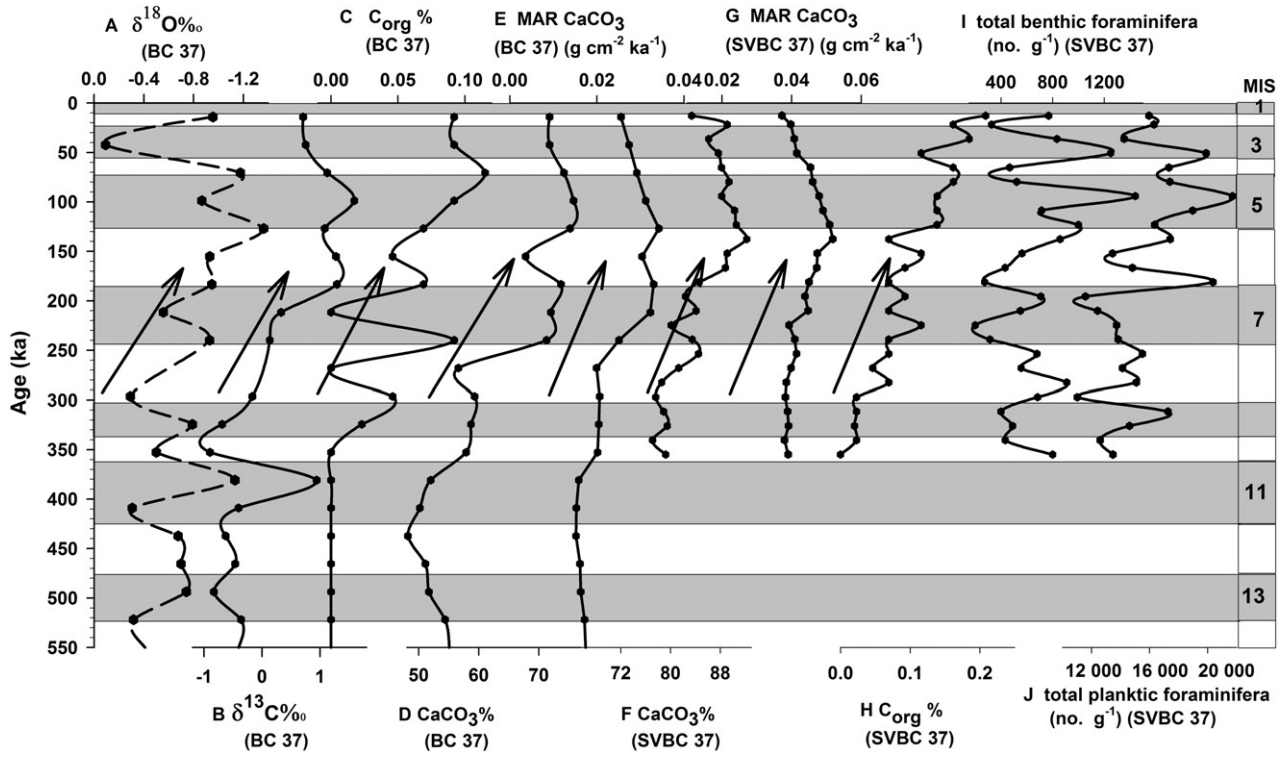

Fig. 4. Records of productivity during the Mid-Brunhes Epoch. A. Oxygen isotope of *Globigerinoides ruber* of core BC 37 (long dashed curves are shown in order to emphasize low-resolution data as a result of very low sedimentation rates). B. $\delta^{13}C$ of core BC 37. C. Organic carbon content (BC 37). D. $CaCO_3$ content (BC 37). E. Mass accumulation rate (MAR) of $CaCO_3$ (BC 37). F. $CaCO_3$ content of core SVBC 37. G. MAR of $CaCO_3$ (SVBC 37). H. Organic carbon content (SVBC 37). I. Total benthic foraminifera in SVBC 37 (in no. g^{-1}). J. Total planktic foraminifera in SVBC 37(in no. g^{-1}). Arrows mark events of increased productivity during the Mid-Brunhes Epoch. MIS refers to marine isotope stages, and the numbers indicate glacial (even) and interglacial (odd) stages.

tropical to subtropical regions of the open ocean (Thierstein *et al*. 1977). Depending on the particular proxy used and the location, the FAD of *E. huxleyi* has been dated at ~270 ka using correlation with planktic foraminiferal $\delta^{18}O$ records (Gartner & Emiliani 1976) and at ~268 ka ago in oxygen isotopic stage 8 (Thierstein *et al*. 1977).

The $^{230}Th_{excess}$-based sedimentation rate of 0.62 mm ka^{-1} is comparable to the 0.72 mm ka^{-1} derived from coccolith and radiolarian-based biostratigraphy (Fig. 3C). A similar record of low sedimentation rate (0.32 mm ka^{-1}) was also reported on the flank of same seamount in the CIB (Mascarenhas-Pereira *et al*. 2006), and such a low sedimentation rate (see Banakar *et al*. 1991; Borole 1993; Gupta *et al*. 1996) limits the extraction of high-resolution variability from these records. Sediments of core BC 37 record a longer age span (550 to 14 ka) compared with SVBC 37, extending to MIS 10 (355 to 13 ka). Thus, these carbonate sediment cores provided us with an opportunity to correlate various dating tools used to reconstruct the late Quaternary (late Middle Pleistocene to Pleistocene–Holocene transition) palaeoceanographic record in the CIB.

Increased productivity at the Mid-Brunhes Epoch

The oxygen and carbon isotope record shows a long-term characteristic change from 300 ka onwards (Fig. 4A, B; Table 4), with a concomitant change also noticed in other productivity proxies of C_{org}, $CaCO_3$, total benthic foraminifera (TBF) and total planktic foraminifera (TPF) (Table 4; Fig. 4C–J) marking a response to the MBCS. This climate shift has been correlated with the so-called 'Mid-Brunhes climate event' centred at 300 ka that has been recorded in many proxies (Kershaw *et al*. 2005 and references therein). The high abundance peaks of C_{org}, $CaCO_3$ and $\delta^{13}C$ and increased MAR of $CaCO_3$ coincide with high abundances of TPF and TBF, suggesting an increase in surface- and bottom-water productivity during the last 300 ka (Fig. 4). Increased carbonate accumulation at the MBCS shown in the sediment record is consistent with the global increase in carbonate productivity (Barker *et al*. 2006 and references therein). A broad maximum in $CaCO_3$ accumulation is seen in the East Equatorial Pacific during the Mid-Brunhes interval (Snoeckx & Rea 1994). Increased global $CaCO_3$ accumulation at the MBCS has been attributed by Barker

Table 4. Organic carbon, $CaCO_3$ data for cores BC 37 and SVBC 37. Oxygen and carbon isotope data for core BC 37.

Core SVBC-37				Core BC-37					
Depth (cm)	Age (ka)	TOC (%)	$CaCO_3$ (%)	Depth (cm)	Age (ka)	$\delta^{18}O$ (‰)	$\delta^{13}C$ (‰)	$CaCO_3$ (%)	TOC (%)
0–1	13	0.21	83.40	0–2	14	–0.96	0.71	71.80	0.09
1–2	22	0.16	89.12	2–4	42	–0.09	0.75	71.80	0.09
2–3	36	0.18	86.13	4–6	70	–1.18	1.12	74.20	0.12
3–4	51	0.12	87.68	6–8	98	–0.87	1.59	75.80	0.09
4–5	65	0.16	88.19	8–10	126	–1.36	1.08	75.20	0.07
5–6	80	0.16	89.39	10–12	155	–0.93	1.28	67.80	0.05
6–7	94	0.14	88.22	12–14	183	–0.95	1.29	73.70	0.07
7–8	109	0.14	90.29	14–16	211	–0.56	0.33	72.00	0.00
8–9	123	0.14	90.58	16–18	239	–0.93	0.14	71.30	0.09
9–10	138	0.07	92.24	18–20	268	–	–	56.60	0.00
10–11	152	0.12	89.12	20–22	296	–0.29	–0.17	59.30	0.05
11–12	167	0.09	88.81	22–24	324	–0.79	–0.69	58.70	0.02
12–13	181	0.07	84.60	24–26	352	–0.50	–0.90	57.90	0.00
13–14	196	0.09	82.39	26–28	380	–1.13	0.94	52.00	0.00
14–15	210	0.07	84.10	28–30	409	–0.31	–0.41	50.20	0.00
15–16	225	0.12	80.11	30–32	437	–0.68	–0.63	48.20	0.00
16–17	239	0.07	83.48	32–34	465	–0.70	–0.46	51.10	0.00
17–18	254	0.07	84.50	34–36	493	–0.74	–0.83	51.70	0.00
18–19	268	0.05	81.30	36–38	521	–0.32	–0.36	54.40	0.00
19–20	282	0.07	78.58	38–40	550	–0.41	–0.40	55.10	0.00
20–21	297	0.02	77.61						
21–22	311	0.02	78.88						
22–23	326	0.02	79.47						
23–24	340	0.02	77.09						
24–25	355	0.00	79.21						

et al. (2006) to an increase in surface ocean carbonate production.

A similar MBCS-related influence is also manifested by a distinct increase in the radiolaria (Rads g^{-1}) in a sediment record located at 7°48′S (~500 miles north of our record) in the CIB (Gupta 2009) at *c.* 250 ka BP (in exact agreement with our sediment record), implying an increase in monsoon-driven productivity (Fig. 5H). Increased amplitudes of high-frequency (suborbital) 17-, 15-, and 13-ka cycles were also evident at the MBCS (Gupta 2009). Gupta *et al*. (2010) also interpreted the abrupt decrease in the *Globigerina bulloides* population at the MBCS across MIS 9 and 8 (~300-250 ka) at Hole 716A (04°56′N; 73°17′E) in the equatorial Indian Ocean as a major decrease in the strength of Indian Ocean equatorial westerlies (IEW) and an increase (positive mode) in the strength of the Indian Ocean Dipole (IOD). This behaviour may relate to IOD-related climate change in the surrounding equatorial regions, including East Africa and Australasia (Fig. 5G). Gupta *et al*. (2010) have further argued that the IEW remained weak following the Mid-Brunhes transition, with significantly reduced variability, suggesting an overall strengthened (positive) IOD. Incidentally, vegetation changes have been shown to have occurred in the regions east and west of the Indian Ocean, with Australasia experiencing wet conditions prior to the transition (~460 to ~300 ka) (Fig. 5G) (Kawamura *et al*. 2006) and tropical Africa experiencing dry conditions (Jansen *et al*. 1986), suggesting a strengthened IEW and negative IOD condition. In contrast, our sediment record, which is further south (20° south of Hole 716, which is about 1200 nautical miles), shows a distinct increase in productivity during the Mid-Brunhes epoch and corresponds to an increased productivity in the NW Arabian Sea in the same time period (Hole 723B; Emeis *et al*. 1995 and Hole 728B; Gupta *et al*. 2010). Thus, the Mid-Brunhes shift in productivity south of the equator (our data) is more probably due to a strengthening of easterlies, as such an event coincides with a shift towards dry conditions in Australasia (Kershaw *et al*. 2005, as quoted in Gupta *et al*. 2010). Low precipitation conditions in the eastern Indian Ocean are also evidenced by an increase in grassland taxa after 300 ka in the Timor Sea (Kawamura *et al*. 2006). At the same time, equatorial East Africa became wetter (Jansen *et al*. 1986) and the Indian summer monsoon intensified (Emeis *et al*. 1995).

A high abundance of the coccolithophore *E. huxleyi* and low abundance of *Gephyrocapsa* spp. are observed from 300 ka onwards, with the increased Shannon–Wiener diversity index (H′) of coccolithophores marking the response to the MBCS (Fig. 6A–E), which is concomitant with the increases in C_{org} and $CaCO_3$ at about the same time. Such a change could reflect either an absolute increase in primary productivity or an increase in the efficiency of C_{org} export from the surface ocean (Barker *et al*. 2006). The ballast hypothesis

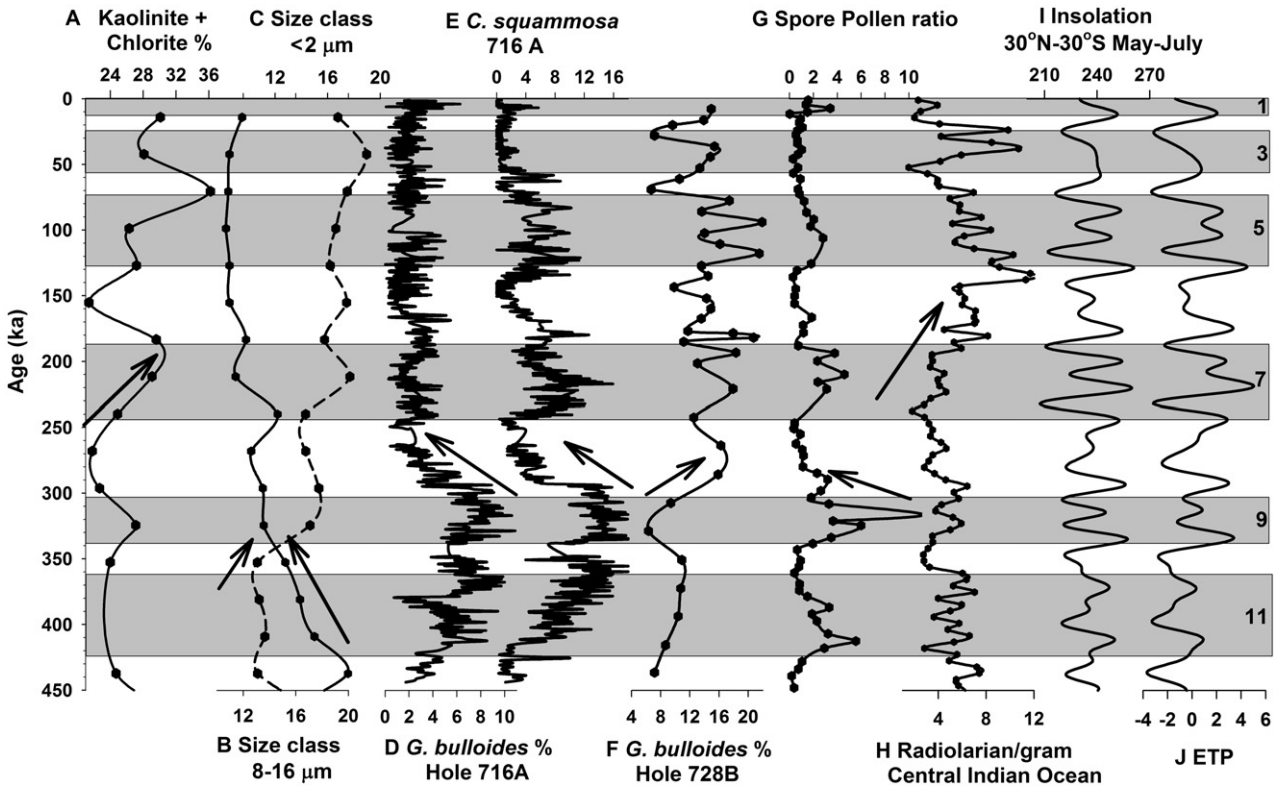

Fig. 5. Records for the Mid-Brunhes productivity and wind regime. A. Kaolinite%+chlorite% content of core BC 37. B. Sediment size class 8–16 μm. C. Sediment size class <2 μm. D. Percentage distribution of *Globigerina bulloides* and (E) percentage of *Cymbaloporetta squammosa* showing a decrease at ~300 ka at Hole 716 A (data fromGupta *et al*. 2010). F. *G. bulloides* percent age at Hole 723B (NW Arabian Sea) (Emeis *et al*. 1995) showing an intensification of SW monsoon from ~300 ka onwards. G. Spore/pollen ratio (Kawamura *et al*. 2006) showing a decrease at ~300-250 ka indicating vegetation changes. H. Radiolarian/gram in the Central Indian Ocean (Gupta 2009), showing an increase at about ~250 ka. I. Insolation (30°N–30°S May–July). J. ETP (MIS = marine isotope stage; MIS and numbers are the same as in Fig. 4).

suggests that $CaCO_3$ may be the most important agent for transporting organic carbon to the deep sea, representing up to 83% of the flux of C_{org} in certain environments (Armstrong *et al*. 2002; Barker *et al*. 2006). Export of C_{org} may strengthen the organic pump and help in the drawdown of CO_2 in the surface ocean, balancing the CO_2 rise from the increased production of $CaCO_3$ in the surface ocean (Barker *et al*. 2006). A distinct peak of $\delta^{13}C$ is noticed during MIS 11 in our record, which is consistent with the global maximum in $\delta^{13}C$ during this period (Wang *et al*. 2004; Barker *et al*. 2006). Relatively heavier $\delta^{13}C$ values at MBCS, however, correspond to higher values of $CaCO_3$ and C_{org} (Fig. 4B–F), which are contemporaneous with increased global carbonate dissolution (Barker *et al*. 2006). Organic carbon is also relatively low during 300 to 550 ka, indicating a well-oxygenated bottom-water environment and low productivity, in contrast to the relatively high C_{org} during the last 300 ka.

Inferring Mid-Brunhes change in wind regime and increased aridity in the Australian region

A distinct increase in the kaolinite% along with chlorite% is noticed at about 270 ka, which coincides with the influence of Mid-Brunhes climatic change (Fig. 5A). At the termination of MIS 11, another distinct increase in the clay-sized lithogenic material (<2 μm) is concomitant with a decreasing trend of coarser fine silt (8–16 μm; Fig. 5B, C). Increased clay size, together with a concomitant increase in kaolinite%, suggests a high supply of kaolinite-rich dust to the CIB. Kaolinite is the dominant mineral of western Australia (in the eastern Indian Ocean), and its source has been attributed to wind transport (Griffin *et al*. 1968; Fagel 2007). Griffin *et al*. (1968) and Kolla & Biscaye (1973) show a tongue of kaolinite-rich sediment extending westwards from the Northwest Cape into the Indian Ocean (Fig. 1), and our study area juxtaposes the kaolinite-rich region off Australia (Fig. 1). Kaolinite-rich dust is blown into the eastern Indian Ocean as a result of the prevailing easterly winds and may increase the overall kaolinite content of the pelagic sediments (McTainsh 1989; Gingele *et al*. 2001). Gingele *et al*. (2001) found kaolinite and illite to be the dominant major minerals both in dust samples and in marine samples. Increased dust in the Mid-Brunhes epoch in our sediment record suggests an intensification of aridity in Australia and dust transport to our

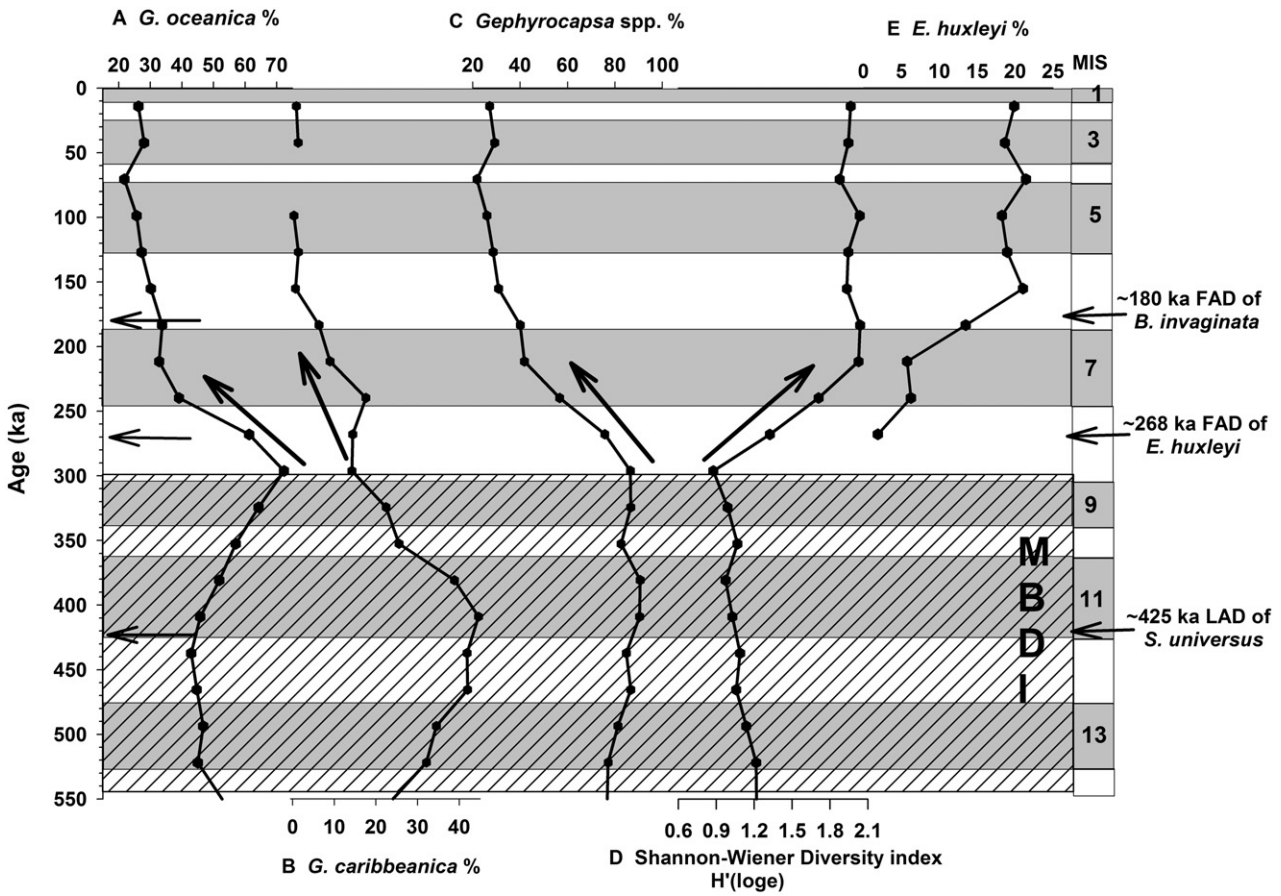

Fig. 6. Coccolithophore records from the CIB demonstrate the dominance of the *Gephyrocapsa* spp. and reduction in the Shannon–Wiener diversity index during the Mid-Brunhes interval. A. *Gephyrocapsa Oceanica* %. B. *Gephyrocapsa Caribbeanica* %. C. *Gephyrocapsa* spp. D. Shannon-Wiener diversity index (H′). E. *Emiliania huxleyi* % (FAD of *B. Invaginata*, *E. huxleyi* and LAD of *S. universus* are marked with arrows). Global Mid-Brunhes dissolution interval (MBDI) is marked by a striped grey box (MIS = marine isotope stage).

site in the middle of the Indian Ocean. This interpretation is consistent with the onset of dry conditions in Australasia at about this time (Kershaw *et al.* 2005; Gupta *et al.* 2010), with the earliest arid landforms dating from at least 300 ka (Bowler 1976). Gupta *et al.* (2010) has related Mid-Brunhes monsoon intensification in the western Indian Ocean and also in eastern Africa to the influence of the Indian Ocean Dipole (IOD) event. The clear manifestation of Mid-Brunhes productivity in our sediment record may also confirm the intensification of the IOD-related monsoon. Monsoon intensification following increased aridity in the eastern Indian Ocean is also a feature of the IOD (Abram *et al.* 2007). The early phase of IOD drought corresponds with the Asian summer monsoon season (~May–September) and is probably caused by strengthened cross-equatorial airflow drawing moisture from the tropical Indian Ocean into the Asian monsoon (Abram *et al.* 2007). A similar process must be responsible for the monsoon intensification during the Mid-Brunhes period, as our study area is located exactly half-way between the areas influenced by the IOD.

Intra- and inter-core carbonate preservation patterns: dissolution related to lysoclinal depth and the glacial–interglacial climatic changes

In the present investigation, carbonate dissolution is evidenced by the presence of corroded planktic foraminiferal specimens and broken keels of *G. menardii*, implying that the cores under investigation were retrieved from close to the lysocline. Based on the ranking of planktic foraminifera susceptible to dissolution, we find that about 60% (SVBC 37; 3992 m) to 80% (BC 37, 4252 m) of foraminifers are resistant (Table 1), reflecting the degree of dissolution intensity in these two cores. Higher $CaCO_3$ content (77 to 92%) in core SVBC 37 than in BC 37 (48 to 75%; Table 4) also supports the foraminifera-based interpretation. This has resulted in low foraminiferal diversity and an abundance of resistant planktic foraminifera. While the number of foraminiferal assemblages present in the two cores is the same, the shallow core SVBC 37 shows a better preservation of foraminifera. The high abundance of resistant species in both cores, however, may

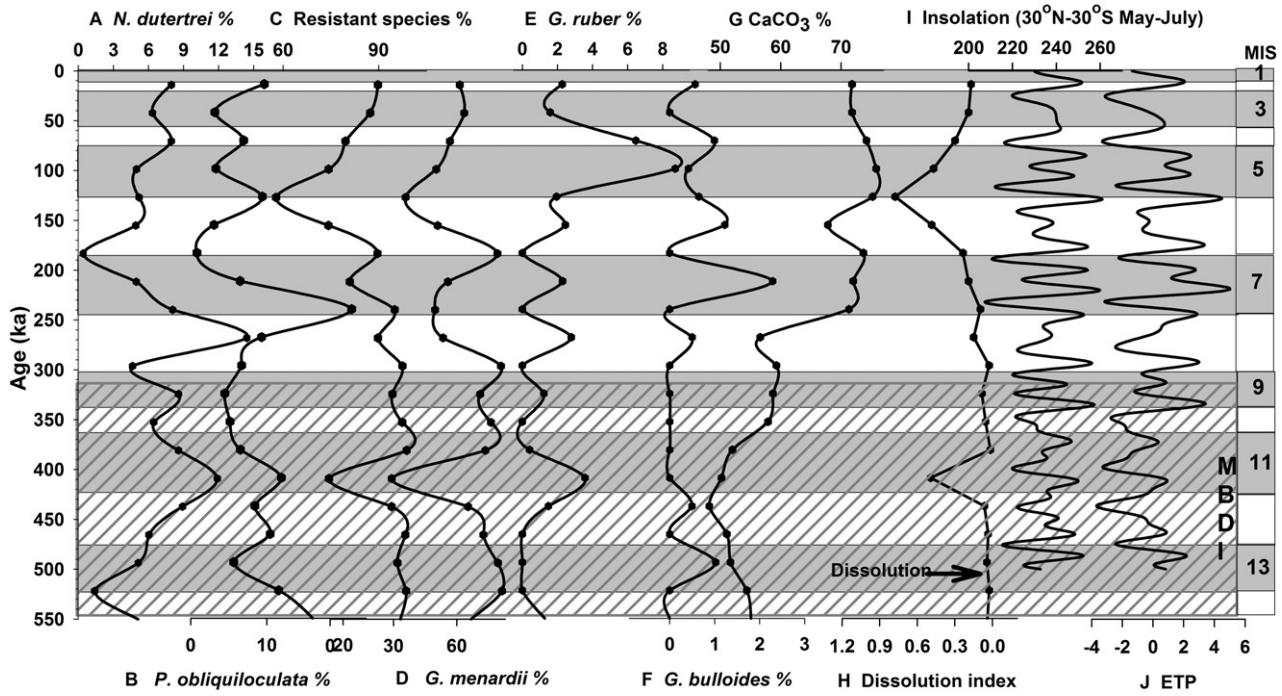

Fig. 7. Mid-Brunhes Dissolution Interval and carbonate dissolution proxies of core BC 37. A. *Neogloboquadrina dutertrei.* B. *Pulleniatina obliquiloculata*. C. Total resistant species. D. *Globorotalia menardii.* E. *Globigerinoides ruber* (dissolution-susceptible species). F. *Globigerinoides bulloides* (dissolution-susceptible species). G. $CaCO_3$%. H. Dissolution index (ratio of non-resistant species to resistant species). I. Insolation (30°N–30°S May–July). J. ETP.

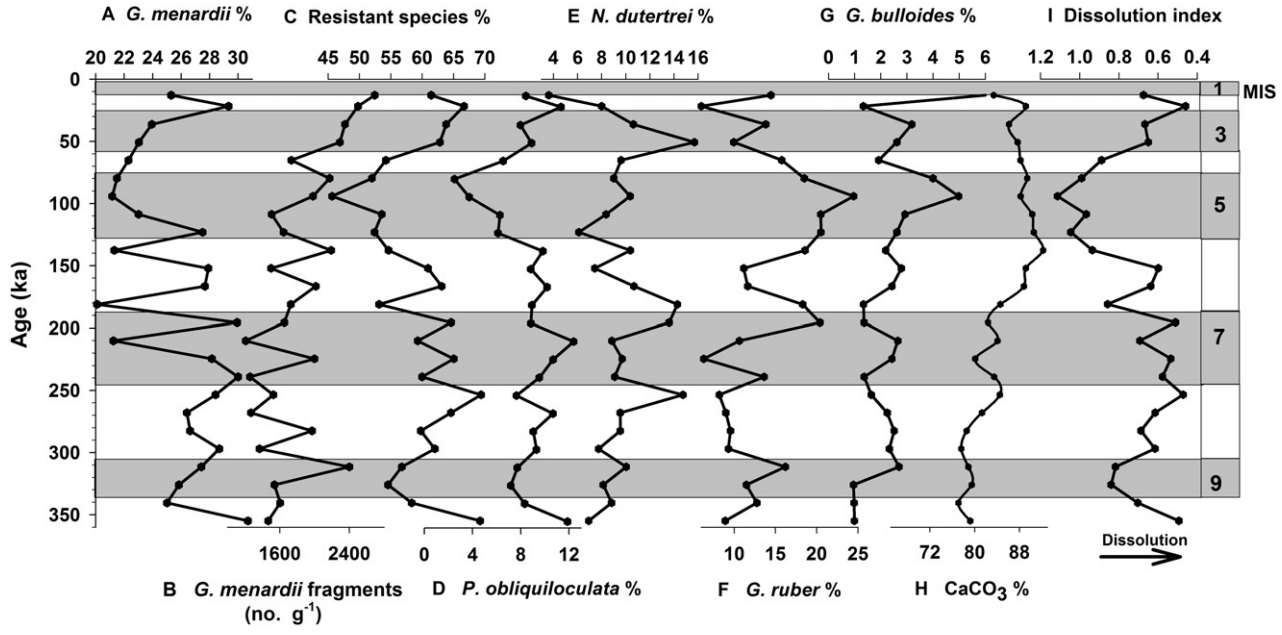

Fig. 8. Carbonate dissolution proxies of core SVBC 37. A. *Globorotalia menardii* %. B. *G. menardii* fragments. C. Resistant species%. D. *Pulleniatina obliquiloculata* %. E. *Neogloboquadrina dutertrei* %. F. *Globigerinoides ruber* %. G. *Globigerina bulloides* %. H. $CaCO_3$%. I. Dissolution index (ratio of non-resistant to resistant species).

suggest some degree of supralysoclinal dissolution. The relative abundance of the most susceptible species *G. ruber* (Rank 1) is very low (eighth most abundant species) in core BC 37, whereas it is significantly high (second most abundant species) in SVBC 37 (Table 1). The significant dissolution in core BC 37 (water depth ~4250 m) relative to SVBC 37 (water depth ~3990 m) suggests that the foraminiferal lysocline is shallower (at a depth of ~4250 m) than the earlier estimate of 4400 m in the CIB (Banakar *et al.* 1998). While the overall differences in $CaCO_3$ content and foraminiferal assemblages between the two cores are related to the lysocline depth, significant dissolution events within each core are seen during the transitional period between MIS 3 and 2 and glacial–interglacial periods such as MIS 6, 7 and 8 (Figs 7, 8), which could reflect the response to past oceanographic/climatic conditions.

In the Pacific Ocean, late Quaternary dissolution maxima were found to correlate with the deglacial periods, and the minima with transitional periods from interglacial to glacial conditions (Wu *et al.* 1991; Murray *et al.* 2000). According to Sexton & Barker (2012), the $CaCO_3$ content of deep-sea sediments in the Pacific Ocean increases during glacials of the Late Pleistocene in comparison to interglacials, whereas records of sedimentary $CaCO_3$ in the Atlantic Ocean show an anti-correlated pattern across glacial–interglacial cycles, this pattern, however, existing only since ~1.10 Ma. Before this, both patterns in both oceans were in-phase, and had 'Atlantic-style' phasing with respect to glacial–interglacial cycles; the change in Pacific $CaCO_3$ dissolution cyclicity at 1.10 Ma was caused by the switching over of the relative ventilation state of abyssal South Pacific waters between glacials and interglacials (Sexton & Barker 2012). Different views exist on the control of carbonate preservation in the Pacific, either in favour of productivity (e.g. Murray *et al.* 2000) or solely in favour of dissolution control (e.g. Anderson *et al.* 2008). Past corrosion of pelagic $CaCO_3$ in the central equatorial Pacific was not found to co-vary with the observed sedimentary concentration of $CaCO_3$ (LaMontagne *et al.* 1996), suggesting a decoupling between $CaCO_3$ content and carbonate dissolution indices, which is also seen in our records from the CIB (Figs 7, 8).

The increased abundance of fragments of the dissolution-resistant species *G. menardii* and *G. menardii*, the higher dissolution index (ratio of non-resistant to resistant species) and the appearance of other resistant species starting from MIS 11 (until MIS 7) suggest selective dissolution processes during this period, which is consistent with other global records (Barker *et al.* 2006). Being a period of global carbonate dissolution, MIS 11 is also marked by increased $CaCO_3$ accumulation in a variety of locations (Barker *et al.* 2006). Our coccolithophore record from the CIB shows a major increase of *Gephyrocapsa* spp. during MIS 14–8, matching well with earlier records (Bollmann *et al.* 1998; Barker *et al.* 2006). According to Barker *et al.* (2006), the global increase in pelagic carbonate production, possibly associated with the proliferation of *Gephyrocapsa* spp., caused widespread dissolution during the Mid-Brunhes. The Shannon–Wiener diversity index of coccolithophores shows a conspicuous decrease during the MBDI and a sudden increase in diversity at 300 ka onwards, marking a response to the MBCS. The MBDI represents a major perturbation to the global ocean carbon system (see Barker *et al.* 2006). Flores *et al.* (2003) noted the correspondence between high $CaCO_3$ and increased abundance of *Gephyrocapsa*, contemporaneous with enhanced dissolution during the Mid-Brunhes at ODP site 1089. The high carbonate dissolution episodes during the transition period of MIS 3/2 and interglacial period MIS 7 and glacial periods MIS 6 and 8 may be a result of the enhanced flow of corrosive AABW or increased productivity during the Late Pleistocene. The CIB is bathed by AABW, which is considered to be significantly corrosive and can induce sediment erosion as recorded in cores from the CIB (Banakar *et al.* 1991). AABW crosses the south eastern Indian Ridge and flows to the western margins of the South Australian Basin and Wharton Basin and continues northwards along the base of the Ninety East Ridge and enters the CIB (Johnson & Nigrini 1982). It causes dissolution of biogenic silica, which is seen in enhanced values of interstitial silica content (Nath & Mudholkar 1989). AABW production has occurred during both glacial and interglacial periods and has shown changes in circulation over the last 500 ka (Corliss 1979). Incidentally, the time periods during which we find intense dissolution in our sediment record and high abundance of diatoms (during the MIS 6/7 and MIS 3/2 boundaries) are correlated with two periods of maximum AABW flow during the last 240 ka (Jones & Johnson 1984).

Conclusions

The chronology of carbonate sediments from a seamount in the CIB was established using fossil markers (radiolarian and coccolith), $^{230}Th_{excess}$, and AMS ^{14}C, providing a sedimentary record of the late middle Pleistocene to Pleistocene–Holocene transition (550 to 11.5 ka). While all the early records of paleoceanographic interpretations from the CIB were based on radiolarian stratigraphy and $^{230}Th_{excess}$ methods, carbonate sediment cores provided us with an opportunity to correlate various dating tools. The sedimentation rates derived from the $^{230}Th_{excess}$ method were ~0.62 mm ka^{-1}, in good agreement with the sedimentation rate of 0.72 mm ka^{-1} obtained from biostratigraphic datum levels. From the chronology established, the following palaeoclimatic inferences are drawn.

- The Late Pleistocene carbonate records from the CIB showed that the monsoon-induced productivity has increased from *c.* 300 ka, displaying a distinct response of monsoon to the MBCS, with an increasing trend at the end of MIS 11. Increased Mid-Brunhes productivity in our record is consistent with a global increase in carbonate productivity. The influence of the MBCS was also reflected in coccolith records, which displayed a distinct change in the species diversity.
- Concomitant changes were also noticed in the wind proxies, such as mean particle size and clay mineral content. Increased clay-sized material (<2 μm) and kaolinite content at the same time (Mid-Brunhes) indicate the intensification of easterlies from Australia.
- The manifestation of Mid-Brunhes productivity in our sediment record may suggest the intensification of the Indian Ocean Dipole (IOD)-related monsoon, similar to earlier reports of IOD-driven Mid-Brunhes monsoon intensification in the northwestern Indian Ocean and eastern Africa.
- Total resistant species, ratio of non-resistant to resistant species and *G. menardii* fragments clearly show that the intensity of carbonate dissolution varied with glacial–interglacial cycles, and dissolution is higher in core BC 37 from a deeper depth (4252 m) than the shallower core SVBC 37 (depth 3992 m), suggesting that the lysocline could be shallower than the previous estimate for the CIB.
- The increased abundance of *G. menardii* and its fragments beginning from MIS 11 and the proliferation of coccolith *Gephyrocapsa* spp. indicate dissolution, which is consistent with the widespread global carbonate dissolution during this period. High carbonate dissolution during the transition period of MIS 3/2 and glacial to interglacial periods (MIS 6, 7 and 8) may result from the enhanced flow of corrosive AABW into the CIB.

Acknowledgements. – We thank the Director of the National Institute of Oceanography, Goa for permission to publish this paper. The Ministry of Earth Science (formerly Department of Ocean Development, Government of India), New Delhi is thanked for providing ship time on RV 'Akademik Boris Petrov' and for funding for Project PMN-EIA. The captain and crew of the ship are also thanked for their help. Ms Trupti Naik helped in shipboard sampling and in sample processing in the onshore laboratory. Mr V.D. Khedekar, Mr Girish Prabhu, Ms Supriya Karapurkar and Dr C. Prakash Babu are thanked for their help during SEM, XRD, IRMS and coulometer analyses, respectively. Sediment grain size and mineralogy were generated as a part of Graduate project work of students of Smt. Parvatibai Chowgule College, Margao. Comments by Dr Richard Murray and the anonymous reviewer, and changes suggested by Professor Jan A. Piotrowski, Editor-in-Chief, helped to improve the manuscript. This is National Institute of Oceanography contribution No. 5232.

References

Abram, N. J., Gagan, M. K., Liu, Z., Hantoro, W. S., McCulloch, M. T. & Suwargadi, B. W. 2007: Seasonal characteristics of the Indian Ocean Dipole during the Holocene epoch. *Nature 445*, 299–302.

Anderson, R. F. & Fleer, A. P. 1982: Determination of natural actinides and plutonium in marine particulate material. *Analytical Chemistry 54*, 1142–1147.

Anderson, R. F., Fleisher, M. Q., Lao, Y. & Winckler, G. 2008: Modern $CaCO_3$ preservation in equatorial Pacific sediments in the context of late-Pleistocene glacial cycles. *Marine Chemistry 111*, 30–46.

Armstrong, R. A., Lee, C., Hedges, J. I., Honjo, S. & Wakeham, S. G. 2002: A new, mechanistic model for organic carbon fluxes in the ocean based on the quantitative association of POC with ballast minerals. *Deep-Sea Research II 49*, 219–236.

Banakar, V. K., Galy, A., Sukumaran, N. P., Parthiban, G. & Volvaikar, A. Y. 2003: Himalayan sedimentary pulses recorded by silicate detritus within a ferromanganese Crust from Central Indian Ocean. *Earth and Planetary Science Letters 205*, 337–348.

Banakar, V. K., Gupta, S. M. & Padmavathi, V. K. 1991: Abyssal sediment erosion in the Central Indian Basin: evidence from radiochemical and radiolarian studies. *Marine Geology 96*, 167–173.

Banakar, V. K., Parthiban, G., Pattan, J. N. & Jauhari, P. 1998: Chemistry of surface sediment along a north-south transect across the equator in the Central Indian Basin: assessment of biogenic and detrital influences on elemental burial on the seafloor. *Chemical Geology 147*, 217–232.

Banakar, V. K., Pattan, J. N. & Mudholkar, A. V. 1997: Palaeoceanographic conditions during the formation of a ferromanganese crust from the Afanasiy-Nikitin seamount, North Central Indian Ocean: geochemical evidence. *Marine Geology 136*, 299–315.

Barker, S., Archer, D., Booth, L., Elderfield, H., Henderiks, J. & Rickaby, R. E. M. 2006: Globally increased pelagic carbonate production during the Mid-Brunhes dissolution interval and the CO_2 paradox of MIS 11. *Quaternary Science Reviews 25*, 3278–3293.

Bé, A. W. H. 1977: An ecological zoogeographic and taxonomic review of recent planktonic foraminifera. *In* Ramsey, A. T. S. (ed.): *Oceanic Micropaleontology*, 1–88. Academic Press, London.

Berger, W. H., Bonneau, M.-C. & Parker, F. L. 1982: Foraminifera on the deep-sea floor: lysocline and dissolution rate. *Oceanologica Acta 5*, 249–258.

Biscaye, P. E. 1965: Mineralogy and sedimentation of recent deep-sea clay in the Atlantic Ocean and adjacent seas and oceans. *Geological Society of America Bulletin 76*, 803–831.

Bollmann, J., Baumann, K. H. & Thierstein, H. R. 1998: Global dominance of Gephyrocapsa coccoliths in the late Pleistocene: selective dissolution, evolution, or global environmental change? *Paleoceanography 13*, 517–529.

Borole, D. N. 1993: Late Pleistocene sedimentation: a case study of the Central Indian Ocean Basin. *Deep-Sea Research Part I: Oceanographic Research Papers 40*, 761–775.

Bowler, J. M. 1976: Aridity in Australia: age, origins and expressions in Aeolian landforms and sediments. *Earth Science Reviews 12*, 279–310.

Clarke, K. R. & Gorley, R. N. 2001: Primer V5: user M/Tutorial, PRIMER-E. Plymoth, UK.

Corliss, B. H. 1979: Quaternary Antarctic bottom water history: deep sea benthonic foraminiferal evidence from the south East Indian Ocean. *Quaternary Research 12*, 271–289.

Emeis, K. C., Anderson, D. M., Doose, H., Kroon, D., Schulz, D. & Schulz-Bull, D. 1995: Sea-surface temperatures and the history of monsoon upwelling in the northwest Arabian Sea during the last 500,000 years. *Quaternary Research 43*, 355–361.

Fagel, N. 2007: Marine clay minerals, deep circulation and climate. *In* Hillaire-Marcel, C. & de Vernal, A. (eds.): *Proxies in Late Cenozoic Paleoceanography*, 139–184. Elsevier, Amsterdam.

Flores, J. A., Marino, M., Sierro, F. J., Hodell, D. A. & Charles, C. D. 2003: Calcareous plankton dissolution pattern and coccolithophore assemblages during the last 600 kyr at ODP Site

1089 (Cape Basin, South Atlantic): palaeoceanographic implications. *Paleogeography, Paleoclimatology, Paleoecology 196*, 409–426.

Flynn, W. W. 1968: The determination of low levels of polonium-210 in environmental samples. *Analytica Chimica Acta 43*, 221–227.

Folk, R. L. 1968: *Petrology of Sedimentary Rocks*. 170 pp. Hemphill, Austin, TX.

Gartner, A. & Emiliani, C. 1976: Nannofossil biostratigraphy and climate stages of Pleistocene Brunhes Epoch. *American Association of Petroleum Geologists Bulletin 70*, 1562–1564.

Gingele, F. X., Deckker, P. D. & Hillenbrand, C. D. 2001: Clay mineral distribution in surface sediments between Indonesia and NW Australia – Source and transport by ocean currents. *Marine Geology 179*, 135–146.

Gordon, A. L., Claudia, F., Giulivi, T. T., Stewart, S., John, M. & Donald, O. 2002: Bay of Bengal nutrient-rich benthic layer. *Deep-Sea Research II 49*, 1411–1421.

Griffin, J. J., Windom, H. L. & Goldberg, E. D. 1968: The distribution of clay minerals in the world ocean. *Deep-Sea Research 15*, 433–459.

Gupta, A. K., Das, M. & Bhaskar, K. 2006: South Equatorial Current (SEC) driven changes at DSDP Site 237, Central Indian Ocean, during the Plio-Pleistocene: evidence from benthic foraminifera and stable isotopes. *Journal of Asian Earth Science 28*, 276–290.

Gupta, A. K., Sarkar, S., De, S., Clemens, S. C. & Velu, A. 2010: Mid-Brunhes strengthening of the Indian Ocean Dipole caused increased equatorial East African and decreased Australasian rainfall. *Geophysical Research Letters 37*, L06706, doi: 10.1029/2009GL042225.

Gupta, S. M. 1988: Radiolarian zonation and volcanic ash-layers in two sediment cores from the Central Indian Basin. *Journal of Palaeontological Society of India 33*, 59–71.

Gupta, S. M. 1996: Quantitative radiolarian assemblages in the surface sediments from the central Indian Ocean and their paleomonsoonal significances. *Journal of Geological Society of India 47*, 339–354.

Gupta, S. M. 2002: Pyloniid stratigraphy – A new tool to date tropical radiolarian ooze from the central tropical Indian Ocean. *Marine Geology 184*, 85–93.

Gupta, S. M. 2003: Orbital frequencies in radiolarian assemblages of the central Indian Ocean: implications on the Indian summer monsoon. *Palaeogeography, Palaeoclimatology, Palaeoecology 97*, 97–112.

Gupta, S. M. 2009: Radiolarian abundance – a monsoon proxy responding to the Earth's orbital forcing: inferences on the mid-Brunhes climate shift. *Earth Science India 2*, 1–20.

Gupta, S. M. & Fernandes, A. A. 1997: Quaternary radiolarian faunal changes in the tropical Indian Ocean: inferences to paleomonsoonal oscillation of the 10°S hydrographic front. *Current Science 72*, 965–972.

Gupta, S. M., Fernandes, A. A. & Mohan, R. 1996: Tropical sea surface temperatures and the Earth's eccentricity cycles. *Geophysical Research Letters 23*, 3159–3162.

Jansen, J. H. F., Kuijpers, A. & Troelstra, S. R. 1986: A Mid Brunhes climatic event: long term changes in global atmosphere and ocean circulation. *Science 232*, 619–622.

Johnson, D. A. & Nigrini, C. 1982: Radiolarian biogeography in surface sediments of the Eastern Indian Ocean. *Marine Micropaleontology 7*, 237–287.

Johnson, D. A., Schneider, D. A., Nigrini, C., Caulet, J. P. & Kent, D. V. 1989: Pliocene-Pleistocene radiolarian events and magnetostratigraphic calibrations for the tropical Indian Ocean. *Marine Micropaleontology 14*, 33–66.

Jones, G. A. & Johnson, D. A. 1984: Displaced Antarctic diatoms in Vema channel sediments: late Pleistocene/Holocene fluctuations in AABW flow. *Marine Geology 58*, 165–186.

Kawamura, H., Holbourn, A. & Kuhnt, W. 2006: Climate variability and land ocean interactions in the Indo Pacific Warm Pool: a 460 ka palynological and organic geochemical record from the Timor Sea. *Marine Micropaleontology 59*, 1–14.

Kennett, J. P. & Srinivasan, M. S. 1983: *Neogene Planktonic Foraminefera, A Phylogenetic Atlas*. 265 pp, Hutchinson Ross, Stroudsburg.

Kershaw, A. P., Moss, P. T. & Wild, R. 2005: Patterns and causes of vegetation change in the Australian wet tropics region over the last 10 million years. *In* Bermingham, E., Dick, C. W. & Moritz, C. (eds.): *Tropical Rainforests: Past and Future*, 375–400. University of Chicago Press, Chicago, IL.

Kleijne, A. 1993: Morphology, taxonomy and distribution of extant coccolithophorids (calcareous nannoplankton). *Ph.D. thesis, Amsterdam Free University,* 321 pp.

Kolla, V. & Biscaye, P. E. 1973: Clay mineralogy and sedimentation in the eastern Indian Ocean. *Deep Sea Research 20*, 727–738.

Kolla, V., Bè, A. W. H. & Biscaye, P. E. 1976: Calcium carbonate distribution in the surface sediments of the Indian Ocean. *Journal of Geophysical Research 81*, 2605–2616.

Krishnaswami, S. & Sarin, M. M. 1976: Procedures for simultaneous determination of Th, Pu and Ra isotopes, Pb-210, Fe-55, Si-32 and C-14 in marine suspended phases. *Analytica Chimica Acta 83*, 143–156.

LaMontagne, R. W., Murray, R. W., Wei, K.-Y., Leinen, M. & Wang, C.-W. 1996: Decoupling of carbonate preservation, carbonate concentration, and biogenic accumulation: a 400 ky record from the central equatorial Pacific Ocean. *Paleoceanography 11*, 553–562.

Lisitzin, A. P. 1996: *Oceanic Sedimentation, Lithology and Geochemistry*. 400 pp. American Geophysical Union, Washington, DC.

Mascarenhas-Pereira, M. B. L., Nath, B. N., Borole, D. V. & Gupta, S. M. 2006: Nature, source and composition of volcanic ash in sediments from a fracture zone trace of Rodriguez Triple Junction in the Central Indian Basin. *Marine Geology 229*, 79–90.

McTainsh, G. H. 1989: Quaternary Aeolian dust processes and sediments in the Australian region. *Quaternary Science Reviews 8*, 235–253.

Murray, R. W., Knowlton, C., Leinen, M., Mix, A. C. & Polsky, C. H. 2000: Export production and carbonate dissolution in the central equatorial Pacific Ocean over the past 1 Myr. *Paleoceanography 15*, 570–592.

Nath, B. N. & Mudholkar, A. V. 1989: Early diagenetic processes affecting nutrients in the pore waters of the Central Indian Ocean cores. *Marine Geology 86*, 57–66.

Nath, B. N., Borole, D. V., Aldahan, A., Patil, S. K., Mascarenhas-Pereira, M. B. L., Possnert, G., Ericsson, T., Ramaswamy, V. & Gupta, S. M. 2008: ^{210}Pb, ^{230}Th, and ^{10}Be in Central Indian Basin seamount sediments: signatures of degassing and hydrothermal alteration of recent origin. *Geophysical Research Letters 35*, L09603, doi: 10.1029/2008GL033849.

Pattan, J. N., Gupta, S. M., Mudholkar, A. V. & Partibhan, G. 1992: Biogenic silica in space and time in sediments of central Indian Ocean. *Indian Journal of Marine Sciences 21*, 116–120.

Pattan, J. N., Masuzawa, T., Borole, D. V., Parthiban, G., Jauhari, P. & Yamamoto, M. 2005: Biological productivity, terrigenous influence and non crustal elements supply to the Central Indian Ocean Basin: paleoceanography during the past approx. 1 Ma. *Journal of Earth System Science 114*, 63–74.

Ramaswamy, V. & Rao, P. S. 2006: Grain size analysis of sediments from the northern Andaman Sea: comparison of laser diffraction and sieve-pipette techniques. *Journal of Coastal Research 22*, 1000–1009.

Ramesh Babu, V., Suryanarayana, A. & Murty, V. S. N. 2001: Thermohaline circulation in the Central Indian Basin (CIB) during austral summer and winter periods of 1997. *Deep-Sea Research II 48*, 3327–3342.

Sexton, P. F. & Barker, S. 2012: Onset of Pacific-style deep-sea sedimentary carbonate cycles at the mid-Pleistocene transition. *Earth and Planetary Science Letters 321*, 81–94.

Snoeckx, H. & Rea, D. K. 1994: Dry bulk density and $CaCO_3$ relationships in upper Quaternary sediments of the eastern equatorial Pacific. *Marine Geology 120*, 327–333.

de Sousa, S. N., Sardessai, S. D., Ramesh Babu, V., Murty, V. S. N. & Gupta, G. V. M. 2001: Chemical characteristics of Central

Indian Basin waters during the southern summer. *Deep-Sea Research II 48*, 3343–3352.

Tchernia, P. 1980: *Descriptive Regional Oceanography*. 253 pp. Pergamon, New York.

Thierstein, H. R., Geitzenauer, K., Molfino, B. & Shackleton, N. J. 1977: Global synchroneity of late Quaternary coccolith datums: validation by oxygen isotopes. *Geology 5*, 400–404.

Thunell, R. C. & Honjo, S. 1981: Calcite dissolution and the modification of planktonic foraminiferal assemblages. *Marine Micropaleontology 6*, 169–182.

Wang, P. X., Tian, J., Cheng, X. R., Liu, C. L. & Xu, J. 2004: Major Pleistocene stages in a carbon perspective: the South China Sea record and its global comparison. *Paleoceanography 19*, PA4005, doi: 10.1029/2003PA000991.

Warren, B. A. 1982: The deep water of the Central Indian Basin. *Journal of Marine Research 40*, 823–860.

Weninger, B., Jöris, O. & Danzeglocke, U. 2010: CalPal-2007 Cologne Radiocarbon Calibration & Palaeoclimate Research Package. http://www.calpal.de (accessed 4 May 2010).

Winter, A., Jordan, R. W. & Roth, P. H. 1994: Biogeography of living coccolithophores in oceanic waters. *In* Winter, A. & Siesser, W. G. (eds.): *Coccolithophores*, 161–177. Cambridge University Press, Cambridge.

Wu, G., Yasuda, M. K. & Berger, W. H. 1991: Late Pleistocene carbonate stratigraphy on Ontong-Java Plateau: effects of winnowing and dissolution. *Marine Geology 96*, 193–209.

Marine Chemistry 121 (2010) 49–66

Contents lists available at ScienceDirect

Marine Chemistry

journal homepage: www.elsevier.com/locate/marchem

Selective leaching studies of sediments from a seamount flank in the Central Indian Basin: Resolving hydrothermal, volcanogenic and terrigenous sources using major, trace and rare-earth elements

M.B.L. Mascarenhas-Pereira *, B. Nagender Nath

Geological Oceanography Division, National Institute of Oceanography, Dona Paula, Goa, 403004, India

ARTICLE INFO

Article history:
Received 27 February 2009
Received in revised form 25 January 2010
Accepted 17 March 2010
Available online 24 March 2010

Keywords:
Major, trace and rare-earth element geochemistry
Selective leaching
Intraplate seamount
Metalliferous sediments
Central Indian basin
Fracture zone

ABSTRACT

We have investigated the sediments from a site where a newly discovered submarine hydrothermal alteration of recent origin is located to identify the source components and estimate their relative contribution. The site is situated on the flank of a seamount in the Central Indian Basin along the 76° 30′ E fracture zone which traces the movement of the Rodriguez triple junction. Detailed analyses of major, trace and rare earth elements (REE) on the bulk, leach, residue and clay fraction, and infra red spectroscopy studies of the clay fraction helped characterize the hydrothermal nature of the sediments. Selective dissolution carried out using HCl has allowed the discrimination between a leach phase (leachable Fe–Mn oxide) and a residue phase (refractory). The sediments are iron-rich, majority of Fe, Mn is in leachable fraction and are compositionally comparable to ridge-crest metalliferous sediments. Elemental ratios and geochemical discrimination plots of major element data reveal that the sediments are a mixture of Fe-rich mineral phases on one hand apparently from hydrothermal sources and aluminosilicates such as illite, zeolites, micaceous clays and smectites contributed from the Bengal fan, weathering of basinal basalts and authigenic processes. Ternary mixing calculations of bulk sediment major element data show that 35–45% metalliferous sediments could reproduce Fe and Mn values of our sediments.

The shale normalized REE patterns of the bulk sediments are remarkably similar to those of the HCl soluble leach fraction, implying that the REEs in the HCl soluble leach fraction dominate the bulk fraction. HCl leacheates exhibit characteristics of vent fluids as well as seawater with pronounced Eu anomaly with HREE enrichment and negative Ce anomaly. The residue on the other hand has a high concentration of Fe, V, Zn, and Pb indicating a sulfidic input to the sediments. Ternary mixing calculations of REEs carried out on the residual fraction indicate that the sulfide-like material dominates (64–72%) over terrigenous (10–20%) and MORB derived (16–18%) components.

This study helped us identify and quantify two types of hydrothermal material in the sediments, dominated by Fe–Mn phases (ferruginous oxides and silicates; Mn-oxides) in leachable fraction and sulfide-like material in residual phases. The clay fraction is mainly composed of dioctahedral smectites and has a composition similar to Alvin nontronite. The geochemical and mineralogical characteristics collectively suggest that these sediment-hosted precipitates formed at relatively low temperatures ranging between 50 and 100 °C from a mixture of seawater and hydrothermal fluids.

The presence of hydrothermal sediments in the vicinity of a fracture zone suggests the occurrence of localized hydrothermal activity associated with intra plate volcanism. This is probably induced by reactivation of tectonic forces along the fracture zones.

1. Introduction

Submarine hydrothermal activity is a widespread feature occurring in all the oceans along the spreading centers at mid oceanic ridges and at subduction areas. Most of the sites discovered in the Indian Ocean so far are located along the mid-oceanic ridge system with some at the Andaman back arc basin (Banerjee and Ray, 2003; Gallant and Von Damm, 2006; Bach et al., 2002; Kurian et al., 2008). In addition to the spreading centers, hydrothermal activity can also occur in oceanic seamount areas. Intraplate seamounts are produced from the upwelling of "small plumes" which transport lower mantle material underneath the ridge axis. The leaking of this lower mantle material gives rise to axial and off axial volcanism (Hékinian et al., 1999). Hydrothermal deposits at intraplate seamounts are less

* Corresponding author. Fax: +91 832 2450602.
E-mail address: mariab@nio.org (M.B.L. Mascarenhas-Pereira).

0304-4203/$ – see front matter © 2010 Elsevier B.V. All rights reserved.
doi:10.1016/j.marchem.2010.03.004

common, although the seamount morphology associated fracturing and volcanism could favor hydrothermalism (Alt, 1988). Such seamounts have been reported from the Pacific viz., Macdonald, Loihi (Karl et al., 1988), Vailulu'u (Staudigel et al., 2004). Signatures of the hydrothermal nature of the Central Indian Basin (CIB) sediments were only reported through microscopic spherules (see Iyer, 2005 and references therein). Native aluminum-rich particles of hydrothermal origin (Iyer et al., 2007), volcanic glass associated with pumice and palagonites (Mascarenhas-Pereira et al., 2006) was recovered from the sediments located on the flank of a seamount along the 76° 30′ E Fracture zone in the CIB and indicated the occurrence of intraplate submarine volcanism and hydrothermal activity. Recent isotopic studies (^{210}Pb, ^{10}Be and ^{230}Th) on the sediments from the same area have revealed hydrothermal alteration of sediments of recent origin through ascending fluid flow (Nath et al., 2008).

In this study, we have employed major, trace and rare-earth element (REE) geochemistry (along with other elements) to characterize the different source components and to estimate their relative contribution to the sediments from the flank of a seamount along the fracture zone. We have extracted the hydrothermal component in the sediments by selective leaching using 50% HCl. The chemistry of hydrothermal component in these sediments allowed a comparison with previously published geochemical data of hydrothermal material from other major spreading centers (Rainbow, TAG, MAR and EPR). Bulk and leach data was used for mixing calculation to find the proportion of the different source components. Based on these studies, we report the occurrence of sediments of distinctly metalliferous nature with ferruginous smectites and nontronite at this intraplate seamount setting. This is the first report of hydrothermal signatures being imprinted on the bulk chemistry of the sediments in an intraplate region of the CIB.

2. Regional setting and hydrothermalism

The CIB is bounded by the Ninety East ridge, the Central Indian ridge and the Southeast Indian ridge, and is between 50 and 60 Ma in age (Mukhopadhyay and Batiza, 1994). There exists three major fracture zones that trend along 73° E (Vishnu or La Boussole), 76° 30′ E and 79° E (Indrani or L'Astrolabe) and the Triple Junction Trace on the Indian Plate (TJT-In) between 76 and 78° E longitude (Kamesh Raju and Ramprasad, 1989). The sediment core studied here is recovered from the southern end of the 76° 30′ E fracture zone (Fig. 1b) which represents the trace of Indian Ocean Triple Junction movement (Kamesh Raju and Ramprasad, 1989; Kamesh Raju, 1993). This is one of the six N–S fracture zones represented in the CIB (Kamesh Raju, 1993, and references therein). Several seamounts were delineated along the fracture zones in the CIB, with the majority clustering along 76° 30′ E and 79° E fracture zones (Fig. 1b). Clustering of seamounts along the fracture zones as seen here, is similar to non-hotspot volcanoes in the Pacific (Das et al., 2007), which preferentially occur either on or very near to the fracture zone. The fracture zones may provide easy conduits for formation of seamounts (Batiza, 1982). There may also be local perturbations to the plumbing system or other zones of weakness that control the location of seamounts (Epp and Smooth, 1989; Kamesh Raju, 1993). Such local perturbations to the plumbing system possibly from tectonic reactivation of the fracture zones may be responsible for the intraplate volcanism and the hydrothermal activity metalliferous sediments in this area.

Possibility of intraplate volcanism and the associated hydrothermal activity in CIB has been reported in the past. Occurrence of volcanic spherules, glass shards (Gupta, 1988; Iyer et al., 1997; Mascarenhas-Pereira et al., 2006; Nath and Rao, 1998; Sukumaran et al., 1999); volcanogenic–hydrothermal material consisting of Fe–Si oxyhydroxides, volcanic spherules, glass shards, ochrous metalliferous sediments and spherules (Iyer et al., 1997), spillites in the vicinity of 79° E fracture zone (Karisiddaiah and Iyer, 1992), zeolitites (Iyer and Sudhakar, 1993), fossil free smectite-rich pyroclastic layers at different subsurface depths representing episodic volcanic activity (Nath and Rao, 1998) in CIB were reported in the past. In a recent study by Iyer et al. (2007), native aluminium of submarine hydrothermal origin was reported from the core AAS 61/BC 8.

3. Sampling and analytical work

A short sediment core AAS 61/BC 8 was collected using a large box corer (50×50×50 cm) at 16° S and 75° 30′ E from the flanks of a seamount from the CIB along the southern end of the76° 30′ E fracture zone from a water depth of 5010 m (Fig. 1) during the 61st cruise of RVAA Sidorenko during the year 2003. The core was sampled from pelagic red clay sediment domain (see Nath et al., 1989 for sediment types in CIB). The core was sub sectioned into 2 cm intervals. Clays of <2 μm size were separated using standard settling velocity technique.

Bulk samples along with clay samples were dissolved following acid dissolution procedure of Balaram and Rao (2003). The resulting solutions were analyzed for REE along with some trace and major elements by Inductively Coupled Plasma Mass Spectrometry (ICP-MS) at the National Geophysical Research Institute, Hyderabad, India. 10 ml of acid mixture containing HF, HNO_3 and $HClO_4$ (in the ratio of 6:3:1) was added to ~50 mg of sample and USGS Marine mud standard MAG-1 in teflon beakers. The solutions were then evaporated to dryness in the fume hood. After 30 min, 2 ml of conc. HCl was added to remove any black particles, if present. The acid mixture was kept on sand bath till it was evaporated to dryness. 5 ml of 1 ppm Rh solution and 20 ml of 1:1 HNO_3 were added and made up to 250 ml and cooled. The clear solutions were then introduced into ICP-MS for elemental analysis.

Following the bulk analyses, selective chemical leaching was carried out using hot 50% HCl on 4 sample intervals and USGS standard MAG-1 (following the technique described in Cronan, 1976). Accurately weighed representative subsamples of 1 g each were leached with hot 50% HCl and kept hot by continuous shaking in a heated water bath for 4 h prior to filtration. The dissolved material was filtered through previously weighed filter papers and the residues were weighed. The leach solutions were analyzed by ICP-MS for the same elements as the bulk samples, using standards made up in the same solutions as the samples. The same leaching procedure (with hot 50% HCl) was carried out on a different subsample (4 sediment sections) for major element analyses. MAG-1 was included during this batch of leaching. Bulk sediments and the residue left after leaching were analyzed for major elements using X-ray Flourescence Spectroscopy (XRF) at NIO, Goa. Elemental data of Fe, Al and Mn are obtained by both ICP-MS (Table 1) and XRF methods (Table 2) for four subsections, The results of Fe and Al by both the methods agree well (<11% variability), while the variability for Mn is relatively large probably due to inhomogeneity between the two subsamples used. It should also be mentioned here that the Mn values for MAG-1 obtained by both the methods concur well with the certified value (Tables 2

Fig. 1. Sampling location of sediment core AAS 61/BC 8 (shown as a star). a) Sampled area in the Central Indian Basin (CIB) with reference to India and shows the sediment distribution (numbers correspond to sediment types shown in the legend) (adopted from Nath et al., 1992b); b) detailed tectonic map showing the fracture zones, ridge axis and location of seamounts (shown as dots). Sampled location falls close to the cluster of seamounts in the vicinity of fracture zone (base map from Kamesh Raju, 1993) and c) 3-dimensional topographic map (bathymetry data set ETOPO 5 (National Geophysical Data Centre (NGDC) 1988). As seen in figures b) and c), the sample location falls on the flank of a seamount.

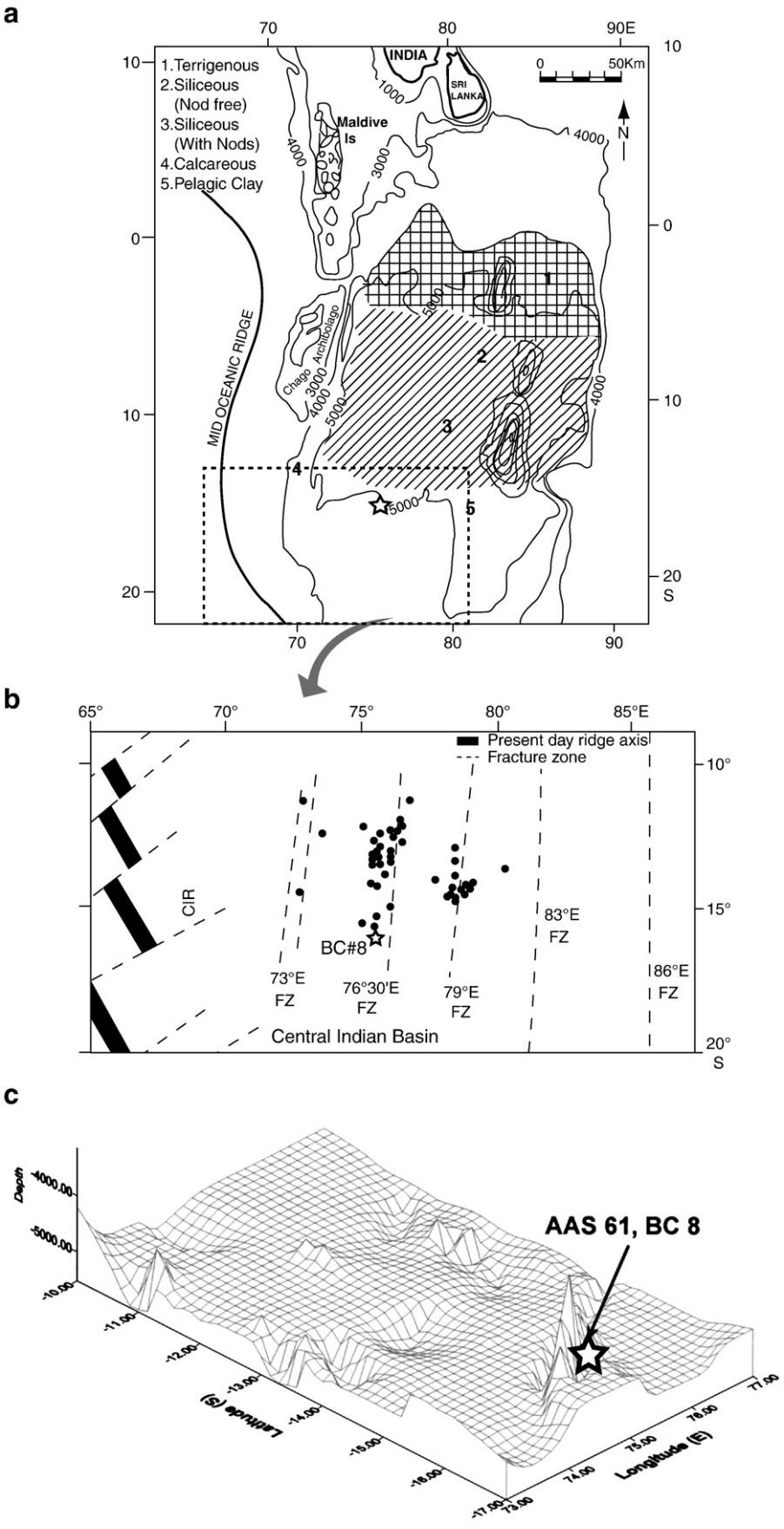

Table 1
Major and rare earth element concentrations in bulk sediments of AAS 61/8.

Element	Depth (cm)									
	0–2	2–4	4–6	6–8	8–10	10–12	12–14	14–16	16–18	18–20
Al (%)	6.43	6.75	6.74	6.82	6.74	6.65	6.61	6.74	6.55	6.63
Mn (%)	1.47	1.47	1.32	1.39	1.45	1.46	1.33	1.31	1.32	1.39
Fe (%)	6.58	7.13	6.20	7.36	8.46	8.26	8.22	8.16	8.14	8.32
V	152	164	125	163	221	221	222	234	231	230
Cr	26	28	29	27	26	25	25	25	25	27
Co	138	147	140	146	149	148	139	137	139	146
Ni	782	761	562	562	490	428	333	300	294	336
Cu	473	452	378	359	332	307	279	264	258	260
Zn	177	178	171	175	184	180	176	185	197	194
Sr	187	195	179	200	224	228	231	233	234	233
Y	257	241	198	221	218	201	191	184	182	192
Zr	281	307	265	322	377	370	384	388	408	399
Ba	732	693	712	598	507	470	480	463	469	525
La	113	121	100	117	123	117	113	110	110	115
Ce	158	169	163	170	177	178	171	168	172	172
Pr	27.15	28.43	24.75	27.26	26.41	25.46	24.29	23.21	22.97	24.18
Nd	121	128	112	123	119	114	108	104	101	107
Sm	29.84	31.22	28.28	29.73	26.88	25.87	24.46	23.17	22.63	24.24
Eu	7.16	7.33	6.71	7.19	6.27	5.84	5.81	5.46	5.42	5.73
Gd	25.70	27.25	23.87	25.69	23.80	22.58	21.92	20.77	20.44	21.80
Tb	5.25	5.50	4.86	5.23	4.75	4.44	4.35	4.11	4.01	4.34
Dy	32.62	33.97	29.54	32.18	29.56	28.20	26.79	25.62	25.35	27.11
Ho	7.03	7.62	6.33	7.00	6.59	6.25	5.93	5.78	5.75	6.17
Er	20.23	22.00	18.02	20.29	19.33	18.41	17.38	16.79	16.87	17.69
Tm	3.06	3.27	2.68	3.02	2.91	2.71	2.64	2.51	2.55	2.64
Yb	17.99	19.24	16.09	17.89	17.41	16.18	15.57	14.83	14.83	15.69
Lu	2.87	3.10	2.58	2.78	2.75	2.58	2.45	2.40	2.33	2.49
Hf	6.65	7.08	6.30	7.71	8.60	8.63	8.79	8.67	8.85	8.37
Pb	19.22	19.82	19.27	19.22	19.05	18.39	18.11	17.78	17.59	17.69
Th	15.79	15.89	18.14	15.95	13.55	13.49	13.28	12.52	12.76	12.79
U	2.27	2.52	2.28	2.67	3.21	3.35	3.34	3.16	3.11	3.27

(All values in ppm).

and 3). We prefer to use ICP-MS data for these 3 elements for interpretations as the data for entire core is available.

The leach was expected to contain amorphous Fe–Mn oxides, carbonate minerals and adsorbed trace elements, crystalline iron oxides, hydrothermal silicates, weathered detrital/clay phases and partially dissolves sulfide component if any (Cronan and Hodkinson, 1997). The residue, on the other hand, was expected to contain mainly the resistant silicates and aluminosilicates insoluble in HCl (detrital phase) and the sulfides if any. Though a large number of leaching techniques are available in the literature, acid based leaching with low pH are found to be suitable for elements like REE (Sholkovitz, 1989; Nath et al., 1994). The leach used here has also been adopted elsewhere for assessing the hydrothermal component in sediments (Chavagnac et al., 2005).

Precision and accuracy of ICP-MS analyses carried out on MAG-1 in duplicate are presented in Table 3. Accuracy was better than 5% for Al, Fe, La, Sm and U, while it was better than 2% for all other elements. Data shows an excellent precision for all the elements studied here (better than 5%: Table 3).

In order to know the recovery of material in the leaching experiment, we compared our results for MAG-1 (bulk and residue) with those of Kryc et al. (2003) (Table 4) who reported sequential extraction procedure for Si, Al, Ti, Fe, Ca, Mn P and Ba in five sedimentary reference materials. It should however be noted that the extraction procedures were different in both the studies. In general, there is a good agreement for all elements (except Fe and Mn) between the results of our study and those of Kryc et al. (2003) (Table 4) despite the difference in techniques and analytical methods adopted for the residual extraction. Our residues contained lower Fe and Mn than Kyrc et al. (2003) probably in view of the stronger leach (hot 50% HCl vis-à-vis the hydroxylamine hydrochloride used by Kryc et al., 2003) used by us.

Table 2
Major element content in (wt %) bulk and leach residues.

Sample (sediment depth)		Residue[a]%	SiO_2	Al_2O_3	TiO_2	Fe_2O_3	MnO	MgO	CaO	Na_2O	K_2O	P_2O_5
AAS 61/8												
4–6 cm	74	Bulk	42.26	12.87	0.61	9.97	5.905	3.07	1.98	1.63	2.54	0.91
		Residue[b]	59.83	12.46	0.75	5.78	0.046	1.44	0.42	0.68	2.09	0.12
8–10 cm	69	Bulk	43.86	13.96	0.73	11.95	2.345	2.81	2.22	1.37	2.85	1.16
		Residue[b]	57.84	12.48	0.87	6.37	0.035	1.45	0.49	0.78	2.22	0.14
12–14 cm	70	Bulk	46.55	14.13	0.77	11.06	2.168	2.73	2.16	1.32	2.87	1.02
		Residue[b]	57.97	12.05	0.95	6.63	0.041	1.47	0.54	0.76	2.03	0.15
18–20 cm	58	Bulk	42.14	13.84	1.05	13.57	2.316	2.64	2.43	1.75	2.86	1.24
		Residue[b]	55.83	12.81	1.05	6.88	0.025	1.57	0.59	0.78	2.16	0.12
MAG-1		Bulk	50.78	16.07	0.72	7.29	0.1	3.09	1.42	3.81	3.70	0.16
		Certified value	50.40	16.40	0.75	6.80	0.098	3.00	1.37	3.83	3.55	0.16
	80	Residue[b]	62.34	16.07	0.78	2.74	0.012	1.11	0.44	1.25	3.52	0.07

[a] Residue left on leaching with hot 50% HCl.
[b] The elemental concentrations are not weight corrected.

Table 3
Analytical results (in duplicate) of USGS geochemical standard MAG_1. (All values in ppm).

Element	Certified values	This work	Accuracy (%)	Precision %
		Mean of 2 analysis	(±)	(±)
Al (%)	8.66±0.16	8.29±0.15	4.28	3.7
Mn (%)	0.076±0.005	0.076±0.0004	0.51	1.03
Fe (%)	4.58±0.42	4.81±0.01	4.89	0.29
V	140±6	136±0.37	2.68	0.54
Cr	97±8	94.56±0.14	2.52	0.31
Co	20±1.6	20.18±0.03	1.06	0.29
Ni	53±8	52.63±0.06	0.71	0.23
Cu	30±3	29.95±0.001	0.17	0.01
Zn	130±6	130±1.3	0.36	2.01
Sr	150±15	145±0.8	3.61	1.11
Y	28±3	27.81±0.21	0.67	1.52
Zr	130±6	125±0.17	3.96	0.27
Ba	480±41	473±2.88	1.43	1.22
La	43±	41.14±0.33	4.33	1.62
Ce	88±9	84.81±0.31	3.62	0.74
Pr	9.3±	9.02±0.03	3.04	0.71
Nd	38±5	37.1±0.2	2.36	1.09
Sm	7.5±0.6	7.81±0.09	4.13	2.43
Eu	1.5±0.14	1.52±0.02	1.37	2.17
Gd	5.8±0.7	5.68±0.06	2.1	2.01
Tb	0.96±0.09	0.97±0.002	1.2	0.31
Dy	5.2±0.3	5.19±0.11	0.19	4.39
Ho	1.02±0.1	1.03±0.02	0.78	4.67
Er	3±	2.94±0.01	2.08	0.58
Tm	0.43±	0.43±0.01	0.35	4.9
Yb	2.6±0.3	2.61±0.01	0.31	0.69
Lu	0.4±0.04	0.39±0.01	1.5	4.06
Hf	3.7±0.5	3.81±0.06	2.91	3.13
Pb	24±3	24.05±0.17	0.21	1.44
Th	11.9±1	12.25±0.28	2.98	4.51
U	2.7±0.3	2.83±0.07	4.78	4.81

Infrared spectroscopic studies were carried out on the <2 μm size clay fraction pellets (pressed with KBr powder) using a Shimadzu 8201 PC at the National Institute of Oceanography, Goa. Organic carbon measurements were made using wet oxidation method of El Wakeel and Riley (1957). The level of precision and accuracy routinely obtained in our laboratory are described in Nath et al. (1997a).

4. Results and discussion

Major and REE data for the bulk sediments is presented in Tables 1 and 2 and those of leach and residues are shown in Table 5.

4.1. Lithological variation

The sediments in the study area show two subsections (units) based on color. While the unit 1 (0–6 cm bsf) display a light brown color, unit 2 (6–20 cm bsf) exhibits a dark brown to black coloration. The coarse fraction (>63 μm) shows an abundance of radiolarians in unit 1, which gradually decreases in abundance, leading to complete absence in unit 2. The transition from pelagic to indurated sediment is marked by the absence of radiolarians and the presence of ichthyoliths. Radiolarian dissolution features were clearly evident in SEM pictures of unit 2 sediments (Nath et al., 2008). Glass shards are present throughout the core, but are abundant in unit 2 (Mascarenhas-Pereira et al., 2006). Aluminium-rich grains of hydrothermal origin were recovered mainly from unit 2 (Iyer et al., 2007). Palagonitic grains were present throughout the core with colors ranging from white, yellow to brown and with a waxy luster. Biostratigraphy and radiometric dating has shown that the unit 1 is younger than 180 kyrs. (Mascarenhas-Pereira et al., 2006).

Table 4
Comparative data results from leaching experiment of MAG-1 (μmol/g).

	Si	Al	Ti	Fe	Mn	Ca
This study						
Residue	8330	2521	78	274	1.35	65.6
Bulk	8477	3149	89.4	910	14.08	263
Certified[a]	8414	3215	94	849	14	254
% element in residue	99	78	83	32	10	26
Kryc et al. (2003)						
Residue	NM	2311	70.9	443	4.3	49.7
Bulk	138	2893	78.7	849	11.8	252
Certified[b]	8381	3212	94	852	13.8	244
% element in residue		72	75	52	31	20

[a] Source USGS website (http://minerals.cr.usgs.gov/geo_chem_stand/marine.html).
[b] As mentioned in Kryc et al. (2003).

4.2. Identification of source

4.2.1. Major element geochemistry and interpretation of mineral associations

The major element composition of bulk and the residues are presented in Table 2. Two major features stand out. In general the sediments have low silica compared to CIB sediments (Nath et al., 1989) and high Fe content suggesting a ferruginous nature. Si/Al ratio in bulk sediments is ~2.8, which is less than that reported for typical quartz mineral/biogenic silica (>5, Ziegler et al., 2007), while the residue has a higher ratio of Si/Al (~ 4). This is consistent with the mineralogy of the core which has low siliceous skeletal remains with dissolution effects seen on some of the radiolarians (Mascarenhas-Pereira et al., 2006; Nath et al., 2008). However Fe/Si ratio of the bulk (0.35–0.48) is comparable to authigenic Fe rich smectites associated with hydrothermal process in other areas (Central Pacific, Ziegler et al., 2007; DOMES area in North Pacific, Hein et al., 1979). The Na/K ratio in leach residues range between 0.32 and 0.37 and closer to ~0.35 assigned to phillipsite (Kastner, 1979; Ziegler et al., 2007) and is consistent with the volcanogenic–hydrothermal content in unit 2 (Mascarenhas-Pereira et al., 2006; Iyer et al., 2007).

Unpublished X-ray diffraction studies have shown that the sediments contain a mixture of quartz, plagioclase feldspars, illite, alteration mineral smectite and authigenic silicate such as zeolites (mainly phillipsite). Earlier studies have shown that the CIB sediments contain illite, chlorite and kaolinite mainly derived from turbiditic currents from Ganges–Brahmaputra through Bengal fan (Rao and Nath, 1988; Debrabant et al., 1993), smectite derived from the weathering of basinal basaltic rocks; with presence of both Al- and Fe-rich montmorillonites (Rao and Nath, 1988). Phillipsite and clinoptilolite are major zeolitic minerals present in CIB sediments (V. P. Rao and B. N. Nath, unpublished data). In the following section on infra-red spectroscopy studies, we have also discussed the presence of nontronite, ferruginous smectites and beidellites in these sediments. We have plotted two x-y scatter diagrams (Al_2O_3 versus. Fe_2O_3 and K_2O versus Al_2O_3), and one ternary diagram (K-A-CN) to infer the mineralogy (Figs. 2 and 3). Literature values of chemical composition for clay minerals (Kaolinite, smectite, illite and chlorite from Grim, 1968 and references therein), plagioclase, zeolites (Deer et al., 1967 and references therein), in addition to Al-Bediellite and nontronite (Aoki et al., 1996) and authigenic Fe-montmorillonite of hydrothermal origin (McMurtry and Yeh, 1981) are used as possible sources. In addition, chemical data on separated clays from the distal Bengal fan (Aoki et al., 1991) are also included.

In the Al_2O_3 vs. Fe_2O_3 plot (Fig. 2a), the bulk sediments fall in between Fe-rich fields of Fe-montmorillonites, nontronites and Bengal fan smectites on one side and Al-rich end members of smectite, beidellite, micaceous clays from Bengal fan, chlorite, zeolite and plagioclase on other. This could be accounted by the presence of a mixture of variable proportions of Al_2O_3 supplied by illite, plagioclase, smectite and zeolites and Fe_2O_3 contributed by nontronite and Fe-

Table 5
Relative proportion in HCl leachates and residue fraction in AAS 61/BC 8. (All values in %).

Sample ID:	4–6 cm		8–10 cm		12–14 cm		18–20 cm	
Analyte (%)	Residue	Leach	Residue	Leach	Residue	Leach	Residue	Leach
Al	66	34	59	41	59	41	57	43
Fe	15	85	13	87	13	87	14	86
V	19	81	14	86	15	85	10	90
Cr	55	45	58	42	45	55	43	57
Co	3	97	3	97	2	98	3	97
Ni	7	93	7	93	8	92	9	91
Cu	8	92	7	93	7	93	6	94
Zn	71	29	80	20	31	69	56	44
Sr	27	73	27	73	24	77	39	61
Y	4	96	4	96	5	95	3	97
La	8	92	8	92	9	91	6	94
Ce	9	91	8	92	7	93	7	93
Pr	6	94	7	93	8	92	5	95
Nd	5	95	6	94	7	93	5	95
Sm	4	96	5	95	7	93	4	96
Eu	5	95	7	93	7	93	6	94
Gd	4	96	4	96	5	95	4	96
Tb	4	96	4	96	6	94	3	97
Dy	4	96	5	96	6	94	4	96
Ho	4	96	4	96	6	94	4	96
Er	4	96	5	95	6	94	4	96
Tm	5	95	5	95	7	93	5	95
Yb	6	94	6	94	8	92	5	95
Lu	6	94	6	94	8	92	5	95
Pb	23	77	25	75	15	85	22	78
Th	34	66	25	75	30	70	19	81
U	38	62	28	72	24	76	26	74

montmorillonite. The residue plot closer to the smectites and micaceous clays of Bengal Fan as compared to the bulk indicating the removal of Fe from the authigenically formed nontronites and Fe-montmorillonite from the bulk sediments. This is also manifested by the Fe/Al ratio of bulk (> 1.02) being more than the residue (< 0.61). The Fe/Al ratio of residue in the surface sediments approaches the

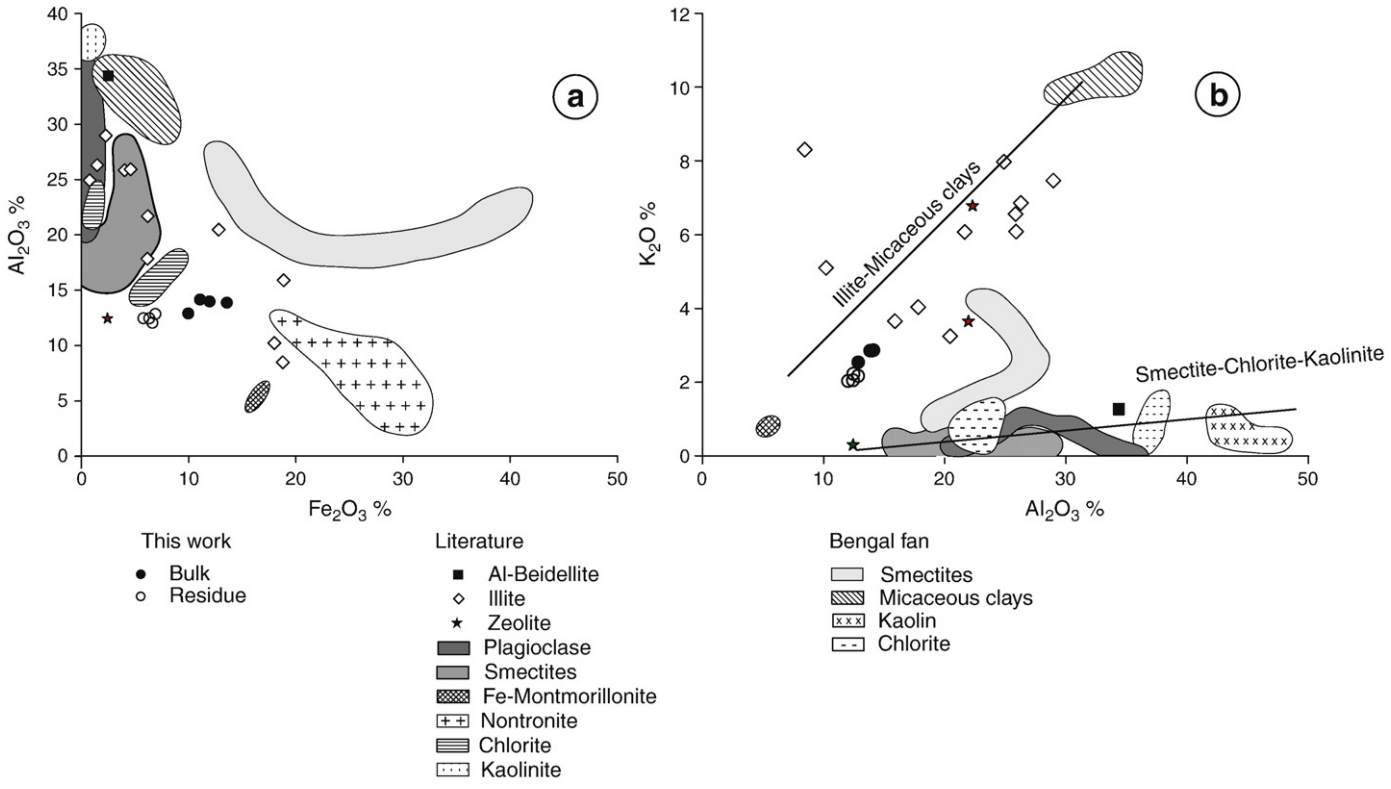

Fig. 2. Discriminating source using composition of sediments. a) Fe_2O_3 versus Al_2O_3 plot and b) Al_2O_3 versus K_2O. The plots illustrate that the bulk sediments are a mixture of variable proportions of Fe-rich and Al-rich end members. References of literature data are given in the text.

value of PAAS (~0.51). The source composition mainly of aluminosilicate fraction is further constrained from the K_2O and Al_2O_3 plot (Fig. 2b), wherein our sediment data plot between two trend lines, first defining illite, Bengal Fan micaceous clays and the other with overlapping compositional fields of plagioclase, smectite, chlorite, kaolinite, beidellite and zeolites. Thus, the aluminosilicates in these sediments may reflect the mixing of these two groups of mineral sources. The residue data fall close to bulk data with slight fall in K and Al values. Support also comes from the ternary diagram of K_2O–Al_2O_3–($CaO + Na_2O$) (Fig. 3), where our bulk sediment data is sandwiched between fields defining zeolite, plagioclase and Fe-smectites on one side and illite, Al-rich beidellite, micaceous clays from Bengal Fan, kaolinite and chlorite on other. The bulk sediments exhibit a loss in $CaO + Na_2O$ on leaching with hot 50% HCl and a concomitant gain in Al_2O_3%. The bulk sediments are apparently stripped off of CaO and Na_2O from the Fe-montmorillonite, phillipsite and plagioclase with the residue exhibiting compositional similarity with Bengal Fan smectites.

4.2.1.1. Fe, Mn and minor element geochemical constraints on metalliferous/hydrothermal contribution. The Fe, Mn contents (Table 1) and Fe/Mn ratios (Table 6) correspond with those found in Central Indian ridge sediments and Fe oxides of hydrothermal origin from the EPR and north Fiji basin (Table 6, Plüger et al., 1986; Walter and Stoffers, 1985; McMurtry et al., 1991) implying the presence of a hydrothermal component in our sediments. The Fe/Mn ratios of our sediments are distinctly similar to ridge flank metalliferous sediments (Fig. 4). Mn concentrations in residues are < 2% of the bulk concentrations indicating that it occurs predominantly in the oxide/oxyhydroxide form. Assuming that majority Mn is of non-crustal origin, excess Fe/Mn (over the crustal ratio) is higher in unit 2 compared to unit 1, indicating a higher hydrothermal component in unit 2 sediments. Iron is present in a significant amount in the fraction soluble in HCl (~86%). Studies have shown that Fe from minerals like goethite and clay minerals of the smectite group can be stripped by HCl attack. Therefore the relatively high iron content in the HCl soluble phase indicates the high concentration of non-detrital iron bearing minerals. In a ternary plot of Al–Fe–Mn, our bulk data fall in the field of Bauer deep metalliferous sediments (Fig. 5).

The "Metalliferous sediment index" 100*Al/(Al + Fe + Mn) values (MSI, based on Boström and Peterson, 1969; Table 6) is higher than those found in Kairei (26–32%; German, 2003) and Rainbow hydrothermal fields (23–26%; Cave et al., 2002) likely due to the presence of "Al-rich" lithic grains of hydrothermal origin in the sediments (Iyer et al., 2007). MSI values are lower in unit 2 suggesting that the metalliferous sediment component is relatively higher in unit 2 sediments.

In all the samples, cobalt, nickel and copper are predominantly present in the HCl soluble phase (up to 98%). In addition, elements like Fe, V, Pb are also principally associated with the non detrital phase (Table 5). Such a combination of elements has been termed as "hydrothermally associated elements" by Cronan and Hodkinson (1997).

We have used Co/Zn ratios to discriminate the sources of Fe–Mn oxides, similar to that adopted for Fe–Mn oxides (e.g., Toth, 1980; Nath et al., 1997b), considering that Co is a typical hydrogenous element enriched in hydrogenous precipitates scavenged from seawater while, Zn can be derived from a hydrothermal source. Analytical data on bulk sediments (AAS 61/ BC 8 core) studied here shows that the Co/Zn ratio (0.70 to 0.83, Table 6) falls close to the value for Fe–Mn oxides of mixed hydrothermal hydrogenous origin from the Rodriguez Triple Junction (RTJ) in the Indian Ocean (Nath et al., 1997a). In a scatter plot (Fig. 6) of Co + Ni + Cu versus Co/Zn (following Toth, 1980), Co + Ni + Cu values of bulk sediments lie between 500 and 1500 ppm and plot very close to the hydrothermal-hydrogenetic boundary line (Fig. 6, modified from Nath et al., 1997a). Although Co/Zn in bulk sediments is almost similar in both the units, the HCl soluble leach phase is clearly differentiated with sediment depth. Data for the HCl leachates of unit 1 (4–6 cm and 8–10 cm) plot away from the hydrothermal-hydrogenetic fields with Co/Zn values between 9 and 12, while those of unit 2 (12–14 cm and 18–20 cm) lie

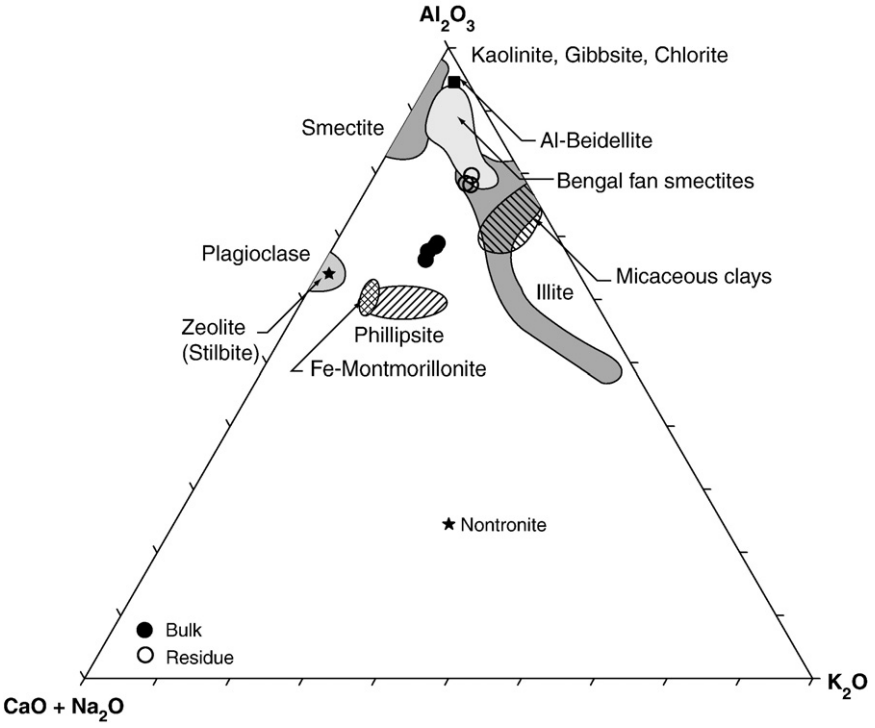

Fig. 3. K_2O–Al_2O_3–($CaO + Na_2O$) diagram shows mixing between zeolite, plagioclase and Fe-smectites on one side and illite, Al-rich beidellite, micaceous clays from Bengal Fan, kaolinite and chlorite on other. Residue exhibits reduction of Ca and Na and compositional similarity with micaceous clays and smectites of Bengal Fan and illites.

Table 6
Important elemental ratios of the sediments of AAS 61/BC 8.

Depth (cms)	0–2	2–4	4–6	6–8	8–10	10–12	12–14	14–16	16–18	18–20
Ratios										
Co + Ni + Cu (ppm)	1393	1360	1080	1068	971	882	751	701	690	743
Co/Zn	0.78	0.83	0.82	0.83	0.81	0.82	0.79	0.74	0.7	0.76
∑REE (ppm)	572	607	539	588	585	567	543	526	527	546
Eu/Eu*	1.22	1.18	1.22	1.22	1.17	1.14	1.18	1.17	1.19	1.17
Ce/Ce*	0.66	0.66	0.75	0.7	0.71	0.75	0.76	0.77	0.79	0.75
$(La/Yb)_{PAAS}$	0.46	0.47	0.46	0.48	0.52	0.53	0.53	0.55	0.55	0.54
Fe/Mn	4.47	4.85	4.71	5.31	5.84	5.67	6.17	6.23	6.18	6
Fe_2O_3/Al_2O_3	0.78	0.8	0.7	0.82	0.95	0.94	0.94	0.92	0.94	0.95
∑REE/Fe	0.0087	0.0085	0.0087	0.008	0.0069	0.0069	0.0065	0.0061	0.0056	0.0052
MSI[a]	44.38	43.97	47.25	43.81	40.5	40.64	40.9	41.58	40.92	40.58
∑REE/Fe(leach)	na	129.5	na	86	na	86	na	na	na	93

Na: not analyzed.
[a] Metalliferous sediment index.

closer to the hydrothermal–hydrogenetic boundary. This is consistent with the variable hydrothermal component in the two units.

Zn/Fe ratios (~ 0.0024 obtained here) are comparable to hydrothermal Fe oxides from the north Fiji basin (Table 7, McMurtry et al., 1991), Fe–Mn oxides of EPR (Walter and Stoffers, 1985), as well as CIR sediments (Plüger et al., 1986). Relative proportion of zinc is higher compared to Cu in residues (Table 5). Hydrothermal precipitates are generally characterized by relatively low Cu but high Zn concentrations (Kastner, 1981). Massive sulfides analyzed from Mt. Jourdanne located on SWIR also show such association (Münch et al., 2001). The presence of high Zn (31–80% of total Zn) in the residue may indicate the presence of sphalerite. The low concentration of Fe along with high Zn content in residue indicates Fe-poor sphalerite formed at temperature below 200 °C (Münch et al., 2001).

CIB sediments in pelagic red clay domain contain 2000–3000 ppm of Ba (Nath et al., 1989) compared to 463 to 732 ppm found in the core under consideration, which is almost 5 times lower than the surrounding sediments. This is consistent with depletion in biologically derived material viz., low organic matter and intense radiolarian dissolution in our core (Nath et al., 2008). Biologically derived barite grains were retrieved and studied earlier from CIB (Fagel et al., 1997). Considering a low biogenic contribution to the core studied here, barium could be from volcanogenic or hydrothermal sources. The

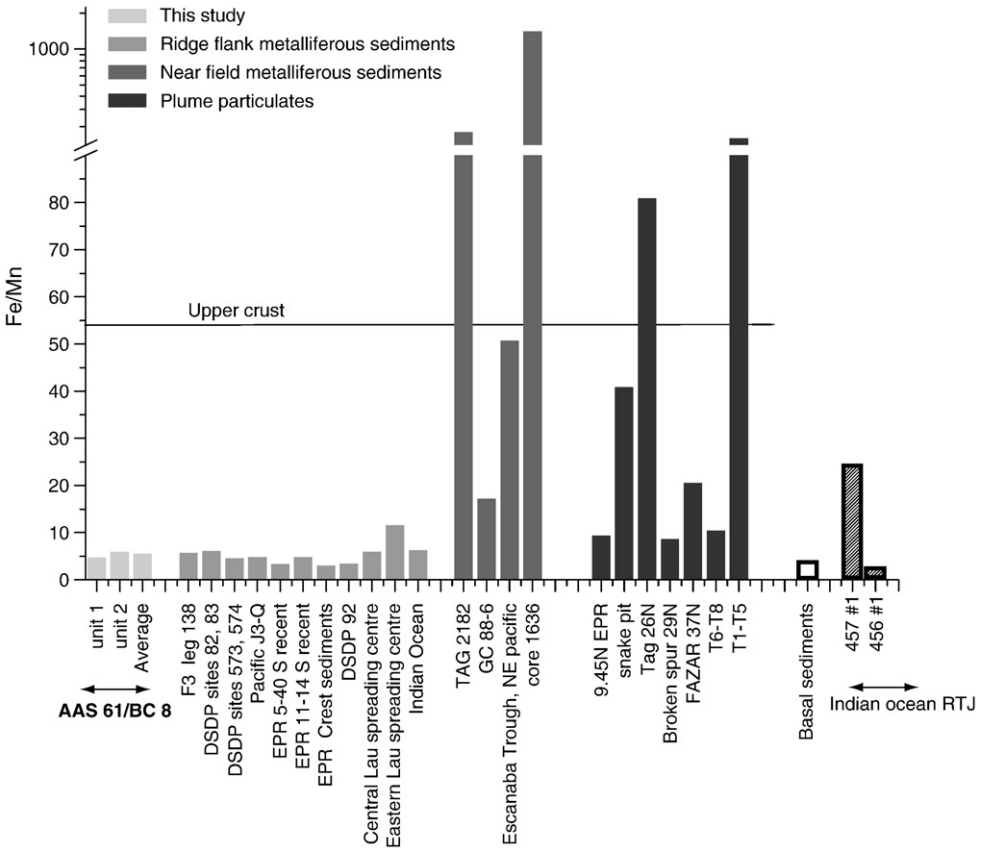

Fig. 4. Fe/Mn ratio of AAS 61/BC 8 is compared with metalliferous sediments form ridge flank as well as near field sediments along with plume particulates. (The literature data for Fe/Mn ratios is taken from Gurvich et al., 1995; Donnelly, 1980; Jarvis, 1985; Lisitzin et al., 1992; Cherkashev, 1992; Li, 2000; Cronan, 1976; German et al., 1993, 1995, 1997, 1999; Barrett et al., 1987; Hodkinson and Cronan, 1991; James et al., 1995; Boström and Peterson, 1969; Sherrell et al., 1999; Ludford et al., 1996 and Mitra et al., 1994). Fe/Mn ratios in our sediments are similar to those of ridge flank metalliferous sediments. Conversely, the near field metalliferous sediments and plume particulates have higher Fe/Mn ratios compared to the ridge flank metalliferous sediments.

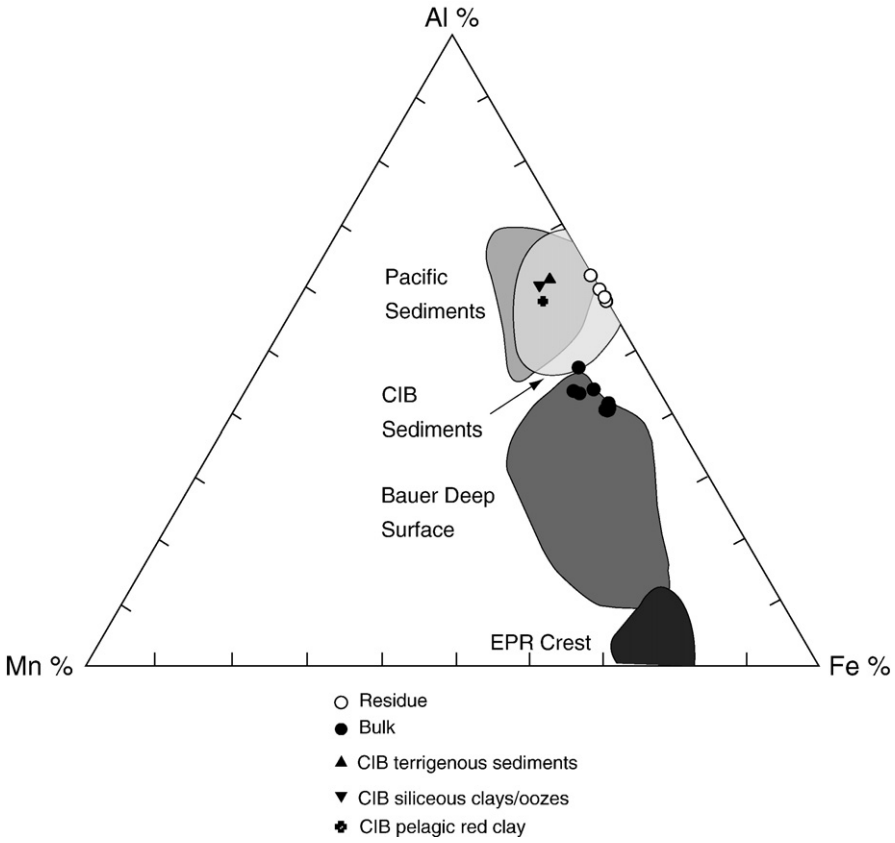

Fig. 5. Ternary plot of Al–Fe–Mn illustrating the compositional similarity of bulk sediments to Bauer deep metalliferous sediments. Compositional fields of CIB (Borole, 1993), Pacific and EPR sediments (Plüger et al., 1985 and references therein) along with mean composition of 3 major sediment types in CIB (Nath et al., 1989) are shown.

values are closer to those found in hydrothermal sediments. For example, similar Ba concentration (550–571 ppm) were also observed in bulk hydrothermal sediments collected from the ODP site 834 and 835 in the Lau basin, SW Pacific (Cronan and Hodkinson, 1997). Ba in the form of barite is a common precipitate from hydrothermal solutions (Dymond, 1981). We have analyzed Ba only in the bulk and thus unable to estimate the presence of barite in the residual phase.

4.2.2. Mixing calculations using major element data of bulk sediments

Based on the possible source components interpreted from above discussion, relative proportion of each end member contributing to the bulk is assessed using ternary mixing equation with mass balance equation (Albarède, 1995; Chavagnac et al., 2005) shown below.

$$\int_{\text{terrigenous}} + \int_{\text{metalliferous}} + \int_{\text{MORB}} = 1$$

$$C^i_{\text{mix}} = \left(\int_{\text{terrigenous}} x C^i_{\text{terrigenous}}\right) + \left(\int_{\text{metalliferous}} x\ C^i_{\text{metalliferous}}\right) + \left(\int_{\text{MORB}} x\ C^i_{\text{MORB}}\right)$$

where f represents the proportion of each end-member contributing to the bulk sediments and C^i_{mix} is the concentration of element i in the mixture of 3 end members. The end members used are metalliferous sediments from Bauer depression (Sayles and Bischoff., 1973), Indian MORB (Sun et al., 1979) and terrigenous sediments (Nath et al., 1989) from northern Indian Ocean (i.e. terrigenous material, metalliferous sediments and, MORB). The mixing calculations show that 35–45% metalliferous sediments could reproduce Fe and Mn values of our sediments. Mixing calculations for other major elements such as Na and Mg also show affinity towards composition of metalliferous sediments, while the MORB contribution is apparently higher to Ti and Al.

4.2.3. REE geochemistry

The behavior of the REE in high temperature seafloor hydrothermal fluids is well characterized (Michard and Albarède, 1986; Mitra et al., 1994). The REE concentrations are enhanced 10–10,000 times over sea water, due to extensive scavenging results in the net removal of these elements from the sea water (German et al., 1990). Based on REE studies on plume particles from EPR (comparing to that of TAG data of German et al., 1990), Sherrell et al. (1999) have shown that (i) the REE fractionation in hydrothermal systems varies over small ranges in each plume, (ii) the middle REE increase linearly with decreasing particulate Fe, (iii) the REE component reflect the mixing of primary hydrothermal precipitates with that of local resuspended material, (iv) the dissolved REE draw down occurs when the particulate Fe content is high (v) continued uptake of REEs by resuspended sediments takes place on at the surface and (vi) the Mn-oxides are not important carrier phases of REE (vis-à-vis Fe which is the prime carrier phase). The distinctive hydrothermal REE pattern of the near field sulfides and oxides is therefore overprinted in metalliferous sediments, which have REE patterns characteristic of seawater (Barrett and Jarvis, 1988).

In this section, we discuss the REE geochemistry of bulk sediments as well as leach and residues of our samples in the light of published literature on plume particles and metalliferous sediments.

4.2.3.1. REE content in bulk sediments. REE content range between 526 and 607 ppm with relatively higher concentration in unit 1 compared to unit 2 (Table 6). The concentrations reported here are higher than those reported for the ridge-flank metalliferous sediments from the EPR (upto 300 ppm, Owen and Olivarez, 1988) and fall in the range of Leg 92 metalliferous sediments concentration (Barrett and Jarvis, 1988).

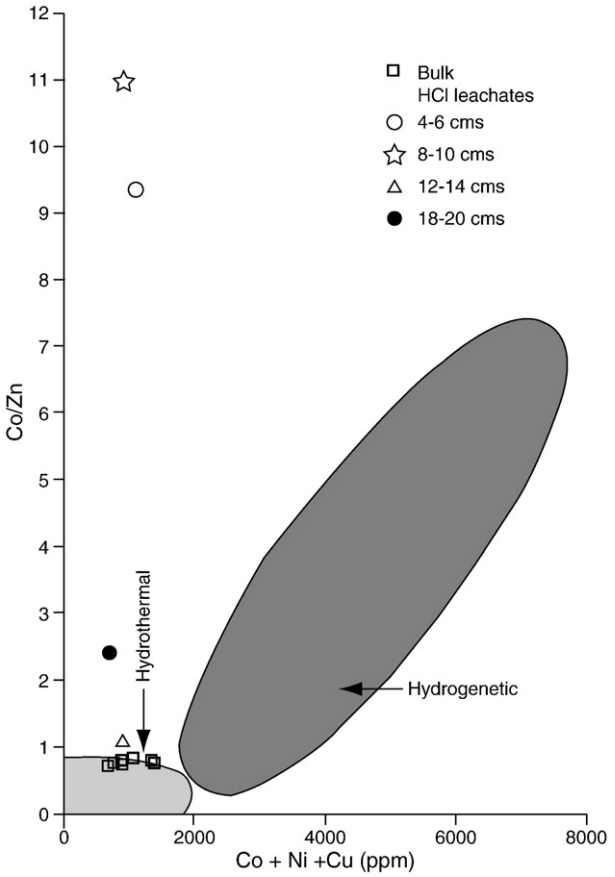

Fig. 6. Co/Zn versus Cu+Ni+Co content (Toth, 1980, modified by Nath et al., 1997a). While the data for all bulk sediments fall in the hydrothermal field, leach data for only unit 2 sediments show hydrothermal signatures. Consistent with their pelagic nature, unit 1 sediments fall away from hydrothermal field.

Post Archaen Australian Shale (PAAS; Taylor and McLennan, 1985) normalized patterns of bulk sediments studied here deviate markedly from a flat pattern (Fig. 7g), with the REE patterns of all the samples showing light REE (LREE) depletion. Uniformity in the REE patterns suggests either that the sediments are derived from a fairly homogeneous source (or sources) with respect to the REE, or may indicate mixing within the sediments (McLennan, 1989).

$(La/Yb)_n = (La/Yb)_{sample}/(La/Yb)_{PAAS}$, which is an indicator of light to heavy REE fractionation, varies from ~0.46 for unit 1 to as much as 0.55 for unit 2 sediments (Table 6), indicating significant downcore HREE enrichment. HREE enrichment (e.g. low Nd_n/Yb_n: 0.56 and 0.59 and La_n/Yb_n:0.46 to 0.55) together with low trace element concentration are indicative of low temperature fluids (Hodkinson et al., 1994; Mills et al., 2001). In contrast high temperature hydrothermal deposits have Nd_n/Yb_n values significantly above 1 (Mills and Elderfield, 1995; Frank et al., 2006).

Further corroboration of a metalliferous nature of the sediments comes from a binary plot of Cu+Ni+Co concentrations v/s ΣREE (Clauer et al., 1984), with the bulk and the HCl leach, representing the non-lithogenic component falling in the same field defined as metalliferous sediments (Fig. 8).

4.2.3.1.1. Ce anomaly. A significant feature of the REE patterns is the presence of negative Ce anomalies, with Ce/Ce* (Ce* obtained by linear interpolation between shale normalized La and Pr) values ranging from 0.66 to 0.79 with an average of 0.73 (Table 6), in contrast to the sediments overlain by nodules (Nath et al., 1992a) and typical hydrogenetic Fe–Mn oxides from the basinal parts of the Indian Ocean which all have positive Ce anomalies (Nath et al., 1992a, 1994; Nath, 1993). A negative Ce anomaly suggests a seawater source for the REEs, scavenged by Fe-oxyhydroxides (German et al., 1990; Sherrell et al., 1999). Previous work on metalliferous sediments has revealed shale-normalized patterns similar to our sediments with negative Ce anomaly and HREE enrichment (Fig. 7f, Marchig et al., 1982; German et al., 1993, 1999; Mills et al., 1993; Chavagnac et al., 2005). The metalliferous sediments are unlikely to have positive Ce anomalies, as long as they have a substantial hydrothermal component in them.

4.2.3.1.2. Eu anomaly. PAAS normalized REE patterns of the bulk sediments reveal another significant feature (Fig. 7g), viz., a positive Eu anomaly compared to its neighboring lanthanides. Positive Eu anomalies reflect a large hydrothermal component in the sediments which is also exhibited by hydrothermal fluids, as well as other hydrothermal phases (German et al., 1993; Mills et al., 1993; Klinkhammer et al., 1994; Mills and Elderfield, 1995; Hrischeva and Scott, 2007). Fractionation of Eu from other REEs and reduction of Eu^{+3} to Eu^{+2} can occur at temperatures above 200–250 °C (e.g., Bau, 1991). REE fractionation controlled by redox equilibrium at high temperatures can lead to LREE enrichment and positive Eu anomalies in reduced metalliferous fluids at active spreading centers (e.g., Bau, 1991). Metalliferous sediments from TAG (German et al., 1993) also have similar REE patterns with respect to LREE depletion and positive Eu anomaly. The degree of Eu anomaly is the result of mixing which indicates a small component of REE sourced from the hydrothermal fluids mixed into the major source of REE from ambient seawater (Chavagnac et al., 2005).

In order to determine whether the degree of Eu anomaly indicates the proximity to hydrothermal source, we plotted Eu/Sm ratios of our sediments along with other ridge flank sediments (Bender et al., 1971), near vent sediments (German et al., 1995, 1997, 1999) along with plume particulates (German et al., 1990, 2002; Sherrell et al., 1999) and vent fluids (Klinkhammer et al., 1994; Michard and Albarède, 1986) (Fig. 7). Eu/Sm ratios of our sediments are more similar to those of ridge flank metalliferous sediments, average plume particulates and far field plume particulates ratios (Fig. 9, and references therein).

4.2.3.2. Leaching studies

4.2.3.2.1. Characterizing the leach fraction. Shale normalized REE patterns of bulk, HCl leachates and residue are plotted along with data from the literature for various possible sources such as i) seawater, ii) plume particulates iii) vent fluids, iv) MORB, v) sulfides and vi) metalliferous sediments in Fig. 7. The REE concentrations and the

Table 7
Fe normalized element concentrations of the bulk sediments of this study compared with literature data.

Element	This study	CIR basalts[a]	RTJ sediments (cfb)[b]	CIR sediments [c]	EPR 10° S Fe–Mn oxides[d]	Fe oxides[e]	TAG nontronite[f]
Mn/Fe	0.1829	0.04	0.077	0.107	0.22	0.15	no data
Zn/Fe	0.0024	0.001	0.001	0.002	0.003	0.002	0.004

[a] Halbach, 1994.
[b] RTJ sediments (Kuhn et al., 2000).
[c] CIR sediments containing 48.5% hydrothermal Fe–Mn oxides from 21° 34′ S (Plüger et al., 1986).
[d] East Pacific Rise (10° S) sediments mainly consisting of Fe–Mn oxides (Walter and Stoffers, 1985).
[e] Hydrothermal Fe oxides from the North Fiji basin (McMurtry et al., 1991).
[f] Hydrothermal clays from TAG zone associated with sulphide debris and Fe oxides (Severmann et al., 2004).

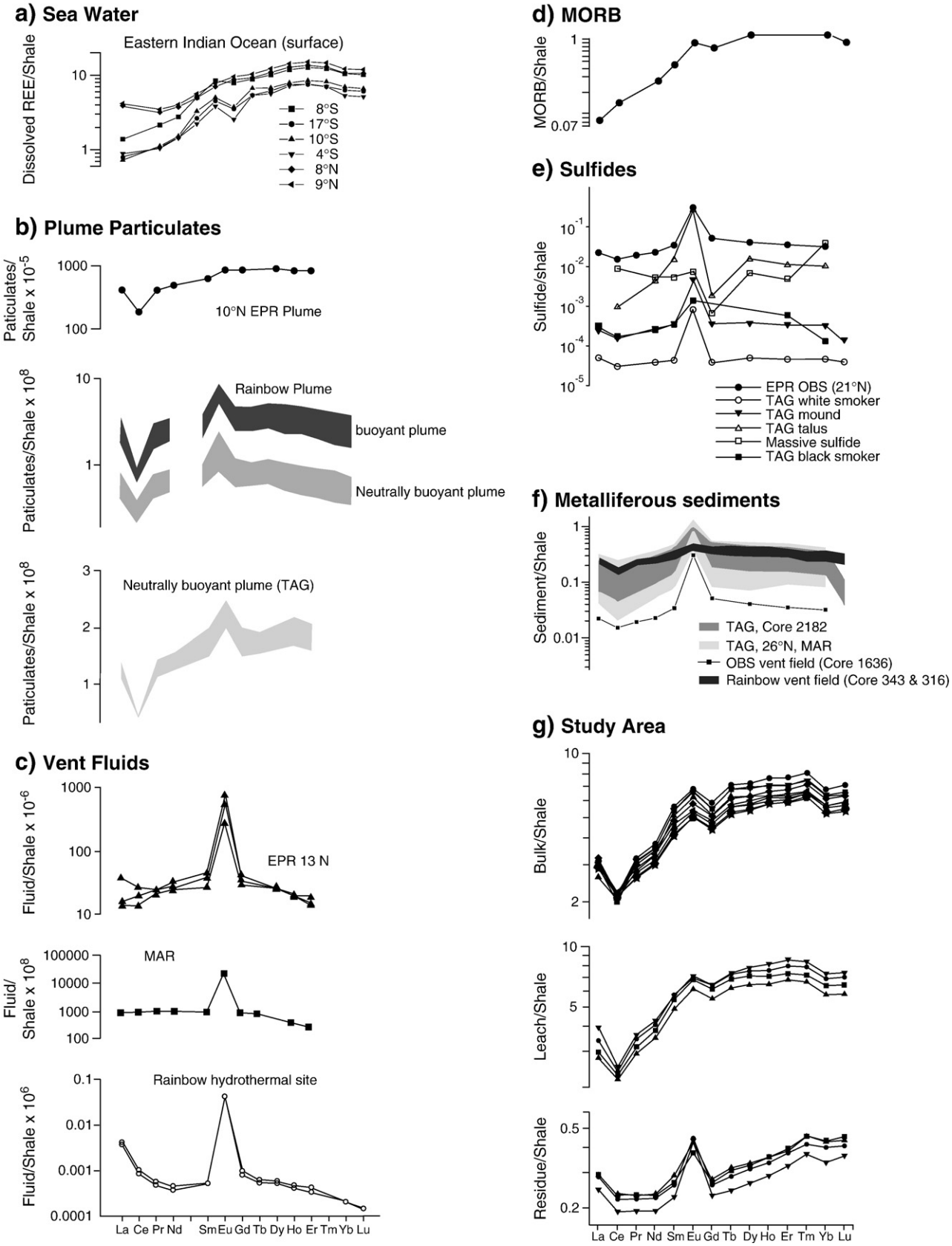

Fig. 7. Shale normalized REE distribution patterns for bulk, HCl leachates and residue of AAS 61/ BC 8 are shown along with a) seawater (Eastern Indian Ocean-Amakawa et al., 2000); b) plume particulates (Rainbow-Edmonds and German, 2004; TAG–German et al., 1990 and EPR–Sherrell et al., 1999), c) vent fluid (EPR–Klinkhammer et al., 1994; MAR–German et al., 1990; Rainbow hydrothermal site–Douville et al., 2002); d) Indian Ocean MORB–Nath et al., 1992b; e) sulfides (TAG–Mills and Elderfield, 1995; OBS vent site at 21° N on EPR–German et al., 1999; West Tasmania, Australia–Whitford et al., 1988) and f) metalliferous sediments–German et al., 1993, 1999; Chavagnac et al., 2005 and Mills et al., 1993. While the patterns for bulk as well as leach closely resemble the plume particulate data, those for residue seem to be a contribution from OBS type sulfides and MORB.

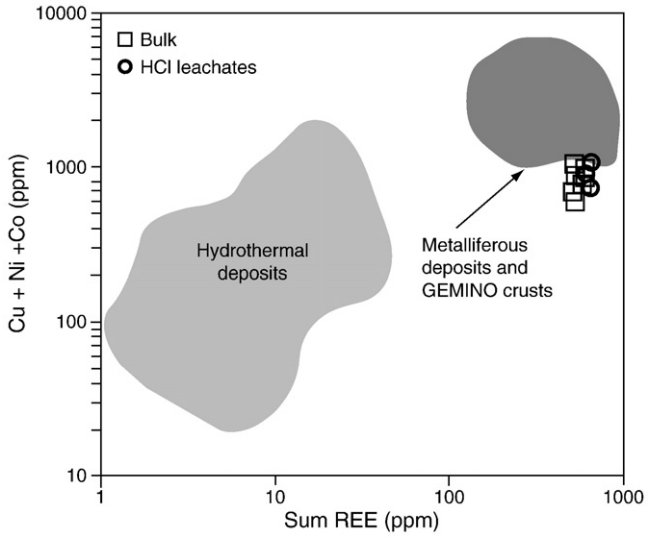

Fig. 8. A plot of ΣREE versus Cu+Ni+Co content (both for bulk and leach) in comparison with literature data for hydrothermal deposits and metalliferous deposits (Clauer et al., 1984, modified by Nath et al., 1997a).

shale normalized patterns of HCl leachates are remarkably similar to that of bulk sediments (Fig. 7g) indicating that most of the REEs in the bulk sediment are dominated by REEs in the leach fraction. Leachates seem to account for >90% of total REEs in the sediments (Table 5) suggesting that they are oxide-bound. The REE patterns of the leachates show a positive Eu anomaly, a negative Ce anomaly and LREE depletion compared to MREE.

The negative Ce anomaly and the HREE enrichment in the sediments (both bulk and leach) are similar to seawater data, and

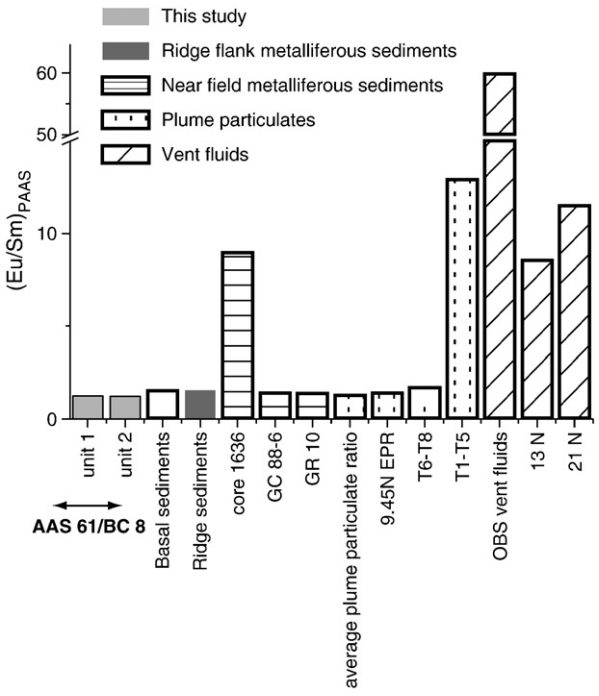

Fig. 9. PAAS normalized Eu/Sm ratios of our sediments are compared with metalliferous sediments from ridge flank as well as near field sediments along with plume particulates and vent fluids. The data is from Jarvis (1985); Bender et al. (1971); German et al. (1990, 1995, 1997, 1999, 2002); Klinkhammer et al. (1994) and Sherrell et al. (1999).

plume particles from the EPR, TAG and Rainbow hydrothermal sites as plume particles essentially scavenge REE from ambient seawater. Negative Ce anomaly, HREE enrichment along with positive Eu anomaly is also similar to the metalliferous sediments of TAG and OBS vent field (Fig. 7). Higher REE concentration in our sediments however are probably due to the extensive scavenging of dissolved REE from seawater onto hydrothermally derived Fe–Mn oxyhydroxide colloidal particles (Barrett and Jarvis, 1988; Olivarez and Owen, 1989; German et al., 1990; Edmonds and German, 2004).

We have normalized REE to Fe in leach in our sediments and compared with that of plume particles as Fe oxides/hydroxides are the host phase in both situations. The $REE/Fe_{(leach)}$ have been calculated and presented in Table 6. The average $REE/Fe_{(leach)}$ in our sediments is 0.96×10^{-2} which is an order higher than the Fe oxy-hydroxides (2×10^{-3}) found in the Rainbow hydrothermal field, which are in turn an order higher (1.6×10^{-4}) than the ratios of plume particulates in that area (Chavagnac et al., 2005). Similarly, particulate REE/Fe ratios in neutrally buoyant plumes of TAG (German et al., 1990) are 10 fold greater than end member vent fluids. This is consistent with what is already known from the study of both plumes and ridge flank hydrothermal sediments that uptake of dissolved REE from seawater causes the REE content of Fe-oxyhydroxides material to evolve continuously with in a dispersing hydrothermal plume, leading to progressive higher REE/Fe ratios with increasing distance from the initial vent source (Mitra et al., 1994; German et al., 2002; Edmonds and German, 2004). Sherrell et al. (1999) contend that in a time scale of plume advection, adsorption reflects near-instanteous equilibrium of hydrothermal precipitates with ambient seawater. Earlier studies on metalliferous sediments from EPR (Ruhlin and Owen, 1986; Olivarez and Owen, 1989) and also the ancient sedimentary sequences in America (Murray et al., 1991) have suggested that the REE uptake will continue until the time of burial and the signatures acquired before burial are retained in the geological record.

It has been suggested that REE content and REE/Fe in metalliferous sediments is a function of by distance from the hydrothermal source (Ruhlin and Owen, 1986; German et al., 1990). Studies by Ruhlin and Owen, 1986, Olivarez and Owen (1989) and Murray et al., 1991 showed that ridge proximal sediments have lower REE/Fe values which increase away from the ridge axis. However, we are not able to ascertain if the variations in Fe/Mn and REE/Fe with depth in our sediments are related to the distance from the hydrothermal source or to the variation in intensity of hydrothermal activity with time. With an average spreading rate of 18 to 35 mm/yr of adjacent ridges (CIR and SEIR — Royer et al., 1989), the site would have moved a small distance of 5 to 11 km during the age span of the core (~300 kyr; see Mascarenhas-Pereira et al., 2006 and Nath et al., 2008 for age details).

4.2.3.2.2. Provenance of the detrital component. The shale normalized REE patterns for the residues shows LREE depletion, HREE enrichment and a pronounced Eu anomaly (Fig. 7g). The residue left after HCl leach would contain detrital phases like silicates, sulfides and resistant minerals (Cronan and Hodkinson, 1997). The possible aluminosilicate contribution to the CIB can come from i) terrestrial sources through turbiditic sedimentation (Kolla et al., 1976; Rao and Nath, 1988; Nath et al., 1989, 1992b; Fagel et al., 1994) ii) dust from the distal sources such as Australia or African or Indian subcontinent (e.g., Kolla and Biscaye, 1977) and iii) local mid oceanic ridge basalts (Rao and Nath, 1988; Nath et al., 1989, 1992a). Terrigenous sediments from the northern part of the CIB are characterized by flat REE patterns, without Ce fractionation (Nath et al., 1992a). The terrigenous input to the core location at 16° S in CIB would be minimal, as it was found that the influx of terrigenous sedimentation is limited to 8–10° S (Nath et al., 1989, 1992b; Fagel et al., 1994; Nath, 2001). There must therefore be an additional source contributing to the HCl-insoluble fraction.

The enrichment in combination with positive Eu anomaly (Fig. 7g) is distinctly similar to the REE patterns of vent fluids from Rainbow

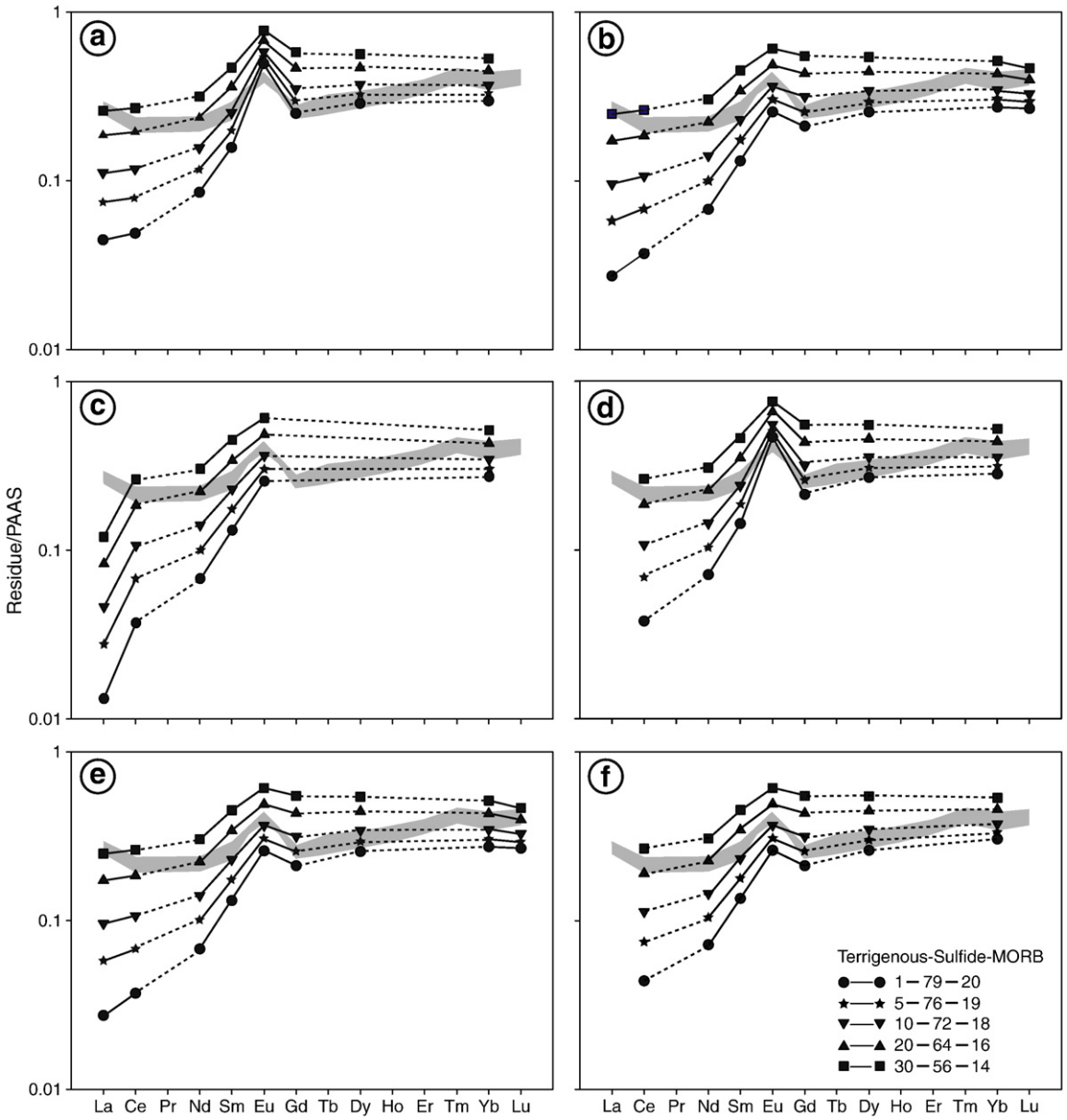

Fig. 10. Ternary REE mixing calculation using 3 end members (Terrigenous sediments in the CIB; sulfides and Indian Ocean MORB) (References for these values are given in text) are presented in PAAS normalized REE patterns for the residue fractions. Relative contribution to the sulfides in the residue was estimated using sulfides from 3 different areas a) EPR (OBS); b–e) TAG (white smoker, black smoker, talus and mound); f) massive sulfides from west Tasmania, Australia. Calculations with varying sulfides have yielded nearly similar contribution (64–72%) of sulfides to residues.

hydrothermal site (Fig. 7c) as well as sulfides from OBS vent field on EPR (German et al., 1999), sulfides from white and black smokers recovered from TAG (Mills and Elderfield, 1995) and west Tasmania, Australia (Fig. 7e) (Whitford et al., 1988). Similar REE patterns are a common feature in many massive sulfides associated with oceanic hydrothermal systems such as Southern Explorer Ridge (Barrett et al., 1990) and Juan de Fuca Ridge (Krasnov et al., 1994). Further, proportion of sulfides forming elements such as Fe, V, Zn and Pb (10 to 80%) are relatively high in the HCl insoluble fraction compared to other elements such as lanthanides, Co and Ni (<9%) and suggests that a sulfidic contribution to residue is possible.

HREE fractionation over MREE in the HCl-insoluble residue suggests a contribution of MORB like source (Fig. 7d, Nath et al., 1992b). Thus, we consider that the residue contains a mixture of three components namely i) sulfide type hydrothermal material, ii) MORB derived weathered detritus and iii) clastic silicates from distal sources.

The importance of the relative proportion these potential sources contributing to the residue (i.e. terrigenous material, sulfides and MORB) is assessed by modeling the REE data using ternary mixing equations as done for major elements (Section 4.2.1.1).

$$\int_{\text{terrigenous}} + \int_{\text{sulfides}} + \int_{\text{MORB}} = 1$$

$$C^i_{\text{mix}} = \left(\int_{\text{terrigenous}} x C^i_{\text{terrigeonus}}\right) + \left(\int_{\text{sulfides}} x\ C^i_{\text{sulfides}}\right) + \left(\int_{\text{MORB}} x\ C^i_{\text{MORB}}\right)$$

Three end-member used here are terrigenous sediments from northern Indian Ocean, published literature on sulfides (Mills and Elderfield, 1995; German et al., 1999; Whitford et al., 1988) and MORB. The results of these calculations are presented on a shale normalized REE pattern in Fig. 10. To avoid a bias, the mixing calculations were repeated using composition of sulfides from different locations viz., TAG, EPR, and west Tasmania, Australia (Fig. 10). The results of sulfidic

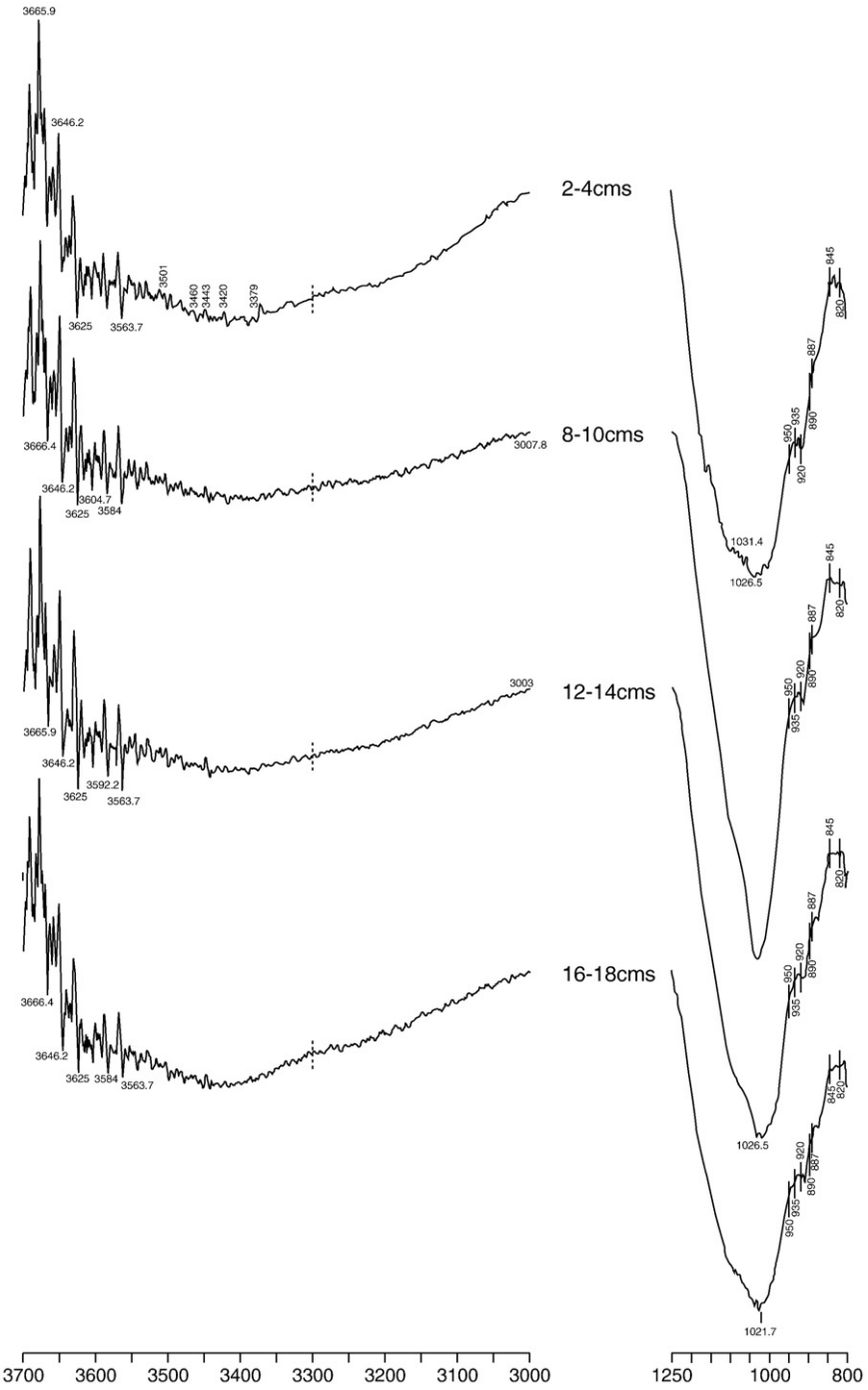

Fig. 11. Infrared spectra of 4 sediment sections (untreated, 2 μm size fractions). Left: OH-stretching region at 3700–3000 cm^{-1} with absorption bands representing ferruginous smectite and nontronite. Right: Si–O stretching region with absorption band at 1020 cm^{-1} corresponding to low Fe content in tetrahedral position of smectite. Absorption bands between 920 and 820 cm^{-1} represent increasing Fe content in octahedral sites and the presence of nontronite, ferruginous smectite and beidellite.

contribution has varied only marginally (between 64 and 72%) when any of the sulfidic end member from different areas was used. Relative proportions of terrigenous component (10–20%), sulfides (64–72%) and MORB (16–18%) reproduce the REE patterns shown for the acid-insoluble residue suggesting that the terrigenous and MORB source contribution to the REEs in the residue is lower than that of sulfidic-type material. However, these calculations should be considered as indicative and may not represent the proportion in which they are incorporated during the sediment formation (see Chavagnac et al., 2005 for discussion).

4.2.4. Evidence for hydrothermal component from the presence of nontronite

SEM-EDAX studies of some of the lithic grains recovered from the core were dense, massive and highly porous, and were similar to some of the lithic grains found in the hydrothermal system on the Juan de Fuca Ridge (Murnane and Clague, 1983). The grains contained Fe and Al (averaging 24% Fe_2O_3 and 14% Al_2O_3) and the calculated formula (based on 24 O atoms) and the composition is close to those of ferruginous smectites (Newman, 1987; Schöps et al., 1993). The Fe_2O_3/SiO_2 ratios are close to 0.51 and fall within the previously

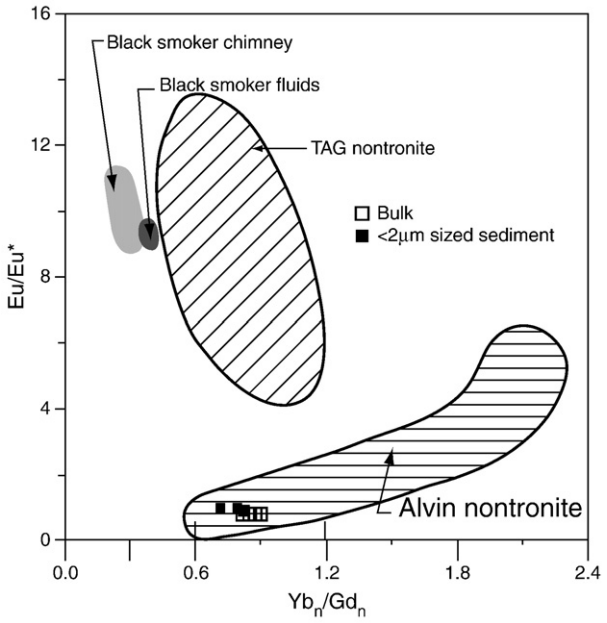

Fig. 12. Chondrite normalized Yb/Gd vs. Eu/Eu* in the bulk and <2 µm sized sediments compared to the composition of nontronites and other hydrothermal precipitates from various areas (modified from Severmann et al., 2004). Samples from this study plot in the Alvin nontronite field.

reported values for nontronites (McMurtry et al., 1983; Murnane and Clague, 1983; Alt, 1988; Severmann et al., 2004). To identify if any ferruginous smectites of hydrothermal origin are present in the sediments studied here, infrared spectroscopy and ICP-MS analyses were carried out on the clay-sized sediment fraction (<2 µm).

IR studies show an intense SiO_2 stretching absorption at ~1020 cm^{-1} for all the four samples studied (Fig. 11), which corresponds to a very low tetrahedral Fe^{3+} content in the sample (e.g., Goodman et al., 1976; Cole, 1985; Schöps et al., 1993). OH bending vibration between 920 and 820 cm^{-1} results from a variable substitution of Al by Fe. Smaller absorption bands occur at 820, ~887 and 935 cm^{-1}, the first two bands suggesting Al–OH deformation in nontronite (Farmer and Russell, 1967), and the third band may suggest the presence of beidellite (White, 1971). The absorption band at ~880 cm^{-1} is attributed to the substitution of octahedral Fe by Al in the smectites (Cole, 1985), or to the Fe–Al–OH substitution in ferruginous smectites (Russell, 1979) and also to the Al–OH deformation in nontronites (Frost et al., 2002, and references therein). The OH-bending vibration at 920 cm^{-1} in this study is similar to that seen in nontronites studied by Farmer and Russell (1967).

Absorption bands are seen at 3625, 3592 and 3563 cm^{-1} in the OH-stretching region which can represent Al–Fe–OH stretching either in ferruginous smectites (Russell, 1979) or in nontronites (Frost et al., 2002, and references therein). This equivalent band at 3564 cm^{-1} is indicative of Fe–FeOH stretching vibration in nontronites (Van der Marcel and Beutel Spacher, 1976). IR studies, therefore, suggest that the clay sized sediments studied here contain smectites of dioctahedral series of monmorillonite-beidellite-nontronite with a dominance of nontronites and ferruginous smectites.

Occurrence of both the ferruginous smectites and the nontronitic clays in these sediments would probably suggest hydrothermal origin (e.g., McMurtry and Yeh, 1981). Iyer et al. (1997) have recovered volcanogenic-hydrothermal material (vhm), and sediments with a composition close to nontronite at 14° S and 75° 56.1′ E which is ~45 km from the 76° 30′ E fracture zone in the CIB and suggested that they form through submarine exhalations and deposition in the surrounding siliceous sediments. Hydrothermal nontronites commonly have very low Al content (Singer et al., 1984), while our sediments contain higher Al (Al_2O_3 ~14 wt%). Nontronites characterized by distinctly elevated Al and Ti content have been described to be formed at low temperatures (32–48 °C) in the Central Pacific seamounts (Schöps et al., 1993). Compositionally, bulk sediments as well as the < 2 µm sized clay fraction studied here; fall in the field of Alvin nontronites (Fig. 12), which were calculated to form at 59+/−5 °C (Severmann et al., 2004). Lack of a well crystallized iron mineral such as hematite in our samples indicates the dominance of amorphous Fe-oxides/oxyhydroxides which may form at temperatures of ~ 100 °C (McMurtry and Yeh, 1981).

In summary, the leaching experiment on sediments has shown that they contain a mixture of Fe and Mn-oxides of metalliferous nature in acid-leachable fraction and sulfides in a fraction of residue in addition to the aluminosilicates from lithogenic sources. A series of deposits ranging from sulfides through iron oxides to Mn oxides with different proportions of these phases have been found in the Red Sea deposited from the same hydrothermal source (Cronan, 1976). Precipitation of sulfides during the cooling of ascending magmatic fluids on contact with seawater and fractionation of Mn and Fe on increase of pH and Eh (Krauskopf, 1957) could be a possible mechanism for the co-occurrence of Fe, Mn oxides and sulfides.

5. Summary

Geochemical studies of the bulk as well as the HCl soluble fraction of sediments collected from the flanks of a seamount near the 76° 30′ E fracture zone complex in the CIB indicate that the major elements have contribution from detrital sources of Bengal Fan and weathering of basinal and mid-oceanic ridge basalts on one hand and hydrothermal (mainly for Fe and Mn) and authigenic sources on the other. Shale-normalized REE patterns are indistinguishable from metalliferous sediments and plume particulates from the EPR, TAG and Rainbow hydrothermal sites. The sediments studied here are estimated to contain ~50–80% and 90–95% hydrothermal component in the bulk and leach fraction, respectively. While the ternary mixing calculations on bulk sediments indicate 35–45% metalliferous sediments could reproduce Fe and Mn values of our sediments, the HCl insoluble fraction indicate that the sulfide-like material dominates (64–72%) over terrigenous (10–20%) and MORB derived (16–18%) components the residue. Occurrence of both Fe–Mn oxides and sulfides is similar to those occurring in Red Sea.

Infrared spectroscopic studies indicate the presence of a dioctahedral smectites of monmorillonite-beidellite–nontronite series, with dominance of nontronite and ferruginous smectite suggesting a hydrothermal nature. Moreover, the composition of clay sized fraction is similar to known hydrothermal nontronitic clays from the Alvin site. The temperature of formation for these smectites is estimated to range from 50 to 100 °C. The presence of metalliferous sediments near the fracture zone suggests that the fracture zones may provide an easy conduit for in-situ volcanic activity in the area. While the earlier reports have shown spherules and lithic grains of metalliferous nature, this is the first study to report hydrothermal features in the bulk sediments of the CIB. The intraplate volcanoes located along the fracture zones, have therefore not only induced hydrothermal activity but also contributed nuclei and metals for the formation of the manganese nodules which are widespread in the CIB.

Acknowledgments

The sampling was carried out as a part of the project “Environmental Impact Assessment of Nodule mining” funded by the Department of Ocean Development, Government of India. M.B.L would like to thank Dr Rahul Sharma for allowing to carry out this work. We thank Director, National Institute of Oceanography, India, for permitting to publish this work, Neetu Singh, M. Aparna for

technical advice and help in data processing, Dr Parameswaran for his guidance during the IR studies, P. Pawaskar and T.C.Vineesh for the plots, Naman, Nivedita, Vitya and Trupti for preparing the samples and analytical assistance, V. D. Khedekar for the SEM photographs and EDAX analyses C. Moraes for XRF analytical work and Drs. V. Balaram and T. G. Rao of National Geophysical Research Institute for the ICP-MS facility. G. P. Glasby has corrected an earlier version of the manuscript. Comments by colleague V. Ramaswamy were helpful. Rick Murray and an anonymous reviewer are thanked for their thorough reviews and helpful suggestions. This is NIO contribution number 4712.

References

Albarède, F., 1995. Introduction to Geochemical Modeling. Cambridge Univ. Press, New York. 543 pp.
Alt, J.C., 1988. Hydrothermal oxide and nontronite deposits on seamount in the Eastern Pacific. Mar. Geol. 81, 227–239.
Amakawa, H., Alibo, D.S., Nozaki, Y., 2000. Nd isotopic composition and REE pattern in the surface waters of the eastern Indian Ocean and its adjacent seas. Geochim. Cosmochim. Acta 64, 1715–1727.
Aoki, S., Kohyama, N., Ishizuka, T., 1991. Sedimentary history and chemical characteristics of clay minerals in cores from the distal part of the Bengal Fan (ODP 116). Mar. Geol. 99 (1–2), 175–185.
Aoki, S., Kohyama, N., Hotta, H., 1996. Hydrothermal clay minerals found in sediment containing yellowish-brown material from the Japan Basin. Mar. Geol. 129 (3–4), 331–336.
Bach, W., Banerjee, N.R., Dick, H.J.B., Baker, E.T., 2002. Discovery of ancient and active hydrothermal systems along the ultra-slow spreading Southwest Indian Ridge 10-16E. Geochem. Geophys. Geosyst. 3 (7). doi:10.1029/2001GC000279.
Balaram, V., Rao, T.G., 2003. Rapid determination of REEs and other trace elements in geological samples by microwave acid digestion and ICP-MS. At. Spectrosc. 24, 206–212.
Banerjee, R., Ray, D., 2003. Metallogenesis along the Indian Ocean Ridge system. Curr. Sci. 85 (3), 321–327.
Barrett, T.J., Jarvis, I., 1988. Rare earth element geochemistry of metalliferous sediments from DSDP Leg 92, the East Pacific Rise transect. Chem. Geol. 67, 243–259.
Barrett, T.J., Taylor, P.N., Lugowski, J., 1987. Metalliferous sediments from DSDP Leg 92: the East Pacific Rise Transect. Geochim. Cosmochim. Acta 51, 2241–2253.
Barrett, T.J., Jarvis, I., Jarvis, K.E., 1990. Rare earth element geochemistry of massive sulfides-sulfates and gossans on the Southern Explorer Ridge. Geology 18, 583–585.
Batiza, R., 1982. Abundance, distribution and size of volcanoes in the Pacific Ocean and implications for origin of non-hotspot volcanoes. Earth Planet. Sci. Lett. 60, 195–206.
Bau, M., 1991. Rare-earth element mobility during hydrothermal and metamorphic fluid-rock interaction and the significance of the oxidation state of europium. Chem. Geol. 93, 219–230.
Bender, M., Broeker, W.S., Gornitz, V., Middel, U., Day, R., Sun, S.S., Biscaye, P., 1971. Geochemistry of three cores from the East Pacific Rise. Earth Planet. Sci. Lett. 12, 425–433.
Borole, D.V., 1993. Deposition of Mn–Cu–Ni enriched sediments during glacial period in the Central Indian Basin. Curr. Sci. 65 (10), 778–782.
Boström, K., Peterson, M.N.A., 1969. The origin of aluminium-poor ferromanganoan sediments in areas of high heat flow on the East Pacific Rise. Mar. Geol. 7, 427–447.
Cave, R.R., German, C.R., Thomson, J., Nesbitt, R.W., 2002. Fluxes to sediments from the Rainbow Hydrothermal plume, 36° 14′ N on the MAR. Geochim. Cosmochim. Acta 66, 1905–1923.
Chavagnac, V., German, C.R., Milton, J.A., Palmer, M.R., 2005. Sources of REE in sediment cores from the Rainbow vent site (36° 14′ N, MAR). Chem. Geol. 216, 329–352.
Cherkashev, G.A., 1992. Geochemistry of metalliferous sediments from ore-forming areas in the ocean. In: Gramberg, I.S., Ainemer, A.I. (Eds.), Hydrothermal Sulfide Ores and Metalliferous Sediments of the Ocean. St. Petersburg, Nedra, pp. 138–152 (in Russian).
Clauer, N., Stille, P., Bonnot-Courtois, C., Moore, W.S., 1984. Nd–Sr isotopic and REE constraints on the genesis of hydrothermal manganese crusts in the Galapagos. Nature 311, 743–745.
Cole, T.G., 1985. Composition, oxygen isotope geochemistry, and the origin of smectite in the metalliferous sediments of the Bauer Deep, southeast Pacific. Geochim. Cosmochim. Acta 49, 221–235.
Cronan, D.S., 1976. Basal metalliferous sediments from the eastern Pacific. Geol. Soc. Am. Bull. 87, 928–934.
Cronan, D.S., Hodkinson, R.A., 1997. Geochemistry of hydrothermal sediments from ODP Sites 834 and 835 in the Lau Basin, southwest Pacific. Mar. Geol. 141, 237–268.
Das, P., Iyer, S.D., Kodagali, V.N., 2007. Morphological characteristics and emplacement mechanism of the seamounts in the Central Indian Ocean Basin. Tectonophysics 443, 1–18.
Debrabant, P., Fagel, N., Chamley, H., Bout, V., Caulet, J.P., 1993. Neogene to Quaternary clay mineral fluxes in the Central Indian basin. Palaeogeogr. Palaeoclimatol. Palaeoecol. 103 (3–4), 117–131.
Deer, W., Howie, R., Zussman, J., 1967. Rock-Forming Minerals, 2nd edition. Pearson Education Ltd publishing.
Donnelly, T.W., 1980. Chemical composition of deep sea sediments-Sites 9 through 425, Legs 2 through 54. In: Rosendahl, B.R., Hékinian, R., et al. (Eds.), Initial. Rep. Deep Sea Drill. Proj., 54. Government Printing Office, Washington, D.C., pp. 899–949.
Douville, E., Charlou, J.L., Oelkers, E.H., Bienvenu, P., Jove Colon, C.F., Donval, J.P., Fouquet, Y., Prieur, D., Appriou, P., 2002. The Rainbow vent fluids (36° 14′ N, MAR): the influence of ultramafic rocks and phase separation on trace metal content in Mid-Atlantic Ridge hydrothermal fluids. Chem. Geol. 184, 37–48.
Dymond, J., 1981. Geochemistry of Nazca Plate surface sediments: an evaluation of hydrothermal, biogenic, detrital, and hydrogenous sources. In: Kulm, L.D., et al. (Ed.), Nazca Plate: Crustal Formation and Andean Convergence: Geol. Soc. Am. Mem., 154, pp. 133–174.
Edmonds, H.N., German, C.R., 2004. Particle geochemistry in the Rainbow hydrothermal plume, Mid-Atlantic Ridge. Geochim. Cosmochim. Acta 68 (4), 759–772.
El Wakeel, S.K., Riley, J.P., 1957. Determination of organic carbon in the marine muds. J. Conseil. Int. Explor. Mer. 22, 180–183.
Epp, D., Smooth, N.C., 1989. Distribution of seamounts in North Atlantic. Nature 337, 254–257.
Fagel, N., Debrabant, P., André, L., 1994. Clay supplies in the Central Indian Basin since the Late Miocene: climatic or tectonic control. Mar. Geol. 122, 151–172.
Fagel, N., André, L., Debrabant, P., 1997. Multiple seawater-derived geochemical signatures in Indian oceanic pelagic clays. Geochim. Cosmochim. Acta 61 (5), 989–1008.
Farmer, V.C., Russell, J.D., 1967. Infra-red absorption spectrometry in clay studies. Proc. 15th Natl. Conf. on Clays and Clay Minerals, pp. 121–142.
Frank, M., Marbler, H., Koschinsky, A., van de Flierdt, T., Klemm, V., Gutjahr, M., Halliday, A.N., Kubik, P.W., Halbach, P., 2006. Submarine hydrothermal venting related to volcanism in the Lesser Antilles: evidence from ferromanganese precipitates. Geochem. Geophys. Geosyst. 7, Q04010. doi:10.1029/2005GC001140.
Frost, R.L., Kloprogge, J.T., Ding, Z., 2002. Near-infrared spectroscopic study of nontronites and ferruginous smectite. Spectrochim. Acta Part A 58, 1657–1668.
Gallant, R.M., Von Damm, K.L., 2006. Geochemical controls on hydrothermal fluids from the Kairei and Edmond Vent Fields, 23°–25°S, Central Indian Ridge. Geochem. Geophys. Geosyst. 7 (6), Q06018. doi:10.1029/2005GC001067.
German, C.R., 2003. Hydrothermal activity on the eastern SWIR (50°–70°E): evidence from core-top geochemistry, 1887 and 1998. Geochem. Geophys. Geosyst. 4((7), 9102. doi:10.1029/2003GC000522.
German, C.R., Klinkhammer, G.P., Edmond, J.M., Mitra, A., Elderfield, H., 1990. Hydrothermal scavenging of rare earth elements in the ocean. Nature 345, 516–518.
German, C.R., Higgs, N.C., Thompson, J., Mills, R., Elderfield, H., Blusztajn, J., Fleet, A.P., Bacon, M.P., 1993. A geochemical study of metalliferous sediments from the TAG hydrothermal mound, 26° 08′ N, Mid Atlantic Ridge. J. Geophys. Res. 98, 9683–9692.
German, C.R., Barreiro, B.A., Higgs, N.C., Nelsen, T.A., Ludford, E.M., Palmer, M.R., 1995. Seawater-metasomatism in hydrothermal sediments (Escanaba Trough, northeast Pacific). Chem. Geol. 1119, 175–190.
German, C.R., Bourlés, D.L., Brown, E.T., Hergt, J., Colley, S., Higgs, N.C., Ludford, E.M., Nelsen, T.A., Feely, R.A., Raisbeck, G., Yiou, F., 1997. Hydrothermal scavenging on the Juan de Fuca Ridge: $^{230}Th_{xs}$, ^{10}Be, and REEs in ridge-flank sediments. Geochim. Cosmochim. Acta 61 (19), 4067–4078.
German, C.R., Hergt, J., Palmer, M.R., Edmond, J.M., 1999. Geochemistry of a hydrothermal sediment core from the OBS vent-field, 21° N East Pacific Rise. Chem. Geol. 155, 65–75.
German, C.R., Colley, S., Palmer, M.R., Khripounoff, A., Klinkhammer, G.P., 2002. Hydrothermal plume-particle fluxes at 13°N on the East Pacific Rise. Deep-Sea Res. Part I 49, 1921–1940.
Goodman, B.A., Russell, J.D., Fraser, A.R., Woodhams, F.W.D., 1976. A Mössbauer and IR spectroscopic study of the structure of nontronite. Clays Clay Miner. 24, 53–59.
Grim, R.E., 1968. Clay Mineralogy. McGraw-Hill, Inc., New York. 596 pp.
Gupta, S.M., 1988. Radiolarian zonation and volcanic ash layers in two Quaternary sediment cores from the central Indian Ocean basin. J. Palaeontol. Soc. India 33, 59–71.
Halbach, P., 1994. Die Entwicklung des Hydrothermalismus und seine strukturgeologische Kontrolle im Gebiet der Rodrigues Triple Junction, Zentraler Indischer Ozean. Technical Cruise Report SO 92. 03G0092A, Freie Universitat Berlin.
Gurvich, E.G., Levitan, M.A., Zuzmina, T.G., 1995. Chemical composition of leg 138 sediments and history of hydrothermal activity. Proc. Ocean Drill. Program Sci. Results 138, 769–778.
Hein, J., Yeh, H., Alexander, E., 1979. Origin of iron-rich montmorillonite from the manganese nodule belt of the North equatorial Pacific. Clays Clay Miner. 27, 185–194.
Hékinian, R., Stoffers, P., Ackermand, D., Révillon, S., Maia, M., Bohn, M., 1999. Ridge-hotspot interaction: the Pacific-Antarctic ridge and the foundation seamounts. Mar. Geol. 160, 199–223.
Hodkinson, R.A., Cronan, D.S., 1991. Regional and depth variability in the composition of cobalt-rich ferromanganese crusts from the SOPAC area and adjacent parts of the central equatorial Pacific. Mar. Geol. 98, 437–444.
Hodkinson, R.A., Stoffers, P., Scholten, J., Cronan, D.S., Jeschke, G., Rogers, T.D.S., 1994. Geochemistry of hydrothermal manganese deposits from the Pitcairn Island hotspot, southeastern Pacific. Geochim. Cosmochim. Acta 58, 5011–5029.
Hrischeva, E., Scott, S.D., 2007. Geochemistry and morphology of metalliferous sediments and oxyhydroxides from the Endeavour segment, Juan de Fuca Ridge. Geochim. Cosmochim. Acta 71, 3476–3497.
Iyer, S.D., 2005. Evidences for incipient hydrothermal event(s) in the Central Indian Basin: A review. Acta Geol. Sin. 79, 77–86.
Iyer, S.D., Sudhakar, M., 1993. A new report on the occurance of zeolitites in the abyssal depth of the Central Indian Ocean Basin. Sediment. Geol. 84, 169–178.
Iyer, S.D., Prasad, S.M., Gupta, S.M., Charan, S.N., 1997. Evidence for recent hydrothermal activity in the Central Indian Ocean Basin. Deep-Sea Res. 44, 1167–1184.

Iyer, S.D., Mascarenhas-Pereira, M.B.L., Nath, B.N., 2007. Native aluminium (spherules and particles) in the Central Indian Basin sediments: Implications on the occurrence of hydrothermal events. Mar. Geol. 240, 177–184.

James, R.H., Elderfield, H., Palmer, M.R., 1995. The chemistry of hydrothermal fluids from the Broken Spur site, 29° N Mid-Atlantic Ridge. Geochim. Cosmochim. Acta 59, 651–659.

Jarvis, I., 1985. Geochemistry and origin of Eocene-Oligocene metalliferous sediments from the central equatorial Pacific: Deep Sea Drilling Project sites 573 and 574. In: Mayer, L., Theyer, F., et al. (Eds.), Initial. Rep. Deep Sea Drill. Proj, vol. 85. U. S. Government Printing Office, Washington, D.C., pp. 781–804.

Kamesh Raju, K.A., 1993. Magnetic lineation, fracture zones and seamounts in the Central Indian Ocean Basin. Mar. Geol. 109, 195–201.

Kamesh Raju, K.A., Ramprasad, T., 1989. Magnetic lineation in the Central Indian Basin for the period A24-A21: A study in relation to the Indian Ocean Triple Junction. Earth Planet. Sci. Lett. 95, 395–402.

Karisiddaiah, S.M., Iyer, S.D., 1992. A note on incipient spilitisation of Central Indian Basin basalts. J. Palaeontol. Soc. India 39, 518–523.

Karl, D.M., McMurtry, G.M., Malahoff, A., Garcia, M.O., 1988. Loihi Seamount Hawaii: a mid-plate volcano with a distinctive hydrothermal system. Nature 335, 532–535.

Kastner, M., 1979. Zeolites. In: Burns, R.G. (Ed.), Marine Minerals. : Reviews in mineralogy, vol. 6. Mineralogical Society of America, Washington, DC, pp. 111–122.

Kastner, M., 1981. Authigenic silicates in deep-sea sediments: formation and diagenesis. In: Emiliani, C. (Ed.), The Sea vol. 7, Wiley J. and Sons, New York, pp. 915–980.

Klinkhammer, G.P., Elderfield, H., Edmonds, J.M., Mitra, A., 1994. Geochemical implications of rare earth element patterns in hydrothermal fluids from mid-ocean ridges. Geochim. Cosmochim. Acta 58, 5105–5113.

Kolla, V., Biscaye, P.E., 1977. Distribution and origin of quartz in the sediments of the Indian Ocean. J. Sed. Res. 47, 642–649.

Kolla, V., Henderson, L., Biscaye, P.E., 1976. Clay mineralogy and sedimentation in the western Indian ocean. Deep Sea Res. 23, 949–961.

Krasnov, S., Stepanova, T., Stepanov, M., 1994. Chemical composition and formation of a massive sulfide deposit, Middle Valley, northern Juan de Fuca Ridge. In: Mottl, M.J., Davis, E.F., Fisher, A.T., Slack, J.F. (Eds.), Proc. ODP, Sci. Results, 139, College Station, TX, pp. 353–372.

Krauskopf, K.B., 1957. Separation of manganese from iron in sedimentary processes. Geochim. Cosmochim. Acta 12, 61–84.

Kryc, K.A., Murray, R.W., Murray, D.W., 2003. Elemental fractionation of Si, Al, Ti, Fe, Ca, Mn, P, and Ba in five marine sedimentary reference materials: Results from sequential extractions. Anal. Chim. Acta 487 (1), 117–128.

Kuhn, T., Burger, H., Castradori, D., Halbach, P., 2000. Volcanic and hydrothermal history of ridge segments near the Rodrigues Triple Junction (Central Indian Ocean) deduced from sediment geochemistry. Mar. Geol. 169 (3–4), 391–409.

Kurian, S., Nath, B.N., Ramaswamy, V., Naman, D., Rao, T.G., KameshRaju, K.A., Selvaraj, K., Chen, C.T.A., 2008. Possible detrital, diagenetic and hydrothermal sources for Holocene sediments of the Andaman backarc basin. Mar. Geol. 247, 178–193.

Li, Y.H., 2000. A Compendium of Geochemistry: from Solar Nebula to the Human Brain. Princeton Uni. Press, Princeton, NJ.

Lisitzin, A.P., Crook, K.A.W., Bogdanov, Yu.A., Zonenshain, L.P., Murav'ev, K.G., Tufar, W., Gurvich, E.G., Gordeev, V.V., Ivanov, G.V., 1992. Hydrothermal fields of the Manus basin rift zone. Int. Geol. Rev. 35, 105–126.

Ludford, E.M., Palmer, M.R., German, C.R., Klinkhammer, G.P., 1996. The geochemistry of Atlantic hydrothermal particles. Geophys. Res. Lett. 23 (23), 3503–3506.

Marchig, V., Gundlach, H., Möller, P., Schley, F., 1982. Some geochemical indicators for discrimination between diagenetic and hydrothermal metalliferous sediments. Mar. Geol. 50, 241–256.

Mascarenhas-Pereira, M.B.L., Nath, B.N., Borole, D.V., Gupta, S.M., 2006. Nature, source and composition of volcanic ash in sediments from a fracture zone trace of Rodriguez Triple Junction in the Central Indian Basin. Mar. Geol. 229, 79–90.

McLennan, S.M., 1989. Rare earth elements in sedimentary rocks: influence of provenance and sedimentary processes. In: Lipin, B.R., Mckay, G.A. (Eds.), Geochemistry and Mineralogy of the Rare Earth Elements: Rev. Mineral., vol. 21, pp. 169–200.

McMurtry, G.M., Yeh, H.-W., 1981. Hydrothermal clay mineral formation of East Pacific Rise Bauer Basin sediments. Chem. Geol. 32, 189–205.

McMurtry, G.M., Wang, C.-H., Yeh, H.-W., 1983. Chemical and isotopic investigations into the origin of clay minerals from the Galapagos hydrothermal mound field. Geochim. Cosmochim. Acta 47, 475–489.

McMurtry, G.M., de Carlo, E.H., Kim, K.H., 1991. Accumulation rates, chemical partitioning, and Q-mode factor analysis of metalliferous sediments from the North Fiji Basin. Mar. Geol. 98, 271–295.

Michard, A., Albarède, F., 1986. The REE content of some hydrothermal fluids. Chem. Geol. 55, 51–60.

Mills, R.A., Elderfield, H., 1995. Rare earth element geochemistry of hydrothermal deposits from the active TAG Mound, 26°N Mid-Atlantic Ridge. Geochim. Cosmochim. Acta 59, 3511–3524.

Mills, R.A., Elderfield, H., Thomson, J., 1993. A dual origin for the hydrothermal component in a metalliferous sediment core from the Mid-Atlantic Ridge. J. Geophys. Res. 98, 9671–9678.

Mills, R.A., Wells, D.M., Roberts, S., 2001. Genesis of ferromanganese crusts from the TAG hydrothermal field. Chem. Geol. 176, 283–293.

Mitra, A., Elderfield, H., Greaves, M.J., 1994. Rare earth elements in submarine hydrothermal fluids and plumes from the Mid-Atlantic Ridge. Mar. Chem. 46, 217–235.

Mukhopadhyay, R., Batiza, R., 1994. Basinal seamounts and seamount chains of the Central Indian Ocean: Probable near-axis origin from a fast-spreading ridge. Mar. Geophys. Res. 16 (4), 303–314.

Münch, U., Lalou, C., Halbach, P., Fujimoto, H., 2001. Relict hydrothermal events along the super-slow Southwest Indian spreading ridge near 63°56′E-mineralogy, chemistry and chronology of sulfide samples. Chem. Geol. 177 (3-4), 341–349.

Murnane, R., Clague, D.A., 1983. Nontronite from a low temperature hydrothermal system on the Juan de Fuca Ridge. Earth Planet. Sci. Lett. 65, 343–352.

Murray, R.W., Buchholtz Ten Brink, M.R., Gerlach, D.C., Russ III, G.P., Jones, D.L., 1991. Rare earth, major, and trace elements in chert from the Franciscan Complex and Monterey Group, California: assessing REE sources to fine-grained marine sediments. Geochim. Cosmochim. Acta 55, 1875–1895.

Nath, B.N., 1993. Rare earth element geochemistry of the sediments, ferromanganese nodule and crusts from the Indian Ocean. Ph.D. thesis. Goa Uni., India.

Nath, B.N., 2001. Geochemistry of sediments. In: Sen Gupta, R., Desa, E. (Eds.), The Indian Ocean: A perspective, vol. 2. Oxford & IBH, New Delhi, India, pp. 645–689.

Nath, B.N., Rao, B.R., 1998. Late Pliocene–Pleistocene sedimentation and episodic volcanism recorded by a sediment core of the central Indian Basin. paper presented at 6th International Conference on Palaeoceanography, Lisbon, Portugal.

Nath, B.N., Rao, V.P.C., Becker, K.P., 1989. Geochemical evidence of terrigenous influence in deep-sea sediments up to 8° S in the Central Indian Basin. Mar. Geol. 87, 301–313.

Nath, B.N., Balaram, V., Sudhakar, M., Plüger, W.L., 1992a. Rare earth element geochemistry of the ferromanganese deposits from the Indian Ocean. Mar. Chem. 38, 185–208.

Nath, B.N., Roelandts, I., Sudhakar, M., Plüger, W.L., 1992b. Rare earth element patterns of the Central Indian Basin sediments related to their lithology. Geophys. Res. Lett. 19 (12), 1197–1200.

Nath, B.N., Roelandts, I., Sudhakar, M., Plüger, W.L., Balaram, V., 1994. Cerium anomaly variation in ferromanganese nodules and crusts from the Indian Ocean. Mar. Geol. 120, 385–400.

Nath, B.N., Bau, M., Rao, B.R., Rao, Ch.M., 1997a. Trace and rare earth elemental variation in Arabian Sea sediments through a transect across the oxygen minimum zone. Geochim. Cosmochim. Acta 61, 2375–2388.

Nath, B.N., Plüger, W.L., Roelandts, I., 1997b. Geochemical constraints on the hydrothermal origin of ferromanganese encrustations from the Rodriguez Triple Junction, Indian Ocean. In: Nicholson, K., Hein, J.R., Bühn, B., Dasgupta, S. (Eds.), Manganese Mineralization: Geochemistry and Mineralogy of Terrestrial and marine Deposits: Geol. Soc. Spec. Publ., vol. 119, pp. 192–221.

Nath, B.N., Borole, D.V., Aldahan, A., Patil, S.K., Mascarenhas-Pereira, M.B.L., Possnert, G., Ericsson, T., Ramaswamy, V., Gupta, S.M., 2008. ^{210}Pb, ^{230}Th, and ^{10}Be in Central Indian Basin seamount sediments: Signatures of degassing and hydrothermal alteration of recent origin. Geophys. Res. Lett. 35, L09603. doi:10.1029/2008GL033849.

Newman, A.C.D., 1987. Chemistry of clays and clay minerals. Longman Scientific and Technical, Harlow.

Olivarez, A.M., Owen, R.M., 1989. REE/Fe variation in hydrothermal sediments: implication for the REE content of seawater. Geochim. Cosmochim. Acta 53, 757–762.

Owen, R.M., Olivarez, A.M., 1988. Geochemistry of rare earth elements in pacific hydrothermal sediments. Mar. Chem. 25 (2), 183–196.

Plüger, W.L., Friedrich, G., Stoffers, P., 1985. Environmental controls on the formation of deep-sea ferromanganese concretions. Monogr. Ser. Miner. Deposits 25, 31–52.

Plüger, W., Schwarz, P., Scholten, J., Stoffers, P., 1986. Geochemie und Mineralogie der Sedimente des Mittelindischen Rückens zwischen 21°S und der Rodriguez Triple Junction (SO 43). GEMINO 2: Geothermale Metallogenese Indischer Ozean. Aachen, RWTH, Aachen, pp. 1–38.

Rao, V.P., Nath, B.N., 1988. Nature, distribution and origin of clay minerals in grain size fractions of sediments from manganese nodule field, Central Indian Ocean Basin. Indian J. Mar. Sci. 17, 202–207.

Royer, J.Y., Sclater, J.G., Sandwell, D.T., 1989. A preliminary tectonic fabric chart of the Indian Ocean. In: Brune, J.N. (Ed.), Proc. Ind. Acad. Sci. (Earth Planet. Sci.), pp. 7–24.

Ruhlin, D.E., Owen, R.M., 1986. The rare earth element geochemistry of hydrothermal sediments from the East Pacific Rise: Examination of a seawater scavenging mechanism. Geochim. Cosmochim. Acta 50, 393–400.

Russell, J.D., 1979. An Infrared spectroscopic study of the interaction of nontronite and ferruginous montmorillonite with alkali metal hydroxides. Clay Miner. 14, 127.

Sayles, F.L., Bischoff, J.L., 1973. Ferromanganoan sediments in the equatorial East Pacific. Earth Planet. Sci. Lett. 19 (3), 330–336.

Schöps, D., Herzig, P.M., Halbach, P., Friedrich, G., Blum, N., 1993. Mineralogy, chemistry and oxygen isotope thermometry of nontronitic smectites from Central Pacific seamounts. Chem. Geol. 106, 331–343.

Severmann, S., Mills, R.A., Palmer, M.R., Fallick, A.E., 2004. The origin of clay minerals in active and relict hydrothermal deposits. Geochim. Cosmochim. Acta 68 (1), 73–88.

Sherrell, R.M., Field, M.P., Ravizza, G., 1999. Uptake and fractionation of rare earth elements on hydrothermal plume particles at 9° 45′ N, East Pacific Rise. Geochim. Cosmochim. Acta 52, 669–677.

Sholkovitz, E.R., 1989. Artifacts associated with the chemical leaching of sediments for rare-earth elements. Chem. Geol. 77, 47–51.

Singer, A., Stoffers, P., Heller-Kallai, I., Szafranek, D., 1984. Nontronite in a deep-sea core from the south Pacific. Clays Clay Miner. 32, 375–383.

Staudigel, H., Hart, S.R., Koppers, A.A.P., Constable, C., Workman, R., Kurz, M., Baker, E.T., 2004. Hydrothermal venting at Vailulu'u Seamount: the smoking end of the Samoan chain. Geochem. Geophys. Geosyst. 5, Q02003. doi:10.1029/2003GC000626.

Sukumaran, N.P., Banerjee, R., Borole, D.V., Gupta, S.M., 1999. Some aspects of volcanic ash layers in the Central Indian Basin. Geo-Mar. Lett. 18, 203–208.

Sun, S.S., Nesbitt, R.W., Sharaskin, A.Y., 1979. Geochemical characteristics of mid-ocean ridge basalts. Earth Planet. Sci. Lett. 44 (119), 138.

Taylor, S.R., McLennan, S.M., 1985. The Continental Crust: Its Composition and Evolution. Blackwell, Malden, Mass. 312 pp.
Toth, J.R., 1980. Deposition of submarine crusts rich in manganese and iron. Geol. Soc. Am. Bull. 91, 44–54.
Van der Marcel, H.W., Beutel Spacher, H., 1976. Atlas of the infrared spectra of clay minerals and their admixtures. Elsevier, Amsterdam, pp. 146–148.
Walter, P., Stoffers, P., 1985. Chemical characteristics of metalliferous sediments from eight areas on the Galapagos rift and East Pacific Rise between 2° N and 42° S. Mar. Geol. 65, 271–287.
White, J.L., 1971. Interpretation of infrared spectra of soil minerals. Soil Sci. 112, 22–31.
Whitford, D.J., Korsch, M.J., Porritt, P.M., Craven, S.J., 1988. Rare-earth element mobility around the volcanogenic polymentallic massive sulfide deposit at Que River, Tasmania, Australia. Chem. Geol. 68 (1–2), 105–119.
Ziegler, C.L., Murray, R.W., Hovan, S.A., Rea, D.K., 2007. Resolving eolian, volcanogenic, and authigenic components in pelagic sediment from the Pacific Ocean. Earth Planet. Sci. Lett. 254 (3–4), 416–432.

SEDIMENTOLOGY the journal of the International Association of Sedimentologists

Sedimentology (2011) **58,** 756–784 doi: 10.1111/j.1365-3091.2010.01183.x

Bacterial response to contrasting sediment geochemistry in the Central Indian Basin

ANINDITA DAS, CHRISTABELLE E. G. FERNANDES, SONALI S. NAIK, B. NAGENDER NATH, I. SURESH, M. B. L. MASCARENHAS-PEREIRA, S. M. GUPTA, N. H. KHADGE, C. PRAKASH BABU, D. V. BOROLE, P. P. SUJITH, ANIL B. VALSANGKAR, BABU SHASHIKANT MOURYA, SUSHANTA U. BICHE, RAHUL SHARMA and P. A. LOKA BHARATHI
National Institute of Oceanography, (Council of Scientific and Industrial Research) Dona Paula, Goa 403004, India (E-mail: loka@nio.org)

Associate Editor – Daniel Ariztegui

ABSTRACT

In order to investigate whether geochemical, physiographic and lithological differences in two end-member sedimentary settings could evoke varied microbe–sediment interactions, two 25 cm long sediment cores from contrasting regions in the Central Indian Basin have been examined. Site TVBC 26 in the northern siliceous realm (10°S, 75·5°E) is organic-C rich with 0·3 ± 0·09% total organic carbon. Site TVBC 08 in the southern pelagic red clay realm (16°S, 75·5°E), located on the flank of a seamount in a mid-plate volcanic area with hydrothermal alterations of recent origin, is organic-C poor (0·1 ± 0·07%). Significantly higher bacterial viability under anaerobic conditions, generally lower microbial carbon uptake and higher numbers of aerobic sulphur oxidizers at the mottled zones, characterize core TVBC 26. In the carbon-poor environment of core TVBC 08, a doubling of the ^{14}C uptake, a 250 times increase in the number of autotrophic nitrifiers, a four-fold lowering in the number of aerobic sulphur oxidizers and a higher order of denitrifiers exists when compared with core TVBC 26; this suggests the prevalence of a potentially autotrophic microbial community in core TVBC 08 in response to hydrothermal activity. Microbial activity at the northern TVBC 26 is predominantly heterotrophic with enhanced chemosynthetic activity restricted to tan-green mottled zones. The southern TVBC 08 is autotrophic with increased heterotrophic activity in the deepest layers. Notably, the bacterial activity is generally dependent on the surface productivity in TVBC 26, the carbon-rich core, and mostly independent in TVBC 08, the carbon-poor, hydrothermally influenced core. The northern sediment is more organic sink-controlled and the southern sediment is more hydrothermal source-controlled. Hydrothermal activity and associated rock alteration processes may be more relevant than organic matter delivery in these deep-sea sediments. Thus, this study highlights the relative importance of hydrothermal activity versus organic delivery in evoking different microbial responses in the Central Indian Basin sediments.

Keywords Autotrophy, bacteria, Central Indian Basin, diagenesis, hydrothermal, non-steady state, numerical simulation, sediment, transition zone.

INTRODUCTION

The deep-sea floor is predominantly a microbial habitat with a relatively low input (0·01% to 1%) of photosynthetically produced organic matter (Suess *et al.*, 1980). The average temperature and pressure generally remain *ca* 2°C and 500 bars, respectively, in these sediments. However, the more subtle differences in organic matter, pore water and sediment geochemistry dictate

variations among the local communities of micro-organisms in terms of numbers and activity. The role played by the number of micro-organisms in terms of total counts and relative abundance is gaining importance. Recent microbiological studies on the Namibian Shelf (GeoB cores) and Eastern Equatorial Pacific [Ocean Drilling Program (ODP) Leg 201] show that culturable bacteria are constant in abundance over large stretches of the ocean. Cultured bacteria vary consistently from one sub-sea floor environment to another and have been shown to contribute significantly to important biogeochemical processes (D'Hondt *et al.*, 2004).

The abundance and activity of culturable bacteria are linked directly to mineralization processes (Schulz & Schulz, 2005) adapted to very low metabolic rates (Teske, 2004). These mineralization processes are dependent on organic matter diagenesis and hydrothermal fluid interactions (Ma *et al.*, 2006). Hydrothermal fluids from magmatic hotspots, faults and fractures are spread over large stretches of the ocean basin (D'Hondt *et al.*, 2002, 2004). These fluid interferences link the nutrient and the rock cycle providing a wide array of electron donors and acceptors for microbial proliferation and activity, including chemosynthesis. Co-occurrence of multiple metabolic pathways (Wang *et al.*, 2008) or overlap of multiple metabolic zones (Canfield & Thamdrup, 2009) emphasizes the extensive chemosynthetic potential of bacteria.

The aim of this study is to investigate how geochemical, physiographic and lithological differences in two end-member sedimentary settings evoke different microbe–sediment interactions. To address this objective, two geochemically and sedimentologically contrasting cores of the Central Indian Basin (CIB; Fig. 1A and B) were examined for distinctions between microbial communities and the extent of chemoautotrophy. Modern microbial and biochemical processes, along with the pore water geochemistry and porosity, have been integrated with stratigraphic data in order to understand and quantify the factors determining the extent of chemosynthetic potential in these two end-member sedimentary settings in the CIB.

GEOLOGICAL SETTING OF THE CENTRAL INDIAN BASIN

The CIB, with an area of $5{\cdot}7 \times 10^6$ km^2 (Ghosh & Mukhopadhyay, 1999), has five sediment types, namely: terrigenous mud, siliceous ooze with and without nodules, pelagic red clays and carbonaceous ooze (Fig. 1A; Nath *et al.*, 1989; Rao & Nath, 1988). The basin is bordered by the Indian Ocean Ridge system and marked by prominent fracture zones (FZ) and seamounts hosting normal to Mid Ocean Ridge Basalts (Fig. 1B; Kamesh Raju & Ramprasad, 1989; Mukhopadhyay *et al.*, 2002; Das *et al.*, 2007).

The oxygen and nutrient-rich Antarctic Bottom Water Current (AABW) entering the CIB from 5°S (Gupta & Jauhari, 1994) maintained oxic conditions during the past *ca* 1100 kyr (Pattan *et al.*, 2005). Terrigenous influx decreases from north to south (Rao & Nath, 1988; Nath *et al.*, 1989). Higher surface productivity, and therefore higher detrital rain from overlying surface waters (Matondkar *et al.*, 2005), make the organic matter supply to the siliceous ooze higher than that to the red clays (Gupta & Jauhari, 1994). Other factors influencing distribution of organic carbon are sedimentation rates, bottom water oxygenation, water depth, topography, bioturbation, recalcitrance and age (Lyle, 1983; Nath *et al.*, 1997; Lochte *et al.*, 2000). The two stations studied here are located along transect 75·5°E, in close proximity to the Trace of Rodriguez Triple Junction.

Geological features of northern siliceous oozes

The sea floor spreading rate at this location is fast at 90 mm kyr^{-1} (Mukhopadhyay *et al.*, 2002). Temperature and dissolved oxygen of bottom water is 0·9 to 1·03°C and 4·2 to 4·3 ml l^{-1}, respectively (Warren, 1982; Nath *et al.*, 1992). Surface C/N ratios of this total organic carbon (TOC)-rich core range from 3 to 6 (Gupta & Jauhari, 1994; Pattan *et al.*, 2005). Illite is the dominant clay type with a SiO_2/Al_2O_3 ratio of 6·7 and biogenic silica varies from 10 to 35%. Early diagenetic processes are attributed to the formation of rough nodules when the Mn/Fe ratio > 1, with higher Mn, Cu, Ni and todorokite mineralogy (Rao & Nath, 1988; Nath *et al.*, 1989).

Geological features of southern pelagic red clay

The sea floor spreading rate is slow at 26 mm kyr^{-1} (Mukhopadhyay *et al.*, 2002). Temperature and dissolved oxygen of bottom waters are >1·03°C and 4·1 to 4·2 ml l^{-1}, respectively (Warren, 1982; Nath *et al.*, 1992). The surface C/N ratio of this TOC-poor core ranges from 3 to 6 (Gupta & Jauhari, 1994). The dominant clay type is montmorillonite

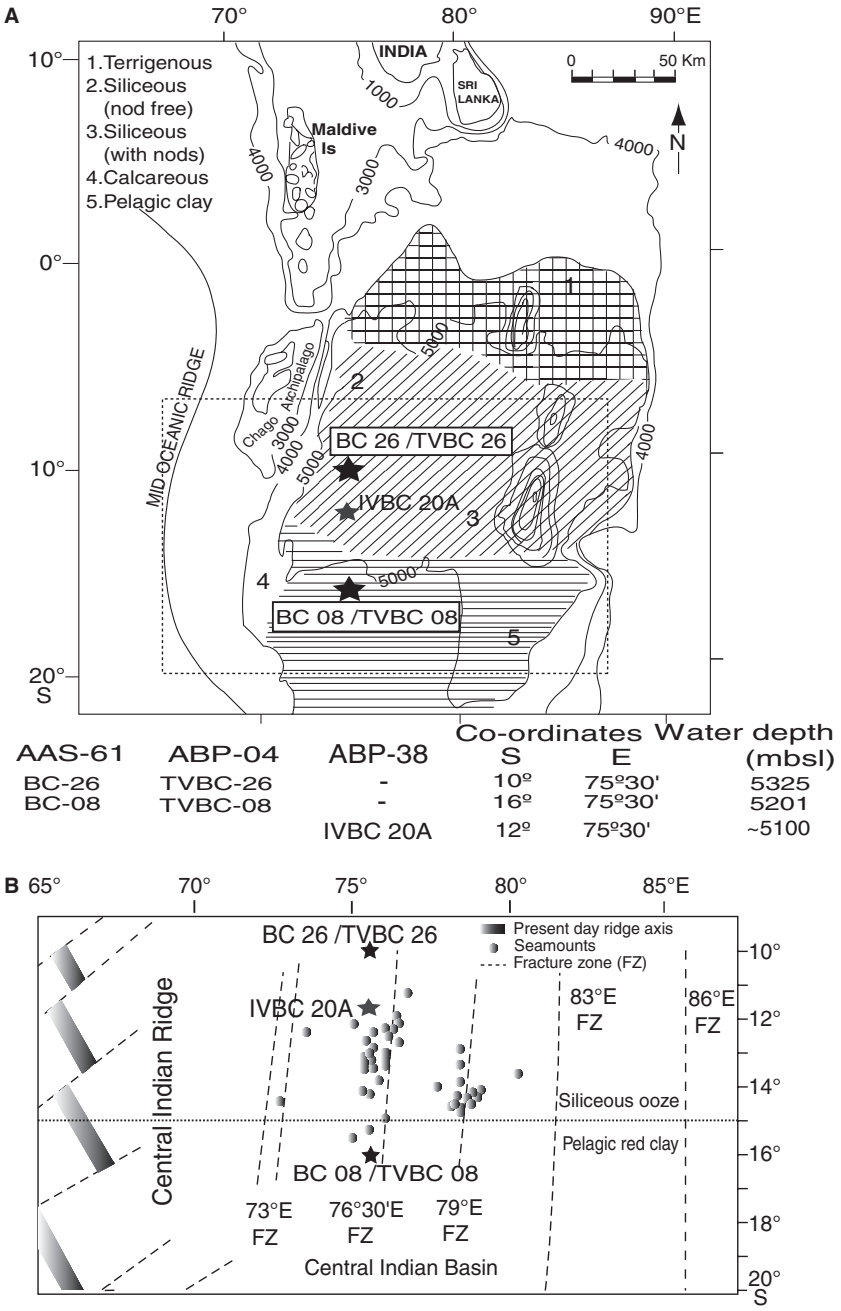

Fig. 1. Area map modified from Mascarenhas-Pereira *et al.* (2006). (A) Station locations with bathymetric and sediment types marked '1' to '5'. (B) Station locations according to topographic features.

with a SiO_2/Al_2O_3 ratio of 4·5 and biogenic silica amounting to 5 to 10%. The Mn/Fe ratio is < 1 suggesting hydrogenetic metal precipitation (Rao & Nath, 1988; Nath *et al.*, 1989). The nature of the glass shards (Mascarenhas-Pereira *et al.*, 2006), native aluminium content (Iyer *et al.*, 2007) and signatures of degassing (Nath *et al.*, 2008) suggest hydrothermal alteration of recent origin in some locations. Late Tertiary sediments probably are exposed in this area due to explosive volcanism (Mascarenhas-Pereira *et al.*, 2006).

GEOMICROBIOLOGY OF THE CENTRAL INDIAN BASIN

Northern siliceous ooze

The northern siliceous setting is rich in TOC with a concentration *ca* 0·3%. Early diagenetic processes and extensive nitrification in this region influence the origin, type and quality of manganese nodules (Nath & Mudholkar, 1989) and sediment biogeochemistry as a whole. The

microbial community might co-express both chemolithotrophy and organotrophy; this would enable efficient recycling of the limited photosynthetically derived organic matter (Stevens, 1997; Ehrlich, 1998). Cultured bacterial representatives showing both phases of nitrification have been isolated from this region (Ram *et al.*, 2001). Microbial processes like manganese oxidation (Ehrlich, 1998 & references therein) and manganese cycling in tan-green mottled zones (Meister *et al.*, 2009) possibly co-occur (Wang *et al.*, 2008) along with the coupling of nitrification–denitrification (Luther *et al.*, 1997). Similarly, sulphide oxidation and iron reduction could co-occur. Here, the mixotrophic combination of chemolithotrophy and organotrophy might be due to simultaneous dependence on the supply of organic matter and possible rock alteration features. The setting might be analogous to that of the hydrocarbon deposits except for the scale and extent (Canfield, 1991; Campbell, 2006; Ma *et al.*, 2006).

Southern pelagic red clay

The southern pelagic red clay setting is TOC-poor with a concentration of <0·1%. It bears the signature of recent hydrothermal alteration due to tectonic reactivation of fracture zones (Mascarenhas-Pereira *et al.*, 2006; Iyer *et al.*, 2007; Nath *et al.*, 2008). Microbiologically, the southern part of the CIB is largely unexplored. It is therefore hypothesized that chemolithotrophy, though widespread, would be more pronounced in the oligotrophic southern CIB than in the detritally dominated northern region. Proximity to tectonic features such as the Trace of Rodrigues Triple Junction (Kamesh Raju & Ramprasad, 1989) may indicate sulphide oxidation with iron reduction (Bach & Edwards, 2003). Thiotrophic nitrate reduction may also be an important contributing process especially in diffuse flow regimes (Childress *et al.*, 1991) with temperatures varying between 2 and 25°C (Chevaldonne *et al.*, 1991). The chemoautotrophy might be totally independent of organic matter rain and this system could be analogous to settings like the Loihi Seamount (Edwards *et al.*, 2004).

MATERIALS AND METHODS

Sampling area and method

The samples for the present study were collected and processed during cruises on-board *R/V Akademik Alexandr Siderenko* (AAS), and *R/V Akademik Boris Petrov* (ABP) as a part of the PMN-EIA (Polymetallic Nodules-Environmental Impact Assessment) programme in the CIB. Two end-member settings, represented by stations TVBC 26 and TVBC 08, were examined in detail for microbial and biochemical parameters during ABP-04 (March to May 2005). Station TVBC 26 (10°S, 75·5°E) lies in the siliceous ooze realm of the northern CIB. Station TVBC 08 (16°S, 75·5°E) is a seamount flank in the volcanic realm of pelagic red clays in the southern CIB. Both stations are situated below the calcite compensation depth, which is *ca* 4500 m below the sea surface (Fig. 1A). Pore water chemistry, porosity, lithology and biostratigraphy were also studied for these two cores during ABP-04. Supporting data on radiometric dating were available from the same locations (BC-26 and BC-08) during an earlier cruise AAS-61 (March to April 2003). Additional pore water data for O_2, Mn, Fe, NH_4^+ and HS^- were acquired from core IVBC 20A, adjacent to core TVBC 26, during Cruise ABP-38 (September to October 2009).

The samples were collected with the help of the United States Naval Electronics Laboratory (USNEL) – using a type box core with dimensions 50 cm × 50 cm × 50 cm. Sub-cores were collected using acrylic cores with a 6·3 cm inner diameter. The sediment cores were sectioned at 2 cm intervals up to 10 cm and at 5 cm intervals thereafter unless mentioned otherwise. The sediments were collected in sterile plastic bags for further processing. Both the cores were analysed up to 25 cm bsf (below sea floor). Hard bottom sediments hindered the collection of deeper cores at TVBC 08. Microbial samples were processed onboard at 4°C and 1 atm pressure immediately after sediment collection.

Lithology, stratigraphy and age

Rock colour was analysed on-board in accordance with the *Rock color chart* of the Geological Society of America, Boulder, Colorado (Courtesy: Cruise report of ABP-04, NIO, Goa, India). The percentage of sand, silt and clay components was determined from desalted samples according to Folk (1968). A lithologue was constructed according to Zervas *et al.* (2009) using the SEDLOG version 2.1.4 software program to show sand, silt and clay content. Neogene radiolarian (NR) biostratigraphy was studied according to Gupta (1991a) and Johnson *et al.* (1989). Radiometric dating using $^{230}Th_{exc}$ was analysed according to Krishnaswami & Sarin

(1976). Details of this analysis are presented in Mascarenhas-Pereira *et al.* (2006) and Nath *et al.* (2008).

Pore water geochemistry and geotechnical properties

Shipboard analysis of modern pore water pH, NO_2^-, NO_3^-, $PO_4^{3-}$and SiO_3^{2-} was performed using the standard methods described in Grasshoff *et al.* (1983). Pore water O_2, NH_4^+ and HS^- were determined according to Pai *et al.* (1993), Grasshoff *et al.* (1983) and Pachmayr (1960), respectively. The determination of Fe and Mn^- in pore water was performed by sampled direct current (Aldrich & van der Berg, 1998) and differential pulse polarographic (Colombini & Fuocco, 1983) methods using a Metrohm voltammeter (Metrohm Limited, Herisau, Switzerland). Porosity, wet bulk density, water content and specific gravity were measured using the standard method described in ASTM (1995).

Total organic carbon and C/N ratio

Total carbon and nitrogen were measured using an NCS 2500 Elemental Analyser (Thermo Quest Italia Spa, Milan, Italy; Patience *et al.*, 1990) using an L-Cistina (Thermo Quest Italia SpA) as a standard. Total carbon was counter-checked with a UIC CM 5014 coulometer and found to be similar in range. Total inorganic carbon was analysed by a UIC CM 5014 coulometer (UIC Inc., Joliet, IL, USA) using $CaCO_3$ (Merck KGAA, Darmstadt, Germany) as a standard. The accuracy of measurements was verified by the analysis of a standard reference material (USGS-MAG-1). The TOC was determined by subtracting total inorganic carbon from total carbon. The C/N was calculated as the ratio between TOC and total nitrogen.

Labile organic matter

Total protein concentrations within sediments were estimated by the Folin Ciocalteu method of Lowry using bovine serum albumin as a standard (Lowry *et al.*, 1951). Total carbohydrate concentrations within sediments were estimated using the phenol-sulphuric acid method of Kochert (1978) with glucose as a standard. Total lipids of sediments were estimated using stearic acid as a standard (Bligh & Dyer, 1959). The sum of total proteins, carbohydrates and lipids was expressed as labile organic matter (LOM). The nature and origin of the organic matter was estimated by the protein/carbohydrate ratio (Cauwet, 1978; Fichez, 1991).

Adenosine triphosphate

Adenosine triphosphate (ATP) was estimated to determine the total biomass of living organisms in deep-sea sediments by luciferin–luciferase reaction (Holm-Hansen & Booth, 1966), using ATP disodium salt as a standard (Sigma Chemicals, St Louis, MO, USA). Photons produced were counted on a Perkin Elmer, Wallac 1409 DSA, Liquid Scintillation Counter (Perkin Elmer Wallac, Waltham, MA, USA) as counts per minute and converted to ATP equivalents (Delistraty & Hershner, 1983).

Bacterial counts

Total counts of bacteria

Total bacterial cells were counted according to Hobbie *et al.* (1977). About 1 g of sediment was diluted with 9 ml of sterile sea water; 3 ml of this slurry was fixed with buffered formalin at an end concentration of 2% and stored at 4°C until analysis. At the on-shore laboratory, the aliquot was sonicated at 15 Hz for 15 sec. The supernatant (1 ml) was stained with 75 μl of 0·01% acridine orange (3 min, in dark) and filtered onto 0·22 μm black polycarbonate filter paper (Millipore, Middlesex County, MA, USA). This procedure minimized masking by sedimentary particles. About 10 to 15 microscopic fields were counted to include a total of 300 to 600 cell counts per sample using a Nikon 80i epifluorescence microscope (Nikon, Tokyo, Japan). The counts were normalized per gram of dry sediment.

Frequency of dividing cells

The frequency of dividing cells (FDC) was enumerated among the total counts (Naganuma *et al.*, 1989) and represented as the natural viable population. In the filtered and stained samples of total bacterial counts, dividing bacteria cells were counted as elaborated above. Bacteria showing an invagination, but not a clear intervening zone between cells were considered as one dividing cell (Hagstrom *et al.*, 1979).

Direct viable counts

Direct viable counts (cell numbers) (DVC) were determined according to Kogure *et al.* (1984). Aerobic viable counts (DVC-a) and anaerobic viable counts (DVC-an) were enumerated sepa-

rately. Three millilitres of sediment slurry was prepared as above by diluting 1 g of sediment with 9 ml of sterile sea water into two sets. The first set was amended with 0·001% final concentration of yeast extract and 0·0016% final concentration of an antibiotic cocktail solution containing piromedic, pipemedic and nalidixic acid in the ratio 1:1:1 and incubated statically in the dark at 4°C for 30 h. In the second set, used to determine viability under anaerobic conditions, in addition to yeast extract and antibiotic cocktail, 12 µl of Na_2S $9H_2O$ was added as a reductant at a final concentration of 0·125% before incubation (Loka Bharathi *et al.*, 1999). At the end of the incubation, the aliquots were fixed with 2% buffered formalin and stored at 4°C until analysis.

The cocktail composition was suitably modified from Joux & Lebaron (1997) by using three of five antibiotics. Antibiotics were dissolved in 0·05 M NaOH [nalidixic, piromidic and pipemidic acids (Sigma)]. All antibiotic solutions were filter sterilized through 0·2 mm pore-size membrane filters (Millipore, USA) before use.

The addition of yeast extract in low concentrations permits cell growth and replication of nucleic acid but the antibiotic cocktail prevents cell division for the period of incubation. The elongated and enlarged dividing cells were counted as DVC-a or DVC-an using a similar procedure to that employed for total counts (Kogure *et al.*, 1984).

Heterotrophic counts

Colony forming units (cfu) on varying concentrations of ZoBell Marine Agar (ZMA) were assessed using three different concentrations of ZoBell Marine broth 2216 (Himedia, Mumbai, India) in 1·5% agar (Difco Lawrence, KS, USA) namely, 100%, 50% and 12·5%. The 100% concentrated broth was prepared according to the manufacturers' instructions, whereas 50% and 12·5% were diluted to half and one-eighth strengths, respectively, with a final pH of 7·6 ± 0·2 (ZoBell, 1941). The plates were incubated at 2 to 5°C. Heterotrophic colonies appeared within four to 10 days.

Potential autotrophs

Nitrifying bacteria were enumerated on modified Winogradsky's media for ammonia oxidizers and nitrite oxidizers by substituting the medium with $(NH_4)_2SO_4$ at 2 mM (final concentration) or $NaNO_2$ at 0·5 mM (final concentration) as an energy source (Ram *et al.*, 2001). The medium for aerobic sulphur oxidizing bacteria was similar to that of denitrifiers, as described below, except for the addition of KNO_3. Inoculation for all oxidizers was carried out by standard plating techniques.

Nitrate reducers were enumerated on modified Leiske's medium (Loka Bharathi, 1989; Loka Bharathi & Chandramohan, 1990; Loka Bharathi *et al.*, 2004). The bacteria cultured on this medium reduce nitrate at the expense of thiosulphate. For simplicity, this group is identified as denitrifiers in the rest of the manuscript as these are known to be functionally similar to *Thiobacillus denitrificans*. Medium composition per litre of aged sea water: $Na_2S_2O_3$ $5H_2O$ – 5 g, K_2HPO_4 – 0·2 g, $MgCl_2$ $6H_2O$ – 0·1 g, $CaCl_2$ $6H_2O$ – 0·01 g, $FeCl_3$ $6H_2O$ – 0·01 g, phenol red indicator – 0·01 g, pure agar (Difco) – 10 g, $NaHCO_3$ – 1 g, pH 8 to 8·3. KNO_3 at 1 g l^{-1} was added as a terminal electron acceptor. Sodium bicarbonate solution was filter sterilized and added to the medium just before inoculation. A second group of nitrate-reducing bacteria (NRB) that reduce nitrate at the expense of organic matter were enumerated. For simplicity, this group is identified as NRB. The medium composition per litre of aged sea water is: 0·101 g KNO_3 and nutrient agar at a pH of 7·5 to 8. The original 14 g l^{-1} of nutrient agar was modified to 25% strength of nutrient broth amended with pure agar to give a final agar concentration of 0·8%. Reducers were inoculated in agar-shake tubes as described in Loka Bharathi (1989).

Fe-oxidizers were cultivated on iron oxidizers medium (Himedia, Mumbai, India). Two parts (A and B) of the medium were prepared separately. Part A consisting of $(NH_4)_2SO_4$ – 3·0 g, KCl – 0·10 g, K_2HPO_4 – 0·5 g, $MgSO_4$ – 0·5 g, $Ca(NO_3)_2$ – 0·01 g was dissolved in 700 ml of sea water containing 1 ml of 10 N H_2SO_4. Part B containing 44·22 g of $FeSO_4$ was dissolved in 300 ml of distilled water and mixed to Part A. The final salinity was adjusted to 35 ppt and the final pH was adjusted to 6·8 ± 0·2 in order to maintain a mild acidic to near neutral condition (Rodina, 1972).

Mn-oxidizers were cultivated on modified Beijerinck's medium (Rodina, 1972; Havert, 1992). Two parts (A and B) of the medium were prepared separately. Part A consisting of $NaHCO_3$ – 0·1 g, $(NH_4)_2SO_4$ – 0·1 g, K_2HPO_4 – 0·5 g, $MgSO_4$ – 0·5 g was dissolved in 900 ml of sea water. Part B containing 12·5 g of $MnCl_2$ was dissolved in 100 ml of distilled water and mixed to Part A. The final salinity was adjusted to 35 ppt and the final pH was adjusted to 7·8 ± 0·2 in order to maintain a near neutral condition.

Microbial uptake of carbon in sediments

Microbial uptake of carbon in sediments was measured using $NaH^{14}CO_3$ uptake [5 μ Ci ml^{-1} activity, Board of Radiation and Isotope Technology (BRIT), Navi Mumbai, India] adopting methods described earlier (Tuttle & Jannasch, 1977; Nelson *et al.*, 1989). Briefly, *ca* 1 g of sediment was suspended in 9 ml sterile sea water and this sediment slurry was incubated with 0·08 μ Ci ml^{-1} final concentration of $NaH^{14}CO_3$ at 4°C with 24 h incubation in the dark. Unincorporated labelled carbon was carefully washed with sterile sea water. The filtered slurry was acidified to remove unbound ^{14}C and trace inorganic carbon. The filter with the trapped sediment was dried further at 35°C and then suspended in a scintillation vial containing cocktail. The sample was counted after 12 to 24 h in a Liquid Scintillation counter (Model Perkin Elmer, Wallac 1409 DSA). Suitable controls for unlabelled and heat-killed sediments, wash water and labelled carbon were included. The incorporation of carbon was read as disintegrations per minute (integrated for 5 min) and was expressed as nmol C g^{-1} day^{-1}.

Calculations of organic carbon flux from surface primary productivity

The organic carbon flux to the sea floor was derived (Schenau *et al.*, 2000) from previously reported productivity values based on values of ^{14}C incorporation by primary productivity (Matondkar *et al.*, 2005). The net primary productivity was derived from the difference between light and dark bottle incubations in this study. The calculations below consider only this net primary productivity. Potential carbon flux to the sea floor $J_{Cx=0}$ was calculated using the relationship:

$$J_{Cx=0} = 2PP^{0.5} \times (PP/100) \times (1/z + 0 \cdot 025) \quad (1)$$

where PP is the integrated column productivity rate in g C m^{-2} $year^{-1}$ and z is the water depth expressed in hundreds of metres (i.e. 5000 m depth is expressed as 50×100, where $z = 50$; Schenau *et al.*, 2000).

The accumulation rate of sediment at the sea floor was calculated as a product of sedimentation rate and dry bulk density as:

$$\text{Sediment accumulation rate}, S_{acc} = S\rho(1-\varphi) \quad (2)$$

where S is the linear sedimentation rate (0·834 and 0·041 cm kyr^{-1} in TVBC 26 and TVBC 08, respectively), ρ is the wet bulk density in g cm^{-3} and φ is the porosity.

The accumulation rate of carbon at the sea floor was calculated as a product of sediment accumulation rate and C_{org} (%) as:

$$C_{org} \times S_{acc} \quad (3)$$

The preservation factor was calculated as the ratio of the rate of carbon accumulation to primary production rate (Wenbo *et al.*, 2008). Palaeoproductivity (PaP) was calculated from TOC:

$$PaP = 5{\cdot}31[C(\rho - 1{\cdot}026\varphi/100)]^{0.71} S^{0.07} Z^{0.45} \quad (4)$$

Palaeoproductivity is a function of carbon flux near the sea floor and is related to both productivity and water depth (Stein, 1991), and expressed as g C m^{-2} kyr^{-1}. Palaeoproductivity profiles are compared with those of autotrophic microbial carbon fixation profiles to understand time-dependent variations in the extent of chemoautotrophy.

Data analysis and statistical significance

In the case of epifluorescence counts, 10 to 15 microscopic fields cumulating in not less than 500 cells were considered for deriving standard deviations. Plate counts, ATP, $NaH^{14}CO_3$ uptake and LOM were analysed in triplicate. All parameters were normalized per gram of sediment dry weight unless mentioned otherwise. Parameters were plotted as averaged profiles with error bars representing the range of individual samples. Two-factor analysis of variance without replication was used for confirming significance in variations. Correlation between the TOC contents, microbial, biochemical parameters and pore water data were analysed for Spearman's rank correlation using STATISTICA version 6 (StatSoft Inc., Tulsa, OK, USA).

Quantification of the influence of non-steady-state diagenetic condition on microbial community by numerical simulation

A non-steady-state diagenetic model was considered to explain the formation of the tan-green mottled zone showing chemoautotrophy in core TVBC 26. A transient diffusion model (Meister *et al.*, 2007), including a sink term, was used to

simulate NO_3^- pore water profiles as shown in Eq. 5:

$$\partial c/\partial t = k\left(\partial^2 c/\partial x^2\right) + s(x) \qquad (5)$$

where $c(x,t)$ is the concentration of NO_3^- (μM), t is time (years) and x is the depth below sea floor (cm bsf):

$$\kappa = \varphi\tau^{-2}D_s \quad \text{and} \quad \tau^2 = \varphi F \qquad (6)$$

where D_s is the diffusion coefficient for NO_3^- (m^2 sec^{-1}), φ is the porosity (dimensionless) and F is the formation factor (dimensionless). Nitrite oxidation rate $s(x)$ and the nitrate reduction rate $s'(x)$ is:

$$\begin{aligned}
&s(x) = 0\,\mu\text{mol m}^{-3}\text{ year}^{-1}, \text{ if } t < 10000 \text{ year}\\
&s(x) = 1000\,\mu\text{mol m}^{-3}\text{ year}^{-1},\\
&\qquad \text{if } 10000 \text{ year} < t < 11200 \text{ year and}\\
&\qquad 3 < x < 7\,\text{cm bsf}\\
&s'(x) = -1000\,\mu\text{mol m}^{-3}\text{ year}^{-1},\\
&\qquad \text{if } 10000\,\text{year} < t < 11200 \text{ year and}\\
&\qquad 5 < x < 9\,\text{cm bsf}
\end{aligned}$$

Thus, $s(x)$ represents nitrification and is substituted by $s'(x)$ in case of denitrification. The following initial conditions and boundary conditions were used:

$$\begin{aligned}
&c = 26{\cdot}13\,\mu\text{M} \quad \text{for } x > 0\\
&c = 8{\cdot}87\,\mu\text{M} \quad \text{for } x = 0\\
&c(0,t) = 8{\cdot}87\,\mu\text{M}\\
&c(L,t) = 26{\cdot}13\,\mu\text{M}
\end{aligned}$$

where L is the length of the model domain.

The explicit finite difference method was used to solve Eq. 5. A time step of 10 years and a grid size of 1 cm were chosen. The tortuosity factor was calculated from porosity and formation factor (Schulz, 2000). A diffusion coefficient for NO_3^- of 9·03E-10 m^2 sec^{-1}, at 0°C was considered (Schulz, 2000). Both $s(x)$ and $s'(x) = 0$ for the first 10 000 years of the computation, which is the time required for an organic matter pulse to reach the present tan-green mottled zone at 13 to 25 cm bsf without being diagenetically altered. After setting these conditions, nitrite oxidation and nitrate reduction are switched on separately in the depth interval $3 < x < 7$ cm and $5 < x < 9$ cm bsf, respectively, to simulate the effect of strong nitrite oxidation followed by nitrate reduction in an organic carbon-rich sediment layer. A nitrite oxidation rate of 1000 μM m^{-3} $year^{-1}$ was assumed in a horizon from 3 to 7 cm bsf (Ward *et al.*, 1989). In the horizon from 5 to 9 cm bsf a maximum nitrate reduction rate of −1000 μM m^{-3} $year^{-1}$ was assumed.

Quantification of hydrothermal alterations on pore water and microbial community by numerical simulation

A modified transient diffusion model (Meister *et al.*, 2007) including a source term was considered to explain the influence of hydrothermal activity on the pore water profile. This model, in turn, was used to explain the enhanced chemoautotrophic microbial activity at the Pleistocene–Tertiary stratigraphic transition zone of core TVBC 08. Pore water NO_3^- profiles were simulated as shown in Eq. 7:

$$\partial c/\partial t = \kappa'\left(\partial^2 c/\partial x^2\right) + \text{sr}(x) \qquad (7)$$

where $c(x,t)$ is the concentration of NO_3^- (μM), t is time (years), and x is the depth below sea floor (cm bsf):

$$\kappa' = \varphi\tau^{-2}D_s \quad \text{and} \quad \tau^2 = \varphi F' \qquad (8)$$

where D_s is the diffusion coefficient for NO_3^- (m^2 sec^{-1}), φ is the porosity (dimensionless) and F is the formation factor (dimensionless). Nitrite oxidation rate sr(x) and the nitrate reduction rate sr′(x) is:

$$\begin{aligned}
&\text{sr}(x) = 0\,\mu\text{mol m}^{-3}\text{ year}^{-1}, \text{ if } t < 1000 \text{ year}\\
&\text{sr}(x) = 1000\,\mu\text{mol m}^{-3}\text{ year}^{-1},\\
&\qquad \text{if } 1000 \text{ year} < t < 1170 \text{ year and}\\
&\qquad 3 < x < 7\,\text{cm bsf}\\
&\text{sr}'(x) = -1000\,\mu\text{mol m}^{-3}\text{ year}^{-1},\\
&\qquad \text{if } 1000 \text{ year} < t < 1170 \text{ year and}\\
&\qquad 5 < x < 9\,\text{cm bsf}
\end{aligned}$$

Thus, sr(x) represents nitrification and is substituted by sr′(x) in the case of denitrification. The following initial conditions and boundary conditions were used:

$$\begin{aligned}
&c = 9{\cdot}71\,\mu\text{M} \quad \text{for } x > 0\\
&c = 4{\cdot}85\,\mu\text{M} \quad \text{for } x = 0\\
&c(0,t) = 4{\cdot}85\,\mu\text{M}\\
&c(L,t) = 9{\cdot}71\,\mu\text{M}
\end{aligned}$$

where L is the length of the model domain.

The explicit finite difference method was used to solve Eq. 7. A time step of one year and a grid size of 1 cm were chosen. The tortuosity factor was calculated from porosity and formation factor (Schulz, 2000). A diffusion coefficient for NO_3^- of 9·03E-10 m^2 sec^{-1}, at 0°C was considered (Schulz, 2000). Both sr(x) and sr′(x) = 0 for the first 1000 years of the computation, when upwelling of hydrothermally derived NO_3^- occurs as a focused jet to the present Pleistocene–Tertiary stratigraphic transition zone at 3 to 12 cm bsf without being dispersed laterally. After setting these conditions, nitrite oxidation and nitrate reduction are switched on separately in the depth interval $3 < x < 7$ cm and $5 < x < 9$ cm bsf, respectively. The effect of strong nitrite oxidation followed by nitrate reduction in the stratigraphic transition zone is simulated due to lateral dispersion and phase separation of solutes carried upward by the hydrothermal fluid and resultant microbial activity. A nitrite oxidation rate of 1000 μM m^{-3} $year^{-1}$ was assumed in a horizon from 3 to 7 cm bsf (Ward *et al.*, 1989). In the horizon from 5 to 9 cm bsf a maximum nitrate reduction rate of −1000 μM m^{-3} $year^{-1}$ was assumed. The model source code in MATLAB 7.0.4 (The Mathworks, Natick, MA, USA) used for this work is available as a '.doc-file' and provided as an electronic supplement to this study.

RESULTS

Northern core TVBC 26

Lithology, stratigraphy and age

The siliceous core TVBC 26 shows tan-green mottled transitions, a distinct feature in northern CIB sediments. Here the moderate yellowish brown (10YR 4/2) sediments from 13 to 25 cm bsf showed intense mottling with light olive grey (5Y 5/2) and dark yellowish brown (10YR 4/2) continuous intercalations. The surface of both cores BC 26 and reoccupied station TVBC 26 were covered with Mn nodules, indicating that the surface was preserved during sample retrieval (Borole, 1993). The sediment of core TVBC 26 is composed of 0·37% to 4·17% sand, 25·37% to 49·45% silt and 49·2% to 74·10% clay. Sand content ≤4% and is not resolvable in the lithologue (Fig. 2).

Neogene radiolarian biostratigraphy of the core TVBC 26 suggested that the first appearance of index species *Collospheara invaginata* is 24 cm bsf, representing an approximate date of *ca* 180 ka (Johnson *et al.*, 1989). *Collospheara tuberosa* and *Collospheara orthoconus* are present from 16 to 3 cm core depth. Most importantly, *Stylatractus universus* is conspicuously absent suggesting that the base of the core was younger than *ca* 300 ka (Fig. 2). The biostratigraphic sedimentation rate of *ca* 1·1 mm kyr^{-1} was consistent with previous findings (Banakar *et al.*, 1991 and Borole, 1993). However, radiometric dating from the same location (BC 26, AAS-61) using $^{230}Th_{exc}$ showed a much higher sedimentation rate of 8·34 mm kyr^{-1} (Fig. 2).

Pore water geochemistry and geotechnical properties

The pore water of TVBC 26 was nearly neutral, with pH averaging 7·30 ± 0·07 (Fig. 3A). NO_2^- concentrations up to 0·14 μM were detected only in the top 0 to 2 cm. The NO_3^- concentration averaged at 21·83 ± 5·97 μM, PO_4^{3-} at 1·79 ± 0·20 μM and SiO_3^{2-} at 478 ± 74 μM (Fig. 3A). Porosity at the tan-green mottled zone shows a decrease indicating relative compaction. Pore water O_2, Mn, Fe, NH_4^+ and HS^- concentrations were obtained from a neighbouring siliceous core IVBC 20A (Fig. 3B). Like TVBC 26, this core also showed mottled structures at 12 to 19 cm bsf. The oxygen concentrations varied from 180 to 370 μM l^{-1} with peaks at 10 and 20 cm bsf indicating consumption of oxygen at the reactive layers above 10 cm and mottles above 20 cm. Ammonium concentrations varied from non-detectable to 0·14 μM l^{-1} of pore water with peaks generally corresponding to oxygen depletion. Sulphide concentrations varied from 0·03 to 0·18 μM l^{-1} with peak concentration at 7 cm bsf. Mn concentrations varied from 0·14 to 9·95 mg l^{-1} with peaks above 7 and 19 cm bsf. Fe concentrations varied from 0·39 to 9·94 mg l^{-1} with the highest peak at 17 cm bsf (Fig. 3B).

Total organic carbon, total inorganic carbon and C/N ratio

The northern siliceous sediment TVBC 26 was twice as rich in TOC when compared with the pelagic red clays from the southern TVBC 08 (Fig. 2). The averaged down-core TOC profile of siliceous TVBC 26 was 0·15% to 0·45%. The TIC varied from non detectable to <0·1 ppm. Total inorganic carbon was detected only at 2 to 4 cm and 20 to 25 cm bsf. A TOC peak at 2 to 4 cm bsf was followed by a TIC peak at 4 to 6 cm bsf in the reactive Layer 1. Total inorganic carbon showed a tendency to increase at the sub-oxic mottled-zone. TVBC 26 showed a C/N ratio ranging from

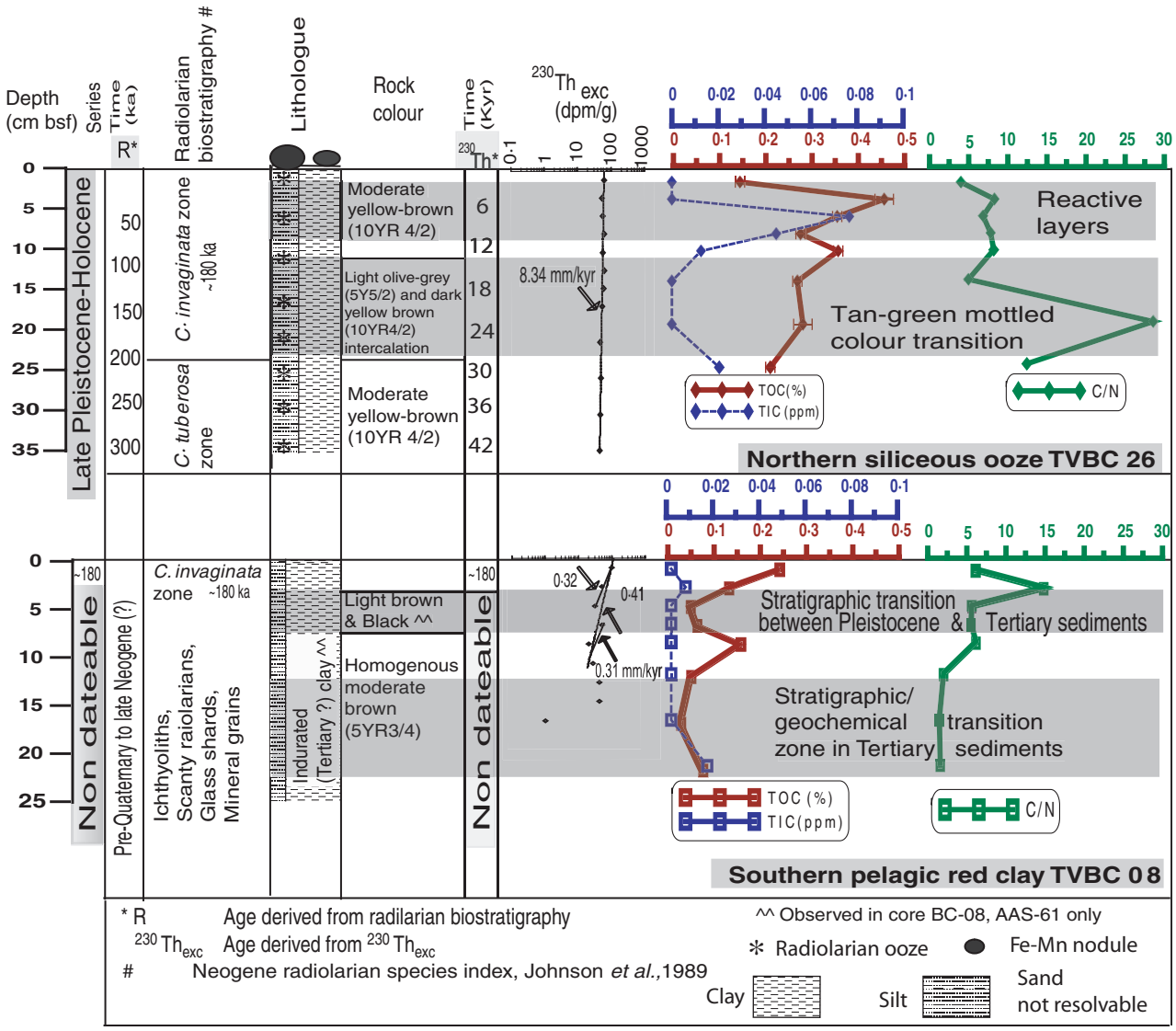

Fig. 2. Age, biostratigraphy, lithology, elemental carbon and nitrogen profiles of TVBC 26 and TVBC 08 (data points on the *y*-axis suggest values below detection limit).

4 to 8·3. At the sub-oxic mottle (15 to 25 cm bsf) ratio was 28·6 (Fig. 2).

Labile organic matter

Though quantities of carbohydrates and lipids were almost similar, proteins were four times higher in TVBC 26 than its southern counterpart. Protein/carbohydrate ratios were > 1 at TVBC 26 indicating fresher LOM content. Significant variations in down-core profiles of all parameters were noted at the reactive layer of TVBC 26 (Fig. 4). In the tan-green mottled zone of TVBC 26, the carbohydrates show relatively better preservation and coincided with a higher C/N ratio (Fig. 2), increasing ATP (Fig. 5), higher aerobic sulphur oxidizers (Fig. 6A) and higher carbon uptake (Fig. 7), indicating a chemo-autotrophic pocket in a predominantly heterotrophic setting.

Adenosine triphosphate

In TVBC 26 the values ranged from 50 to 105 ng g^{-1} dry wt with the highest value at 20 to 25 cm bsf (Fig. 5).

Bacterial counts

Total bacterial counts and frequency of dividing cells. The total bacterial counts in core TVBC 26 varied from 3·6E + 08 to 7·2E + 08 cells g^{-1}. The down-core profile was almost homogenous. In core TVBC 26, 14% of the total bacteria were naturally viable. The FDC was two and a half

times higher in the surface layer of 0 to 10 cm at TVBC 26 than in the subsequent sub-surface layer (Fig. 5).

Direct viable counts (DVC-a and DVC-an). DVC-an was three times higher at the TOC-rich TVBC 26 than at TVBC 08 ($P > 0{\cdot}05$) (Fig. 5). Prominent variations in TC, FDC, DVC-a and DVC-an are seen at or near the reactive Layer 1. DVC-an shows an increase in the sub-oxic mottled zone of TVBC 26.

Heterotrophic counts. Triplicate plate counts on ZMA showed that the retrievability from organic-rich TVBC 26 was strangely lower than TVBC 08 with a few exceptions. A conspicuous depletion of heterotrophs on 12·5% ZMA was noted at the tan-green mottled colour transition zone (Fig. 6A).

Potential autotrophs. The ammonium and nitrite oxidizer population generally was lower in TVBC 26 than the southern counterpart. The aerobic sulphur oxidizers, however, followed a different pattern with the average values at TVBC 26 being nearly four times the value in TVBC 08 (Fig. 6A and B). The deep sea bacterial isolates from the CIB were able to grow almost equally well at 28 and 5°C. Nitrifiers and aerobic sulphur oxidizers appeared within 10 to 35 days. Culturable denitrifiers and nitrate reducers generally took longer to grow than aerobe. The incubation period was often as long as three to 12 months, or more, at 5° ± 2°C.

Denitrifiers showed a peak culturability at 4 to 6 cm bsf (in between reactive Layers 1 and 2) with 10^3 cfu g^{-1} dry sediment in the northern TOC-rich core. A second peak with 10 cfu g^{-1} dry sediment was seen at the commencement of the mottled zone. The NRB that are dependent on organic matter showed two peaks at 2 to 4 cm and 6 to 8 cm bsf with 670 and 20 cfu g^{-1}, respectively. An increase in NRB counts was noted at the tan-green mottled zone, perhaps representing the remnant of an older reaction front (Fig. 6A).

Fe-oxidizers varied from 1·11E + 02 to 1·12E + 03 cfu g^{-1} in the northern core TVBC 26. Mn-oxidizers varied from 2·22E + 02 to 1·06E + 03 cfu g^{-1} in core TVBC 26. The peaks of Mn- oxidizers lie in the reactive layers and tan-green mottled zone (Fig. 6A). The pore water Mn profile of a similar neighbouring core, IVBC 20A (Fig. 3B), corroborates with that of Mn-oxidizers of core TVBC 26.

Microbial uptake of carbon in sediments

Measurement of autotrophic microbial carbon fixation by whole sediment slurries showed maximum uptake at 4 to 6 cm and 20 to 25 cm bsf in core TVBC 26. The heat-killed controls showed markedly lower values than the actual experimental uptake (Fig. 7).

Organic carbon flux, palaeoproductivity and modern microbial autotrophic uptake

The rate of column productivity recorded over the siliceous oozes was 103 mg C m^{-2} day^{-1} corresponding to 18·91 to 37·74 g C m^{-2} $year^{-1}$ (Matondkar *et al.*, 2005). About 0·4 to 0·6% of carbon from surface production reaches the sea floor as organic carbon flux over the northern siliceous ooze of TVBC 26. The organic C flux was between 0·07 to 0·205 g C m^{-2} $year^{-1}$. The corresponding carbon accumulation rates were 0·028 g C m^{-2} $year^{-1}$. Preservation factors for these sediments were extremely low with $1{\cdot}04 \times 10^{-6}$ for siliceous TVBC 26. Palaeoproductivity calculated from organic carbon content in the sediment cores ranged from 0·097 to 0·157 g C m^{-2} kyr^{-1} in the siliceous oozes. This palaeoproductivity profile was compared with autotrophic carbon uptake in the present Quaternary times. The modern microbial autotrophic uptake profile showed a similar trend to the palaeoproductivity profile except at 3 to 5 cm and 20 to 25 cm bsf where the trend was opposite. This trend was observed at the reactive layer (age 6 kyr) and the tan-green mottled transition (age 24 kyr) (Fig. 8). Here, the low surface productivity layer was superimposed on a layer with high chemosynthetic activity.

Inter-relationship between bacterial and geochemical parameters in northern core TVBC 26

The TOC and LOM significantly correlated to each other ($P > 0{\cdot}05$) highlighting the interdependence of organic flux to sea floor and lability of organic matter enhanced by bacteria. Total organic carbon related to pore water pH, nitrite oxidizers, carbon uptake rates ($P > 0{\cdot}01$) and to ammonium oxidizers ($P > 0{\cdot}05$) signifying its stimulatory role on the microbial population while promoting diagenetic reactions. Labile organic matter determined total bacterial counts, FDC, DVC-a and heterotrophs recoverable on 50% ZMA ($P > 0{\cdot}05$). These relations are suggestive of aerobic heterotrophic degradation of organic matter. Pore water NO_2^- showed a negative relationship with NO_3^- ($P > 0{\cdot}01$), SiO_3^{2-} ($P > 0{\cdot}001$), TOC ($P > 0{\cdot}05$) and ammonium oxidizers ($P > 0{\cdot}001$) indicating coupling of a heterotrophic degradative process with nitrification during early diagenetic reactions. The ^{14}C uptake ($P > 0{\cdot}05$) is correlated positively with nitrite

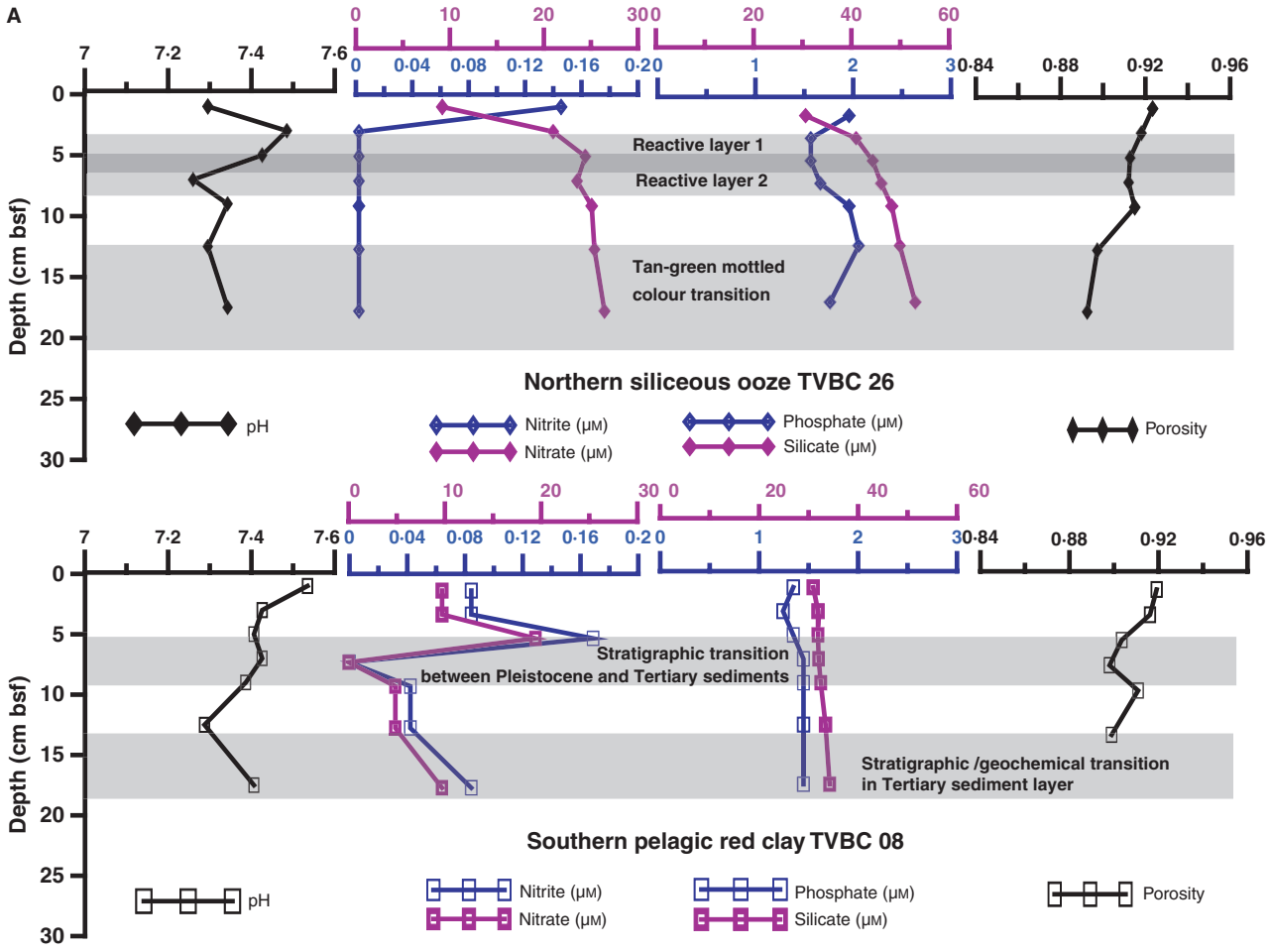

Fig. 3. (A) Pore water profiles of NO_2^-, NO_3^-, PO_4^{3-}, SiO_3^{2-} (data points on y-axis suggest values below detection limit), pH and porosity. (B) Pore water O_2, Mn, Fe, NH_4^+ and HS^- of core IVBC 20A in the vicinity of TVBC 26 (data points on the *y*-axis suggest values below detection limit).

oxidizers. The strong correlation at $P > 0{\cdot}001$ existed between aerobic sulphur oxidizers and DVC-an suggesting their affinity with facultative anaerobic heterotrophy.

Quantification of the influence of non-steady-state diagenetic condition on microbial community by numerical simulation

The NO_3^- concentration profile measured by shipboard analysis was simulated using a transient diffusion numeric model (Fig. 9A). At the sea floor interface, the observed NO_3^- concentration of 8·87 μM was used as a starting condition. It is also assumed that NO_3^- in sediment pore water is 0. The model calculated the concentration as a function of time and depth. Considering the residence time of NO_3^- and the sedimentation rate of an organic matter pulse, a 10 000 year time scale is required for NO_3^- to reach 17·5 cm bsf. Assuming a surface layer with a nitrite oxidation rate of 1000 μM m^{-3} $year^{-1}$ in the section 3 to 7 cm bsf, the model also shows that the reactant, NO_2^-, will be consumed within a time period of 1000 years in this zone. Conversely, at 5 to 9 cm bsf the reactant NO_3^- would be reduced at a reduction rate of −1000 μM m^{-3} $year^{-1}$. The reactant NO_3^- will be consumed within 1000 years. The profile returns to its original shape within another 1000 years soon after the consumption of NO_2^- in the upper 3 to 7 cm layer and the simultaneous reduction of NO_3^- in the lower 5 to 9 cm ceases. In both halves of the reaction couple a steady nitrification profile is finally achieved and they reproduce the pore water NO_3^- profile measured in the core TVBC 26 (Fig. 9A), showing net nitrification. The effect of advection in this single core system is neglected; this is because the variations in TOC (Fig. 2) are more important than the variation in porosity (Fig. 3).

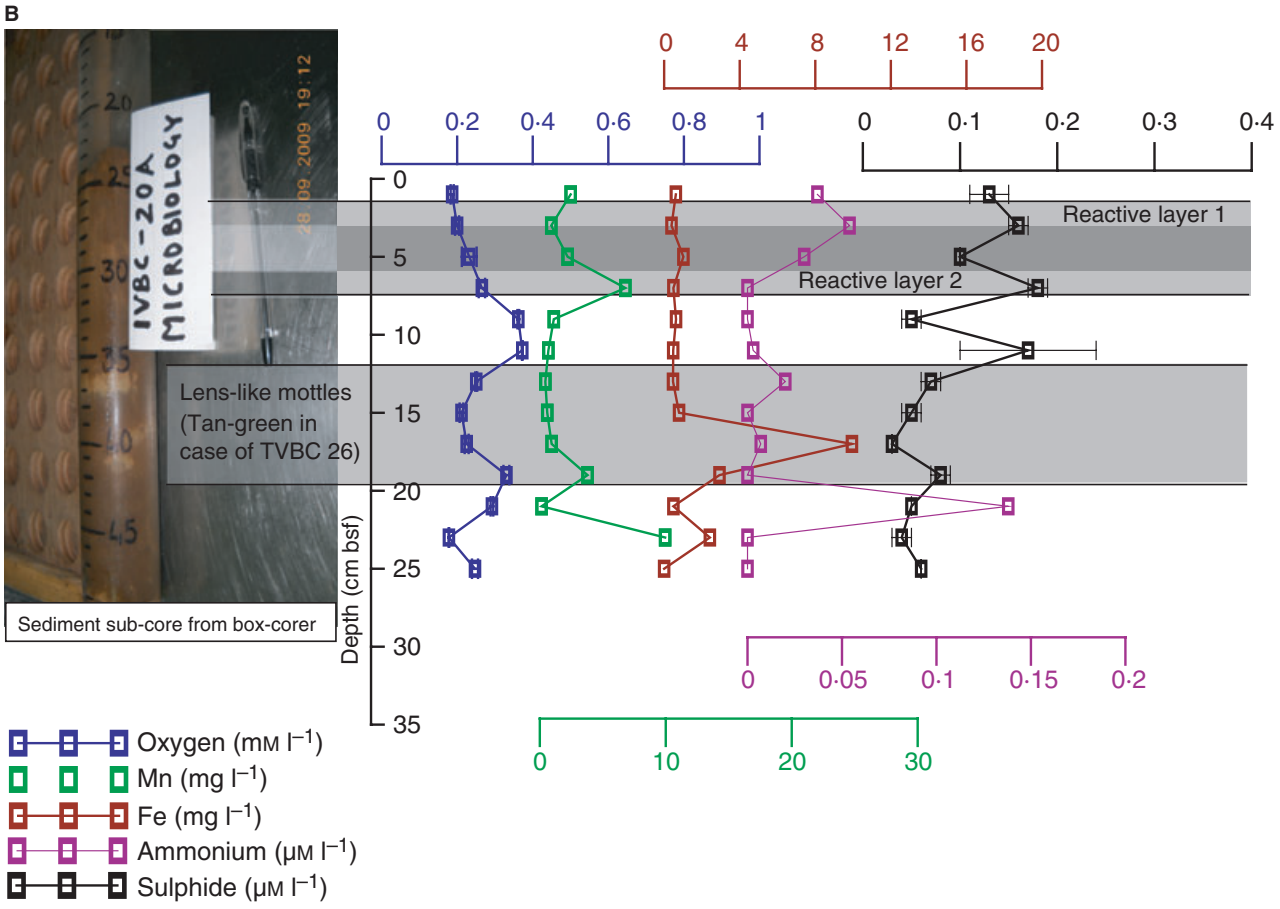

Fig. 3b. continued.

Southern core TVBC 08

Lithology, stratigraphy and age

The recently reoccupied location TVBC 08 was a different colour from the earlier occupied station BC 08. The sediment of core TVBC 08 was composed of 0·19% to 0·56% sand, 16·85% to 26·92% silt and 72·18% to 82·84% clay (Figs 1 and 2).

In core TVBC 08, *C. invaginata* and *C. tuberosa* are found only in the 0 to 2 cm section, representing an approximate date of *ca* 180 ka, whereas *S. universus* and older index fossils are not found in the core suggesting that the top 0 to 2 cm indicate an approximate age of *ca* 180 ka. This young layer overlies a very old (pre Quaternary to late Neogene) pelagic clay represented by mineral grains, glass shards, and occasional radiolarian and ichthyoliths at 4 to 18 cm, with little biostratigraphic value (Gupta, 1991b). Based on these observations no geological age can be inferred for the older substratum. The biostratigraphic record of TVBC 08 (Cruise ABP 04) is consistent with the published results from station BC 08 (Cruise AAS-61) albeit the precise depth of disappearance of above the NR index species (Fig. 2).

Pore water geochemistry and geotechnical properties

The pore water of core TVBC 08 was marginally more alkaline than the northern core TVBC 26, with the pH averaging 7·41 ± 0·07 (Fig. 3A). NO_2^- averaged 0·07 ± 0·05 μM and NO_3^- 8·32 ± 6·08 μM. The NO_2^- and NO_3^- concentrations show similar trends and are undetectable at 6 to 8 cm bsf. Sharp variations in NO_2^-, NO_3^-, pH and porosity are seen at the Tertiary to Pleistocene stratigraphic transition at TVBC 08. The PO_4^{3-} concentration averaged 1·39 ± 0·08 μM whereas silica at 324 ± 11 μM showed a steady profile (Fig. 3A).

Total organic carbon, total inorganic carbon and C/N ratio

The TOC content of the southern pelagic red clays TVBC 08 was highly depleted with average downcore TOC profile varying between 0 to 0·24%. Total organic carbon depletion was maximum

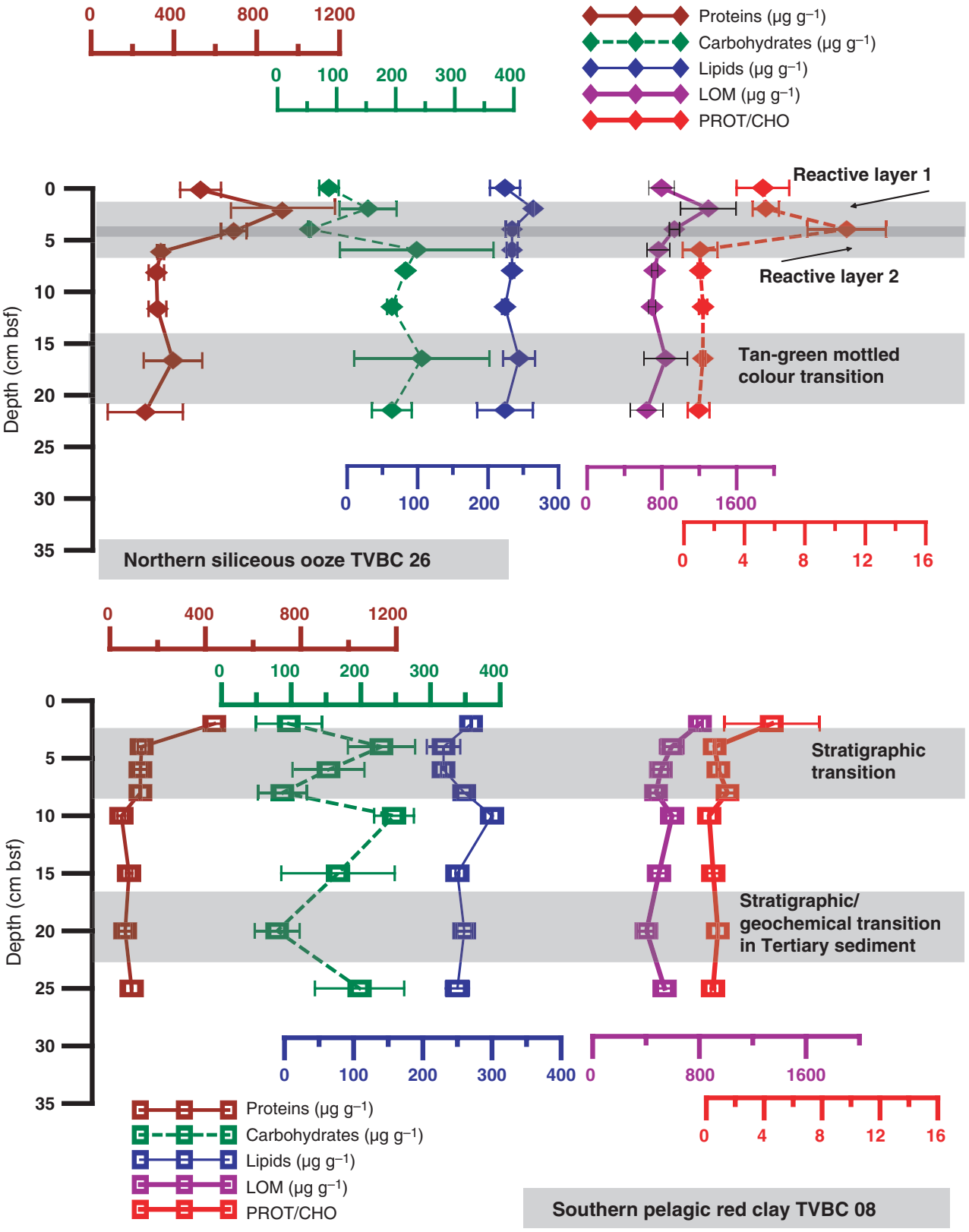

Fig. 4. Biochemical parameters per gram dry sediment (error bars represent sample ranges at individual depths).

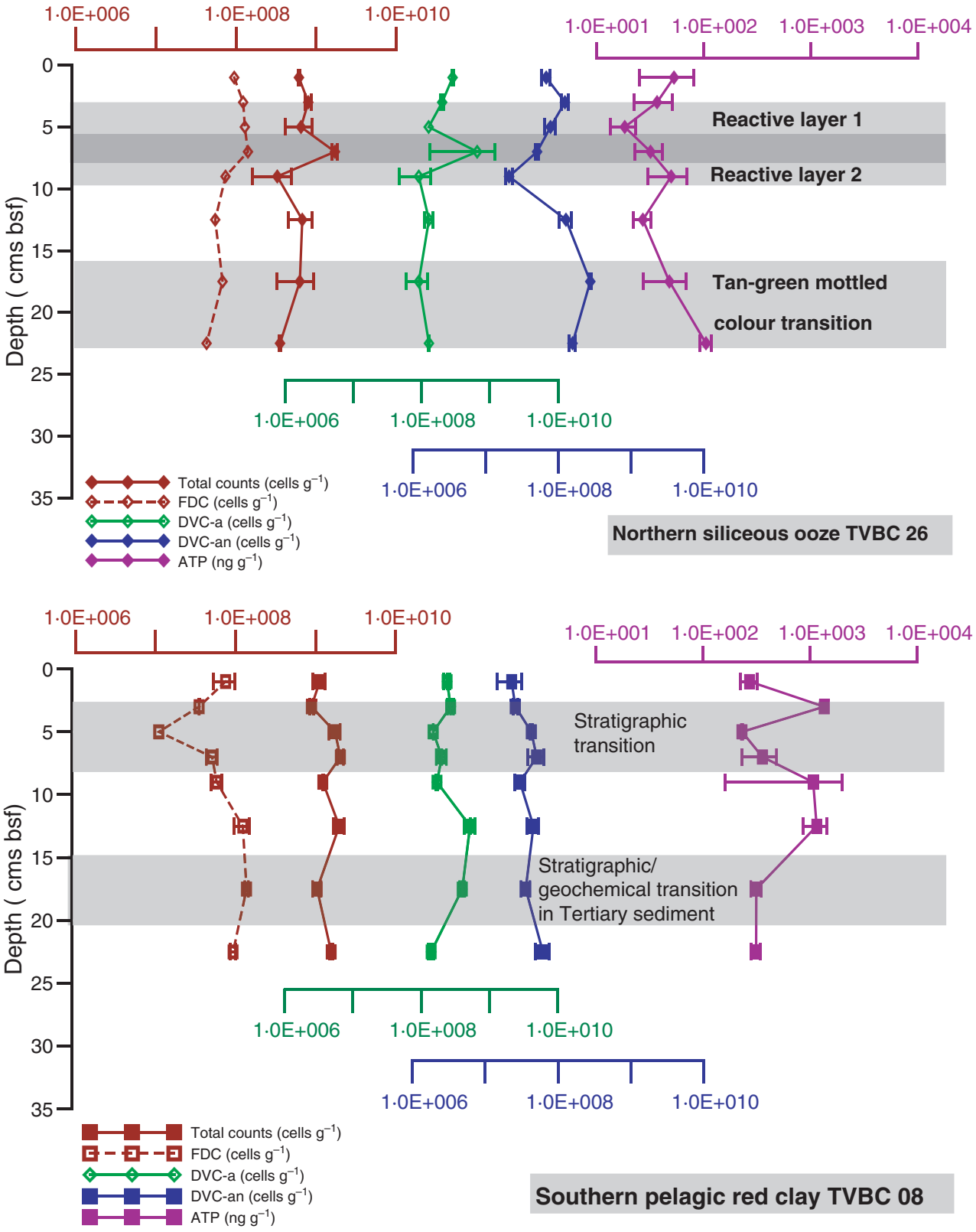

Fig. 5. Bacterial counts and ATP content per gram dry sediment (error bars represent range for samples at individual depths).

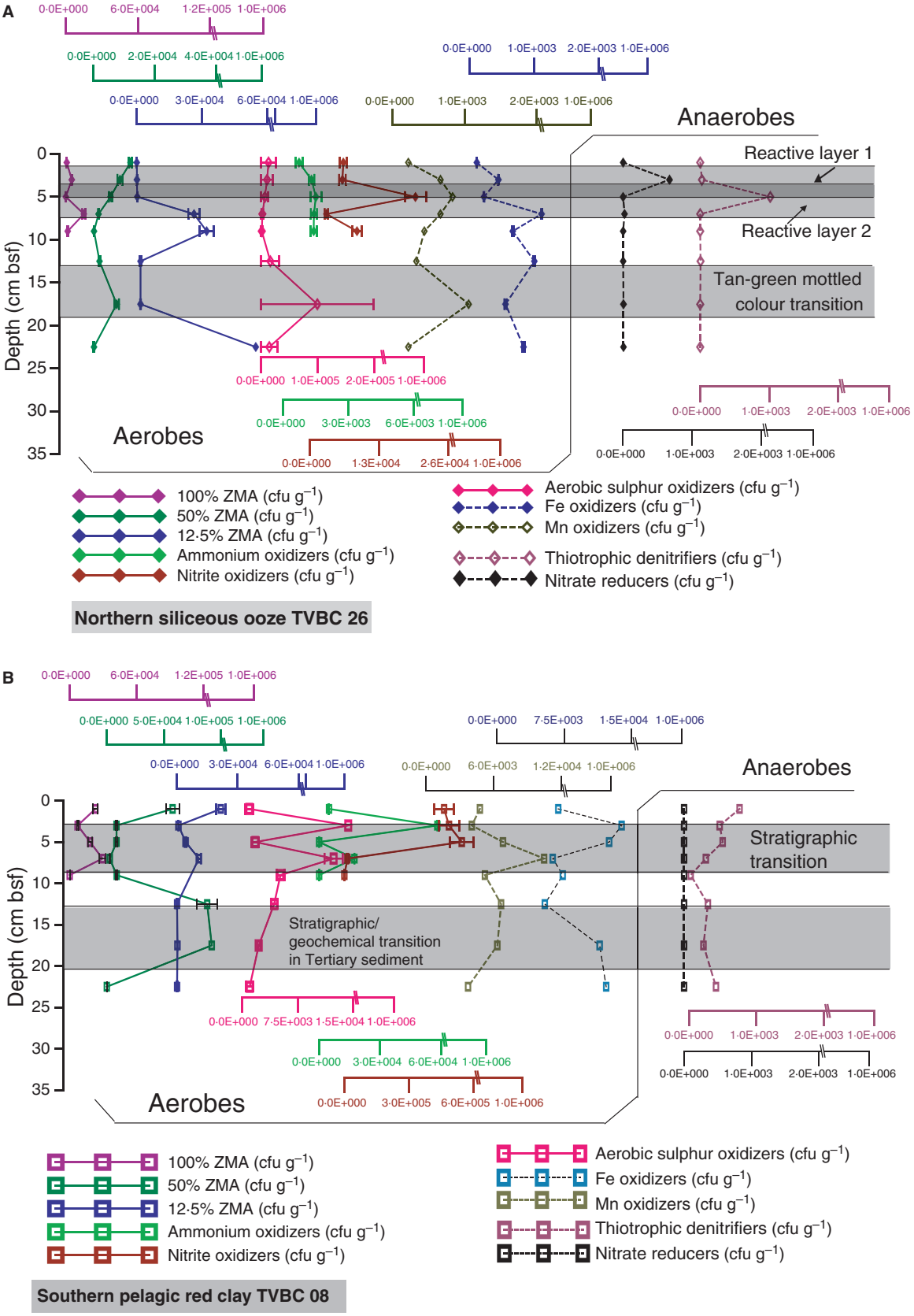

Fig. 6. (A) Culturable bacteria per gram dry sediment in core TVBC 26. (B) Culturable bacteria per gram dry sediment in core TVBC 08 (data points on the *y*-axis suggest very low culturability; the narrow range of less than ± 0·01% variation for individual samples does not appear on this scale).

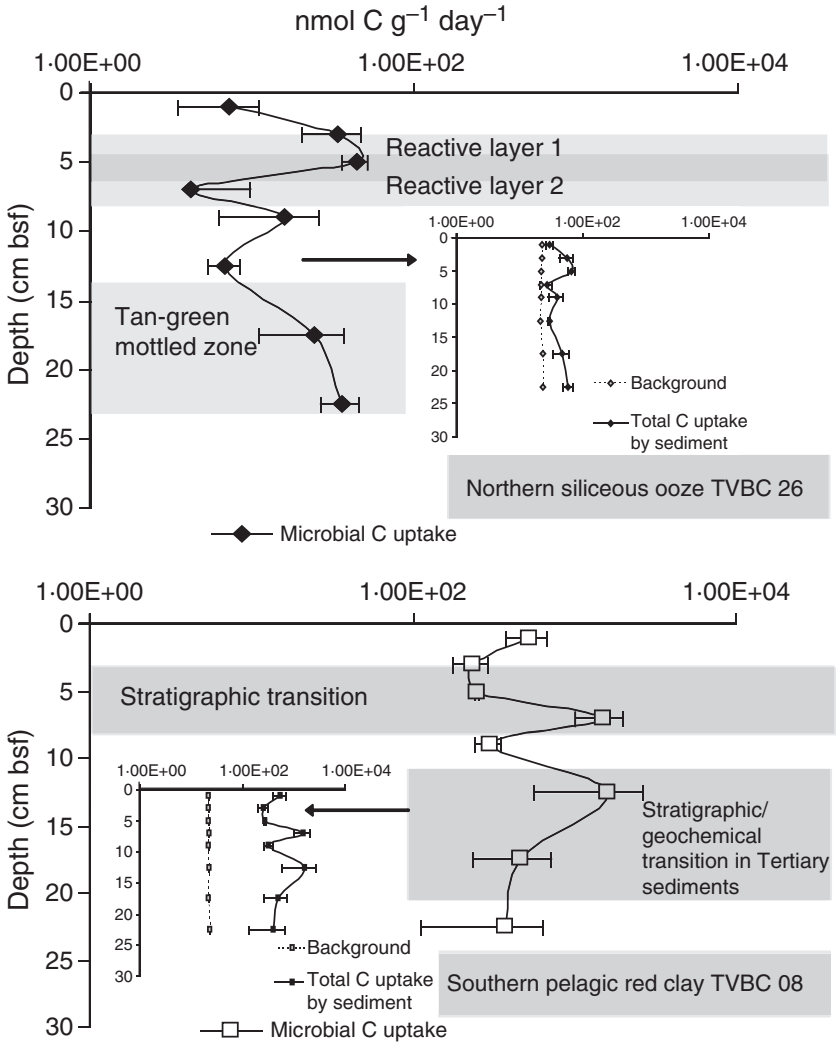

Fig. 7. Microbial carbon uptake by sediments of TVBC 26 and TVBC 08 expressed in nmol C g^{-1} dry sediment day^{-1}. Insets show background values representing heat-killed controls and experimental C uptake.

both in the upper stratigraphic transition and in the deeper 15 to 20 cm bsf layer (Fig. 2). C/N ratio averages *ca* 5 except for a high peak of 14 at the upper limit of the stratigraphic transition zone (2 to 4 cm bsf) indicating preferential nitrogen loss. At greater depths (15 to 25 cm bsf) C/N ratios < 1 were observed indicating relative nitrogen enrichment (Fig. 2). The Tertiary–Pleistocene stratigraphic transition in TVBC 08 coincided with that of geochemical and geotechnical boundaries at 2 to 8 cm bsf with abrupt changes in the C/N ratio, pore water NO_2^- and NO_3^- (Fig. 3A).

Labile organic matter

Labile organic matter values at TVBC 08 were only *ca* 50% of TVBC 26. Protein/carbohydrate ratios were < 1 at TVBC 08, except at 0 to 2 cm and 6 to 8 cm bsf indicating greater recalcitrance (Cauwet, 1978). Significant variations in down-core profiles of all parameters were noted at the stratigraphic transitions of TVBC 08 (Fig. 4). At the deeper layer at 15 to 20 cm bsf, the carbohydrate oxidation coincided with a lower ATP (Fig. 5), higher heterotrophic counts (Fig. 6B) and carbon uptake (Fig. 7), indicating chemo-heterotrophic sections in a predominantly autotrophic core.

Adenosine triphosphate

Adenosine triphosphate values were an order higher in TVBC 08 than in northern TVBC 26 with values ranging from 232 to 1069 ng g^{-1} (Fig. 5).

Bacterial counts

Total bacterial counts and frequency of dividing cells. The total bacterial counts in core TVBC 08 ranged from 8·9E + 08 to 2·0E + 09 cells g^{-1}.

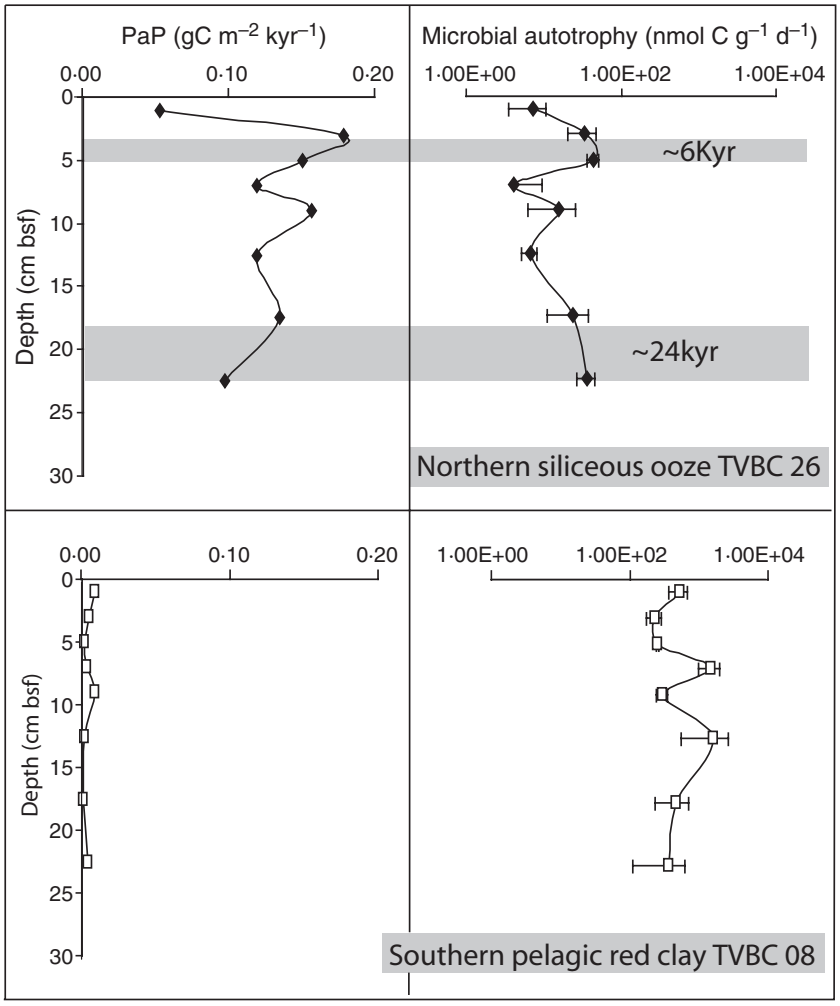

Fig. 8. Comparative profiles of palaeoproductivity and modern autotrophic carbon uptake with respect to geochemical boundaries in the radiometrically determined late Pleistocene to Holocene time scale.

Down-core profiles were almost homogenous (Fig. 5). In core TVBC 08, 5% of the total bacteria were naturally viable. The FDC at station TVBC 08 was two times higher in sub-surface depths of 10 to 25 cm than at the surface (Fig. 5).

Direct viable counts (DVC-a and DVC-an). DVC-a were nearly two times higher at the southern TVBC 08 than at TVBC 26 but the difference was not statistically significant. Prominent variations in TC, FDC, DVC-a and DVC-an were noted at the upper stratigraphic transition and at the deeper 15 to 20 cm bsf layer of TVBC 08 (Fig. 5).

Heterotrophic counts. Triplicate plate counts on ZMA showed that the retrievability from TVBC 08 was generally higher than that from TVBC 26 with a few exceptions. It was more than 15 times higher than TVBC 26 at 100% ZMA, seven times higher at 50% ZMA and almost 1·2 times higher at 12·5% ZMA. A conspicuous peak of $>10^4$ cells g^{-1} of heterotrophs on 50% ZMA was observed at the stratigraphic transition within the Tertiary sediments (Fig. 6A and B).

Potential autotrophs. Total nitrifiers estimated on mineral agar amended with ammonium salt were 250 times higher in TVBC 08. The difference was less in nitrite-amended medium. The retrievability of nitrite oxidizers in TVBC 08 was twice that of TVBC 26 (Fig. 6A and B). Denitrifiers were present uniformly in the southern core TVBC 08 ranging from 250 to 750 cfu g^{-1}, with an order of magnitude less at 8 to 10 cm bsf. The NRB were notably absent in the TOC-poor south in contrast to the northern core (Fig. 6A and B).

In core, TVBC 08, both the Fe-oxidizers and Mn-oxidizers were one order higher than in core TVBC 26. Here, Fe-oxidizers varied from 5·33E + 03 to 1·39E + 04 cfu g^{-1}. Mn-oxidizers

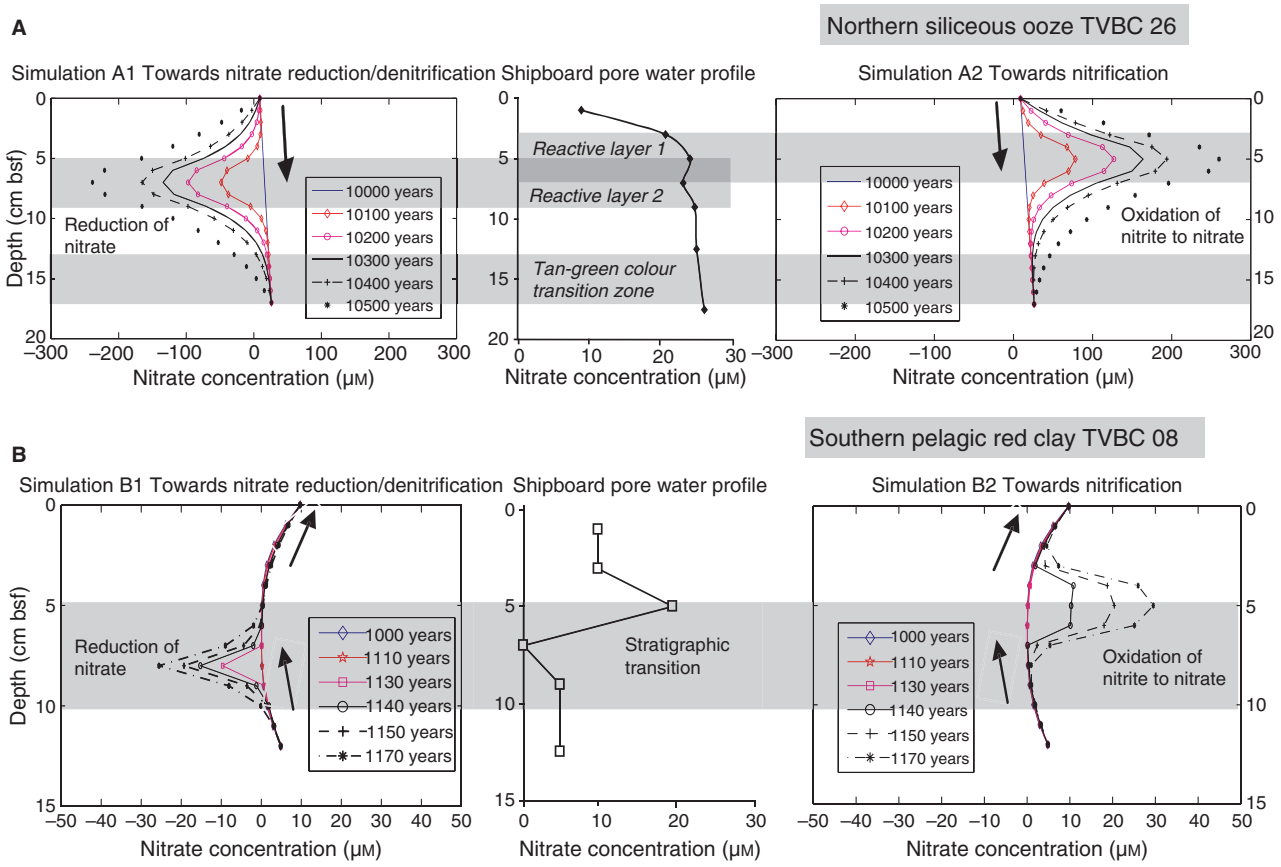

Fig. 9. Numerical simulations (A) Core TVBC 26. Simulation of non-steady state of NO_3^- concentrations in pore water due to diffusion, production and consumption, showing the prevalence of a nitrification–denitrification coupling at 3 to 9 cm bsf. (B) Core TVBC 08. Simulation of hydrothermal alteration of pore water NO_3^- concentrations affected by production, upward diffusion, dispersion due to phase change and consumption by microbes showing the existence of nitrification–denitrification couple at 3 to 9 cm bsf.

varied from 3·72E + 03 to 1·05E + 04 cfu g^{-1} dry sediment. A distinct increase in the abundance of these groups is noted at the stratigraphic transition zones (Fig. 6B).

Microbial uptake of carbon in sediments

Measurement of autotrophic microbial carbon fixation by whole sediment slurries showed marked differences, with nearly 30 times more uptake at TVBC 08 than at TVBC 26. Occasionally, at certain depths of TVBC 08, the carbon uptake was 300 times or more than that of TVBC 26. Core TVBC 08 showed two mid-depth maxima at 6 to 8 cm and 10 to 15 cm, respectively (Fig. 7).

Organic carbon flux, palaeoproductivity and modern microbial autotrophic uptake

Pelagic red clays showed a lower productivity of 30 to 50 mg C m^{-2} day^{-1} corresponding to 10·95 to 18 g C m^{-2} $year^{-1}$ (Matondkar *et al.*, 2005). Less than 0·3% of carbon produced from surface production rains over reaches the red clays. Organic C flux was 0·03 g C m^{-2} $year^{-1}$ and carbon accumulation rates were 0·00046 g C m^{-2} kyr^{-1}. The preservation factor was $3{\cdot}07 \times 10^{-8}$ for pelagic red clay at TVBC 08. Palaeoproductivity ranged from 0·0016 to 0·0097 g C m^{-2} $year^{-1}$ in the pelagic red clays (Fig. 8). Palaeoproductivity and modern microbial autotrophic uptake were independent of each other.

Inter-relationship between bacterial and geochemical parameters

Lower surface productivity (Matondkar *et al.*, 2005), lower sedimentation rates and negligible continental influx are attributed to the low TOC, recalcitrant LOM and the lack of a relationship between the two parameters in the southern TVBC 08 (Figs 2 and 4). The total bacterial counts are dominated by a viable anaerobic population ($P > 0{\cdot}01$) that is correlated negatively with TOC, LOM and C/N ratio. The ^{14}C uptake correlated positively with total bacterial counts and ($P > 0{\cdot}05$).

The ^{14}C uptake related positively only to nitrite oxidizers ($P > 0{\cdot}05$) in the north suggesting that chemosynthesis is highly dependent on the reducing agents that are limited in availability. On the contrary, in the southern core the absence of such a relationship suggests that the chemosynthetic activity is not limited either by availability of reduced substrates. Further, this relationship is not restricted to any specific group.

Quantification of hydrothermal alterations on pore water and microbial community by numerical simulation

The NO_3^- concentration profile measured by shipboard analysis was simulated using a transient diffusion numeric model (Fig. 9B). At 12·5 cm bsf, i.e. below the stratigraphic transition, the observed NO_3^- concentration of 4·85 μM was used as a starting condition. It was also assumed that NO_3^- in sediment pore water is 0. The model calculated the concentration as a function of time and height of core using the core bottom as height zero. The precise time and duration of the explosion is unknown. However, the alteration features indicate a 200 year time span between the explosion and the present time (Nath *et al.*, 2008). Thus an assumption of a 1000 year focused jet-flow was made to simulate the model. For the first 1000 years of explosive volcanism, NO_3^- had diffused upwards as a focused jet after which it started dispersing laterally. Assuming a surface layer with a nitrite oxidation rate of 1000 μM m^{-3} $year^{-1}$ at 9 to 5 cm bsf, the model also shows that the reactant, NO_2^-, will be dispersed and consumed by microbes within a time period of 100 to 200 years in this zone. Conversely, at 7 to 3 cm bsf, the reactant, NO_3^- will be dispersed and consumed within 100 to 200 years with a nitrate reduction rate of −1000 μM m^{-3} $year^{-1}$. The profile returns to its original shape within another 100 to 200 years soon after the utilization of NO_2^- in the lower 9 to 5 cm layer and the simultaneous reduction of NO_3^- in the upper 7 to 3 cm ceases. Due to the continuous abiotic supply of NO_2^- and NO_3^-, in both halves of the reaction, a non-steady nitrification–denitrification coupled profile is sustained and they reproduce the pore water NO_3^- profile measured in the core TVBC 08 (Fig. 9B).

DISCUSSION

Although it was argued that the culturable fraction could wield greater influence on the environment, such inferences remained controversial for two decades, as only 0·001% to 0·01% of the total bacterial count is amenable to cultivation techniques (Van Es & Meyer-Reil, 1982). Prokaryotic processes are now known to be operating on geological time scales and culturable prokaryotes are reported to be stimulated at interfaces (Parkes *et al.*, 2005). The present work reiterates the prevalence of such enhanced bacterial culturability in the CIB that was earlier shown in the Eastern Equatorial Pacific (Parkes *et al.*, 2005; Meister *et al.*, 2007; Wang *et al.*, 2008). This study also demonstrates the occurrence of chemoautotrophic activity coinciding with geochemical and stratigraphic transition zones in both diagenetic and hydrothermally altered sedimentary settings.

Northern core TVBC 26

Influence of organic carbon on microbial carbon uptake

The comparison of a modern microbial autotrophic uptake profile with the palaeoproductivity profile shows a similar trend suggesting heterotrophy dependent on surface-based production. The microbial degradation and recycling of organic matter is evident in reactive layers 1 and 2 representing two halves of any redox cycle in metabolic zones (Fig. 2; see Schulz, 2000 for detailed definitions). Interestingly, the occurrence of this process is evident at the tan-green colour transition zone (Konig *et al.*, 1997) and appears to have operated at a *ca* 10 000 year time span on the Late Pleistocene to Holocene scale (age derived from ^{230}Th decay). Surprisingly, the biostratigraphic change at 180 ka BP also coincides with the tan-green mottled zone; however, its relationship with elemental carbon and nitrogen, if any, is not clear (Fig. 2). Although, a clear dependence on surface derived organic matter is shown by the heterotrophic microbes of TVBC 26, the enhanced chemoautotrophic features at the reactive layers and tan-green transition show that this process is also operational.

Bacteria response to pore water geochemistry in the tan-green mottled zone

The tan-green mottled zones are colour transitions associated with the iron redox boundary. These layers, often referred to as 'sub-oxic' mottles, had been correlated with dissolved NO_3^-, Mn and Fe (Lyle, 1983; Konig *et al.*, 1997). The tan-green mottled zones are found generally below reactive layers 1and 2 which, in turn, are

prominent below the sediment–water interface (Fig. 2). Formations of these mottles in the Pacific Ocean sediments were attributed to high palaeo-productivity, differential sedimentation rates and fluctuations in oceanic redox conditions caused by changes in bottom water oxygen content (Lyle, 1983). Formation of metal enrichment zones in the upper part of the deep-sea sediment column (Colley *et al.*, 1984; Colley & Thomas, 1985) with the active involvement of microbes (Froelich *et al.*, 1979) are also believed to be the cause of these formations.

Non-steady-state diagenetic processes due to downward diffusing oxidants, such as O_2 and NO_3^-, result in the depletion of initially deposited organic carbon. Both oxidized and reduced forms of nitrogen are produced in the active oxidation zones (Buckley & Cranston, 1988). More recently, the temporal shift of geochemical interfaces from shallower temporary reactive to deeper layers results in mottle formation in predominantly detrital settings (Meister *et al.*, 2007, 2009).

Tan-green transitions in the sediment columns from the northern CIB were reported to influence pore water and sedimentary organic carbon profiles. Extensive nitrification coupled with oxic respiration and the possible involvement of bacteria was suggested previously (Nath & Mudholkar, 1989). However, the relevant direct microbial evidence is now presented in this study. Microbiologically, the zone is characterized by an increasing trend of ^{14}C uptake and higher values for the C/N ratio, ATP, DVC-an and denitrifiers (Figs 2, 5, 6 and 7A). Higher C/N ratios in sub-oxic depths of sediments with TOC < 1% has been associated with bacterial oxidation of metals (Farrimond *et al.*, 1989) and reworking of residual organic matter.

Earlier studies on bacteria from these tan-green mottles at 20 to 25 cm bsf highlighted their capability of showing different phases of nitrification (Ram *et al.*, 2001). Nitrate reduction coupled to oxidation of organic matter, followed by fixing of CO_2, is suggestive of recycling and conservation of available organic matter. The depleted NO_2^- concentration (Fig. 3A) and its negative correlation to NO_3^- indicate a coupled bacterial nitrification–denitrification process if explained traditionally. However, formation of dinitrogen and loss of nitrogen under the influence of reactive Mn (Luther *et al.*, 1997) can be attributed to elevated C/N ratios at these depths. Bacterial chemo-denitrification is known to exist in oxygen containing sediments (Luther *et al.*, 1997). Non-steady Mn diagenesis resulting in the enrichment of Mn below these sub-oxic or tan-green transition depths has been suggested earlier in these sediments (Pattan & Jauhari, 2001).

Organic carbon in the reactive layers (Fig. 2) stimulates oxygen consumption by active micro-aerophilic or facultative anaerobic bacteria (for example, nitrifiers, nitrate reducers, aerobic sulphur oxidizers and heterotrophs) during oxic respiration. This oxic process is followed by nitrate reduction within the total 6 cm thick overlapping reactive layers 1 and 2. Also, in these layers, manganese reduction possibly synchronizes with sulphide oxidation. Consequently, the resultant upward diffusion of dissolved metals could feed the nodule accretion process at the sediment water interface (see IVBC 20A pore water profiles in Fig. 3B).

Pore water oxygen concentrations are within ranges previously reported for the deep-sea (Jahnke & Jahnke, 2004). Warren & Johnson (2002) reported *ca* 4 to 4·5 ml l^{-1} (175 to 197 μM) in waters of the northern CIB at *ca* 4600 m below the surface, along 90°E longitude. The convex profile of NO_3^- (Fig. 3A) is indicative of predominantly oxic conditions with net nitrification (Soetaert *et al.*, 1996). A distinct early diagenetic reactive layer is seen at 3 to 9 cm bsf in station TVBC 26. The PO_4^{3-} concentrations are depleted at the diagenetic reactive layer (Schulz, 2000) and within the tan-green mottled zone, and are possibly related to the nitrification–denitrification coupled zones where nitrification is more prominent. The SiO_3^{2-} concentration shows a typical downward increasing trend in TVBC 26 indicating a diffusive flux from the sediment water interface (Nath & Mudholkar, 1989).

The presence of iron-bacteria and manganese-bacteria in higher numbers, along with the thiotrophs, suggests the possible occurrence of sulphide-oxidation along with iron and manganese oxido-reduction in this diagenetic setting, especially at the mottled zone. These associations are common in hydrothermally altered sediments or diffuse flow systems (Bach & Edwards, 2003). Although bacterially mediated Mn^{2+} oxidation by O_2 or NO_3^- may be restricted near oxic zones, processes like thiotrophic nitrate reduction in deep-sea settings are gaining importance. These processes over time lead to the formation of tan-green mottled zones dominated by facultative heterotrophs, manganese-oxidizers and aerobic sulphur oxidizers (Fig. 6A). These bacteria conserve the organic matter chemolithotrophically

by recycling (Stevens, 1997) and re-fixing CO_2 formed during breakdown of organic matter.

The occurrence of sulphide in some of these oligotrophic sediments highlights the greater importance of hydrothermal influence and requires renewed investigations. Although, the co-existence of sulphide and oxygen in 'sub-oxic' or 'oxic-anoxic' transitions are well-known (Glazer *et al.*, 2006), the trends suggest that an inverse distribution of oxygen versus sulphide in pore waters may not always be true. Co-existence of detectable amounts of sulphide, ammonium and oxygen (Fig. 3B), and the presence of manganese oxidizers and thiotrophic bacteria, indicate the possibility of co-occurrence (Wang *et al.*, 2008) or overlap of multiple metabolic zones (Canfield & Thamdrup, 2009). The present results reiterate the importance of sulphide and a possibly underestimated hydrothermal influence in the formation process of ferro-manganese nodules (cf. Glasby, 2006).

Alternatively, rock alteration and volcanic degassing could be a significant process in station TVBC 26 due to its proximity to the Trace of Rodrigues Triple Junction. Under such conditions, autotrophy at the mottled zones could be associated with fluid percolation through these sediment strata (Sizaret *et al.*, 2009). Even then, station TVBC 26 would not be an independent chemoautotrophic system as a major fraction of the organic flux is derived from the highly productive South Equatorial Boundary Current-driven surface waters. Core TVBC 26 would be analogous to hydrocarbon rich layers mutually influenced by organic matter rain and hydrothermal fluid flow. However, the scale and extent of the processes could be highly reduced.

Quantification of the influence of non-steady-state diagenetic condition on microbial community by numerical simulation

The numerical simulation (Fig. 9A) suggests the prevalence of bacterial nitrate reduction–nitrite oxidation coupling at the reactive layers. Consequently, a mottled zone forms at deeper layers and reduced metal species oxidize near the sediment–water interface. Sigmoid profiles of NO_3^- concentration at the reactive layers are suggestive of formation and subsequent utilization of the ion at this shallow depth. The deposition of a 4 cm thick organic carbon-rich layer and upward migration of reduced metal species like Mn^{2+} leads to the coupling of nitrate reduction to nitrite oxidation. These coupled processes may reach a rate of $\pm$ 1000 $\mu M\ m^{-3}\ year^{-1}$; consequently, this leads to rapid formation and removal of NO_3^- and a new nitrite oxidizing–nitrate reducing interface may be formed. This interface may potentially migrate upwards from 3 to 9 cm bsf to the surface, thus allowing manganese nodule precipitation in the form of MnO_2 at the surface. The precipitation of these manganese nodules could be analogous to dolomite precipitation above sulphate–methane interfaces (Rao *et al.*, 2003; Meister *et al.*, 2007, 2009). High chemosynthetic activity has been noted in these reactive layers similar to that in sulphate–methane interfaces and dolomite deposits observed at Blake Ridge (Rodriguez *et al.*, 2000) and ODP site 1229 in the Eastern Equatorial Pacific (Meister *et al.*, 2007). The relative compactness of porous siliceous ooze sediments at these depths (Fig. 3A) reduces permeability, partially restricting horizontal transfer and utilization of NO_3^-, in these clay-rich sediments; this results in the formation of horizontal mottled layers (Figs 2 and 3).

Southern core TVBC 08

Influence of organic carbon on microbial carbon uptake

The microbial autotrophic uptake profile of core TVBC 08 shows no relationship to the palaeoproductivity profile suggesting greater chemoautotrophy and independence from surface based production (Fig. 8). The depletion of organic content and the additional influence of hydrothermally derived pore-fluids appear to have triggered a greater microbial carbon uptake. A net autotrophic bacterial community with higher nitrifiers and nutritionally flexible heterotrophs inhabit the southern TOC-poor sediments of TVBC 08. These observations are further supported by a positive correlation ($P > 0{\cdot}05$) between ^{14}C uptake and total bacterial counts. The greater number of FDC at the TOC-depleted lower depths suggests the utilization of inorganic substrates in hydrothermally altered fluids promoting greater autotrophic activity.

Influence of hydrothermal alterations on pore water and bacterial activity

Mid-plate volcanic and hydrothermally altered area, TVBC 08 (Mascarenhas-Pereira *et al.*, 2006; Iyer *et al.*, 2007; Nath *et al.*, 2008) hosts a predominantly chemoautotrophic microbial population. The possibility of nitrogen species emanating out of the circulating hydrothermal fluids (Gieskes *et al.*, 2002) and advecting upwards before spreading laterally at 4 to 8 cm bsf (Fig. 3A)

due to diffusive transport at the stratigraphic interface (Gieskes *et al.*, 2002) is explored in the present work.

Fluid phase separation during hydrothermal alterations is known to produce higher and lower phases of solutes. Although the higher phases rapidly migrate by advection towards the surface, presumably along cracks and faults, the lower ones get transported laterally along more porous zones in the sediments; here they may get utilized by bacteria. A recent study by Nath *et al.* (2008) interpreted the influence of neutral chloride type hydrothermal fluids to be predominant in these altered sediments. Intense hydrothermal alteration features were reflected in: (i) the depleted sedimentary organic carbon (also observed in the present study, see Fig. 2); (ii) dissolution features of radiolarian skeletons; (iii) the presence of altered minerals such as smectite and zeolites; and (iv) distinctly different magnetic properties in the altered sediments. An excess of ^{210}Pb over its parent was recorded in the lower semi-indurated sediments. Bioturbation and slumping of older sediments from the shallower portions of the seamount were ruled out for the $^{210}Pb_{exc}$ as the sediments lacked benthic biota, organic matter and detectable carbonate content (Nath *et al.*, 2008).

The PO_4^{3-} in TVBC 08 is lower than TVBC 26. However, the presence of a PO_4^{3-} concentration > 1 μM in organically depleted environments with distinct enrichment in Fe in an oxidized state, compared to the pelagic clays occurring in the CIB (Nath *et al.*, 2008) indicates possible hydrothermal origin and co-precipitation with the metal oxides (Yamagata *et al.*, 1991; Karl, 1995). The SiO_3^{2-} concentrations show little variation and a lower diffusional gradient in TVBC 08.

Adenosine triphosphate values (Fig. 5) are similar to the range reported from Guaymas Basin (Table 1). Although extensively reported from waters and bacterial mats of vent fields, reports on ^{14}C incorporation rates of whole sediments are still scanty. It is noted that ^{14}C incorporation rates (Fig. 7) of CIB sediments when normalized to bacterial numbers are similar to some water samples of Juan de Fuca and white smokers of the 21°N East Pacific Rise (Table 2).

The contribution of LOM and faunal numbers to higher measurements of ATP at TVBC 08 is minimal. Negligible numbers of macrofauna and meiofauna (Ingole *et al.*, 2005) suggest that there could be little contribution by these organisms. Moreover, ATP does not relate to any of the other parameters measured, suggesting that the higher ATP in the south could be due more to hydrothermally produced analogues rather than being organically derived (Liu *et al.*, 1982; Yamagata *et al.*, 1991). The high ATP in TVBC 08 (Fig. 5, Table 1) could therefore be due to the inclusion of large amounts of pyrophosphate or polyphosphates formed during rapid cooling in hydrothermal systems (Yamagata *et al.*, 1991). The presence of Fe in an oxidized state (Nath *et al.*,

Table 1. Comparison of ATP values of other established vent fields to Central Indian Basin stations.

Location	Type	Range of ATP (ng g^{-1})	Reference
21°N EPR	Particulate matter, black smoker	71–125	Karl *et al.*(1989)
Guaymas Basin	Sediments	68–1005	Haberstroh & Karl (1989)
	Control deep-sediments	100–200	Haberstroh & Karl (1989)
TVBC-26, 10°S, 75°30′E	Sediments (northern, TOC-rich)	18–106	Present work
TVBC-08, 16°S, 75°30′E	Sediments (southern, TOC-poor)	232–1354	Present work

Table 2. Comparison of ^{14}C incorporation values of Central Indian Basin stations to other established vent fields.

Location	Type	^{14}C incorporation*	Condition	Reference
21°N, EPR	Water, White smoker	12·7	1 atm, 3 °C, 24 h, dark	Wirsen *et al.* (1986)
Juan de Fuca	Water	201·7	1 atm, dark	Chase *et al.* (1985)
Guaymas Basin	Bacterial mats	444 000	1 atm, dark, 28 °C	Nelson *et al.* (1989)
Guaymas Basin	Bacterial mats	12 000	1 atm, dark, 8 °C	Nelson *et al.* (1989)
TVBC-26	Sediments	5–45	1 atm, dark, 5°C	Present work
TVBC-08	Sediments	230–1600	1 atm, dark, 5 °C	Present work

*^{14}C incorporation units are nmol l^{-1} day^{-1} CO_2 for water samples and nmol g^{-1} dry wt day^{-1} for sediments and bacterial mats. The rates are normalized to bacterial numbers for comparison.

2008) and the anomalous bulk phosphate (Nath *et al.*, 2005) suggests scavenging of hydrothermal phosphorus by iron, leading to the formation of bio-available pyrophosphate and its subsequent utilization as an alternate pathway for channelling geothermal-based energy in the biosphere (Liu *et al.*, 1982).

The hydrothermal origin of ammonium or other reduced nitrogenous species from deeper layers is indicated by the pore water profiles of NO_2^- and NO_3^-. Higher total nitrogen values and a C/N ratio < 1 at 20 to 25 cm bsf both indicate excess of nitrogen. The high C/N ratio and depletion of NO_2^- and NO_3^- is probably caused by the preferential loss of N during metamorphic volatilization (Bebout & Fogel, 1992) at the upper stratigraphic transition between Pleistocene and Tertiary sediments (Fig. 2). Where there is minimal contribution of organic matter, this excess can only be derived from hydrothermal fluids. Similar findings have been reported from Suiyo Seamount at Izu-Bonin backarc system (Takano *et al.*, 2004) and the shallow vent systems of Vulcano Islands (Gugliandolo & Maugeri, 1998). Rapid conversion of dissolved NO_3^- and NO_2^- to NH_4^+ rather than to N_2, particularly in the presence of Fe and Ni as seen in ODP Leg 201 pore water data (Smirnov *et al.*, 2008), could explain the abrubt fluctuations of nitrogen. Different transport routes for higher and lower phases of hydrothermally altered fluids while cooling can produce distinct changes both in bacterial number and activity. These alterations occur (Figs 5 to 7) at sediment layers with varying porosity and pH (Figs 2 and 3; Gieskes *et al.*, 2002).

The high peak of the C/N ratio with low TOC (Fig. 2) and LOM in the upper 2 to 4 cm bsf (Fig. 4) corresponds to the highest ATP, ammonia oxidizers and aerobic sulphur oxidizers (Figs 5 and 6). This layer is sandwiched between carbon uptake maxima (Fig. 7) suggesting the chemolithotrophic utilization of inorganic substrates made available during phase separation of solutes.

Venting activities can produce ammonia where nitrifying bacteria can thrive (Karl, 1995). The higher number of autotrophic nitrifiers and the significant correlation between ammonium oxidizers and aerobic sulphur oxidizers suggests a more hydrothermal origin for the ammonium feeding the nitrite oxidizers (Wirsen *et al.*, 1986; Karl, 1995). The presence of large numbers of thiotrophs, iron-oxidizers and manganese-oxidizers indicates that hydrothermal alterations or diffuse flow might influence the sulphide-oxidation and iron metabolism in this core (Bach & Edwards, 2003).

Synchronization of carbohydrate maxima with the zone of high ^{14}C uptake at 15 to 20 cm bsf possibly is suggestive of chemoautotrophy by mixotrophs. Large fractions of heterotrophic bacteria inhabited this lower non-dateable stratigraphic transition within the Tertiary sediments. Higher adaptability and resilience of bacteria are associated with relatively oligotrophic sediments (Harder & Dijkhuizen, 1982; Goltekar *et al.*, 2006) like the organically depleted core TVBC 08. Similar unexplained high heterotrophic populations have been reported in some earlier findings in vent sites with low organic carbon (Karl, 1995).

Although the nitrifiers, aerobic sulphur oxidizers and heterotrophs exist in large numbers and contribute partly to ATP and ^{14}C uptake, they do not have a statistically significant relationship with the pore water nitrogen species or the C/N ratio in TVBC 08. This observation is contrary to the diagenetic TVBC 26 where these retrievable bacteria show a statistically significant relationship with other biochemical and pore water parameters. The results indicate the predominance and activity of a distinct functional group capable of exhibiting chemolithotrophy through multiple metabolic pathways. These microbes flourish in the remnant inorganic substrates derived from explosive hydrovolcanism that geochemists believe to have occurred *ca* 200 years ago (Nath *et al.*, 2008). Examining the whole community at the molecular level would complement the present studies and throw more light on both their taxonomy and function.

Quantification of hydrothermal alterations on pore water and microbial community by numerical simulation

The numerical simulation (Fig. 9B) suggests the prevalence of a nitrite oxidation–nitrate reduction coupling at the Pleistocene–Tertiary stratigraphic interface due to lateral dispersion and phase separation of solute during cooling of upwelled hydrothermal fluid. Consequently, there is an enhancement of bacterial abundance and activity at the stratigraphic transition zone (Figs 5 to 7) due to the availability of inorganic substrates made utilizable by processes such as phase separation of solutes. Sigmoid profiles of NO_3^- concentration at the stratigraphic transition are suggestive of formation and subsequent utilization of the ions at this transition zone. The 6 cm

transition zone in core TVBC 08 and upward migration of reduced chemical species from hydrothermally altered fluids leads to the coupling of nitrate reduction to nitrite oxidation; consequently, this leads to rapid formation and removal of NO_3^-. A new nitrite oxidizing–nitrate reducing transition gets formed. The pore water NO_2^- profile would run parallel to that of NO_3^- and would not be analogous to those derived from organic matter diagenesis (for example, Core TVBC 26) when there is continuous supply. Hence, the NO_3^- profile is altered by the presence of hydrothermally derived reduced substrates.

An initial vertical focused-jet of hydrothermally altered fluid evolves into a lateral diffusion at the Pleistocene–Tertiary stratigraphic transition and allows for hydrothermal precipitation of Fe, Ti, P, etc., as reported earlier by Nath *et al.* (2008). A negative rock alteration index denoting precipitation (Zhao *et al.*, 2009) may be expected at 3 to 7 cm bsf sandwiched between positive ones denoting dissolution. Although neutral chloride type hydrothermal activity is indicated by previous studies (Nath *et al.*, 2008), more comprehensive data on thermal and Cl^- anomalies would be helpful for simulating improved models.

Variation in porosity (Fig. 3B) at the stratigraphic transition zone is sharp. The effect of advection and interactions between fluid flow, heat transfer, mass transport and chemical reactions needs to be considered in a comprehensive manner using coupled transport models or finite element models (Yang *et al.*, 2004; Ma *et al.*, 2006; Zhao *et al.*, 2009) taking into account the complex stratigraphic features.

CONCLUSION

The distinctions between types of microbial autotrophic activity at different geological end-member settings are identifiable and quantifiable by multi-disciplinary approaches. Content and quality of organic matter and flow of hydrothermal heat, fluid and solutes are the most important factors controlling autotrophic activity in deep-sea sediments. The present study explores the domain of chemoautotrophy in the deep-abyssal basins of the Central Indian Basin with a combination of low organic content and diffuse low temperature hydrothermal alterations.

In Central Indian Basin sediments, a decrease in organic matter tends to elevate microbial carbon uptake in the bacterial communities. The northern core TVBC 26 is predominantly heterotrophic with chemosynthetic signatures at the tan-green mottled zones. The bacterial activity is only partially dependent on the surface productivity at core TVBC 26. The depth of reactive layers and tan-green mottled zones coincides with high chemosynthetic activity and low palaeosurface productivity. The autotrophy prevailing in the tan-green transition is analogous to the organic matter fossilization and hydrocarbon formation in organic rich sedimentary settings (Campbell, 2006; Ma *et al.*, 2006; Mazumdar *et al.*, 2009).

The southern core TVBC 08 is predominantly autotrophic with heterotrophic microbial signatures in the deeper layers. Here chemoautotrophy is totally independent of surface productivity. The heterotrophy in the deeper parts of southern core TVBC 08 is possibly akin to the formation of new degradable organic compounds in hydrothermal settings. This system is possibly analogous to settings like the Loihi Seamount. Further study of this location may provide interesting insights into tracing pre-biotic origins and explorations for lunar, martian or jovian planetary systems (Goodman *et al.*, 2004).

The role of thiotrophs in deep-sea sediments is prominent in both diagenetic and hydrothermally altered sediments. Processes like thiotrophic nitrate reduction may be more influential in the northern total organic carbon and sulphide-rich sediments. The data highlights the necessity for renewed investigations involving pore water NH_4^+, HS^-, Mn and Fe in oxic conditions. Thiotrophs in hydrothermally altered sediments or diffuse flow systems might be influencing sulphide-oxidation and iron metabolism. The presence of large numbers of iron-oxidizers, manganese-oxidizers and thiotrophs at the mottled zones of TVBC 26 and in hydrothermally altered core TVBC 08 indicate their close relationship to rock alteration and mineralization processes.

These findings could stimulate the pursuit of chemosynthesis for sequestering CO_2 in the deep sea floor. The present study also adds a theoretical dimension for expanding the potential for hydrocarbon exploration in the ocean as discussed earlier in the Pacific nodule province by Wenxuan *et al.* (2002). In these stretches of metal-rich oligotrophic abyssal sediments, hydrothermal activities may predominate, at least over a 100 to 1000 year time scale and require further quantification. However, hydrothermal activity and associated rock alteration processes may be

more relevant than organic matter delivery in these deep-sea sediments.

ACKNOWLEDGEMENTS

The authors are grateful to S. R. Shetye, Director, National Institute of Oceanography for his encouragement. V. Subramaniam and M.-J. B. D. De Souza helped with the microbial ^{14}C uptake analyses. J. N. Pattan, K. P. Krishnan and Siby Kurian are acknowledged for their help during the course of the work. V. Nanjundaiah (IISc, India), Deiter Wolf-Gladrow (AWI, Germany), D. Shankar, A. Mazumdar and N.T. Manoj introduced AD to the field of numerical simulations and codes, conceptual biogeochemical and biological modelling. Facilitation on-board by the shipboard scientific party and crew of *Akademik Alexandr Sidorenko* (Cruise 61, 2003), *Akademik Boris Petrov* (Cruise 4, 2005) and *Akademik Boris Petrov* (Cruise 38, 2009) is acknowledged. Special thanks are due to Patrick Meister (ETH-Zürich/ Bremen University) and other anonymous reviewer(s) for their critical guidance leading to the significant improvement in the manuscript. This work was financially supported by the Ministry of Earth Sciences, Government of India. AD, CEGF and SPP acknowledge the Council of Scientific and Industrial Research (CSIR), New Delhi, for funding their research work. This study is NIO Contribution No. 4786.

REFERENCES

Aldrich, A.P. and **van der Berg, C.M.G.** (1998) Determination of Fe and its redox speciation in seawater using catalytic cathodic stripping voltametry. *Electroanalysis*, **10,** 369–373.

ASTM (1995). *Annual Book of ASTM Standards, 04.08*. Soil and Rocks (I) D420-D4914, ASTM, Philadelphia, PA, 981 pp.

Bach, W. and **Edwards, K.** (2003) Iron and sulphide oxidation within the basaltic ocean crust: implications for chemolithoautotrophic microbial biomass production. *Geochim. Cosmochim. Acta*, **67,** 3871–3887.

Banakar, V.K., Gupta, S.M. and **Padmavathi, V.K.** (1991) Abyssal sediment erosion in the Central Indian Basin: evidence from radiochemical and radiolarian studies. *Mar. Geol.*, **96,** 167–173.

Bebout, G.E. and **Fogel, M.L.** (1992) Nitrogen-isotope compositions of metasedimentary rocks in the Catalina Schist, California: implications for metamorphic devolatilization history. *Geochim. Cosmochim. Acta*, **56,** 2839–2849.

Bligh, E.G. and **Dyer, W.J.** (1959) A rapid method of total lipid extraction and purification. *Can. J. Biochem. Physiol.*, **37,** 911–917.

Borole, D.V. (1993) Late Pleistocene sedimentation: a case study of the Central Indian Ocean Basin. *Deep-Sea Res.*, **40,** 761–775.

Buckley, D.E. and **Cranston, R.E.** (1988) Early diagenesis in deep sea turbidites: the imprint of palaeo-oxidation zones. *Geochim. Cosmochim. Acta*, **52,** 2925–2939.

Campbell, K.A. (2006) Hydrocarbon seep and hydrothermal vent paleoenvironments and paleontology: past developments and future research directions. *Palaeogeogr. Palaeoclimatol. Palaeoecol.,* **232,** 362–407; doi: 10.1016/j.palaeo.2005.06.018.

Canfield, D.E. (1991) Sulfate reduction in deep sea sediments. *Am. J. Sci.*, **291,** 177–188.

Canfield, D.E. and **Thamdrup, B.** (2009) Towards a consistent classification scheme for geochemical environments, or, why we wish the term 'suboxic' would go away. *Geobiology*, **7,** 385–392.

Cauwet, G. (1978) Organic chemistry of seawater particulates: concepts and developments. *Oceanol. Acta*, **1,** 99–105.

Chase, R.L., Delaney, J.R., Karsten, J.L., Johnson, H.P., Juniper, S.K., Lupton, J.E., Scott, S.D., Tunnicliffe, V., Hammond, S.R. and **McDuff, R.E.** (1985) Hydrothermal vents on an axis seamount of the Juan de Fuca ridge. *Nature*, **313,** 212–214.

Chevaldonne, P., Desbruyeres, D. and **Le Haitre, M.** (1991) Time-series of temperature from three deep-sea hydrothermal vent sites. *Deep-Sea Res. A*, **38,** 1417–1430.

Childress, J.J., Fisher, C.R., Favuzzi, J.A., Kochevar, R.E., Sanders, N.K. and **Alayse, A.M.** (1991) Sulphide-driven autotrophic balance in the bacterial symbiont-containing hydrothermal vent tubeworm *Riftia pachyptila*. *Biol. Bull.*, **180,** 135–153.

Colley, S. and **Thomas, J.** (1985) Recurrent uranium relocations in distal turbidites emplaced in pelagic conditions. *Geochim. Cosmochim. Acta*, **49,** 2339–2348.

Colley, S., Thomson, J., Wilson, T.R.S. and **Higgs, N.C.** (1984) Post depositional migration of elements during diagenesis in brown clay and turbidite sequences in the North East Atlantic. *Geochim. Cosmochim. Acta*, **48,** 1223–1235.

Colombini, M.P. and **Fuocco, R.** (1983) Determination of manganese at ng/ml levels in natural water by differential pulse polarography. *Talanta*, **30,** 901–905.

Das, P., Iyer, S.D. and **Kodagali, V.N.** (2007) Morphological characteristics and emplacement mechanism of the seamounts in the Central Indian Ocean Basin. *Tectonophysics*, **443,** 1–18.

Delistraty, D.A. and **Hershner, C.** (1983) Determination of adenine nucleotide levels in Zostera marina (eelgrass). *J. Appl. Biochem.*, **5,** 404–405.

D'Hondt, S., Rutherford, S. and **Spivack, A.J.** (2002) Metabolic activity of sub-surface life in deep-sea. *Science*, **295,** 2067–2070.

D'Hondt, S., Jørgensen, B.B., Miller, D.J., Batzke, A., Blake, R., Cragg, B.A., Cypionka, H., Dickens, G.R., Ferdelman, T., Kai-Uwe Hinrichs, K.-U., Holm, N.G., Mitterer, R., Spivack, A., Wang, G., Bekins, B., Engelen, B., Ford, K., Gettemy, G., Rutherford, S.D., Sass, H., Skilbeck, C.G., Aiello, I.W., Gue'rin, G., Christopher, H., House, C.H., Inagaki, F., Meister, P., Naehr, T., Niitsuma, S., Parkes, R.J., Schippers, A., Smith, D.C., Teske, A., Wiegel, J., Padilla, C.N. and **Juana Luz Solis Acosta, J.L.S.** (2004) Distributions of microbial activities in deep subseafloor sediments. *Science*, **306,** 2216–2221.

Edwards, K.J., Bach, W. and **McCollom, T.M.** (2004) Neutrophilic iron-oxidizing bacteria in the ocean: their habitats,

diversity, and roles in mineral deposition, rock alteration, and biomass production in the deep-sea. *Geomicrobiol. J.*, **21,** 393–404.

Ehrlich, H.L. (1998) Geomicrobiology: its significance for geology. *Earth-Sci. Rev.*, **45,** 45–60.

Farrimond, P., Eglinton, G., Brassell, S.C. and **Jenkyns, H.C.** (1989) Toarcian anoxic event in Europe an organic geochemical study. *Mar. Petrol. Geol.*, **6,** 136–147.

Fichez, R. (1991) Composition and fate of organic matter in submarine cave sediments: implications for the biogeochemical cycle of organic carbon. *Oceanol. Acta*, **14,** 369–377.

Folk, R.L. 1968. *Petrology of Sedimentary Rocks*. University of Texas, Austin, TX, 170 pp.

Froelich, P.N., Klinkhammer, G.P., Bender, M.L., Luedtke, G.R., Heath, G.R., Cullen, D., Dauphin, P., Hammond, D., Hartman, B. and **Maynard, V.** (1979) Early oxidation of organic matter in pelagic sediments of the eastern equatorial Atlantic: sub-oxic diagenesis. *Geochim. Cosmochim. Acta*, **43,** 1075–1090.

Ghosh, A.K. and **Mukhopadhyay, R.** (1999) Exploration. In: *Mineral Wealth of the Ocean*, pp. 176–203. Oxford and IBH Publishing Co. Pvt. Ltd, New Delhi.

Gieskes, J.M., Simoneit, B.R.T., Goodfellow, W.D., Baker, P.A. and **Mahn, C.** (2002) Hydrothermal geochemistry of sediments and porewaters in Escanaba Trough – ODP Leg 169. *Appl. Geochem.*, **17,** 1435–1456.

Glasby, G.P. (2006) Manganese: predominant role of nodules and crusts. In: *Marine Geochemistry* (Eds H.D. Schulz and M. Zabel), pp. 371–428. Springer, Berlin.

Glazer, B.T., Luther III, G.W., Konovalov, S.K., Friederich, G.E., Trouwborst, R.E. and **Romanov, A.S.** (2006) Spatial and temporal variability of the Black Sea suboxic zone. *Deep-Sea Res. II*, **53,** 1756–1768.

Goltekar, R.C., Krishnan, K.P., DeSouza, M.J.B.D., Paropkari, A.L. and **Loka Bharathi, P.A.** (2006) Effect of carbon source concentration and culture duration on retrievability of bacteria from certain estuarine, coastal and offshore areas around peninsular India. *Curr. Sci.*, **90,** 103–106.

Goodman, J.C., Collins, G.C., Marshall, J. and **Pierrehumbert, R.T.** (2004) Hydrothermal plume dynamics on Europa: implications for chaos formation. *J. Geophys. Res.*, **109,** E03008; doi: 10.1029/2003JE002073.

Grasshoff, K., Ehrhardt, M. and **Kremling, K.** (1983) *Methods of Seawater Analysis*, 2nd edn. Verlag Chemie, Weinheim, Deerfield Beach, FL, 419 pp.

Gugliandolo, C. and **Maugeri, T.L.** (1998) Temporal variations in heterotrophic mesophilic bacteria from a marine shallow hydrothermal vent off the Island of Vulcano (Eolian Islands, Italy). *Microb. Ecol.*, **36,** 13–22.

Gupta, S.M. (1991a) Radiolarian zonation and volcanic ash-layers in two sediment cores from the Central Indian Basin. *J. Paleontol. Soc. India*, **33,** 59–71.

Gupta, S.M. (1991b) New ichthyoliths from ferromanganese crusts and nodules from the Central Indian Ocean Basin. *Micropaleontology*, **37,** 125–147.

Gupta, S.M. and **Jauhari, P.** (1994) Radiolarian abundance and geochemistry of the surface sediments from the Central Indian Basin. *Curr. Sc.*, **66,** 659–663.

Haberstroh, P.R. and **Karl, D.M.** (1989) Dissolved free amino acids in hydrothermal vent habitats of the Guaymas Basin. *Geochim. Cosmochim. Acta*, **53,** 2937–2945.

Hagstrom, A., Larsson, U., Horstedt, P. and **Normark, S.** (1979) Frequency of dividing cells, a new approach to the determination of bacterial growth rates in aquatic environments. *Appl. Environ. Microbiol.*, **37,** 805–812.

Harder, W. and **Dijkhuizen, L.** (1982) Strategies of mixed substrate utilization in microorganisms. *Philos. Trans. Roy. Soc. London B*, **297,** 459–480.

Havert, H.H. (1992) Genus *Siderocapsa* (and other iron or manganese-oxidizing eubacteria). In: *The Prokaryotes – A Handbook on the Biology of Bacteria, Ecophysiology, Isolation, Identification and Applications* (Eds A. Balows, H.G. Trüper, M. Dworkin, W. Harder and K.-H. Schleifer), Vol. IV, pp. 4102–4113. Springer-Verlag, New York, Inc.

Hobbie, J.E., Daley, R.J. and **Jasper, S.** (1977) Use of Nucleopore filters for counting bacteria by fluorescent microscopy. *Appl. Environ. Microbiol.*, **3,** 1225–1228.

Holm-Hansen, O. and **Booth, C.R.** (1966) The measurement of adenosine triphosphate in the ocean and its ecological significance. *Limnol. Oceanogr.*, **11,** 510–519.

Ingole, B.S., Pavitran, S., Goltekar, R. and **Gonsalves, S.** (2005) Faunal diversity and abundance. In: *Benthic Environmental Variability in the Central Indian Ocean Basin-I*, pp. 83–103. Project report submitted to Department of Ocean Development, Government of India, New Delhi.

Iyer, S.D., Mascarenhas-Pereira, M.B.L. and **Nath, B.N.** (2007) Native aluminium (spherules and particles) in the Central Indian Basin sediments: implications on the occurrence of hydrothermal events. *Mar. Geol.*, **240,** 177–184.

Jahnke, R.A. and **Jahnke, D.B.** (2004) Calcium carbonate dissolution in deep sea sediments: reconciling microelectrode, porewater and benthic flux chamber results. *Geochim. Cosmochim. Acta*, **68,** 47–59.

Johnson, D.A., Schneider, D.A., Nigrini, C.A., Caulet, J.P. and **Kent, D.V.** (1989) Pliocene–Pleistocene radiolarian events and magnetostratigraphic calibrations for the Tropical Indian Ocean. *Mar. Micropaleontol.*, **14,** 33–66.

Joux, F. and **Lebaron, P.** (1997) Ecological implications of an improved direct viable count method for aquatic bacteria. *Appl. Environ. Microbiol.*, **63,** 3643–3647.

Kamesh Raju, K.A. and **Ramprasad, T.** (1989) Magnetic lineations in the Central Indian Basin for the period A24-A21: a study in relation to the Indian Ocean Triple Junction trace. *Earth Planet. Sci. Lett.*, **95,** 3–4.

Karl, D.M. (1995) Ecology of free-living, hydrothermal vent microbial communities. In: *The Microbiology of Deep-Sea Hydrothermal Vents* (Ed. D.M. Karl), pp. 35–124. CRC press, Boca Raton, FL.

Karl, D.M., Brittain, A.M. and **Tilbrook, B.D.** (1989) Hydrothermal and microbial processes at Loihi seamount, a mid plate hot-spot volcano. *Deep-Sea Res.*, **36,** 1655–1673.

Kochert, G. (1978) Carbohydrate determined by the phenol-sulfuric acid method. In: *Handbook of Physiological Methods: Physiological and Biochemical Methods* (Eds J.A. Hellebust and J.J. Craigie), pp. 95–97. Cambridge University Press, Cambridge.

Kogure, K., Simidu, U. and **Taga, N.** (1984) An improved direct viable count method for aquatic bacteria. *Arch. Hydrobiol.*, **102,** 117–122.

Konig, I., Drodt, M., Suess, E. and **Trautwein, A.X.** (1997) Iron reduction through the tan-green color transition in deep-sea sediments. *Geochim. Cosmochim. Acta*, **61,** 1679–1683.

Krishnaswami, S. and **Sarin, M.M.** (1976) The simultaneous determination of Th, Pu, Ra isotopes, ^{210}Pb, ^{55}Fe, ^{32}Si and ^{14}C in marine suspended phases. *Anal. Chim. Acta*, **83,** 143–156.

Liu, C.-L., Hart, N. and **Peck Jr, H.D.** (1982) Inorganic pyrophosphate: energy source for sulfate-reducing bacteria of the genus *Desulfotomaculum*. *Science*, **217,** 363–364.

Lochte, K., Boetius, A. and **Petry, C.** (2000) Microbial food webs under severe nutrient limitations: life in the deep sea. In: *Microbial Biosystems: New Frontiers. Proceedings of the 8th International Symposium on Microbial Ecology* (Eds C.R. Bell, M. Brylinsky and P. Johnson-Green), pp. 95–102. Atlantic Canada Society for Microbial Ecology, Halifax, Canada.

Loka Bharathi, P.A. (1989) The occurrence of denitrifying colourless sulphur-oxidizing bacteria in marine waters and sediments as shown by the agar shake technique. *FEMS Microbiol. Ecol.*, **62,** 335–342.

Loka Bharathi, P.A. and **Chandramohan, D.** (1990) Sulfate-reducing bacteria from the Arabian Sea – their distribution in relation to thio-sulfate oxidizing and heterotrophic bacteria. *Bull. Mar. Sci.*, **47,** 622–630.

Loka Bharathi, P.A., De Souza, M.J.B.D., Nair, S. and **Chandramohan, D.** (1999) Abundance, viability and culturability of antarctic bacteria. *Fifteenth Indian Expedition to Antarctica, Scientific Report*, Department of Ocean Development, New Delhi, Technical Publication No. 13, pp. 79–92.

Loka Bharathi, P.A., Pradeep Ram, A.S., Nair, S., Nath, B.N. and **Chandramohan, D.** (2004) Distribution of baroduric, psychrotrophic and culturable nitrifying and denitrifying bacteria in the Central Indian Basin. In: *Proc. Natl. Seminar on New Frontiers in Mar. Biosci. Res.*, (Eds S.A.H. Abidi, M. Ravindran, R. Venkatesan and M. Vijaykumaran), 319–330. Allied Publishers Pvt Ltd., Chennai.

Lowry, O.H., Rosebrough, N.J., Farr, A.L. and **Randall, R.J.** (1951) Protein measurement with the Folin-Phenol reagents. *J. Biol. Chem.*, **193,** 265–275.

Luther III, G.W., Bjørn, S., Brent, L.L., Brendel, P.J. and **Silverberg, N.** (1997) Interactions of manganese with the nitrogen cycle: alternative pathways to dinitrogen. *Geochim. Cosmochim. Acta*, **61,** 4043–4052.

Lyle, M. (1983) The brown-green colour transition in marine sediments: a marker of Fe(III)-Fe(II) redox boundary. *Limnol. Oceanogr.*, **28,** 1026–1033.

Ma, F., Al-Aasm, I. and **Yang, J.** (2006) Numerical modeling of hydrothermal fluid flow coupled with mass transport: an example from the Devonian Wabamun Group, northeast British Columbia, Canada. *J. Geochem. Explor.*, **89,** 247–250.

Mascarenhas-Pereira, M.B.L., Nath, B.N., Borole, D.V. and **Gupta, S.M.** (2006) Nature, source and composition of volcanic ash in sediments from a fracture zone trace of Rodriguez Triple Junction in the Central Indian Basin. *Mar. Geol.*, **229,** 79–90.

Matondkar, S.G.P., Nair, K.K.C. and **Ansari, Z.A.** (2005) Biological characteristics of Central Indian Basin water during the Southern Summer. *Mar. Georesour. Geotechnol.*, **23,** 299–314.

Mazumdar, A., Dewangan, P., Joäo, H.M., Peketi, A., Khosla, V.R., Kocherla, M., Badesab, F.K., Joshi, R.K., Roxanne, P., Ramamurty, P.B., Karisiddaiah, S.M., Patil, D.J., Dayal, A.M., Ramprasad, T., Hawkesworth, C.J. and **Avanzinelli, R.** (2009) Evidence of paleo–cold seep activity from the Bay of Bengal, offshore India. *Geochem. Geophys. Geosyst.*, **10,** 1–15.

Meister, P., McKenzie, J.A., Vasconcelos, C., Frank, M. and **Gutjahr, M.** (2007) Dolomite formation in the dynamic deep biosphere: results from the Peru margin (ODP Leg 201). *Sedimentology*, **54,** 1007–1032.

Meister, P., Bernasconi, S.M., Aiello, I.W., Vasconcelos, C. and **Mckenzie, J.A.** (2009) Depth and controls of Ca-rhodochrosite precipitation in bioturbated sediments of the Eastern Equatorial Pacific, ODP Leg 201, Site 1226 and DSDP Leg 68, Site 503. *Sedimentology*, **56,** 1552–1568; doi: 10.1111/j1365-3091.2008.01046.x.

Mukhopadhyay, R., Iyer, S.D. and **Ghosh, A.K.** (2002) The Indian Ocean nodule field: petrotectonic evolution and ferromanganese nodules. *Earth-Sci. Rev.*, **60,** 67–130.

Naganuma, T., Otsuki, A. and **Seki, H.** (1989) Abundance and growth rate of bacterioplankton community in hydrothermal vent plumes of the North Fiji Basin. *Deep-Sea Res.*, **36,** 1379–1390.

Nath, B.N. and **Mudholkar, A.V.** (1989) Early diagenetic processes affecting nutrients in the porewaters of Central Indian Ocean cores. *Mar. Geol.*, **86,** 57–66.

Nath, B.N., Rao, V.P. and **Becker, K.P.** (1989) Geochemical evidence of terrigenous influence in deep-sea sediments up to 8°S in the Central Indian Basin. *Mar. Geol.*, **87,** 301–313.

Nath, B.N., Roelandts, I., Sudhakar, M. and **Plüger, W.I.** (1992) Rare earth element patterns of the Central Indian Basin sediments related to their lithology. *Geophys. Res. Lett.*, **19,** 1197–1200.

Nath, B.N., Bau, M., Rao, B.R. and **Rao, Ch.M.** (1997) Trace and rare earth elemental variation in Arabian Sea sediments through a transect across the oxygen minimum zone. *Geochim. Cosmochim. Acta.*, **61,** 2375–2388.

Nath, B.N., Mascarenhas-Pereira, M.B.L., Kurien, S., Selvaraj, K., Naman, D., Desai, N., D'souza, V. and **Naik, T.** (2005) Porewater nutrients and sediment chemistry. In: *Benthic Environmental Variability in the Central Indian Ocean Basin-I*, pp. 45–64. Project report submitted to Department of Ocean Development, Govt. of India, New Delhi.

Nath, B.N., Borole, D.V., Aldahan, A., Patil, S.K., Mascarenhas-Pereira, M.B.L., Possnert, G., Ericsson, T., Ramaswamy, V. and **Gupta, S.M.** (2008) ^{210}Pb, ^{230}Th, and ^{10}Be in Central Indian Basin seamount sediments: signatures of degassing and hydrothermal alteration of recent origin. *Geophys. Res. Lett.*, **35,** L09603.

Nelson, D.C., Wirsen, C.O. and **Jannasch, H.W.** (1989) Characterization of large, autotrophic Beggiatoa spp. abundant at hydrothermal vents of the Guaymas basin. *Appl. Environ. Microbiol.*, **55,** 2909–2917.

Pachmayr, F. (1960) *Vorkommen und Bestimmug Von Schwefelverbindungen in Mineralwasser*. Dissertation, University of Munchen, Munich, Germany, 48 pp.

Pai, S.C., Gong, G.C. and **Liu, K.K.** (1993) Determination of dissolved oxygen in seawater by direct spectrophotometry of total iodine. *Mar. Chem.*, **41,** 343–351.

Parkes, R.J., Webster, G., Cragg, B.A., Weightman, A.J., Newberry, C.J., Ferdelman, T.G., Kallmeyer, J., Bo Jørgensen, B., Ivano W. Aiello, I.W. and **Fry, J.C.** (2005) Deep subseafloor prokaryotes stimulated at interfaces over geological time. *Nature*, **436,** 390–394.

Patience, R.L., Clayton, C.J., Kearsley, A.T., Rowland, S.J., Bishop, A.N., Rees, A.W.G., Bibby, K.G. and **Hopper, A.C.** (1990). An integrated biochemical, geochemical, and sedimentological study of organic diagenesis in sediments from Leg 112. In: *Proceedings of the Ocean Drilling Program, Scientific Results*, (Eds E. Suess, R. von Huene), Vol. 112, pp. 135–153. *Proc. ODP, Sci. Results*, College Station, TX (Ocean Drilling Program); doi: 10.2973/odp.proc.sr.112.191.1990.

Pattan, J.N. and **Jauhari, P.** (2001) Major, trace, and rare earth elements in the sediments of the central Indian Ocean basin: their source and distribution. *Mar. Georesour. Geotechnol.*, **19,** 85–106.

Pattan, J.N., Masuzawa, T., Borole, D.V., Parthiban, G., Jauhari, P. and **Yamamoto, M.** (2005) Biological productivity, terrigenous influence and noncrustal elements supply to the Central Indian Ocean Basin: Paleoceanography during the past *ca* 1 Ma. *J. Earth Syst. Sci.*, **114,** 63–74.

Ram, A.S.P., Loka Bharathi, P.A., Nair, S. and **Chandramohan, D.** (2001) A deep-sea bacterium with unique nitrifying property. *Curr. Sci.*, **80,** 1222–1224.

Rao, V.P. and **Nath, B.N.** (1988) Nature, distribution and origin of clay minerals in grain size fractions of sediments from Manganese Nodule Field, Central Indian Ocean Basin. *Ind. J. Mar. Sci.*, **17,** 202–207.

Rao, V.P., Kessarkar, P.M., Krumbein, W.E., Krajewski, K.P. and **Schneiders, R.J.** (2003) Microbial dolomite crusts from the carbonate platform of western India. *Sedimentology*, **50,** 819–830.

Rodina, A.G. (1972) Methods of culturing iron bacteria. In: *Methods in Aquatic Microbiology* (Eds R.R. Colwell and M.S. Zambruski), pp. 358–367. University Park Press, Baltimore, CA.

Rodriguez, N.M., Paull, C.K. and **Borowski, W.S.** (2000) Zonation of authigenic carbonates within gas hydrate-bearing sedimentary sections on the Blake Ridge: offshore southeastern North America. In: *Proceedings of the Ocean Drilling Program, Scientific Results* (Eds C.K. Paull, R. Matsumoto, P.J. Wallace and W.P. Dillon), Vol. 164, pp. 301–312. Ocean Drilling Program, College Station, TX.

Schenau, S.J., Slomp, C.P. and **De Lange, G.-J.** (2000) Phophogenesis and active phosphorite formations in sediments from Arabian Sea oxygen minimum zone. *Mar. Geol.*, **169,** 1–20.

Schulz, H.D. (2000) Quantification of Early Diagenesis: dissolved constituents in Marine porewater. In: *Marine Geochemistry* (Eds H.D. Schulz and M. Zabel), pp. 87–122. Spriger Verlag, Berlin-Heidelberg.

Schulz, H.N. and **Schulz, H.D.** (2005) Large sulfur bacteria and the formation of phosphorite. *Science*, **307,** 416–418.

Sizaret, S., Branquet, Y., Gloaguen, E., Chauvet, A., Barbanson, L., Arbaret, L. and **Chen, Y.** (2009) Estimating the local paleo-fluid flow velocity: new textural method and application to metasomatism. *Earth Planet. Sci. Lett.*, **280,** 71–82.

Smirnov, A., Hausner, D., Laffers, R., Strongin, D.R. and **Schoonen, M.A.A.** (2008) Abiotic ammonium formation in the presence of Ni-Fe metals and alloys and its implications for the Hadean nitrogen cycle. *Geochem T*, **9,** 5–24.

Soetaert, K., Herman, P.M.J. and **Middelburg, J.J.** (1996) A model of early diagenetic processes from the shelf to abyssal depths. *Geochim. Cosmochim. Acta*, **60,** 1019–1040.

Stein, R. (1991) Accumulation of organic carbon in marine sediment. *Lect. Notes Earth Sci.*, **34,** 1–217.

Stevens, T. (1997) Lithoautotrophy in the subsurface. *FEMS Microbiol. Rev.*, **20,** 327–337.

Suess, E., Muller, P.J., Powell, H.S. and **Reimers, C.E.** (1980) A closer look at nitrification in pelagic sediments. *Geochem. J.*, **14,** 129–137.

Takano, Y., Kobayashi, K., Yamanaka, T., Marumo, K. and **Urabe, T.** (2004) Amino acids in the 308°C deep-sea hydrothermal system of the Suiyo Seamount, Izu-Bonin Arc, Pacific Ocean. *Earth Planet. Sci. Lett.*, **219,** 147–153.

Teske, A.P. (2004) The deep subsurface biosphere is alive and well. *Trends Microbiol.*, **13,** 402–404.

Tuttle, J.H. and **Jannasch, H.W.** (1977) Thiosulfate stimulation of microbial dark assimilation of carbon dioxide in shallow marine waters. *Microb. Ecol.*, **4,** 9–25.

Van Es, F.B. and **Meyer-Reil, L.-A.** (1982) Biomass and metabolic activity of heterotrophic marine bacteria. In: *Advances in Microbial Ecology* (Ed. K.C. Marshal), pp. 111–170. Plenum Press, New York, 6.

Wang, G., Spivack, A.J., Rutherford, S., Manor, U. and **D'Hondt, S.** (2008) Quantification of co-occurring reaction rates in deep subseafloor sediments. *Geochim. Cosmochim. Acta*, **72,** 3479–3488.

Ward, B.B., Kilpatrick, K.A., Renger, E.H. and **Eppley, R.W.** (1989) Biological nitrogen cycling in the nitracline. *Limnol. Oceanogr.*, **34,** 493–513.

Warren, B.A. (1982) The deep water of the Central Indian Basin. *J. Mar. Res.*, **40**(Suppl.), 823–860.

Warren, B.A. and **Johnson, G.C.** (2002) The overflows across the Ninetyeast Ridge. *Deep-Sea Res. II*, **49,** 1423–1439.

Wenbo, S., Yongbiao, W., Cramer, B.D., Munnecke, A., Zhiming, l. and **Lipu, F.** (2008) Preliminary estimation of Paleoproductivity via TOC and habitat types: which method is more reliable? – A case study on the Ordovician–Silurian Transitional Black Shales of the Upper Yangtze Platform, South China *J. China Univ. Geosci.*, **19,** 534–548.

Wenxuan, H., Zhijun, J., Suping, Y., Xiancai, L., Zhilin, C., Linye, Z., Xuejun, Z. and **Huaiyang, Z.** (2002) Discovery of low-mature hydrocarbon in manganese nodules and ooze from the Central Pacific deep sea floor. *Chinese Sci. Bull.*, **47,** 939–944.

Wirsen, C.O., Tuttle, J.H. and **Jannasch, H.W.** (1986) Activities of sulfur-oxidizing bacteria at the 21°N East Pacific Rise Vent site. *Mar. Biol.*, **92,** 449–456.

Yamagata, Y., Watanabe, H., Saitoh, M. and **Namba, T.** (1991) Volcanic production of polyphosphates and its relevance to prebiotic evolution. *Nature*, **352,** 516–519.

Yang, J., Bull, S. and **Large, R.** (2004) Numerical investigation of salinity in controlling ore-forming fluid transport in sedimentary basins: example of the HYC deposit, Northern Australia. *Mineral. Deposita*, **39,** 622–631.

Zervas, D., Nichols, G.J., Hall, R., Smyth, H.R., Charlotta, L. and **Murtagh, F.** (2009) SedLog: a shareware program for drawing graphic logs and log data manipulation. *Comput. Geosci.*, **35,** 2151–2159.

Zhao, C., Hobbs, B.E. and **Ord, A.** (2009) Theoretical and numerical investigation into roles of geofluid flow in ore forming systems: integrated mass conservation and generic model approach. *J. Geochem. Explor.*, **106,** 251–260.

ZoBell, C.E. (1941) The cultural requirements of heterotrophic aerobes. *J. Mar. Res.*, **4,** 42–75.

Manuscript received 8 October 2008; revision accepted 6 July 2010

Supporting Information

Additional Supporting Information may be found in the online version of this article:

Material S1. Explicit finite difference model.

Please note: Wiley-Blackwell are not responsible for the content or functionality of any supporting materials supplied by the authors. Any queries (other than missing material) should be directed to the corresponding author for the article.